AGARD-R-827

AGARD-R-827

AGARD

ADVISORY GROUP FOR AEROSPACE RESEARCH & DEVELOPMENT
7 RUE ANCELLE, 92200 NEUILLY-SUR-SEINE, FRANCE

AGARD REPORT 827

High Speed Body Motion in Water

(le Mouvement des corps évoluant à grande vitesse dans l'eau)

This Report is a compilation of the proceedings of a Fluid Dynamics Panel Workshop held at the National Academy of Sciences in Kiev, Ukraine, 1-3 September 1997.



NORTH ATLANTIC TREATY ORGANIZATION

DISTRIBUTION STATEMENT A
Approved for public release;
Distribution Unlimited

Published February 1998

Distribution and Availability on Back Cover

AGARD-R-827

AGARD

ADVISORY GROUP FOR AEROSPACE RESEARCH & DEVELOPMENT
7 RUE ANCELLE, 92200 NEUILLY-SUR-SEINE, FRANCE

AGARD REPORT 827

High Speed Body Motion in Water

(le Mouvement des corps évoluant à grande vitesse dans l'eau)

This report is a compilation of the proceedings of a Fluid Dynamics Panel Workshop held at the National Academy of Sciences in Kiev, Ukraine, 1-3 September 1997.

DTIC QUALITY INSPECTED 3



North Atlantic Treaty Organization
Organisation du Traité de l'Atlantique Nord

19980410 131

The Mission of AGARD*

According to its Charter, the mission of AGARD is to bring together the leading personalities of the NATO nations in the fields of science and technology relating to aerospace for the following purposes:

- Recommending effective ways for the member nations to use their research and development capabilities for the common benefit of the NATO community;
- Providing scientific and technical advice and assistance to the Military Committee in the field of aerospace research and development (with particular regard to its military application);
- Continuously stimulating advances in the aerospace sciences relevant to strengthening the common defence posture;
- Improving the co-operation among member nations in aerospace research and development;
- Exchange of scientific and technical information;
- Providing assistance to member nations for the purpose of increasing their scientific and technical potential;
- Rendering scientific and technical assistance, as requested, to other NATO bodies and to member nations in connection with research and development problems in the aerospace field.

The highest authority within AGARD is the National Delegates Board consisting of officially appointed senior representatives from each member nation. The mission of AGARD is carried out through the Panels which are composed of experts appointed by the National Delegates, the Consultant and Exchange Programme and the Aerospace Applications Studies Programme. The results of AGARD work are reported to the member nations and the NATO Authorities through the AGARD series of publications of which this is one.

Participation in AGARD activities is by invitation only and is normally limited to citizens of the NATO nations.

* AGARD merged with the Defence Research Group of NATO (DRG) on 1 January 1998 to form the Research and Technology Organization (RTO) of NATO. However, both AGARD and DRG will continue to issue publications under their own names in respect of work performed in 1997.

The content of this publication has been reproduced
directly from material supplied by AGARD or the authors.



Printed on recycled paper

Published February 1998

Copyright © AGARD 1998
All Rights Reserved

ISBN 92-836-1071-7



Printed by Canada Communication Group Inc.
(A St. Joseph Corporation Company)
45 Sacré-Cœur Blvd., Hull (Québec), Canada K1A 0S7

High Speed Body Motion in Water

(AGARD R-827)

Executive Summary

This report is a compilation of the edited proceedings of a Workshop on "High Speed Body Motion in Water" held at the National Academy of Sciences Kiev, Ukraine, 1-3 September 1997. The material assembled in this report was prepared under the combined sponsorship of the NATO Partnership for Peace Program, the AGARD Fluid Dynamics Panel, the Institute of Hydromechanics in Kiev, and the United States Air Force European Office of Aerospace Research and Development. It was appropriate that the Workshop be co-sponsored with the Institute of Hydromechanics in Kiev, where for many years there has been an active research effort in many aspects of high speed motion in water. One of the main purposes of this Workshop was to showcase the research of the Institute in this area to participants from the NATO countries.

The technical topics covered during the Workshop included Hydrobionics, Boundary Layer Flows, Supercavitating Flows, Air-Water Penetration, and Control of Cavitation. Hydrobionics is the science of studying the structure, form, and movement of swimming animals in order to determine possible ways to achieve better efficiency, such as drag reduction and an increase of propulsion efficiency with minimum possible energy expenditures, for bodies such as submarines and missiles.

A general summary of noise generation by high speed bodies in water was given. It was clear that this field is not well understood at the present time, and that a great deal more research effort is required in this area. In addition, presentations were given on a Simple Model for the Aero-Hydrodynamics of Ekranoplans, and on the Movement of a Wing Above a Wavy Water Surface. Of the 35 presented papers, 18 came from the Ukraine, 5 from Russia and 12 from the NATO nations.

Le mouvement des corps évoluant à grande vitesse dans l'eau

(AGARD R-827)

Synthèse

Ce rapport est un recueil des travaux de l'atelier sur "le mouvement des corps évoluant à grande vitesse dans l'eau", organisé à l'Académie nationale des sciences à Kiev, en Ukraine, du 1er au 3 septembre 1997. Les textes inclus dans ce rapport ont été rédigés sous l'égide conjointe du Programme OTAN de Partenariat pour la Paix, du Panel AGARD de la dynamique des fluides, de l'Institut d'Hydromécanique de Kiev et du Directorat européen pour la recherche et les réalisations aérospatiales de l'Armée de l'air des Etats-Unis.

Ce partenariat avec l'Institut d'Hydrodynamique de Kiev était tout à fait indiqué car cet Institut travaille activement sur les différents aspects des mouvements à grande vitesse dans l'eau depuis de nombreuses années. L'un des principaux objectifs de cet atelier a été de montrer les travaux de recherche de l'Institut dans ce domaine aux participants des pays de l'OTAN.

Les sujets techniques couverts par l'atelier comprenaient l'hydrobionique, les écoulements de couche limite, les écoulements supercavitants, la pénétration air/eau, et le contrôle de la cavitation. L'hydrobionique est la science de la structure, la forme et le mouvement des animaux aquatiques, qui sont étudiés dans le but d'obtenir une meilleure efficacité des corps en mouvement tels que les sous-marins et les missiles, par la réduction de la traînée et l'amélioration de la propulsion par la réduction au minimum des dépenses d'énergie.

Un résumé global de la génération du bruit par les corps évoluant à grande vitesse dans l'eau a été présenté. Il est apparu très clairement que ce sujet n'est pas très bien connu à l'heure actuelle et que des efforts de recherche supplémentaires considérables sont demandés dans ce domaine. Des communications ont également été présentées sur un modèle simple de l'aérohydrodynamique des Ekranoplans, et sur le mouvement d'un profil au-dessus d'une surface d'eau ondulée. Des 35 communications présentées, 18 ont été proposées par l'Ukraine, 5 de la Russie et 12 des pays de l'OTAN.

Contents

	Page
Executive Summary	iii
Synthèse	iv
Recent Publications of the Fluid Dynamics Panel	viii
Workshop Staff	x

	Reference
The Swimming Hydrodynamics of a Pair of Flapping Foils Attached to a Rigid Body by P.R. Bandyopadhyay and M.J. Donnelly	1
Substitution of Rolling for Slipping as an Effective Mechanism of Decreasing Hydrodynamic Drag by V.I. Merkulov	2
Hydrobionics Principles of Drag Reduction by V.V. Babenko	3
Turbulent Boundary Layer Over a Compliant Surface by G.A. Voropaev and N.V. Rozumniuk	4
Non-Linear Nonsteady Effects in the Hydrodynamics of the Oscillating Wing by S.A. Dovgiy	5
Distinctive Features of the Wave Plate (or Fish) Motion by L.I. Korennaya	6
A New View of the Dynamics of Reynolds Stress Generation in Turbulent Boundary Layers by B.J. Cantwell and J.M. Chacín	7
Control of Görtler Vortices by W.S. Saric	8
Experimental Investigation of the Boundary Layer over Rigid and Elastic Plates by V.V. Babenko	9
Modeling of Turbulent Near-Wall Shear Flows Properties by V.T. Movchan and E.A. Shkvar	10
Direct Numerical Simulation of Transitional Near-Wall Flow by V.S. Chelyshkov, V.T. Grinchenko and C. Liu	11
A New Approach to the Study of Organised Vortical Motion Affected by Body Forces by E.I. Nikiforovich	12

Experimental Studies on the Boundary Layer Development in Penguins: Mechanisms of Turbulence Control and Their Applicability to Engineering 13
by R. Bannasch

Compliant Coatings for Transitional Boundary Layer Control 14
by N. Yurchenko

Dynamics of Vortices in Near-Wall Flows: Eigenfrequencies, Resonant Properties, Algorithms of Control 15
by V. Gorban and I. Gorban

A Simple Model for the Aero-Hydrodynamics of Ekranoplans 16
by U.P. Bulgarelli, M. Greco, M. Landrini and C. Lugni

About Movement of a Wing Above Wavy Surface of Water 17
by V.G. Belynsky

Some Problems of Supercavitating Flows 18
by G.V. Logvinovich

Cavity Shapes in Three Dimensions 19
by M.P. Tulin

Investigation of High-Speed Supercavitating Underwater Motion of Bodies 20
by Yu.N. Savchenko

Supercavitating Flows at Supersonic Speed in Compressible Water 21
by A.D. Vasin

Computer Simulation of Unsteady Supercavitating Flows 22
by V.N. Semenenko

Some Problems of the Supercavitation Theory for Sub or Supersonic Motion in Water 23
by V.V. Serebryakov

Water Entry of Ship Sections and Axisymmetric Bodies 24
by O. Faltinsen and R. Zhao

Asymptotics Theories of Incompressible Water Entry 25
by E. Fontaine and R. Cointe

Spray Influence on the Drag of a Gliding Body 26†
by O.P. Shorigin (lecture given by Dr. Vasin)

Stability of Supercavitating Slender Body During Water Entry and Underwater Motion 27
by S.I. Putilin

Emergence of Cavitating Profile 28
by M. Arnaud and L. Dieval

Reduction of Overload on a Body Entering Water at High Speed 29
by V.T. Savchenko

† Paper not available at time of printing.

Cavitation Scale Effects: A Representation of its Visual Appearance and Empirically Found Relations 30
by A.P. Keller

Tip Vortex Roll-Up and Cavitation in Water and Polymer Solutions 31
by D.H. Fruman and J-Y. Billard

Cavitation Self-Oscillations Intensify Technological Processes 32
by V.V. Pilipenko, I.K. Man'ko and V.A. Zadontsev

Control of Cavity Parameters at Supercavitating Flow 33
by Yu.D. Vlasenko

High Speed Body Motion and Sound Generation 34
by V.T. Grinchenko

Supercavitating Projectile Experiments at Supersonic Speeds (Abstract) 35
by I.N. Kirschner

Recent Publications of the Fluid Dynamics Panel

AGARDOGRAPHS (AG)

Turbulent Boundary Layers in Subsonic and Supersonic Flow
AGARD AG-335, July 1996

Computational Aerodynamics Based on the Euler Equations
AGARD AG-325, September 1994

Scale Effects on Aircraft and Weapon Aerodynamics
AGARD AG-323 (E), July 1994

Design and Testing of High-Performance Parachutes
AGARD AG-319, November 1991

Experimental Techniques in the Field of Low Density Aerodynamics
AGARD AG-318 (E), April 1991

Techniques Expérimentales Liées à l'Aérodynamique à Basse Densité
AGARD AG-318 (FR), April 1990

A Survey of Measurements and Measuring Techniques in Rapidly Distorted Compressible Turbulent Boundary Layers
AGARD AG-315, May 1989

REPORTS (R)

Turbulence in Compressible Flows
AGARD R-819, Special Course Notes, June 1997

Advances in Cryogenic Wind Tunnel Technology
AGARD R-812, Special Course Notes, January 1997

Aerothermodynamics and Propulsion Integration for Hypersonic Vehicles
AGARD R-813, Special Course Notes, October 1996

Parallel Computing in CFD
AGARD R-807, Special Course Notes, October 1995

Optimum Design Methods for Aerodynamics
AGARD R-803, Special Course Notes, November 1994

Missile Aerodynamics
AGARD R-804, Special Course Notes, May 1994

Progress in Transition Modelling
AGARD R-793, Special Course Notes, April 1994

Shock-Wave/Boundary-Layer Interactions in Supersonic and Hypersonic Flows
AGARD R-792, Special Course Notes, August 1993

Unstructured Grid Methods for Advection Dominated Flows
AGARD R-787, Special Course Notes, May 1992

Skin Friction Drag Reduction
AGARD R-786, Special Course Notes, March 1992

Engineering Methods in Aerodynamic Analysis and Design of Aircraft
AGARD R-783, Special Course Notes, January 1992

ADVISORY REPORTS (AR)

Ice Accretion Simulation
AGARD AR-344, Report of WG-20, December 1997

Sonic Nozzles for Mass Flow Measurement and Reference Nozzles for Thrust Verification
AGARD AR-321, Report of WG-19, June 1997

Cooperative Programme on Dynamic Wind Tunnel Experiments for Manoeuvring Aircraft
AGARD AR-305, Report of WG-16, October 1996

Hypersonic Experimental and Computational Capability, Improvement and Validation
AGARD AR-319, Vol. I, Report of WG-18, May 1996

Aerodynamics of 3-D Aircraft Afterbodies
AGARD AR-318, Report of WG-17, September 1995

A Selection of Experimental Test Cases for the Validation of CFD Codes
AGARD AR-303, Vols. I and II, Report of WG-14, August 1994

Quality Assessment for Wind Tunnel Testing
AGARD AR-304, Report of WG-15, July 1994

Air Intakes of High Speed Vehicles
AGARD AR-270, Report of WG-13, September 1991

Appraisal of the Suitability of Turbulence Models in Flow Calculations
AGARD AR-291, Technical Status Review, July 1991

Rotary-Balance Testing for Aircraft Dynamics
AGARD AR-265, Report of WG11, December 1990

Calculation of 3D Separated Turbulent Flows in Boundary Layer Limit
AGARD AR-255, Report of WG10, May 1990

CONFERENCE PROCEEDINGS (CP)

Aerodynamics of Wind Tunnel Circuits and Their Components
AGARD CP-585, June 1997

The Characterization & Modification of Wakes from Lifting Vehicles in Fluids
AGARD CP-584, November 1996

Progress and Challenges in CFD Methods and Algorithms
AGARD CP-578, April 1996

Aerodynamics of Store Integration and Separation
AGARD CP-570, February 1996

Aerodynamics and Aeroacoustics of Rotorcraft
AGARD CP-552, August 1995

Application of Direct and Large Eddy Simulation to Transition and Turbulence
AGARD CP-551, December 1994

Wall Interference, Support Interference, and Flow Field Measurements
AGARD CP-535, July 1994

Computational and Experimental Assessment of Jets in Cross Flow
AGARD CP-534, November 1993

High-Lift System Aerodynamics
AGARD CP-515, September 1993

Theoretical and Experimental Methods in Hypersonic Flows
AGARD CP-514, April 1993

Aerodynamic Engine/Airframe Integration for High Performance Aircraft and Missiles
AGARD CP-498, September 1992

Effects of Adverse Weather on Aerodynamics
AGARD CP-496, December 1991

Manoeuvring Aerodynamics
AGARD CP-497, November 1991

Vortex Flow Aerodynamics
AGARD CP-494, July 1991

Missile Aerodynamics
AGARD CP-493, October 1990

Aerodynamics of Combat Aircraft Controls and of Ground Effects
AGARD CP-465, April 1990

Computational Methods for Aerodynamic Design (Inverse) and Optimization
AGARD CP-463, March 1990

Applications of Mesh Generation to Complex 3-D Configurations
AGARD CP-464, March 1990

Fluid Dynamics of Three-Dimensional Turbulent Shear Flows and Transition
AGARD CP-438, April 1989

Workshop Staff

WORKSHOP COORDINATORS

Professor B. Cantwell
Stanford University
Departmant of Aeronautics and Astronautics
Stanford, California
94305 USA

IGA B. Masure
Université d'Orléans
6, rue Eudoxe Marcille
45000 Orléans
France

Professor V.T. Grinchenko
Director, Institute of Hydromechanics
8/4 Zhelyabov Str.
KYIV, 252057
Ukraine

Col W. Kauw
Chief, Technical Cooperation Programme
AGARD-NATO
7, rue Ancelle
92200 Neuilly-sur-Seine
France

PANEL EXECUTIVE

Mr. J.K. Molloy

Mail from Europe:
AGARD/OTAN
Attn: FDP Executive
7, rue Ancelle
92200 Neuilly-sur-Seine
France

Mail from USA and Canada:
AGARD/NATO
Attn: FDP Executive
Unit PSC 116
APO AE 0977

Tel: 33 (1) 55 61 22 75

THE SWIMMING HYDRODYNAMICS OF A PAIR OF FLAPPING FOILS ATTACHED TO A RIGID BODY

Promode R. Bandyopadhyay
Naval Undersea Warfare Center Division
Weapons Technology and Tactical Vehicle Systems Dept.
Newport, Rhode Island 02841 U.S.A.
and
Martin J. Donnelly
Virginia Polytechnic Institute and State University
Department of Engineering Mechanics
Blacksburg, Virginia 24061 U.S.A.

SUMMARY

Inspired by the natural action of flapping in aquatic locomotion, a dual flapping foil device was developed. The performance of the device in providing propulsive and maneuvering forces to small rigid axisymmetric bodies will be detailed. Two modes of flapping were investigated: waving and clapping. The clapping motion of wings is a common mechanism for the production of lift and thrust in the insect world, particularly in butterflies and moths. Waving is similar to the motion of the caudal fin of a fish. A model was built (1 m long, 7.6 cm diameter) with flapping foils at the end of the tail cone and various measurements were performed in a water tunnel. (In hindsight, the model can be described as a rigid-bodied mechanical seal because seals have remarkably similar dual flaps in their tails.) Time-dependent tests of thrust, drag, and yawing moment were conducted for several flapping frequencies commonly observed in relevant aquatic animals. Phase-matched laser Doppler anemometry measurements of the near wake were carried out and detailed vorticity-velocity vector maps of the vortex shedding process have been obtained for the axial and cross-stream planes. Dye visualization of wake was documented and a video recording was prepared of the entire dynamic process.

The ability of the dual flapping foil device to produce a net thrust and maneuvering cross-stream forces has been demonstrated, although the main body is rigid. Its wake, which is composed of jets, is extremely wide, nonrotating, and rapidly decaying. The thrust production greatly increases with Strouhal number. The results have been compared with two-dimensional inviscid flapping foil theories and measurements. The effect of the rigid cylinder on the flapping performance is extracted. The efficiency of thrust production generally increases in the waving mode which mimics the side-to-side head motion of a fish. Efficiency also tends to peak roughly in the Strouhal number range popular among fish. Axial thrust shows sensitivity to Strouhal number in the range popular among fish. However, existing non-linear inviscid theories do not capture this aspect and the strong viscous effects observed also need to be included.

1.0 INTRODUCTION

In nature, the inherent actions of swimming and flying have been perfected over millions of years. These actions have been the inspiration for many inventions in the fields of aero-dynamics and hydrodynamics. However, most studies have concentrated on mechanisms of thrust. The aspect of maneuverability has received scant attention. Aquatic locomotion generally deals with low absolute speeds. A more relevant speed parameter is body length traversed per second, which is frequently large. Thus, considering our current interest in shallow water and small vehicles, a natural place to look for new ideas for maneuvering and propulsion would be the hydrodynamics of aquatic locomotion. The transition from hydrodynamics in nature to engineering is not straightforward. Some recent developments are described in Bandyopadhyay et al. (ref. 1). This paper is a continuation of that effort.

Many varieties of fish use caudal fins for propulsion and pectoral fins for maneuvering. In this paper, we will consider the engineering reproduction of these control surfaces and use a pair of foils to simulate motions that are qualitatively similar. Propulsive and lifting forces produced by flapping foils were studied by Knoller and Betz from 1909-1912 (see ref. 2). From 1924-1936, Birnbaum, von Kármán, Burgers, and Garrick conducted theoretical studies that proved propulsive efficiency improved with slower flapping. Though there is no verification, it appears that German scientists tested a flapping foil device for torpedo propulsion during the early 1940s (see ref. 3). Gopalkrishnan et al. (ref. 4), Hall and Hall (ref. 5), and Jones et al. (ref. 2) have made recent progress. These works provide insight on the mechanism of propulsion and drag, and describe advanced diagnostics of the forces and turbulence in wake. Most importantly, the former authors (ref. 4) have indicated the existence of an optimum standard number for flapping, which squarely places the vortex shedding process at the center of the mechanisms for propulsion and maneuvering.

Several past studies of flapping foils dealt with flexible bodies and propulsion. However, we deal with the maneuvering of rigid bodies by means of flapping foils. A simplified momentum model of the dual flapping foil device (ref. 6) will first be described. Then, we will report the results of a detailed laboratory experimental investigation. An instrumented robust model (1 m long with a 7.6-cm diameter) was built with a pair of flapping foils installed at the end of the tail cone (Figs. 1 and 2). The flapping frequencies and flow speeds were varied. Phase-matched measurements of force and moments were carried out using a six-component dynamic drag balance.

Paper presented at an AGARD FDP Workshop on "High Speed Body Motion in Water", held in Kiev, Ukraine, 1-3 September 1997, and published in R-827.

Phase-matched measurements of the vortex shedding in the wake were also conducted using a laser Doppler anemometer. Data analysis included ensemble averaging of forces and moments and determination of net axial forces. The anemometry data were processed to produce phase-matched maps of vorticity-velocity vectors and circulation distributions. Vortex threading diagrams are constructed to gain insight into the mechanism for the production of maneuvering and propulsive forces.

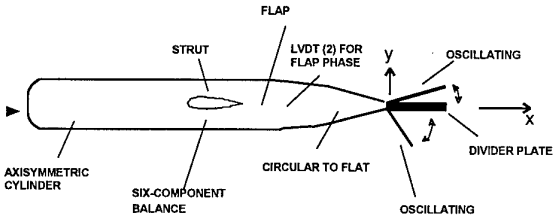


Fig. 1. Schematic diagram of the dual flapping foil device mounted at the end of the tail cone of a rigid cylinder. Axis z is along span of flap.

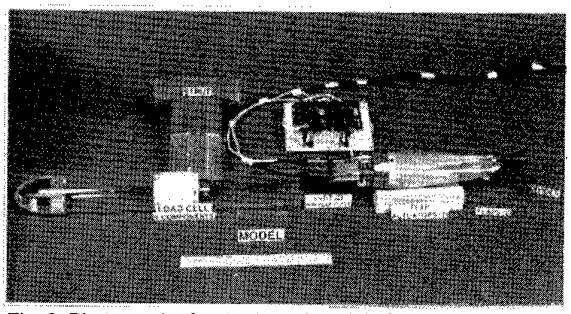


Fig. 2. Photograph of water tunnel model of the dual flapping foil device. Dual flapping foils and divider plate are shown on the right end; to the left of foils lie the actuators, two phase transducers, and actuator control circuits. The six-component load cell is located at the junction of the strut and cylinder.

The present work, while engineering in approach, needs to be placed in the perspective of hydrobionics. Unambiguous identification of the mechanism of maneuvering, thrust, and lift in swimming and flight in nature continues to be extremely difficult because of a lack of objective diagnostics and controlled experiments. The present experiment could help biology in this regard. Many quasi-steady aerodynamic explanations of biolocomotion have actually been an impediment to the uncovering of dynamic stall mechanisms for force enhancement believed to be widely practiced in nature (Ellington, 1995 ref. 7). Three-dimensional time-dependent accurate calculation methods need to be developed that can compute dynamic stall characteristics accurately. Measurements reported herein could help validate such methods.

What are the hydrodynamic differences between foils mounted on rigid and flexible bodies? According to Rayner (1995, ref 8), "For a swimming fish, drag is enhanced substantially because of body flapping (estimates range to up to five times the gliding drag; Webb, 1975, ref. 9). The fish must generate thrust to balance this enhanced flapping drag, but this force will not be reflected in the total momentum flow far from the fish if — as seems intuitively reasonable — much of the enhancement is due to induced drag. If the fish is well-streamlined, there may be only a weak thrust wake in steady swimming. Momentum representing the flapping-enhanced profile drag wake that will be transported in vortices generated close to the body; one explanation for the paradox is that these vortices approach and interact with the lifting vortices at the tail and annihilate one another before reaching the wake (Lighthill, ref 10)." The present experiment on the rigid body is unambiguous in the sense that the flap behavior and wake are not contaminated by any body flapping drag or associated vortices. Furthermore, because circulation is proportionate to the angular velocity of rotation, it is clearly ascribable to the flapping foils on a rigid body, but less so when the body is flexible.

The present work originated from a desire to apply the mechanisms of fish locomotion to rigid bodies and to focus on devices that would allow precision maneuvering. This led to a design of a tail on which two or three flapping foils are mounted on a ring and where they could be operated differentially. After the dual-flapping foil model was built (Figs. 1 and 2) and the measurements were completed, one of the authors (P. R. Bandyopadhyay) observed during a trip to the Mystic Marinelife Aquarium that seals and sea lions, which have a streamlined body and are known as wonderful swimmers, also have dual-flapping foils (Fig. 3). Figure 4 shows that the present experiment was carried out in the parameter range popular among fish.

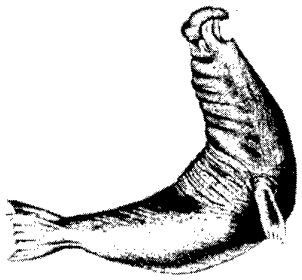


Fig. 3. The caudal fins of seals and sea lions are examples of dual-flapping foils which make them wonderful swimmers.

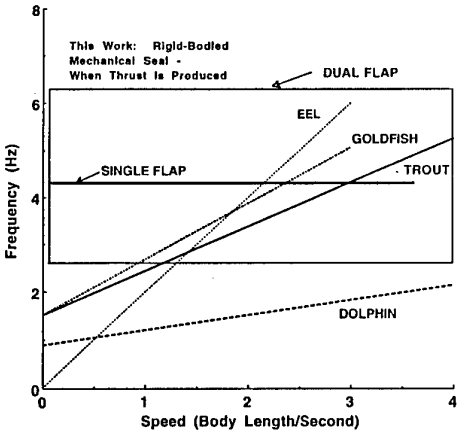


Fig. 4. Comparison of flapping frequencies of the rigid-bodied mechanical seal with those of aquatic animals (refs. 19, 20, 21, and 26). At a given speed, frequency range may be ±0.5 Hz.

2.0 SIMPLIFIED TWO-DIMENSIONAL MOMENTUM MODEL

A simplified two-dimensional momentum model of the maneuvering forces produced by the differential flapping device is developed here. This model assumes that the kinematics of the trailing edge of the flap holds the key to modeling the effects of the device. The basic importance of the trailing edge bears some similarity to the modeling of the propulsive forces produced by the caudal fins of fish (see refs. 10-13). In this simple model, induced drag and flap tip vortices are not considered.

2.1 Maneuvering and Axial Thrusts Generated

Consider the two-dimensional maneuvering device shown schematically in Fig. 5. Two flaps, numbered 1 and 2, are shown, although the basic approach is applicable if three flaps are mounted on a rotatable ring for finer control of maneuvering. Figure 5 pertains to thrust-producing maneuvering devices, rather than drag-producing maneuvering devices (Fig. 25 versus Fig. 26 — the two modes will be discussed later). In the thrust mode, two jets are assumed to be produced, each consisting of starting vortices as sketched. These jets are assumed to be similar to those observed behind a flexible tuna by Triantafyllou (see ref. 13).

As mentioned earlier, the differential flaps are both maneuvering as well as propulsive devices. The drag of the rigid body in Fig. 1 can be accounted for by proposing that the thrust-producing jets are produced after the drag is overcome. Consider flap #1.

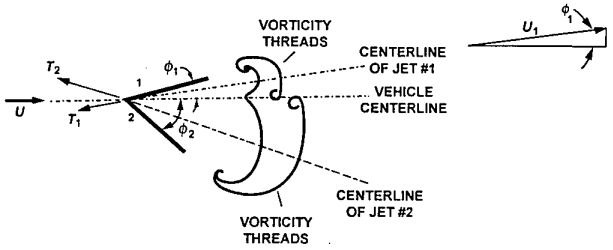


Fig. 5. Schematic of thrusts due to a pair of differentially operated oscillating flaps.

Propose that the thrust generated is proportional to the product of the mass of water affected and the increase in velocity given to that mass. The following definitions apply:

m_1, m_2 = Mass of water affected per unit span (normal to page in Fig. 5) by flaps 1 and 2, respectively,

T_1, T_2 = Thrusts due to flaps 1 and 2, respectively.

t_1, t_2 = Time periods of oscillation of flaps 1 and 2, respectively,

U = Forward speed of the vehicle generated by its propulsor,

U_1, U_2 = Velocities of water due to flapping acting at angles of $\phi_1/2$ and $\phi_2/2$, respectively, to the axial direction,

V_1, V_2 = Speeds imparted by flapping normal to the direction of vehicle motion,

x, y = Axial and normal directions, respectively, and

ϕ_1, ϕ_2 = Maximum flapping angles.

Therefore, thrust in the axial direction is

$$T_{1x} \propto m_1 \frac{U_1 \cos(\phi_1/2) - U}{t_1}, \tag{1}$$

and

$$T_{2x} \propto m_2 \frac{U_2 \cos(\phi_2/2) - U}{t_2}. \tag{2}$$

If $t_1 \neq t_2$ and if the phase is different when $t_1 = t_2$, a complex, perhaps even chaotic, pitching motion could result. Therefore, to simplify, assume that $\tau = t_1 = t_2$ and that both flaps oscillate at the same or opposite phase. Thrust vectors (Fig. 6) are then as follows:

Net Axial Thrust

$$T_a = T_0 + T_{1x} + T_{2x} \quad (\textit{in the } x\textit{ - direction}),$$

$$T_a = T_0 + \Delta T_x, \tag{3}$$

where T_0 is vehicle axial thrust due to any additional independent means of propulsion, and ΔT_x is the contribution from the oscillating flaps.

Net Maneuvering Thrust

$$T_m = T_{2y} - T_{1y}. \tag{4}$$

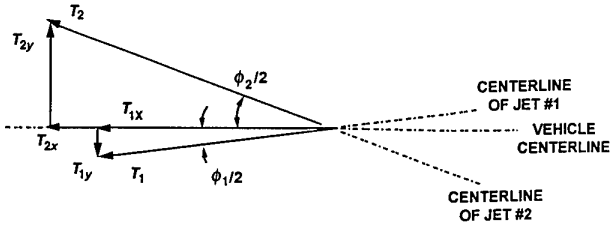


Fig. 6. Maneuvering and axial thrust vectors.

The vertical velocity vectors (in the y-direction) would be T_{1y} and T_{2y} (see Fig. 6).

Total axial thrust due to flapping is

$$\Delta T_x = m_1 \frac{U_1 \cos(\phi_1/2) - U}{\tau} + m_2 \frac{U_2 \cos(\phi_2/2) - U}{\tau}, \quad (5)$$

$$\Delta T_x = \frac{1}{\tau}[\{m_1 U_1 \cos(\phi_1/2) + m_2 U_2 \cos(\phi_2/2)\} - U\{m_1 + m_2\}].$$

(component determined by flaps alone) (component influenced by steady forward speed generated by main propulsor)

2.1.1 Axial thrust versus braking

Equation (5) shows that if $U_1, U_2 < U$, the flaps can be used as brakes. If both flaps are oscillated identically, then,

$$U_1 = U_2, \quad T_m = 0.$$

In this manner, the dual flaps can be used as brakes. If the vehicle is perfectly neutrally buoyant, and if the flaps are also slowed down in the manner of U, then the vehicle would come to a dead stop gradually.

However, if $U_1 \neq U_2 > U$, or $U_1 \neq U_2 < U$, then maneuvering thrusts will be produced.

In equation (5), if $U = 0$, $T_0 = 0$, then,

$$\Delta T_x = \frac{1}{\tau}[\{m_1 U_1 \cos(\phi_1/2) + m_2 U_2 \cos(\phi_2/2)\}].$$

If $(\phi_1, \phi_2)\uparrow, \Delta T_x \uparrow$. Note that $\phi_1, \phi_2 \neq 0$ when the flaps are operational.

2.1.2 Maneuvering thrust

From equation (4),

$$T_m = \frac{m_1 U_1 \sin(\phi_1/2)}{t_1} - \frac{m_2 U_2 \sin(\phi_2/2)}{t_2}.$$

If $t_1 = t_2 = \tau$,

$$T_m = \frac{1}{\tau}[m_1 U_1 \sin(\phi_1/2) - m_2 U_2 \sin(\phi_2/2)].$$

As $\phi_1 \uparrow$, or $\phi_2 \uparrow$, each part of T_m increases. The value of $|T_m|$ will be maximum if all flap variables are held the same when either flap is turned off.

It is implied that the rate of momentum shed by the flap trailing edge vortices is equal to the thrust produced. Therefore, the kinematics of the trailing edge gives the thrust and power generated. The key factors are the mass of water affected by flapping and movements of the trailing edge leading to acceleration of the water. These issues are considered next.

2.2 Mass of Water Affected

The mass of water affected by the flap's oscillation can be modeled in several ways. A simple body-geometry-based assumption would be that the diameter of the vortices produced is related to the distance of cross-stream travel of the oscillating flap. The following approach is based on the property of the vortices produced.

Consider the vortex doublet control volume shown in Fig. 7(a). These two contrarotating vortices are produced by one flap, say #1, in one time period of oscillation τ. The following assumptions are made:

1. The flaps are two-dimensional,

2. Both vortices are of the same strength ($|\Gamma|$) but of opposite signs,

3. There is no viscous dissipation, and

4. Vortex distance from flap center is c_1, i.e., the first vortex has not propagated downstream significantly more compared to c_1 during one cycle of flap oscillation.

Assume that the radial (r) distribution of azimuthal velocity v_θ within each shed vortex is as shown in Fig. 7(b). The distribution is linear in the core, followed by an exponentially dropping velocity (see ref. 14, fig. 5.5, p. 89):

$$v_\theta = k_1 r, \quad 0 \le r \le \ell, \quad (6)$$

$$v_\theta = k_2 \exp(-r^2), \quad r > \ell. \quad (7)$$

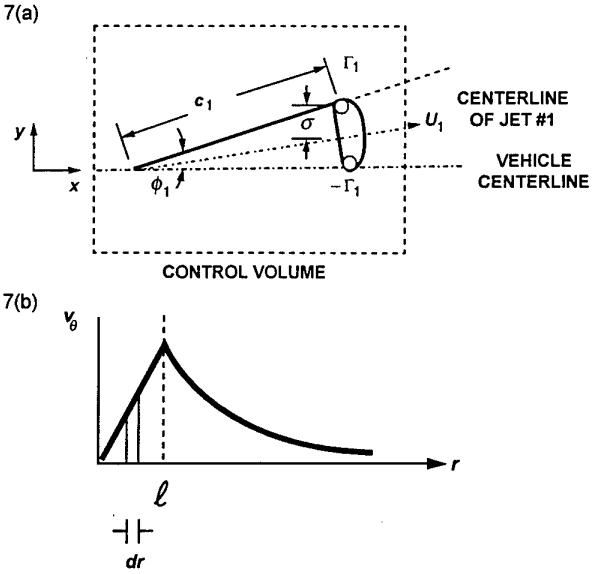


Fig. 7. Vortex doublet (a) and cross-sectional distribution of azimuthal velocity in the shed vortices (b).

Here, k_1 is a constant denoting the vortex property, viz., its vorticity (whose dimension is $1/T$), and k_2 is another constant that is largely dependent on vortex diffusion rate. Structural modeling of turbulent boundary layers (Bandyopadhyay and Balasubramanian, ref. 15) shows that, as a first approximation,

the distribution in equation (7) may be neglected, i.e., the decaying region due to viscous effects is ignored soon after the formation of the vortices. As proved successful in that model, it was also assumed that $\ell =$ the local mixing length ≈ 0.07 of the local width of the trailing jet.

Considering the two vortices in the control volume in Fig. 7(a), the mass of water affected by flap #1 per unit span is

$$m_1 = \rho k \pi \frac{(\ell_1)^2}{4}, \tag{8a}$$

where k is a constant dependent on the flap's sectional shape and is a property of the vortex, and ρ is the fluid density. Similarly,

$$m_2 = \rho k \pi \frac{(\ell_2)^2}{4}. \tag{8b}$$

Therefore, the maneuvering thrust is given by:

$$T_m = \frac{\rho k}{\tau}\frac{\pi}{4}\left[(\ell_1)^2 U_1 \sin(\phi_1/2) - (\ell_2)^2 U_2 \sin(\phi_2/2)\right], \tag{9}$$

where U_1 and U_2 may be obtained by Biot-Savart's law, if Γ is known from measurements. The vortices in Fig. 7(a) would move in a direction normal to the line joining them (see Batchelor, ref. 16, p. 441).

2.3 Velocity of Propagation of Shed Vortices

Let

c_1, c_2 = Chord lengths of flaps 1 and 2,

$\Gamma_1, -\Gamma_1$ = Strengths of vortices shown in Fig. 7(a), and

σ = Half-gap between the two vortex foci (Fig. 7(a)).

Referring to Batchelor (ref. 16, sec. 2.6.4) and Schlichting (ref. 14, p. 89) for a doublet,

$$U_1 = 2\frac{\Gamma_1}{2\pi\sigma} = 2\frac{\Gamma_1}{2\pi c_1 \sin(\phi_1/2)}. \tag{10}$$

2.4 Strength of Shed Vortices

Circulation from Joukowski's hypothesis is (see Batchelor, ref. 16, p. 441)

$$\Gamma_1 = A\sqrt{V_r^2}, \tag{11}$$

where A is a constant of proportionality that depends on the shape and orientation of the flap. For example, it will be different for a rigid or a flexible flap. (Note that a flexible flap would have a variable chord length.) The value of A would be different if trailing edge serrations are present. If a divider plate is present between the two flaps, it would alter the effective shape and orientation of the flap by introducing another length scale into the problem, whose effect would be to alter the value of the constant A. In equation (11), V_r is a representative speed of the flap.

2.5 Speed of Flap Oscillation

There are two forms of flapping speed, i.e., pendulum-like sinusoidal rotational speed and constant rotational, square wave speed. The sinusoidal pattern would be obtained if a pendulum-like variable torque is used to oscillate the flap. The square wave pattern would be generated by a drive that produces a constant rotational speed. In the model design, a pattern that is close to a square wave is expected. In this case, if W is the tip speed, c is flap's chord length, and Ω is the rotational speed (rad/s), then

$$W = c\Omega. \tag{12}$$

A flexible flap would have a variable chord length and the time signature of the tip speed would be distorted compared to those for rigid flaps.

In the present model design, a brushless magnet actuator, known commercially as Ultimags, was chosen to oscillate the flaps. The input current to the Ultimags was observed to follow a square wave pattern. This finding confirmed that, in the model, the flaps indeed operate at a constant rotational speed.

A relationship is required for the transfer of momentum between the solid and the liquid, i.e., between the rotational variables Ω and Γ. This relationship is modeled in section 4.3.2 where comparisons with measurements are presented.

2.6 Effects of Flap Travel, Body Thickness, Viscosity, and Virtual Mass

There may be a relationship, yet unknown, between maximum flap travel and body thickness (Fig. 1). Experiments are needed to determine if results become independent of body thickness when the maximum flap travel exceeds the body thickness (Webb, ref. 12, p. 208).

Virtual mass would be affected by viscosity via boundary layer displacement thickness δ^* on the flaps. An estimate suggests that virtual mass is reduced to

$$m - 2\rho\delta^* c, \tag{13}$$

where ρ is the density of water and c is the flap chord length. Equation (13) is analogous to that for a fish where virtual mass correction is of the order of only 1 percent. The viscosity correction to the mass of water affected can therefore be neglected.

The added mass effects due to the potential flow also need to be considered. The pressure drag, or the frontal area, is an indication of this effect. Therefore, it is expected that, as long as the flap travel is small or the flaps oscillate within the base of the tailcone, the added mass effect due to the potential flow would be low. However, if the flap tips protrude beyond the vehicle, the added mass effect would increase.

2.7 Power of Flap

Let

m_1 = Mass of water affected by flap #1 per unit span (in direction normal to page in Fig. 5),

U_1 = Velocity imparted to mass of water m_1 by flap #1, and

U = Vehicle speed.

Then, the momentum given to water by the flap = m_1U_1, and the rate of momentum shedding into the wake (thrust) = m_1U_1U.

The flap is working against the fluid at the rate of tip speed W. Power is always positive—when accelerating and braking the vehicle. The flap power is, therefore,

$$P = m_1U_1UW. \quad (14)$$

(Units for equation (14) are: $(ML^3/LT^3) = ML^2/T^3)$ = watts. In SI units: Power = watts = J/s) = (N/m)/s = (kgm/s^2) (m/s) = kg(m^2/s^3) = M(L^2/T^3).)

However, all this power is not available for maneuvering and thrust. Some of it is used to overcome drag. The lost kinetic energy in the shed vortices is

$$P_k = 1/2m_1U_1^2U. \quad (15)$$

Therefore, the available power for maneuvering and thrust is

$$P_m = P - P_k. \quad (16)$$

3.0 DESCRIPTION

3.1 The Dual-Flapping Foil Maneuvering Device

A schematic diagram of the water tunnel model is shown in Fig. 1. Figure 2 is a photograph of the partially assembled model. The cylinder diameter is 7.62 cm and the length is about 1 m. The two flaps are 7.62 cm x 7.62 cm in size. A fixed divider plate of the same size is located between the two flaps. The divider plate serves to reduce the rigid body drag and it also "trains" the vortex array allowing accurate phase-averaged wake vortex measurement. The flaps are activated by two magnetic actuators and phase is determined by two differential transducers that measure displacement. The actuators and phase sensors are housed internally. The entire model 'floats,' mounted on a six-component balance located under the strut. The strut is fixed and hangs from the tunnel's top wall. The vortices shed by the flapping foils are created by salient edge separation and, thus, their effects are independent of any boundary layer tripping. The data presented here are mostly for natural transition on the main cylinder because tripped cases show little effect. The two flaps can be operated in one of two modes, i.e., in a clapping or waving mode—so named because of the kind of animation they simulate (see Fig. 8). In the clapping mode, the two flaps approach or recede from each other simultaneously, while in the waving mode, the flaps always follow the direction of motion of each other. In other words, in clapping, the phase of the two flaps is opposite to each other, while phase is the same in the waving mode.

3.2 Experiment Details

All measurements were performed for both flapping modes, i.e., waving and clapping. The balance measurements were conducted with a single flap as well as the dual flap. The actions of the maneuvering device and the phase sensors in air and in a water tunnel were video taped (Bandyopadhyay et al., ref. 17). The robustness of the device was demonstrated by the fact that it worked in the water tunnel nonstop for about five days during which time the phase-matched turbulence measurements were carried out. These measurements were conducted in the water tunnel at Virginia Polytechnic Institute (Zeiger et al,. ref. 18). The cross-section of the test section is large for our purpose: 0.56 m wide and 0.61 m deep. The balance data were collected for flow speeds between 10 and 80 cm/s and flap frequencies of 2.65, 4.237, and 6.2 Hz. As shown in Fig. 4, these parameters are in the same range as those in several relevant aquatic animals. The flow visualization was carried out at 5 cm/s and the laser Doppler velocity data were collected at 20 cm/s with a flap frequency of 2.65 Hz. The flap tip travel was commonly 38 mm which made an angle of 30 degrees about the axis. Data acquisition was carried out in the following manner. First, the balance data were collected. One desk-top computer was used to operate the balance and another was used to read out, process, and store the data. Next, a two-component laser Doppler anemometer was used to make phase-matched turbulence measurements in the wake. The measurements were conducted first in three axial planes downstream of the flaps. Then they were conducted in three cross-stream planes. The data were processed to produce phase-averaged vorticity-velocity vector contours in the axial and cross-stream planes. Finally, distributions of circulation were calculated by two integral methods, i.e., velocity time integrals and vorticity areas. The efficiency measurements were carried out in the NUWC water tunnel which is 30 cm x 30 cm in cross-section.

4.0 RESULTS AND DISCUSSION

4.1 Flow Visualization

Dye flow visualization was carried out to examine the vortex shedding process at a flow speed of 5 cm/s. The vortex rollup at the flap tip is shown in Fig. 8 for the clapping and waving modes. The complete wake can be seen in the video (Bandyopadhyay et al., ref. 17). For a flap angle of 30°, the outer tip vortices were spread at an angle of 70° to the axis, the resulting wake spread angle being 140°. This is a very wide wake that produces thrust and maneuvering forces. As shown later, this wake dissipates very quickly.

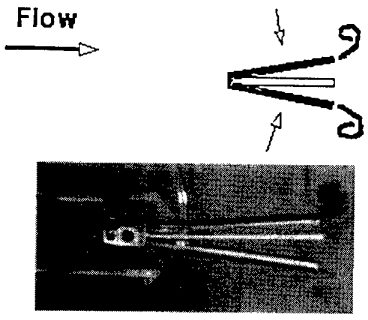


Fig. 8(a). Flow visualization tests of clapping mode: flaps closing (top, graphic depiction; bottom, photograph).

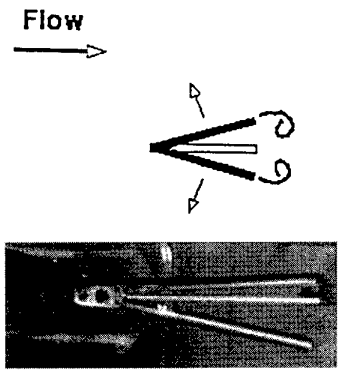


Fig. 8(b) Flow visualization tests of clapping mode: flaps opening (top, graphic depiction; bottom, photograph).

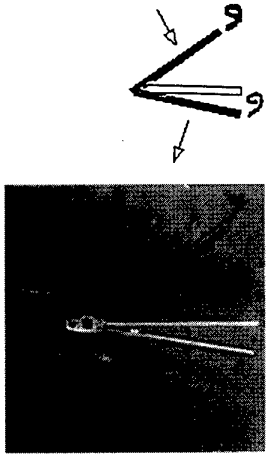


Fig. 8(c). Flow visualization tests of waving mode: Flaps toward port (top, graphic depiction; bottom, photograph).

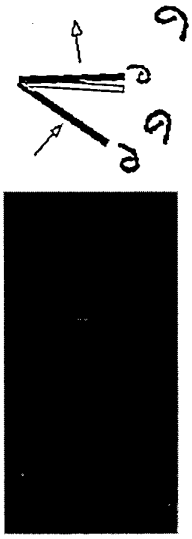


Fig. 8(d). Flow visualization tests of waving mode: Flaps toward starboard (top, graphic depiction; bottom, photograph).

4.2 Definition of Coefficients

The coefficient of axial force, c_a, is defined as

$$c_a = \frac{F}{\frac{1}{2}\rho U_\infty{}^2 D^2}, \tag{17}$$

where F is axial force, being positive for thrust, ρ is density of water and U_∞ is freestream velocity. When F is positive, $c_a = c_t$, the coefficient of thrust, and when F is negative, $c_a = c_d$, the coefficient of drag.

The coefficient of yawing moment is defined as

$$c_m = \frac{T}{\frac{1}{2}\rho U_\infty{}^2 D^3}, \tag{18}$$

where T is yawing moment, D is the length scale of the model and flaps. Time, t, is nondimensionalized as $t^* = tU_\infty/D$. The Reynolds number is defined as

$$\mathrm{Re} = \frac{U_\infty D}{\nu}, \tag{19}$$

where ν is kinematic viscosity of water. In calculating vorticity, velocity and circulation, nondimensionalization is performed using U_∞ for velocity scale, D for length scale, and D/U_∞ for time scale.

The Strouhal number, St, is defined as

$$St = \frac{fA}{U_\infty}, \tag{20}$$

where f is flapping frequency and A is maximum cross-stream travel of a flap tip.

Efficiency of the flapping foils was defined as

$$\eta = \frac{OutputPower}{InputPower} = \frac{T \cdot U_\infty}{\eta_a \int 2VIdt}, \tag{21}$$

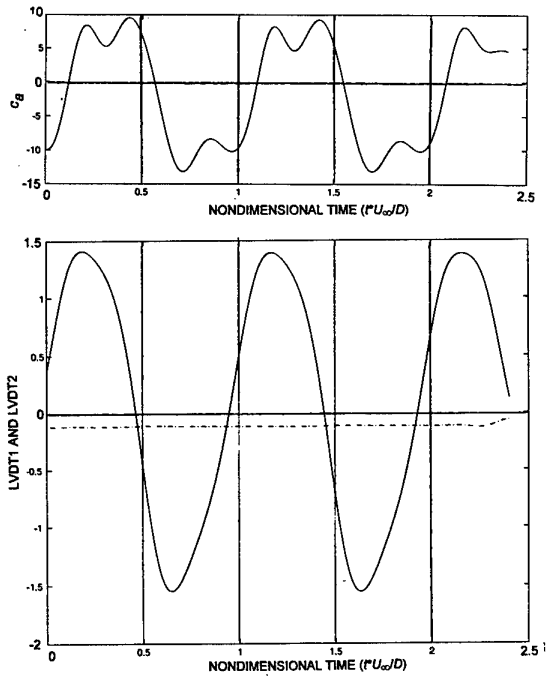
where T is integrated thrust, η_a is actuator efficiency, V and I are actuator volts and currents, respectively. The factor 2 accounts for two actuators.

4.3 Forces and Moments

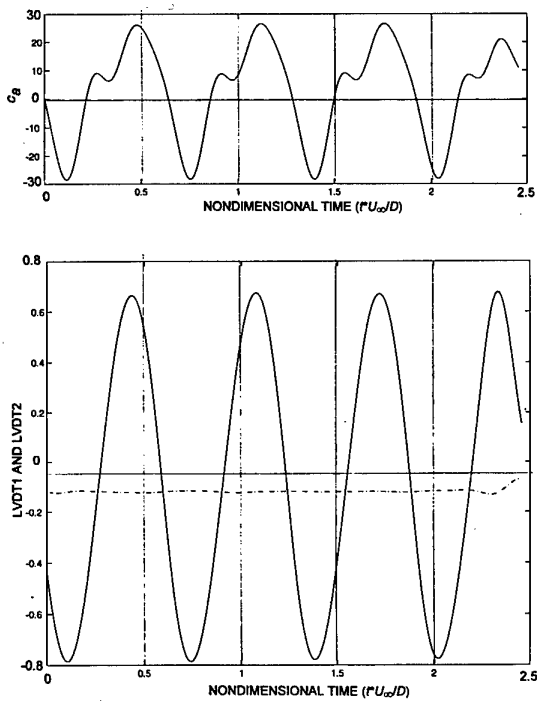
4.3.1 Time signatures

The ensemble-averaged coefficient of axial force (c_a) due to a single flapping foil is shown in Fig. 9(a-c). A net thrust is produced only at 4.24 Hz. For the dual-flapping foil case, the ensemble-averaged time histories of axial force and yawing moment are shown in Figs. 10 and 11, respectively. A thrust is produced at all three frequencies. In Fig. 10, positive values of force indicate thrust and negative values indicate drag. Clearly, the device has produced more thrust than drag. The net values of the moment can be made non-zero and acting toward port or starboard by operating the flaps differentially. The data in Fig. 11 can be used to design control laws for maneuvering. Observe the 90° phase difference between axial force and yawing movement.

9(a) 2.6 Hz



9(b) 4.24 Hz



9(c) 6.2 Hz

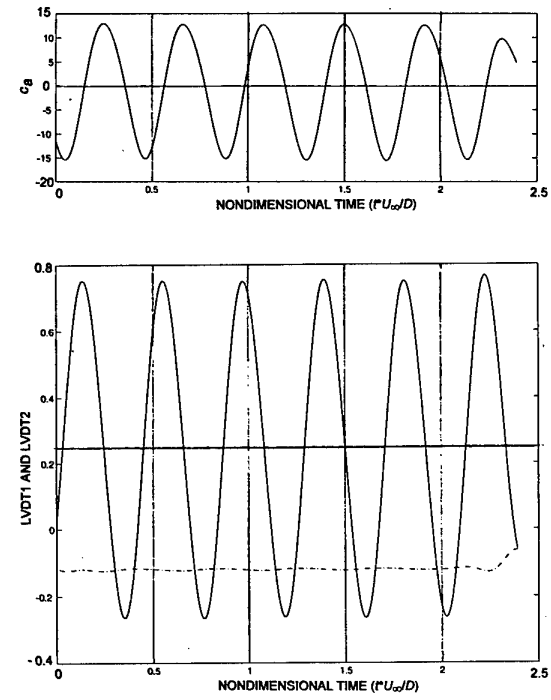


Fig. 9. Ensemble-averaged coefficient of axial force (c_a) due to a single flapping foil; positive values indicate thrust (c_t) and negative values indicate drag (c_d); U_∞ = 20 cm/s: (a) 2.6 Hz, (b) 4.24 Hz, and (c) 6.2 Hz. LVDT signature indicates flap phase ≡ highest values: flap fully open; lowest values, flap fully closed.

10(a) 2.6 Hz

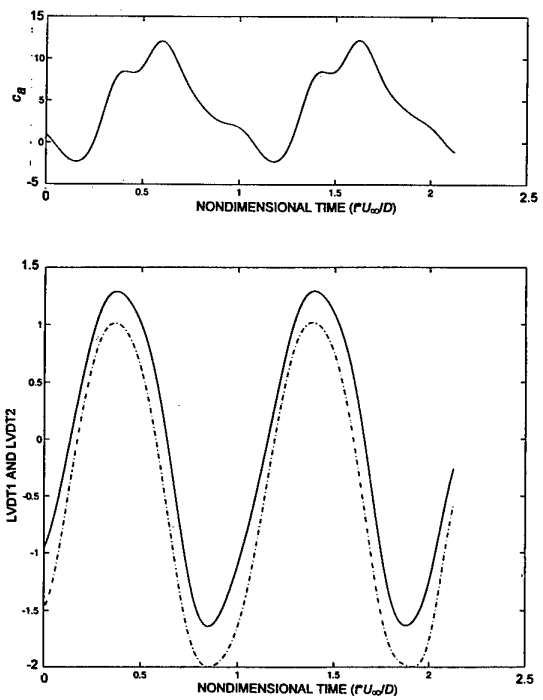
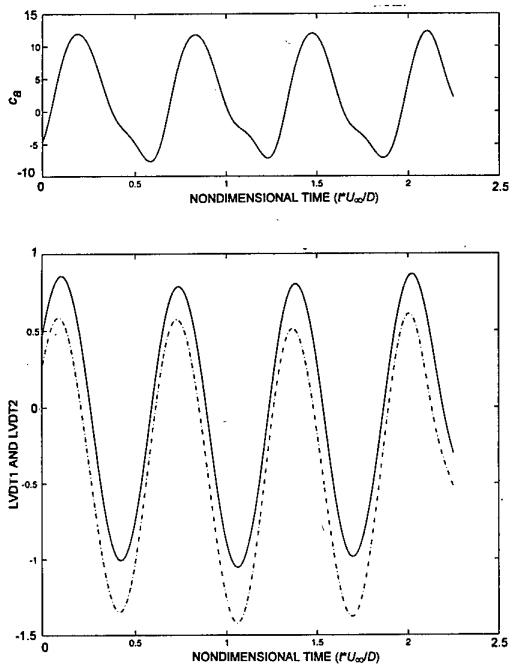


Fig. 10. Ensemble-averaged axial force and flap opening due to dual-flapping foils. High LVDT values ≡ flap fully open; low LVDT values ≡ flap fully closed. The flaps are actually in opposite phase.

10(b) 4.24 Hz



10(c) 6.2 Hz

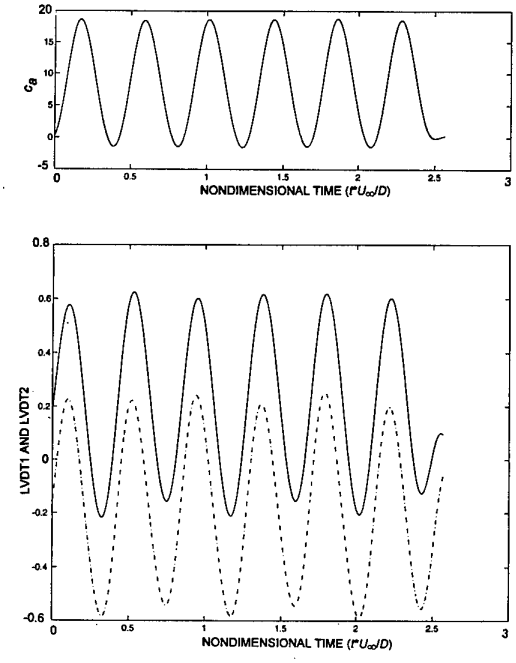


Fig. 10. (Cont'd) Ensemble-averaged axial force and flap opening due to dual-flapping foils. High LVDT values ≡ flap fully open; low LVDT values ≡ flap fully closed. The flaps are actually in opposite phase.

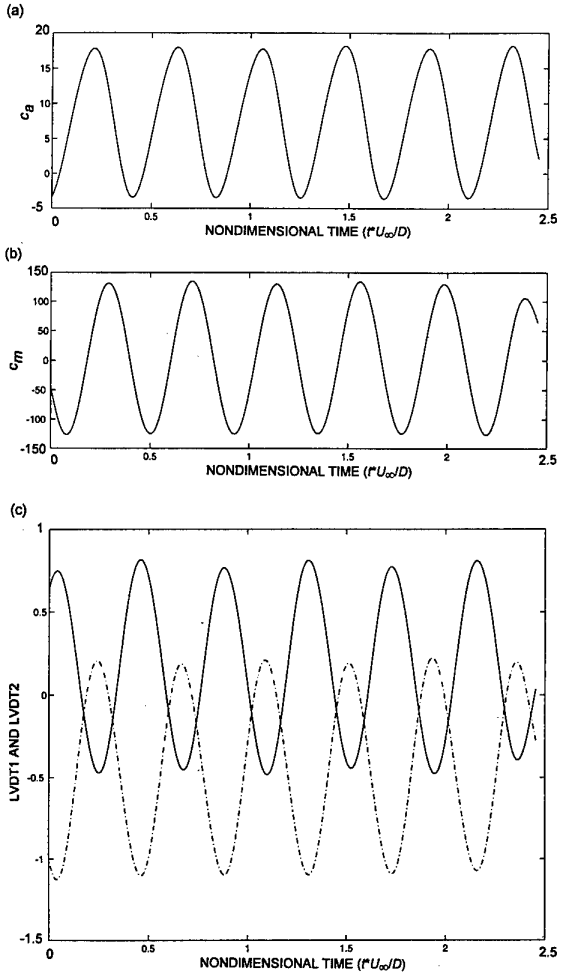


Fig. 11. Ensemble-averaged (a) axial force, (b) yawing moment, and (c) flap phase in waving mode; U_∞ = 20 cms/s; f = 6.2 Hz. The flaps are actually in phase.

4.3.2 Thrust coefficient

The distributions of coefficient of axial force with Strouhal number are shown in Fig. 12. The dual flapping foil data are compared with the two-dimensional theories of Lighthill (ref. 10) and Chopra (ref. 22) and the two-dimensional measurements of Triantafyllou et al. (refs. 23, 24) and Isshiki and Murakami (ref. 25). There is good agreement in the trend. Our measurements are also compared with the two-dimensional momentum model of Bandyopadhyay (ref. 6) described in section 2. In this model, the mass of water affected per unit span of flap was taken to be

$$2v_\theta \cdot R_v, \tag{22}$$

where $v_\theta = c \cdot \Omega$. Here v_θ is azimuthal speed of the flap time, R_v is vortex radius at the flap tip, c is flap chord = D; Ω is rotational speed of flap = $2\pi f$, and the factor 2 accounts for two vortices formed in each cycle of flapping.

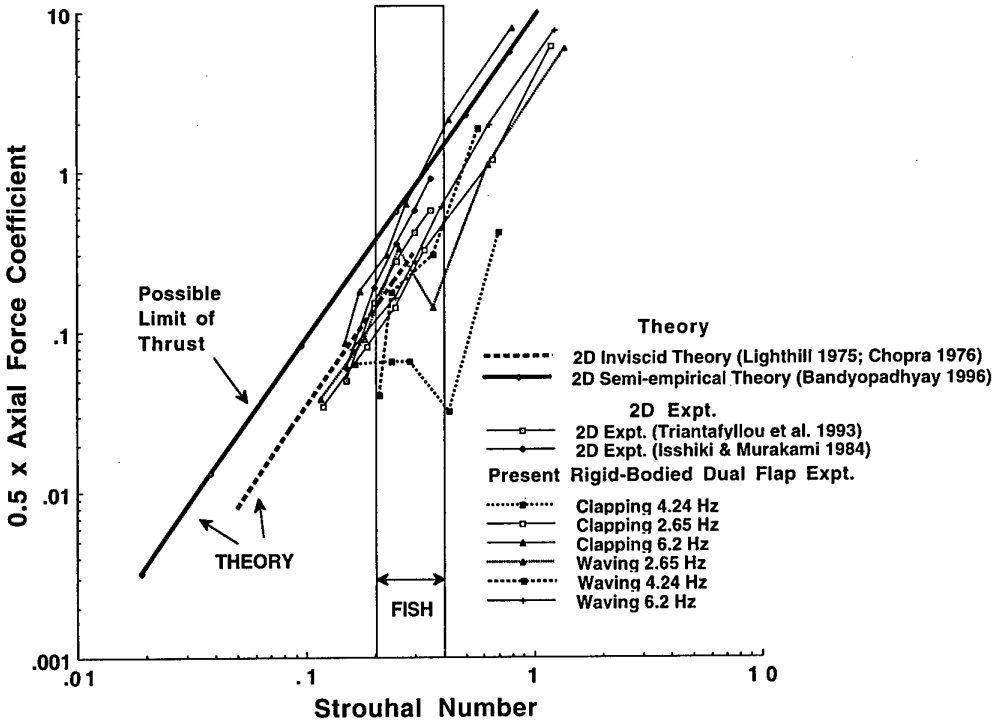


Fig. 12. Comparison of measurements of axial force (thrust) coefficient.

From flow visualization experiments, R_v was taken to be 0.173 cm at all values of U_∞ and f. From the phase-matched LDV measurements shown in Fig. 13, the axial jet speed relative to U_∞ was taken to be 60 cm/s at all values of U_∞ and f. Thrust coefficients calculated using these values of mass of water affected and jet speed are also shown in Fig. 12. The momentum model may be the asymptotic limit of thrust that can be produced by the flapping foil technique. In the St range common among fish (Triantafyllou, ref. 23), some of the dual flapping foil data exhibit sensitivity to St.

In the case of the rigid body, the shed vortices do not propagate tangential to the trailing edge when the flap is at the outer extremity. At 5-20 cm/s, while the flap trailing edge is at 30° to the axis, the outboard vortex moves away from the axis at 70°. There is also a rapid decay in the vortex circulation (discussed later, Figs. 23 and 24). Thus, the vortex self-induced dynamics is strong and the wake is affected by viscous non-linear mechanisms. Although, the two-dimensional non-linear theories generally agree with the mean data trend in Fig. 12, the detailed sensitivity in the range $0.2 < St < 0.4$ is not captured. We suggest that, in order to determine sensitivity to St and f, viscous non-linear stability dynamics need to be included in the theories.

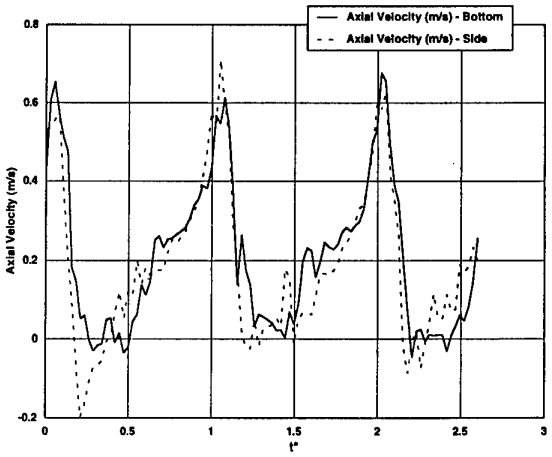


Fig. 13. Phased-average measurements of axial jet speed due to dual-flapping foil. Axial velocities shown are relative to U_∞ of 20 cm/s. Measurements in two different planes are compared.

The efficiency of the flapping foil (equation (21)) is shown in Fig. 14. The efficiency of the magnetic actuator, η_a , was assumed to be 18% as supplied by the manufacturer. The actual η_a is lower and, thus, the actual values of η of the dual flaps shown are higher. There is a general agreement with Triantafyllou's (ref. 23) experiment on a two-dimensional heaving and feathering foil. It is interesting to note that the dual flaps show a tendency to achieve a higher efficiency in the waving mode. This is intriguing. We propose that in the waving mode, the model nose yaws and sheds vortices. This either lowers the drag on the rigid body or it enhances the thrust (by augmenting jet speed) due to the vortices produced by flapping.

Because the efficiency plots shown in Fig. 14 include the cylinder drag, an attempt was made to estimate the efficiency of the flapping foils alone. The viscous and form (small) drag coefficient of the cylinder was estimated to be 0.145. When this is taken into account, the efficiency of the flapping foils alone are higher as shown in Fig. 15. At lower St, there is a tendency for the efficiency to depend on f. This has not yet been explained.

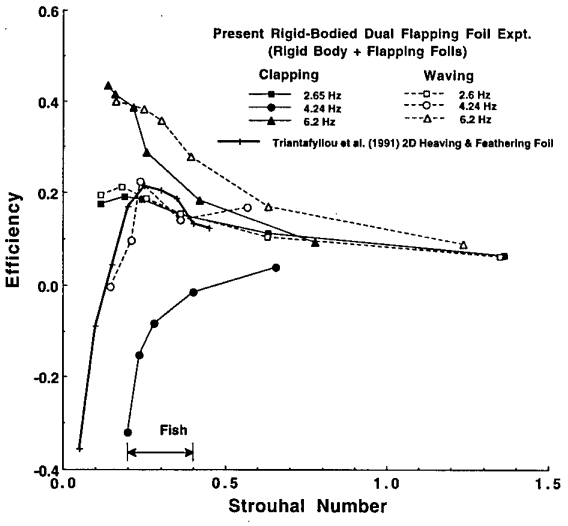


Fig. 14. Measurements of the axial force efficiency of the dual-flapping foils.

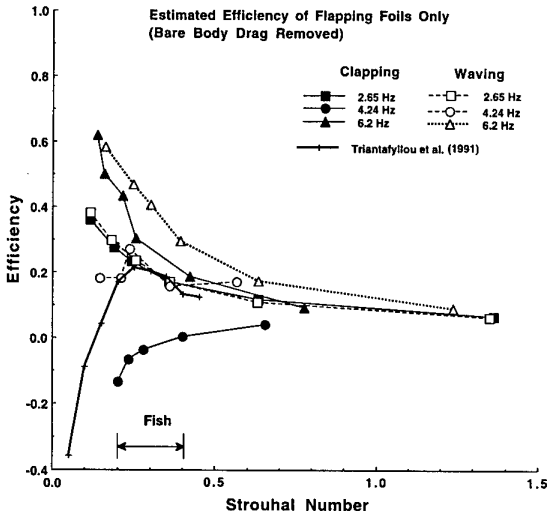


Fig. 15. Estimated efficiency of dual-flapping foils. Estimated values of bare body drag (viscous + form) removed from measurements of total efficiency (rigid body + flapping foils) shown in Fig. 14.

Measurements of all axial force coefficients due to single- and dual-flapping tails are shown in Fig. 16. Both thrust and drag production cases are included. Except at 4.25 Hz, one single foil is unable to produce thrust. This is due to the drag of the rigid cylinder. Tripping of the cylinder boundary layer has no effect on the thrust produced because that mechanism is inviscid — tripping only affects the drag of the rigid cylinder. The data indicate that the thrust produced is governed by *St*, drag of the rigid cylinder, and the total mass of water affected. The mass of the water affected is doubled when two flaps are used and the thrust produced overcomes the drag of the rigid cylinder. According to Triantafyllou (Pvt. Comm. 1997), the "robotuna" vortex cores make an angle of 10-15° to the forward direction. However, the wake angle is 140° in the present case. (The divider plate probably lowers the cylinder drag slightly.) This suggests that the drag of the flexible robotuna's main body could well be lower, but this remains a speculation. The two-dimensional flapping foil experiments do not have a main body and, thus, have the pure thrust produced. We believe that, in the future, by comparing our results with those of the robotuna of Triantafyllou, insight can be gained on the effect of a flexible body.

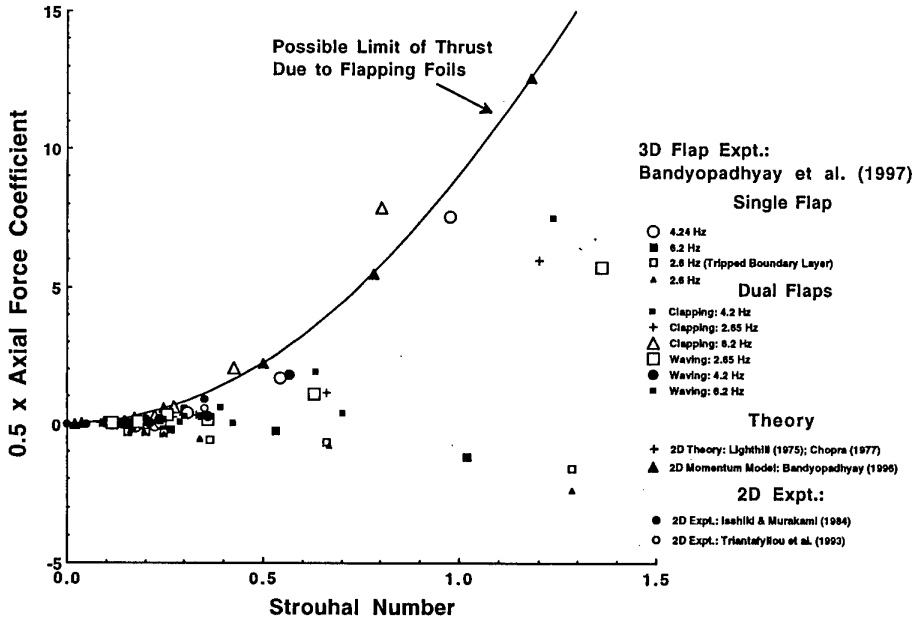


Fig. 16. Summary of all single- and dual-flap axial force coefficients. Both thrust- and drag-producing cases are shown. Note that body drag is included in axial force.

4.4 Vortex Shedding: Vorticity-Velocity Vector Maps

4.4.1 Vorticity-velocity vector maps

The phase-matched vorticity-velocity vector measurements were carried out at a flow speed of 20 cm/s. Their maps in the axial (diametral) midplane (z = 0) are shown in Figs. 17, 18 and 19 for waving and clapping modes (phase is given by $t^* = tU_\infty/D$). Similarly, the phase-matched vorticity-velocity vector maps in the cross-stream plane at the trailing edge of the flap ($x/D = 0.066$) are shown in Figs. 20 and 21 for the waving and clapping modes, respectively. Such maps were used to compute circulation values of the vortices by two methods: by calculating velocity line integrals and vorticity area integrals. The circulation distributions are shown in Figs. 22 and 23 for x/D = 0.0656 and 0.5577, respectively. The two methods of circulation calculation are in reasonable agreement. We note that within a short length after formation ($x/D \cong 0.5$), the minimum circulation has dropped by a factor of 3.

Measurement resolution is higher in Fig. 17. This figure captures the radially far-flung vortices. The maps in Figs. 17, 18, and 19 show the jets between vortex pairs which gives rise to thrust. The vortex arrays and the mechanism of thrust and yawing moment are depicted schematically in Figs. 27 and 28.

Figures 18 and 19 indicate that, in the clapping mode, the two flaps produce arrays of vortices that are mirror images. Thus, they would produce thrust but no maneuvering cross-stream forces (Fig. 27). On the other hand, in the waving mode, the two arrays of vortices from the two flaps are staggered in the streamwise direction. Due to this fact, the waving mode produces both axial and cross-stream forces (Fig. 28). The vortex shedding process is clarified in Figs. 25 - 28. Figure 25 shows a drag-producing wake behind a hydrofoil where the induced flow between a pair of shed vortices is pointed upstream. When the foil is oscillated, the wave train shown in Fig. 26 is produced when the induced velocity points in the downstream direction, which gives rise to thrust. The clapping mode produces the mirror-image vortex train shown in Fig. 27 and the waving mode produces the staggered vortex train shown in Fig. 28.

The cross-stream maps in Figs. 20 and 21 were examined to look for clues for higher efficiency in the waving mode. The wake is three-dimensional due to the finite nature of the flaps. The figures show that the shed axial vortex lying within the divider propagates inward towards the axis of the model while the outer shed axial vortex shows no such tendency. This is shown schematically in Fig. 24. After it is fully formed, the inner axial vortex is elliptic and takes an inclined position in the y-z plane. In the clapping mode, during the outward motion of the flaps, four axial vortices would tend to converge near the model axis increasing vortex-vortex and vortex-wall interactions. We suspect that induced drag will be affected more in the clapping mode than that in the waving mode.

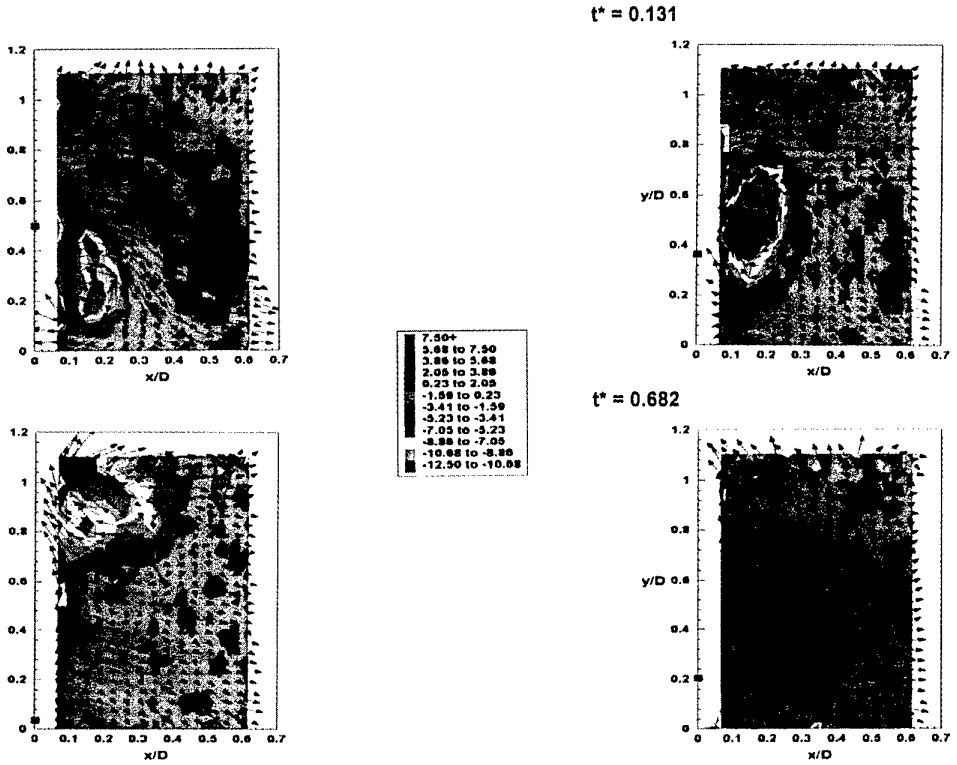


Fig. 17. Vorticity-velocity vector plots in the axial plane for clapping. The velocity perturbations are with respect to freestream velocity. Filled squares on the y-axis indicate the location of flap trailing edge in this and succeeding figures. Note that, when the flap is at outboard extremity, the outer-most vortex trajectory is at 70° to the x-axis which is much larger than the flap trailing edge angle of 30°.

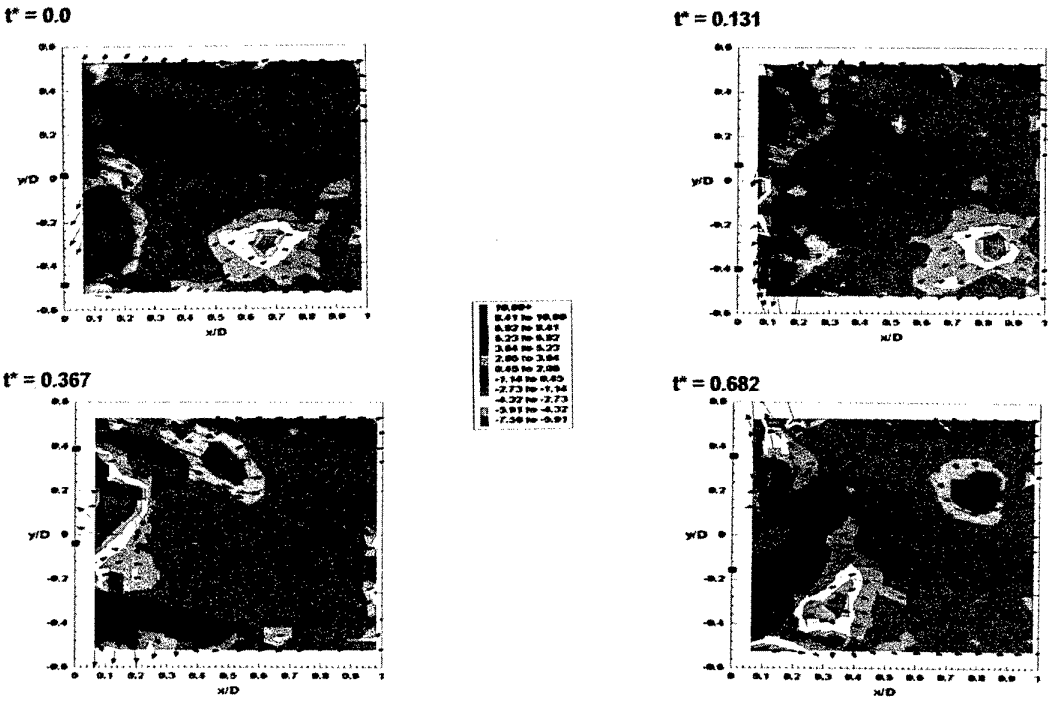


Fig. 18. Vorticity-velocity vector maps in the axial plane in the waving mode.

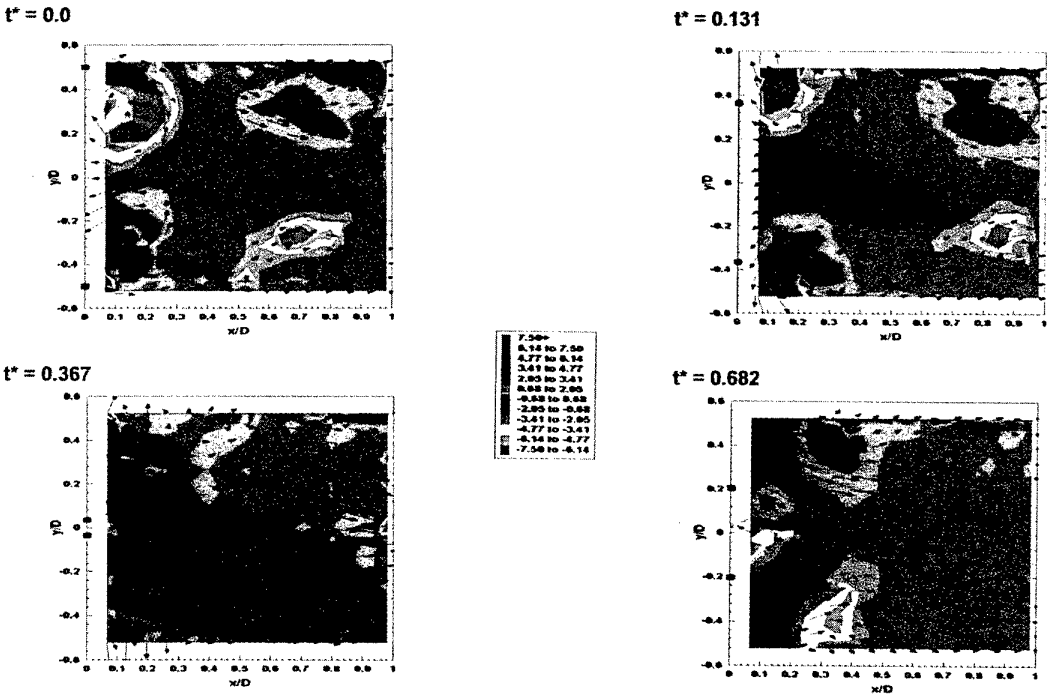


Fig. 19. Vorticity-velocity vector maps in the axial plane in the clapping mode.

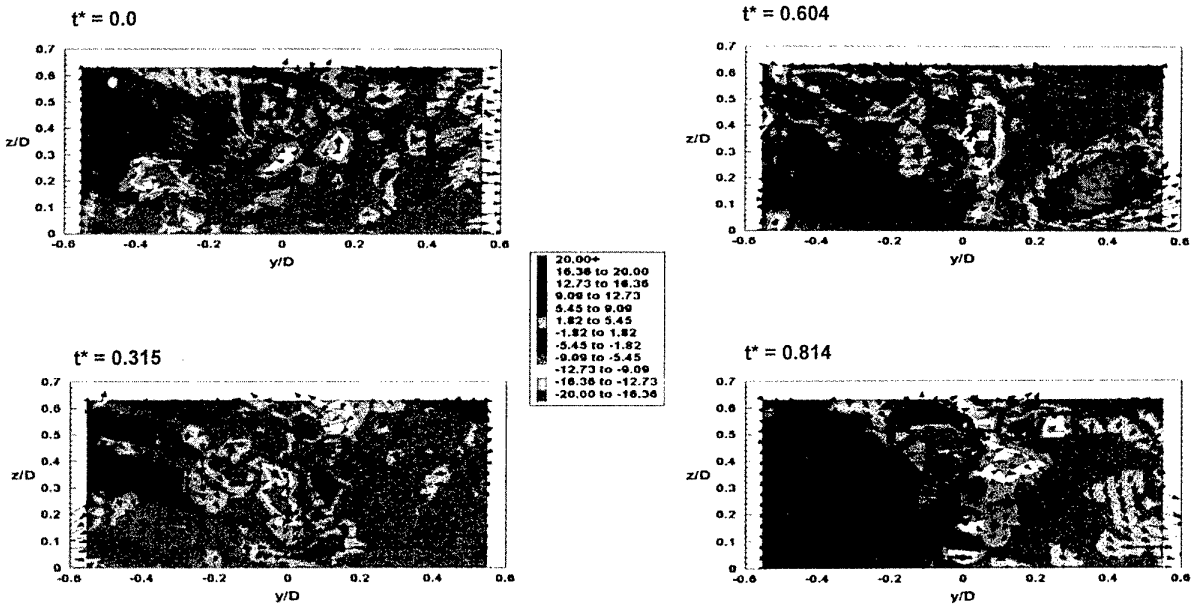


Fig. 20. Vorticity-velocity vector maps in the cross-stream plane in the waving mode; x/D = 0.066. Filled square markers at z/D = 0.5 within each frame indicates flap location.

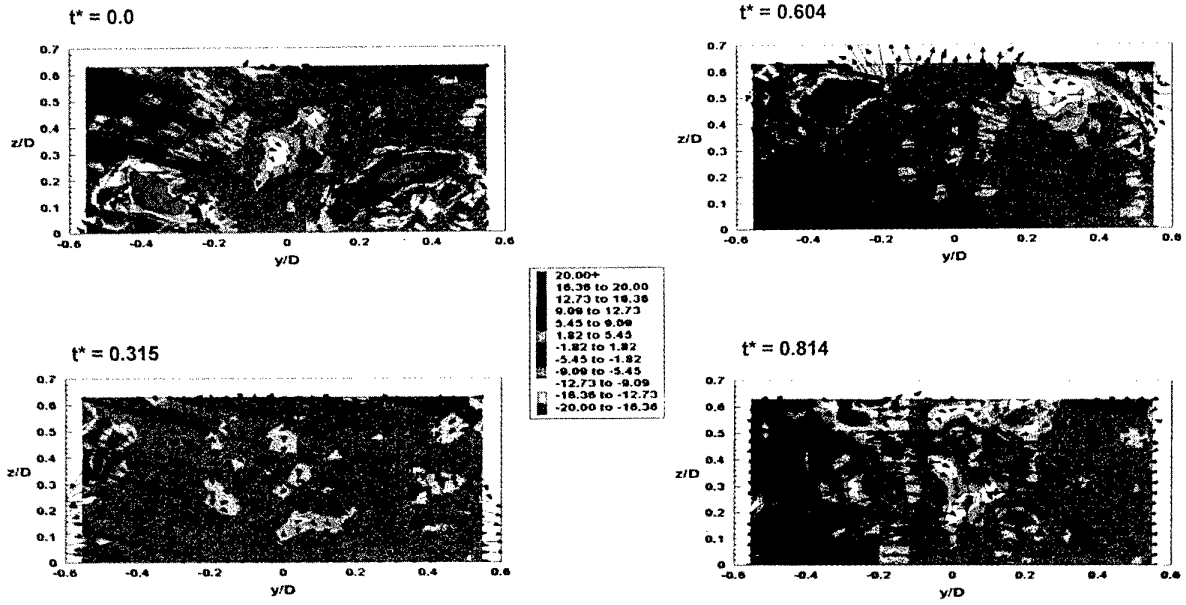


Fig. 21. Vorticity-velocity vector maps in the cross-stream plane in the clapping mode; x/D = 0.066. Filled square markers at z/D = 0.5 within each frame indicates flap location.

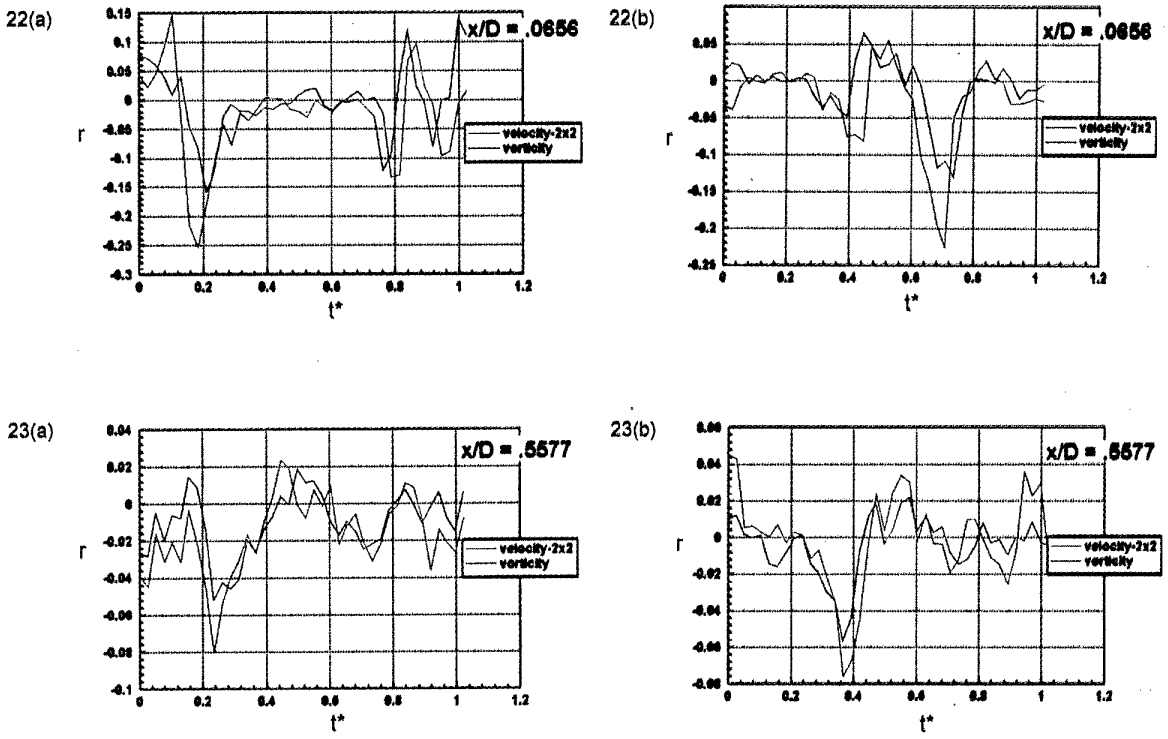


Fig. 23. Circulation distribution at a downstream station (x/D = 0.5577) compared to that in Fig. 22, (a) waving and (b) clapping

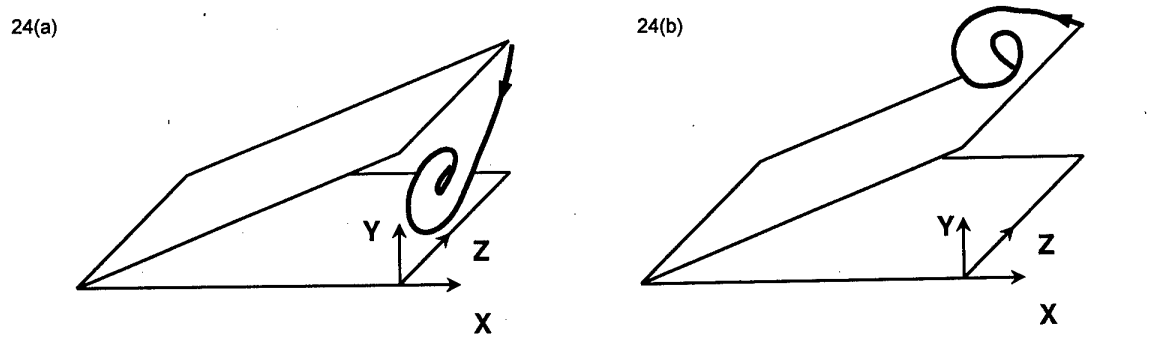


Fig. 24 Schematic diagram showing the inward trajectory of the inner shed axial vortex (a) as opposed to the outer shed axial vortex (b) in both modes of flap oscillation.

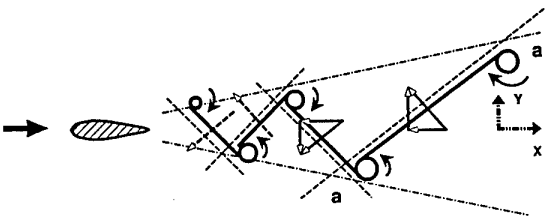


Fig. 25. Schematic of production of drag (momentum deficit) and yaw force due to a Kármán vortex train.

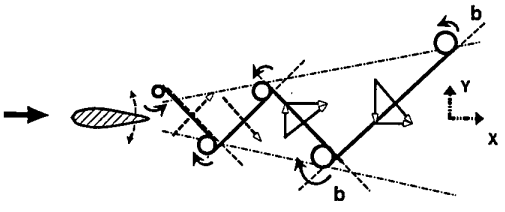


Fig. 26. Schematic of production of thrust (momentum excess) and yaw force due to a negative Kármán vortex train.

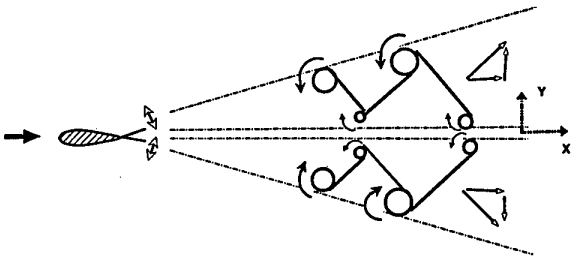


Fig. 27. Schematic of vortex train in clapping mode showing the origin of axial and cross-stream force vectors.

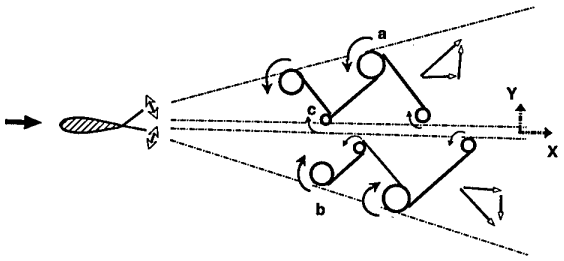


Fig. 28. Schematic of vortex train in waving mode showing the origin of axial and cross-stream force vectors.

5.0 CONCLUSIONS

A laboratory investigation has been conducted to examine the performance of a dual flapping foil device used as a maneuvering and propulsive tool for a rigid body. A model was built (1 m long, 7.6 cm diameter) with flapping foils at the end of the tail cone and various measurements were performed in a water tunnel. The flow speed range in water was between 5 and 80 cm/s and the flapping frequency varied from 2.6 to 6.2 Hz. These parameters, as well as the body length, are in the range popular among fish and seals. The flaps were operated in two modes: waving and clapping. These flaps mimic the motion of the caudal and pectoral fins of a fish. (This clapping motion is also found among insects.) It was demonstrated that, although attached to a rigid body, the device can produce a net thrust. By operating the flaps differentially, the device can also be used to produce a yawing moment for maneuvering purposes. The waving mode of the flaps is more efficient as a thruster compared to the clapping mode. This explains why a fish may use a caudal fin for propulsion and the pectoral fins for maneuvering. The waving mode involves a yawing motion of the nose. Thus, its higher propulsive efficiency suggests that the side-to-side motion of the head of a fish may have hydrodynamic benefits.

Comprehensive measurements of the vortex shedding process in the wake, matched to the phase of the flaps, have been carried out. These data can be useful to validate dynamic numerical simulation codes incorporating the effects of moving surfaces. Existing non-linear inviscid theories are inadequate to account for sensitivity to Strouhal number in the range $0.2 < St < 0.4$. Viscous stability effects also need to be included. In the dual-flapping foils attached to a rigid body, while the net drag is less than the net thrust, the wake is very wide compared to that for a fixed cylinder of same diameter and the wake decays rapidly. This is explained by clearly demonstrating that the wake of the device is predominantly composed of down-stream-pointing jets lying between pairs of shed vortices.

Past two-dimensional theoretical and experimental results in the low Strouhal number-axial force coefficient range, as well as the present work over a larger range, indicate that there is an universal asymptotic limit of thrust that can be produced by the flapping foil technique. However, the axial force produced may fall short when flapping foils are attached to rigid bodies. The interaction of the drag of the rigid body with the flapping foil flow is complicated. There is systematic variation in force generation with the mode of flap oscillation, flapping foil frequency (in addition to Strouhal number) and the number of flapping foils. Three-dimensional viscous non-linear theories are required to account for these effects.

When the present work was started, we were intrigued by the fact that the clapping motion of the wings of insects for propulsion is common in air, but is rare in water. On the other hand, the waving motion of the caudal fin of fish is common in water but is rare in air. Because clapping of wings in air produces both thrust and a large amount of lift force, it involves a complicated rotary motion of the wings as well. The ability of small insects to fly in the air remains a mystery. Quantitative experiments are required to ascertain the mechanisms involved. However, aquatic animals have separate means for handling the buoyancy forces and the thrust-producing role of the waving motion of the caudal fin is relatively better understood.

With aquatic animals, the main lacuna in our understanding is the element of drag. There is considerable uncertainty in the drag data of aquatic animals. This has led to much controversy in the past. Even our understanding of lift-based force generation is often based on inviscid non-linear theories. They do not adequately account for viscous effects, which influence the behavior in narrow Strouhal number ranges where optimum efficiency is reached. Careful laboratory experiments on simplified engineering models of aquatic animals and physical modeling might bring some clarity to the subject.

ACKNOWLEDGMENT

This research was funded by the Office of Naval Research (program managers J. Fein and Dr. T. McMullen) and the Naval Undersea Warfare Center Independent Research Program (program manager Dr. S. Dickinson). This support is gratefully acknowledged. The authors would also like to acknowledge the assistance of W. Nedderman, J. Castano, J. Dick, M. Zeiger, C. Straney, M. Savoie, and B. Doyle.

REFERENCES

1 Bandyopadhyay, P. R., Castano, J. M., Rice, J. Q., Philips, R. B., Nedderman, W. H., and Macy, W. K., "Low-Speed Maneuvering Hydrodynamics of Fish and Small Underwater Vehicles," J. Fluids Eng., *119*, 1997, pp. 136-144.

2. Jones, K. D., Dohring, C. M., and Platzer, M. F., "Wake Structures Behind Plunging Airfoils: A Comparison of Numerical and Experimental Results, Paper No. AIAA 96-0078, 1996.

3. "HSVA Towing Tests on a G7e Torpedo with SSR-Drive and with Normal Propeller Drive," PG/21600, translated by the British from the German, September 1944.

4. Gopalkrishnan, R., Triantafyllou, M. S., Triantafyllou, G. S., and Barrett, D., "Active Vorticity Control in a Shear Flow Using a Flapping Foil," J. Fluid Mech., *274*, 1994, pp. 1-21.

5. Hall, K. C., and Hall, S. R., "Minimum Induced Power Requirements for Flapping Flight," J. Fluid Mech., *323*, 1996, pp. 285-315.

6. Bandyopadhyay, P. R., "A Simplified Momentum Model of a Maneuvering Device for Small Underwater Vehicles," NUWC-NPT Technical Report 10,552, Naval Undersea Warfare Center Division, Newport, RI, 1996.

7. Ellington, C. P., "Unsteady Aerodynamics of Insect Flight," The Society of Experimental Biology," No. XLIX, pp. 109-129 (Eds. C. P. Ellington and T. J. Pedley), 1995.

8. Rayner, J. M., "Dynamics of the Vortex Wakes of Flying and Swimming Vertebrates," The Society of Experimental Biology, No. XLIX, 1995, pp. 131-155 (Eds. C. P. Ellington and T. J. Pedley).

9. Webb, P. W., Hydrodynamics and Energetics of Fish Propulsion, Bull. Fish. Res., BD., Canada, *190*, 1975, pp 1-158.

10. Lighthill, M., J., Mathematical Biofluidynamics, Philadelphia, SIAM, 1975.

11. Wu, T. Y., "Hydromechanics of Swimming Propulsion," J. Fluid Mech., *46*, 1971, pp. 337-355.

12. Webb, P. W., "Hydrodynamics: Nonscombroid Fish," in *Fish Physiology, Vol. VII,* eds., W. S. Hoar and D. J. Randall, Academic Press, 1978, pp. 189-237.

13. Gopalakrishnan, R., "Vortex-Induced Forces on Oscillating Bluff-Cylinders," Ph.D. Thesis, MIT, Cambridge, MA, 1993.

14. Schlichting, H., *Boundary-Layer Theory*, McGraw-Hill, New York, 1979.

15. Bandyopadhyay, P. R., and R. Balasubramanian, "Vortex Reynolds Number in Turbulent Boundary Layers," J. Theor. Comp. Fluid Dynamics, *7*, 1995, pp. 101-117.

16. Batchelor, G. K., *An Introduction to Fluid Dynamics*, Cambridge University Press, 1967.

17. Bandyopadhyay, P. R., Nedderman, W. H., Castano, J. M., and Donnelly, M., 1996, "A Small Maneuvering Device for Energetic Environment," NUWC-NPT Video, Naval Undersea Warfare Center Division, Newport, RI.

18. Zeiger, O. K. Rediniotis, Donnelly, M. J., and Telionis, D. P., "Temporal Evolution of the Flow Field Over a Pitching Tangent-Ogive Cylinder," AIAA Paper No. 95-0441, 1995.

19. Bainbridge, R., "The Speed of Swimming of Fish as Related to Size and the Frequency and Amplitude of the Tail Beat," J. Exp. Biol., *35*, 1963, pp. 109-133.

20. Kashin, S. and Greelner, S., "On the Generation of End Performance of Fish Swimming," in "Neurocontrol of Locomotion," (Eds. Stein, Greelner, and Stuart), 1976, pp. 81-102.

21. Kashin, S., "Fish Locomotion," Dr. Sci. Thesis, Inst. of Oceanology, Academia of Science of USSR, Lenin State Library, Moscow, 1985.

22. Chopra, M. G., "Hydromechanics of Lunate Tail Swimming Propulsion," J. Fluid Mech., *7*, 1977, pp. 46-69.

23. Triantafyllou, M. S., Triantafyllou, G. S., and Gopalakrishnan, R., "Wake Mechanics for Thrust Generation in Oscillating Foils," Phys. Fluids, *3*(12), 1991, pp. 2835-2837.

24. Triantafyllou, G. S., Triantafyllou, M. S., and Grosenbaugh, M. A., "Optimal Thrust Development in Oscillating Foils with Application to Fish Propulsion," J. Fluids and Structures, *7*, 1995, pp. 205-224.

25. Isshiki, H., and Murakami, M., "A Theory of Wave Devouring Propulsion," J. Soc. Naval Architects of Japan, *156*, 1984, pp. 102-114.

26. Fish, F., "Power Output and Propulsive efficiency of Swimming Bottlenose Dolphins (Tursiops Truncatus," J. Exp. Bio., *185*, 1983, pp. 179-193.

Substitution of rolling for slipping as an effective mechanism of decreasing hydrodynamic drag

V. I. Merkulov .

Institute of Theoretical and Applied Mechanics SB RAS, Novosibirsk, 630090, Russia
tel: (383-2) 355622 fax: (383-2) 352268 e-mail: merkulov@itam.nsc.ru

1. SUMMARY

As is shown by theoretical and experimental researches, the general mechanism of crucial reduction of hydrodynamic drag consists in substituting rolling friction for slipping friction [1]. This mechanism is realized at a boundary layer reconstruction with formation of periodic transverse vortices that are rolling without slipping over the body surface. A small velocity gradient characterizing such a motion conditions low energy dissipation. A travelling wave on elastic body surface works as a mechanism of formation of a periodic vortex structure for some water animals, such as dolphins. At appropriate elastic parameters of the surface, the wave is excited in a regime of hydroelastic flutter. The surface roughness, as it takes place with sharks, expands the range of velocities at which travelling waves are excited, though it decreases their energy efficiency.

2. INTRODUCTION

Another vortex formation mechanism abundant in nature employs the specifics of the flow along a slender rough body. Analytical calculations validated by direct experiments showed that helical vortices with a high amplitude growth increment are generated on a slender rough body. Arriving at the fish body, well-developed helical vortices reconstruct the boundary layer in such a way that the normal flow with slipping of fluid layers with a high velocity gradient is replaced by a motion with rolling of vortices with a small velocity gradient and, as a consequence, with low hydrodynamic drag.

The rostrum of a sword-fish is a slender body covered by small-scale roughness. Nearly parallel flow is formed at a small distance from the leading edge, which changes weakly downstream due to both viscosity and slight thickening of the rostrum. One can try to approximate this flow by fluid motion along an infinite thin rough needle.

The needle surface roughness generates continuously small disturbances in the flow. The stability of initial laminar flow guarantees the absence of other disturbances except for those diffusing from the cylinder surface. For one-scale roughness, we will have one-scale turbulence with a known mixing path length.

The presence of turbulent oscillations causes the appearance of turbulent viscosity that exceeds multiply the molecular viscosity in the gradient flow region. The flow which is of interest to us can be described by the Reynolds equations with a certain turbulent viscosity which can be determined using the Prandtl technique [1] in terms of known, in the present case constant mixing path length. The solution obtained can be analyzed for stability. Inviscid solutions depend on turbulent viscosity only via the averaged velocity profile.

3.MATHEMATICAL FORMULATION OF THE PROBLEM.

The equation of the average momentum in the boundary layer model in the cylindrical coordinate system r, z is written as

$$\rho[\frac{\partial U}{\partial z} + V\frac{\partial U}{\partial r}] = -\frac{1}{r}\frac{\partial}{\partial r}(r\rho\overline{uv})$$

Here, U and V are components of the averaged velocity profile, u, v are components of the fluctuating velocity.

According to the Prandtl model [2], the Reynolds stress can be expressed in terms of the averaged velocity gradient $(\partial U/\partial r)$ and mixing path l as follows:

$$\overline{uv} = -l^2(\partial U/\partial r)^2.$$

Thus, the averaged momentum equation is reduced to the equation

$$U\frac{\partial U}{\partial z} + V\frac{\partial U}{\partial r} = \frac{l^2}{r}\frac{\partial}{\partial r}[r(\frac{\partial U}{\partial r})^2]. \qquad (1)$$

The continuity equation has a usual form.

$$\frac{\partial(Ur)}{\partial z} + \frac{\partial(Vr)}{\partial r} = 0 \qquad (2)$$

Assuming the needle diameter to be equal to zero, we obtain the following boundary conditions for unknown functions U and V.

$U = V = 0$ for $r = 0, z > 0$

$U = 1, V \to 0$ for $r \to \infty$

One can conclude from the form of equation (1) that it is independent of velocity scale but depends on the roughness scale. Assuming the coordinates r, z be normalized to a certain size L, the quantity l will be a measure of relative roughness.

4. SOLUTION OF THE PROBLEM

Paper presented at an AGARD FDP Workshop on "High Speed Body Motion in Water", held in Kiev, Ukraine, 1-3 September 1997, and published in R-827.

From the analysis of dimensionality of equation (1), it follows the existence of a self-similar solution of the form $U = U(\eta)$ where $\eta = r/(l^2 z)^{1/3}$. Let us represent the function $U(\eta)$ in terms of the second derivative of some other unknown function $\phi(\eta)$

$$.U = \phi''(\eta)$$

and determine the second component of velocity from the continuity equation (2).

For this purpose, let us pass to new variables $..z = \xi; \quad \eta = r/(l^2 z)^{1/3}$.

Then we will need the relations $\partial\eta/\partial r = \eta/r = 1/(l^2\xi)^{1/3}$

$\partial\eta/\partial z = -\eta/3z$

$\partial\xi/\partial r = 0; \quad \partial\xi/\partial z = 1.$

Let us substitute in equation (2) the relation for the function U.

$$.\frac{\partial(Ur)}{\partial r} = -r\frac{\partial U}{\partial z} = r\phi'''\frac{\eta}{3\xi}.$$

whence we can obtain

$$..\frac{\partial}{\partial\eta}(Vr)/(l^2\xi)^{1/3} = \frac{\eta^2(l^2\xi)^{1/3}}{3\xi}\phi'''.$$

$$V = \frac{(l^2\xi)^{1/3}}{3\xi\eta}\int \phi'''\eta^2 d\eta = \frac{(l^2\xi)^{1/3}}{3\xi\eta}[\eta^2\phi'' - 2\eta\phi' + 2\phi]. \tag{3}$$

Now we will turn to the momentum equation (1).

After substituting the above formulas for U and V, the left-hand side is converted to the following form

$$.\frac{\phi'''}{3\xi\eta}(-2\eta\phi' + 2\phi)$$

Let us now transform the right-hand side of this equation.

$$\frac{l^2}{r}\frac{\partial}{\partial r}[r(\frac{\partial U}{\partial r})^2] = \partial\phi'''\xi\eta(\phi''' + 2\eta\phi'''')$$

Finally, we obtain an equation for $\phi(\eta)$

$$\phi'''(2\eta\phi'''' + \phi''' + \frac{2}{3}\eta\phi' - \frac{2}{3}\phi) = 0 \tag{4}$$

with the boundary conditions

$\phi'' = 0$ for $\eta = 0$

$lim(\phi/\eta - \phi') = 0$ при $\eta \to 0$

$lim(\phi''\eta - 2\phi' + 2\phi/\eta) = 0$ при $\eta \to \infty$

5. ANALYSISOF EQUATION (4).

For small values of argument η in equation (4), the main terms are the highest derivatives that describe viscous forces

$$2\eta\phi'''' + \phi''' = 0,$$

which has the following solution

$$\phi'' = \sqrt{\eta}.$$

For large values of η the main terms are the convective terms

$$\phi'' = \sqrt{\eta}$$

which vanish at $\phi = \eta^2$.

6. ANALYSIS OF STABILITY OF THE SOLUTION.

Let us designate by the letters u, v, w, p the small perturbations of components of velocity vector and pressure, which will be sought in the form

$$u, v, w, p = Reel[Fr, iGr, Hr, \rho Pr]\exp(in\phi + i\alpha(x - ct)).$$

Here, α is the wave number and c is the phase velocity. For unknown functions $F(r), G(r), H(r)$ after eliminating $P(r)$, we obtain the following system of ordinary differential equations

$$n(U-c)G + \frac{d}{dr}[(U-c)rH] = 0$$

$$\alpha(U-c)(nF - \alpha rH) + nU'G = 0$$

$$\alpha rF + r\frac{d}{dr}G + G + nH = 0$$

, that must be solved with uniform boundary conditions $F, G, H, P \to 0$ at $r \to 0$ and $r \to \infty$.

The second equation of this system is an algebraic one and makes it possible to exclude the function F.

As a result, one can obtain a system of two equations of the first order for two unknowns H, G.

$$n(U-c)G + \frac{d}{dr}[(U-c)rH] = 0 \tag{5}$$

$$n(U-c)(r\frac{dG}{dr} + G) - nrU'G + (n^2 + \alpha^2 r^2)(U-c)H = 0 \tag{6}$$

Excluding H from this system, we obtain one second-order equation with one unknown.

$$(U-c)\frac{d}{dr}[\frac{r}{n^2 + \alpha^2 r^2}\frac{d}{dr}(rG)] - \tag{7}$$

$$(U-c)G - G\frac{d}{dr}(\frac{rU'}{n^2 + \alpha^2 r^2}) = 0$$

The system of equations (5)-(6) or equation (7) equivalent to it with uniform boundary conditions can have a solution only for certain values of c and α that are called eigenvalues.

Stability of various axisymmetric flows is studied in detail in a well-known paper of Batchelor and Gill [4]. In particular, they showed that the flow can lose stability with respect to inviscid form of perturbations if the following condition is satisfied at some internal point:

$$\frac{d}{dr}(\frac{rU'}{n^2 + \alpha^2 r^2}) = 0.$$

Here, as usually, n is the number of the azimuthal mode, and α is the wave number of the longitudinal travelling wave.

This condition is a generalization of the known condition on an inflection point in the profile of a parallel-plane flow to an axisymmetric flow.

It is easy to see that this condition is not valid for the Poiseuille flow with a logarithmic profile and for any profile if we confine ourselves to axisymmetric disturbances ($n = 0$).

At the same time, for a profile on a rough cylinder obtained by us, this condition is always valid at point $r_k = n/\sqrt{3}\alpha$.

Batchelor and Gill showed that most unstable are disturbances with the number $n = 1$.

Concerning the conditions of physical realization, we are interested in the case when the product $\alpha c = \omega$ is a real number, hence, α is a complex number conjugated with c. In this case, the real part of the wave number α_r determines the wave length λ in accordance with the relation $\alpha_r = 2\pi/\lambda$, and the imaginary part α_i determines the downstream change of disturbance amplitude according to the law $\exp(-\alpha_i z$.

The reference length in the problem under consideration can be only the wave length, which will be accepted as a unit of measurement. With such normalization, $\alpha_r = 2\pi$, and

$$r_k = Reel\frac{1}{\sqrt{3}\alpha} = \frac{\alpha_r}{\alpha_r^2 + \alpha_i^2} = \frac{1}{2\pi\sqrt{3}[1 + (\alpha_i/\alpha_r)^2]}$$

Since $\alpha_i < \alpha_r$, then the dimensionless distance to the critical layer will be determined by a small number 0.092.

Let us rewrite equation (7) in the following way:

$$r\frac{d}{dr}[\frac{r}{n^2 + \alpha^2 r^2}\frac{d}{dr}(rG)] - rG = \frac{r^2 G}{U - c}\frac{d}{dr}(\frac{rU'}{n^2 + \alpha^2 r^2}) \qquad (8)$$

Let us represent an approximate solution to this equation, which satisfies uniform boundary conditions, in the following form:

$rG = 0$ for $r < r_k$

$rG = rK_l'(r\alpha)$ for $r > r_k$

Here K_l is the Hankel function of the lth order.

The condition of continuity of this function at point $r = r_k$

$$K_1'(r_k\alpha) = 0 \qquad (9)$$

can be provided by choosing an arbitrary value of the wave number α.

Using direct substitution, one can verify that the chosen function satisfies equation (8) for velocity profile

$$U = \sqrt{r} \quad at \quad r < r_k$$

$$U = const \quad at \quad r > r_k$$

and is an approximate solution for all profiles similar to this one.

The first root of equation (9) has the following complex value: $0.90 - i0.58$. The negative imaginary part ensures a rapid growth of disturbance amplitude.

7. CONCLUSION.

The conducted qualitative analysis of solution properties and the estimate of some of its parameters allows one to prepare an experimental verification of the hypothesis according to which a thin rough rostrum of a sword-fish performs a function of vortex generator.

Firstly, we found out that dimensionless parameters of the flow along a rough cylinder are independent of velocity scale. This makes it possible to carry out experiments with an arbitrary velocity convenient for the experimentor.

Secondly, we found out that the velocity profile formed by the rough cylinder is stable with respect to axisymmetric disturbances. At the same time, helical disturbances of the travelling wave shape

$f(r)exp[i\alpha(z - ct) + in\theta]$

are unstable with a continuous spectrum of frequencies. This means that forced generation of such disturbances with a small initial amplitude ensures an onset of increasing disturbances which, having achieved a certain amplitude, as we suppose, form a steady periodic flow. The most unstable form is a helical vortex filament corresponding to the value $n = \pm 1$. Superposition of two such forms provides an intersecting vortex geometry that will then evolve into inclined circular vortices embracing the cylinder. Such waves can be generated by transverse oscillations of the cylinder in one plane, two disturbance waves being excited during one period of oscillations.

References.

1. Merkulov V.I. Fluid Flow Control, Nauka, Novosibirsk, 1981, 180 p.

2. Schlichting H. Grenzschicht-Theorie, Verlag G.Braun, Karlsruhe, 1951.

3. Betchov R., Criminale W.O., Jr. Stability of Parallel Flows, Academic Press, New York, London, 1967.

4. Batchelor F.K., Gill A.E. Analysis of the axisymmetric jets, J.Fluid Mech., 14, pp.529-551, 1962.

HYDROBIONICS PRINCIPLES OF DRAG REDUCTION

V.V. Babenko.

Department of hydrobionics and boundary layer control
Institute of hydromechanics
National Academy of Sciences of Ukraine,
8/4 Zheliabov Street
252057, Kiev, Ukraine

SUMMARY

General principle of optimization of alive organism consists, as a result of many-centuries evolution, in attainment of minimal energy expenditures for maintaining the process of life. Principal attention in this investigation is payed to study of peculiariries of organism systems and their interaction in the process of motion of water animals, which are directed at the reduction of energy expenditures. On dolphin example, considered are peculiarities of morphology and physiology of skeleton, muscles, skin coating, blood system and innervation. As the motion takes place in the water medium, considering those systems the force influence of medium onto the organism is taken into account. Studied are influence of swimming speed, non-steadiness of flow, unusual method of trust creation, specific structure of body surface onto the body systems. Also considered are some peculiarities of hydrodynamic influence onto the body when moving in water medium. In accordance with these peculiarities, specific structure of mentioned systems of water animals are analyzed.

Here there are detailed description of skeleton and location of innervation ganglions as well as layer-by-layer location, along diameter and body length, of moving muscles. Structure of skin coatings is given in details especially. The peculiarities of blood system and structure of that in skin coating are analyzed. Presented are results of measurements of temperature distribution on the surface of body skin and results of theoretical estimation of controlled heat conductivity of skin.

By means of apparatus developed, the measurements of distribution for elasticity and damping properties of skin of different dolphin types are carried out.

Presented are results of direct and indirect measurements of other mechanical parameters of skin, in particular phase velocity of disturbances development. The results of measurements of turbulent boundary layer in different regimes of dolphin motion are given. Described are the functioning the body systems and mechanisms for regulation of mechanical features of skin.

The ways of reduction of body motion drag are shown.

1. INTRODUCTION

The attention to hydrodynamic functions of skin covers and bodies of cetaceans was paid for the first time in the works [11, 30-33, 37 etc.]. The greatest attention to these investigations was attracted by the publication of the Gray's book [13], were the estimated calculation has shown that the energy of dolphins does not correspond to swimming speeds developed by them. The book of Hertel [12] has shown ways of the hydrobionics technical applications and has formed the basis for development of this direction in the different countries. The fundamental theoretical [17, 21, 22, 27, 38] and series of experimental [20, 36 etc.] investigations in hydrobionics were carried out.

It is known, that high-speed hydrobionts, in particular dolphins, have developed as a result of evolution the adaptations for economical energy expenditure and efficient drag reduction.

The principal purpose of research consists in finding the corresponding laws of structure of skin and other organism systems as well as explanation of that on the basis of laws of physics and hydromechanics.

Hydrobionics is new science based on complex studying the phenomena using knowledge of different scientific directions including biological and technical ones. As a new science hydrobionics needs development of methodology and, in particular, of new techniques for experimental investigations carrying out. Present section of research includes development of methodology of carrying out the mainly experimental hydrobionical investigations.

About 30 years of research in Institute of Hydromechanics of National Academy of Science of Ukraine and in other institutions show the perfect flowing around the high-speed marine animals and the difference from that for corresponding rigid bodies [17, 25].

Study of living organisms should not be conducted in the same manner as it is done in case of rigid bodies in technics. This gives the new notion in the field of modelling in technical problems. Well elaborated bionical approach can create a bridge between investigations of marine animals and development of methodology for identification of more effective technical systems.

Paper presented at an AGARD FDP Workshop on "High Speed Body Motion in Water", held in Kiev, Ukraine, 1-3 September 1997, and published in R-827.

The most important is insight into understanding of basic principles of organism construction which would permit to develop the reliable methodics of research.

The purpose of present investigation consists in identification and study the adaptation mechanisms of systems in a hydrobiont organism which are energy saving at high speeds of swimming.

The hypothesis of present investigation consists in the fact that all organism systems are interconnected and function towards achievement of highest efficiency: drag reduction and increase of propulsion efficiency at minimum possible energy expenditures.

Formulation of the problem consists in determitanation of the relationship between morfology of hydrobiont body and its hydrodynamics.

Approach consists in characterization of hydrobiont morphology systems including hydrodynamic correspondence and mutual interaction of organism systems.

2. BASIC PRINCIPLES OF THE GYDROBIONIC

The most important for undestanding the peculiarities of structure of hydrobionts and their systems as well as for modelling those pecularities in technics is study and systematization of hydrobionics principles. Let enumerate the basic functional principles [4, 5, 8, 9, 25].

- *Principle of buoyancy force* balance. Average density of hydrobiont body is close to that of water, so animal is more or less balanced by static force buoyancy. Positive or negative buoyancy is neutralized during the motion by hydrodynamic resultant force of body and fins.
- *Biological principle of convergence* (likeness of signs) affirms that in long- and stable-uniform conditions of life the animals of different type, under influence of natural selection, draw nearer concerning some signs, which are connected directly with influence of environment.
- *Biological principle of divergence* (discrepancy of signs) means that in the range of one single species there are not absolutly equal organisms. Being uniform initially groups of them, during natural selection in some different conditions of environment, have been specializing in different directions. As a result new varieties and binds have appeared with more expressed distinctions of structure, functions and way of life. For example, skin elasticity of dolphins which swim with different speeds is essentially different.
- *Important is biological principle of embriogenes.* It was found out that is process of embrio growth the common signs of large group of animals are found themselves earlier than special ones. So, different signs caused by historical influence of environment appear successfully.
- *Principle of progressive swimming* consists in that that, as hydrobiont dimensions increase and strenghtening the level of organizing, the maximum swimming speed essentially increases. It is stipulated by the fact that effective power of hydrobiont is proportional to cube of linear dimensions (to mass), and hydrodynamic drag - to square of linear dimensions (square of wetted surface).
- *The principle of cyclic motion.* Swimming of water animals is always non-stationary, usually periodical, close to harmonic. Besides, usually the active swimming alternates with motion by its own momentum (coasting). This principle may be explained by important-for-life biological properties of regulating the parameters of living tissues, which (properties) are stipulated by cycles of energy exchanges, acts of breathing and blood circulation as well as unexplored jet efficiency of non-stationary swimming.
- *Principle of propulsor unification.* Among hydrobionical objects the most widely distributed are wave-like propulsors with elastic bending-oscillatory complex of different structure which become localized as the dimensions and swimming speeds increase.
- *Principle of relative hydrodynamic conformity* is characterized by that that, as Reynolds number increases, there is succesive localization of hydrobionts parameters range with changing, in law-governed way, characteristics of propulsors and methods of swimming in accordance with hydrodynamic modes of flow in boundary layers and vortical wakes. However the generic Reynolds numbers differ essentially from those for rigid bodies because of specific flexible skin covers and non-steadiness of flowing around.
- *Principle of receptoric regulation consists in the following.* If rigid body moves then various hydrodynamic forces influence its surface. However the rigid body is insensitive to those forces, it does not perceive them because designers set beforehand such a margin of safety that this body would not be deformed. For all hydrobionts and in particular cetaceans the nerve endings are located in skin very close to flowing around surface: at distance of several tens of microns from body surface. Our predictions showed that pressure fluctuations and boundary layer velocities are registered by such receptors very well. Since the hydrobiont body surface is very innervated then force influence of hydrodynamic field of outer medium when moving and especially the gradients of hydrodynamic loads are perceived sensitively by a living organism. An animal feels any vortical perturbation. And this principle (law) of receptoric sensitivity means that as a result of many-centure evolution a hydrobiont organism has developed the adaptations in such a way that to eliminate the painful feelings. Yet on the basis of this principle one can search the organism adaptations intended for elimination of painful feelings and directed toward reduction of hydrodynamic drag.
- *Principle of interconnection consists* in that that all systems in a living organism work only in an interconnected manner.

- *Principle of polyfunctionality* means that majority of organism systems has not one function only but several ones.
- *Principle of combinationness of adaptive systems* consists in that that, in order to achieve the most efficiency, working are not single organism system but the greatly large number of systems.
- *Principle of automatic regulation* consists in that that all adaptations in organism work automatically.
- *Principle of thermal regulation* consists in that that there are hydrobiont's mechanisms for control of heat flux and, besides, heating is directed not on forming the heat boundary layer but on regulation of mechanical characteristics of skin covers, the latter being directed to control of coherent vortical structures of boundary layer.

3. GEOMETRIC PARAMETERS OF BODY.

In conformity with hypothesis of research, at first the geometric parameters of body and its parts (fins) are considered. Geometric parameters have to provide minimum hydrodynamic drag. Laminarized airfoil of B-TSAGI series for airplane wing is shown on Fig. 1 at its top [25]. On the airfoil the boundary layer remains laminar one on the extent of 80...90% of wetted surface, that is such profile has minimum friction drag and minimum thicknesses of boundary layer and wake behind the airfoil. Below are the vertical longitudinal projections of cetacean body: II - Orcinus orca, III - cetacean dolphin, IV - common dolphin, V - coalfish whale, VI - grey whale; VII - sperm whale, VIII - smooth whale. It is seen that all bodies have laminarized shape. Moreover, the geometry of body shape is such that resultant lifting force for some cetaceans is directed upwards and for another ones down. This is connected with way of life and contributes to diving and rising to the surface. It is to be noted that, from one side, cetaceans are able to regulate the body shape unlike rigid bodies and can change the direction of resultant force. From another side, they have almost zero buoyancy and can move in fluid with different position of the body. This promote effective body manoeuvrability. On Fig. 2 one can see the body shape of having been just caught cachalot (sperm whale), and represented on Fig. 3 [29] are bodies of revolution which are equivalent to trunk of cachalot (1), coalfish whale (2) and dolphin (3) [17]. It is seen that all animals belong to different speed groups: high-speed dolphin has obviously laminarized shape; as low swimmer but good diver, cachalot has middle section located in the forebody part. All cetaceans have well-streamlined body shape.

The shape of cetacean fins is also of optimal geometry which corresponds to best airfoils [15, 25]. Fins of cetacean are able to change their geometry, and tail fin changes the span and profile shape cyclically in process of oscillation [28].

4. SPEEDS OF MOTION.

In order to estimate correspondence of adaptations of organism systems to hydrodynamic laws of body flowing around it is necessary to know the real speeds of the hydrobiont swimming. Distingnished are three typical speeds of swimming: slow swimming with infinite time of motion, cruise swimming speeds which can be maintained by animal for 15...20 minuts and full speeds (rush-like) that are the maximum possible speeds which can be maintained for several seconds [17, 25].

Thus, the speed of motion is determined by the time of sustaining the loading. Besides, speed of motion is determined by the size of motive musculature that is dimensions and leugth of animal.

Shown on Fig. 4 is dependence for cruising mode of swimming on duration of swimming for wild dolphins: common dolphin (1), orca (2), white whale (3) and for whales: blue (4), grey and sperm whales (5, 6), and also for pro-dolphin having been trained (7), bottle-nosed dolphin (8) and striped one (9). Experiments with fishes in hydro-tubes represent: a - pulsed mode, b - long-time, c - migrating mode, and also sports swimming of champions: d - with flippers, e - "free-style" method, and the last one: f - salmon of 0.18 meters length [17].

Comparison of hydrodynamic parameters for hydrobionts of different type with technical objects is shown on Fig. 5 [25]; 1 - fishes: a - trout, b - salmon, c - vakhu, d - barracuda, e - tuna, f - sword-fish, g - maco shark, h - blue shark; 2 - cetaceans - dolphins: i - common dolphin, j - bottle-nosed, k - howling, l - orca, m - white whale; whales: n - finback whale, coalfish, fin-whale, blue, o - grey, humpback, sperm; 3 - transportation of light divers; 4 - self-propelled inhabited vehicles; 5 - small submarines; 6 and 7 - foreign submarines; KT and 0B - regions of parameters for hydrodynamic models having been tested in cavity tube and test tank.

Majority of high-speed hydrobionts are just as good as american submarines as to speed of motion, and some of hydrobionts have the speeds more than those of technical objects.

5. ENERGETICS.

The question arises, at what expense the high-speed hydrobionts can move with such speeds. Presence of laminarized shape does not explain the phenomena found out. It may be suggested that there is a complex of means of adaptation in organism structure for the sake of observed swimming velocity achievement. The hypothesis has been put forward that all is determined by energetics of animal. Measurements of energy capabilities (power to weight ratio) of some kinds of high-speed hydrobionts have been carried out. Shown on Fig. 6 are the power of basic and active exchange in dependence of total mass for: 1 - dog, 2 - human being, 3 - horse and dolphins (MC - porpoise, A - common dolphin). Line 1-prime shows energetics of animal in a state of excitement [17]. It is seen that laws for warm-blooded animals are the same. The more mass the higher power developed. Shown on Fig. 7 is the dependence of maximum specific power output to external mechanical work on duration of swimming [17]. Curve 1 is predicted one according to

approximating formula $Q_{max}=1,73[\ln(1+T)]^{-1,25}$ here T in seconds, Q_{max} in W/N, 2 and 3 - physiclogical evaluations for sportsmen - champions and well-trained sportsmen. Experimental points: 1 - dolphin jumps, 2 - salmon jumps, 3 spawning migration of Siberian salmon; sportsmen: 4 - boat-racing, 5 - running on track and uphill, 6 - exercises with cycle-ergometer. Maximum speed of swimming as a function of motion duration is represented of Fig. 8 [25]. The designations are as follows: $\overline{U}_{max} = U_{max} / U^*_{max}$, $\overline{T}_{max} = T_{max} / T^*_{max}$, $\overline{q}_{max} = q_{max} / q^*_{max}$, $\overline{U}_{max}$ - typical average maximum speed of every species swimming at characteristic, for all species, swimming duration $T^*=10^3$ sec., q^* - specific output of power at $T= T^*$.

There are some methods for finding the energy capabilities of hydrobiont. One of them is based on results of gas composition analysis of air breathed out depending on fulfilled loading (work). Second method deals with estimation of jump height and motion kinematic during the jump. All measurement showed that energy capabilities of high-speed hydrobionts are of the same order as that of well-trained sportsmen, in particular of olympic champions. Phenomenal differences as to energy capabilities of high-speed hydrobionts were not found out. Discovered in cetacean tissues was myoglobin which contributes to accumulation and reservation of oxygen. Myoglobin promotes the deep-sea diving and forcing the speed, but does not exercise essential influence on magnitude of cruising speed and energy capabilities.

Body shape and energy capabiliities do not permit to explain the reason of the high swimming speeds. Consequently, hydrobionts must have another means of adaptation for fast swimming.

6. NON-STEADINESS OF MOTION.

All hydrobionts move along non-steady trajectory and are flowed around by non-steady flow. There are three types of hydrobiont swimming [17] (Fig. 9): - undulatory (shake-like) type: 1 - Squalus acantias, 2 - Rabidus furiosus, 3 - Heterodontus francisci, 4 - Lampetra, 5 - Anguilla rostrata, 6 - Chlamydoselachus anquineus, 7 - Lophotes, 8 - Gastrostomus; - Scombroid type, when tail part of body oscillates: 9 - Cephalorhyndus commersonil, 10 - Tunnus saliens, 11 - Lamna distropis, 12 - Katsuwonus pelamit, 13 - Balcenoptera borealis, 14 - Pneumatophorus garonicus, 15 - Clupea pallasii, 16 - Ladis marocephalus, 17 - Oncorhyndins nerka; - fin-twinkle type: 18 - tetraodon melengris. Shown on Fig. 10 is the typical trajectory of tail fin during scombroid mode of motion (curve 1), with that the centre of gravity (curve 2) moves along straight trajectory. Cinema frames of motion for high-speed bottle-nosed dolphin (at the top) and low-speed Phocaena phocaena (at the bottom) [17, 19, 25] are given on Fig. 7. Investigation of kinematics of hydrobiont motion is as separate and very important part of hydrobionics. A large amount of experimental researches of kinematics of fish and dolphin swimming has been carried out. Developed were the theories which describe method of motion and allow to calculate the hydrodynamic characteristics of hydrobionts. A drawing-in force, arised at the tail part of hydrobiont body, is introduced into prediction. Measurements of pressure distribution along the body showed that, when active swimming, there is redistribution of pressure along the body, which promote the laminarization of boundary layer.

However the calculations have shown that even in this case the drawing-in force and pressure redistribution don't allow to explain the phenomena of fast hydrobiont swimming.

Next problem is study the laws of non-steady boundary layer on the dolphin body. On Fig. 11 there is the general picture (pattern) of coherent vortical structures development in the boundary layer of flat rigid plate during laminar, transitional and turbulent modes of flow [7]. Shown there below is general scheme of morphological structure of outer layers of dolphin skin and generation in the boundary layer, with help of skin, of two types of coherent vortical structures: sinusoidal wave and longitudinal vortexes. Of course, this idealized picture in real non-steady boundary layer on vibrating surface will have another character (behaviour). Carried out were direct measurements, with thermoanemometer, of longitudinal fluctuative component of velocity in the dolphins boundary layer at different modes of its motion [18, 19, 26]. On Fig. 12 curve 2 corresponds to longitudinal fluctuative velocity along rigid body and curve 1 [17-19] is that along dolphin body. It's seen that transition to turbulence happens at high speed of motion. Maximums of fluctuations are less for curve 1 and, what is most important, it is smooth that is there are not large gradients of velocity change as it is when flowing the rigid dolphin model. Fig. 13 shows that value of fluctuations and their behaviour change essentially, depending on modes of acceleration. Also compared were distributions between fluctuative velocity along dolphin body and its rigid skin (Fig. 14): 1...6 - points on the animal body at x/L=0,22; 0,56; 0,75; 0.8; 0.84; 0.89; 7 - data for rigid model at U=4.7 m/s; 8...11 - data at passive swimming at U=1.0, 2.7, 2.5, 3.3 m/s; 12...15 - active swimming at the same speeds. One can see the essential difference of fluctuations in the boundary layer of alive dolphin and its rigid model. During active swimming the boundary layer fluctuations are intrinsicly smaller [26]. Magnitude of fluctuations determines the friction drag. Thus, from those date it is seen that friction drag of actively moving dolphin is considerably less than that of rigid body. What is an explanation of results obtained. To understand this one should consider morphological structure of dolphin skin and its systems.

7. MORPHOLOGY OF ORGANISM SYSTEMS.

In the centre of Fig. 15 there is classical structure of dolphin skin by academician V. E. Sokolov [31-33]. In outer skin layers one can see clearly the dermal nipples and dermal rolls. At the left there is the scheme of skin structure according to Surkina and Babenko [9]. The

basic distinction from Sokolov's scheme is skin musculature and specific peculiarities of outer layers structure shown below. Fig. 16 depicts the skin development during ontogenesis. This means that, as embryoe developes, in its organism the signs appear which have been developed in the process of many-century selection. Dermal nipples and rolls arised in comharatively recent time. Millions years ago the dolphin skin was the same as we have. This testifies that specific structure in the skin has appeared under the action of force-type stresses of flow and was directed towards friction drag reduction.

On Fig. 17 there are dimensions of transverse microfolds on skin surface [9]. It is seen how the skin layers in the region of microfolds peel, that is connected with hydrodynamics of flowing the micro-hollow. Shown on Fig. 18 on the right are the angles of inclination of dermal mipples as regards to body surface at different places along the body [9]. From the left there is topography of dermal nipples inclination angles along dolphin body. It is seen that these angles of inclination correlate with gradients of hydrodynamic loads on the body arised when moving in water medium. Angles of inclination along the body change essentially and are stipulated by hydrodynamics of body flowing only.

Fig. 19 shows along-the-body direction of dermal rolls in the dolphin skin [35]. Let remind that dermal nipples are located in form of rows along dermal rolls. Such location corresponds, as if, to streamlines in boundary layer when flowing the dolphin body.

On Fig. 20 there is distribution of skin muscle along the body of bottle-nosed dolphin and Phocaena phocaena [34]. Skin muscle plays important role during regulation of mechanical features of skin. General scheme of location of motive musculature and skin muscle along the dolphin body [2, 34] is represented on Fig. 21.

Also longitudinal distribution of skin thickness both as a whole and of separate layers were measured [10] (Fig. 22). Near-surface thin layer has uniform thickness along the body. More deep layers have different thickness distribution along the body that is connected with hydrodynamic functions.

Represented on Fig. 23 is general scheme of circulatory system and innervation of dolphin body [1, 2] as well as typical pattern of web of circulatory and lymphatic systems in a skin cover of mammals. In the region of each vertebra there exists the autonomous circulatory, lymphatic and innervative system which control narrow circular areas of skin.

8. MEASUREMENT OF MECHANICAL CHARACTERISTICS OF DOLPHIN SKIN

Peculiarities of structure of dolphin's organism systems show that there exist the definite morphological means of adaptation directed, first of all, on intensive section-by-section blood-supply of skin covers. Autonomous section-by-section innervation of skin testifies about fast regulation of blood-supply and lymphatic system. As it follows from data represented on Fig. 12-14, 16, skin covers as a result of long evolution have developed the adaptations for decrease the power stress of friction.

In this connection it is of interest to measure the mechanical characteristics of skin covers. On the basis of analysis of skin structure, a mechanical model of element of skin cover has been developed [3, 7]. Differential equation of motion for the model has been made (Fig. 24), while making the coefficients of the equation dimensionless ones allows to define the basic criterions of similarity.

Apparatus and techniques for determination of mechanical characteristics of dolphin skin covers have been developed [6, 7]. At first, measurements of skin elasticity along the body were carried out with specially produced instrument. Fig. 25 shows topography of dolphin skin elasticity.

On Fig. 26 there are results of measurement of skin elasticity distribution along the body for high-speed (common and bottle-nosed dolphins) and low-speed (Phocaena phocaena) dolphins as well as for having been trained (a) and just cought (b) ones [6, 17]. It is seen that in the middle part of the body elasticity decreases and in tail part increases.

One of the most important characteristic is rigidity determined as ratio of elasticity to thickness of measured material. On Fig. 27 there are results of measurements of skin rigidity for above mentioned dolphins. The empirical equations of rigidity distribution along the dolphins body were made [4]. On Fig. 28 there is distribution of elasticity parameter for common (1) and bottle-nosed (2) dolphins at fast and slow swimming. The shaded area corresponds to optimal parameters for drag reduction. It is seen that skin elasticity becomes optimal at fast swimming only.

Represented on Fig. 29 are the measurement results of damping dolphin skin features determined by height H of rebounding the metal balls of different mass M from dolphin skin with respect to initial fall height H_0. Plotted on horizontal axis is potential energy of perturbation (by balls) which (energy) influence the dolphin skin. It is seen the relationship of damping coefficient for skin of living dolphin is essentially different from that for skin of sick or just the deceased dolphin as well as from that for rubber-like and constructive materials. The principal difference consists in that that damping coefficient comes near to 100% at values of perturbation energy which corresponds to energy of pressure fluctuations of turbulent or transitional boundary layers [39].

Investigated also were another mechanical parameters of skin covers: oscillated mass, coefficient of skin tension, phase velocity of skin oscillations. All those parameters become optimal ones, from the point of view of friction drag reduction, at fast-swimming speeds only.

9. INTERACTION OF BIOLOGICAL SYSTEMS.

Mechanical characteristics of skin covers become optimal from hydrodynamical positions at high speeds of swimming only, it means that energetics of organism is enough for swimming at low speeds. When moving with cruising speeds the energy in not enough and joined into the work must be the adaptations for friction drag reduction, which were acquired during evolutional development. Evidently, the adaptations work during the interaction of all the organism systems.

Scheme of section-by-section distribution of organism systems and their interconnection is represented on Fig. 30. It is seen that, in the region of each vertebra, blood and lymphatic vessels and nervous stems are directed vertically upwards. It permits in a shoretst way to provide with blood and regulate automatically the blood current in outer layers of skin. Also two layers saturated with horizontal layers of circulatory systems are seen on Fig. 30. The layer of skin muscle can regulate mechanical features of skin layers located upper of this layer, and stress of motive musculature changes, cyclically in time with propulsor, the stress of all skin.

On the basis of analysis of organism systems interaction and Fig. 30, the following classification of methods of interaction of biological systems has been developed. As a result of such interaction, occurred is:

1. Regulation of shape of body and fins.
2. Regulation of geometric parameters of skin covers.
3. Adaptation of mechanical characteristics of skin with help of both the skin tension by muscle and the oscillation of elastic medium (skin).
4. Control of mechanical characteristics of skin with help of systems of blood-circulation and innervation.
5. Specific regulation of body and skin temperature.
6. Optimization of mechanical characteristics of skin.
7. Regulation of vibration on skin surface.

On Fig. 31, 32 it is shown how the regulation of body shape happens. Conformity between dolphin sceleton and motive musculature along the body is represented on Fig. 31 [24]. Fig. 32 shows structure of organism systems. When bracing the motive musculature, the body volume and cross suction as well as body shape can change itself due to large mobility and specific structure of sceleton and lungs filled with air. On Fig. 33 it is shown how the shape of vertical fin changes. Such change ocurres owing to specific complex vessels and regulation of their blood filling [24, 25, 37].

On Fig. 34 it is shown how the thickness and shape of skin covers change owing to specific structure of skin muscle [1]. With that, along the body at fast swimming, a longitudinal fold is formed.

Calculations showed that mechanical characteristics of skin and its stabilizing the boundary layer features can be changed essentially by small changes of body diameter and thickness of skin cover.

Fig. 35 shows how elasticity of skin is regulated due to changes of tension in skin with help of skin muscle [4]. Curves 1 and 2 denote elasticity of sick dolphin of length L=2.4 m; curve 3 - for just the deceased dolphin, L=2.55 m; for healthy dolphins: curves 4,5 - L=1.9 m and curve 6 - L=2.2 m.

Shown on Fig. 36 are calculations of oscillations of conical panel made with rubber IRP-1347. It is seen that there are the resonant frequencies of oscillation at which the maximum temperature of rubber heating is reached.

In the process of motion dolphin represents the elastic oscillatory beam. Skin surface can be represented in form of conical elastic shell. Owing to specific structure of skin and under-skin fat cellulose, heat insulation of body from outer water medium is realized. In this consequence, when swimming with high speed, heating both the body and skin owing to oscillation of elastic systems occurs. It is known that elastic characteristics of flexible materials depend essentially on temperature. Thus the adaptation of mechanical characteristics of skin to external hydrodynamic loads is realized.

On Fig. 37 there is the scheme of hydrodynamic loads that act on a body of revolution which is similar, as to shape, to dolphin body [7, 8]. Curve 1 denotes shear stresses on the inner surface of skin; 2 - shear stresses; 3 - static pressure; 4 - displacement thickness of laminar boundary layer. It is seen that in certain places of the body the gradients of hydrodynamic loads are different. Accordingly, regulation of mechanical characteristics of skin covers must be by sections.

Represented on Fig. 38 is dependence for length of section of self-regulation of damping the cetaceam skin on relative maximum speed of swimming and Reynolds number [25]: 1 - high-speed and II - low-speed cetaceans; 1 - common dolphin, 5 - bottle-nosed dolphin, 7 - howling whale, 8 - orca, 10 - porpoise, 11 - white-wing porpoise, 12 - white whale, 13 - coalfish whale, 14 - fin whale, 15 - blue whale, 16 - humpback whale, 17 - grey whale, 18 - cochalot (sperm whale).

The warm-blood cetaceans provide the regulation of elastic prorerties of skin with help of circulatory and innervation systems. On Fig. 39 there is the scheme of blood circulation in dolphin skin [5, 23]: 1 - venules, 2 - arterioles, 3 - epidermis, 4 - under-nipple layer, 5 - derm, 6 - hypoderm, 7 - skin musculature, 8 - under-skin fat cellulose, 9 - sceleton musculature; I and II - first and second layers of horizontal location of vessels respectively. Such horizontal two-layer structure in combination with skin muscle allows to create a heat screen and regulate effectively the thermal regime of body and skin covers [5]. Complex vessels were found out in under-nipple layer, which permits regulating the heat transfer effectively.

Capillars of venules and arterioles in epidermis have between themselves the straight cross-pieces, that allows blood to flow effectively from arterial system into venose one. Owing to specific system of innervation such flowing can be controlled actively.

Owing to regulation with skin muscle the vessels may become closed or opened at all. Thus, with help of circulatory system, heat flux can from one side remain inside the body and from another side be directed into external layers of skin for change of mechanical characteristics of skin.

On Fig. 40 there is a prediction of specific heat flux through unit of length of dolphin skin for common (1) and bottle - nosed (2) dolphins. Curves 3 and 4 denote calculations from below and from above respectively. Calculations have been fulfilled according to formulas from work [5]. As the base of calculations, taken were measurements of temperature of exterior surface of skin, which were carried out with different kinds of living dolphins [5].

Measurements showed that at quiet state and slow swimming the temperature of skin surface differs from that of outer medium insignificantly, of the order 0.5°...0.7° degrees (Fig. 41) [5]. On fins the difference is several degrees. At such difference of temperature the thermal boundary layer is of no importance for boundary layer stabilization.

At high speeds of swimming the blood circulation increases and pressure in capillars of dermal nipples increases too. Nipples become of bottle-like form [9], Fig. 42. This happens also owing to vessels contraction. With this, from one side, elasticity of skin increases, however, from another side, damping properties of skin increases due to specific form of nipples. Thereby adjuistment of stabilizing properties of skin onto optimal regime occures.

Vessels of lymphatic system have a system of valves intended for flow of lymph in one direction (Fig. 43) [2]. Undoubtedly, lymphatic system participates also in generation of optimal mechanical properties of skin covers.

To determine the optimal properties of skin covers, theoretical and experimental investigations have been carried out with analogs of dolphin skin cover. On passive analogs of skin covers a range of optimal parameters has been determined. Those data are to be compared with results of measurement of mechanical characteristics of skin covers and can, as a first approximation, serve as landmarks for determination of corresponding characteristics for artificial (cynthetic) elastic coatings.

Executed also were direct measurements of vibration of skin covers at different speeds of swimming [16, 25]. Calculations of mechanical characteristics based on modelling approach showed good agreement with just mentioned results. Besides, active oscillation of external covers shows resonant mechanism of their interaction with disturbances of boundary layer.

10. SOME EXPERIMENTAL VERIFICATIONS ON MODELS AND DEVELOPMENT OF ANALOGS OF SKIN COVERS.

Direct measurements of kinematics of dolphin swimming have been carried out [12, 15, 17]. On the basis of processing the cinema frames and direct measurent of dolphin body and fins, predicted were all corresponding parameters on which basis the relations on Fig. 44 were built [17]. Curves 1 and 2 denotes relations for laminar and turbulent boundary layers on flat plate respectively. When dolphin moving with different accelerations the curves mean: 3 - a=0,35÷0,7 m/s^2, 4 - 0,1÷0,3 m/s^2, 5 - 0,0÷0,07 m/s^2, 6 - - (0,08÷0,15) m/s^2, 7 - motion by inertia with put-off engine.

Obtained with quasi-stationary approach the coefficients of dolphins hydrodynamic drag, whose propulsor is considered as working one in the regime of flapping wing (points in double small circles), are in all cases approximately twice as much than those obtained at the same regimes of dolphin swimming, whose propulsor generates thrust by bending-oscillatory movements of all the body (points 3-7).

The bigger (longer) regime of accelezation and the larger body stress the smaller body drag. In this case all organism systems begin operating in the work.

Comparison of drag for dolphin and models is on Fig. 45: 9 - laminar, 10 - transitional and 7 - turbulent flowing around the rigid plate; 8 - drag of rigid body of revolution in turbulent mode; 1 - dolphin drag predicted according to theory of flapping propulsor; 2 - dolphin drag at active braking; 3 - dolphin drag (L=2.2m) when moving on inertia; 4 - numerical calculation of drag of equivalent rigid body; 5 - drag of dead porpoise when towing in basin (dolphin dimensions 1×0,21×0,25 m); 6 - drag of model "Dolphin" with profile of body of revolution NACA-66; 11 and 12 - experiments by Kramer [14, 17, 25].

Tests on analogs of skin covers of dolphins [7] are represented on Fig. 46, 47. Fig.46 shows measurements of oscillations propagation on rigid surface (from the left) and on two types of elastic plates. Fig.47 describes measurements of drag of elastic plates.
Developed constructions of elastic plates which model the skin covers of dolphins [7] are shown on Fig.48.

11. CONCLUSIONS.

Adduced results of hydrobionic investigations as an example of cetaceans with consideration of main hydrobionic principls permit to confirm that there is a complex of adaptations for high-speed marine animals drag reduction.

On the basis of research carried out it is possible to conclude that a number of means of adaptation has been found out which:

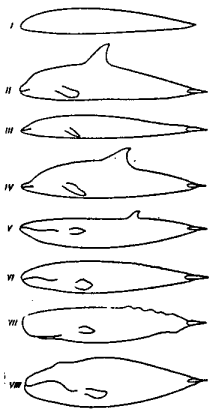
- function separately/simultaneously depending on swimming mode
- interconnect toward achieving higher results, in particular for increase the efficiency and drag reduction
- influence as active control with feedback system
- have been modelled and tested with different extent of approximation to real properties.

In nature all adaptations are interconnected. However for technical applications individual systems optimisation may be used. Peculiarities of body shape and fins shape, of push-motion complex, polymer injection system for high-speed fishes of kinematics motions, also regularities of unstady motion and body oscillations, peculiarities of resonant mechanisms and so on were consider in detail acording to analog plan.

REFERENCES

1. Agarkov, G. B., Babenko, V. V., Ferenets ,Z. I., «On innervation of dolphin skin and skin musculature in connection with hypothesis of flow stabilization in a boundary layer», Problems of Bionics, Proceedings, Moscow, Nauka, 1973, pp 478-483.
2. Agarkov, G. B., Khomenko, B. G., Khadzhinskiy, V. G. «Morphology of dolphins», Kiev, Ukraine, Naukova Dumka, 1974, 167 pp.
3. Babenko, V. V., «Principal characteristics of flexible coatings and similarity criteria», Bionika, 5, 1971, pp 73-76.
4. Babenko, V. V., «Investigation of the elasticity of living dolphins skin», Bionika 13, 1979, pp 43-52.
5. Babenko, V. V., «Some peculiarities of thermal regulation of external covers of water animals», Bionika, 17, 1983, pp 35-39.
6. Babenko, V. V., Gnitetsky, N. A., Kozlov, L. F, «Preliminary results of elastic properties investigation of living dolphins skin», Bionika, 3, 1969, pp 12-19.
7. Babenko, V. V., Kanarsky, M. V., Korobov, V. I., «Boundary layer on elastic plates», Kiev, Ukraine, Naukova dumka, 1993, 264 pp.
8. Babenko, V. V., Nikishova, O. D., «Some hydrodynamic regularities of the skin structure of nautical animals», Bionika, 10, 1976, pp 27-33.
9. Babenko, V. V., Surkina, R. M., «Some hydrodynamic peculiarities of dolphins swimming», Bionika, 3, 1969, pp 19-26.
10. Babenko V. V., Surkina, R. M., «Determination of parameter of oscillatory mass of skin covers for some marine animals», Bionika, 5, 1971, pp 94-98.
11. Bainbridge, R., «The speed of swimming of fish as related to size and to the frequency and amplitude of tail beat», J. Exp. Biol., *1*, 5, 1958.
12. Hertel, H., «Structure, Form and Movement», Biology and Technology, Reinhold Publ. Corp., 1966, 251 pp.
13. Gray, J., «Animal Locomotion», L, Weidenfeld and Nicholson, 1961, 479 pp.
14. Kaian, V. P., «On dolphin drag coefficients», Bionika, 8, 1974, pp 31-35.
15. Kaian, V. P., «On hydrodynamic characteristics of fin-type propulsor of dolphin», Bionika, 13, 1979, pp 9-15.
16. Kidun, S. M., «Investigation of oscillations propagation on dolphin cover», Bionika, 13, 1979, pp 52-58.
17. Kozlow, L. F., «Theoretical biohydrodynamics», Kiev, Ukraine, Vischa Shkola, 1983, 238 pp.
18. Kozlov, L. F., Shakalo, V. M., «On mode of flow in quasi-stationary boundary layer of some cetaceans», Bionika, 14, 1980, pp 74-81.
19. Kozlov, L. F., Shakalo, V. M., Burianova, L. D., Vorobiev, N. N., «On influence of non-steadiness on flow regime in the boundary layer of Black-sea-bottle-nosed dolphin», Bionika, 8, 1974, pp 13-16.
20. Lang, T. G., «Hydrodynamic analysis of dolphin fin profiles», Nature, pp 1110-1111.
21. Lighthill, J., «Mathematical biofluid dynamics», SIAM, Philadelphia Pa, 281 pp.
22. Logvinovich, G. V., «Hydrodynamic of thin flexible body», Bionika, 4, 1970, pp 3-5.
23. Parry, D. A., «The Structure of Whale Blubber, and a Discussion of its Thermal Properties», Quart. J. Microsc. Sc., *90*, 1, 1949, pp 273-279.
24. Pershin, S. V., «Self-adjustement of skin damping and reduction of hydrodynamic drag when active swimming the cetaceans», Bionika, 10, 1976, pp 33-40.
25. Pershin, S. V., «Fundamentals of hydrobionics», Leningrad, UdSSR, Sudostroenie, 1988, 263 pp.
26. Piatetskiy, V. E., Shakalo, V. M., Tsiganiuk, A. I., Sizov, I. I., «Investigation of regime of flowing around the water animals», Bionika, 16, 1982, pp 31-36.
27. Romanenko, E. V., «Theory of fishes and dolphins swimming», Moscow, UdSSR, Nauka, 1986, 148 p.
28. Semenov, N. P., Babenko, V. V., Kaian, V. P., «Experimental investigation of some peculiarities of hydrodynamics of dolphins swimming», Bionika, 8, 1974, pp 23-31.
29. Shpet, N. G., «Shape peculiarities of trunk and tail fin of whales», Bionika, 9, 1975, pp 36-41.
30. Sickmann, J., «Investigation into the movement of swimming animals», ZWDI, *10*, 104, 1962, pp 433-439.
31. Sokolov, V. E., «The structure of skin cover of some cetaceans», Bull. of Moscow Society of Nature investigators, Dep. of biology, *6*, 60, 1955, pp 45-60.
32. Sokolov, V. E. «Morphology and ecology of water mammals», Moscow, UdSSR, Nauka, 1971.
33. Sokolov, V. E., «Skin cover of mammals», Moscow, UdSSR, Nauka, 1973, 487 pp.
34. Surkina, R. M., «On structure and function of skin musculature of dolphins», Bionika, 5, 1971, 81-87.
35. Surkina, R. M., «Location of dermal rolls on the body of common dolphin», Bionika, 5, 1971, pp 81-94.
36. «Swimming and Flying in Nature», 1, N-Y., L., Plenum Press, 1975, 421 pp.
37. Tomilin, A. G., Cetaceans, «Animals of the USSR and border countris», v.9. -Academy of Sc. of USSR Publ. (1957), 756 pp.
38. Wu, T. Y., «Hydromechanics of swimming of fishes and cetaceans», Adv. Appl. Mech., 11, N-Y.,L., 1971, pp 1-63.
39. Yurchenko, N. F., Babenko, V. V. «On modelling the hydrodynamic functions of external covers of water animals», Hydrodynamic questions of bionika, Proceedings, Kiev, Ukraine, Naukova dumka, 1983, pp 37-46.

GEOMETRIC PARAMETERS OF BODY



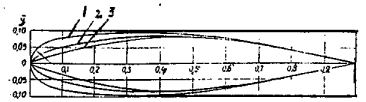


Fig.3 Body of revolution which is equivalent to body of cachalot (1), coalfish whale (2), dolphin (3)



Fig.2 Body shape of cachalot

Fig.1 Vertical longitudinal projections of airplane wing of B – TSAGI series and various representatives of whale type

ENERGETICS

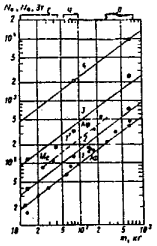


Fig. 6.
Power No of principal (lines 1,1') and Na active (2-4) exchange in dependence of total mass for warm-blooded animals and man

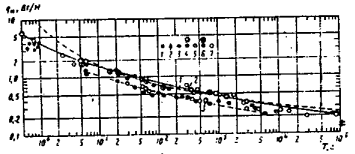


Fig.7. Maximum specific power output on external mechanical work of big warm-blooded hydrobionts as a function of swimming duration

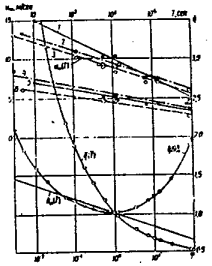


Fig.8
Dependences for whales (1,6) and dolphins (2-5)

SPEEDS OF MOTION (SWIMMING)

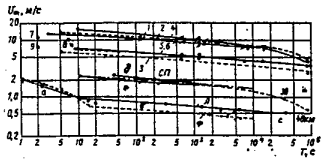


Fig.4 Dependence of absolute maximum speed of cruise swimming of hydrobionts on duration of swimming

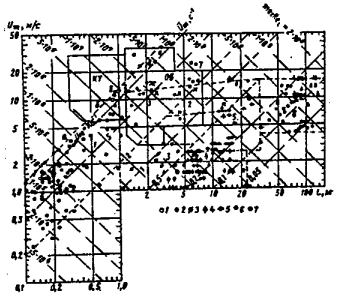
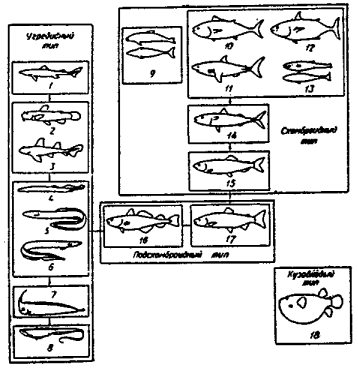


Fig.5 Hydrodynamic parameters of hydrpobiont species and technical objects. Four - parameter diagram

INSTITUTE OF HYDROMECHANICS, KIEV

NON-STEADINNESS OF MOTION



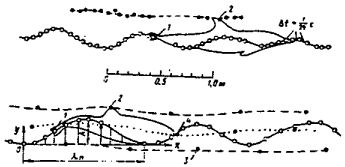


Fig.10 Results of shooting processing while slow swimming the Black-sea-dolphins

Fig.9 Correlation between morphological structure and modes of swimming for water animals

INSTITUTE OF HYDROMECHANICS, KIEV

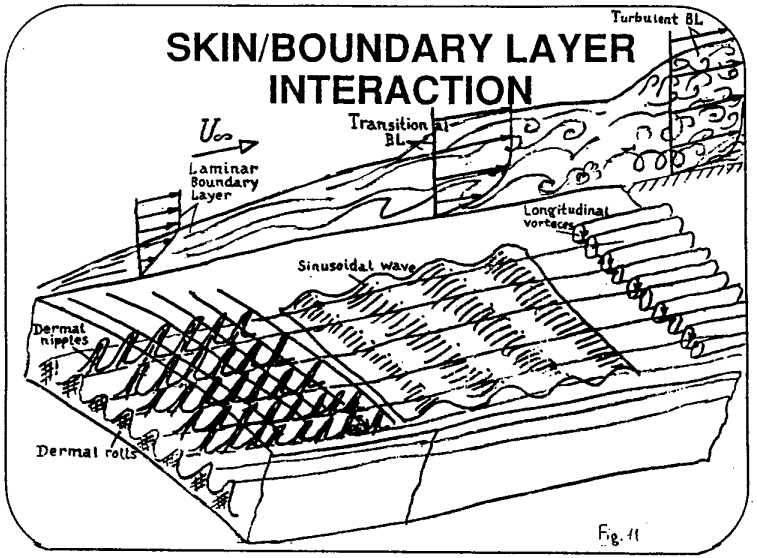


Fig. 11

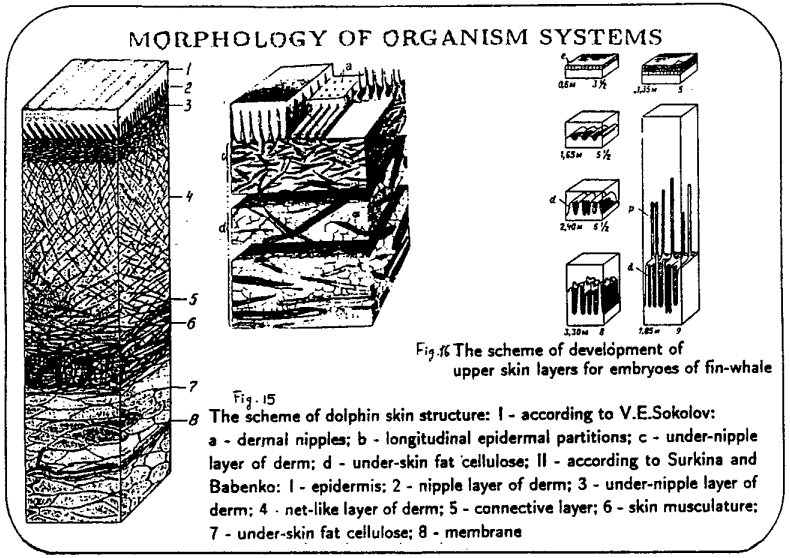


Fig. 15 The scheme of dolphin skin structure: I - according to V.E.Sokolov: a - dermal nipples; b - longitudinal epidermal partitions; c - under-nipple layer of derm; d - under-skin fat cellulose; II - according to Surkina and Babenko: 1 - epidermis; 2 - nipple layer of derm; 3 - under-nipple layer of derm; 4 - net-like layer of derm; 5 - connective layer; 6 - skin musculature; 7 - under-skin fat cellulose; 8 - membrane

Fig. 16 The scheme of development of upper skin layers for embryoes of fin-whale

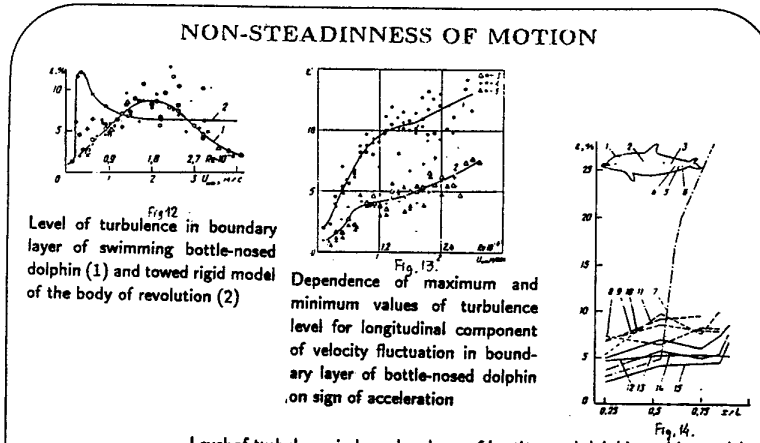


Fig. 12

Level of turbulence in boundary layer of swimming bottle-nosed dolphin (1) and towed rigid model of the body of revolution (2)

Fig. 13.

Dependence of maximum and minimum values of turbulence level for longitudinal component of velocity fluctuation in boundary layer of bottle-nosed dolphin on sign of acceleration

Fig. 14.

Level of turbulence in boundary layer of bottle-nosed dolphin and its model: 1–6 points of the animal body; 7 – experimental data for dolphin model at v=4.7 m/s; 8–11 - data for passive mode of the dolphin swimming

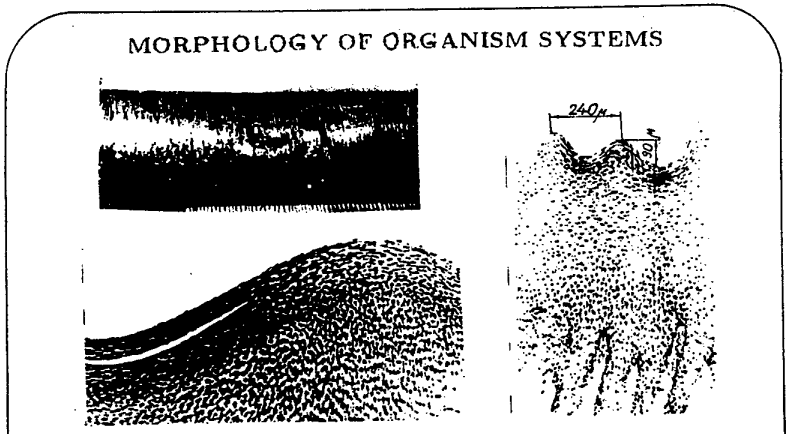


Fig. 17 Transverse micro-wrinkles on the skin surface

MORPHOLOGY OF ORGANISM SYSTEMS

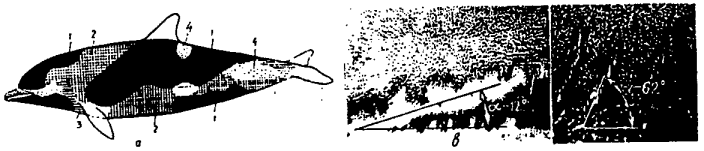


Fig. 18 The scheme of distribution (a) and angles of inclination (b) of dermal nipples in the dolphin skin:
$1 - \alpha = 10 - 25^0$; $2 - \alpha = 25 - 40^0$;
$3 - \alpha = 40 - 55^0$; $4 - \alpha = 55 - 80^0$



Fig. 19 Direction of dermal rollers along the body

MORPHOLOGY OF ORGANISM SYSTEMS

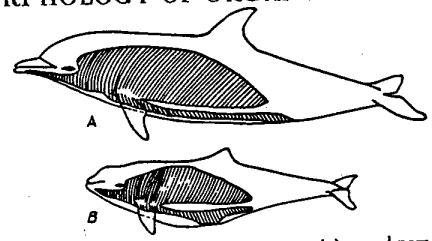


Fig. 20 Direction of fibres of skin muscle for common dolphin (a) and porpoise (b)

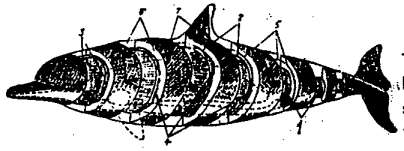


Fig. 21
The scheme of common dolphin skin structure:
1 - sceleton musculature; 2 - ano-neurosis of sceleton musculature which are wedged into the skin thickness; 3 - sub-skin fat celulose; 4 - muscular portion of skin musculature; 5 - ano-neurosis of skin muscle; 6 - derm; 7 - epidermis

MORPHOLOGY OF ORGANISM SYSTEMS

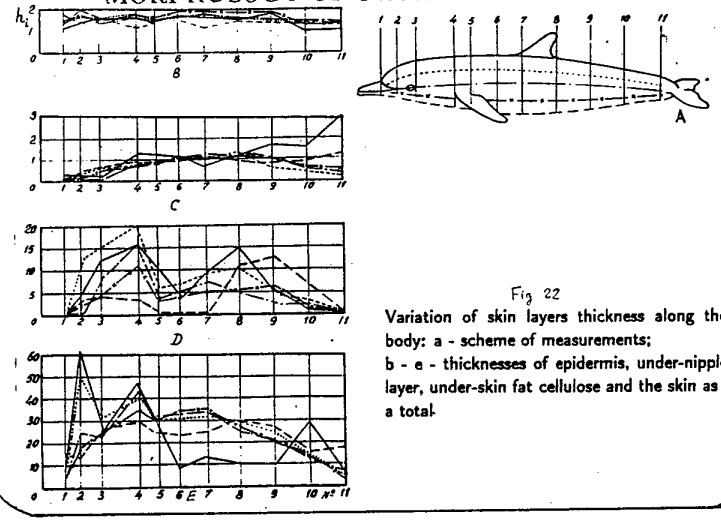


Fig 22
Variation of skin layers thickness along the body: a - scheme of measurements;
b - e - thicknesses of epidermis, under-nipple layer, under-skin fat cellulose and the skin as a total

MORPHOLOGY OF ORGANISM SYSTEMS

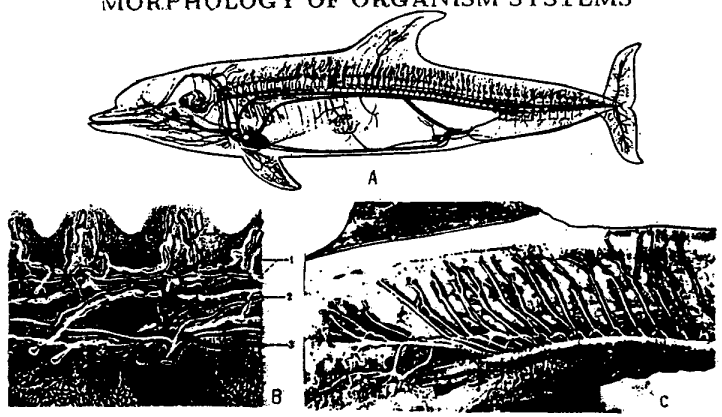
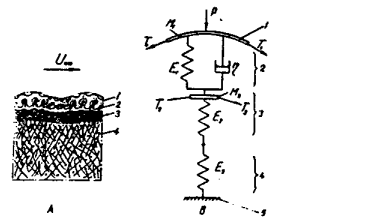


Fig. 23. The scheme of circulatory system (arterial and venose) (A), lymphatic capillars of skin (according to V.N.Nadezdin) (B): 1 - lymphatic capillars; 2 - veins; 3 - arteries, and Segment-by-segment innervation of epaxial muscles and skin of dorsal area (C)

MEASUREMENT OF SOME MECHANICAL CHARACTERISTICS OF DOLPHIN SKIN



$$(T_1+T_2)\frac{\partial^2 y}{\partial t^2}-(M_1+M_2)\frac{\partial^2 y}{\partial t^2}-\eta\frac{\partial y}{\partial t}-(E_1'+E_2'+E_3')\varepsilon_y=P-\sigma$$

Fig. 24

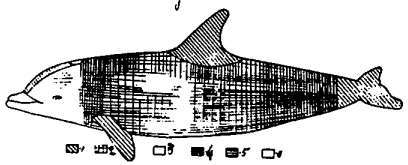


Fig. 25

Topography of skin elasticity for common dolphin: 1 - 1.9 g/mm^2; 2 - 1.8 ÷ 1.85; 3 - 1.75 ÷ 1.77; 4 - 1.85 ÷ 1.9; 5 - 1.77 ÷ 1.8; 6 - not measured

MEASUREMENT OF SOME MECHANICAL CHARACTERISTICS OF DOLPHIN SKIN

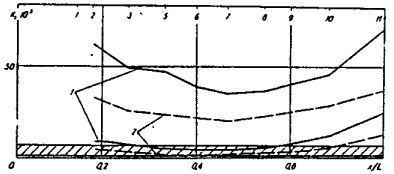
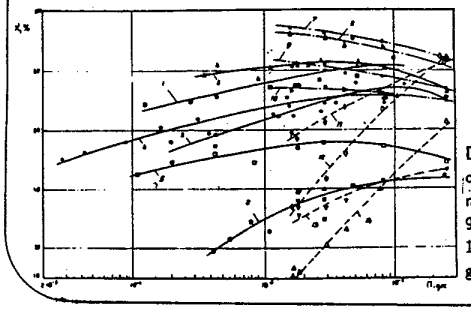


Fig. 28

Distribution of parameter of elasticity along the body of common dolphin (1) and bottle-nosed dolphin (2)



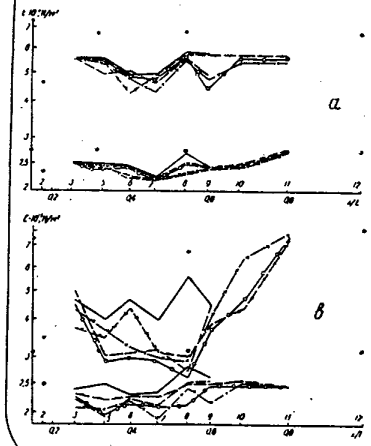
$$K=(1-h/h_0)\cdot 100$$

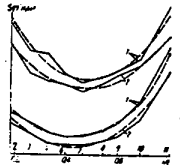
$$\Pi=mgh_0$$

Fig. 29

Dependence of the coefficient of damping on the energy of impact: 1-6 - elastic materials; 7,8 - dolphins in health; 9 - sick dolphin; 10 - dead dolphin; 11 - non-secured stel strip; 12 - line silicate glass; 13 - wood; 14 - organic glass

MEASUREMENT OF SOME MECHANICAL CHARACTERISTICS OF DOLPHIN SKIN





$$1-S\cdot 10^{-7}=67\frac{x}{L}\left(\frac{x}{L}-0{,}98\right)+23;$$

$$2-S\cdot 10^{-7}=48{,}7\frac{x}{L}\left(\frac{x}{L}-0{,}94\right)+17{,}5;$$

$$1-S\cdot 10^{-7}=49{,}4\frac{x}{L}\left(\frac{x}{L}-0{,}84\right)+10{,}5;$$

$$2-S\cdot 10^{-7}=53\frac{x}{L}\left(\frac{x}{L}-0{,}84\right)+10.$$

Fig. 27

Distribution of skin rigidity for common dolphin (a) and bottle-nosed dolphin (b) at different speeds of swimming

Fig. 26

Distribution of skin elasticity along the body of common dolphin (a) and bottle-nosed dolphin at (b) different speeds of swimming

INSTITUTE OF HYDROMECHANICS, KIEV

SKIN/BOUNDARY LAYER INTERACTION

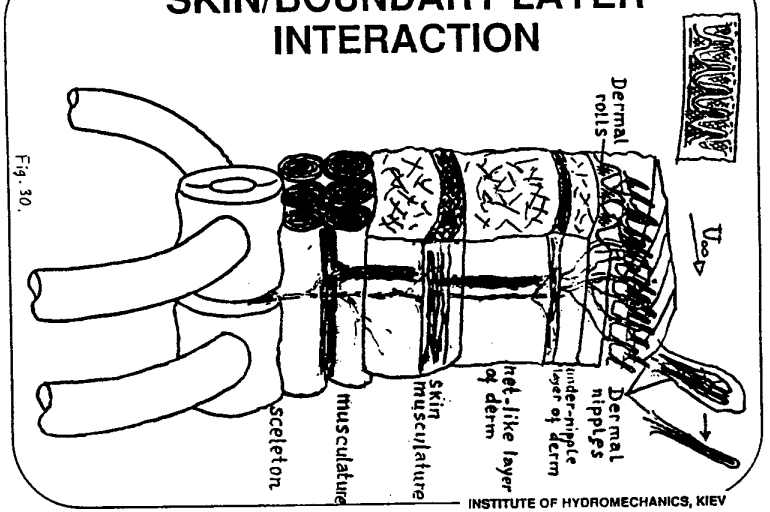
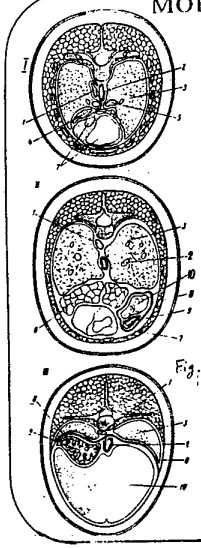


Fig. 30.

INSTITUTE OF HYDROMECHANICS, KIEV

MORPHOLOGY OF ORGANISM SYSTEMS



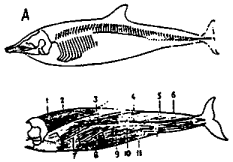


Fig. 31 The scheme of dolphin sceleton (a) and motor musculature (b): 2 – longest muscle; 3 – loin-rib-muscle; 4 – dorsal muscle; 5 – surface muscle; 6 – deep muscle

Fig. 32 Cross-sections of dolphin (Phocoena phocoena) body: 1 - 33 cm from nose tip; II - 37 cm III - 42 cm. I - aorta; 2 - acsophagus; 3 - lungs; 4 - auricle; 5 - pulmonary artery; 6 - lymphatic node; 7 - heart ventricles; 8 - diaphragm; 9 - stomach; 10 - liver

INTERACTION OF BIOLOGIC SYSTEMS

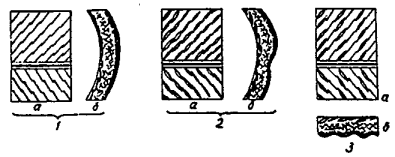


Fig. 34 The scheme of the body shape change due to skin musculature: a - side view; b - cross section

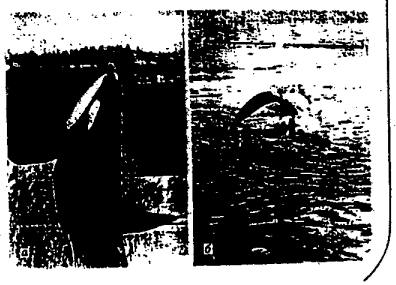


Fig. 33 Trained killer-whales in oceanarium: a - jump for ball (all fins are straightened, extremely elastic); b - lies in shallow-water (dorsal fin is relaxed).

INTERACTION OF BIOLOGIC SYSTEMS

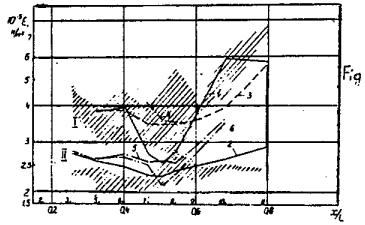


Fig. 35 Regulation of skin elasticity for four bottle-nosed dolphins: I - measurements in the first time, II - measurements after training

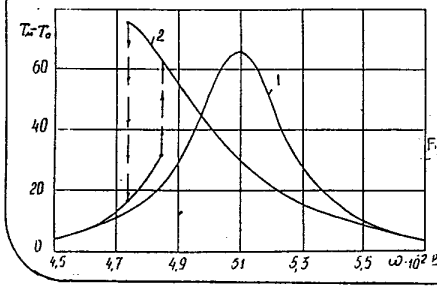


Fig. 36 Variation of increment in maximum temperature as a function of oscillation frequency of conic panel of rubber IRP-1347: 1 - linear, 2 - non-linear task

INTERACTION OF BIOLOGIC SYSTEMS

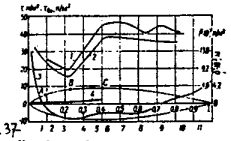


Fig. 37 Distribution of hydrodynamic characteristics along the body of revolution which is geometrically similar to dolphin body

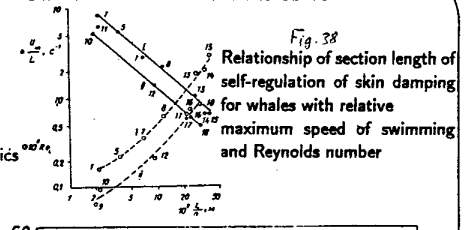


Fig. 38 Relationship of section length of self-regulation of skin damping for whales with relative maximum speed of swimming and Reynolds number

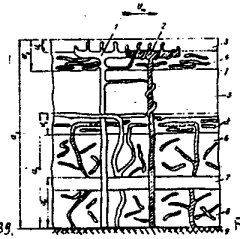


Fig. 39 The scheme of blood circulation in dolphin skin



Fig. 40 Specific heat flux through the unit of skin length for common dolphin and bottle-nosed dolphin

INTERACTION OF BIOLOGIC SYSTEMS

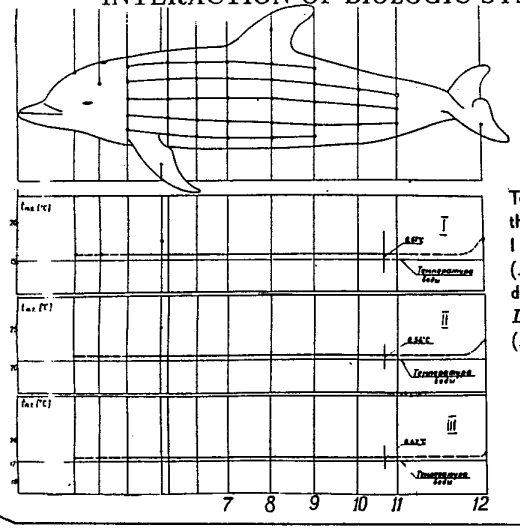


Fig.41.
Temperature distribution on the surface of dolphin skin: I - common dolphin ($L = 1,3m$), II - bottle-nosed dolphin ($L_1 = 1,7m$; $L_2 = 1,6m$); III - porpoise ($L_1 = 0,7m$; $L_2 = 0,8m$)

NON-STEADINNESS OF MOTION

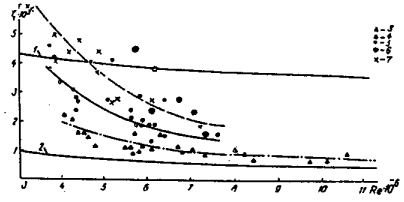


Fig.44 Coefficient of hydrodynamic drag of dolphin, Reynolds number and average acceleration of motion

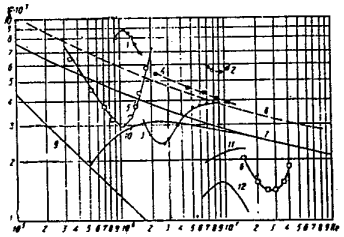


Fig.45 Dependence of drag coefficients for dolphins and models on Reynolds number

INTERACTION OF BIOLOGIC SYSTEMS



Fig.42 Change of blood-filling of dermal nipples



Fig.43 The scheme of structure of valves of lymphatic vessels

SOME EXPERIMENTAL VERIFICATIONS ON MODELS AND DEVELOPMENT OF ANALOGS

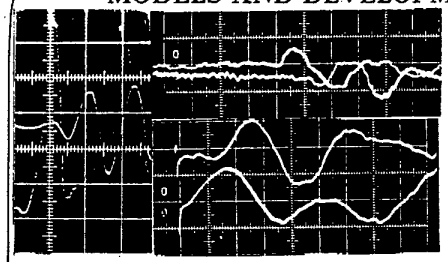


Fig.46

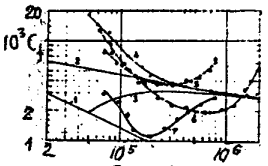


Fig.47.



Fig.48

TURBULENT BOUNDARY LAYER OVER A COMPLIANT SURFACE.

Voropaev G.A., Rozumniuk N.V.
Institute of Hydromechanics, National Academy of Sciences of Ukraine
8/4 Zheliabov Str., Kiev, 252057, Ukraine

Summary.

Numerical results of modeling of turbulent boundary layers over deformable viscoelastic surfaces are presented. A qualitative interpretation of friction drag reduction on a deformable surface is given. Quantitative characteristics of interaction of a turbulent boundary layer with the deformable surface at various magnitudes of parameters describing viscoelastic properties of the material are obtained.

1. Introduction.

During the time after Kramer's publication [28], a large number of both experimental and theoretic works have been performed to investigate a back influence of the surface which is deformed by flow pulsations on the structure of laminar or turbulent boundary layer. As a rule, first experiments [1,28] investigated how the integral characteristics of bodies with polymer coatings differ from those on rigid bodies of the same shape. Friction drag reduction was attributed to delaying transition from laminar boundary layer to turbulent one.

First theoretic works of Benjamin [13], Landahl [29], Nonweiler [35], Korotkin [9] was also devoted to the laminar boundary layer stability on a deforming surface. But these results stated new questions rather then asked the question what is possible interaction mechanism of the deforming surface with flow disturbances. It was shown there, that delaying transition is possible on a deforming surface, but the coating parameters were not in accordance completely with the Kramer's coating ideology. At the same time, the experiments of Kozlov, Babenko [7] on the laminar boundary layer transition on viscoelastic coating verified the transition point displacement towards high Reynolds numbers and, that is the most important, showed that the disturbance amplitude enlarging rate decreases as compared with that for laminar boundary layer on rigid smooth surface. But even qualitative confirmation of some insignificant delaying of transition could not explain quantitative friction drag reduction at high Reynolds numbers.

The experiments of Blick [14], Lissaman [33], Hansen & Hunston [24], Babenko [2], Semenov[11] investigated the internal structure of the turbulent boundary layer together with friction drag. Longitudinal velocity U profiles and the Reynolds stress $-\overline{uv}, \overline{u^2}$ were measured in different section of the boundary layer on a compliant surface. Blick [14], Lissaman [33], Babenko [2], Semenov [11] reported friction drag coefficient reduction that correlates with turbulent pulsation intensity reduction and viscous sublayer thickening. Logarithmic velocity profiles for streamlining over different surfaces have the same slope in the "logarithmic region" that means the Karman's constant κ is the same for different boundary layers. There was not detect any noticeable change of turbulence anisotropy in the near-wall region of the boundary layer. Some anomalous behavior of $u_*, -\overline{uv}, \overline{u^2}$ obtained by Blick was corrected by Lissaman. But these articles did not contain any information about the deforming surface behavior during interaction with flow, and therefore the conclusions could not contain any recommendations how to choose the coating material a priori, except those parameters which was suggested by Kramer.

Further, both the turbulent flow characteristics and spatial and temporal quantitative characteristics of the streamlined surface displacement amplitudes were studied by Bushnel & Hefner & Ash (BHA) [15], Gad-el-Hak [22,23], Lee & Fisher & Schwarz (LFS) [32]. The coating material was chosen based on theoretic evaluation of the coating reaction to fluctuate load which are equivalent to those referred by Duncan [19] and Buckingham & Hall & Chun [16]. In the USSR, analogic evaluations were done independently by Voropaev [3].

It must be noted, that the BHA's and Gad-el-Hak's conclusions differ essentially from LFS's conclusions. Gad-el-Hak proceeding from his researches supported the hypothesis suggested by Bushnel. The essence is that the coating is capable to friction drag reduction, if short running waves of large amplitude appear on its surface, i.e. kinematic interaction of the boundary layer disturbances with the deforming surface takes place. It is only possible for low-dissipate coating material at shear modulus $G<\rho_s U_o^2$, where ρ_s is the material density, U_0 is the flow speed, i.e. for such the coating parameters at which inherent oscillations of the coating will show themselves.

LFS obtained friction drag reduction at $G>\rho_s U_o^2$ and small (much more less than the viscous sublayer thickness) amplitudes of the surface oscillation, that means absorbing nature of the interaction mechanism.

Paper presented at an AGARD FDP Workshop on "High Speed Body Motion in Water", held in Kiev, Ukraine, 1-3 September 1997, and published in R-827.

Last 10-15 years, the boundary layer stability and initial stage of the disturbance evolution in laminar boundary layer at varied boundary conditions were analyzed by Carpenter [18,19], Kirejko [6], Yeo [40,41], Thomas [38] using both linear and quasi-linear treatment.

Theoretic evaluations of a possible dissipative mechanism of interaction of a turbulent boundary layer with the absorbing coating at $G>\rho_* U_\infty^2$ is suggested in [8], based on the k-ε model for the turbulent boundary layer and a flow boundary conditions at the partition boundary of mediums.

2. Theoretic model.

Usually when a turbulent boundary layer characteristics are studied, they are separated rather relatively in mean and fluctuate ones. The investigations of these both characteristics are conducted by means of direct physical measurements, as well as simulation of such flows on basis of elaboration and solution of closed systems of equations and boundary conditions.

Determination of dependencies of turbulent characteristics on dimensionless flow parameters (Re, Fr, Pr,Gr), as well as a type and quality of the streamlined surface permits to systematize experimental data and formulate laws of these characteristics or their combinations variations, that provide a possibility to plan new experiments.

This process is often called numerical experiment. If the model describes adequately a turbulent flow in varying conditions, then results of the numerical experiment often compete with those of expensive direct physical experiment

The problem of interaction of a turbulent flow with the deformable surface of viscous-elastic medium includes the system of differential equations for parameters describing movement of fluid and oscillations of viscous-elastic medium under action of disturbances in the flow over some undisturbed surface, as well as boundary conditions for displacements or velocities and forces on partition boundary of two mediums.

2.1. To describe a movement of viscous, homogeneous and incompressible liquid, the following equations are used:

$$\frac{\partial \vec{U}}{\partial t}+(\vec{U}\cdot\mathrm{grad})\vec{U}=-\frac{1}{\rho}\mathrm{grad}\ P-\nu\cdot\mathrm{rot}\cdot\mathrm{rot}\ \vec{U};$$

$$\mathrm{div}\ \vec{U}=0,$$

and for viscoelastic medium:

$$\frac{\partial^2\vec{\xi}}{\partial t^2}=L(\vec{\xi}),$$

where $L(\vec{\xi})$ is a generalized viscoelastic operator.

Though it is impossible to solve this classical system of equations at large Re numbers exceeding some threshold Re values, even at a simplest boundary conditions.

Therefore it is necessary to design a model of turbulence, i.e. a system of equations describing adequately turbulent flows at fixed sets of parameters characterizing such flows.

Nowadays the Reynolds stress transfer model named after the Launder-Reece-Rodi model [30] is the most informative turbulence model. It permits to obtain as mean velocity profile as the Reynolds stress components, and to conclude about energy balance components at each points of flow, as well. Application of this model to the boundary-layer problems has required to introduce the nearwall functions and to modify the model equation for dissipation velocity, that permits the no-slip condition for the Reynolds stress to be satisfied.

In a boundary-layer approach, the model system of equations is the following [5,39]:

$$U\frac{\partial U}{\partial x}+V\frac{\partial U}{\partial y}=\nu\frac{\partial^2 U}{\partial y^2}-\frac{\partial}{\partial y}\overline{u'v'};$$

$$\frac{\partial U}{\partial x}+\frac{\partial V}{\partial y}=0;\ (1)$$

$$U\frac{\partial}{\partial x}\left(\frac{\overline{u'^2}}{2}\right)+V\frac{\partial}{\partial y}\left(\frac{\overline{u'^2}}{2}\right)=\frac{1}{2}P_{11}-\Pi_{11}f_n+\nu\frac{\partial^2}{\partial y^2}\left(\frac{\overline{u'^2}}{2}\right)+\frac{\partial}{\partial y}\left(2\varepsilon_\tau\frac{\partial}{\partial y}\left(\frac{\overline{u'^2}}{2}\right)\right)-\varepsilon_{11};$$

$$U\frac{\partial}{\partial x}\left(\frac{\overline{v'^2}}{2}\right)+V\frac{\partial}{\partial y}\left(\frac{\overline{v'^2}}{2}\right)=\frac{1}{2}P_{22}-\Pi_{22}f_n+\nu\frac{\partial^2}{\partial y^2}\left(\frac{\overline{v'^2}}{2}\right)+\frac{\partial}{\partial y}\left(6\varepsilon_\tau\frac{\partial}{\partial y}\left(\frac{\overline{v'^2}}{2}\right)\right)-\varepsilon_{22};$$

$$U\frac{\partial}{\partial x}\left(\frac{\overline{w'^2}}{2}\right)+V\frac{\partial}{\partial y}\left(\frac{\overline{w'^2}}{2}\right)=\frac{1}{2}P_{33}-\Pi_{33}f_n+\nu\frac{\partial^2}{\partial y^2}\left(\frac{\overline{w'^2}}{2}\right)+\frac{\partial}{\partial y}\left(2\varepsilon_\tau\frac{\partial}{\partial y}\left(\frac{\overline{w'^2}}{2}\right)\right)-\varepsilon_{33};$$

$$U\frac{\partial}{\partial x}\left(\overline{u'v'}\right)+V\frac{\partial}{\partial y}\left(\overline{u'v'}\right)=P_{12}-\Pi_{12}f_n+\nu\frac{\partial^2}{\partial y^2}\left(\overline{u'v'}\right)+\frac{\partial}{\partial y}\left(4\varepsilon_\tau\frac{\partial}{\partial y}\left(\overline{u'v'}\right)\right)-\varepsilon_{12};$$

$$U\frac{\partial\varepsilon}{\partial x}+V\frac{\partial\varepsilon}{\partial y}=C_{\varepsilon_1}f_1\frac{\varepsilon}{k}P_\Sigma-C_{\varepsilon_2}f_2\frac{\varepsilon}{k}\left[\varepsilon-2\nu\left(\frac{\partial k^{1/2}}{\partial y}\right)^2\right]+\frac{\partial}{\partial y}\left(2\varepsilon_\tau\frac{\partial\varepsilon}{\partial y}\right)+\nu\frac{\partial^2\varepsilon}{\partial y^2},$$

where P_{ij} are components of production tensor, Π_{ij} are components of energy redistribution tensor:

$$P_{11} = -2\overline{u'^2}\frac{\partial U}{\partial x} - 2\overline{u'v'}\frac{\partial U}{\partial y} \approx -2\overline{u'v'}\frac{\partial U}{\partial y};$$

$$P_{12} = -\overline{u'^2}\frac{\partial V}{\partial x} - \overline{v'^2}\frac{\partial U}{\partial y} \approx -\overline{v'^2}\frac{\partial U}{\partial y};$$

$$D_{11} = -2\overline{u'^2}\frac{\partial U}{\partial x} - 2\overline{u'v'}\frac{\partial V}{\partial x} \approx 0;$$

$$D_{22} = -2\overline{u'v'}\frac{\partial U}{\partial y} - 2\overline{v'^2}\frac{\partial V}{\partial y} \approx -2\overline{u'v'}\frac{\partial U}{\partial y};$$

$$D_{33} = 0;$$

$$D_{12} = -\overline{u'^2}\frac{\partial U}{\partial y} - \overline{v'^2}\frac{\partial V}{\partial x} \approx -\overline{u'^2}\frac{\partial U}{\partial y};$$

$$P_\Sigma = \frac{1}{2}\left(P_{11} + P_{22} + P_{33}\right) = -\overline{u'v'}\frac{\partial U}{\partial y};$$

$$k = \frac{1}{2}\left(\overline{u'^2} + \overline{v'^2} + \overline{w'^2}\right).$$

$$\Pi_{ii} = C_1\frac{\varepsilon}{k}\left(\frac{\overline{u_i'^2}}{2} - \frac{1}{3}k\right) + C_2\left(\frac{1}{2}P_{ii} - \frac{1}{3}P_\Sigma\right) + \pi'_{ii,1} + \pi'_{ii,2} + \pi'_{ii,3}; \quad (2)$$

$$\Pi_{12} = C_1\frac{\varepsilon}{k}\overline{u'v'} + C_2P_{12} + \pi'_{12,1} + \pi'_{12,2} + \pi'_{12,3};$$

$$\varepsilon_{11} + \varepsilon_{22} + \varepsilon_{33} = \varepsilon;$$

$$\Pi_{11} + \Pi_{22} + \Pi_{33} = 0;$$

$$\pi'_{ij,1} = -C_1'\frac{\varepsilon}{k}\left(\overline{v'^2}\delta_{ij} - \frac{3}{2}\left(\overline{v'u_i'}\delta_{j2} + \overline{v'u_j'}\delta_{i2}\right)\right)f\left(\frac{\ell}{y}\right);$$

$$\pi'_{ij,2} = -C_2'\left(\frac{P_{ij}}{2} - \frac{1}{3}P_\Sigma\delta_{ij}\right)f\left(\frac{\ell}{y}\right);$$

$$\pi'_{ij,3} = -C_3'\left(\frac{1}{2}D_{ij} - \frac{1}{3}P_\Sigma\delta_{ij}\right)f\left(\frac{\ell}{y}\right),$$

where $\pi'_{ij,1}$, $\pi'_{ij,2}$ are the additional redistribution tensors [30] appeared owing to the wall influence and satisfying the condition:

$$\pi'_{ii,j} = 0.$$

The wall influence function has been written as:

$$f\left(\frac{\ell}{y}\right) = \frac{R_t}{R_k}\left(1 + \sqrt{1 + \frac{A_\tau}{R_t}}\right)$$

The nearwall functions f_n, f_1, f_2 are:

$$f_n = \left[1 - \exp(-a_\mu R_k)\right]\sqrt{1 + \frac{a_\tau}{R_t}};$$

$$f_1 = 1 + 0.8e^{-R_t}; \qquad f_2 = 1 - 0.2e^{-R_t^2},$$

where $R_k = \frac{k^{1/2}y}{\nu}$; $R_t = \frac{k^2}{\nu\varepsilon}$, A_τ, a_τ, a_μ are the model constants.

The kinematic coefficient of turbulent diffusion is assumed to be equal to: $\varepsilon_\tau = C_\tau\overline{v'^2}k/\varepsilon$; ($C_\tau = 0.12$ and in the equation for dissipation velocity $C_t = 0.15$).

The dissipation velocity tensor is [31]:

$$\varepsilon_{ij} = f_s\frac{\overline{u_iu_j}}{2k}\varepsilon + (1 - f_s)\frac{1}{3}\delta_{ij}\varepsilon,$$

where $f_s = 1/\left(1 + 0.06R_t\right)$.

Assuming the turbulent flow to be homogeneous statistically over a deforming surface (without resonance effects of eigen frequencies of the surface) the application of Reynolds's averaging to the problem of streamlining over a deforming surface results in the analogical system of equations with the boundary conditions for Reynolds stresses and turbulent diffusion components on the deforming surface:

$$-\overline{u_iu_j}\Big|_s = f_{ij}; \quad -\overline{u_ip}\Big|_s = Y_i,$$

and usual conditions of undisturbed flow far from the surface.

2.2. Movement of incompressible viscoelastic medium movement can be described by the system of linearized equations of motion:

$$\rho\frac{\partial^2\xi_i}{\partial t^2} = \sigma_{ij,j} \qquad (3)$$

with the dynamic boundary conditions imposed at undisturbed partition boundary of two mediums:

$$\sigma_{22}\Big|_0 = -p'; \quad \sigma_{21}\Big|_0 = \tau,$$

where p', τ are pressure and shear stress fluctuations on the surface.

For isotropic incompressible viscoelastic mediums, the shear modulus is determined by the decay function which may be simulated by the exponential function:

$$\mu(t) = \sum_{j=0}^{N}\mu_j\,e^{-t/\tau_i}.$$

In a case of harmonic load, it is possible to obtain a frequency dependence for the shear modulus:

$$\mu(\omega) = \mu_r(\omega) + i\mu_i(\omega)$$

$$= \mu_0 + \sum_{j=1}^{N}\mu_j\left[\frac{(\omega\tau_j)^2}{1 + (\omega\tau_j)^2} + i\frac{\omega\tau_j}{1 + (\omega\tau_j)^2}\right]$$

Assuming the volume modulus K to be independent on time ($K=\lambda+2/3\mu$), we can also obtain an expression for $\lambda(\omega)$.

Thus we can use a convinced expression for stress σ_{ij}:

$$\sigma_{ij} = \tilde{\lambda}(\omega)\theta\delta_{ij} + 2\tilde{\mu}(\omega)\varepsilon_{ij},$$

where $\theta = \varepsilon_{ii}$, $\varepsilon_{ij} = \frac{1}{2}\left(\frac{\partial\xi_i}{\partial x_j} + \frac{\partial\xi_j}{\partial x_i}\right)$.

Eigen values analysis of viscoelastic coating [8] permits to select such range of phase velocities of the load at which the eigen frequencies do not show itself and the coating response to the boundary layer

disturbances is homogeneous in whole range of frequencies. Proceeding from this conditions, the principle of nonresonance interaction of a boundary layer and a viscoelastic coating has been formulated. Once we determined the amplitudes of surface displacement and dissipation velocity inside of coating at a unit load, it is possible to define boundary conditions for characteristics of the nearwall turbulence at arbitrary Reynolds number.

In absence of resonance ($U_0 < \sqrt{\mu_0/\rho}$), the averaging by the all wave numbers per unit time does not cause any problems and it is possible to obtain linearized values of Reynolds stress carried to the undisturbed surface:

$$-\overline{u_1 u_2} = -\frac{1}{2}\omega_e^2 |\xi_2||\xi_1|\cos(\varphi_2 - \varphi_1);$$

$$\overline{u_1^2} = \frac{1}{2}\omega_e^2\left(|\xi_1|^2 + 2\frac{U'}{\omega_e}|\xi_1||\xi_2|\sin(\varphi_2 - \varphi_1) + \frac{U'^2}{\omega_e^2}|\xi_2|^2\right);$$

$$\overline{u_2^2} = \frac{1}{2}\omega_e^2|\xi_2|^2;$$

$$\overline{u_3^2} = \frac{1}{2}\omega_e^2|\xi_1|^2\tan^2\theta,$$

where $\omega_e = \frac{U_0}{\delta}$; $U' = \frac{u_*^2}{\nu}$; $\theta = \arctan\frac{u_{3max}}{u_{1max}}$, and the amplitude of the surface displacement is determined using the calculated values of the function $\beta_i(\omega)$ (normalized amplitudes at the unit load) and the pressure fluctuation intensity at the coating surface:

$$\xi_i = H\beta_i(\omega)\frac{p'}{|\mu|} = H\beta_i(\omega)\frac{\rho K_p U_0^2}{|\mu|}\tilde{u}_*^2,$$

where H is the coating thickness, u_* is dynamic velocity.

Then

$$\overline{u_1^2} = \frac{1}{2}\left(\frac{H}{\delta}\right)^2\left(C_{k1} + \tilde{u}_* Re_* C_{k2}\right)^2\tilde{u}_*^4;$$

$$\overline{u_2^2} = \frac{1}{2}\left(\frac{H}{\delta}\right)^2 C_{k2}^2\tilde{u}_*^4; \qquad (4)$$

$$\overline{u_3^2} = \frac{1}{2}\left(\frac{H}{\delta}\right)^2 C_{k1}^2\tilde{u}_*^4\tan^2\theta;$$

$$-\overline{u_1 u_2} = 0,$$

where $C_{ki} = K_p\beta_i(\omega)\frac{\rho U_\infty^2}{|\mu|}$, $Re_* = \frac{u_*\delta}{\nu}$; K_p is Kraichnan's parameter, δ is local boundary layer thickness.

Taking into account that we dealt with one-mode approach the stresses are determined by energy-carrying frequency $\omega_e = U_0/\delta$, dynamic frequency of flow $\omega_b = u_*^2/\nu$, the amplitudes $\xi_{1,2}$ and do not depend practically on phase shift between them because φ_2-$\varphi_1 \approx \pi/2$ for isotropic materials of viscoelastic layer. Therefore regularly oscillating surface does not generate the Reynolds shear stresses on the surface, i.e. $-\overline{u_1 u_2} = 0$, or generated shear stresses became to be negative under oscillations decaying in time.

Thus, assuming the surface oscillations to be regular we qualify a possible friction drag reduction. Zero values of the shear stresses permit to assume that the turbulent viscosity coefficient in the nearwall layer is the same on a deforming surface in comparison with a rigid smooth one.

While oscillating, the viscoelastic coating absorbs fluctuate energy of the flow, where dissipation velocity is determined by diffusive flux of fluctuate energy through the boundary, that is equal to the Poiting's vector $\overline{p'u_2}$. On the surface of an absorbing layer, $\overline{p'u_2} \neq 0$, while at ideal elastic surface or rigid one, $\overline{p'u_2} = 0$, and consequently, the coefficient of turbulent diffusion in a turbulent boundary layer on the absorbing surface is not equal to zero:

$$-\overline{u_2 p'} = -\frac{\overline{u_2 p'}}{\rho U_\infty^3} = \frac{1}{4}\frac{H}{\delta}\frac{\beta_2(\omega)\rho U_\infty^2}{|\mu(\omega)|}K_p^2\gamma(\omega)\tilde{u}_*^4$$

$$= \frac{1}{4}\frac{H}{\delta}C_{k3}\tilde{u}_*^4; \qquad (5)$$

$$\tilde{\varepsilon}_q = -\frac{\overline{u_2 p'}}{\frac{\partial k}{\partial n}} = \frac{1}{4}C_{k3}\frac{\tilde{u}_*^3\Delta_{max}}{k_{max} - k_q},$$

where

$C_{k3} = K_p C_{k2}\gamma(\omega)$, $\Delta_{max} = \frac{y_{max}^+}{Re_*}$, $y^+ = yu_*/\nu$, k_q is energy of oscillating surface, and consequently, dissipation velocity on the boundary is:

$$\tilde{\varepsilon} = \frac{\partial}{\partial\tilde{n}}\left[\left(\frac{1}{Re} + \tilde{\varepsilon}_q\right)\frac{\partial\tilde{k}}{\partial\tilde{n}}\right].$$

Thus, boundary conditions may be characterized by three parameters: C_{k1} and C_{k2} are responsible for additional generation of turbulence energy for account of nonzero Reynolds stresses on the boundary; C_{k3} is responsible for additional sink of fluctuate energy from turbulent boundary layer into the coating. It is more conveniently to use in calculations the generated coefficient $Cd_i = C_{k_i}H/\delta\tilde{u}_*$, which connects dynamic velocity of the flow with generated stresses.

3. Calculation results.

The boundary problem (1)-(5) has been solved by finite difference technique on the 5-dot template of nonuniform grid [10].

Calculation results for local and integral characteristics of turbulent boundary layer on a rigid smooth surface are shown in Fig.2, as well as LFS's

results at corresponded Reynolds numbers based on the momentum thickness (+ - Re_{**}=897, * - Re_{**}=1349, ◊ - Re_{**}=1952, × - Re_{**}=2347). Integral drag coefficient calculated along the plate length is represented in Fig.2e in comparison with two empirical curves which approximate a great number of experimental data mentioned in [32]. All this results were obtained at the model constants written in the Fig 2.

The results of numerical experiments for streamlining over the plate at fixed Re number are shown in Figs.2-9. There were varied the parameter Cd_2 describing additional generation of turbulent stress on account of normal amplitudes of the surface oscillations, and Cd_3 describing intensity of absorption of fluctuate energy. The parameters vary in limits $Cd_2 \sim (0 \div 3 \cdot 10^{-3})$ and $Cd_3 \sim 0 \div 1$.

Calculation results for boundary layer thickness, displacement thickness and momentum thickness along the plate are shown in Fig.3a,3b. When intensity increases, boundary layer thickness grows more fast on the oscillating surface and more slowly on absorbing one, than that on the rigid smooth surface. Friction drag of the plate increases on the oscillating surface in comparison with that on rigid smooth one by $\delta^{**}/\delta_0^{**} - 1 = 0.05$. Drag reduction by 11% has been obtained on the absorbing surface that coincides with the results of [32].

Curves of drag coefficient variation along the plates are shown in Fig.4. The friction drag coefficient increases at additional generation of turbulence and decreases at absorption of turbulence energy. But when insignificant additional generation of turbulence energy occurs ($Cd_2 = 1 \cdot 10^{-3}$) we can only observe influence of the oscillating surface on the beginning part of the plate where the boundary layer thickness is small and viscous sublayer is thin. When the boundary layer thickness (viscous sublayer thickness) increases, the dynamic roughness does bring a noticeable change in the integral result. Further development of the boundary layer is similar to that on rigid smooth surface with somewhat larger the boundary layer thickness. We can see coincided velocity profiles (Fig.5), profiles of kinetic energy of turbulence (Fig.6) and dissipation velocity (Fig.8) in the section at x/L=0.94.

The curve 1 on Fig.5 corresponds to the velocity profile on the rigid smooth surface, 2 corresponds to $Cd_2=3 \cdot 10^{-3}$, 3 corresponds to $Cd_3=5/Re_\delta$. At $Cd_2=1 \cdot 10^{-3}$, the velocity profile coincides with that on the rigid smooth surface. Thus, if a memory effect exists along the boundary layer thickness, i.e. local increase in friction on the trailing edge of the plate results in total drag increase of the whole plate, than the effect can not be seen in measurements of the velocity profile in dynamic variables on the oscillating plate in sections close to end. Therefore the velocity profile in dynamic variables only reflects local effects, practically do not taking into account previous history. The curve 4 shows the local friction drag reduction, that is accompanied by relative growth of viscous sublayer. The velocity profile in a core of the boundary layer ($70<y^+<1000$) lies in parallel to the logarithmic profile, that shows the constant κ does not vary in the boundary layer on a damping surface.

Energy grows somewhat in the viscous sublayer on oscillating surface at $Cd_2 = 3 \cdot 10^{-3}$ in comparison with rigid surface (Fig.6). Turbulent energy maximums in the boundary layers coincide practically by magnitude and their location relatively the surface. At $Cd_3 = 5/Re_\delta$, turbulent energy in the boundary layer on the absorbing surface is much more less through whole the boundary layer thickness. Energy maximum on deforming surface less by almost 20% than energy maximum on rigid smooth surface and displaced from the surface to $\sim y^+ \approx 32$ while maximum k on rigid plate lies in the region of $y^+ \approx 20$.

Coincident velocity profiles in sections close to the end of the plate correspond to coincident shear stresses $\overline{-u_1 u_3}/u_*^2$ on the rigid smooth surface and oscillating one (Fig.7). In the nearwall region, at $y^+<80$, shear stresses are less on the absorbing surface than those on the rigid smooth surface, and they reach maximal values more smoothly. Far from the wall, shear stresses in dynamic variables practically do not depend on a type of the streamlined surface.

The most variations in turbulence energy dissipation velocity appear in a region of viscous sublayer (Fig.8). Dissipation velocity tends to zero on the oscillating surface, while it reaches absolutely maximal value in a boundary layer on the absorbing surface, and in region $5<y^+<20$, it is essentially less then corresponding values of dissipation velocity in a boundary layer on the rigid smooth surface. Thus, typical time (k/ε) of turbulent structures existence near the surface varies. So, turbulence degeneration is more intensive on the absorbing surface than that on rigid one, and typical time in a viscous sublayer on the oscillating surface can have a concrete magnitude. Therefore, a viscous sublayer can not exist on the oscillating surface in usual understanding, like to that on a rough surface. At $|\xi_{1l}|>\nu/u_*$, it results in increase of mixing near the surface. A size of the mixing area is proportional to the root-mean-square value of the surface oscillation amplitude. Hypothesis of gradient diffusion is not applicable in this area. But, at small amplitudes ($|\xi_{1l}|<<\delta$), the integral scales do not vary and the inaccuracy introduced by hypothesis of gradient diffusion can only be visible in the area $y^+< 2$, where it is comparable with viscous diffusion.

In addition, when the surface is deformed so that wave length is small in comparison with the boundary layer thickness ($\alpha>>1$), at certain phase shift φ between maximum energy disturbances and the surface displacement, and at certain phase velocity of the surface travelling wave c, such velocity pulsations appear which provide negative viscous diffusion near the surface (Fig.1). As a result, the area of maximum turbulent stresses moves away from the surface.

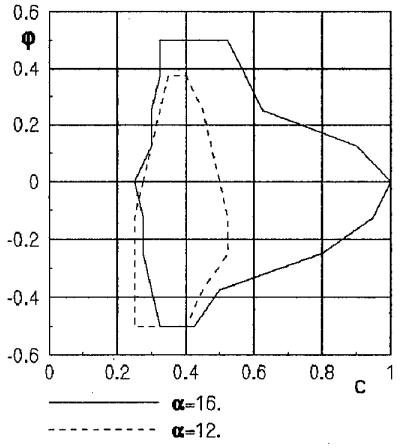


Fig.1.

The domains enclosed by the curves correspond to such magnitudes of φ and c at which the viscous diffusion is negative near the surface.

Experimental results are absent in this field, therefore it is impossible to confirm or disprove this statement.

An indirect confirmation can be given by numerical solutions of the linearized Navier-Stokes equations in approximation of Stenberg on the oscillating surface.

Moving away from the wall, at $y^+>5$, the turbulent diffusion coefficient becomes to be less on the absorbing surface, and diffusive flux of turbulence energy decreases, that leads to deceleration of the boundary layer thickness growth and consequently, to friction drag reduction.

For stable flows, as it was noted, we can observe practically unequivocal connection between dynamic velocity and energy balance components at changing both Re number and conditions of the flow (for example, a flow of polymer solutions). This fact confirms universality of the dynamic velocity as a scale parameter, but does not make more clear physics of energy balance formation.

In turbulent boundary layers on a plate and in a pipe, on greater part of boundary layer thickness or pipe radius, the energy balance is determined by local equality of production and dissipation. In direct vicinity from the surface, the turbulence energy dissipation is counterbalanced by viscous diffusion,.Far from the surface, the last can be neglect. At last, in the layer "of constant stress" and on external border of the boundary layer or on axis of the pipe, where all these quantities are small in comparison with their maximal values, turbulent diffusion is comparable with production and dissipation.

There always exists a thin area of boundary layer, from the surface to the layer "of constant stress", which corresponds to such flows at large Re numbers, where the cross pressure gradient is small. This area is of shares of percent from the whole boundary layer thickness ($0.005\div0.01\delta$), and it is responsible for formation of maximal values of the Reynolds stress (in the first place, $\overline{u^2}$) and dissipation velocity ε. Therefore, very small variation of turbulence energy in the nearwall region can results in a significant variation of friction drag. Such variation of energy can provide fluctuate energy absorption by viscoelastic coating in nonresonance area of interaction on a wide enough range of frequencies.

All the components of turbulence energy balance (production, diffusion, dissipation and redistribution) are comparable by magnitude in a region of their maximal values, that requires an appropriate level of simulation. Fixing a certain energy balance of total turbulence energy, it is possible to analyze present structure of the flow and its integral characteristics, but practically we could say nothing about a reason of this state. It has already been shown in the work [8], that turbulence energy diffusion coefficient variation can results in energy balance with less values of turbulence energy intensity and dissipation velocity, and consequently, in reduction of u_*.

This statement, giving explanation to the fact of changed energy balance, describes only schematically the mechanism of establishment of this balance in terms of (k-ε) model, connecting this result with change of turbulent viscosity coefficient. So, anisotropy of the Reynolds stress tensor components in the nearwall region of turbulent flow emphasizes unequivalent influence of the streamlined surface on the turbulence energy components and, consequently, on mechanism of redistribution, as well.

Calculations of the turbulence energy components and shear stresses on the deforming and the absorbing surfaces has shown that longitudinal component of fluctuate energy and turbulence energy dissipation velocity are the most varied, and it occurs in the nearwall region only.

At the same time, calculation results for terms of the equation of turbulence energy conservation have

demonstrated the qualitative difference of the balance components during streamlining over various surfaces. So, streamlining an absorbing surface, there is energy changed considerably production of the longitudinal component of total fluctuate energy, which is equivalent to production of total turbulence energy in whole at interaction of disturbances in the flow with mean flow, because direct production of the components $\overline{v^2}$ and $\overline{w^2}$ may be neglected in a stable boundary-layer flow. These components receive energy on account redistribution from component $\overline{u^2}$ only.

Behavior of diffusion and turbulence energy dissipation velocity varies qualitatively. When the fluctuate energy absorption is $Cd_3>3/Re_\delta$, then maximums of these variables reaches the absorbing surface, while the maximum of production moves away from the surface (Fig.10). Distribution of the conservation equation component in a turbulent boundary layer on the oscillating nonabsorbing surface repeats qualitatively behavior of corresponding components on the rigid smooth surface, even at large values of the surface oscillation amplitude.

On basis of calculation results for turbulent boundary layer on the absorbing surface, we can see interrelation of energy frequency $\omega_e \sim U_0/\delta$ [17] and dynamic frequency $\omega_b = u_*^2/\nu$ with coefficient of anisotropy of turbulence $q = \overline{v^2}/\overline{u^2}$ and with variation of friction drag coefficient. So, at $\omega_e>\omega_b$, the coefficient of anisotropy q decreases in comparison with boundary layer on rigid smooth plate, but friction drag grows. At $\omega_e<\omega_b$, the flow anisotropy rate remains the same or grows somewhat, and friction drag changes proportionally to the Reynolds stress intensity.

If to assume behavior of the components of the stress tensor near a surface to be described by the following dependencies:

$$u^2 \approx a\cdot y^2+\ldots;$$
$$v^2 \approx b\cdot y^4+\ldots;$$
$$w^2 \approx c\cdot y^4+\ldots,$$

then redistribution Π_{11} is equivalent to the dissipation velocity at $y\to 0$ in the boundary-layer approximation, i.e.:

$$\Pi_{11} = \varepsilon - \varepsilon_{11},$$

because turbulence energy production and the longitudinal components of the stress tensor $\overline{u^2}$ are equal, and the turbulent diffusion k and $\overline{u^2}$ are equivalent.

Thus, $\Pi_{33}=2/3\ (1-f_s)\varepsilon$, and consequently $\Pi_{33}=0$ on the rigid smooth surface, because $f_s\to 1$ at $y\to 0$.

On a deforming surface $Re_t \neq 0$, and consequently $\Pi_{33}\neq 0$, that can be seen in calculation results (Fig.9) for redistributions on the oscillating and absorbing surfaces. The redistribution on the absorbing surface changes essentially: maximum of the 'pressure-deformation' correlation decreases considerably and moves away from the surface, at contrary that on the oscillating one.

In this view, the question about reliability of the redistribution description is not trivial, though it is not trivial in more simple flows too. The work [37] compares in detail three last models for the correlation 'pressure-deformation' with results of direct simulation of uniform shift on basis of numerical solution of the Navier-Stokes equations. These are the models of Shih-Lamley(SL), Fu-Launder-Theleridakis (FLT) and Speziale-Sarkar-Gatski (SSG). The results of simulation of all three models are admitted to be insufficient for relatively simple flow. Now there is nothing to compare with the calculation results shown in Fig.9.

4.Conclusions.

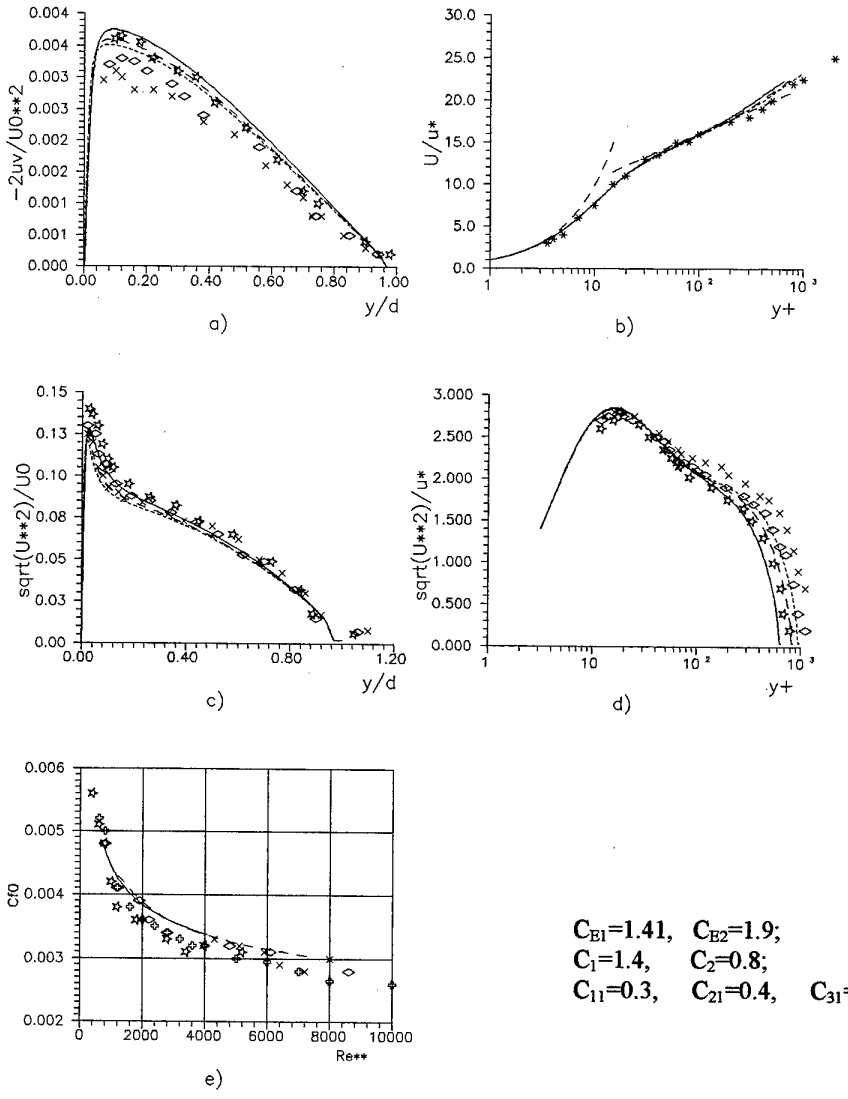
In a turbulent boundary layer over the absorbing surface of the viscoelastic coating, the turbulence anisotropy and normal diffusive flux of the turbulence energy will changes, production of the normal component of the Reynolds tensor decrease, the turbulence energy maximum decrease and move away from the surface and the viscous sublayer thicken against the corresponding characteristics of the turbulent boundary layer over a rigid smooth surface. It will lead to noticeable (by 10-12%) friction drag reduction.

References:

1. Amfilohiev, V.B., "Turbulent Flow with Elastic Bounaries", Bionics, 3, 1969, pp.46-53 (in Russian).
2. Babenko, V.V., Kanarskij, M.V., Korobov,V.E., "Boundary Layers on Elastic Plates", Kiev, Ukraine, Naukova Dumka, 1993 (in Russian).
3. Voropaev, G.A., "Investigation of Influence of Cetaceous Skin Analog onto Turbulent Boundary Layer", Ph.D. Dissertation, Kiev, Ukraine, 1977 (in Russian).
4. Voropaev, G.A., Popkov, V.I., "The Mechanism of Interaction of a Compliant Surface with the Viscous Sublayer of the Turbulent Boundary Layer",

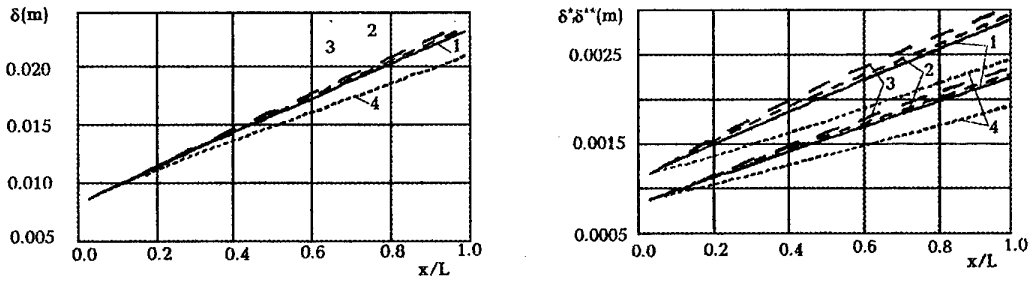
Hydromechanics, 58, 1988, pp.20-25 (in Russian).
5. Voropaev, G.A., Ptuha, Yu.A., "Modeling of Turbulent Flows over Deformable Surfaces", Kiev, Ukraine, Naukova Dumka, 1991, 165p (in Russian).
6. Kirejko, G.V., "On Interaction of the Near-Wall Turbulence with a Compliant Surface", Механика жидкости и газа. - 1990.-№4. -С.67-72 (in Russian).
7. Kozlov, L.F., Babenko, V.V., "Experimental Investigations of a Boundary Layer", Kiev, Ukraine, Naukova Dumka, 1978 (in Russian).
8. Kozlov, L.F., Voropaev, G.A., "The Possible Mechanism of Interaction of the Turbulent Flow in a Pipe with the Elastic-Dumping Surface", // ДАН УССР, Сер.А, Физ.-мат. и техн. науки. -1981. -№9. -С.48-52 (in Russian).
9. Korotkin, A.I., "Stability of the Laminar Boundary Layer in an Incompressible Fluid over an Elastic Surface", Известия АН СССР. МЖГ. -1966. -№3. -С.39-44 (in Russian).
10. Paskonov, V.M., Polezhaev, V.I., Chudov, L.A., "Numerical Modeling of the Process of Heat and Mass Transfer", Moscow, Sciences, 1984, 288p (in Russian).
11. Semenov, B.N., "The Influence of the Elastic Coatings on the Turbulent Boundary Layer", *in* Recearch in Control of the Boundary Layer, Novosibirsk, 1976, pp.92-101 (in Russian).
12. Semenov, B.N., "An Analysis of Deformation Characteristics of Viscoelastic Coatings", *in* Hydrodynamics and Acoustics of Near-Wall and Free Flows, Novosibirsk, 1981, pp.57-76 (in Russian).
13. Benjamin, T.B., "Effect of a Flexible Boundary on Hydrodynamic Stability", J.Fluid Mech.,**9**, 1960, 513p.
14. Blick, F.B., Walters, R.R., "Turbulent Boundary Characteristics of Compliant Surfaces", J. Aircraft, **5**, 11 (1968).
15. Bushnel, D.M., Hefner, J.N., Ash, R.L., "Effect of Compliant Wall Motion on Turbulent Boundary Layers", Phys. Fluids, **20**, N10, pt.II, 31 (1977).
16. Buckingham, A.C., Hall, M.S., Chun, R.C., "Numerical Simulations of Compliant Material Response to Turbulent Flow", AAIA Journal, **23**, N7, 1046 (1985).
17. Cantwell, B.J., "Organized Motion in Turbulent Flow", Ann. Rev. Fluid Mech., 13, 1981, pp.457-515.
18. Carpenter, P.W., "Status of Transition Delay using compliant walls", in *Viscous Drag Reduction in Boundary Layers. Progress in Astronautics and Aeronautics,* (ed. Bushnell D.M., Hefner S.N.) **123,** 79, AIAA(1990).
19. Carpenter, P.W., Garrad, A.D., "The Hydrodynamic Stability of Flow over Kramer-type Compliant Surfaces. Part 2. Flow-induced surface instabilitties", J. Fluid Mech., **170**, 439 (1987).
20. Duncan, J.H., "The Responce of an Incompressible Viscoelastic Coating to Pressure Fluctuations in a Turbulent Boundary Layer", J. Fluid Mech., **171**, 339 (1986).
21. Duncan, J.H., "The Dynamics of Waves of the Interface Between a Two-layer Viscoelastic Coating and a Fluid Flow", J. of Fluids and Structures, vol.2, 11. pp.35-52, N1, 16 (1988).
22. Gad-el-Hak, M., "The Responce of Elastic and Viscoelastic Surfaces to a TBL", Trans. ASME E: J. Appl. Mech., **53**, N3, 206 (1986).
23. Gad-el-Hak, M., Blackwelder R.F., Riley J.J. On the Interaction of Compliant Coatings with Boundary-Layer flows", J. Fluid Mech., **140,** 257 (1984).
24. Hansen, R.J., Hunston, D.J., "An Experimental Study of Turbulent Flows over Compliant Surfaces", J. Sound Vib., **34**, 297 (1974).
25. Hansen, R.J., Hunston, D.J., "Fluid-Property Effects on Flow-generated Waves on a Compliant Surface", J. Fluid Mech., **133,** 161 (1983).
26. Hansen, R.J., Hunston, D.J., Ni, C.C., "An Experimental Study of Flow-Generated Waves on a Flexible Surfaces", J. Sound Vib., **68**,317 (1980).
27. Hess, D.E., Peattie, R.A., Schwarz, W.H., "A Non-Invasive Method for the Measurement of Flow-Induced Surface Displacement of a Compliant Surface", Exp. Fluids, **8,** 137 (1993).
28. Kramer, M.O., "Boundary Layer Stabilization by Distributed Dumping", ASME J.,**72**, N2, 25 (1960).
29. Landahl, M.T., "A Wave/Guide Model for Turbulent Shear Flow", J.Fluid Mech., **29**, N3, 441 (1967).
30. Launder, B.E., Reece, G.I., Rodi W., "Progress in the Development of a Reynolds Stress Turbulent Closure", J.Fluid Mech., **68**, 537 (1975).
31. Launder, B.E., Reynolds, W.C., "Asymptotic Near Wall Stress Dissipation Rates in Turbulent Flow", Phys. Fluids, **26,** 1157 (1993).
32. Lee, T., Fisher, M., Schwarz, W.H., "Investigation of the Stable Interaction of a Passive Compliant Surface with a Turbulent Boundary Layer", J. Fluid Mech., **257**, 373 (1993).

33. Lissaman, P.B.S., Gordon, L.H., "Turbulent Skin Friction on Compliant Surfaces", AIAA Paper, N164, 1 (1969).
34. McMichael, J.M., Klebanoff, P.S., Mease N., "Experimental Investigation of Drag on a Compliant Surface", in *Viscous Flow Drag Reduction* (ed. G.R. Hough), AIAA Astro. Acro.,**72**, 410 (1979).
35. Nonweiler, T., "Qualitative Solution of the Stability Equation for a Boundary Layer in Contact with Various Forms of Flexible Surface", ARC Rep., **22**, N670, 75 (1963).
36. Riley, J.J., Gad-el-Hak, M., Metcalf, R.W., "Compliant coating", Ann.Rev. Fluid Mech. **20**,393 (1988).
37. Speziale, C.G., Gatski, T.B., Sarkar, S., "On Testing Models for the Pressure-Strain Correlation of Turbulence using Direct Simulations", Physics of Fluids, **4**, N12, 2887 (1992).
38. Thomas, M.D., "The Nonlinear Stability of Flows over Compliant Walls", J. Fluid Mech., **239**, 657 (1992).
39. Wolfstein, M., Naot, D., Lin, A., "Models of Turbulence", *Topics on transport phenomena in bioprocesses, mathematical treatment and mechanisms*, 3-45 (1975).
40. Yeo, K.S., "The Stability of Boundary-Layer Flow over Single- and Multi-Layer Viscoelastic Walls", J.Fluid Mech., **196**, 359 (1988).
41. Yeo, K.S., "The Hydrodynamic Stability of Boundary-Layer Flow over a Class of Anisotropic Compliant Walls", J. Fluid Mech., **220**, 125 (1990).



C_{E1}=1.41, C_{E2}=1.9;
C_1=1.4, C_2=0.8;
C_{11}=0.3, C_{21}=0.4, C_{31}=0.046.

Fig.2.



a) b)

Fig.3. Dimensional value of a) the boundary layer thickness and b) displacement thickness and momentum thickness over:
rigid smooth plate (curves 1);
elastic surface with $Cd_2=1*10^{-3}$ (curves 2);
elastic surface with $Cd_2=3*10^{-3}$ (curves 3);
absorbing surface with $Cd_3=5/Re$ (curves 4).

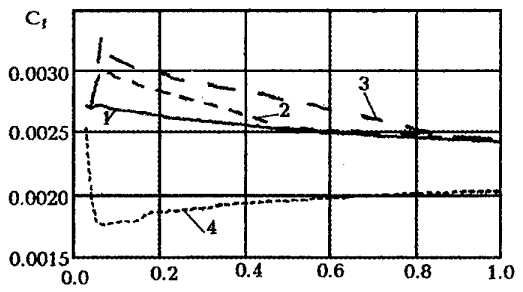


Fig.4. Friction drag coefficient.

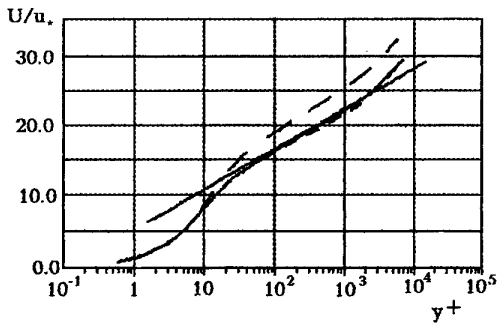


Fig.5. Velocity profiles.

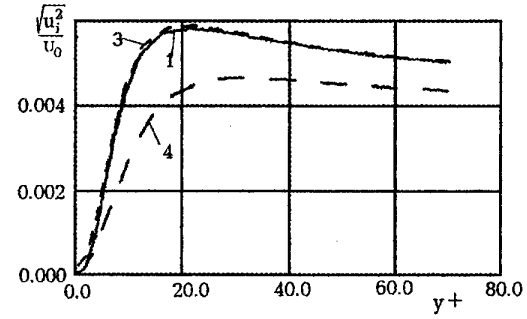


Fig.6. Turbulence energy components.

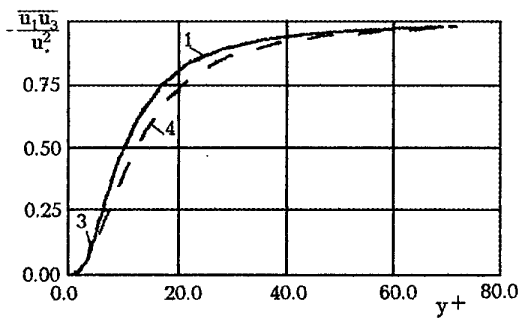


Fig.7. Shear stresses.

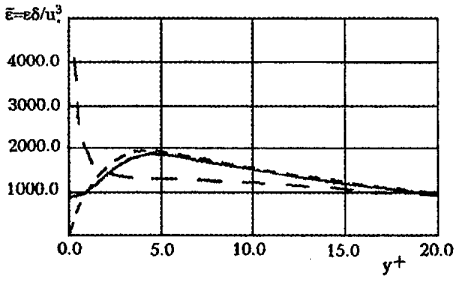


Fig.8. Turbulence energy dissipation velocity.

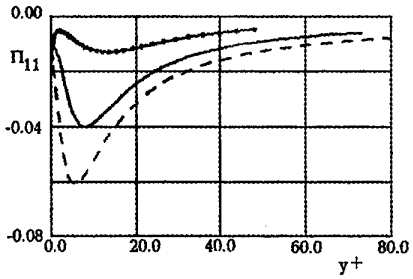


Fig.9. The redistribution term of the transition equation for the longitudinal component of the Reynolds stress tensor on rigid, elastic and absorbing surfaces.

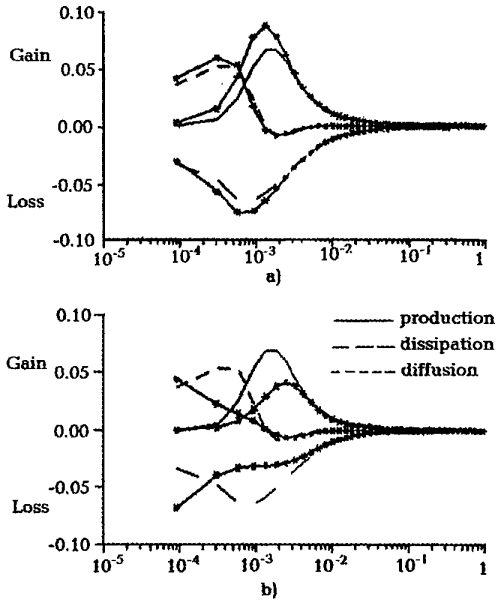


Fig.10. Components of fluctuate energy balance of the turbulent flow in the pipe: a) elastic surface; b) absorbing surface (curves without markers correspond to a rigid smooth surface).

NON-LINEAR NONSTEADY EFFECTS IN THE HYDRODYNAMICS OF THE OSCILLATING WING

S.A. Dovgiy
Hydromechanics Institute, The National Academy of Science of Ukraine
8/4 Zheliabov str., 252057 Kyiv,Ukraine

SUMMARY

The article presents the analysis of the nonsteady hydroaerodynamic characteristics of the oscillating wing with the infinite span performing the function of the propulsor. The results are received for the non-linear theory by means of the discrete vortices method. The comparison of data is conducted based on the quasi-steady approach, linear and non-linear theories. It is also noted that for those modes of the wing motion which are able to simulate the operation of the wing propulsors of hydrobionts, valid results can be given with the help of the nonsteady theory only.

THE LIST OF SYMBOLS

b	wing chord
ν	oscillations frequency
h	vortex street width
l	vortex street step
y	wing's heave coordinate
θ	angular oscillations amplitude
a	linear oscillations amplitude
$\bar{U}_n$	progressive wing velocity
$\bar{U}^*$	characteristic velocity, $\overline{\bar{U}_n}$
α	angle of attack
p^*	Strouhal number, $2\pi\nu b / U^*$
λ_p	relative wing velocity, $1 / ap^*$
T	oscillations period
τ	dimensionless time
w	velocity in the nearest wake
P	pressure in the nearest wake
ΔP	pressure differential on the wing
$\bar{R}$	main vector of external forces
C_T	thrust force coefficient
C_Q	suction force coefficient
C_Y	lift force coefficient
C_N	normal force coefficient
C_M	leading edge moment coefficient
C_{X_P}	pressure drag coefficient
C_{X_F}	frictional drag coefficient
C_W^*	output power
C_W	input power
φ	phase shift between C_Y and y
η	efficiency
k_T	reduced thrust coefficient, $C_T / (a^2 p^2)$
k_W	reduced power coefficient, $C_W / (a^2 p^3)$
k_Y	reduced lift force coefficient, $C_Y / (a\, p^*)$

Subscripts and superscripts

k	quasi-steady theory
L	linear theory
--	Averaging symbol for the period of oscillations

INTRODUCTION

The major part of the theoretical papers in the nonsteady hydroaerodynamics of the wing-propulsor are fulfilled on basis of linear theories. The linear theories are still traditionally more developed ones. This is mainly connected with fact that the non-linear approaches need the clearing of great mathematic and computational difficulties. In the available scientific literature there are few papers specially devoted to the comparison of results of the non-linear and linear theories, the analysis of the effects of nonstationarity, displaying in the non-linear statement of the problem [1,11].

The most effective method for the solution of the non-linear nonsteady problems of the wing theory at present is the discrete vortices method.[1, 2, 5]. The main advantage of it consists in the universal approach to the solution of various problems, in particular, the plane and spatial ones. The author of the present paper together with his colleagues accumulated a good deal of experience while solving various non-linear nonsteady problems on the motion of oscillating wing and wing systems using this method as well as an experience in the carrying out of numerical and physical experiments. (see, e.g.[3-12]). The results of the present paper are received on basis of the following assumptions: the wing with infinite span is moving in the non-limited fluid and performs reciprocating or angular harmonic oscillations in a predetermined manner, the fluid is supposed to be ideal, incompressible, and the fluid stream-vortexfree. These assumptions let us reduce the solution of the physical problem to the non-linear initial boundary value problem for the velocity potential. The main feature of this problem consists in the fact that at every time moment there is a part of the potential existence field boundary - the boundary of the vortex sheet (vortex wake) unknown. The investigation of the vortex wake evolution behind the wing is one of the most difficult issues of the nonsteady theory. At present it can be solved with the satisfactory degree of precision for many cases using the vortex method and basing on the conservation feature of free vortices circulation.

COMPARISON OF THE NON-LINEAR THEORY WITH THE OTHER THEORIES

The characteristic property of all approaches based on linearization consists in the fact that the vortex wake form is postulated in advance. There are three approaches known:

I. The position of free vortices trailing from the wing is carried onto the plane (line) which is parallel to the velocity of the external flow. The velocity of their motion is considered to be equal to the velocity of the external flow [13-15].

II. The form of the vortex wake "follows" the track of the wing's trailing edge motion. In case of harmonic oscillations the wake form is also a harmonic function.

Paper presented at an AGARD FDP Workshop on "High Speed Body Motion in Water", held in Kiev, Ukraine, 1-3 September 1997, and published in R-827.

III. The inverted vortex street observed in the experiment is simulated by two vortex rows. The condition of the stability $h / l = 0{,}281$ is introduced from the classical Karman theory.

Having restricted the values of τ to small ones, it is possible to observe the linear forms of the vortex sheet. However, when continuing the calculations until great values of time are achieved, we will see the appearing of disturbances, their development and creation of spiral curls. The experiments also show that even under small disturbances caused in the flow by the wing the wake differs essentially from the Schemes I and II that are stipulated by the linear approaches. And the more the amplitude and the frequency of oscillations are, the more this difference is. As to Scheme III, so it is unsteady that is proven by many authors in a theoretical way. So, it is necessary to attract the non-linear approaches for the description of the real flows.

Apart from the linear approaches that make it possible to take into account the nonsteady effects, the quasi-steady approach is also widely used in the engineering applications. This approach is based on the hypothesis of stationarity and gives the satisfactory results for the progressive oscillations with the relative wing velocities $\lambda_p \geq 4$. Some inconvenience of this approach, besides from the restriction on λ_p, is connected with the fact that it demands the knowledge of values of steady characteristics of the wing used.

The comparative investigation of the oscillating wings characteristics based on the aforementioned approaches is a matter of interest. As we are interested in thin wings only, it is natural to regard the projections of steady values of lift force for the plane plate in the velocity coordinates system as the instantaneous quasi-steady values:

$$C_{Yk}(\tau) = 2\pi \sin\alpha(\tau)\cos\alpha(\tau),$$
$$C_{Tk}(\tau) = 2\pi \sin^2\alpha(\tau). \qquad (1)$$

For the cases of the linear and non-linear theories the thrust force was determined by the projection of the main vector of external forces $\bar{R}(\tau)$ onto the direction of the averaged wing's motion. As in the case given this direction is parallel to the wing chord, so the thrust force will be determined fully by the suction force and the lift force will be determined by the normal force. :

$$C_T(\tau) = C_Q(\tau),$$
$$C_Y(\tau) = C_N(\tau).$$

Apart from the thrust coefficient, the second important characteristic of the oscillating wing that performs a function of a wing-propulsor, is its efficiency coefficient.

$$\eta = \frac{\overline{C_W^*(\tau)}}{\overline{C_W(\tau)}},$$

where $\overline{C_W^*}$ - is the averaged output power, spent for the creation of the thrust effort, $\overline{C_W}$ - is the averaged input power to the wing during the period, which can be found using the equations:

$$\overline{C_W^*} = -\frac{1}{T}\int_{\tau_0}^{\tau_0+T} U_{0X} C_T(\tau)\,d\tau,$$
$$\overline{C_W} = -\frac{1}{T}\int_{\tau_0}^{\tau_0+T} U_{0Y}(\tau) C_Y(\tau)\,d\tau. \qquad (2)$$

For the case of progressive wing oscillations with the amplitude $a = 0{,}05$ and the frequency $\nu^* = 10$ in the Fig. 1 the values of the angle of attack α, the reduced thrust coefficient k_T and the reduced power coefficient k_W for the oscillations period are represented. The Curves 1 show the quasi-steady approach (1); the Circles 2 show the linear theory; the Curves 3 show the non-linear theory. It can be seen that for this mode of oscillations the quasi-steady approach is not able to reflect the real situation either qualitatively or quantitatively: the instantaneous values of k_{W_K} and k_W differ both in the amplitude and in the phase,

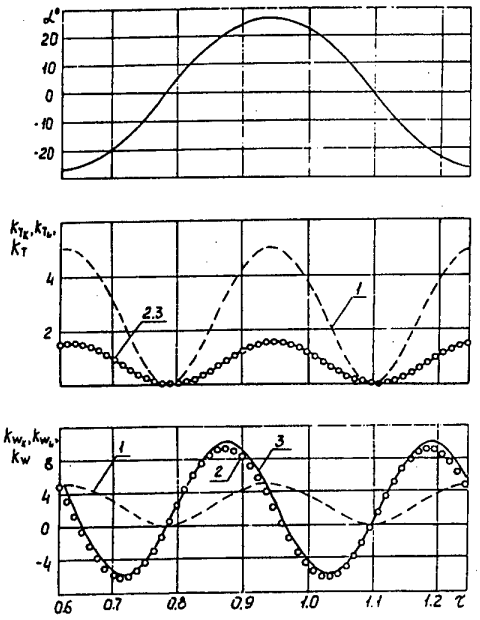


Fig. 1

and k_{W_K} does not have the sections that are characteristic for the nonsteady modes when the part of the power that is given to the fluid by the wing, returns to the wing - (the negative values of k_W). The simulation of the wing oscillations on basis of the linear theory describes the bahaviour of k_T and k_W in a qualitatively correct way; however, although the oscillations amplitude is small, the differences in amplitude and in phase can already be observed for the reduced power coefficient.

Now, let's clear it up what is the trend in the bahaviour of k_{T_K}, k_T and η_K, η for the values of the relative wing velocity $\lambda_p > 1$. Let's examine the low frequency modes of the progressive oscillations under the amplitude value $a = 0{,}5$. In the Fig. 2 Curve 1 corresponds to the non-linear theory, and Curve 2

shows the quasi-steady circulation. It can be seen that under $\lambda_p > 4$ the results does not asymptotically tend to each other, as it was traditionally stated in the experimental papers using the engineer summarising. The thrust coefficient k_{T_K} exceeds k_T almost twice and $\eta_K = 100\%$ for the whole range of λ_p.

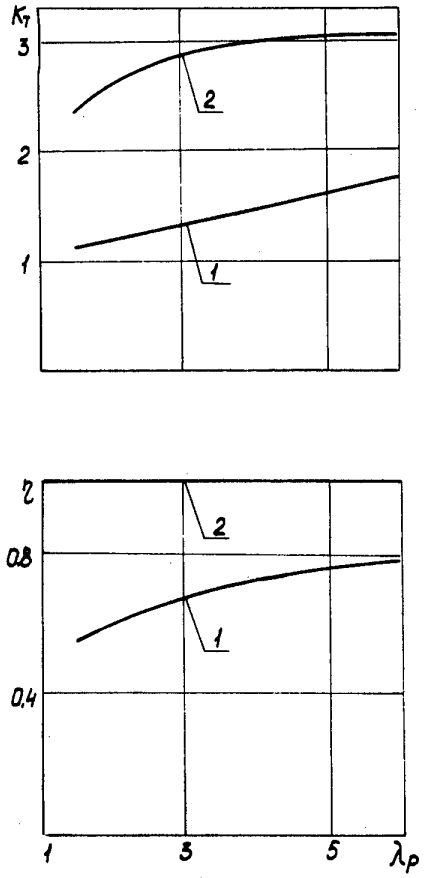


Fig. 2

This fact is unusual at first glance and can be explained as follows. First, the distinction between the approach (1) and the traditional one consists in the fact that the approach (1) does not take into account the wing profile drag (the sum of the pressure drag C_{XP} and the frictional drag C_{X_F}), that causes the afore mentioned asymptotic trend within the framework of the traditional approach.

Second, under the condition $C_{XP} = 0$ and $C_{X_F} = 0$ all the input power C_W to the wing will be equal to the output power C_W^* because the energy will not be spent for the vortex's separation and for the creation of the needed circulation round the wing as well as for the acceleration and the deceleration of the fluid added masses.

That is why the quasi-steady approach (1) corresponds to such ideal situation when only the steady Zhukowski force affects the wing.

THE VORTEX WAKE CHARACTERISTICS

Now let's study the vortex wake characteristics behind the oscillating wing.

In the Fig. 3 the comparison is given of computational and experimental flow patterns in the nearest wake that are reduced to a universal scale. The amplitude of the angular wing's oscillations is $\theta = 3.8°$, Strouhal number $p^* = 9$. Five consequent frames are shown during a halfperiod to characterise the flow patterns in development. Near the last top position of the wing (the top couple of the frames) the vortex of the maximal intensity is separated, creating the core of the vortex blob that involves the part of the ambient fluid in the rotational movement. This vortex takes place in the top row of the inverted vortex street. The similar processes take place during the creation of the vortex in the low row. A good qualitative agreement characterises not only the reliability of the computational method, but also the speciality of the experiment, during which only the field of the intensive vortex flow behind the wing was coloured.

The cycle of investigations was conducted on the averaged flow characteristics of the nearest wake behind the oscillating wing.

The Fig.4 shows the profiles of the averaged lengthwise velocity $\overline{w}_X$, the root-mean-square pulsation of the lengthwise velocity $\overline{w'^2_X}$, the averaged lateral velocity $\overline{w}_y$ and the averaged pressure $\overline{P}$ in the vertical section at the distance of d=0,1 from the trailing edge of the wing for the progressive oscillations with the amplitude $a = 0{,}02$ and the frequencies $p^* = 2\pi$, $p^* = 3\pi$, $p^* = 6\pi$.

The maximum $\overline{w}_X$ on the symmetry axis indicates the existence of the lengthwise averaged flow in the wake that is created by the wing in the process of oscillations. Two separating sections of the vortex sheet with different signs being centres of the vortex core concentration correspond to the position of the maximums $\overline{w'^2_X}$. The relative minimum $\overline{w'^2_X}$ on the axis is stipulated by some mutual compensation of them at the cost of symmetry of the oscillations law. Fig.4 also shows that there are two averaged lateral flows, directed in various sides from the symmetry axis of the oscillations. This acceleration of the flow, in accordance with the Koshee-Lagrange integral, leads to the averaged pressure reduction at some distance from the trailing edge of the wing in the field near the symmetry axis of the oscillations.

DYNAMIC HYSTERESIS

As the wing movement occurs under the harmonic law such that U_{0X} doesn't depend from the time and U_{0Y} depends from it, so the expended power C_W (2) will

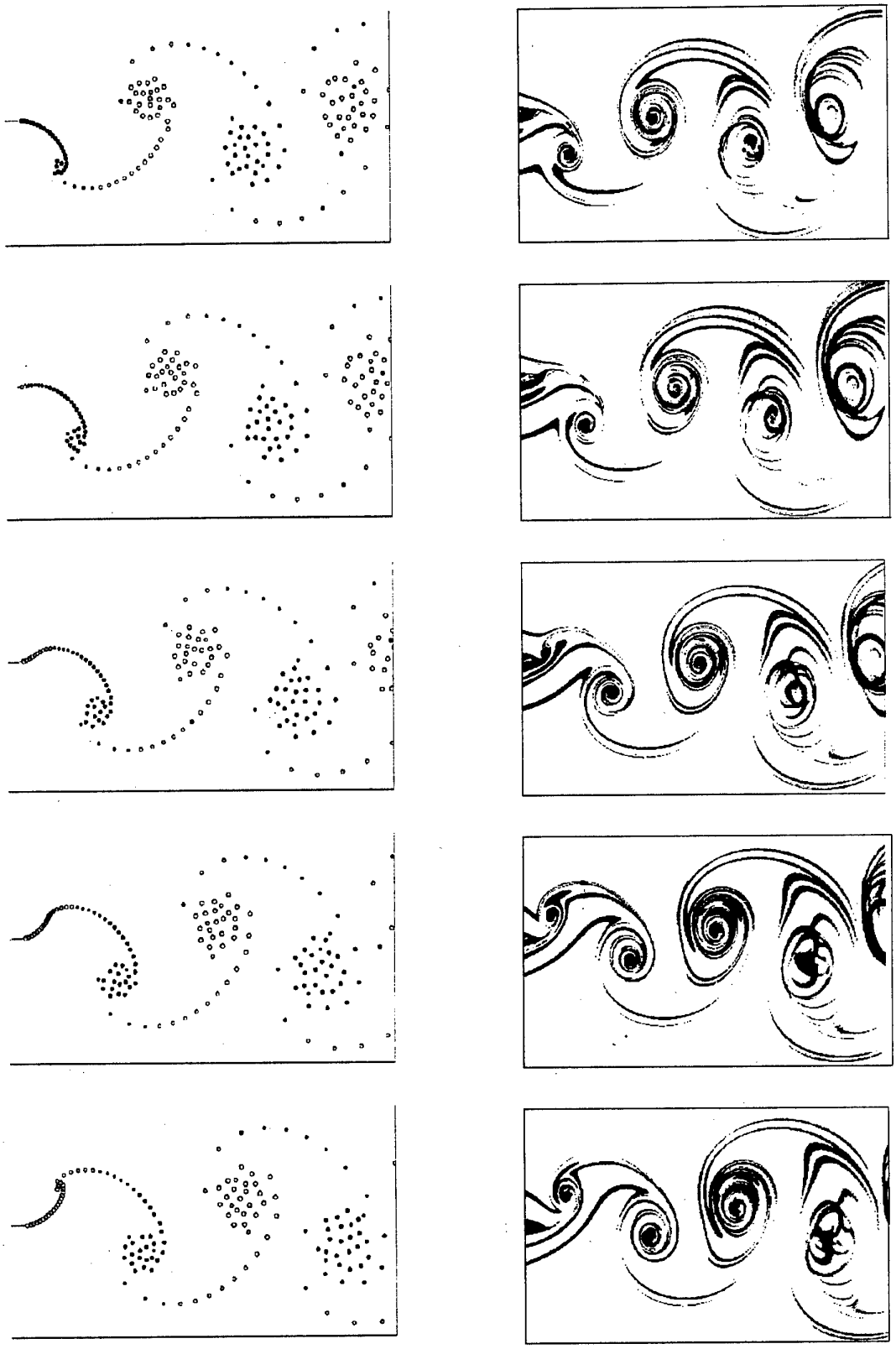


Fig.3

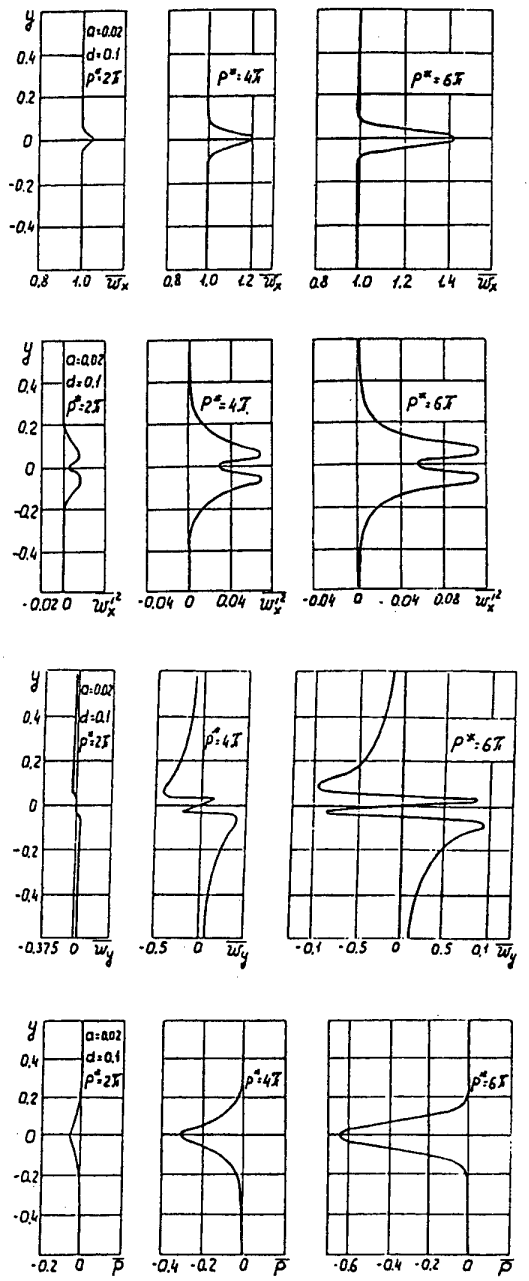


Fig.4

be determined not only by the amplitude values U_{0Y} and C_Y, but also by the value of the phase shift between them. The phase shift can change in dependence from the oscillations frequency. The influence of the value of this phase shift upon the wing efficiency is big enough, that is why it is a matter of interest to investigate the limits of its variation for the cases of the linear and the non-linear theories.

For convenience we will determine the shift φ between the phases C_Y and y (the oscillations law). It's more natural as the phase y coincides with the wing's acceleration phase $\ddot{y}$. So, for the quasi-steady lift force coefficient C_{Y_K} we receive the shift value $\varphi = 90^0$ with reference to the oscillations law. This corresponds not to the maximum of the acceleration but to the maximum of the wing's velocity, as the quantity

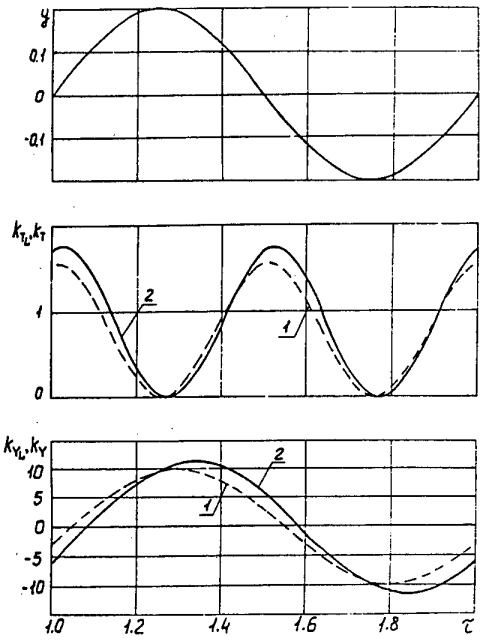


Fig.5

C_{Y_K} is directly proportional to the velocity circulation around the wing under conditions of the steady flow. Fig.5 illustrates the bahaviour of the reduced thrust coefficient k_T and the reduced lift force coefficient k_Y for the case of the progressive oscillations with the amplitude $a = 0{,}2$ and the frequency $p^* = 2\pi$. Curve 1 serves for the linear theory and Curve 2 shows the non-linear one. It can be seen that k_Y has the bigger shift value $\Delta\tau$ than k_T with reference to $\varphi = 90^0$,such that this shift is more in case of the non-linear theory. The bahaviour of the shift $\varphi = p^* \Delta\tau / T$ in degrees (between k_Y and Y) in dependence from the amplitude a under the frequency $p^* = 2\pi$ and in dependence from the frequency p^* under the amplitude $a = 0{,}2$ is shown in the Fig.6. The linear theory is marked with figure 1, and the non-linear one is marked with figure 2. It can be seen that before values $p^* = 1{,}5$ this shift is the same for both approaches, however, under $p^* > 1{,}5$ the higher values of φ are observed for the non-linear case than for the linear one. The fact of independence of shift value from the amplitude for the case of the linear theory and the dependence of them in case of the non-linear theory causes the divergence of the values $\eta(p^*)$ for various amplitudes represented in the Fig.11. Together with the increase of the external disturbing periodical factor the time lag increase of the phase of one characteristic with reference to some other independent one occurs. This

phenomenon is named, as it is known, a dynamic hysteresis.

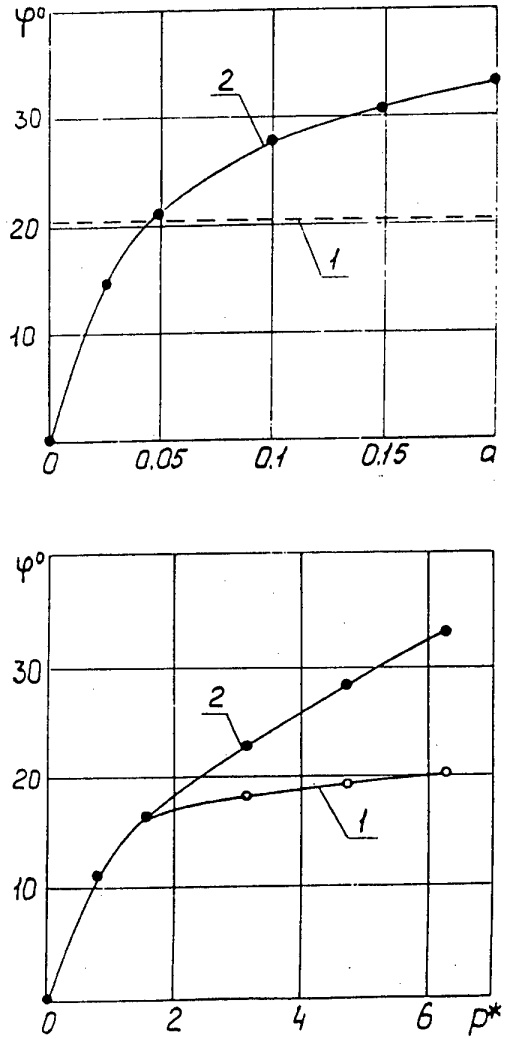


Fig.6

The dynamic hysteresis of hydroaerodynamic characteristics in the sweep under the instantaneous angle of attack is a matter of special interest. In the Fig. 7 the so-called phase portraits of the thrust force coefficient C_T, the lift force coefficient C_Y, the momentum C_M and the input power C_W for the frequency $p^* = 2\pi$ and the amplitudes $a = 0{,}03$ (Curves 1), $a = 0{,}06$ (Curves 2), $a = 0{,}09$ (Curves 3) are represented. The arrows mark the directions of the curves path-tracing when the angle of attack $\alpha(\tau)$ changes.

Let's study the bahaviour of the thrust force coefficient C_T (Fig. 7). Let's take a right halfloop and follow the change $C_T(\alpha(\tau))$. It is visible that the increasing of α from 0 to α_{max} causes the change of C_T along the low part of the half loop, and the decreasing of it causes the change of C_T along the top part of the half loop. It is known that the increasing of α from 0 to α_{max} approximately corresponds to the acceleration section of

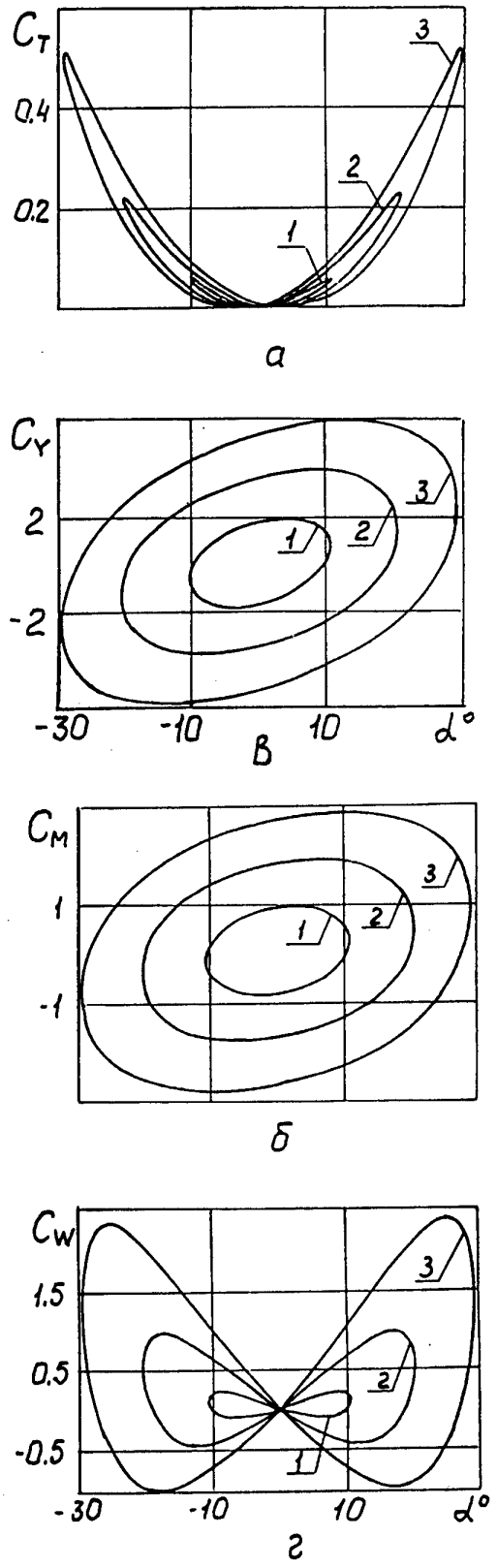


Fig. 7

the wing movement track and vice versa, the reduction of it corresponds to the deceleration mode. During this process the intensive overflow of the flow through the leading edge of the wing is formed near the end of the acceleration track section. The phase of the deceleration following after this process leads to the short-term increase of the velocity of this overflow relative to the wing. In future the wing will pass the same angles of attack in the reverse order in the conditions of the circulation having been generated round the leading edge that finally causes the occurence of the suction force dynamic hysteresis.

In the similar way the inertial influence of the added mass of the fluid causes the correction of the pressure differential ΔP on the wing that is nonsymmetric in sign. In its turn it causes the dynamic hysteresis of other hydrodynamic coefficients.

THE INFLUENCE OF FORCES OF VARIOUS NATURE

Let's examine the contribution of the forces of various nature acting on the oscillating wing : the inertial forces, the forces of the circulatory and vortical nature. The circulatory component is the quasi-steady analog of Zhukowski force and is determined by the current value of the circulation along the contour near the wing. (without taking into account the separated vortices) and by the relative undisturbed velocity. The inertial component is the nonsteady component dependent from the current added mass of the wing that is determined by the velocity of change of the circulation along the liquid contour encompassing the separated vortex street. The vortical component is determined by the current value and distribution of the vortices round the wing [10].

Let's consider first the case of the rotational oscillations with the frequency $p^* = 9$ and the angular amplitude $\theta = 3.8^0$ round the leading edge of the wing. We can note that the wake form for such small amplitude has a slight distinction from the wake form in case of progressive oscillations with the linear amplitude a, being equal to the linear vertical travel of the wing's trailing edge.

For this case Fig.8a and Fig.8b show the contribution of each component into the thrust force and the lift force of the oscillating wing. The continuous curve numbered 1 corresponds in all pictures to the summary thrust force coefficient, (Fig. 8a), and the lift force one (Fig.8b).

It can be observed that for this case the main contribution in C_T and C_Y is made by the force of inertial nature; the vortical one is near zero during the whole cycle of oscillations and the circulatory one oscillates with small values of amplitude near zero values.

To test the influence of Strouhal number p^* value upon the redistribution of the contribution of these forces the calculations were held represented in Fig. 9. There are the components of the thrust force coefficient laid off on the ordinates axis referring to the full thrust force coefficient ($i = 1$ means the contribution of the inertial force, $i = 2$ - the contribution of the circulatory one, $i = 3$ the contribution of the vortical one).

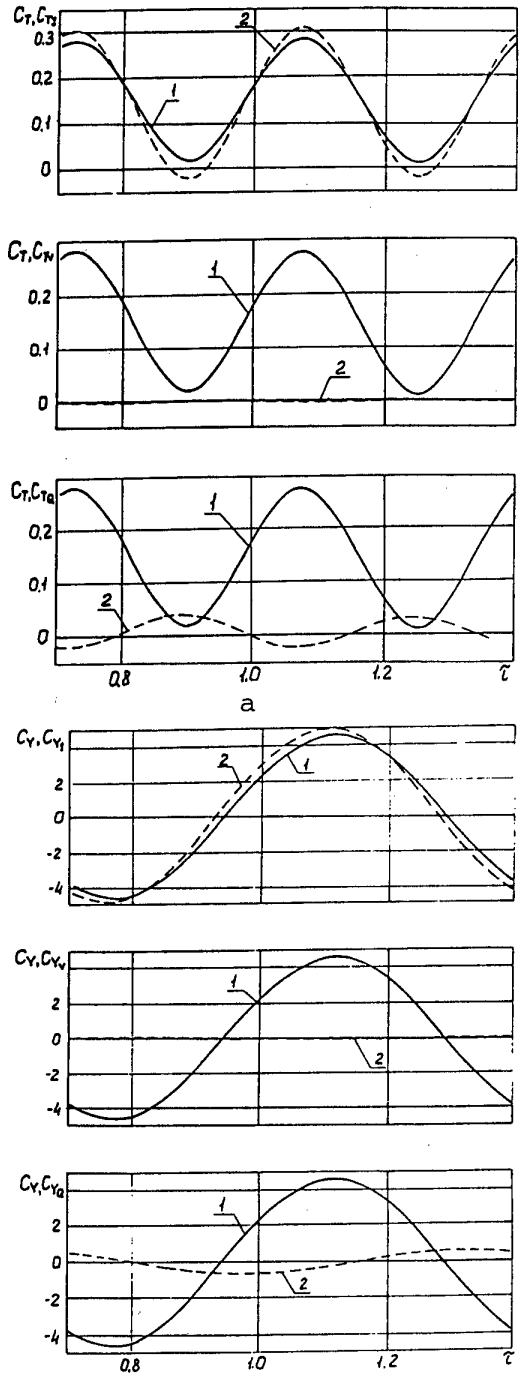


Fig. 8

It can be seen from the figure that for this case the indicated redistribution of forces is valid in a whole for all values of p^*. For values of $p^* < 4$ the negative contribution of the circulatory component merely appears and is compensated with the increase of the inertial component.

In the same time it is known that under progressive oscillations of the thin wing the whole thrust force is created by the suction force of the circulatory nature.

The investigation of the contribution of all three components for this oscillations type is also a matter of interest.

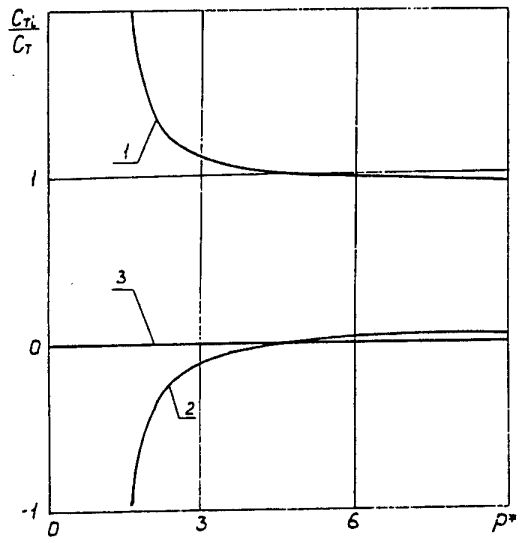


Fig. 9

Fig. 10 shows the results of these calculations for the case $\alpha = 0{,}05$, $p^* = 10$.

It can be observed that although the thrust force in this case is fully determined by the force of the circulatory nature, the main contribution into the lift force is still made by the inertial component.

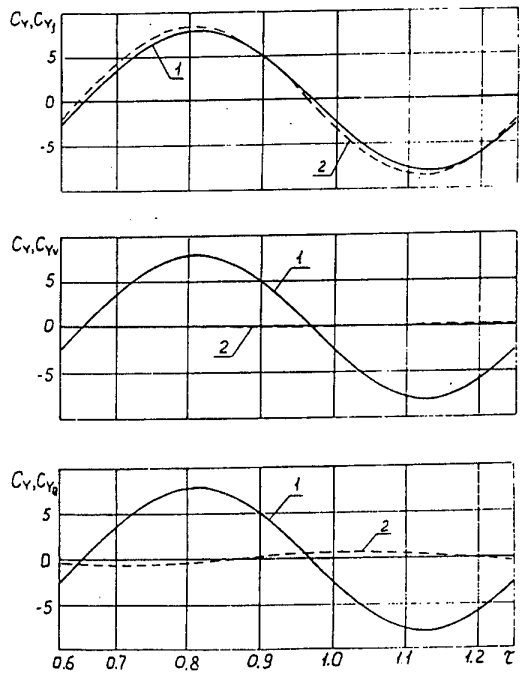
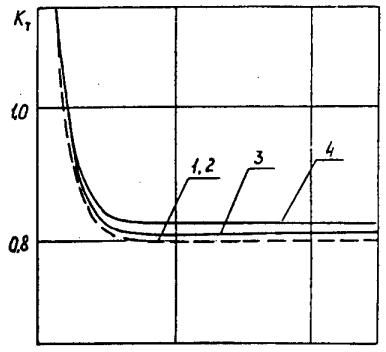


Fig. 10

The results received convincingly prove the afore mentioned explanations of mechanisms of the appearance of the nonsteady phase shifts and of the dynamic hysteresis of hydroaerodynamic characteristics of oscillating wings.



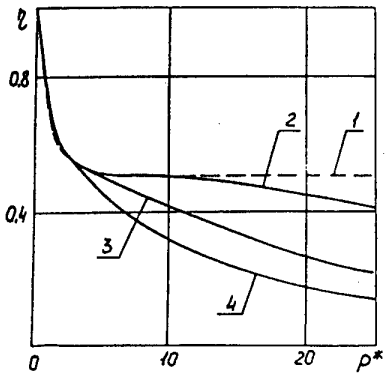


Fig. 11

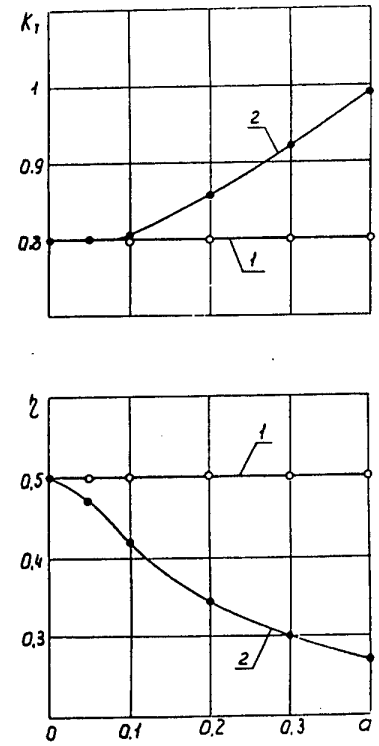


Fig. 12

And finally, let's study the bahaviour of the reduced thrust force coefficient and the efficiency dependent from the amplitude and the frequency of oscillations. As

it was noted above, the linear theory is not able to simulate the process of vortex sheet deformation.

The second argument in favour of necessity of the non-linear simulation is the assumption of the linear theory regarding the small values of the angles of attack and the oscillations amplitudes does not give the possibility to correctly simulate the oscillations with the finite amplitudes. This fact is illustrated in the Fig.11, 12 where the Curves 1 correspond to the linear theory and the other line corresponds to the non-linear theory under amplitude values a = 0,01 (Curves 2), a = 0,04 (Curves 3), a = 0,08 (Curves 4) (Fig. 11), and the frequency $p^* = 5$ (Fig. 12). It can be seen from the figures that the linear theory significantly highers the values of efficiency under big values of Strouhal number and finite amplitudes of progressive oscillations.

It can be also seen that the behaviour of the thrust force coefficient C_T in dependence from the amplitude a deviates from the square dependence, and the efficiency deviates from the linear dependence having been obtained on basis of the linear theory.

CONCLUSIONS

The linear theories describe the behaviour of the thrust coefficient and the efficiency in a qualitatively correct way only for small values of frequency and oscillations amplitudes. For efficiency the distinction from the non-linear theory can already be observed under small values of amplitude.

The adequate description of the vortex wake structure behind the oscillating wing by means of the non-linear theory and the discrete vortices method gives us the possibility to compute the propulsive characteristics more precisely. In particular, the investigation of such phenomenon as dynamic hysteresis of hydroaerodynamic characteristics shows that the results of the linear and the non-linear theories coincide only under frequency values $p^* < 1.5$.

On basis of computations under the non-linear theory it was stated that the main contribution in the thrust force and in the lift force of the wing-propulsor for the examined oscillations type is made by the forces of inertial nature.

REFERENCES

1. Белоцерковский С.М., Ништ М.И. "Отрывное и безотрывное обтекание тонких крыльев идеальной жидкостью", Москва, Наука, 1978, 352с.
2. Белоцерковский С.М., Лифанов И.К. "Численные методы в сингу+лярных интегральных уравнениях", Москва, Наука, 1985, 256с.
3. Довгий С.А. "Численный расчет гидродинамических характеристик колеблющегося крыла конечного размаха" в "Математические методы МЖГ", Днепропетровск, 1982, с.156 - 161.
4. Довгий С.А. "Исследования вихревых течений за колеблющимися крыльями", в "Наука - механике", Киев, 1983, с.109-116.
5. Довгий С.А., Шеховцов А.В. "Усовершенствованный метод дискретных вихрей", Киев, 1995, 9с.(Деп. рук., ИГМ НАН Украины, ГНТБ Украины, 06.07.95., N 1692, Ук.95).
6. Dovgiy S.A., Babenko V.V., Kozlov L.F. "The influence of the outflow generated vortex structures on the boundary layer characteristics" LTT, IVTAM Symposium, SpringerVerlag, Berlin, Heidelburg, 1985, pp. 41-49.
7. Довгий С.А., Копейка О.В. "Влияние твердой поверхности на гидродинамические характеристики двух колеблющихся крыльев при их нелинейном взаимодействии", Бионика, Вып.24, 1990, с. 28 - 33.
8. Довгий С.А.,Шеховцов А.В. "Об одном механизме образования высокой подъемной силы при трепещущем полете насекомых", Бионика, Вып. 26, 1993, с. 74-83.
9. Довгий С.А., Шеховцов А.В. "Оптимальные режимы работы крыльевого движителя с двумя степенями свободы", Киев, 1995, 36с, (Деп. рук., ИГМ НАН Украины, ГНТБ Украины 06.07.95.; N 1695 - Ук.95).
10. Довгий С.А.,Шеховцов А.В. "К вопросу о роли вихревого следа в создании силы тяги на машущем крыле" в "Гидродинамика больших скоростей (Труды VI Всероссийской научной школы)", 1996, с. 48 - 52.
11. Шеховцов А.В. "Проявление эффектов нестационарности при расчете пропульсивных характеристик плавникового движителя в нелинейной постановке" в "Гидродинамика больших скоростей. (Труды VI Всероссийской научной школы)", 1996, с. 210 - 216.
12. Довгий С.А. "Нестационарная нелинейная гидроаэродинамика колеблющихся крыльев в ограниченных потоках", Дисс. д.ф.-м.н. Киев, 1996, 335с.
13. Бисплингхоф Р., Эшли Х., Халфмен Р. "Аэроупругость", Москва, 1958, 800с .
14. Karman Th.,Sears W.R. "Airofoil theory for non-uniform motion", J. of Aeron. Sciences, 5,N9-10, 1938, pp.415-462.
15. Седов Л.И. "Плоские задачи гидродинамики", Москва, Наука, 1966, 448с.

DISTINCTIVE FEATURES OF THE WAVE PLATE (OR FISH) MOTION

L.I.Korennaya
National Academy of Sciences - Institute of Hydromechanics
8 / 4 Zhelyabov str., Kyev, 252057
Ukraine

SUMMARY

The measurements of the thrust force of the wave-like deformable plate in three-dimensional flow were carried out on specially constructed equipment. The laws which were found out by other authors in researches of water animals (fish and dolphins) were reviewed. The vortical model of the wave-like deformable plate reflects three-dimensional flow space. This model was used to calculate the hydrodynamic forces and coefficients of the wave-like deformable plate (the mechanical model of wave propulsion). Our measurements, calculations, comparisons with ideal hydraulic propulsion have shown the distinctive features of the wave-like deformable plate as it creates the thrust force.

The distinctive features of boundary layer formation on the wave-like deformable body are also considered. There is a boundary layer control system in nature with running waves. Concepts similar to Prandtl's about boundary layer control by means of the moving surface of the body has existed in nature for centuries.

1. INTRODUCTION

The results of research of a wave-like deformable plate in three-dimensional flow are discussed.

Our experiments were carried out in the flume of the Institute of Hydromechanics, the Ukrainian National Academy of Sciences. Actually the wave plate is a mechanical model of wave propulsion having prescribed kinematic parameters. The range of these parameters was wider in comparison with the range for water animals.

The data for water animal kinematics for comparisons and calculations were taken from earlier reports of the Institute of Hydromechanics.

2. GEOMETRICAL AND KINEMATIC PARAMETERS OF THE WAVE PLATE

The plate was made from 2 mm thick rubber. It was aligned horizontally and had streamwise length $L = 400$ mm and the width across the flow $H =$ 100 mm. Hence its aspect ratio was small, 0.25.

The coordinate system $oxyz$ connected with the plate moves uniformly and with the velocity V relative to the stationary fluid, Figure 2. The running wave

$$y = A(x)sin(\omega t + \beta x + \varphi_0) \qquad (1)$$

propagates along the plate in the direction from the leading edge to the trailing adge with the constant relative velocity $C = \lambda f$.

Here, $A(x)$ is the amplitude function, $\omega = 2\pi f$ is the circular frequency, $\beta = \frac{2\pi}{\lambda}$ is the wave number, λ is the wavelength, f is the frequency, φ_0 is the phase angle.

The wave was generated the following way. Seven links were fixed to the plate, Figure 1. They produced phase-shifted sine oscillations so that the running wave was created.

It is possible to imagine the running wave as follows. We take a rigid "infinite" sinusoid enclosed in a piece of a flexible sleeve. This sleeve plays the role of the fish body. When the sinusoid is moved inside the sleeve, all elements of the sleeve are subjected to transverse oscillations. The sleeve represents a transversely deformable body according to the wave propagation. The velocity of the sinusoid inside the sleeve is the wave velocity, C. The body begins its motion opposite to the direction of the running wave with velocity V, and always $V < C$.

The thrust force of the plate was measured experimentally for successively modified parameters: 1) the velocity of uniform and rectilinear motion of neutral axis of the wave-like deformable plate V, in our experiments (in inverted motion) this is the velocity of water in the flume $V^* = -V$, which was $V^* = 0$ and $V^* \approx 0.33 - 1.2m/s$ (the asterisk is for inverted flow everywhere in this paper); 2) the oscillation frequency $f \approx 1.5 - 4Hz$; 3) the number of waves that are on the length of the plate $L/\lambda = 0.25, 0.5, 0.75, 1$; 4) the amplitude function $A(x)$ of seven types: the constant oscillation amplitudes along the plate and the amplitudes increasing by linear or square law along the plate toward the

Paper presented at an AGARD FDP Workshop on "High Speed Body Motion in Water", held in Kiev, Ukraine, 1-3 September 1997, and published in R-827.

back edge.
The velocity of the running wave and the velocity of the neutral axis of the wave-like deformable plate were held constant for each experiment.

The Reynolds numbers $R_L = VL/\nu$, where ν is the kinematic viscosity of fluid, and the Strouhal number $S_L = fL/V$ were changed respectively in limits from 1.25 to 4.6×10^5 and from 0.6 to 6. The ratio of velocities $C/V = S_\lambda$ was limited from 0.64 to 21.

3. PROPULSION REGIME OF THE WAVE PLATE

3.1. Thrust Force and Effect of Non-Stationarity

The experimental researches have shown the following.
– Vhen $V < C$ and in opposite directions is the necessary condition for the creation of propulsion force (thrust). This occurs in nature.
– The thrust force decreases when the velocity of the uniform motion of the neutral axis of the wave-like deformable plate V (in our experiments the velocity of water in the flume) increases.
– The thrust force at $V = 0$ is proportional to square of the oscillation frequency .
– The thrust force for the constant oscillation amplitude along the plate and $V = 0$ is approximately proportional to square of amplitude of oscillations.
– The law of change of oscillation amplitude along the plate has decisive significance. It is possible to obtain considerably larger values of the thrust force if the oscillation amplitude is increased in the direction from the forward edge of plate to back one.
– The nature of dependence of the thrust force from the wavelength and from the running wave velocity is more complicated. With increase of Strouhal number fL/V the transition from the greater wavelength to the smaller one is desirable.

The results agreed with the kinematic data of the water animals as well as with results of the wave-like deformable body researches of other authors. Earlier the particular case of the wave-lake deformable plate in two-dimensional flow was investigated experimentally [1].
It is necessary to draw attention to the regimes of plate deformations on which the thrust of the plate is equal zero. These regimes are analogous to those of fish motion as the thrust force created by the wave-like deformable body is equal on value and is directed oppositly to the resistance force of the wave-like deformable body. For these regimes Strouhal numbers calculated with the wavelength $S_\lambda = f\lambda/V = C/V$ were within the limits 1.18 to 1.44. For fish and dolphins Strouhal numbers $S_\lambda = f\lambda/V = C/V$ range from 1.05 to 1.59 in experiments done earlier by other authors in the water tunnel of the Institute of Hydromechanics. The range of Strouhal numbers for our plate is within the range of Strouhal numbers for water animals. So there is identity of the conditions for formation of the hydrodynamic forces on the wave-like deformable plate and for active motion of water animals. And also this fact shows the reliability of data obtaind in experiments with the plate and in experiments with the subjects.

The mechanism of thrust force creation by the wave-like deformable body is a naturel phenomenon. Let us compare the wave-like deformable plate, the mechanical model of the wave propulsion, with other types of propulsion created by man.

The parts of the wave 1, 2, 3, 4, 5 in Figure 2a located within the extreme points of the sinusoid act similarly to an oar blade or the paddle of a water wheel. They push the fluid in the opposite direction of the body motion. They are the working elements of the wave propulsion. The fluid that is pushed by the running wave carries with it the definite momentum of the fluid. By the law of conservation of the momentum the opposite momentum is obtained by the deformable body. Thus, the part of the energy that was spent on creation of the running wave was transformed into work of the thrust force.

Let us show that the conditions of creation of the thrust are $V < C$ and in opposite directions. When a body moves in fluid, the direction of the resistance force coincides with the direction of the flow velocity in inverted motion. It is clear from Figure 2a that in the case $V < C$ and in the opposite direction the flow velocity in inverted motion $U^* = -(C - V)$ and the velocity of the uniform rectilinear motion of the neutral axis of the wave-like deformable body V have identical directions. Thus, the thrust that is necessary for motion of the wave-like deformable body with the velocity V is due to the resistance force to motion in water of the sinusoid moving on the body with velocity C. The inclination of the axis of the deformable body of the water animals to the neutral axis of the wave is equal to 40 degrees on the average. Such a body is a badly streamlined one . The main contribution to its resistance is the form resistance. Really the system of vortices is formed near to the extreme points of the sinusoid and the edges of the plate, Figure 2c, 3 . The thrust force has the greatest value when $V = 0$ because then the velocity U^* is maximum. At $V = C$ and in the opposite direction the velocity U^* and the thrust are equal to zero. If the wave-like deformations occur in regime $V > C$, the flow velocity U^* and the resistance force of the sinusoid are directed opposite to the motion of the plate and there is no thrust.

Let us look at the wave propulsion working elements 1, 2, 3 at $t = t_0$, Figure 2a, then at elements 2, 3, 4 at $t = t_0 + 1/2f$, then at 3, 4, 5 at $t = t_0 + 1/f$. It is visible that the working elements arise gradually, move on the plate, and gradually disappear. They exist during the final time interval, $\Delta t = L/C = L/\lambda f$. Hence the final interval Δt depends on the kinematic and geometrical parameters of the plate. The events are similar to those at a sudden start of a body with constant velocity. It is known that at the initial moment of the body motion at constant velocity the hydrodynamic forces considerably exceed the hydrodynamic forces at stationary motion [2, 3]. Therefore, if the period Δt is small, the hydrodynamic forces should be calculated with regard to non-stationarity. The non-stationarity coefficient k is equal to the ratio of non-stationary (experimental) forces to quasi-stationary ones (calculated in according to the quasi-stationary theory) T_{exp}/T_{calc}, Figure 4. Let us compare L/λ in Figure 4 and $\Delta t = L/\lambda f$. In Figure 4 L and f are constant for each curve. Therefore, Δt is only a function of λ. So L/λ is dimensionless time number. At $L/\lambda = 0.25$ Δt is one-fourth at $L/\lambda = 1$. The k has the greatest value at $L/\lambda = 0.25$ where Δt has the minimum value. The non-stationarity coefficient approaches unity as Δt tends to infinity. The experiments have shown that the most influence on the nonstationarity coefficient have: a) the wave length, namely, the number of the waves present along the plate length, b) the law of change along the plate of the oscillation amplitude $A(x)$. But the non-stationarity coefficient depends on the oscillation frequency to a lesser degree, Figure 4. The body shape and the shape of the lateral edges considerably influence the process of vortex formation, and the research of the effect of non-stationarity is considerably complicated.

Each element of the wave-like deformable body (it is "n" in Figure 2) makes a transverse oscillatory motion. Therefore the values of instantaneous flow velocity and instantaneous angle of attack of each element change continuously. This helps to justify logically the vortex model of the wave-like deformable plate [4], Figure 3. Usually the occurrence of a vortex is considered as a negative phenomenon. However it is a good idea to increase the intensity of the vortex in the case of wave propulsion. This phenomenon takes place in nature. There are sharp edges of the flippers of the water animals. And experiments [1] have shown that the thin metal wave-like deformable plate with the sharp edges had thrust considerably larger than the rubber plate.

We have two main paradoxical conclusions.
– The thrust force of the wave propulsion is stipulated by the resistance force of the sinusoid. So the thrust, that is useful force, arises from the resistance force, that is usually a harmful force.
– Hydrodynamic forces of the wave propulsion are greater than their calculated quasi-stationary values. Hence, it is necessary to take into consideration the non-stationary effect.

3.2. Wave plate efficiency

The calculations of the wave-like deformable plate in accordance with [4] were carried out. The dependence of the wave-like deformable plate efficiency η on the thrust load coefficient $\sigma_T = 2T/\rho F_T V^2$, where ρ is fluid density, F_T is the hydraulic section of the wave-like deformable plate that is equal to the product of width of the plate and the total amplitude of the trailing edge of the plate. Figure 5 represents one wavelength on the length of the plate and the linear change of the oscillation amplitude along the plate. The seven links for setting of the running wave had the cross oscillation amplitudes A = 0.01, 0.014, 0.018, 0.022, 0.026, 0.030, 0.34 m.

Curve 2 in Figure 5 for experimental values of the thrust load coefficient shows that the wave-like deformable plate for small aspect ratio has low efficiency.
The calculations of efficiency for imaginary propulsion were carried out:
– without friction forces (without internal losses in the propulsion) – Curve 3;
– without friction forces and inertia forces – Curve 4;
– without friction forces, inertia forces and without inductive velocities – Curve 5.
The relative position of Curves 2, 3, 4, 5 in Figure 5 shows that friction forces and inertia forces considerably reduce the efficiency of the wave-like deformable plate. The efficiency decreases, but in less degree, under the influence of inductive velocities.
Curve 1 for the ideal hydraulic propulsion [5] is in Figure 5. It is calculated by the formula

$$\eta_i = \frac{2}{1 + \sqrt{1 + \sigma_{T_i}}} \qquad (2)$$

Here σ_{T_i} is the thrust load coefficient of the ideal propulsion.
The wave-like deformable plate efficiency, Curve 2, is far below the ideal hydraulic propulsion efficiency, Curve 1.

There were assumptions about high efficiency of wave propulsion in the literature. They were not verified. It is impossible in nature to realize the rotary motion of parts of the body relative to each other, and so much energy is spent for overcoming the inertia forces at cross oscillations of a body. However it should be noted in relation to the water animal motor-propulsion complex that its common efficiency can be sufficiently high. In the first

place, the same body fulfils functions of motor and propulsion. Secondly, it is not excluded that in most cases the water animals use resonance regimes that are economical ones. It is possible in the future designers offer the devices using principles of energy transformation existing in nature. Then application of such devices will be very effective.

4. FRICTION FORCES OF THE WAVE-LIKE DEFORMABLE BODY AT PROPULSION REGIME

An idea of Prandtl was to reduce the velocities in the boundary layer by means of moving surface of the body in the flow direction. It is possible to remove completely the boundary layer if the surfac of the body has the velocity that is equal to the external flow velocity.

We come back to the model used for demonstration of the running wave. This is a body having the form of a sinusoid in the flow. The surface (or boundary) of this sinusoid is moving along the sinusoid. Really in each following moment of time the very same element of the plate takes the new element of the sinusoid.

The theoretical and experimental researches of moving surfaces were undertaken more than once including the question of boundary layer control. The parameter of the moving surface p was introduced into the theoretical research [6] for the plate in the form of the half-plane as the ratio of the velocity of the moving surface to the mainstream velocity. The following conclusions were derived which reveal the effects of moving surfaces.
— When the velocity of the moving surface equals the value and direction of the mainstream velocity, $p = 1$, the hydrodynamic forces do not act on the plate. The flow around the plate is potential.
— When the velocity of the moving surface is more than the mainstream velocity, $p > 1$, the plate has no resistance force, it has thrust force.
— When the velocity of the moving surface and the mainstream velocity are directed opposite to each other, $p < 0$, the plate has a resistance force less than on stationary surface at $p = 0$.
The effects of the moving surfaces in applications in engineering could be very useful. But complexity of design and increase of cost block the way to the technical applications of the effects of the moving surfaces. At the same time nature makes wide use of the effects of moving surfaces as will be shown below.

Let us enter the parameter p, similar by structure to the parameter for the half-plane. This is the ratio of the velocity of the moving surface W_L to tangential component of the external flow velocity W_t^* on the plate element. Naturally this parameter has another value for each element of the wave-like deformable plate and in each following moment of time on the individual plate element.

$$p = \frac{W_L}{W_t^*} \tag{3}$$

For the regime of propulsion under consideration the surface moving in flow direction takes place in the extreme points of our sinusoid necessarily, as the velocities $W_L = -C$ and $W_t^* = U^* = -(C-V)$ are directed to one side, Figure 2b. Bearing in mind that $S_\lambda = \lambda f/V = C/V$ we have

$$p_{y_{max}} = \frac{C}{C-V} = \frac{S_\lambda}{S_\lambda - 1} \tag{4}$$

The parameter $p_{y_{max}}$ at the extreme points of the sinusoid depends only on Strouhal number. The regimes $L/\lambda = 1$ and $T = 0$ for experiments with the plate are the closest to the regimes of the water animal's motion. The range of parameter $p_{y_{max}}$, 3.28—6.55, for the plate in this regime is within the range of parameter $p_{y_{max}}$, 2.7—21, in experiments with live water animals.

Going over to the general case, not the extreme points of the sinusoid, we must take into account the velocity of oscillatory motion of the considered plate element $V_y = \frac{dy}{dt}$, Figure 2b. The angle α formed by the neutral axis of the running wave and the considered element of the plate, $\alpha = tan^{-1}\frac{dy}{dx}$, indicates the position of the considered plate element.

In general case

$$p = \frac{C + V_y \frac{dy}{dx}}{C - V - V_y \frac{dy}{dx}} \tag{5}$$

The surface moving in the flow direction is realized only if

$$C - V > V_y \frac{dy}{dx} \tag{6}$$

The kinematic data of the water animals were used for calculations. The following results were obtained.
— The ratio (6) is fulfilled on all points of the dolphin body. The scheme of the moving surface in the flow direction is fully realized here.
— The ratio $C - V < V_y \frac{dy}{dx}$ is fulfilled for fish on a significant part of their body. Consequently $p < 0$ and the scheme of the moving surface opposite to the direction of the flow takes place here.
It is necessary to note, that p for the different fish varieties has close values, in the range from -2.54 to -2.68 for the caudal flipper at $y = 0$. It is considerably different from $p = 389$ for the dolphin, see the table, Figure 6.

So, the scheme of the moving surface in the flow direction, $p > 0$, is realized for the entire length

of the dolphin body moving at $R > R_{cr}$, and the scheme of the moving surface opposite to the flow direction, $p < 0$, is realized on a significant part of the fish body moving at $R < R_{cr}$,

From structure of formula (5) follows that when $V = 0$, p has the least significance and $p_{y_{max}} = 1$. Hence, friction forces at extreme points of the sinusoid are absent, and in other points of the sinusoid are less than they were at regimes when V is not equal to 0. Therefore, in oder to reduce the influence of the friction forces (internal losses in propulsion), the regimes $V = 0$ were used in the analysis of experimental results.

The knowledge of physical processes taking place in the boundary layer of the wave-like deformable body is necessary for successful use of the effects of the running wave and the moving surface in engineering. The method of geometrical summation of the velocity profiles in the boundary layer of the wave-like deformable plate is here offered for the case of a moving surface in the flow direction and for the case of a moving surface against the flow direction, Figure 7. This is the first step to uncovering the physical processes and for qualitative comparisons. The two regimes below, which were close to the regimes of the live moving water animals and to the regimes in both [7] and the author's experiments, were chosen for accuracy and clearness.

Regime A: $p = 4.33$;
$V = 0.5m/s$; $C = 0.65m/s$; $C/V = 1.3$

Regime B: $p = -2.33$;
$V = 0.5m/s$; $C = 0.35m/s$; $C/V = 0.7$

All velocity profiles are constructed in the same scale, Figure 7. The theoretical Blasius profile for the laminar boundary layer was used for construction of the velocity profiles a for W_t^* and b for W_L. It was taken into consideration that the velocity W_t^* and W_L complete the total cycle of changes for the distance that equals $1/2$ wavelength. The velocity profile c is obtained by geometrical summation of the profiles a and b. The resulting profile c is constructed in coordinate system connected with the element of the "sinusoid". It is necessary to take up the coordinate system connected with the moving surface (with the plate). They were given velocities equal in magnitude W_L and opposite W_L directed for the plate element and for the environmental fluid, profile d. The velocity of the external flow in the resulting profile e is equal in magnitude of the velocity V and in the opposite direction.

Comparing the calculated velocity profiles for wave-like deformable plates at $p > 0$ and $p < 0$ we will note the following important properties of these profiles.

The resulting profile e at $p > 0$, Regime A, is similar in form to the experimental velocity profile in the boundary layer of the wave-like deformable plate [7]. This velocity profile is more convex in comparison with the one on the flat plate and is similar to the profiles of the stable type. Transition from laminar to turbulent boundary layer is delayed in this case [8].

The scheme of the moving surface in the flow direction is realized on the entire body length of the dolphin moving at Reynolds numbers which are larger than critical ones. Hence the velocity profile in the boundary layer of the dolphin body should be the profile of the stable type, and transition in the boundary layer is delayed.

Really, there are interesting results in [9]. The amplitude of the pressure pulsations in the boundary layer depends on the type of the dolphin motion at $R > R_{cr}$. The level of the pressure pulsations in the boundary layer corresponds to the developed turbulent flow for passive motion (inertial). But for active motion the level of the pressure pulsations is considerably less (1.5 - 2 times) and corresponds to insufficiently advanced turbulent flow.

The theoretical Blasius profile for the laminar boundary layer on the flat plate is the dot-and-dash curve in the profile e.

In case of $p < 0$ (the scheme of the moving surface against the flow direction) the value of the velocity gradient (du/dy_1) at $y_1 = 0$ is less in comparison to the velocity gradient (du/dy_1) at $y_1 = 0$ on the flat plate. As the local viscous shear on the body surface is directly proportional (du/dy_1) at $y_1 = 0$, then the surface friction should be slightly smaller than on the flat plate. This agrees with the conclusions in [6].

The scheme of the moving surface against the flow direction is realized for a significant part of the fish body moving at Reynolds numbers which are lower than critical. Hence the local viscous shear for fish should be smaller than on the flat plate.

We see that these features of the boundary layer for wave deformations of the body are successfully used in nature. The delay of transition from the laminar to turbulent boundary layer takes place at greater critical Reynolds numbers. And the reduction of the surface friction takes place at Reynolds numbers which are less than critical ones.

The wave-like deformable body can be used not only as the mechanism for creation of a thrust force but also as the mechanism influencing the boundary layer in control systems for decrease of the resistance forces.

REFERENCES

1. Kelly, H.R., Rentz, A.W., Siekmann, J., " Experimental Studies on the Motion of a Flexible Hydrofoil ", J. Fluid Mechanics, 19, part 1, 1964, pp 30–48.

2. Schehlova, M.G., Ohnev, V.I., " Experimental Results of Forming of Force at Pulsed and Accelerated Motion, Trudi TsAHI, issue 1379, 1971, pp 1–24.

3. Byelotzercovsky, '.M., Nisht, M.I., Sokolova, O.N, " Calculation of Separated Flow around Slender Wing of Finite Aspect Ration" Izvestiya Akademii Nauk SSSR, Mekhanika Zhidkosti i Gaza, 2, 1975, pp 107–112.

4. Korennaya, L.I., " Method of Calculation of Wave Propulsion ", Bionika, Issue 15, 1981, pp 59–63.

5. Bacin, A.M., Miniovich, I.J., " Theory and Calculation of Propeller Screws ", Leningrad, Russia, Sudpromhiz, pp 24–58.

6. Cherny, H.H., " Boundary Layer on a Plate with Moving Surface ", Reports Akademii Nauk SSSR, 213, 4, pp 802–803.

7. Taneda, S., Tomonari, Y., " An Experiment on the Flow around a Waving Plate ", J.Physical Society of Japan, 36, 5, May 1974, pp 1683–1689.

8. Schlihting, H., " Theory of Boundary Layer ", Moscow, Russia, Nauka, 1974, cc 197–205.

9. Romanenko, Ye.V., " Foundations of Statistical Biohydrodynamics ", Moscow, Russia, Nauka, 1976.

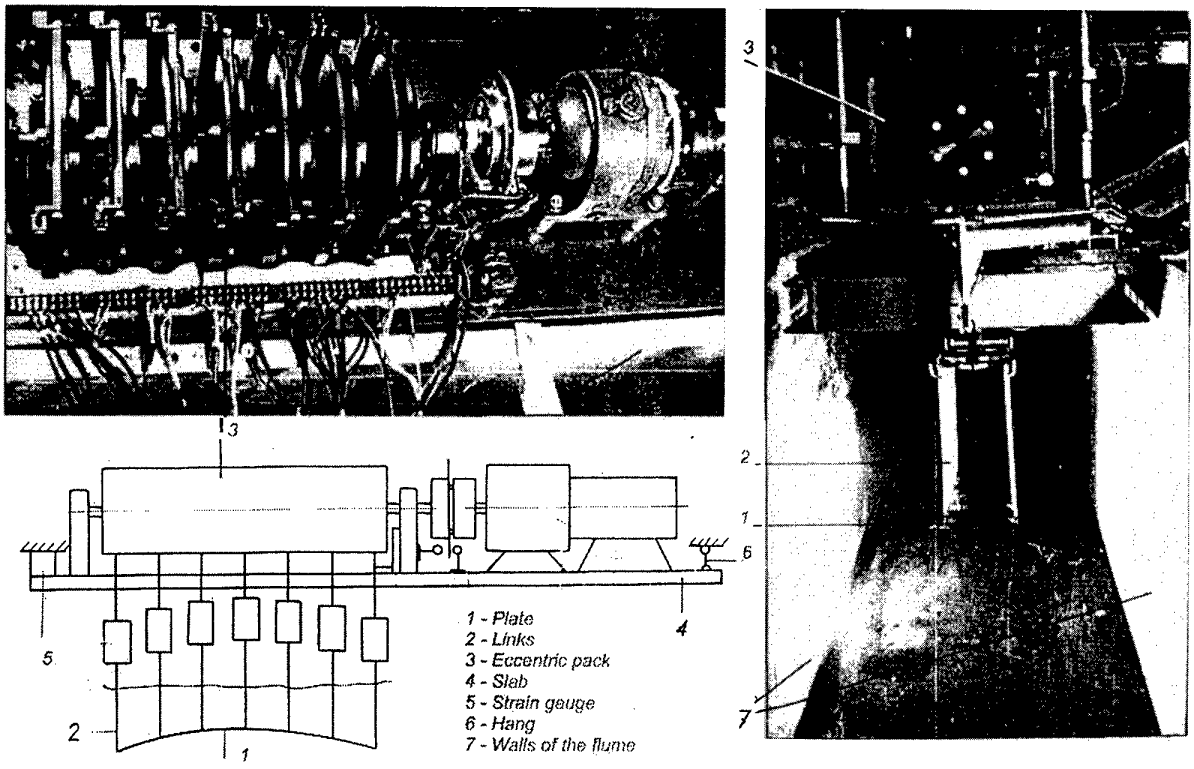


Fig. 1. Experimental installation.

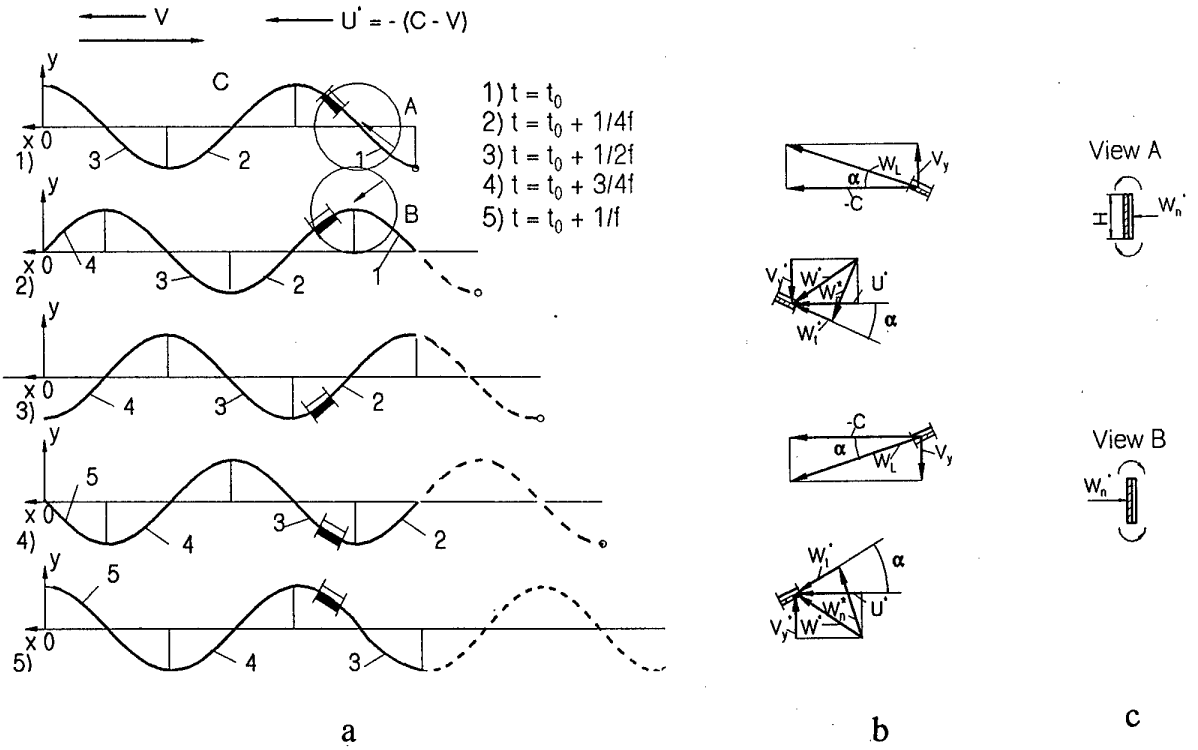


Fig. 2*a*, *b*, *c*. Regime of propulsion of the wave plate.

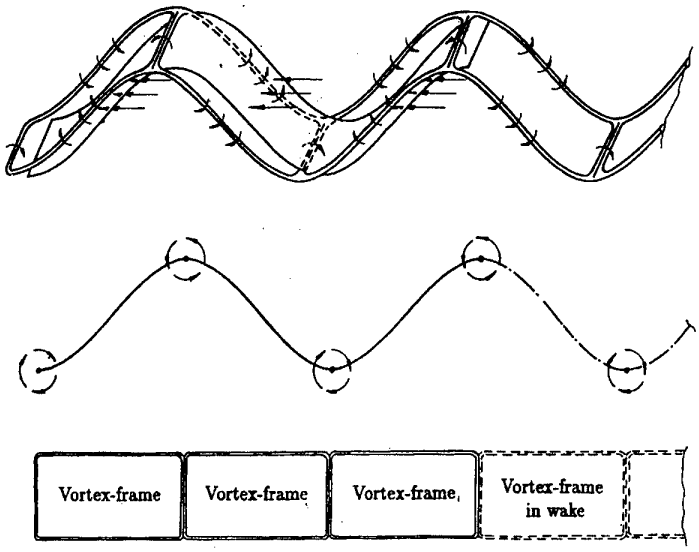


Fig. 3. Wortex model of the wave plate.

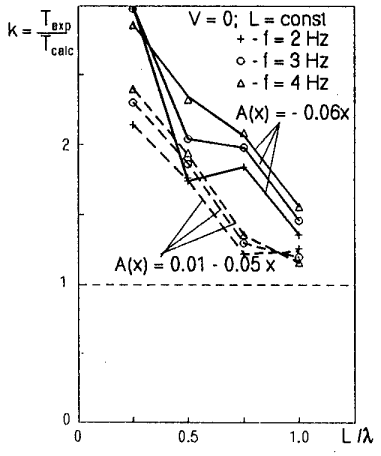


Fig. 4. Coefficient of non-stationarity.

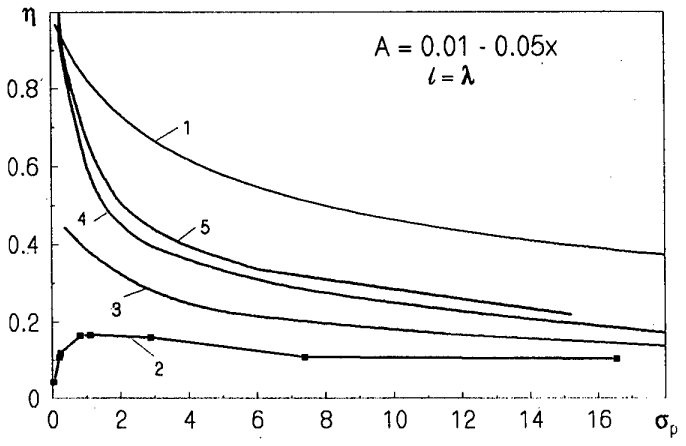


Fig. 5. Wave plate efficiency.

Water animal varictics (Latin)	L [m]	V [m/s]	$Re = \frac{VL}{\nu}$	C [m/s]	$C-V$ [m/s]	λ [m]	A [m]	f [Hz]	$\left(v_y \frac{dy}{dx}\right)_{y=0}$ [m/s]	$\frac{\left(v_y \frac{dy}{dx}\right)_{y=0}}{C-V}$	p
Tursiops truneadus	2.60	2.34	$6 \cdot 10^6$	3.12	0.78	1.90	0.15	1.64	0.77	0.99	389
Belone	0.48	1.05	$4.5 \cdot 10^5$	1.21	0.16	0.22	0.03	5.58	1.04	6.53	-2.55
Pomatomus saltatrix	0.42	1.72	$6.5 \cdot 10^5$	1.95	0.23	0.37	0.05	5.27	1.61	7.00	-2.58
Sarda sarda	0.16	1.12	$1.6 \cdot 10^5$	1.25	0.13	0.13	0.02	9.58	0.94	7.53	-2.68
Cristivomer namaycush	0.21	1.33	$2.5 \cdot 10^5$	1.48	0.15	0.15	0.02	9.74	1.21	8.10	-2.54

Fig.6. Parameter of the moving surface p for the caudal flipper of the dolphin (Tursiops truneadus) and for the fish (Belone, Pomatomus saltatrix, Sarda sarda, Cristivomer namaycush).

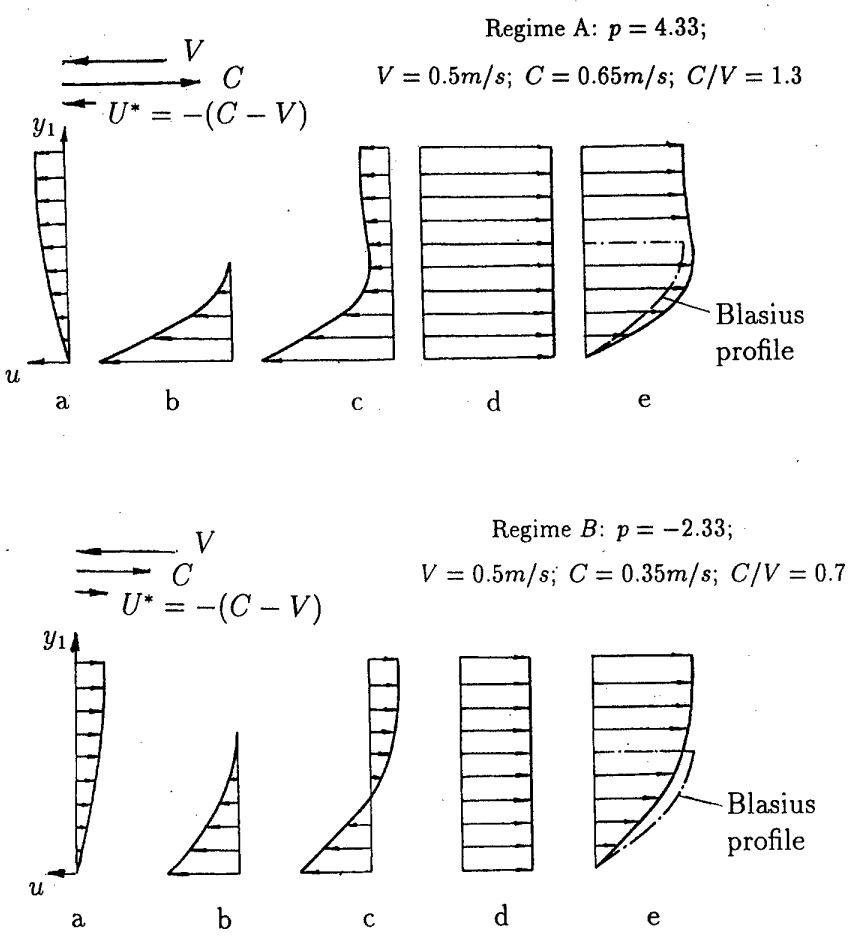


Fig. 7. Scheme of the moving surface of the wave plate.

A New View of the Dynamics of Reynolds Stress Generation in Turbulent Boundary Layers

Brian J. Cantwell
Dept. of Aeronautics and Astronautics, Stanford University
Stanford, CA 94305 USA
and
Juan M. Chacín
Dept. of Mechanical Engineering, Stanford University
Stanford, CA 94305 USA

Abstract

The structure of a numerically simulated turbulent boundary layer over a flat plate at $Re_\theta = 670$ (Spalart [17]) was studied using the invariants of the velocity gradient tensor (Q and R) and a related scalar quantity, the cubic discriminant ($D = 27R^2/4 + Q^3$). These invariants have previously been used to study the properties of the small-scale motions responsible for the dissipation of turbulent kinetic energy (Chen *et al.* [6], Soria *et al.* [16] and Blackburn *et al.* [3]). In addition, these scalar quantities allow the local flow patterns to be unambiguously classified according to the terminology proposed by Chong *et al.* [8]. The use of the discriminant as a marker of coherent motions reveals complex, large-scale flow structures that are shown to be associated with the generation of Reynolds shear stress $-\overline{u'v'}$. These motions are characterized by high spatial gradients of the discriminant and are believed to be an important part of the mechanism that sustains turbulence in the near-wall region.

Nomenclature

Roman Symbols

$\mathbf{A}_{ij}$	Velocity gradient tensor ($\partial U_i/\partial x_j$)
D	Discriminant of the velocity gradient tensor $\mathbf{A}_{ij}$
P	First invariant of the velocity gradient tensor $\mathbf{A}_{ij}$
p	Instantaneous pressure
Q	Second invariant of the velocity gradient tensor $\mathbf{A}_{ij}$
R	Third invariant of the velocity gradient tensor $\mathbf{A}_{ij}$
Re_θ	Reynolds number based on momentum thickness
$\mathbf{S}_{ij}$	Rate of strain tensor
U_i	Instantaneous velocity component
$u'v'$	Instantaneous Reynolds shear stress
u_τ	Wall shear velocity
x_j	Cartesian coordinate direction
x^+, y^+, z^+	Cartesian coordinate axis normalized by wall units (u_τ and ν)
$\mathbf{W}_{ij}$	Rate of rotation tensor

Greek Symbols

λ	generic eigenvalue of the velocity gradient tensor
ν	kinematic viscosity
ρ	Fluid density
θ	Boundary layer momentum thickness

Introduction

Since the early 1980's there has been tremendous progress in our ability to directly simulate wall-bounded turbulent flows at moderate Reynolds number. However, for the foreseeable future, simulations will be restricted to a relatively small number of flows. Therefore the vast majority of engineering applications, especially those involving high Reynolds number, will continue to require the use of phenomenological models. Unfortunately, there has been much less progress in the development of models capable of handling all but the narrow range of flows and conditions for which they have been tailored. Part of the reason why progress has been slow is that we still lack a complete physical picture of what Townsend [20] called the "main turbulent motion" and which, as Klebanoff [11] showed, contains most of the turbulent kinetic energy and is responsible for the generation of most of the Reynolds stress. Nor do we have an adequate picture of the fine scale motion responsible for the dissipation of kinetic energy. This is not surprising in

Paper presented at an AGARD FDP Workshop on "High Speed Body Motion in Water", held in Kiev, Ukraine, 1-3 September 1997, and published in R-827.

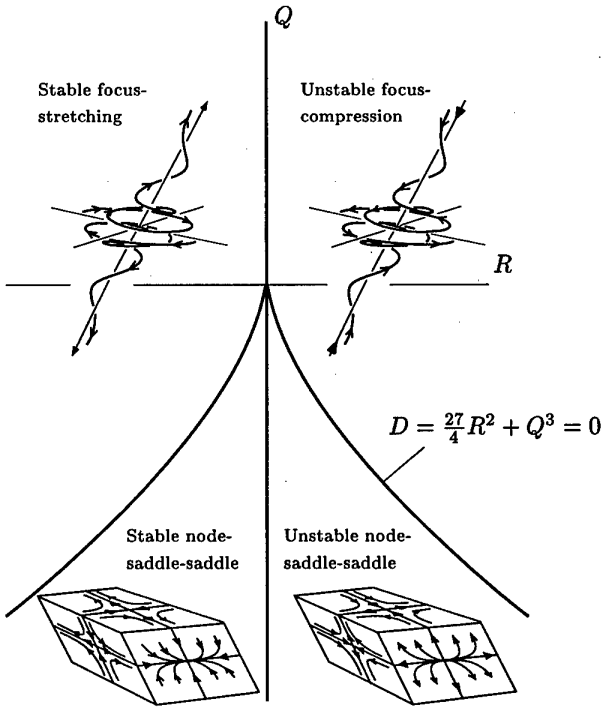


Figure 1: Summary of three-dimensional incompressible topologies (from Soria *et al.* [16]).

view of the difficulties inherent in the description of such a complex, highly elliptic, time-dependent, three-dimensional phenomenon.

The first step toward understanding the physics of turbulent motion is to develop a robust, unambiguous method for identifying dynamically important flow structures. This paper is mainly concerned with this issue. The methodology described here is based on the use of the invariants of the velocity gradient tensor and a related scalar quantity, the cubic discriminant. Identification of turbulent structure in terms of the discriminant provides a useful connection between Reynolds stress producing motions and dissipating motions. The method is particularly effective near the wall where the low-speed streaks, first documented by Kline *et al.* [12], are clearly defined along with their physical connection to the outer flow. New insights also emerge into the concept, introduced by Townsend [19], of active versus inactive turbulence. Finally, the turbulent structure can be compared with Theodorsen's [18] original vision of a hierarchy of horseshoe eddies as well as with Townsend's [19] attached eddy model of wall flow as recently extended by Perry and Marušić [14].

Discriminant-based structure identification

Chong *et al.* [8] provide a road map to linear, three-dimensional flow patterns in terms of the invariants of the velocity gradient tensor. The approach is useful for the classification of compressible and incompressible flows. The method treats every point in a flow field as a critical point as seen by an observer moving with the fluid particle at the point in question at the instant of time in question. The local flow is the solution of a third-order system of autonomous, linear ordinary differential equations whose solution behavior is determined by the invariants of the velocity gradient tensor. We consider fluid motions that are describable by the leading terms in a Taylor series expansion of the velocity field about a point.

$$U_i(\vec{x},t) = U_i(\vec{x}_o,t) + \left.\frac{\partial U_i}{\partial x_j}\right|_{\vec{x}_o} \Delta x_j + \frac{1}{2}\left.\frac{\partial^2 U_i}{\partial x_j \partial x_k}\right|_{\vec{x}_o} \Delta x_j \Delta x_k + \cdots . \quad (1)$$

We will exclude singular cases such as vortex sheets or shock waves as well as highly degenerate flows where the local flow is determined by quadratic or higher order terms in eqn. 1. If the origin of the coordinate system translates at the local velocity of the expansion point ($U_i(\vec{x}_o,t) = 0$), then eqn. 1 reduces to the following, autonomous set of ordinary differential equations

$$U_i(\vec{x},t) = \frac{dx_i}{dt} = \mathbf{A}_{ij}x_j, \quad (2)$$

where $\mathbf{A}_{ij}$ is the velocity gradient tensor ($\mathbf{A}_{ij} = \partial U_i/\partial x_j|_{\vec{x}_o}$). Using standard linear algebra tech-

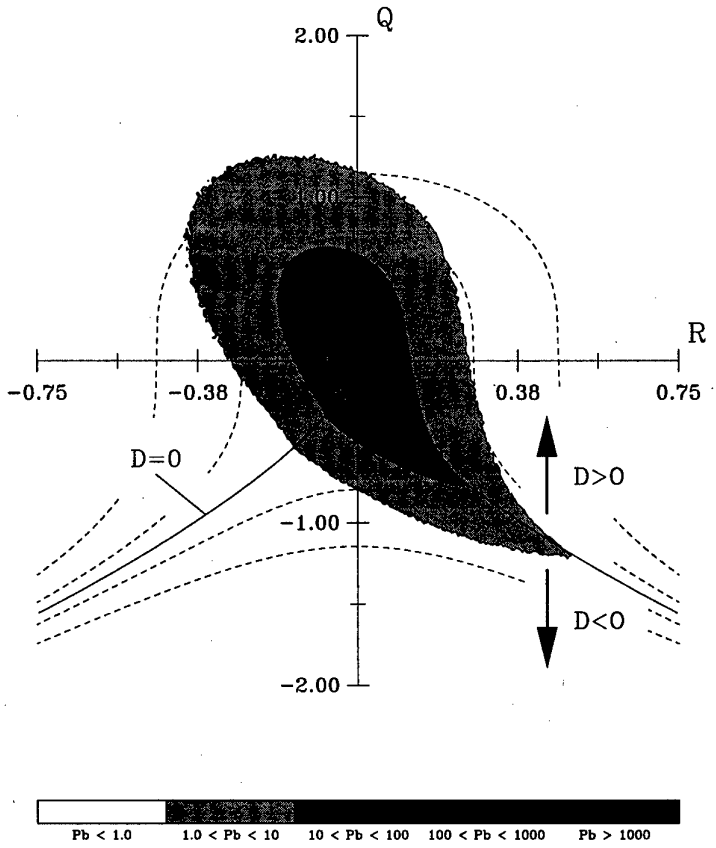


Figure 2: Contour plot of joint probability distributions of the invariants of the velocity gradient tensor at $Re_\theta = 670$ (from Chacin *et al.* [5]).

niques, the shape of the solution trajectories — instantaneous streamlines in this case—can be uniquely classified according to the nature of the eigenvalues, and associated eigenvectors, of $\mathbf{A}_{ij}$. The eigenvalues are the roots of the characteristic cubic equation for this tensor, given by

$$\lambda^3 + P\lambda^2 + Q\lambda + R = 0. \tag{3}$$

The coefficients of this polynomial are the invariants of the velocity gradient tensor given by

$$P = -\mathbf{A}_{ii}, \tag{4}$$

$$Q = \frac{1}{2}P^2 - \frac{1}{2}\mathbf{A}_{ik}\mathbf{A}_{ki}, \tag{5}$$

$$R = -\frac{1}{3}P^3 + PQ - \frac{1}{3}\mathbf{A}_{ik}\mathbf{A}_{kn}\mathbf{A}_{ni}. \tag{6}$$

The first invariant P is identically zero for incompressible flow. It can be readily shown that the nature of the roots of eqn. 3 is determined by the sign of the discriminant of $\mathbf{A}_{ij}$, defined as

$$D = \frac{27}{4}R^2 + Q^3. \tag{7}$$

If the discriminant is positive, eqn. 3 admits two complex and one real root. If $D < 0$, all the roots are real. Using these quantities, the local geometry of three-dimensional instantaneous streamlines around any point in a turbulent flow field can be cataloged using the invariants Q and R and the discriminant D. Figure 1 summarizes all the possible streamline shapes that can exist in an incompressible flow, classified according to the values of these invariants.

An important feature of this method is that both Q and R, and consequently the discriminant, are invariant under non-uniform translations and are independent of the orientation of the coordinate system. More generally, they are invariant under any affine transformation. As pointed out by Perry and Chong [13], this technique also avoids the dangers involved in trying to study a flow field by projecting three-dimensional streamlines onto two-dimensional planes.

This method was used by Blackburn *et al.* [3], Soria *et al.* [16], Cheng and Cantwell [7] and Chacin *et al.* [5], to study the flow structure of numerically simulated turbulent flows. The data considered here are from the direct simulation of a turbulent boundary layer

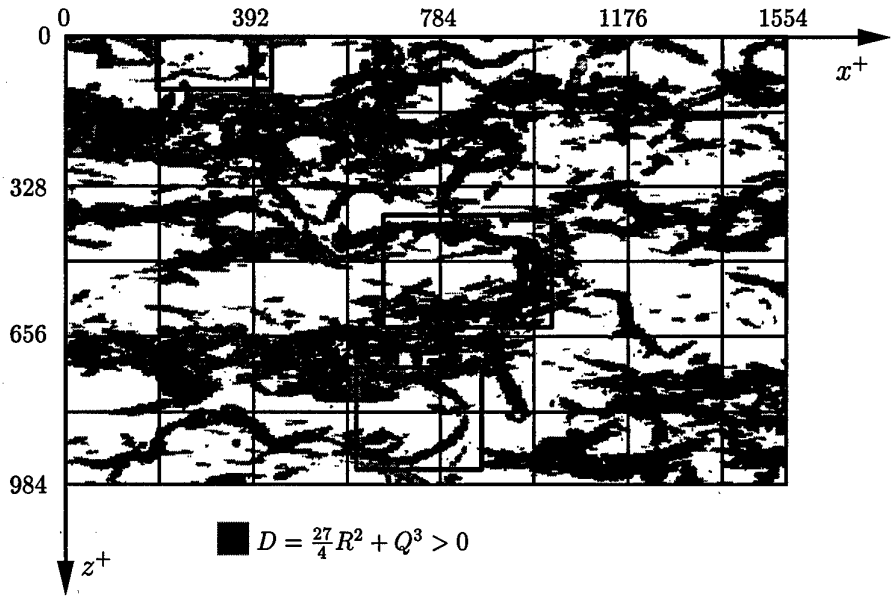


Figure 3: Top view of the zero pressure gradient, turbulent boundary layer showing flow structures of positive discriminant (focus topology). The vertical extent of the domain is from $y^+ \approx 1$ to $y^+ \approx 138$. All the areas that are not colored have topology of the type node-saddle-saddle (from Chacin *et al.* [5]).

over a flat plate under zero pressure gradient computed by Spalart [17] at $Re_\theta = 670$. The invariants of the velocity gradient tensor were obtained at every point in the flow and cross-plotted in the $Q-R$ plane. The result, shown in fig. 2, is a joint probability distribution for these two invariants. Four contour levels with logarithmic spacing are plotted and the value Pb shown in the legend corresponds to the density of data points ((R, Q) pair) per unit area of the plot, per simulation time step. The total number of samples, obtained over 500 time steps was approximately 7.9×10^8 data points. The tear-drop shape of the distribution, as well as the tendency of the data to gather near the origin (as indicated by the darkest contour), have been observed in several different flows—including decaying turbulence (Cheng and Cantwell [7]), time-developing compressible and incompressible mixing layers (Soria *et al.* [16] and Chen *et al.* [6]) as well as in turbulent channel flow (Blackburn *et al.* [3])—and seem to be a distinctive and universal trait of turbulence. Furthermore, the second invariant Q can be broken into two terms

$$Q = \frac{1}{2}\left(\mathbf{W}_{ij}\mathbf{W}_{ij} - \mathbf{S}_{ij}\mathbf{S}_{ij}\right), \qquad (8)$$

where $\mathbf{W}_{ij}$ is the antisymmetric, rate-of-rotation tensor and $\mathbf{S}_{ij}$ is the symmetric rate-of-strain tensor. The first term in eqn. 8 is proportional to the enstrophy density whereas the second one is proportional to the mechanical dissipation of kinetic energy. This expression, together with the sketches in fig. 1, highlight the fact that the local flow pattern is determined by a tradeoff between rotation and strain.

The invariants of the velocity gradient, rate-of-rotation and rate-of-strain tensors were used by Blackburn *et al.* [3] to conduct detailed studies of regions of high dissipation in a simulation of turbulent channel flow. The authors observed a strong tendency towards alignment between the vorticity vector and the intermediate, principal eigenvector of the rate-of-strain tensor ($\mathbf{S}_{ij}$). This is consistent with the numerical studies of Ashurst *et al.* [2] and the experiments of Tsinober *et al.* [21] in free shear flows. In wall bounded flows, for these highly dissipative areas of the flow, both terms on the right hand side of eqn. 8 tend to be of comparable magnitude particularly very near the wall where all three scalars, Q, R and D go rapidly to zero.

While the joint probability distribution of Q and R shown in fig. 2 is useful for the study of some of the characteristics and properties associated with certain specific flow patterns, it is also important to study the relationship between the joint pdf's and physical features of the flow structure. As shown in fig. 1, the curve $D = 0$ marks the boundary between focus-type and node-saddle-saddle-type flow patterns in the $Q-R$ plane. Therefore, a surface of $D = 0$ in physical space will identify regions of the flow within which the eigen-

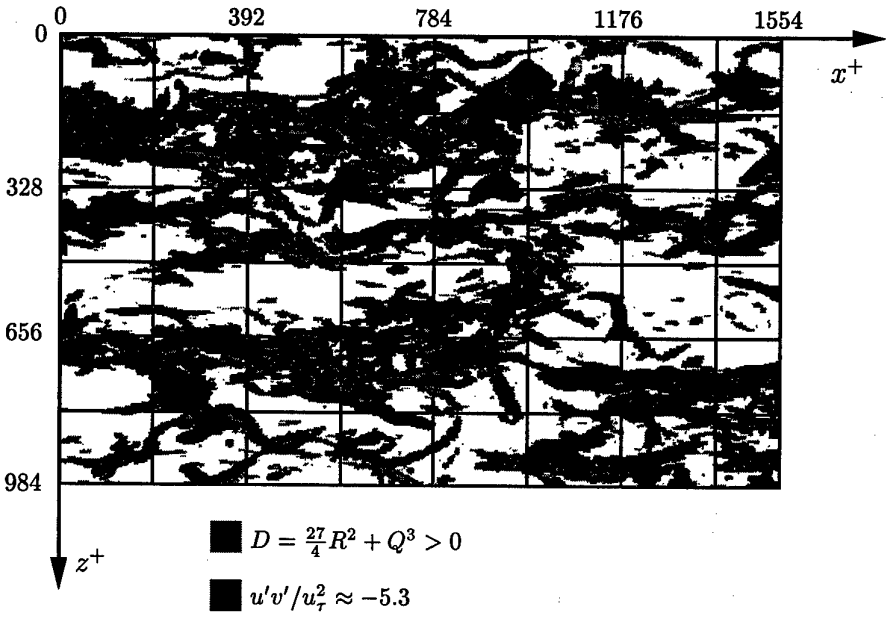


Figure 4: Top view of the computational domain showing regions of positive discriminant (light gray) and isocontours of instantaneous $-u'v'$ (dark gray).

values of the velocity gradient tensor are complex and thus may be a useful marker of dynamically important motions (see Blackburn *et al.* [3]). These tend to be mainly regions dominated by vortex stretching. This approach was used to produce fig. 3. The dimensions shown in the figure were normalized using wall variables (u_τ and ν). As a practical matter, to avoid interpolation errors, a surface of $D = 0.04$ was used to make the plot. The maximum value of D was approximately four orders of magnitude larger.

The isocontours of $D = 0.04$ show that the points in the flow where the local topology is of focus type are grouped together forming complicated flow structures of dimensions comparable to the boundary layer thickness which extend almost all the way to the wall. The majority of them are tilted streamwise tubes inclined away from the wall that seem to bundle and twist creating long braids. Farther away from the wall, into the logarithmic region, some of these tubes turn in the spanwise direction and form horseshoe shaped eddies reminiscent of the coherent motions first proposed by Theodorsen [18]. Three of these structures are indicated by the square outlines in fig. 3. The surface $D = 0.04$ delineates the flow structure all the way down to the viscous sublayer. Within the sublayer Q, R and D fall rapidly to zero and are identically zero at the wall. This figure depicts a boundary layer structure which is consistent with the picture proposed by a number of investigators since Theodorsen [18] including Townsend [20], Head and Bandyopadhyay [9], Robinson [15] and more recently Perry and Marušić [14]. However, it needs to be pointed out that these pictures are based purely on the vorticity and do not take into account the fundamental balance between vorticity and strain which is essential for the formation and shape of the coherent structure and which is accounted for by the discriminant. This distinction becomes crucial near the wall where, as pointed out by Blackburn *et al.* [3], the vorticity is very diffuse and is therefore a poor marker of flow structure.

Relationship to Reynolds stresses

The importance, and usefulness, of the study of these organized motions hinges on whether or not they can help clarify the mechanism by which the flow of energy from the mean flow to the small dissipative scales is sustained. It is believed that a significant fraction of the turbulent kinetic energy in wall bounded flows is produced in short, intermittent, quasi-periodic events called bursts (see for example Kim *et al.* [10] or Antonia *et al.* [1]) which are associated with the passage of large eddies. Of similar interest is the mechanism by which the components of the Reynolds shear stress tensor are generated since they constitute the closure problem of turbulence modeling. Figure 4 shows the same view of the flow previously presented in fig. 3. In the light shade of gray are, again, the regions where the discriminant of the velocity gradient tensor is positive (focus topology). Superimposed on this view, in

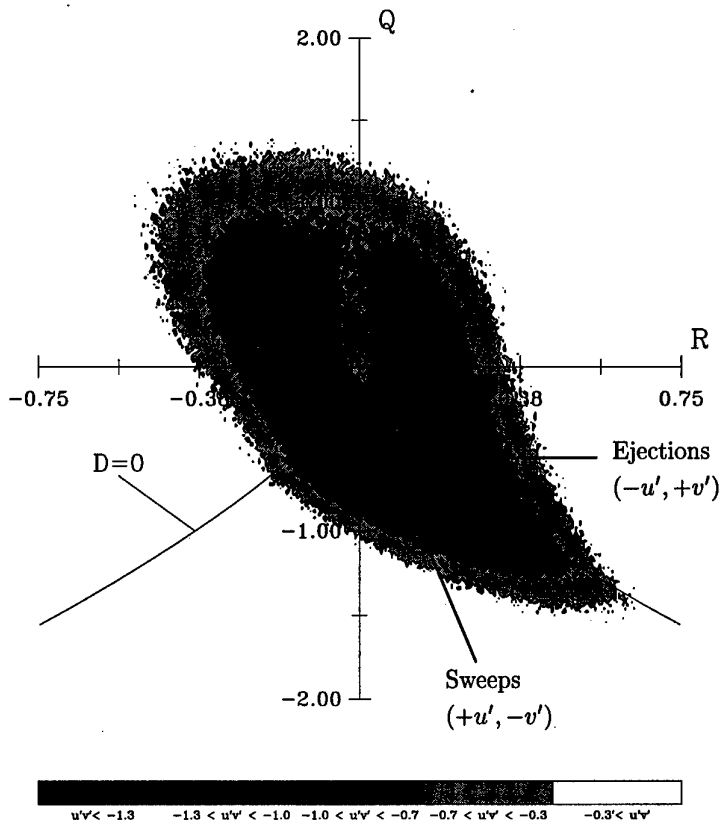


Figure 5: Time-averaged Reynolds shear stress ($-u'v'$) generating events associated with the four incompressible flow topologies. The values of the contour levels shown are normalized by u_τ^2 (from Chacin *et al.* [5]).

the darker shade of gray, are isocontours of high, instantaneous values of $-u'v'$.

This particular component of the Reynolds stress tensor is the most important one for this particular flow as it is the only one that appears in the production term of the turbulent kinetic energy equation ($-\overline{u'v'}\partial U/\partial y$). The events shown in fig. 4 are about 6 times stronger than the peak, time-averaged value of this stress. There is a clear spatial association between these bursts and the structures visualized using the discriminant as they seem to occur in the immediate neighborhood of these eddies. A close inspection of this figure reveals that the Reynolds stress generating motions actually occur where the discriminant is close to zero and rapidly changing sign. Statistical evidence of this observation will be discussed shortly. Notice also that the areas of fig. 4 where there are no visible, nearby structures of focus-type topology are also devoid of motions with high values of $-u'v'$. A computer-based flow animation prepared using several hundred, consecutive realizations shows these bursts growing, convecting and dissipating together with the $D > 0$ eddies. This figure gives new meaning to the notion of active and inactive turbulence once proposed by Townsend [19].

The nature of these active motions can be further studied using the $Q - R$ plane. Figure 5 shows the time-averaged value of the $-u'v'$ stress associated with each one of the four possible three-dimensional topologies. The peculiar shape of this figure shows that the strongest events are located toward the lower right branch of the $Q - R$ distribution with the highest values of $-u'v'$ corresponding to local flow patterns with either unstable-focus compression or unstable node-saddle-saddle motions (with the events of these latter type being located, in physical space, adjacent to regions of positive discriminant). It can also be seen that there are two distinctive peaks for the strongest $-u'v'$ motions, one located right above the $D = 0, R > 0$ curve and one right below it. These two peaks were further studied using the quadrant decomposition technique first proposed by Wallace *et al.* [22]. As shown in fig. 5, it was observed that the strong $u'v'$ motions below the $D = 0$ line were composed mostly of sweeps (positive u', negative v') or high speed fluid moving downward. Those located above the aforementioned curve, in the region of unstable-focus compression topology were almost entirely comprised of ejections (negative u', positive v'); low speed fluid moving away from the wall.

In addition to suppressing turbulent fluctuations, the

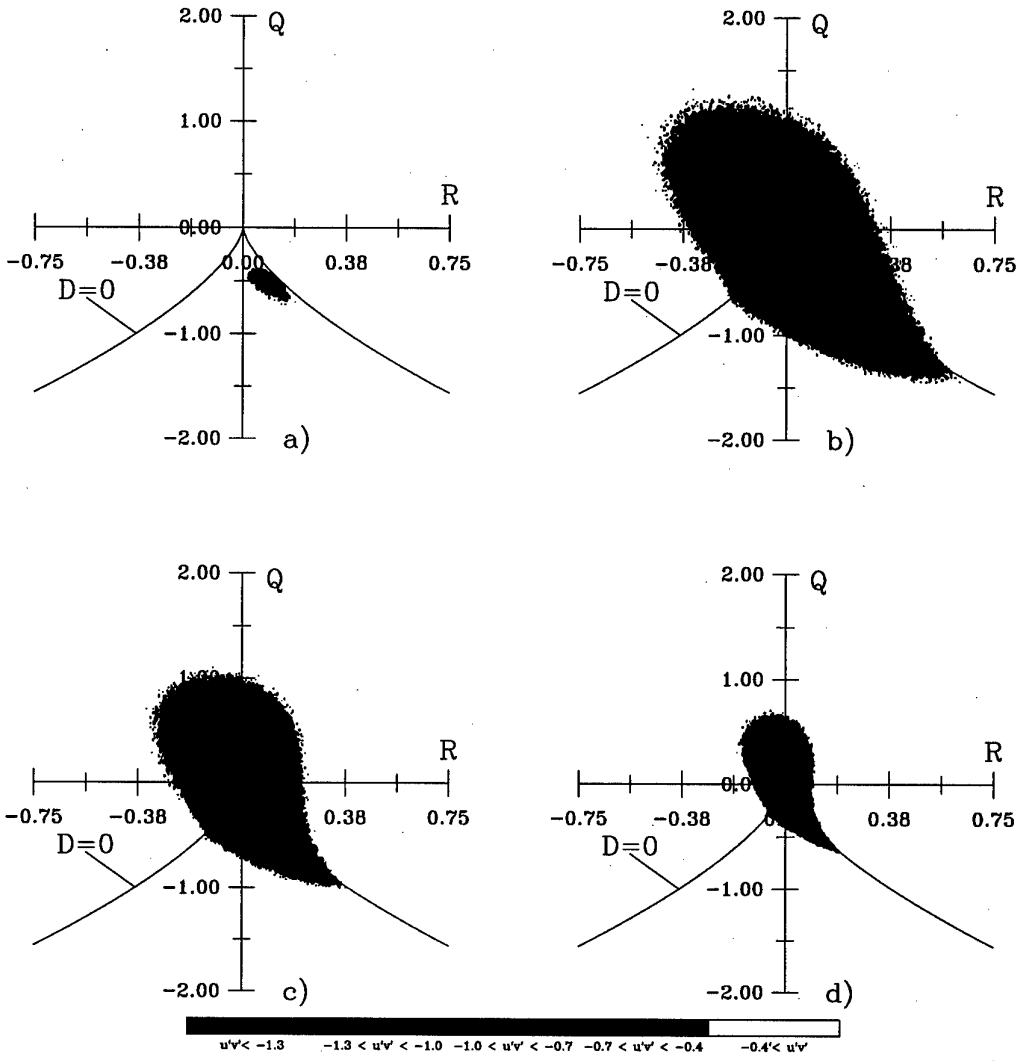


Figure 6: Time-averaged Reynolds shear stress ($-u'v'$) generating events associated with the four incompressible flow topologies as a function of distance to the wall. a) $y^+ < 5.0$, b) $5.0 < y^+ < 41$, c) $41 < y^+ < 107$, d) $y^+ > 107$. The values of the contour levels shown are normalized by u_τ^2.

presence of a no-slip boundary also creates a strong shear. As a consequence, the flow is strongly inhomogeneous in the direction normal to the wall. Since the data used to create fig. 5 comes from the entire layer, the effects of the shear cannot be observed. This issue is addressed in fig. 6. As indicated in the figure, the boundary layer was divided into four regions (viscous layer, buffer region, log layer and the wake) and the same calculation for $-u'v'$ was repeated in each separate zone. In the viscous sub-layer (fig. 6a)), where the turbulence level is predictably low, the unstable node-saddle-saddle topology is the only kind of flow pattern that contributes significantly to the Reynolds shear stress and, as can be observed, these events are almost exclusively sweeps (positive u', negative v') or high speed fluid moving downward. Farther away from the wall, from the buffer region to the outer layer (figs. 6b) through d)), the profiles are similar to that shown in fig. 5. The only noticeable effect of the diminishing role of viscosity is the change in the scales, with the largest range of contours occurring in the buffer region (where the production term and the turbulence intensities also peak). In these regions (buffer, log layer and wake) the strongest Reynolds stress events are associated with motions of unstable node-saddle-saddle and unstable focus-compression topology. As pointed out above, these events are located in regions where the discriminant changes sign rapidly.

Finally, fig. 7 shows a similar view to that presented in fig. 4. The dark gray contours indicate motions with very high instantaneous turbulent kinetic energy ($u_i' u_i'/2$). There is a similar spatial correlation between these energetic motions and the eddies iden-

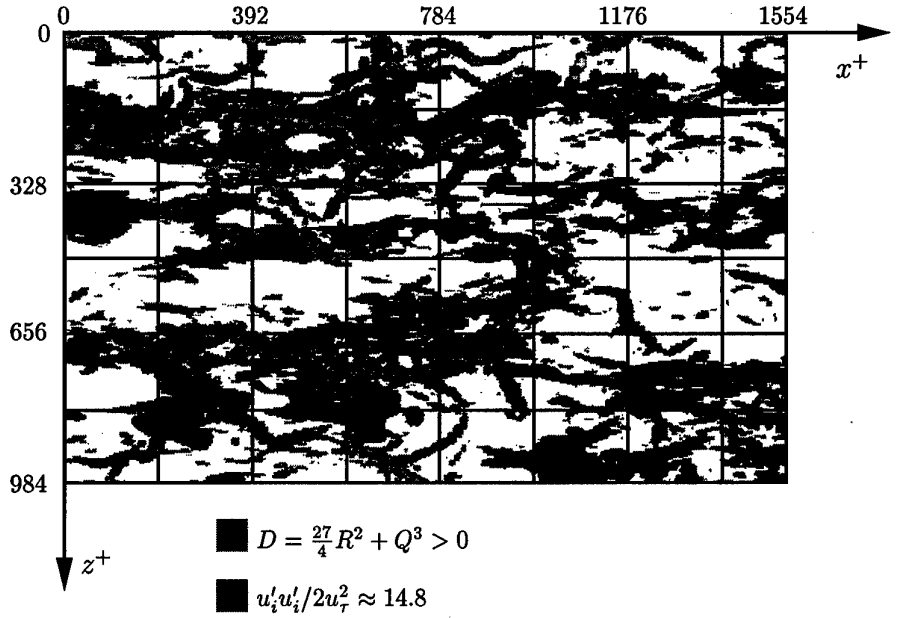


Figure 7: Top view of the computational domain showing regions of positive discriminant (light gray) and isocontours of instantaneous turbulent kinetic energy $u_i' u_i'/2$ (dark gray).

tified using the discriminant of the velocity gradient tensor, shown once again in the light gray tone. As before, active and inactive regions are evident.

Relationship to the pressure field

A comprehensive study of the kinematics of turbulence was carried out by Robinson [15] on the same numerical simulation data presented here. In that work, the author presents a taxonomy of coherent events that have been observed in turbulent flows. He points out the importance of vortical motions and how they could be used to connect various types of structures. He uses the pressure field as a means of identifying these vortical motions. The rationale is that, for a two-dimensional vortex with near-circular streamlines the pressure has to reach a minimum at the vortex center. In the absence of such near-circular streamlines, the extrema in the pressure field need not occur.

Figure 8 shows the same view of the computational domain used in fig. 3 with surfaces of constant pressure superimposed onto the structures visualized using the discriminant. These latter contours were made transparent to facilitate the comparison since pressure minima commonly lie inside the surface $D = 0.04$. The pressure threshold chosen was $p/(\rho u_\tau^2) \approx -4.3$. This level encloses the regions of the flow with the lowest, instantaneous pressure and is the same one used by Robinson [15] in his study. As can be seen in the figure, there is a general correspondence between the two fields. In particular, pressure minima generally occur where the discriminant is positive. Again, this is consistent with the view that active regions are located at the boundary of the $D > 0$ surfaces. The association however is not universal.

This issue can be further explored by examining some of the properties of the pressure field, which is governed by Poisson's equation. This equation can be recast as (see for example Cantwell [4])

$$\nabla^2 p = 2Q. \tag{9}$$

For any three-dimensional function, a necessary condition for the existence of a local minimum is given by

$$\nabla^2 p > 0, \tag{10}$$

so local pressure minima and regions of positive discriminant can only coincide in areas where $Q > 0$. As was shown in the joint probability distributions of Q and R in fig. 2, there is a significant number of flow structures where $D > 0$ and $Q < 0$. These regions can not be seen using isocontours of low pressure and, as indicated by fig. 5, these areas are important in Reynolds shear stress generation.

In addition, the use of the pressure field presents the additional complication that a threshold level must be chosen. For a relatively simple flow, with no mean pressure gradient like this one, this selection is not unduly cumbersome. For a more complex flow with pres-

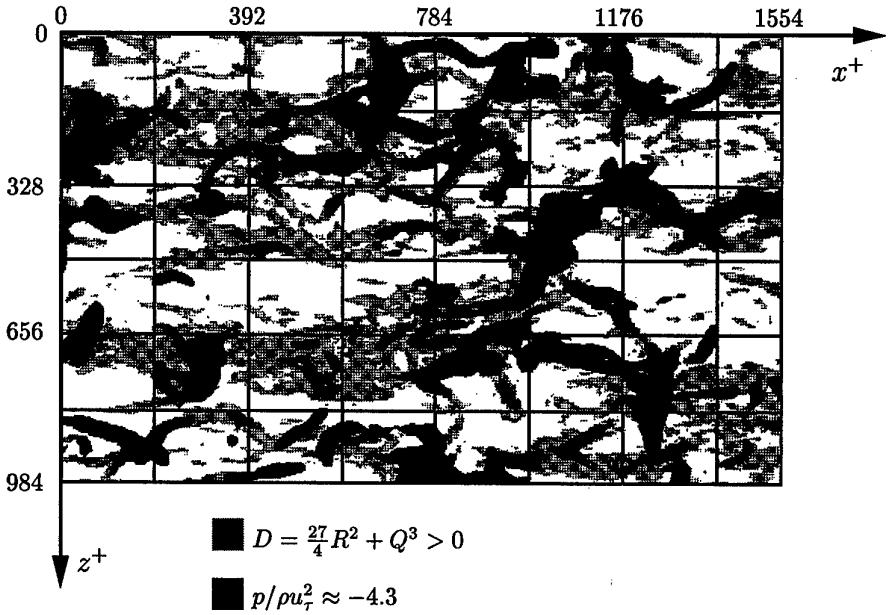


Figure 8: Top view of the computational domain showing regions of positive discriminant (light gray) and isocontours of instantaneous pressure (dark gray). The pressure threshold level is $p/\rho u_\tau^2 \approx -4.3$.

sure gradients it may not be possible to do so without a certain degree of arbitrariness. This problem is avoided by the use of the velocity gradient tensor invariants, and the discriminant, since the threshold value used ($D = 0$) is unmistakably determined by the boundary between complex and real roots for the characteristic equation (eqn. 3).

Conclusions

Perhaps no other problem in fluid mechanics has received as much attention as that of the structure of a turbulent boundary layer. In spite of all this effort the lack of a unified framework for identifying and describing the structure has been a continuing hindrance to progress. As a result, a substantial fraction of the effort has been devoted to settling nagging issues of nomenclature and communication. In this paper we have described a methodology which identifies dynamically significant features in an unambiguous and coordinate-independent way. The method relies on scalar measures of the velocity gradient field and is generally applicable to all flows regardless of pressure gradient, boundary conditions or Reynolds number. Moreover the extension to compressible flows is straightforward. The method gives new meaning and definition to the concept of active versus inactive turbulence. It also gives new meaning to the concept of an attached eddy and provides a physical connection between the flow very close to the wall and the outer part of the layer.

That the invariants of the velocity gradient tensor, and in particular the discriminant formed from them, are closely associated with Reynolds stress generating motions as depicted in fig. 5 is an important new finding which may have significant implications for turbulence modeling.

Acknowledgments

This work was supported by NASA Grant NAG-1-1610 and by the NASA Ames-Stanford Joint Institute for Aeronautics and Acoustics Grant NCC-2-55. Supercomputer resources have been provided by the San Diego Supercomputer Center and NASA's Ames Research Center. Computer flow visualization facilities were provided by the Large-scale Interactive Flow Visualization Environment (LIVE) at the National Aerodynamics Simulation facilities at NASA's Ames Research Center. The numerical simulation code was graciously supplied by Dr. Philippe Spalart.

Figures 2, 3 and 5 are reprinted by permission of the publisher from "Study of turbulent boundary structure using the invariants of the velocity gradient tensor". *Experimental Thermal and Fluid Science*, **13** (4), 308 - 317. Copyright 1996 by Elsevier Science Inc.

References

[1] Antonia, R. A., Browne, L. W. B. and Bisset, D. 1989. "Effect of Reynolds number on the organized motion in a turbulent boundary layer". In *Near Wall Turbulence*, Proc. Zaric Meml. Conference, S. J. Kline and N. H. Afgan Eds., Hemisphere Pub. Corp., 488 - 506.

[2] Ashurst, W. T., Kerstein, A. R., Kerr, R. M. and Gibson, C. H. 1987. "Alignment of vorticity and scalar gradient with strain rate in simulated Navier-Stokes turbulence". *Phys. Fluids* **30** (8), 2343 - 2353.

[3] Blackburn, H. M., Mansour, N. N. and Cantwell, B. J. 1996. "Topology of fine-scale motions in turbulent channel flow". *J. Fluid Mech.* **310**, 269 - 292.

[4] Cantwell, B. J. 1992. "Exact solution of a restricted Euler equation for the velocity gradient tensor". *Phys. Fluids A* **4** (4), 782 - 793.

[5] Chacin, J. M., Cantwell, B. J. and Kline, S. J. 1996. "Study of turbulent boundary layer structure using the invariants of the velocity gradient tensor". *Experimental Thermal and Fluid Science*, **13** (4) 308 - 317.

[6] Chen, J. H., Chong, M. S., Soria, J., Sondergaard, R., Perry, A. E., Rogers, M., Moser, R. and Cantwell, B. J. 1990. "A study of the topology of dissipating motions in direct numerical simulations of time-developing compressible and incompressible mixing layers". *Proceedings of the Summer Program*, Center for Turbulence Research, Stanford University, 139 - 161.

[7] Cheng, W. and Cantwell, B. J. 1996. "Study of the velocity gradient tensor in turbulent flow". *Joint Institute for Aeronautics and Acoustics*, Report No. TR-114.

[8] Chong, M. S., Perry, A. E. and Cantwell, B. J. 1990. "A general classification of three-dimensional flow fields". *Phys. Fluids A* **2** (5), 765 - 777.

[9] Head, M. R. and Bandyopadhyay, P. 1978. "Combined flow visualization and hot wire measurements in turbulent boundary layers". In *Lehigh Workshop on Coherent Structure in Turbulent Boundary Layers*, C. R. Smith Ed., Department of Mechanical Engineering, Lehigh University, Bethlehem, Pennsylvania, 98 - 125.

[10] Kim, H. T., Kline, S. J. and Reynolds, W. C. 1971. "The production of turbulence near a smooth wall in a turbulent boundary layer". *J. Fluid Mech.* **50**, 133 - 160.

[11] Klebanoff, P. S. 1955. "Characteristics of turbulence in a boundary layer with zero pressure gradient". NACA Report No. 1247.

[12] Kline, S. J., Reynolds, W. C., Schraub, F. A. and Runstadler, P. W. 1967. "The structure of turbulent boundary layers". *J. Fluid Mech.* **30**, 741 - 773.

[13] Perry, A. E. and Chong, M. S. 1994. "Topology of flow patterns in vortex motions and turbulence". *Applied Scientific Research*, **53**, 357 - 374.

[14] Perry, A. E. and Marušić, I. 1995. "A wall-wake model for the turbulence structure of boundary layers. Part 1. Extension of the attached eddy hypothesis". *J. Fluid Mech.* **298**, 361 - 388.

[15] Robinson, S. K. 1991. "The kinematics of turbulent boundary layer structure". NASA TM-103859.

[16] Soria, J., Sondergaard, R., Cantwell, B. J., Chong, M. S. and Perry, A. E. 1994. "A study of the fine-scale motions of incompressible time-developing mixing layers". *Phys. Fluids* **6** (2) Pt. 2, 871 - 884.

[17] Spalart, P. R. 1988. "Direct simulation of a turbulent boundary layer up to $Re_\theta = 1410$". *J. Fluid Mech.* **187**, 61 - 98.

[18] Theodorsen, T. 1955. "The structure of turbulence". In *50 Jahre Grenzschichtforsung.* H. Görtler, W. Tollmein, Eds., Braunschweig, Vieweg & Sohn. Germany, 55 - 62.

[19] Townsend, A. A. 1956. "The Structure of Turbulent Shear Flow". Cambridge Univ. Press. First ed. Cambridge.

[20] Townsend, A. A. 1976. "The Structure of Turbulent Shear Flow". Cambridge Univ. Press. Second ed. Cambridge.

[21] Tsinober, A., Kit, E. and Dracos, T. 1992. "Experimental investigation of the field of velocity gradients in turbulent flows". *J. Fluid Mech.* **242**, 169 - 192.

[22] Wallace, J. M., Eckelmann, H. and Brodkey, R. S. 1972. "The wall region in turbulent shear flow". *J. Fluid Mech.* **54**, 39 - 48.

Control of Görtler Vortices

William S. Saric
Mechanical and Aerospace Engineering
Arizona State University
Tempe, AZ 85287
USA

SUMMARY

It is shown that convex curvature is a strong nonlinear stabilizer of Görtler vortices. It is also conjectured that sub-critical roughness can prevent the growth of more unstable modes and hence delay transition.

1 INTRODUCTION

In a boundary-layer flow over a concave surface, the *Rayleigh circulation criterion* is satisfied and the flow is subject to a centrifugal instability. This instability of an *open* system with a *weakly nonparallel* basic state is commonly associated with Görtler and is in the form of stationary counter-rotating vortices. Saric (1994) presents arguments for considering this problem to be different from Taylor instabilities and Dean instabilities. For general reviews of the subject, see Hall (1990), Floryan (1991) and Saric (1994).

The Görtler instability is an important boundary-layer instability that, under some conditions, leads the flow through a transition to turbulence. It is known that a Görtler instability can cause transition on the wall of a supersonic nozzle in a boundary layer that would be otherwise laminar (Beckwith et al 1985; Chen et al 1985). Moreover, the Görtler vortex structure exists in a turbulent boundary layer over a concave surface such as turbine-compressor blades (e.g. see Floryan 1991 for a review). This instability is visualized, for example, with surface striations on the reentry vehicles in the Smithsonian Air & Space Museum where differential surface ablation caused locally concave surfaces. On the other hand, recent experiments (Swearingen & Blackwelder 1987, Peerhossaini & Wesfreid 1988*a,b*) show that the breakdown to turbulence in the presence of Görtler vortices is typically through a strong secondary instability caused by distortion of the steady velocity profile. This leads to arguments regarding the *linear* nature of this instability. In addition, the spanwise modulations of the steady flow caused by the Görtler vortices can also destabilize Tollmien-Schlichting waves (Nayfeh & Al-Maaitah 1987, Hall & Seddougui 1989, Malik & Hussaini 1990). These brief comments serve to illustrate that this is a rich area of study.

1.1 Nonlinear mean flow distortion

The significant feature of a stationary, streamwise-oriented vortex in a spatially developing flow is the convection of streamwise momentum normal to the wall. Figure 1 is a sketch of such behavior and Figure 1a, shows the orientation of the vortex motion. At the $z = 0$ position, the combined action of the two vortices produces an upwelling of the flow. At the $\pm\pi$ position, there is a downwelling. If the low-momentum fluid is identified by the shaded area of Figure 1b as an initial condition, the upwelling at $z = 0$ raises the low-momentum fluid and reduces the shear. On the other hand, the downwelling at $\pm\pi$ decreases the region of low-momentum fluid and increases the shear. As the motion continues, a mushroom shaped distribution is formed as shown in Figure 1d.

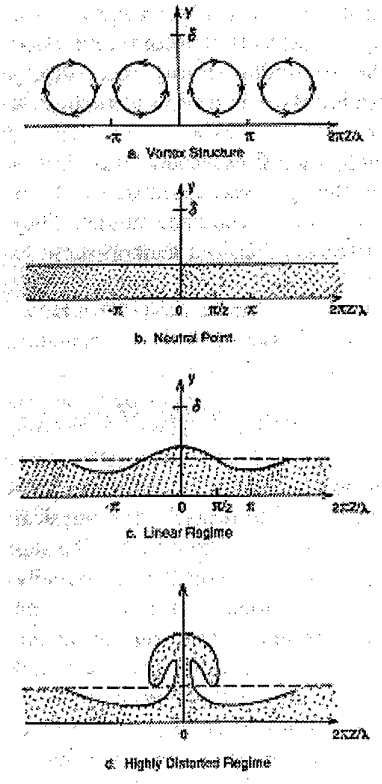


Figure 1.Evolution of mean profile distortion

Paper presented at an AGARD FDP Workshop on "High Speed Body Motion in Water", held in Kiev, Ukraine, 1-3 September 1997, and published in R-827.

This behavior is verified experimentally by Peerhossaini (1987) and with a typical nonlinear calculations by Liu & Sabry (1990), Sabry & Liu (1991), Lee & Liu (1992), Liu & Domaradzki (1993), and Benmalek (1993). This phenomenon also exists in other flows with a stationary streamwise vortex structure such as the crossflow instability on a swept wing (Kohama et al 1990) and the curved channel problem (Guo & Finlay 1994).

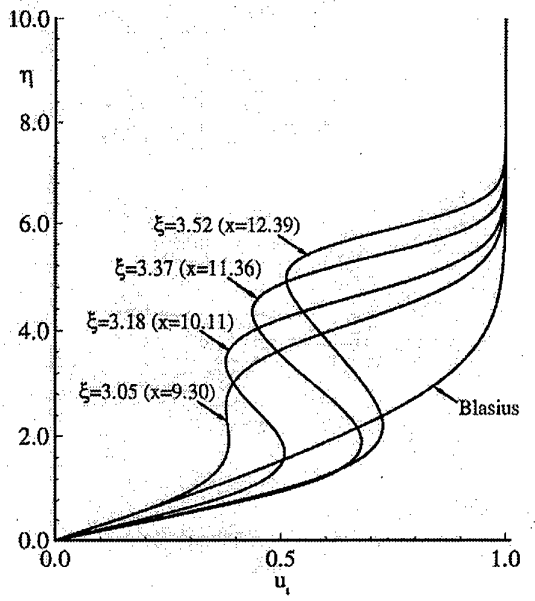


Figure 2. Streamwise evolution of mean profiles of total velocity for constant curvature case.

The consequence of this behavior is shown in Figure 2. In this figure, the velocity profile is calculated for the different streamwise locations and shows the development of the highly inflectional velocity profiles that would give rise to a Rayleigh instability. Here, x is the streamwise distance from the leading edge normalized with the with distance from the leading edge where the curvature is first applied, η is the Blasius variable, and u_t is the total mean velocity (Benmalek & Saric 1994). The computations are for the nonlinear, parabolized disturbance equations and should be considered as generic features that are characteristic of these distorted profiles. One can do a comparable development of the spanwise gradients of the velocity profiles and show that these are subject to a Kelvin-Helmholtz instability. The spanwise gradients are as large as the wall-normal gradients and that flows such as this are subject to strong secondary instabilities.

1.2 Saturation and breakdown

The other feature of this nonlinear profile distortion is saturation. At some streamwise location, the disturbance energy saturates as shown in the generic Figure 3. This figure contains the trajectories of the integrated mode shapes for different curvatures. The constant curvature case is $\kappa/\kappa_0 = 1$. Saturation does not occur at a particularly large Görtler number.

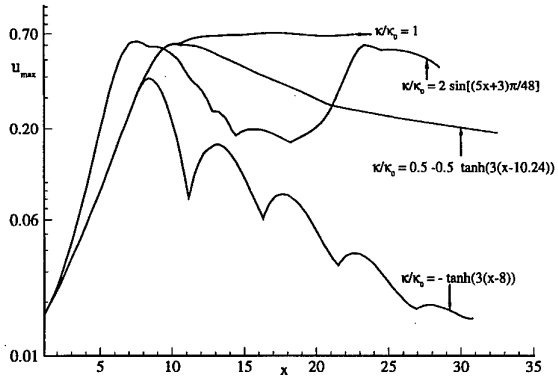


Figure 3. Sreamwise evolution of maximum streamwise velocity disturbance for different curvature conditions.

The first measurements of the strong distortion of the mean flow and the description of the nonlinear process are found in Aihara (1979), Yurchenko et al (1980), Yurchenko (1981), and Ito (1980). Yurchenko also noted the importance of the spanwise gradient of the streamwise flow, $\partial u/\partial z$, which is as large as the wall-normal gradient, $\partial u/\partial y$. This was followed by the work of Aihara & Koyama (1981) who identified the breakdown of the vortex structure as a secondary instability due to a horseshoe-vortex structure.

The Görtler vortex problem is really a nonlinear, nonparallel instability where the basic state cannot be decoupled from the disturbance state or the initial conditions. In fact, the only reliable assumptions about the Görtler problem are that it is spanwise periodic and initially stationary. Prior to the onset of the secondary instability, the experiment teaches us (i) that there is significant profile distortion from mean flow (Figure 2); (ii) saturation will occur (Figure 3); and (3) the low-momentum streaks form a mushroom-shaped cross section (Figure 1).

Sabry & Liu (1988, 1991) and Liu & Domaradzki (1993) did a temporal calculation of the spatially developing vortex and they were able to achieve good agreement with experiment. Lee & Liu (1992) did the nonlinear spatial computations of the parabolized Navier-Stokes equations as did Guo & Finlay (1994), Benmalek (1993), and Benmalek & Saric (1994). Whereas some numerical details differ between these computations, they are stable computational models of the steady spatial evolution of the Görtler vortex structure. Both Lee & Liu (1992) and Guo & Finlay (1994) give the successful comparisons with the data of Swearingen & Blackwelder (1987). Lee & Liu go one step further and show that the initial

conditions typically used by Hall (1983, 1988) do not give as good a comparison with experiment as compared with initial conditions chosen as eigen solutions to the separation of variable solution (e.g. Day et al 1990). A more complete review is given by Saric (1994).

2 CONTROL OF CURVATURE

2.1 The concave/convex wall

We consider a concave circular arc attached to a convex circular arc of the same radius $1/\kappa_0$ by a section with continuously varying curvature. The curvature distribution between the circular arcs is chosen as

$$\kappa/\kappa_0 = -\tanh[3(x-8)]$$

The convex curvature starts at $x = 8$ which is upstream of the location where the mushroom-shaped contours are established; that is before the onset of the associated secondary instabilities. This allows us to study whether the mushroom-like structures and the associated streamwise velocity inflectional profiles and secondary instabilities can be prevented by convex curvature.

Benmalek & Saric (1994) show that in the convex region, the primary pair of vortices is lifted upward away from the wall while a new pair of vortices with opposite sense of rotation is created. These vortices appear initially as recirculating eddies near the wall at each side of the interface $z = \pi/\alpha$ separating the vortices of the preceding primary pair. These new vortices strengthen and expand for some distance downstream while the preceding pair weakens. The new vortices move the low-speed fluid, that was initially ejected from the wall by the preceding pair, back towards the wall. They also eject low-speed fluid away from the wall at the spanwise locations $z = 0$ and $2\pi/\alpha$, where high-momentum fluid was moved towards the wall by the initial vortices. While strengthening for some downstream distance immediately after its creation, the new pair of vortices does not reach the maximum amplitude of the preceding pair as indicated by the streamwise evolution of their amplitude in Figure 3. This process of creation of new sets of vortices with opposite rotation to that preceding each set near the upwelling interface on the convex wall continues downstream and eventually, the vortices are too weak to affect the flow. Eventually, the iso-contours of mean velocity are dissipated from the mushroom shape, the flow becomes two-dimensional with a similar distribution of iso-contours as the Blasius flow. The effect on the meanflow contours is shown in Figure 4. The mean flow is observed to go from the highly inflectional state to a benign profile as x increases.

Thus, convex curvature is a strong stabilizing influence on Görtler vortices and can be used effectively as a control device.

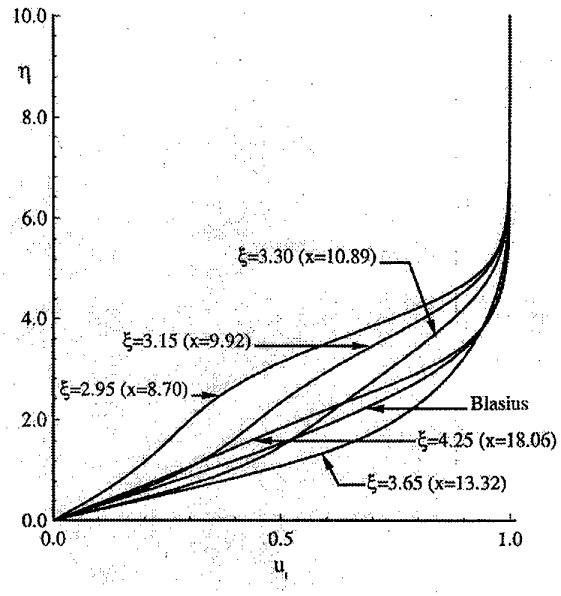


Figure 4. Streamwise evolution of mean profiles of the total streamwise velocity for concave/convex curvature.

2.2 Periodic Curvature

Saric & Benmalek (1991) and Benmalek & Saric (1994) show that in the case of periodic curvature, the stabilizing effect of the convex region is greater than the destabilizing effect of the concave region. This is shown in Figure 3. Thus, the well-worn Görtler-Wittig mechanism (see Lesson & Koh 1985 for a recent example) for destabilizing the boundary layer does not exist and in fact is stabilizing. If one needed to sustain a region of convex curvature over a body at moderate Reynolds numbers, judicious use of periodic curvature could permit one to sustain an overall concave surface.

3 CONTROL WITH ROUGHNESS

In Saric et al (1998), stationary crossflow waves are investigated on a swept airfoil within a low-disturbance environment. A review of this mechanism can be found in Reed & Saric (1989). Although the stationary crossflow waves are co-rotating vortices, the same distortion of the mean flow occurs as in the case of the Görtler vortices and the secondary instability pattern leading to transition is similar. Thus there may be an analogy between the control of these two mechanisms. Therefore, a brief description of the results of Saric et al (1998) are given here.

Stationary crossflow waves dominate the transition process even though the surface is polished to 0.25 μm

rms roughness. The results of Reibert et al (1996) show that the spectral content of the stationary instability can be controlled by the careful addition of artificial roughness at a particular wavelength. For reference, it is necessary to note that under the conditions of Reibert et al (1996), the most unstable wavelength was 12 mm. The roughness initiated waves at integral multiple wavenumbers of the primary mode i.e. harmonics in wavenumber space but not subharmonics.

Saric et al (1980 showed that the disturbance field obtained with 18 mm spaced roughness is qualitatively consistent with the experiments of Reibert et al (1996), with one important new discovery. Applying the roughness elements such that the spacing is not a multiple of the most unstable wavelength, effectively suppresses growth of this most unstable mode. The strong growth of the 9 mm mode (the harmonic in wavenumber space) prevents the naturally occurring dominant mode from appearing. This suggests that forcing modes that do not grow strongly (or have harmonics that grow strongly) may yield smaller total disturbance growth.

Saric et al (1998) then examined a subcritical roughness spacing of 8 mm for elements that were of 6 μm high. Under certain conditions, the subcritical spacing effectively delays transition past that of even the natural roughness case (0.25 μm). This behavior was sustained for roughness heights of 48 μm. The excited disturbance shows initial exponential growth, but then saturates and decays dramatically. The strong initial growth of the subcritical disturbance inhibits the growth of the most unstable wavelengths. The decay allows longer-wavelength background disturbances to grow downstream (as linear theory predicts) which may eventually lead to transition.

The implications of the subcritical roughness spacing results are profound. Although some issues remain to be addressed in terms of appropriate roughness height, subcritically spaced roughness shows promise as an effective passive transition-control mechanism for cases where stationary structures dominate.

ACKNOWLEDGMENT

This work was supported in part by the Air Force Office of Scientific Research, USAF, under grant number F49620-96-1-0369.

REFERENCES

Aihara, Y. 1979. Görtler vortices in the nonlinear region. In *Theoretical and Experimental Fluid Mechanics*, ed. U. Müller, K.G. Roesner, B. Schmidt, pp. 331-38. Berlin: Springer-Verlag

Aihara, Y., Koyama, H. 1981. Secondary instability of Görtler vortices: formation of periodic three-dimensional coherent structure. *Trans. of the Japan Soc. for Aero & Space Sciences.* 24: 78-94

Beckwith, I.E., Malik, M.R., Chen, F.J., Bushnell, D.M. 1985. Effects of nozzle design parameters on the extent of quiet test flow at Mach 3.5. In *Laminar-Turbulent Transition*, ed. V.V. Kozlov, pp. 589-600. New York: Springer-Verlag

Benmalek, A. 1993. Nonlinear development of Görtler vortices over variable curvature walls. *PhD Thesis*, Arizona State University

Benmalek, A., Saric, W.S. 1994. Effects of curvature variations on the nonlinear evolution of Görtler vortices. *Phys. Fluids 6* (10) 3353-67.

Bippes, H. 1972. Experimentelle Untersuchung des laminar-turbulenten Umschlags an einer parallel angestrîmten konkaven wand. *Sitzungsberichte der Heidelberger Akademie der Wissenschaften Mathematischnaturwissenchaftliche Klasse* 3: 103-80 (also NASA TM-75243, 1978)

Chen, F.J., Malik, M.R., Beckwith, I.E. 1985. Instabilities and transition in the wall boundary layers of low-disturbance supersonic nozzles. *AIAA Pap. No.* 85-1573

Day, H.P., Herbert, T., Saric, W.S. 1990. Comparing local and marching analyses of Görtler instability. *AIAA J.* 28(6): 1010-5

Floryan, J.M. 1991. On the Görtler instability of boundary layers. *Prog. Aerospace Sci.* 28: 235-71

Guo, Y., Finlay, W.H. 1994. Wavenumber selection and irregularity of spatially developing nonlinear Dean & Görtler vortices. J. *Fluid Mech.264*, 1.

Hall, P. 1983. The linear development of Görtler vortices in growing boundary layers. *J. Fluid Mech.* 130: 41-58

Hall, P. 1988. The nonlinear development of Görtler vortices in growing boundary layers. *J. Fluid Mech.* 193: 243-66

Hall, P. 1990. Görtler vortices in growing boundary layers: The leading edge receptivity problem, linear growth, and nonlinear breakdown stage. *Mathematika* 37: 151-189

Hall, P., Seddougui, S. 1989. On the onset of three-dimensionality and time dependence in the Görtler vortex problem. *J. Fluid Mech.* 204: 405-20

Ito, A. 1980. The generation and breakdown of longitudinal vortices along a concave wall (in

Japanese). *J. Japan Soc. Aero. Space Sci.* 28: 327-33

Kohama, Y., Saric, W.S., Hoos, J.A. 1990. A high-frequency secondary instability of crossflow vortices that leads to transition. *Proc. Roy. Aero. Soc.: Boundary-Layer Transition and Control*, Cambridge

Lee, K., Liu, J.T.C. 1992. On the growth of mushroomlike structures in nonlinear spatially developing Görtler vortex flow. *Phys. of Fluids A* 4(1): 95-103

Lesson, M., Koh, P.H. 1985. Instability and turbulent bursting in the boundary layer. In *Laminar-Turbulent Transition*, ed. V.V. Kozlov, pp. 39-52. New York: Springer-Verlag

Liu, J.T.C., Sabry , A.S. 1990. Concentration and heat transfer in nonlinear Görtler vortex flow and the analogy with longitudinal momentum transfer. *Proc. R. Soc. London Ser. A* 432: 1-12

Liu, W., Domaradzki, J. 1993. Direct numerical simulation of transition to turbulence in Görtler flow. J. *Fluid Mech.* 246: 267 (also AIAA Pap. No. 90-0114)

Malik, M.R., Hussaini, M.Y. 1990. Numerical simulation of interactions between Görtler vortices and Tollmien-Schlichting waves. *J. Fluid Mech.* 210: 183-9

Nayfeh, A.H., Al-Maaitah, A. 1987. Influence of streamwise vortices on Tollmien-Schlichting waves. *AIAA Pap. No.* 87-1206

Peerhossaini, H. 1987. *L'Instabilite d'une couche limite sur une paroi concave (les tourbilons de Görtler). These de Doctorat, L'Universite de Pierre et Marie Curie, Paris*

Peerhossaini, H., Wesfreid, J.E. 1988a. On the inner structure of streamwise Görtler rolls. *Intl. J. Heat and Fluid Flow*, 9(1): 12-8

Peerhossaini, H., Wesfreid, J.E. 1988b. Experimental Study of the Taylor- Görtler Instability. In *Propagation in Systems Far from Equilibrium*, Eds. J.E. Wesfreid et al., pp. 399-412. Berlin: Springer-Verlag

Reed, H.L., Saric, W.S. 1989. Stability of three-dimensional boundary layers. *Ann. Rev. Fluid Mech.* 21: 235-84

Reibert, M.S., Saric, W.S., Chapman, K.L. 1996 Experiments on Nonlinear Saturation of Stationary Crossflow Vortices in a Swept-Wing Boundary Layer. *AIAA Paper No. 96-0184.*

Sabry, A.S., Liu, J.T.C. 1988. Nonlinear Development of Görtler vortices and the generation of high shear layers in the boundary layer. Appl. Math. Fluid Mech. Astrophysics, 175-83

Sabry, A.S., Liu, J.T.C. 1991. Longitudinal vorticity elements in boundary layers: nonlinear development form initial Görtler vortices as a prototype problem. *J. Fluid Mech.* 231: 615-63

Saric, W.S. 1994. Görtler Votices. *Ann. Rev. Fluid Mech. 26*: 379-409.

Saric, W.S., Carrillo, R., Reibert, M. 1998. Leading-edge Roughness as a Transition Control Mechanism. *AIAA Paper No. 98-0781.*

Saric, W.S., Benmalek, A. 1991. Görtler vortices with periodic curvature. In Boundary Layer Stability and Transition to Turbulence, *ASME-FED* 114: 37-42.

Swearingen, J.D., Blackwelder, R.F. 1987. The growth and breakdown of streamwise vortices in the presence of a wall. *J. Fluid Mech.* 182: 255-90

Yurchenko, N.F, Babenko, V.V., Kozlov, L.F. 1980. Experimental investigation of the Görtler instability in boundary layers (in Russian). In *Stratified and Turbulent Flows* 50-9. Kiev: Naukova Dumka

Yurchenko, N.F. 1981. Method of experimental investigation of a system of streamwise vortices in a boundary layer (in Russian). *Inzhenerno-Fiz. Zh.* XLI(6):996-1002.

EXPERIMENTAL INVESTIGATION OF THE BOUNDARY LAYER OVER RIGID AND ELASTIC PLATES

V. V. Babenko.
Department of hydrobionics and boundary layer control
Institute of hydromechanics
National Academy of Sciences of Ukraine,
252057, Kiev, Ukraine

SUMMARY

Boundary layer in natural conditions is influenced by disturbances of different types coming from outside. An approach was developed for experimental study of disturbance interaction. It was realized using a special hydrodynamic complex including a water channel with the regulated freestream turbulence level, different kinds of strain gauges and devices for the introduction of small disturbances into a boundary layer from its outer and inner edges. There were used in experiments visualization methods (in particular, tellurium method) thermo- and laser anemometry and strain-gauging. Besides, a technique was developed to carry out measurements of space-time characteristics of disturbing motion.

Kinematic, spectral and correlation characteristics were investigated at different stages of natural boundary layer transition including the turbulent state on flat and concave plates. The model of disturbance transformation through all the transition stages was proposed. Each stage was considered from the point of view of mechanisms driving the disturbance development resulted in a next stage. Some empirical relations were obtained for wave lengths of two and three-dimensional disturbances depending on the Reynolds number. Conditions of the occurance of two transition types and their connection with two distincet intermittency factors proposed were analysed. Results were presented in the form of profiles of mean and fluctuation longitudinal velocity components and also of neutral curves and curves of maximum amplification in Tollmien-Schlichting and Gortler diagram.

Structural and kinematical-dynamical principles of boundary layer interaction with compliant surfaces were formulated.

Interactions of different disturbances were studied in boundary layers on resonant and dissipative compliant plates.

1. INTRODUCTION

It is considered that investigations of İ. Kramer [14] on the elastic surfaces published in 1957 was the beginning of development of a new direction in a hydromechanics. Actually, the announcement about the developed theory of liquid flow in elastic pipes [12] was made by the Russian professor I. S. Gromeko on May 14, 1883.

The main stages of development of a flow over elastic surfaces problem are explained in reviews and monographs [2, 5, 6, 8, 9, 10, 11, 13, 15, 18].

The M. Kramer considered that the effect of elastic surfaces interaction with a flow is stipulated by damping of Tollmien-Schlichting waves. Therefore, the problems of hydrodynamic stability during a flow over elastic plates were widely investigated in the beginning after publication of results of his experiments.

The study of a problem with the purpose of examination and substantiation of Cramer's idea was executed for the first time by Benjamin and Landahl [6, 15].

Among the home scientists the experimental researches of a boundary layer on elastic plates were carried out by A. I. Korotkin [5], V. B. Amphilohiev [1], B. N. Semenov [20]. Recently, Gad-el-Hack [11], Bushnel [9], Fisher [16], Carpenter [17] etc. fruitfully worked in this direction.

The results of experimental researches of laminar [13], transitional [10] and turbulent [4] boundary layers at a flow over various kinds of elastic surfaces are presented in this work.

2. MEASURING METHODS OF BOUNDARY LAYER PARAMETERS

Boundary layer velocity field is visualized with tellurium method [21] and with coloured streaks. Velocity measurements are carried out with the laser Doppler anemometer (LDA) and DISA thermoanemometer [10].

The hydrodynamic bench, equipment and devices are described in [10] and detail in Fig. 1.

A low-turbulence hydrodynamic test bench comprises special equipment and devices. The following are the basic technical data of the test bench: length of test bench 7 m, length of test section 3 m, cross-section of test section 0.09×0.25 m, range of operating speeds 0.05÷1.5 m/sec, effuser contraction factor equal to 10. Mounted on the test bench are the following main devices: a duplex bottom of the test section, a removable cover of the test section. The test bench is equipped with a boundary-layer bleed in the corners of the test section. The cover of the test section can be tilted to various angles and rails are laid out along the test section, over which the car with special apparatus, LDA and DISA moves.

The tellurium method was employed and a set of special equiment was constructed for measuring the

Paper presented at an AGARD FDP Workshop on "High Speed Body Motion in Water", held in Kiev, Ukraine, 1-3 September 1997, and published in R-827.

velocity field and recording the neutral oscillations. Tellurium wires were attached to special supports.

Small oscillations of various types were introduced into the boundary layer with the help of specially designed oscillators for measuring neutral oscillations. Supports were arranged further downstream, making it possible to obtain small tellurium jets. The oscillator vibrational frequency changes in the course of the experiment, the amplitude of the tellurium jet oscillations being recorded. The voltage applied to the tellurium wires during photography of the velocity profile was approximately 500÷600 V, whereas 10÷20 V were required when recording the tellurium jets.

Small oscillations were introduced into the boundary layer mainly with the help of two oscillators. The mechanical oscillator consisted of a frame on which two motors were mounted, making it possible to obtain the required range of the oscillator ribbon oscillating frequencies. The oscillation amplitudes varied due to the eccentricity of the various bearings through which the oscillations were transferred from the axle to the rod. Attached to the rod were two pushers to which the oscillator ribbon was fastened.

The experimental investigation of hydrodynamic stability was conducted on the bottom of the test section of the hydrodynamic bench [19]. The method of obtaining dots on the neutral curve consisted in determining the maximum amplitude of tellurium jet oscillations at a fixed point in the test section with the help of photography. The velocity profiles were photographed simultaneously. In this way the dots of the second branch of the neutral curve were determined.

A series of the above-mentioned measurements was carried out in various places of the test section to permit experimental plotting of the neutral curve, the distance between the oscillator and the supports not exceeding 20 cm.

The method of investigation of natural transition at nonlinear stages consists in the following. First of all a boundary layer is examined in different aspects with the tellurium method along the test section. On Fig. 2 there are examples of visualization, with tellurium-method, of stream-lines and profiles of mean longitudinal velocity and also the form of nonlinear Tollmien wave modeled on a computer. The particular attention is paid to the registration of the velocity distribution transverse to the flow, the tellurium wire being placed here on varying distance from the floor.

Fig. 3 shows the velocity profile in boundary layer in transverse direction: (a) - for rigid plate at zero pressure gradient, (b) - the same at adverse pressure gradient. In first case small deformation of velocity profile was observed, in second one - very large. Fig. 3 (c) shows the velocity profile on elastic surface. The pattern is different from both previous cases. Such procedures are carried out under U_∞=const along x axis; so the increase of Re allowes to fix up different transition stages at specific positions along x.

Simultaneus photography of velocity profiles in vertical and transverse directions and also of longitudinal tellurim small jets gives the possibility to construct the spatial-temporary picture of exciting motion and velocity field during different stages of transition. The example of such pictures is given in Fig. 4.

Analysis of profiles U(z) gives the possibility for determining the characteristic points along y and z axes where the boundary layer kinematic parameters are measured with LDA and DISA. All these measurements are made under a low turbulence level ($\varepsilon \leq 0{,}05\%$).

Further the transition features are studied over the inserting floor section at x=const, U_∞=var.

The main method of experimental determination of neutral stability curves was worked out by Schubauer and Scremstead on the basis of theoretical analysis of Tollmien and Schlichting and was fully covered in my book.

3. DISTRIBUTION OF PARAMETERS OF DISTURBING MOTION THROUGH THE LAMINAR BOUNDARY LAYER.

Determined was distribution of amplitudes of exciting motion transverse velocities throughout the thickness of the boundary layer at varying oscillation amplitude of the oscillator. Velocity v' is directly proportional to value A_V. With the A_V>0,7 mm, velocity v' becomes so significant (velocities u' and w' rising correspondingly) that a turbulence takes place immediately beyond the oscillator. The amplitudes of exciting motion velocities were at maximum when the disturbance source was within $(0{,}1 \div 0{,}3)y/\delta$.

Dimensionless wave number $\alpha\delta^*$ and the velocity c_r/u of exciting motion propagation are practically independent of the disturbance source location in the boundary layer thickness. At the same time the measurements have shown that values $\alpha\delta^*$ and c_r/u depend on the amplitude of the oscillator (Fig. 5). When the disturbance amplitude rises to 0.7 mm, quantities $\alpha\delta^*$ and c_r/u tend to attain ultimate values throughout the entire thickness of the boundary layers under given experimantal conditions and with $\beta_T\nu/U^2=525\cdot10^{-6}$, $Re_{\delta^*}=653$ these being 0.5 and 0.65 respectively.

It has been revealed that in the investigations of the hydrodynamic stability the following conditions have to be adhered to. The degree of turbulence in water should not exceed 0.04%. The amplitude of oscillator strip oscillations should be of the order of 0.2-0.5 mm at selected range of velocities 10 to 20 cm/sec. The cross velocities v' built up by the oscillator should not exceed 2% of the main flow velocity.

Investigated was the distribution of wave numbers and phase velocities of the exciting motion throughout the boundary layer thickness at optimum oscillator ribbon positioning and at its optimum amplitude (Fig. 6). With the Reynolds number being constant, each oscillation frequency has its own nature of wave number variation throughout the boundary layer thickness, whereas in the phase velocity the differences in dependences are manifested slighter. It has been discovered that with the advance toward the outer limit of the boundary layer the wave numbers decrease, i. e. the wave length increases and at the same time the phase velocity steadily rises. These results show that dependences of quantities $\alpha\delta^*$ and c_r/u on the boundary layer thickness and on the exciting oscillation frequency are quite complex.

On Fig. 7 there are results of measurements of distribution c_r/u versus δ (u - local velocity in point of measuring). General behaviour is opposed to that on Fig. 6, where it can be seen that value of c_r increases with y/δ. Growth rate of averaged velocity u with increase of y/δ forestalls that of c_r, that stipulates the behaviour of curves on Fig. 7. From above data it follows that $c_r \sim u$ at $y=\delta^*$ in only the case when frequency of fluctuation of disturbing motion is equal to frequency of neutral oscillation, and disturbance is introduced and located in the region of critical layer. In all other cases, when the frequency of disturbing motion more or less than that of second neutral oscillation, $c_r \sim u$ only at $y/\delta=0.4\text{-}0.6$ being the more ratio n/n_{II} then at higher values y/δ equality mentioned is valid and the steeper the curves. General behaviour is as follows: near the wall c_r considerably exceeds u, and the more x the more exceeding; above $y/\delta=0.4\div0.6$ value c_r becomes less than u. However near the wall the fluctuations damp due to viscosity in spite of large values of c_r. Not far from $Re_{l.s.}$ the curves, as functions of y/δ,change not so strongly in comparison with that at large x.

On Fig. 8, there are plots of c_r/u versus oscillation frequency. It was found out that if $y_V \sim y_{p.l.} \sim \delta^*$ then, under all test conditions for (x, U_∞), $c_r \sim u$ only at $n=n_{II}$ that is at frequency of second neutral oscillation, but at $n \neq n_{II}$ this relation becomes $c_r/u>1$. At frequency $n<n_{II}$, that is in the region of unstable oscillation of neutral curve, c_r is more close to u than when crossing neutral curve into the region of stable oscillations. At $n>n_{II}$ the value of c_r increses sharply at the beginning, until it becomes from 1.2 to 1.5 times as much as u, and then, as n increases the value of c_r decreases smoothly. It is typical that as x decreases or U_∞ growthes, value of n increases that is $\beta_r/U_\infty \neq \omega_r(II)$, that is accompanied by curves smoothing (Fig. 8, b, curves 7, 12, 13), and not far from $Re_{l.s.}$ at any n practically the equality $c_r/u \sim 1$ is valid.

Thus, depending on frequency and location through the boundary layer thickness for introduced disturbances, velocities of their propagation are significantly different. Only disturbances, which were introduced in the region of critical layer at $Re_{l.s.}$, propagated with velocity $c_r=u$ in wide region of frequencies. Disturbances generated, for example, by wall (at $y/\delta<0.33$) propagates faster, and those which come into boundary layer from outside ($y/\delta>0.33$) propagates more slowly than u. As a general one, remains the fact that when these disturbances come to region of critical layer, they propagate with velocity $c_r=u$ at $n=n_{II}$. Also remained in force is the following: oscillations with frquency more than n_{II} propagates with velocity $c_r>u$. This is the reason of extra harmonics appearance, even if all conditions are met and specified is only oscillation with $n=n_{II}$, as well as one of the reason for origin and development of non-linear stages of transition.

Taking into account the test accuracy, one will have:

$$\frac{c_r}{u} = \left(\frac{n}{n_{II}} - 1\right)^2 \quad \text{from} \quad n < n_{II}, \tag{1}$$

$$\frac{c_r}{u} = 1{,}6 \lg \frac{n}{n_{II}} + 1 \quad \text{from} \quad n > n_{II}. \tag{2}$$

The investigations have shown that at each point along the working part oscillations were observed in a strictly definite frequency range. Fig. 9 represents dependences of wave numbers and phase velocities upon disturbing motion oscillation frequency. By the maximum values of these points a region has been plotted, limited by a dot-and-dash curve outside, of which no oscillations of any frequency in the boundary layer were observed. This curve has been defined as ultimately neutral curve. Dashed curves show dependences of wave numbers and phase velocities on the oscillation frequency along which the cluster of points is layed out at a definite velocity of the main flow. Neutral curves were not plotted experimentally within these coordinates.

Despite the scatter of the experimantal points, the obtained measurement results have shown that certain regularities are observed between the wave length and phase velocity on the one hand and the oscillation frequency of the exciting motion - on the other. These regularities are, however, not single-valued and depend on the main flow velocity.

Neutral curves, plotted in non-traditional coordinates "the wave number - phase velocity", have allowed to obtain the empirical dependences for disturbances that develop with frequency of second neutral oscillation

$$\left.\begin{aligned} \alpha\delta^* &= 1{,}4 \cdot 10^3 \frac{\beta_r \nu}{U_\infty^2} + 0{,}15 \\ \frac{c_r}{U_\infty} &= 0{,}7 \cdot 10^3 \frac{\beta_r \nu}{U_\infty^2} + 0{,}2 \end{aligned}\right\} \tag{3}$$

Here $\alpha=2\pi/\lambda$ - wave number of disturbing fluctuation; λ - length of Tollmien-Schlichting's wave; δ^* - replacement thickness, $\beta_r=2\pi n$ - circular frequency; ν - coefficient of kinematic viscosity.

4. PHYSICAL PATTERN OF STAGES OF LAMINAR-TURBULENT BOUNDARY LAYER TRANSITION

On Fig. 10 there are schemes of different variants of disturbing motion behaviour obtained on the basic of photoes of disturbance development visualization with tellurium-method.

Shown is behaviour of tellurium streaks (a) as frequency increases, at x=const. Amplitude of wave increases at first and then decreases. On Fig. 10, b the streak behaviour downstream is shown at U_∞=const at two vibrator frequencies.

While simultaneous shooting from the side and from above, a helical motion of streak (Fig. 10, c) was found out, that is non-linear behaviour of wave.

Development of disturbing motion is shown at adverse pressure gradient, Fig. 10, d and at non-sinusoidal oscillation of vibrator ribbon, Fig. 10, e.

We have the large enough amount of experimental data in order to conclude that at the low turbulence level the transition process is characterised by the succesive change of disturbing motion types. The model of this succession was developed (Fig. 11) on the basis of the study of the natural boundary layer transition and the well-known results of Knapp and Roach, Klebanoff and oth., Tani, Morkovin, Kline and many others. The wave transformation process during transition to turbulence can be devided into the following stages (Fig. 11):

- plane disturbances amplification;
- wave modulation in phase - three-dimensional effect emergency;
- generation of the longitudinal rows of Λ-shaped vortices;
- arrangement of the longitudinal vortex system;
- transformation of votices in form and intensity, indulation of vortices;
- breakdown of peripherical parts of undulating vortices;

generation of turbulent spots, their growth confluence and turbulent boundary layer development.

At present there are two concepts explaining the successive development of the transition process:

- it is defined by modes development and interaction in a boundary layer;
- it is defined by the vortex filaments behaviour.

Both concepts are reasonable - the conditions and mechanism of their interaction are discussed in detail in my book.

Small particle of liquid contains double information concerning its movement:

- as the vibrating element it is characterized by frequency-wave and other parameters;
- as the moving element it is characterized by vorticity, i.e. by the trajectory of its movement.

In any case it is necessary also to analyse the structure of disturbances: for example, the form of linear and nonlinear waves, the form and direction of vortices and, besides, the disturbing motion intensity.

5. INVESTIGATION OF DEVELOPMENT OF DISTURBING MOTION ON CURVILINEAR SURFACES

Regularities of disturbances evolution and of alternation of transition stages have common properties under different conditions of flat plate flowing.

For much more approaching to real conditions of flowing, analogous measurements on curvilinear surfaces have been carried out (Fig. 13) [10].

In Figure 13, *a* there is a visualization of profiles U(z) evolution along x on various curved surfaces. At plate curvature R=4 m, it is seen that yet before the beginning of diffuser region, still on horizontal part at x=0,3 m (*a*), one can see strong bend of the profile in comparison with that on flat horizontal plate. At the beginning of diffuser part at x=0.6 m (*b*) a quite stable, in time, flow braking happens along the channel axis. Measurements over the most low part (that is higher, along y, above braked area) have shown that profile U(z) was bended weakly at x=1.1 m (*c,d*) just as downstream at x=1.52 m (*e*).

In convergent region, at x=1,8 m (*f, g*) and 2,15 m (*h*), the wave length of longitudinal vortical system as well as amplitude of deformation decrease - that is like a stabilization of flow happens under influence of centrifugal forces and negative pressure gradient. However, now non-steadiness of U(z)-distribution is manifested greatly, being much more intensive than on horizontal surface at large ε. Change in shape of U(z) takes place within 3 to 8 seconds, that is 4 to 6 times faster, especially at $y>\delta_1$ (*g, h*). At $y<\delta_1$ non-steadiness is revealed in oscillative motion of disturbances in transversal direction (*f*) rather than in change of shape U(z), that is in-layer (layered) development of disturbances is observed. Zigzag-like shape arises at $y<\delta_1$ and then propogates all over the thickness δ.

At smaller curvature, distribution of U(z) along all the working section is constant: at R=12 m, x=0,6 m, $y=4\cdot10^{-3}$ m (*i*) and x=0.6 m, $y=6\cdot10^{-3}$ m (*j*). On the contrary, at bigger curvature (R=1 m) the more intensive deformation of profile takes place: x=2,22 m, $y=3\cdot10^{-3}$ m (*k*). Profiles *a, b, g, h* have been obtained at $y=6\cdot10^{-3}$ m. *c, e* - $1\cdot10^{-2}$ m, *d* - $2\cdot10^{-2}$ m, *f* - $4\cdot10^{-3}$ m.

Measurement concerning disturbances development in cylindrical channel (Fig. 13, *b*) at R=1m has shown that both on convex and concave surfaces of the channel distribution of U(z), though remaining non-stationary, has much more stable character than in opened channel. Data for Fig. 13, *b* are as follows: U_∞=0.044 m/s (*a-c, h-j*) and 0.037 m/s (*d-g*); x=0.8 m(*a-c*), 0.93 m (*d-g*), 1.05 m (*h-j*); $y_T=2\cdot10^{-3}$ m (*a*), $6\cdot10^{-3}$ (*b*), $1\cdot10^{-2}$ (*c*), $5\cdot10^{-3}$ (*d*), $1\cdot10^{-2}$ (*e, f*), $1.5\cdot10^{-2}$ (*g*), $1\cdot10^{-3}$ (*h*), $5\cdot10^{-3}$ (*i*), $1.5\cdot10^{-2}$ (*j*). Non-steadiness is

manifested mainly in oscillation of velocity minimum in transversal direction.

6. BOUNDARY LAYER EVOLUTION ON ELASTIC CURVILINEAR PLATES

As it was shown above, increase of intensity of three-dimensional disturbances and change of their parameter λ_z has resulted in fast forming, in boundary layer over elastic plates, and stable preserving, at all stages of transition, longitudinal vortical structures which have minimum friction coefficients (Fig. 14).

Investigation of complex interactions has been carried out on curvilinear plates at increased degree of turbulence and on cylindrical surface too. Intensity of disturbing motion was being increased too by using vortex-generators B4 which had the twice height as compared to height of B3 (Fig. 14). Like on rigid plate (section 2), measurements were carried out on the same curved bottoms which were stuck around with sheets of elastic material of PE-3 type having thickness 0,003 m and 0,01 m.

Under the most unfavourable conditions (at curvature radius R=1 m), elastic material of 0,003 m thickness was stuck not throughout the all surface, but in longitudinal stripes of λ_z=0,042 m step (on flat rigid plate at natural transition, vortical systems had λ_z=0,045 m). Air layer in non-glued places increased the damping ability of elastic material [4]. If on rigid curved plate in duffuser section observed was separate flow, then on elastic one - system of longitudinal vortices with λ_z=0,042 m. Vortex generators B3, mounted at the beginning of diffuser section, created disturbances which suppressed mentioned system of longitudinal vortices during natural evolution of boundary layer. However at distance 0,2 m from vortex generators their influence disappeared. The step of forced vortical structure corresponded to λ_z of vortex generators, and deformation of U(z) profile was the same pointed one (means non-linearity) as on flat elastic plate too as well as on linear stages of transition [10].

Once elastic material (of 0,01 m thickness) was pasted through all area, its absorbing/damping properties have deteriorated. This has resulted in that separate flow arised in diffuser section as on rigid surface too. Introduction of disturbances by means of vortex generators B3 stabilized the flow.

During investigation in cylindrical section there were mounted vortex generators of different step λ_z, then U(z) profiles were photographed along curvilinear section from above, through the transparent lid. With help of LDA and tellurium method, velocity U(y) profiles were measured which were used to determine the momentum thickness. Using the character of evolution of U(z)-profile along elastic curved plate, parameters of neutral longitudinal vortical systems as well as systems of maximum amplification were determined.

In the same way determined were values of λ_z and δ_2 on curved elastic plates during natural transition and when introducing, into boundary layer, three-dimensional disturbances from vortex generators B3. For neutral three-dimensional disturbances value of λ_z was equal λ_z=0,01÷0,02 m on curved elastic plate of 0,01 m thickness, R=4 m, at U_∞=0,033 m/s, x=2,2 m and y=0,006 m. Corresponding Gertler's parameters have the values: G=2,1; $\alpha\delta_2$=0,5÷0,84, and for becoming more intensive disturbances introduced: λ_z=0,028 m, G=2.1; $\alpha\delta_2$=0,36. Just on this plate, natural disturbances with λ_z=0,05 m are characterized by: G=2,1; $\alpha\delta_2$=0,2. On curved plate with R=1 m at U_∞=0,213 m/s, x=1,35 m, for growing forced disturbance with λ_z=0,02 m, one has: G=13,8 and $\alpha\delta_2$=0,55.

Pairs of parameters obtained are plotted in form of points on diagram of Gertler's stability (Fig. 15). First Gertler's number for rigid curved plate is G_0=0,3 and for elastic one G_0=2,1. Increased too is the second critical Gertler's number G^* which characterized destruction of ordered motion in boundary layer and transition to turbulence. Like that, in [10] for rigid surface during artificial generation of vortical disturbances it was obtained: G^*=6.3. On elastic surface for curved section that was correspondingly G^*=18,8 and for cylindrical one (using B4): G^*=80, that is 3-13 times higher. If one would take into account the less velocities of growth too, then non-linear area of transition when flowing elastic surfaces stretched essentially. Range of values of wave lengthes of unstable longitudinal vortices decreases too.

7. PHYSICAL SUBSTANTIATION OF THE MECHANISM OF A FLOW INTERACTION WITH AN ELASTIC SURFACE

The static or quasi-static interaction of a flow with an elastic surface is considered in the majority of work, and the field of external loads is represented as a bend wave of pressure. At such simplified approach many peculiarities of an elastomer interaction with a boundary layer are not taken into account.

During the computation of hydroaerodynamic interaction it is necessary to considerate the specific schemes of an elastic surface and modes of external loads under various conditions of a flow over for construction and the descriptions of a complete rheologic model of a material.

Principles of structural and kinematics-dynamic interaction of a boundary layer with a streamline surface are based on development of elastic surfaces schemes. These principles are stated in [4].

The structural principle consists in fulfillment of conformity between structures of a disturbing movement in a boundary layer (or its characteristic areas) and elastic plate. It means, that if there is the intensive flat wave in a critical layer on the initial stages of transition, it is desirable that an outside layer of an elastomer had the structure generating also flat

disturbing movement under action of a pressure field of a boundary layer.

The kinematics-dynamic principle is, that the mechanical properties of all layers or outside layer of a composite elastic plate should provide kinematics and dynamic conformity to the characteristics of a boundary layer. In this case, energy of a flat wave in a critical layer on the initial stages of transition should be enough to cause deformation of an outside layer of an elastomer. Thus, the frequency of forcing force of a boundary layer should correspond to own frequency of this layer (or several layers) of elastomer. Then, the fluctuations will appear in an elastomer under action of an external load, which will damping an external load at a certain ratio with a phase of forcing force . In a case of a waveguide structure of an elastomer, there will be the superficial waves in an elastomer and on the wall - liquid border under action of an external load. The energy of a flat wave of a boundary layer will be picked out to maintain this waves and will be damp by that.

The coordination principle consists in fact that two first principles should take place on length of a streamline surface in each place. In other words, the structure and properties of an elastomer (or its outside layer) should change at modification of structure and properties of a disturbing movement in a boundary layer.

The elastic surface section in region of a stage of longitudinal whirlwinds formation arrangement should have the other structure: it should correspond to a structure, sizes and direction of these whirlwinds. The structure of a surface should correspond to structure of current in viscous sublayer at a stage of an advanced turbulent boundary layer.

8. PROFILES OF AVERAGE SPEED ON ELASTIC PLATES

Various kinds of monolithic and composite elastic plates established and tested in an insert were developed on the basis of results of researches. The mechanical characteristics of these plates were measured with the help both standard and specially developed devices [4]. A boundary layer on these elastic plates both in a hydrodynamic pipe, and in an aerodynamic pipe [4] was investigated. In the latter case the tests were carried out with the help of a hot-wire anemometer DISA at ~10 and 18 m/s speeds of a running flow. The value of a turbulence degree of a flow ε made about 1.7% at $U_\infty<10$ m/s, and at $U_\infty>10$ m/s - $\varepsilon\approx2\%$.

Calculations shown the majority of investigated elastic plates π-parameters were unoptimum in a range of working speeds during tests in an aerodynamic pipe. Therefore, it is possible to explain positive effects fixed in experience most likely not by resiliently damping properties of elastic plates, but by fulfillment of structural and kinematic-dynamic principles of interaction of a flow with an elastic surface. The conformity of structure of a disturbing movement in viscous sublayer to a structure of an elastic plate is characterized by parameters

$$\lambda_z^+ = \frac{\tilde{\lambda}_z u_\tau}{\nu}, \qquad (4)$$

$$\overline{y}^+ = \frac{\overline{y} u_\tau}{\nu}. \qquad (5)$$

Here $u_\tau=(\tau_w/\rho)^{1/2}$ - dynamic speed, τ_w - pressure of friction on a wall, ν - factor of kinematics viscosity.

The distance between Kline-stripes equal to double length of a wave λ_z of longitudinal whirlwinds in viscous sublayer as it is shown in [7].

The dynamic conformity of a disturbing movement and elastic plate is characterized by parameters

$$T^+ = \frac{T u_\tau^2}{\nu}, \qquad (6)$$

$$f^+ = \left(T^+\right)^{-1}, \qquad (7)$$

where T and f - period and frequency of ejections from viscous sublayer.

Here and hereinafter the efficiency of elastic plates will be understood as set of positive attributes, testified reduction of hydrodynamic friction resistance in comparison with a case of a flow around the rigid standard.

The measurements were carried out on eleven elastic plates in the following sequence: the standard, 1, 1a, 5, 9, 2a, 11a, 10a, 7, 3, 8a, 11, the standard. The speeds of the basic flow in the appropriate sections of measurements are resulted in tab. 1. The Reynolds numbers changed in $7.7\cdot10^5\div1.5\cdot10^6$ limits in III section of the standard.

Except of π-parameters describing mechanical properties of elastic of plates [3, 4] and parameters (4)-(7), essential criterion determining efficiency of complex interactions is also parameter of roughness K_s^+:

$$K_s^+ \approx \frac{K_s u_\tau}{\nu} \le 5; \qquad (8)$$

$$K_{admis} = \frac{K_s U_\infty}{\nu} \le 100, \qquad (9)$$

where K_s - height of roughness.

During flow around elastic plates, the "dynamic" roughness caused by bend fluctuations of the whole plate or by local fluctuations of the plate under action of a pressure pulsation of a boundary layer [4] takes place along with the "static" roughness. These parameters are considered in [4] more in detail. Parameter of "dynamic" roughness was also less then allowable one in the present measurements.

The results of measurement of average speed profiles on the rigid standard are well coordinated with results of similar measurements [2, 5, 6, 8] and coincide with the "1/7" degrees law:

$$\frac{u}{U_\infty} = (y/\delta)^{1/7} \qquad (10)$$

During a flow around elastic plates, the experimental points place below reference curve, as though increase the value 1/n in the sedate law of speeds distribution. The profiles of speed constructed in linear scale in form of $\frac{u}{U_\infty} = f(y/\delta)$ find out smooth bends at a flow around elastic plates, which is typical for complex interactions of various disturbances in a boundary layer.

The profiles of average speed are resulted in logarithmic coordinates in Fig. 16, that enables to study behavior of a liquid in direct affinity from a wall in more details. During a flow around the rigid standard (the series *a*), experimental points are stacked along curve 2 and 3 depending on speed of the basic flow. The vertical lines designate disorder of experimental points. The curves 1 and 2 characterize the flow in attached to wall area and have an identical inclination. Their distinction is caused by different values of the Reynolds numbers and especially by a turbulence degree of the basic flow in aerodynamic pipes. The curve 3 corresponds to greater Reynolds number and smaller thickness of viscous sublayer, and also has other inclination in attached to wall area in comparison with a curve 2.

Thus, profiles of speed in logarithmic coordinates allow to determine thickness of viscous sublayer and characteristic inclination of a profile in attached to wall area. A role of this inclination and metrology kind of the profile form are estimated in a series of measurements *b*.

The curve 9 designates Blasius-profile received on the hydrostand at a low degree of turbulence (the first stage of transition) on rigid and elastic plates. The profile remained rectilinear (curve 10) during heating of elastic plate.

Increase of a turbulence degree resulted in change of Blasius-profile (curve 5); the rectilinear dependence was changed to parabolic one (II stage of transition). With growth of speed and alternation of transition stages the form of profiles remains parabolic but ever more comes nearer to form characteristic for a turbulent profile; curve 6 - IV stage of transition, curve 7 - VI stage of transition. We shall note a good conformity of the profile form (curve 4) to transitive profiles [10]. At last, the form of profile becomes again rectilinear but with other inclination than at curves 9, 10 in a turbulent boundary layer (curve 8) in viscous sublayer.

It is possible to characterize property of the average speed profile on elastic plates on the basis of these data. For convenience of the analysis, the plates on Fig. 16 are grouped as follows. The results of measurements on an open sheet of a polyurethane foam (*c*) and pasted over outside by an elastic film (*d*), in series *e, f, g, i* - on compliant, and in series *j, k, l, m* - on elastic plates are listed in series *c, d*. In a series *i*, the plate 10 a can be related simultaneously to elastic and rough plates owing to its structure and properties.

Thickness of viscous sublayer is important characteristic for a physical picture of a liquid flow in a turbulent boundary layer and for closing of its various half-empirical theories. There are few techniques of this value determination. So, the formula for calculation of viscous sublayer thickness is offered in work of Niysing on the basis of viscous sublayer analogy to a laminar boundary layer:

$$\bar{\delta}_L = 4.64\left(\frac{\nu x_0}{u_0}\right)^{1/2} \qquad (11)$$

where x_0 - extent of viscous sublayer up to an ejection or its destruction, and u_0 - speed on external border of viscous sublayer at the moment of its destruction.

A few ways of viscous sublayer thickness determination are cited in [4, 8], the most simple of which are two: on vertical coordinate of a longitudinal pulsating speed maximum and on a conditional point of crossing of the speed profiles laws in viscous sublayer and area of the logarithmic law.

On the basis of the dimension theory Karmann offered a simple ratio for calculation of viscous sublayer thickness :

$$\bar{\delta}_L = \alpha \frac{\nu}{\sqrt{\tau_w/\rho}}. \qquad (12)$$

Factor α was made 11.6 on Nikuradze tests. According to theoretical conclusions, the turbulent movement along a rigid plate is characterized by two empirical constants: $\aleph \approx 0.41$ and $\alpha \approx 11.5$, and the value α is defined by the formula

$$\alpha = \frac{\bar{\delta}_L u_\tau}{\nu}. \qquad (13)$$

The value α can be determined also from a ratio

$$u^+ = \alpha - 2.5\ln\alpha + 2.5\ln y, \qquad (14)$$

where u^+ and y^+ are chose from a point of the specified speeds crossing.

Experimental data have recently collected, from which follows that $\alpha = 10 \div 12.5$, and $\aleph = 0.39 \div 0.41$.

We shall calculate constant α for researched plates according to the formula (13). The value δ_L was counted by experimental data Fig. 16, on a point of laws of a profiles in viscous sublayer and logarithmic area crossing, and the value u_τ was determined by a method of Klauser [4]. The results of calculations are shown in tab. 2. The received dependence $\delta_L/\delta = f(Re^{**})$ is completely coordinated with data of work [2, 7, 8].

Measurements on a rigid plate shown $\alpha_{mid} = 11.55$. However, at smaller speed $\alpha > \alpha_{mid}$, and at greater one $\alpha < \alpha_{mid}$. It occurs due to fact that the value u_τ grows slower than δ_L decreases with growth of U_∞. In the

majority of tests on elastic plates, increase of parameter α at the expense of viscous sublayer thickness growth was fixed, as thus u_τ decreased. Values δ_L/δ increased accordingly.

In series of tests *e*, *f*, *g*, as well as in series *c*, *d* (Fig. 16) elastic plates were tested, the outside layer of which was made from monolithic plates. At plates investigated in these series the thickness of an outside layer was increased so that the thickness of a plate in a series *f* was in 1.5 and in a series *g* - in 2.5 times more than in a series *e*. The influence of the mechanical characteristics to efficiency of complex interactions was studied on all these plates. According to criteria of similarity, the efficiency of interaction depend on Reynolds number: factor α indirectly testified to it and depend on a place of measurement on a plate and speed of a running flow. In a series *e* the value α increased at greater speed of a flow-around only in sections III and IIIa.

As a whole, the efficiency of compliant plates much depend on the mechanical characteristics and appreciably changed at their small deviations. For elimination of this lack the compliant plate was made so that it generated from below system of longitudinal whirlwinds. The test of such plate (10a) shown essential increase of δ_L and α, and the form of a profile in viscous sublayer become transitive (parabolic).

As the elasticity of this plate increased, it can be related to elastic plates, the analysis of which should be made according to principles and criteria (4)-(7). Determination of these criteria was made as follows (tab. 3). The value λ_z^+ and frequency of ejections from viscous sublayer f_b^+ for the standard are accepted the same as in tests [7]. By using the formulas (6), (11), the period of viscous sublayer updating is determined from a ratio

$$T^+ = \left(\frac{u_\tau \bar{\delta}_L}{4.64\nu}\right)^2. \qquad (15)$$

As in the formula (11), the value $\bar{\delta}_L$ is understood as thickness of viscous sublayer including laminar and buffer layers , it was determined from crossing curves of a speed profile in a turbulent nucleus and in buffer zone. The values $\bar{\delta}_L$ accordingly is more than in tab. 2, and it is more convenient to determine them from profiles of speed, given in universal coordinates. The calculation made for I section and the speed U_∞=10.15 m/s on rigid plates determined T^+=215, and $f^+=4.65\cdot10^{-3}$, that is well coordinated with known data.

For compliant plates is taken from the tab. 3 λ_z^+ the same as for the standard. Thus, λ_z^+ is underestimated as follows from results of measurements of correlation factors. The value f_b^+ is determined by results of measurement of frequency of elastic plates own fluctuations, as fluctuations of a plates surface influence strongly on ejections from viscous sublayer.

For elastic plates λ_z^+ was determined on the basis of their outside layer design, f_b^+ - on measurements of dynamic properties of plates.

The compliant plates 1, 1a, 9 and 10a are characterized by such values f_b^+, that according to a hypothesis about preexplosive modulation [9] they could effectively cooperate with a boundary layer at the expense of regulation of ejections from viscous sublayer frequency. However, this mechanism does not work because of their large compliance, conformity of large values f_b^+ in tab. 4 to small values α in tab. 2 testifies about that.

The efficiency of such compliant materials elasticity of which increased, can be increased at the expense of increase of structural interaction. Really, the increasing values α corresponds to λ_z^+=201÷252 at a plate 10a. λ_z^+ also increased up to 200 at polymeric solutions. The same tendency is fixed at large negative gradients of pressure.

All elastic plates (see Fig. 16, series *j*, *k*, *l*, *m*) without exception are characterized by increase of values α (up to two times in comparison with the standard). Thus, λ_z^+ was either the same as the standard had, or less in 1.5÷2 times, and f_b^+ - in 1.5÷5 times more.

It is obvious that the efficiency of these plates is caused by the mechanism of preexplosive modulation (f_b^+ increased). However, the principle of structural interaction plays an essential role. So, the maximum increase of viscous sublayer thickness is fixed at a plate 11, which λ_z^+ twice times less than the standard have. But taking into account, that λ_z of vortical system in viscous sublayer of the standard, also in twice times less then Kline-stripes, there is the good conformity λ_z of vortical system to distance between longitudinal structures in an elastic material. From here follows, that λ_z of an elastic plate structures have to be either equaled to λ_z of longitudinal vortical system in viscous sublayer, or to be twice more to correspond to "peaks" or "valleys" of whirlwinds.

11. CONCLUSIONS.

Results of researches adduced before allow to make the following conclusions concerning effects of a flow interaction with elastic plates:

- Simple membrane plates accelerate or slow down the change of transition stages, increase or reduce area of unstable frequencies of flat disturbances and number $Re_{l.s.}$, depending on their structure and mechanical characteristics;
- The elastic plates promote of longitudinal whirlwinds system formation in a boundary layer;

- Change of a current structure and character of disturbing movement in a boundary layer is fixed at a flow over of elastic plates. If the boundary layer is considered as a waveguide, the characteristics of a waveguide can be adjusted by changing of property and structure of a streamline surface. For example, it is possible to organize longitudinal vortical systems in a boundary layer with the help of elastomers the properties of which vary periodically in a given direction.

REFERENCES

1. Amphilochiev, V. B., Droblenkov, V. V., «The boundary layer stability on elastic plate on different bonder conditions», Drag reduction and ships seaworthiness, Leningrad, Shipbuilding, 89, 1967, pp 16-21.
2. Ash, R. L., Bushnell, D. M., «Compliant wall turbulent skin-friction reduction», AIAA Paper, 833, 1975, pp 1-33.
3. Babenko, V. V., «Principal characteristics of flexible coatings and similarity criteria», Bionika., 5, 1971, pp 73-76.
4. Babenko, V. V., Kanarsky, M. V., Korobov, V.V., «Boundary layer on elastic plates», Kiev, Ukraine, Naukova dumka, 1993, 264 pp.
5. Basin, A. M., Korotkin, A.. I., Kozlov, L. F., «Boundary layer control for ship», Leningrad, UdSSR, Shipbuilding, 1968, 491 pp.
6. Benjamin, T. B., «The threefold classification of unstabl disturbances in flexible surfaces bounding inviscid flows», J. Fluid Mech., 16, 1963, pp 436-450.
7. Blackwelder, R.F., «Analogies between transitional and turbulent boundary layers», Phys. of Fluids, *26*, 10, 1983, pp 2807-2816.
8. Borshevskij, U. T., Rudin, S. N., «Turbulent boundary layer control», Kiev, Ukraine, Vishcha shkola, 1978, 184 pp.
9. Bushnell, D.M., «Turbulent Drag Reduction for External Flows», AIAA Paper, 0227, 1983, pp 1-20.
10. «Forming of turbulence in shear flows» Kozlov, L. P., Tsiganiuk, A. I., Babenko V. V. and other, Kiev, Ukraine, Naukova dumka, 1985, 281 pp.
11. Gad-el-Hak, M., Blackwelder, R. J., Riley, J. F., «On the interaction of compliant coatings with boundary layer flow», J. Fluid Mech., 140, 1984, pp 257-280.
12. Gromeko, N. S., «Collection of writings», Moscow, UdSSR. Nauka, 1952, 295 pp.
13. Kozlov, L. P., Babenko, V. V., «Experimental investigations of the boundary layer», Kiev, Ukraine, Naukova dumka, 1978, 184 pp.
14. Kramer, M. O., «Boundary layer stabilization by distributed damping», Naval Eng. J., *72*, 1, 1962, pp 25-73.
15. Landahl, M. T., Kaplan, R. E., «The effects of compliant walls on boundary layer stability and transition», Naples, AGARD, Boundary layer Technology Mecting, 1965, 67 pp.
16. Lee, T., Fischer, M., Schwarz, W. H., «Investigation of the stable interaction of a passive compliant surface with a turbulent boundary layer», J. Fluid Mech., 257, 1993, pp 373-401.
17. Lucey, A. D., Carpenter, P. W., «Boundary layer instability over compliant walls. Comparson between theory and experiment», Phys. Fluids, *7*, 10, 1995, pp 2355-2363.
18. Merkulov, V. I., «Fluid movement control», Novosibirsk, UdSSR, Sibirian Branch of «Nauka», 1981, 173 pp.
19. Schubauer, G. B., Skramstad, H. K., «Laminar boundary layer oscillations and stability of laminar flow». J. Aeronaut. Sci., 14, 1947, pp 69-81.
20. Semenov, B. N., «Interaction of flexible boundary with viscous sublayer of turbulent boundary layer» J. Appl. Mech. and Techn. Phys., 12, 3, 1971, pp 58-62.
21. Wortmann, F. X., «Eine Methode zur Beobachtung und Messung von Wasserstromung mit Tellur», Z. Fur Angew. Phys., *5*, 6, 1953, ss 200-206.

Range of working speeds at test of elastic plates

Table 1.

Number of plate	I section			II section			III section		
	U_∞ m/s	u_τ m/s	u_τ/U_∞ 10^2	U_∞ m/s	u_τ m/s	u_τ/U_∞ 10^2	U_∞ m/s	u_τ m/s	u_τ/U_∞ 10^2
The standard	10.15	0.46	4.5	9.62	0.488	5.1	10.0	0.475	4.75
	15.98	0.744	4.66	16.99	0.778	4.6	17.06	0.774	4.53
5	9.88	0.488	4.94	-		-	10.07	0.44	4.4
	17.04	0.758	4.4	-		-	16.94	0.746	4.4
11a	10.13	0.425	4.2	-		-	9.9	0.439	4.4
	17.67	0.758	4.3	-		-	17.43	0.701	4.02
11	-	-		-		-	9.9	0.414	4.8
	-	-		-		-	16.37	0.558	3.4
8a	-	-		-		-	9.94	0.418	4.2
	-	-		-		-	15.54	0.652	4.2
3	-	-		-		-	9.93	0.398	4.0
	-	-		-		-	15.64	0.734	4.7
1	9.92	0.418	4.2	10.27	0.377	3.67	10.09	0.447	4.4
	15.53	0.595	3.83	15.69	0.562	3.58	15.86	0.549	3.5
1a	9.36	0.414	4.4	9.904	0.394	3.94	9.36	0.373	3.99
	15.69	0.578	3.7	15.69	0.545	3.5	17.01	0.68	3.99
9	9.49	0.371	3.9	-	-	-	9.77	0.412	4.2
	16.12	0.691	4.3	-	-	-	15.92	0.628	3.9
2a	-	-	-	-	-	-	9.58	0.451	4.7
	-	-	-	-	-	-	16.17	0.562	3.48
10a	-	-	-	-	-	-	10.07	0.42	4.17
	-	-	-	-	-	-	15.81	0.75	4.74

The thickness of viscous sublayer determined on Fig. 7.

Table 2.

Number of plate	Number and designations of curve	Number of section	u_τ, m/s	$10^4\delta_L$	$10^2\delta$, m	$10^2\delta_L/\delta$, m	$\alpha = \frac{u_\tau \delta_L}{\nu}$
The standard series *a*	2	I	0.46	3.8	2.51	1.51	11.73
	3	I	0.744	2.0	2.21	0.9	9.99
	2'	II	0.488	4.1	2.78	1.47	13.4
	3'	II	0.778	2.2	2.63	0.84	11.5
	2"	III	0.475	3.7	2.93	1.33	11.8
	3"	III	0.774	2.1	2.75	0.76	10.9
5, series *c*	11	I	0.488	4.7	3.32	1.42	15.39
	12	I	0.758	2.6	3.4	0.76	13.23
	13	III	0.44	4.0	4.1	0.98	11.8
	14	III	0.746	3.7	3.6	1.03	18.5
2a, series *d*	15	III	0.451	6.7	3.71	1.8	20.3
	16	III	0.562	2.8	3.76	0.75	11.24
9, series *e*	17	I	0.371	4.2	2.31	1.82	10.46
	18	I	0.691	2.1	2.18	1.01	9.74
	19	III	0.412	4.4	2.73	1.61	12.17
	20	III	0.628	3.4	2.67	1.27	14.33
	21	IIIa	0.594	2.3	2.94	0.78	9.2
	22	III	0.562	3.5	3.0	1.17	13.2
1a, series *f*	23	I	0.414	3.9	2.57	1.51	10.84
	24	I	0.578	2.3	2.75	0.83	8.9
	25	II	0.39	3.1	2.74	1.12	8.1
	26	II	0.545	3.4	2.64	1.3	12.4
	27	III	0.373	3.7	2.93	1.2	9.26
	28	III	0.68	3.7	2.96	1.24	16.9
1, series *g*	29	I	0.418	4.5	2.7	1.67	12.6
	30	I	0.595	4.0	2.73	1.5	15.97
	31	II	0.377	4.3	2.96	1.45	10.88
	32	II	0.562	4.0	2.93	1.37	15.1
	33	III	0.447	4.7	3.42	1.37	14.1
	34	III	0.549	1.64	3.28	0.5	6.04
10a, series *i*	35	III	0.42	2.0	3.83	0.52	5.64
	36	III	0.75	4.2	2.66	1.6	21.14
11a, series *j*	37	I	0.425	4.4	2.49	1.76	12.6
	38	I	0.758	3.6	2.51	1.4	18.3
	39	III	0.439	3.7	2.89	1.28	10.9
	40	III	0.701	3.9	2.82	1.38	18.35
	41	IIIa	0.672	3.2	2.92	1.1	14.4
	42	III	0.635	3.0	2.825	1.06	12.8
11, series *k*	43	III	0.414	6.3	2.9	2.17	17.5
	44	III	0.558	4.6	2.82	1.63	17.23
8a, series *l*	45	III	0.418	4.6	2.93	1.6	12.9
	46	III	0.652	3.8	2.82	1.35	16.6
3, series *m*	47	III	0.398	5.1	2.95	1.73	13.62
	48	III	0.734	3.1	2.87	1.08	15.3

Parameters of flow in viscous sublayer.

Table 3.

Number of plate	I section						III section					
	U_∞, m/s	λ_z^+	$10^2\lambda_z$, m	$10^3 f_b^+$	f, 1/s	Re^{**}	U_∞, m/s	λ_z^+	$10^2\lambda_z$, m	$10^3 f_b^+$	f, 1/s	Re^{**}
The standard	10.15	80-100	0.26-0.32	3.5-4.1	49.7-58.2	1662	10	80-100	0.25-0.31	3.5-4.1	53-62	1912
	15.98	80-100	0.16-0.2	3.5-4.1	130-152	2304	17.06	80-100	0.15-0.19	3.5-4.1	141-165	3061
5	9.88	80-100	0.24-0.3	4.88	78	2140	10.07	80-100	0.27-0.34	6.0	78	2676
	17.04	80-100	0.16-0.2	2.02	78	3794	16.94	80-100	0.16-0.2	2.1	78	3968
11a	10.13	48.5	0.17	19.72	239	1645	9.9	50.1	0.17	18.5	239	1867
	17.67	86.5	0.17	6.2	239	2894	17.43	80	0.17	7.25	239	3207
11	-	-	-	-	-	-	9.9	47.2	0.17	16.1	185	1872
	-	-	-	-	-	-	16.37	63.7	0.17	8.85	185	3012
8a	-	-	-	-	-	-	9.94	80-100	0.29-0.36	19.9	233	1901
	-	-	-	-	-	-	15.54	80-100	0.18-0.23	8.2	233	2859
3	-	-	-	-	-	-	9.93	80-100	0.3-0.37	15.9	169	1910
	-	-	-	-	-	-	15.64	80-100	0.16-0.2	4.67	169	2929
1	9.92	80-100	0.29-0.36	18.2	214	1748	10.09	80-100	0.27-0.33	16	214	2251
	15.53	80-100	0.2-0.25	9.0	214	2766	15.86	80-100	0.2-0.27	10.6	214	3394
1a	9.36	80-100	0.29-0.36	20.1	246	1569	9.36	80-100	0.32-0.4	26.3	246	1789
	15.69	80-100	0.2-0.26	11	246	2815	17.01	80-100	0.17-0.22	7.9	246	3283
9	9.49	80-100	0.32-0.4	14.8	137	1430	9.77	80-100	0.29-0.36	12	137	1739
	16.12	80-100	0.17-0.2	4.3	137	2292	15.92	80-100	0.19-0.24	5.2	137	3773
2a	-	-	-	-	-	-	9.58	80-100	0.26-0.33	6.1	83	2319
	-	-	-	-	-	-	16.17	80-100	0.21-0.27	3.9	83	3965
10a	-	-	-	-	-	-	10.07	112.8-141	0.4-0.5	19.5	231	2516
	-	-	-	-	-	-	15.81	201-252	0.4-0.5	6.1	231	2743

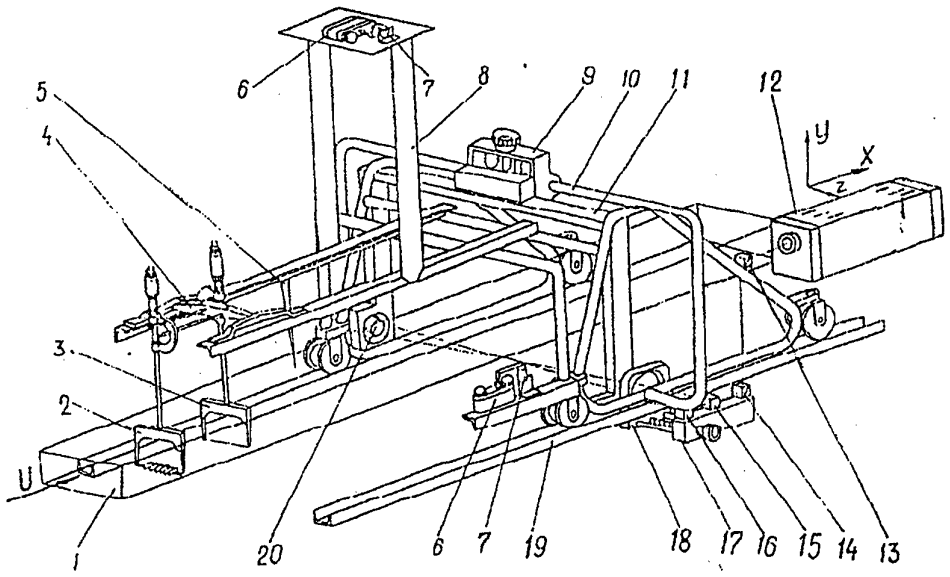


Figure 1 The sketch of the hydrodynamic channel test section with devices

1 - the test section; 2 - vortex generators; 3,4 - tellurium wire with a holder, 5 - anode (visualization system), 6,7 - photoregistration system, 8-11 - moving truck with devices, 12-19 - system of laser anemometry.

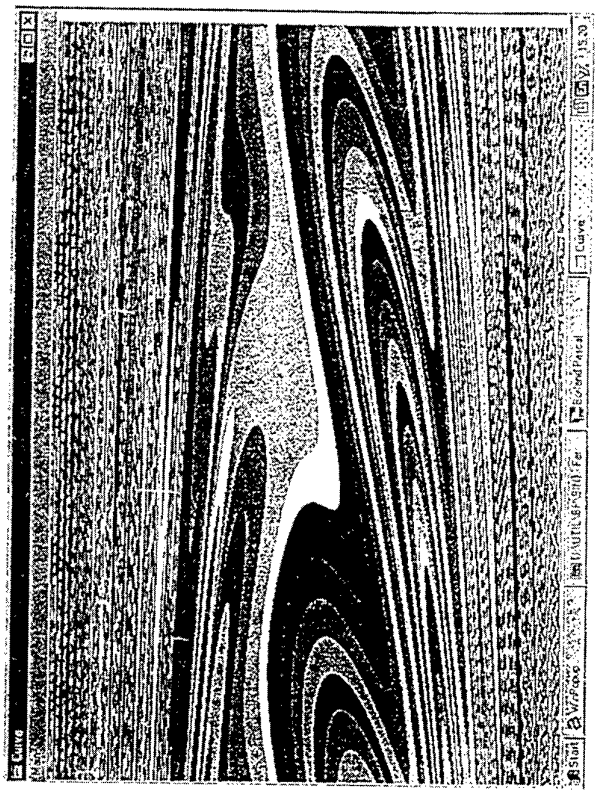


Fig. 2,b

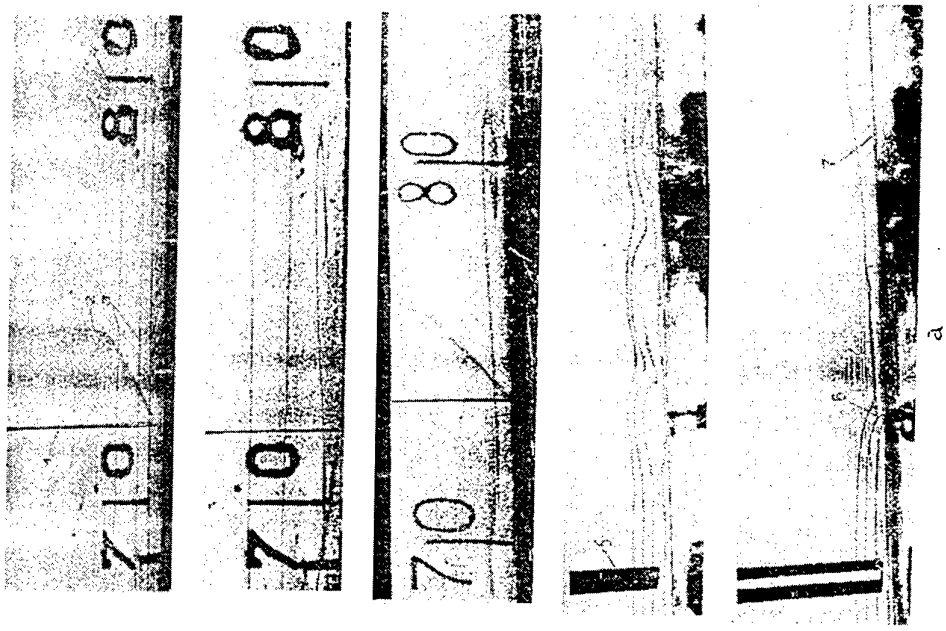


Figure 2 The tellurium method was used to photograph the velocity profile and streamlines in the flow

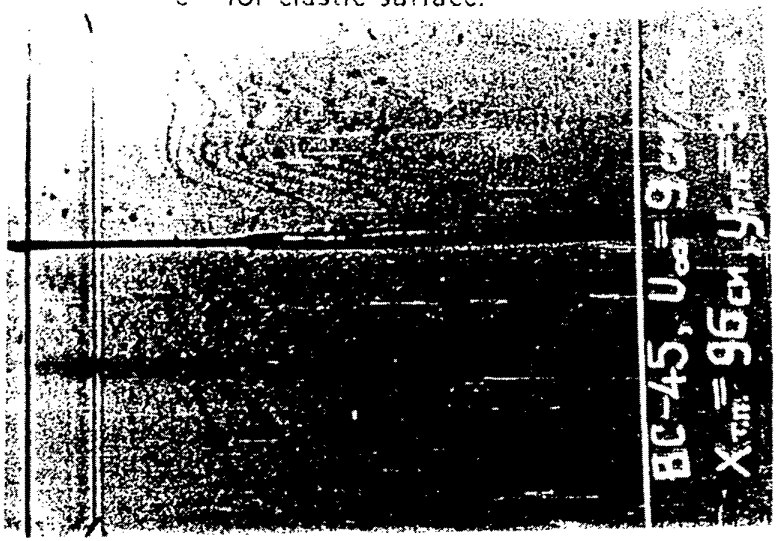


Fig.3. Velocity profile in boundary layer in transverse direction:

a - for rigid plate at zero pressure gradient;

b - the same at adverse pressure gradient;

c - for elastic surface.



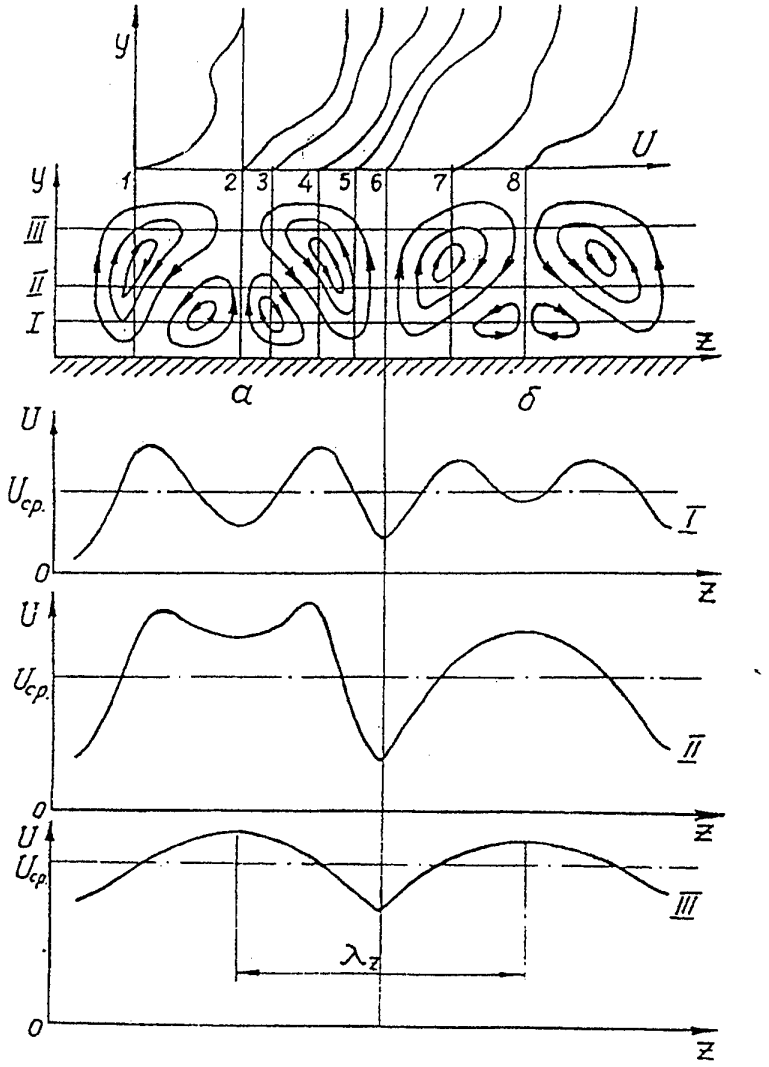


Figure 4. The scheme of flow structure at initial stages of non-linear deformation of plane wave at large

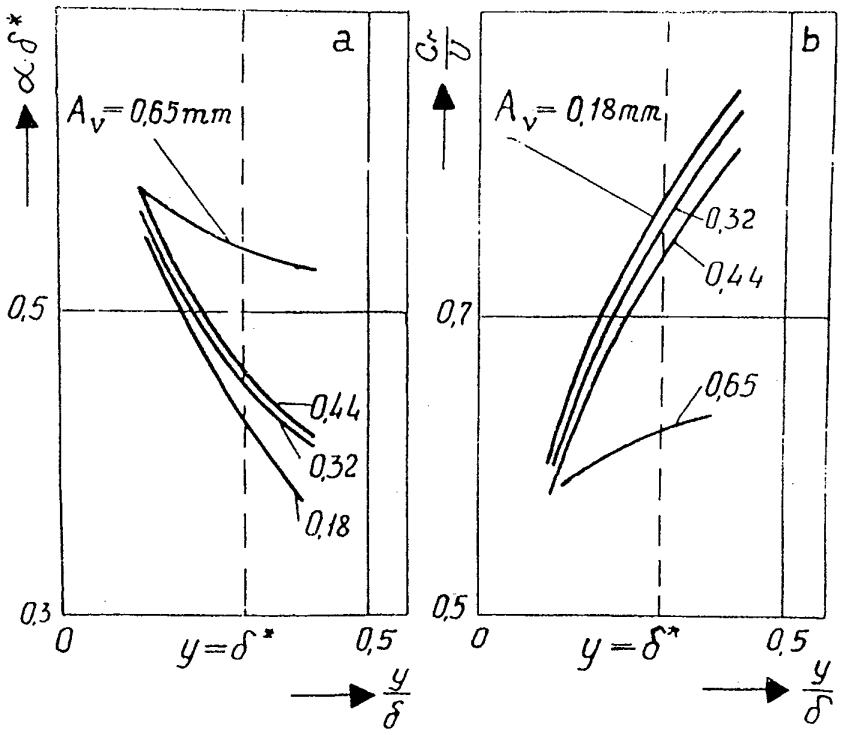


Fig.5. Effect of oscilllation ribbon oscillation amplitude upon wave number distribution (a) and phase velicity (b) of the exciting motion the boundary layert thickness.

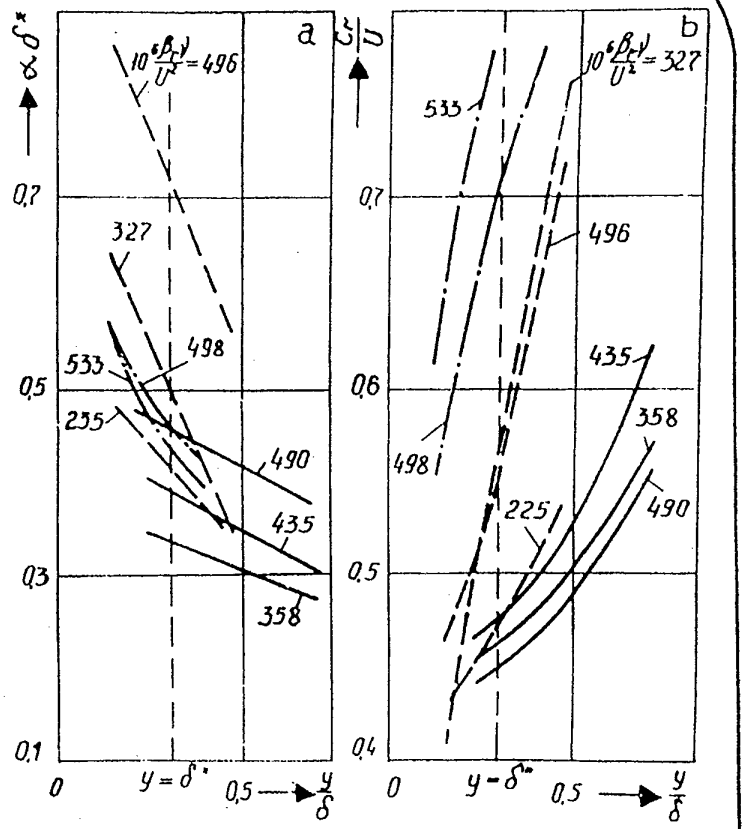
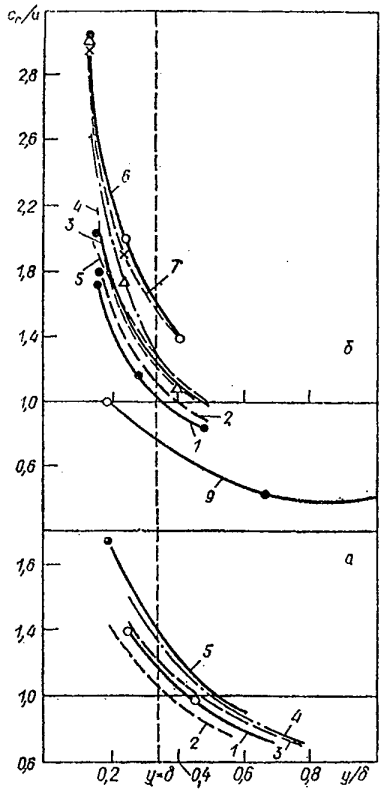
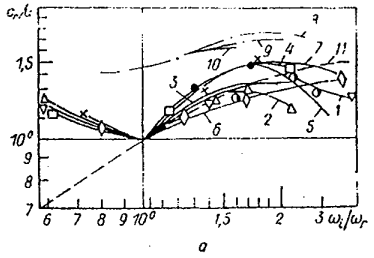
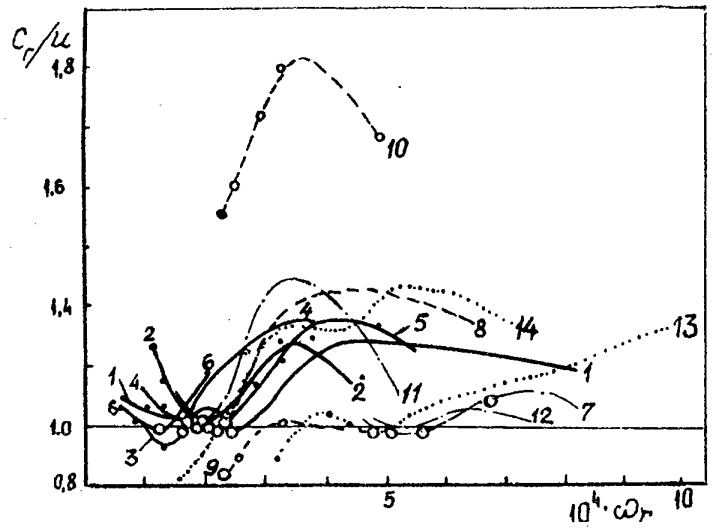


Fig.6. Distribution of values $\alpha\delta_*$ and $C_r/U(b)$ theroughout the boundary layer thickness at $Re_{\delta^*} = 653$ (dot - and - dash curves



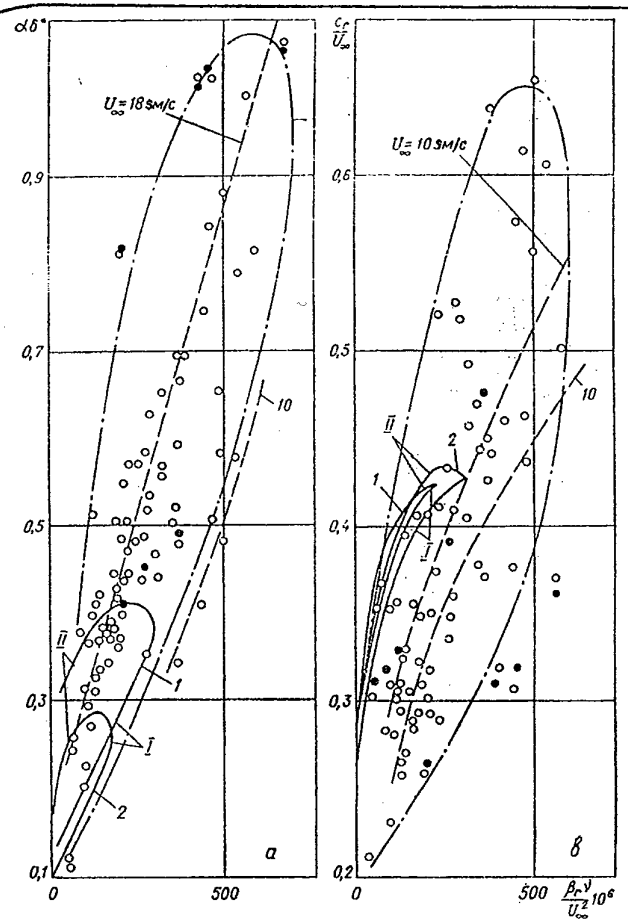




$$c_r/u = (n/n_{11} - 1)^2 \qquad n < n_{11},$$
$$c_r/u = 1.6\log(n/n_{11}) + 1) \qquad n > n_{11}.$$

Fig. 8. Dependence of phase velocity on frequency of disturbing motion

Fig.7. Distribution of dimensionless velocity C_r/u through the boundary layer thickness near $R_{l.s.}$ (a) and at $Re > Re_{l.s.}$(b)



$$\left.\begin{aligned} \alpha\delta^* &= 1.4 \cdot 10^3 \beta_r \nu / U^2_{infty} + 0.15, \\ c_r / U_{infty} &= 0.7 \cdot 10^3 \beta_r \nu / U^2_{infty} + 0.2. \end{aligned}\right\}$$

Fig. 9 . Ultimately neutral curves. Dependence for wave number (a) and phase velocity (b) on frequency of disturbing motion: predictions: 1 - according to Tollmien for dimensionless frequency and Shen for phase velocity; 2 - according to Schlichting; I, II - branches of neutral curve; ○ - author's • measurement from v' end w'.

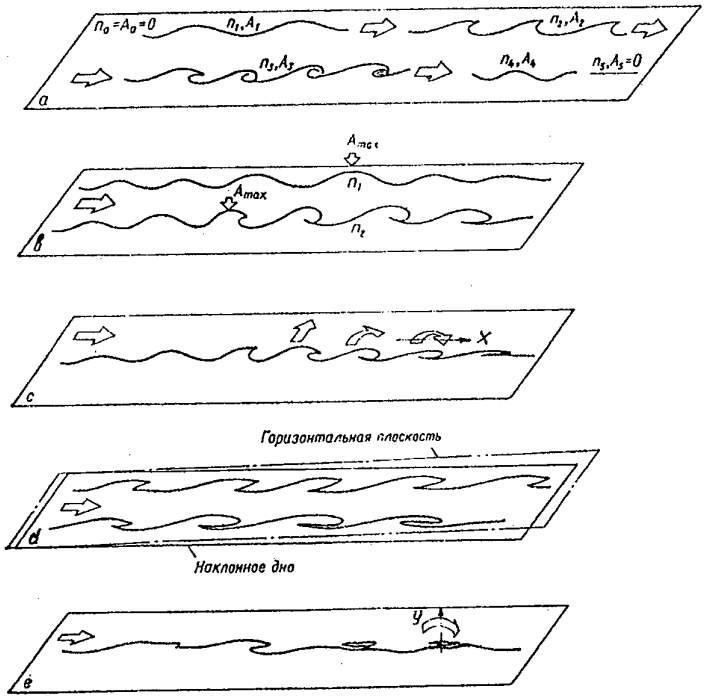


Fig.10.The scheme of disturbing motion development along plate: a - at $x = const$; b - at $n = const$; c - simultaneous shooting from above and from the side; d - at adverse pressure gradient; e - at non-sinusoidal character of disturbance.

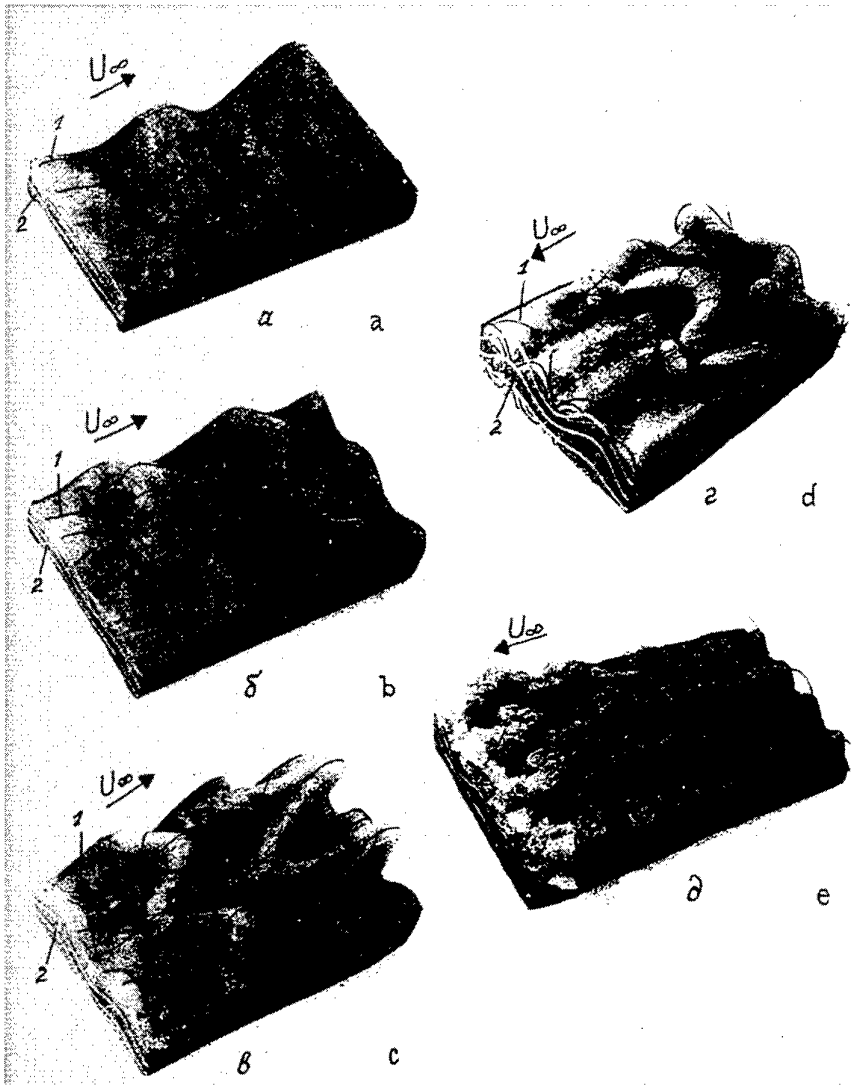
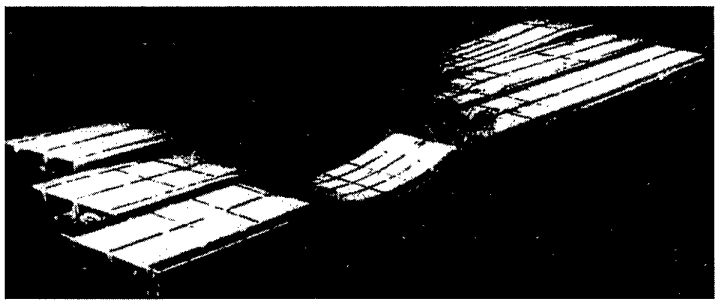
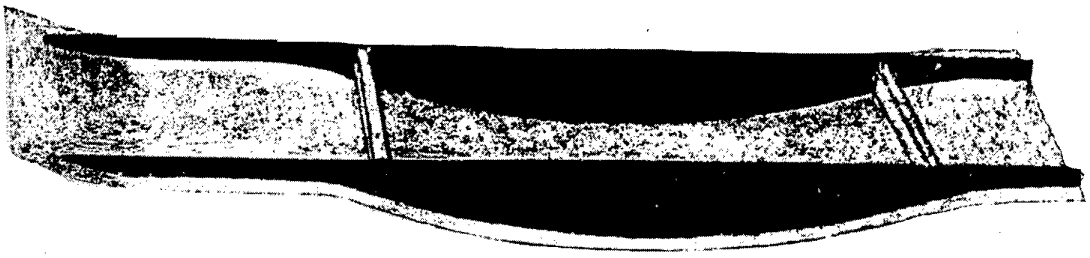


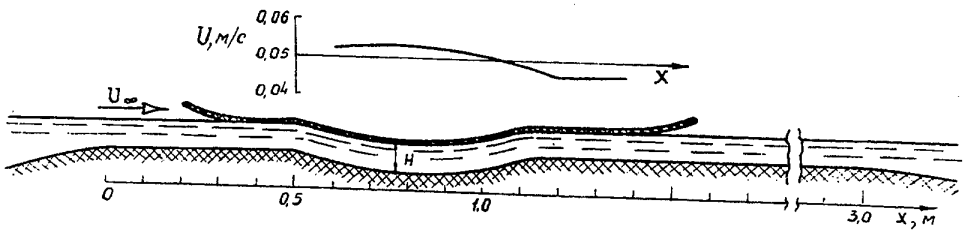
Fig.11. The physical model of the disturbances type successive transformation during the transition to turbulence: a — amplification of plane disturbances; b — phase modulation of the wave, three-dimensional effects appearance; c — amplitude modulation of the wave, "peaks" and "valleys" forming; formation of longitudinal rows of Λ — shaped vortices; d — organization of the longitudinal vorteces system; e — vorteces form and intensity changes in space and time; transition to a zigzag trajectory of the vorteces movement; breakdown of peripherical parts of the meandering vortices. Active formation of turbulent spots, their growth, amalgamation and turbulent boundary layer development.



a



b



c

Fig.12. Curvilinear bottom (a), lid (b) and the schemeof their disposal in working section of the hydrostand (c).

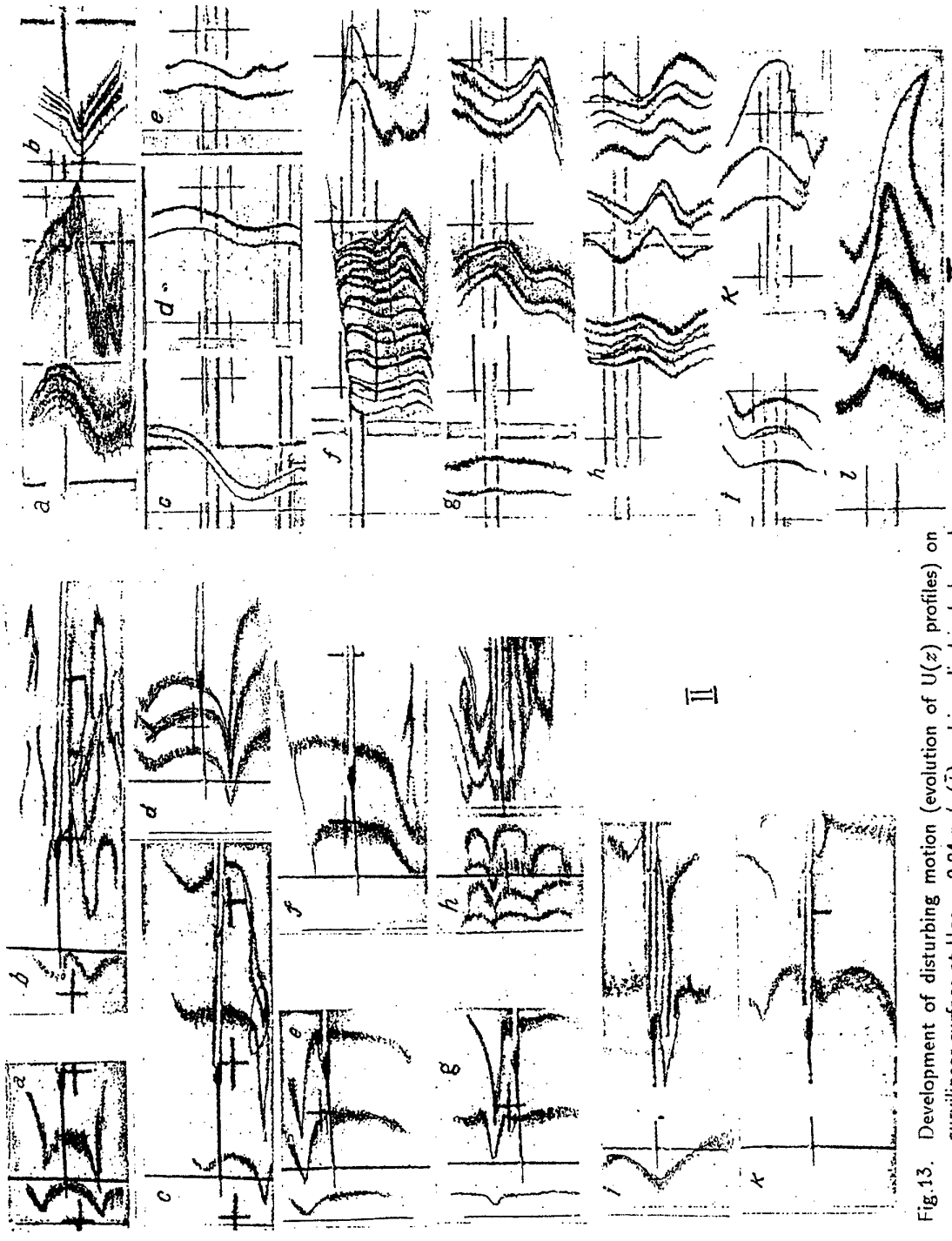


Fig.13. Development of disturbing motion (evolution of $U(z)$ profiles) on curvilinear surface at $U_\infty = 0.04$ m/s (I) and in cylindrical channel near convex wall (II).

Fig. 13

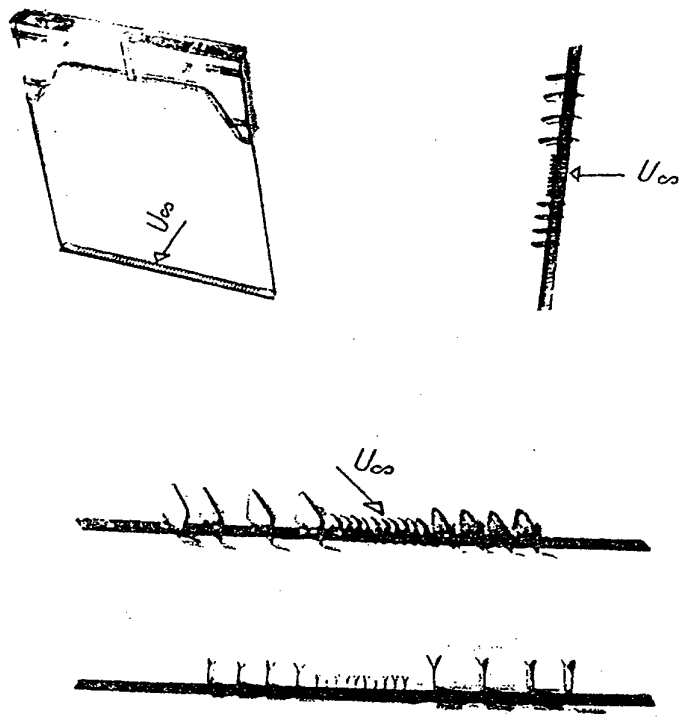


Fig.14. Support1 with vortex-generators 2 for introducing three-dimensional disturbances into a boundary layer.

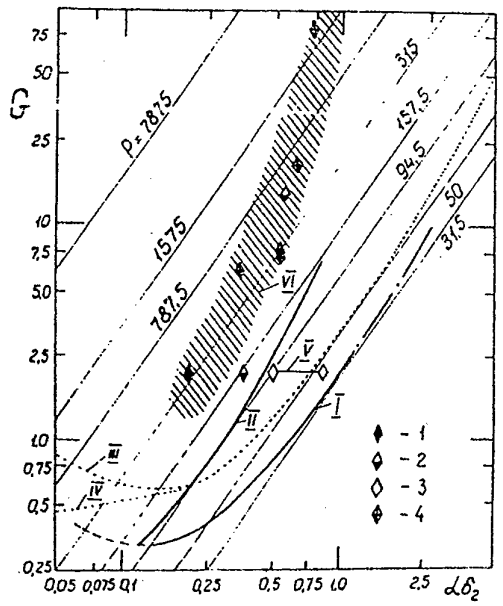


Fig. 15. Stability of three-dimensional disturbances on concave elastic surface: I,II - experimental neutral curve and curve of maximum amplification for rigid surface; III-IV - calculated neutral curves [9.14]; V,VI - regions of neutral and maximum grown disturbances for elastic surface: Characteristics for concave elastic surface: 1- natural disturbances, 2- growing forced ones, 3- disturbances forced, close to neutral, 4- growing forced disturbances on cylindrical part.

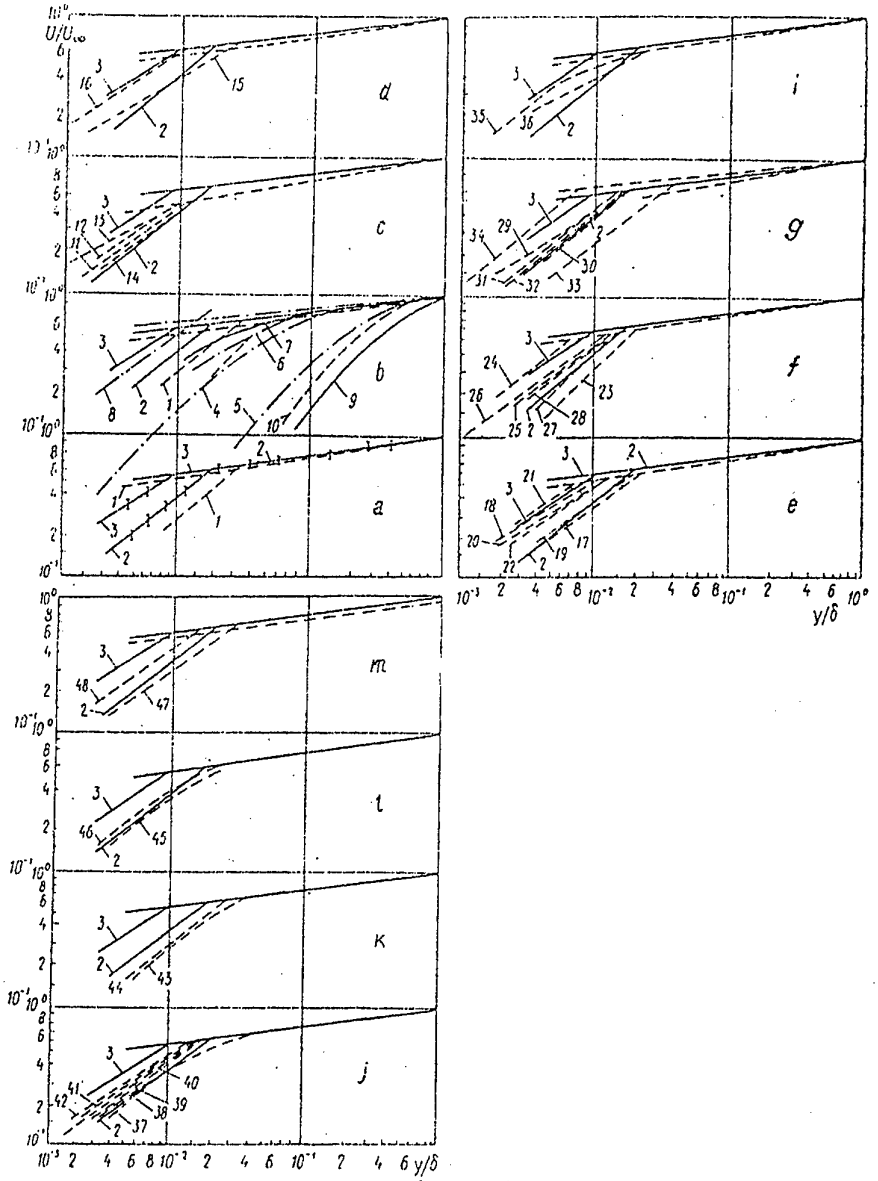


Fig.16. Distribution of longitudinal averaging speed on thickness of a boundary layer on the standard (a), rigid (b) and elastic plates 5 (c), 2a (d), 9 (e), 1a (f), 1 (g), 10a (i), 11a (j), 11 (к), 8a (л), 3 (м):

1,4 - data from work [8] for turbulent and transitive boundary layers accordingly;

2, 3 - measurement at small and large speeds of a flow accordingly;

5, 8 - measurement on the hydrostand at various stages of transition at U_∞ equal to 0.1; 0.18; 0.27 and 0.6 m/s [illegible], and $\varepsilon>0.1\%$ accordingly;

9 - the same at $U_\infty=0{,}08\div0.15$ m/s and at $\varepsilon<0.05\%$ on rigid and elastic plates;

10 - as well as 9, but at a heating of a membrane surface [13]. The other designations are given in tab. 3.

MODELING OF TURBULENT NEAR-WALL SHEAR FLOWS PROPERTIES

V.T. Movchan,
E.A. Shkvar
Department of Higher Mathematics,
Kiev International University of Civil Aviation,
Cosmonaut Komarov ave. 1, Kiev, 252058, Ukraine,
fax: (044) 488-30-27

SUMMARY

The given paper deals with mathematical and numerical modeling of shear flows in the vicinity of boundary layer. The half-empirical algebraic models of turbulent viscosity and turbulent conductivity coefficients for predictions of two- and three-dimensional gradient flows on smooth and rough surfaces are proposed. These models of turbulent exchange coefficients can be effectively applied both for approximate-analytical and numerical solutions of flows characteristics on fixed or moving surfaces. The results of approximate - analytical and numerical predictions of different kinds of boundary layers are presented.

LIST OF SYMBOLS

- a empirical coefficients in Eq.(9).
- B constant of logarithmic law for shear flow over rough surface, dimensionless
- C_f skin friction coefficient, dimensionless
- C_p specific heat at constant pressure, J/kg K
- C_{sm} constant of logarithmic law for shear flow over smooth surface, dimensionless
- D integral characteristic of velocity profile, m
- H shape factor,dimensionless
- k model coefficient, dimensionless
- l mixing length, m
- N anisotropy coefficient, dimensionless
- p pressure, kg/m s ^{2}
- Pr Prandtl number, dimensionless
- q heat stream density, J/m ^{2} s
- Re^{**} momentum - deflect thickness Reynolds number, dimensionless
- Re^L Reynolds number of liquid film, dimensionless
- T temperature, K
- u velocity, m/s
- U_{L0} velocity of motion of liquid - gas phase separation boundary, m/s
- U_h free stream velocity, m/s
- U_{max} maximum value velocity of near-wall jet velocity profile, m/s
- U_{min} minimum value velocity of near-wall jet velocity profile, m/s
- v_* shear velocity, m/s
- x axis of ortogonal coordinate system, m

Greek symbols

- β_w surface cross flow angle
- β_{τ_w} wall shear-stress angle
- γ intermittency function, dimensionless
- δ shear flow thickness, m
- δ^* displacement thickness, m
- δ^{**} momentum - deflect thickness, m
- Δ Rotta-Clauser parameter, dimensionless
- ΔT shift of logarithmic part of the temperature profile, K
- Δu shift of logarithmic part of the velocity profile, m/s
- Δx_2 roughness influence function, m
- λ heat conductivity coefficient, W/m K
- μ absolute coefficient of viscosity, kg m/s
- ν kinematic coefficient of viscosity, m^2/s
- ϱ density, kg/m^3
- τ shear stresses, kg/m s^2
- $\bar{\tau}$ non-dimensional shear stresses
- χ model coefficient, dimensionless
- χ_1 model coefficient, dimensionless
- χ_2 model coefficient, dimensionless
- Φ Fedyaevsky parameter, dimensionless

Subscripts

- j parameter in joint point
- L parameter for liquid
- h parameter for heat transfer processes
- n direction of secondary flow
- r summary velocity
- s direction of main flow
- t turbulent
- w wall
- Σ summary parameter

1 INTRODUCTION

Nowadays there is a good choice to use the most simple and calculatively effective algebraic models of turbulent exchange coefficients in the process of prediction of turbulent boundary layer properties. Meanwhile, modeling on algebraic level can meet some problems to be overcome. They are: pressure gradient, low Reynolds numbers, peculiarities of flow development influences and difficulty of turbulence structure description. The aim of the present paper is to discribe a new approach for modeling of turbulent viscosity and turbulent conductivity coefficients, which has been proposed and worked out by authors.

2 TURBULENT VISCOSITY MODEL (TVM)

TVM for turbulent boundary layer

The given method of simulation is based on the fact that coefficients of turbulent exchange are presented

Paper presented at an AGARD FDP Workshop on "High Speed Body Motion in Water", held in Kiev, Ukraine, 1-3 September 1997, and published in R-827.

by means of one continuous dependence along the shearing layer thickness. This allows to take into account the effects of nonlinear interaction, to avoid the problem of joining, to create some advantages during elaboration of the design method. In case of three-dimensional turbulent flow the modification of Rotta' approach has been worked out. According to this the turbulent viscosity coefficient for boundary layer applications can be presented as follows

$$(\nu_t)_{11} = \nu_t(\frac{u_1^2 + Nu_3^2}{u_\tau^2}); \qquad (\nu_t)_{33} = \nu_t(\frac{u_3^2 + Nu_1^2}{u_\tau^2});$$

$$(\nu_t)_{13} = (\nu_t)_{31} = \nu_t(1-N)\frac{u_1 u_3}{u_\tau^2}; \; u_\tau^2 = u_1^2 + u_3^2, \quad (1)$$

where $(\nu_t)_{ij}$ $(i,j=1,3)$ – components of turbulent viscosity tensor; ν_t – scalar turbulent viscosity; $N = \nu_{tn}/\nu_{ts}$ – non-isothropy coefficient; s, n – directions of main and secondary flows respectively; u_k – velocity projections on ortogonal coordinates directions $x_k, (k=1,2,3)$ where x_1 and x_3 being in the plane, tangentional to streamlined surface and x_2 axis is normal to this plane. Scalar turbulent viscosity is expressed by the continuous equation for the shearing layer thickness

$$\nu_t = \chi U_h D \gamma \tanh \frac{l(v_{*1}^4 \bar{\tau}_1^2 + v_{*3}^4 \bar{\tau}_3^2)^{1/4}}{\chi U_h D}, \qquad (2)$$

where χ – Clauser coefficient; U_h – free stream velocity; D – integral characteristic of three-dimensional velocity profile; $v_{*i} = \sqrt{\tau_i/\varrho}$ – shear velocity; $\bar{\tau}_k = \tau_k/\tau_{wk}$ – non-dimensional shear stresses in the wall vicinity; ϱ – density; l – mixing length; $\gamma = \sqrt{1-\eta}$ – the function with effect of non-continuous turbulence (intermittency function); $\eta = x_2/\delta$ – non-dimensional lateral coordinate; δ – shear layer thickness. To calculate the above mentioned parameter D two approaches have been used, one elaborated by Cebeci and other - by Mellor, Herring. According to these

$$D_1 = \int_0^\delta (1 - \frac{u_\tau}{U_h}) dx_2;$$

$$D_2 = \int_0^\delta \frac{x_2}{U_h} \sqrt{\left(\frac{\partial u_1}{\partial x_2}\right)^2 + \left(\frac{\partial u_3}{\partial x_2}\right)^2} dx_2. \qquad (3)$$

Calculation of $\bar{\tau}_k$ have been done using the expressions:

$$\bar{\tau}_k = \begin{cases} 1 + \Phi_k \eta, & \text{if} \quad \Phi_k \geq 0; \\ 1/(1 - \Phi_k \eta), & \text{if} \quad \Phi_k < 0, \end{cases}$$

where $\Phi_k = \delta/\tau_w \frac{\partial p}{\partial x_k}$ – parameter of Fedyaevsky; $\frac{\partial p}{\partial x_k}$ – pressure gradient along the axis x_k.
Mixing length is expressed by

$$l = k x_{2*} \tanh \frac{\sinh^2[\chi_1 x_{2*}^+] \tanh\{\sinh^2[\chi_2 x_{2*}^+]\}}{k x_{2*}^+ (v_{*1}^4 \bar{\tau}_1^2 + v_{*3}^4 \bar{\tau}_3^2)^{1/4}/v_{*\Sigma}}, \quad (4)$$

where $k = 0.4$, $\chi = 0.0168 - 0.0215$ $\chi_1 = 0.068 - 0.072$, $\chi_2 = 0.023$ – model coefficients; $v_{*\Sigma} = (v_{*1}^4 + v_{*3}^4)^{1/4}$ – total shear velocity; $x_{2*} = x_2 + \Delta x_2$; $x_2^+ = x_2 v_{*\Sigma}/nu$; Δx_2 – roughness dynamical influence function; $\Delta x_2^+ = \Delta x_2 v_{*\Sigma}/\nu$. The better way is to determine model coefficients with using the dependences $\chi = f_1(\frac{\partial p}{\partial x})$, $k = f_2(\frac{\partial p}{\partial x})$, $\chi_1 = f_3(\frac{\partial p}{\partial x})$, $\chi_2 = f_4(\frac{\partial p}{\partial x})$, which have been found by V.T. Movchan [14] as a result of numerical experiment. They are

$$\chi_2 = \chi_{20}(1 + 30,18p^+);$$

$$\chi_1 = \chi_{10}\chi_{1R}(1 + 15,09p^+ r_1 r_2);$$

$$k = 0,4 + 0,182\left(1 + p^+\right)\left(1 - e^{-0,321\beta}\right), \text{ if } p^+ \geq -1;$$

$$k = 0,4 + 58,51\frac{p^+}{\beta}\left(1 - e^{-0,321\beta}\right), \qquad \text{if } p^+ < -1;$$

$$\chi = \chi_R\left\{0,0095 + 1/\left[74,6 + (2,4+\beta)^2\right]\right\};$$

$$r_1 = 1 - 0,5e^{-0,144\beta} + 0,5e^{-0,353\beta}; \quad \chi_{10} = 0,072;$$

$$\chi_{20} = 0,223; \quad r_2 = 1 - e^{-76,1528p^+/\beta} + e^{-361,41p^+/\beta};$$

$$\chi_{1R} = 1 + 0,01\left[1 - e^{-14/(1+Z^2)}\right]; \; Z = R^{**} \cdot 10^{-3};$$

$$R^{**} = \frac{U_h \delta^{**}}{\nu}; \quad p^+ = \frac{\nu}{\rho v_*^3}\frac{\partial p}{\partial x}; \quad \beta = \frac{\delta^*}{\tau_{w\Sigma}}\frac{\partial p}{\partial x};$$

$$\chi_R = 1,55/\left[1 + 0,55\left(1 - e^{-0,243\sqrt{Z_1} - 0,2981 Z_1}\right)\right];$$

$$Z_1 = \frac{R^{**}}{425} - 1,$$

The mentioned above roughness dynamical influence function is determined by the following equations

$$\Delta x_2^+ = \begin{cases} \operatorname{arctanh}(\chi_1 \Delta u^+)/\chi_1, & \text{if } h^+ \leq h_j^+; \\ h^+ \exp(-kB(h^+)), & \text{if } h^+ > h_j^+; \end{cases} \quad (5)$$

$$\Delta u^+ = \frac{1}{k}\ln h^+ - B(h^+) + C_{sm};$$

$$h_j^+ = x_{2j}^+ \exp\left(kB(h_j^+)\right),$$

where Δu^+ – shift of logarithmic part of the velocity profile in half-logarithmic coordinates relative to its position in case of smooth surface; h – roughness height; $h^+ = h v_{*\Sigma}/\nu$; B – constant in Nicuradze equation for velocity profile at rough surface; C_{sm} – logarithmic law constant for smooth surface; x_{2j} - the joining point coordinate of buffer and logarithmic zones. The value of x_{2j} is defined as the level of smoothness of velocity profile in the joining point

$$x_{2j}^+ = \frac{\cosh^2(x_{2j}^+ + \Delta x_2^+)}{k\sqrt{1 + p^+ x_{2j}^+}} - \Delta x_2^+, \qquad (6)$$

where $p^+ = (\nu/(\varrho v_{*\Sigma}))\frac{\partial p}{\partial s}$ – pressure gradient parameter; ν – kinematic viscosity. When the streamlined surface is smooth $\Delta x_2^+ = 0$, $k = 0.4$, $\chi = 0.072$ and $x_{2*\,sm}^+ \approx 26$.

Modification TVM for near-wall jet

In the case of near-wall jet characteristics prediction the model of turbulent viscosity [1–6] is

used in the frame of near-wall flow ($0 \le u \le U_{max}$) as is, but with following two differences. 1) Intermittency is absent, that is why intermittency function is determined as $\gamma = 1$. 2) Free-stream velocity U_h in [2] is replaced onto maximum velocity significance U_{max}.
In the jet region ($U_{max} < u \le U_{min}$) the well-known traditional Clauser' approach has been used

$$\nu_t = \chi_j \delta_j (U_{max} - U_{min})\gamma,$$

where $\chi_j = 0.011$, – empirical coefficient; δ_j – thickness of the jet region;
In the wake region ($U_{min} < u \le U_h$) the mentioned above approach has been used too

$$\nu_t = \chi_w \delta_w (U_h - U_{min})\gamma,$$

where $\chi_w = 0.011$, – empirical coefficient; δ_j – thickness of the wake region;

Modification TVM for two-phase shear layer with phase separation boundary
In this case shear flow may be presented as two layers, one of which (ie gas boundary layer) is located over thin liquid film, which is spread immediately at the streamlined surface. It is obviously, that the gas–liquid boundary is moveable. In connection with this circumstances the TVM for gas flow can be used in the same form as [1–6] equations, but with following modification of velocity scale in wake region of gas shear flow. Free-stream velocity U_h in [2] is replaced onto value $(U_h - U_{L0})$, where U_{L0} – velocity of motion of liquid–gas separation boundary.

3 TURBULENT HEAT CONDUCTIVITY MODEL

Turbulent heat conductivity is expressed by the continuous equation for the shear layer thickness

$$\lambda_t = \lambda Pr \chi_h \Delta v_{*\Sigma} D\gamma \tanh \frac{l_h (v_{*1}^4 \bar{\tau}_1^2 + v_{*3}^4 \bar{\tau}_3^2)^{1/4}}{\chi_h U_h D}; \quad (7)$$

$$l_h = k_h x_{2*h} \tanh \frac{\sinh^2(\chi_{1h} f(Pr) x^+_{2*h}) v_{*\Sigma}}{k_h Pr x^+_{2*h} (v_{*1}^4 \bar{\tau}_1^2 + v_{*3}^4 \bar{\tau}_3^2)^{1/4}}, \quad (8)$$

where λ – molecular heat conductivity coefficient; $\chi_h = 0.0217$, $k_h = 0.44$, $\chi_{1h} = 0.0743$ – model coefficients; Pr – molecular Prandtl number; $x_{2*h} = x_2 + \Delta x_{2h}$; Δx_{2h} – roughness influence function on heat transfer processes; $f(Pr)$ – empirical function of Prandtl number, which can be presented as follows

$$f(Pr) = \sum_{i=1}^{6} a_i \lg^{i-1} Pr, \quad (9)$$

where $a_1 = 1$, $a_2 = 1.124$, $a_3 = -0.363$, $a_4 = 0.538$, $a_5 = -0.136$, $a_6 = 0.0344$. The roughness influence function for heat conductivity is determined by the following equations

$$\Delta x^+_{2h} = \begin{cases} \operatorname{arctanh}(\chi^f_{1h} \Delta T^+ / Pr)/\chi^f_{1h}, & \text{if } T^+ \le T^+_j; \\ \exp(k_h(\Delta T^+ - C_{sm})), & \text{if } T^+ > T^+_j; \end{cases} \quad (10)$$

$$\Delta T^+_j = \frac{1}{k_h} \ln x^+_{2hj} + C_{h\ sm},$$

where $\chi^f_{1h} = \chi_{1h} f(Pr)$; ΔT^+ – shift of logarithmic part of the temperature profile in half-logarithmic coordinates relative to its position in case of smooth surface; $C_{h\ sm}$ – constant of logarithmic law for temperature distribution over smooth surface; $x_{2hj\ sm}$ – the coordinate of joining point of buffer and logarithmic zones for temperature profile. The value of x_{2hjsm} is defined as the level of smoothness of temperature profile in the joining point in connection with following expression

$$x^+_{2hj\ sm} = \frac{\cosh^2(\chi_1 x^+_{2hj\ sm})}{k_h \sqrt{1 + p^+ x^+_{2hj\ sm}}}. \quad (11)$$

In case when secondary flow is absent the models Eq.(1 - 11) are transformed into the two-dimensional versions which has well proved itself. The application of these two-dimensional models for different types of boundary layers allows to set the relation between model coefficients and the parameters of the flow itself. These models can be also applied for the description of turbulent viscosity in the wall region of wall jets and also in case of two-phase flows with phase separation (fluid-air).

4 APPROXIMATE-ANALYTICAL SOLUTIONS

The next advantage of this approach of simulation is the elaboration of approximate-analytical solution for stress friction distribution across the boundary layer and profiles of velocity and temperature. These distributions correspond well with the law of simularity applied to wall flows. For example, in case of two-dimensional flow on smooth surface under the influence of adverse pressure gradient the shear stress distribution in cross section of the boundary layer is well approximated by means of the equation

$$\tau = \tau_w (1-\eta) \left(1 + (1+\Phi)\eta - (2+\Phi)\eta^n \tanh \frac{l\sqrt{\bar{\tau}}}{\chi_h \Delta}\right), \quad (12)$$

where $\Delta = U_h D / v_{*\Sigma}$ – Rotta-Clauser length parameter.
Equations (2-4, 12) allow to find the following velocity profile in buffer and viscous zones:

$$u^+ = \frac{1 + p^+ x^+_2}{\chi_1} \tanh(\chi_1 x^+_2) - \frac{p^+}{\chi_1^2} \ln[\cosh(\chi_1 x^+_2)], \quad (13)$$

$$u^+ = \frac{u}{v_*}.$$

By using Fourier equation with expressions Eq.(7,8), we are found the temperature distribution in mentioned above zones as

$$T^+ = \frac{Pr}{\chi^f_{1h}} \tanh(\chi^f_{1h} x^+_2), \quad T^+ = \frac{T - T_w}{T_*}, \quad (14)$$

where $q_w/(\varrho C_p v_*)$; q_w – heat stream density; C_p – specific heat at constant pressure; T_w – temperature of wall. The expressions for velocity and temperature distributions in logarithmic zone of turbulent boundary layer may be presented as follows:

$$u^+ = \frac{1}{k}\left[\ln\frac{\sqrt{1+p^+x_2^+}-1}{\sqrt{1+p^+x_2^+}+1} + 2\sqrt{1+p^+x_2^+}\right] + C_{sm} \tag{15}$$

$$T^+ = \frac{1}{k_h}\ln x_2^+ + C_{h\ sm}. \tag{16}$$

In case, when pressure gradient is zero, these constants may be determined with using following expressions

$$C_{sm} = \frac{1}{\chi_1}\tanh(\chi_1 x^+_{2j\ sm}) - \frac{1}{k}\ln x^+_{2j\ sm},$$

$$C_{h\ sm} = \frac{1}{\chi^f_{1h}}\tanh(\chi^f_{1h} x^+_{2hj\ sm}) - \frac{1}{k_h}\ln x^+_{2hj\ sm}.$$

The same approaches have been used to get expressions for distributions in outer regions, under favourable pressure gradient, with or without suction or injection through the streamlined surface and in case when the surface is rough. The calculated results are compared with experimental data and we can get the relationship of models coefficients versus pressure gradient and low Reynolds parameters and etc. The results of comparison between velocity profiles, which were obtained by expressions for rough surface (line), and experimental data of M.D. Millionschikov [1] for pipes with different technical roughness of surface (circles) are shown on Fig. 1. Figure 2 is presented the correlation of temperature distributions Eq.(14, 16) (line) and experimental data of N.M. Galin and P.L. Kirillov [2] for boundary layers on smooth surface with different values of Prandtl' number (circles).

5 NUMERICAL PREDICTIONS AND THE RESULTS OF THEIR COMPARISON WITH EXPERIMENTAL DATA

To evaluate the characteristics and the fields of application of the given turbulent viscosity model we have used it in some numerical methods of turbulent boundary layers predictions. They are: differential-difference (direct line method) according to which the boundary layer equations are transformed into a system of ordinary differential equations; two versions of grid method which are based on finite-difference patterns of Crank-Nicolson and Pasconov, Polezhaev, Chudov [3]. Besides, the applications of the model in the frame of integral method has been also analysed. It has been stated that the most applicable method from the point of view of necessary accuracy and high effectiveness of separated turbulent boundary layer computation is the grid method based on the pattern suggested by Paskonov, Polezhaev, Chudov. The given pattern ensures noniterational algorythm for solution on each step along the evolutionary coordinate and effectively stabilizes disturbances of computation. The results presented in the paper have been obtained with the help of this version of the grid method. It should be noted that the divergency of computations when other methods have been used is in the limits of data scattering and is practically the same. But the computations with the help of integral method ensure satisfactory correlation with experimental data only in case of small pressure gradients and did not allow to the forecast the separation process.

Figures 3-5 present the results of comparison of the given computation (continuous line) with experimental data (circles) and also with predictions given by the different authors (interrupted lines). All the results refer to separated flows under influence adverse pressure gradient: 1)Moses experiment (id.3800) on two-dimensional boundary layer with smooth surface [4] (Fig. 3); 2) Scottorn-Power experiment on two-dimensional boundary layer with rough surface [5] (Fig. 4); 3) Van-Den-Berg and Elsenaar experiment on infinite swept wing [6] (Fig. 5).

Figure 6 demonstrates the application of presented here approaches for calculation the two-phase flows with phase separation boundary (liquid-gas). In this case laminar liquid film covered the streamlined surface and spread under influence of shear stresses, which are generated in turbulent boundary layer of gas over the liquid film. The phase separation boundary is considered as wavy and moveable. According to this the model of turbulent viscosity has been modify on case of moveable rough surface influence. The height of liquid h_L and velocity of motion of phase separation boundary U_{L0} are calculated by the following equiation

$$h_L = \sqrt{\frac{2Q_L\nu_L}{\tau_w}};$$

$$U_{L0} = \frac{\tau_w h_L}{\mu_L},$$

where $Q_L = \varrho_L h_L u_{Lav}$; $\mu = \nu\varrho$; $u_{Lav} = U_{L0}/2$ - average velocity across the liquid film; index "L" means liquid phase of flow. The results of liquid height prediction for described above flows with different values of Reynolds number of film are shown on Fig. 6, Fig.7 where continuous line – predictions by using integral method [7], dashed lines – predictions by using numerical method [8] circles – experimental data of S.V. Ryshkov, V.V. Yershov, V.N. Miroshnichenko [9] (on Fig. 6) and O.A. Povarov, G.A. Phillipov, E.A. Vasylchenko [10] (on Fig. 7). Figure 8 reflects the comparison between numerical predictions of near-wall jets velocity distributions and experimental data of Kacker and Whitelaw [15].

The results presented here and the matherials given by the authors allow to come to a conclusion that the use of the developed approaches to the modeling of turbulent exchange coefficients while elaboration of numerical methods ensures the high reliability of flow development and separation process forecast.

REFERENCES

1. Millionschikov, M.D.; Subbota, V.I. and others, "Hydraulics drag and velocity fields in pipes with artifical roughness of walls", *in* "Nuclear energy", Vol. *34*, 4, 1973, (in Russian).
2. Galin, N.M.; Kirillov, P.L., "Heat–mass exchange (in nuclear energy production)", Moscow, "Energoizdat", 1987, (in Russian).
3. Pasconov, V.M., Polezhaev, V.I., Chudov, L.I., "Numerical modeling of heat- and mass transfer processes", Moscow, "Nauka", 1984, (in Russian).
4. "Computation of turbulent boundary layer", *in* AFOSR - IFR -Stanford Conference, *Vol. 1*, Ed. Kline, S.J., Morcovin, M.V., Sovran, G., Cockrell, D.J., 1968; *Vol. 2*, Ed. Coles, D.E., Hirst, E.A., 1969.
5. Cebeci, T., Chang, K.C., "Calculation of incompressible rough-wall boundary layer flows", J. AIAA, *16*, 730, 1978.
6. Van den Berg, B., "The turbulence modeling and discussion of results of the experimental researches in three-dimensional boundary layers", *in book* "Three-dimensional turbulent boundary layers", Moscow, "Mir", 1985.
7. Movchan, V.T., Kozlova, T.V., Shkvar, E.A., "The integral method for predictions of two-phase turbulent boundary layer with phase separation", State Scientific-Engineering Library of Ukraine, N 2417-Yk95 from 21.11.95., 1995, (in Russian).
8. Ageyev, S.E., Movchan, V.T., Mkhitaryan, A.M., Shkvar, E.A., "Modeling of two-phase flows with phase separation boundary", J. of Applic. Mechanics and Tec. Physics, Novosibirsk, "Nauka", *6*, 1990, (in Russian).
9. Ryshkov, S.V., Yershov, V.V., Miroshnichenko, V.N., "About liquid flow properties on short horisontal plate, which streamlined by gas flow", J. "Teploenergetika", Works of Nikolaev Ship-Build. Inst., *33*, 1970, (in Russian).
10. Povarov, O.A., Phillipov, G.A., Vasylchenko, E.A.,"Experimental investigation of wavy modes of liquid films flow under influence co-directed gas flow", J. "Teploenergetika", *4*, 1978 (in Russian).
11. Fedyaevsky K.K., Gynevsky A.S., Kolesnikov A.V., "Prediction of inviscid turbulent boundary layer", Leningrad, "Sydostroenie", 1973 (in Russian).
12. Sivykh, G.F., "Turbulent viscosity for inviscid boundary layer prediction over rough surface", J. of Applic. Mechanics and Techn. Physics, Novosibirsk, "Nauka", *2*, 1984, (in Russian).
13. Dvorak, F.A., "Prediction of turbulent boundary layer on rough surface with presence of pressure gradient", J. "Rockets Technics and Cosmonautics", *7*, 9, 1969, (in Russian).
14. Movchan, V.T., "Approximate-analytical turbulent boundary layer research", J. "Applic. Mechanics and Techn. Physics", Novosibirsk, *3*, 1982, (in Russian).
15. Kacker, S.C., Whitelaw, J.H., "Some properties of two-dimensional, turbulent wall jet in a moving stream", ASME New-York, 1-5, December, 1968.

ILLUSTRATIONS

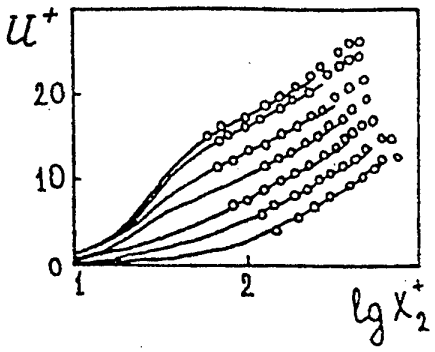


Fig. 1 Comparison of approximate-analytical prediction (line) of velocity profile on rough surface (line) and experimental data of M.D.Millionschikov [1] for pipes with different technical roughness (circles).

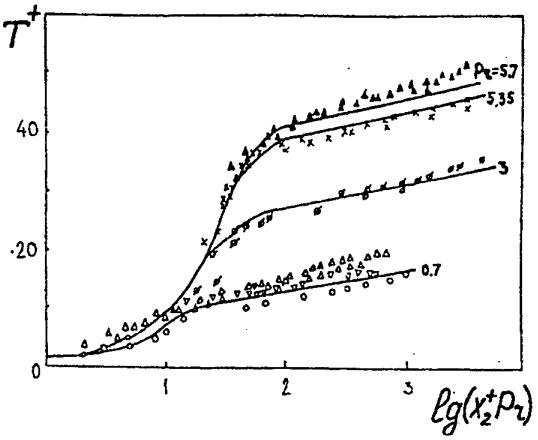


Fig. 2. Comparison of temperature distributions (line) and experimental data of N.M. Galin and P.L. Kirillov [2] for boundary layers on smooth surface with different values of Prandtl number (circles).

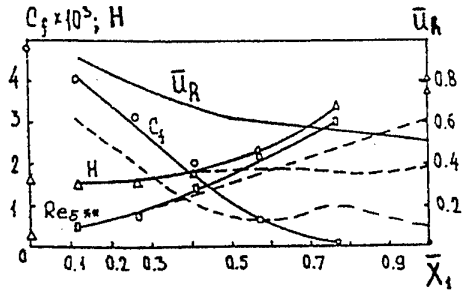


Fig. 3. Comparison of computation (continuous line) and Moses' experimental data (id. 3800) [4] (circles), where $C_f = 2\tau_w/(\varrho U_h^2)$ – skin friction coefficient; $H = \delta^*/\delta^{**}$ – shape factor; δ^*, δ^{**} – displacement and momentum-deflect thicknesses respectively; Re^{**} – momentum-deflect thickness Reynolds number; $\bar{u}_h = U_h/u_\infty$ -nondimensional velocity. Dash line – predictions of K.K. Fedyaevsky, A.S. Gynevsky, A.V. Kolesnikov [11].

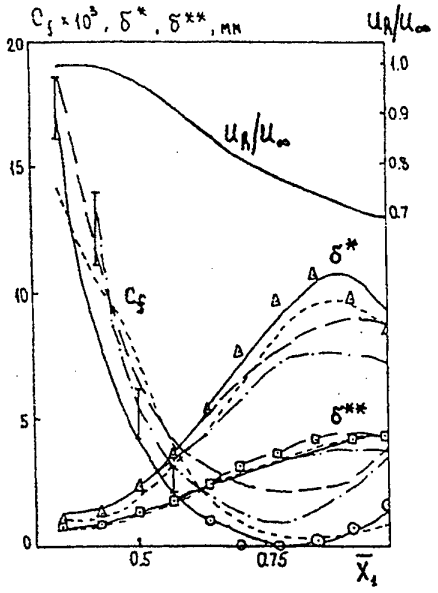


Fig. 4. Comparison of computation (continuous line) and Scottorn - Power' experimental data on two-dimensional boundary layer with rough surface [5] (⊙, □, Δ). Nomenclature is the same as in Fig. 3., except dash lines – predictions of different researches: – · – T. Cebeci, K.C. Chang [5]; – – G.F. Sivykh [12]; – – – F.A. Dvorak [13].

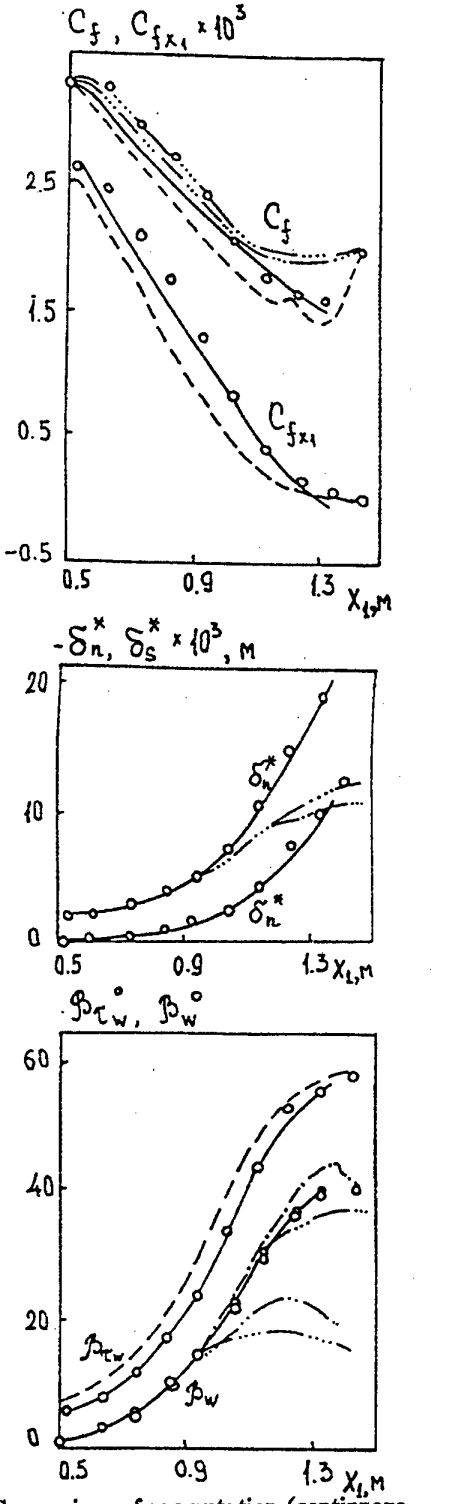


Fig. 5. Comparison of computation (continuous line) and B. van den Berg experimental data on infinite swept wing (35 °) [6] (circles), where $C_f = 2\tau_{w\Sigma}/(\varrho U_h^2)$ – total skin friction coefficient; $C_{fx_1} = 2\tau_{w_1}/(\varrho U_h^2)$ – skin friction coefficient projection on x_1 axis, which normal to the leading edge; δ_s^*, δ_n^* –displacement thickness in main and secondary flows directions respectively. β_w – surface cross-flow angle; β_{τ_w} – wall shear-stress angle. Dash lines – predictions of different authors: – – – Redven and Lekydis; – · – , – · · – Custey; – · · · – Swafford and Yitfild; – · · · · – T. Cebeci.

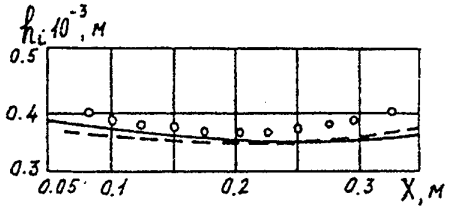


Fig. 6. Comparison of liquid film thickness h_L computation (lines) and S.V. Ryshkov, V.V. Yershov, V.N. Miroshnichenko experimental data [9] (circles), where $Re_L = 198$, Re_L – Reynolds number of liquid film ; $u_{hG} = 20$ m/s , u_{hG} – velocity of gas flow; dash line – numerical method of calculations [8]; continuous line – integral method of predictions [7].

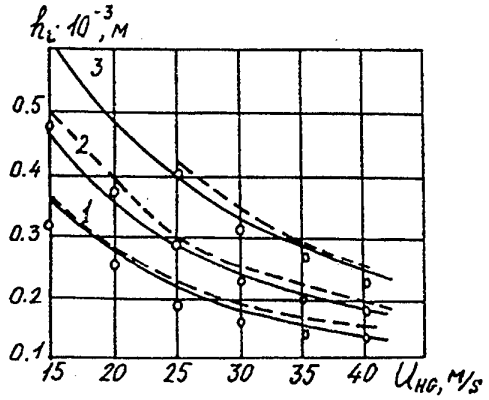


Fig. 7. Comparison of liquid film thickness h_L computation (lines) and O.A., Povarov, G.A., Phillipov, E.A., Vasylchenko experimental data [10] (circles), where: 1 – $Re_L = 100$; 2 – $Re_L = 200$; 3 – $Re_L = 400$; dash line – numerical method of calculations [8]; continuous line – integral method of predictions [7].

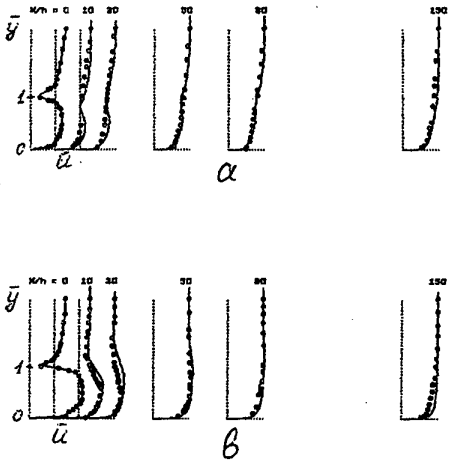


Fig. 8. Comparison of predicted velocity distribution $u = u(x, y)$ (lines) with S.C., Kacker and J.H., Whitelaw [15] experimental data (circles): a – $U_k/U_{Cav} = 0.75$; b – $U_k/U_{Cav} = 1.33$.

DIRECT NUMERICAL SIMULATION OF TRANSITIONAL NEAR-WALL FLOW

V.S. Chelyshkov†, V.T. Grinchenko†, and C. Liu‡

†Institute of Hydromechanics, NAS of Ukraine,
8/4, Zhelyabov st., Kiev, 252057, Ukraine

‡Louisiana Tech University,
Ruston, LA 71272-0001, USA

Abstract

Local approach that can be applied for investigation of near-wall flows, jets, and wakes is discussed. The approach is developed on the basis of examining the flow near a flat plate. Coupled equations, which describe both slow and fast changing of flow in longitudinal coordinate, are utilized. Possible ways of excitation of slow disturbances are studied. Direct numerical simulation (DNS) of near-wall flow is carried out. Phase speeds of propagation of 2D-disturbances are calculated.

1. Introduction

There is a wide class of laminar flows that can be described with Prandtl equations [16]. These flows are boundary layers near bodies with small curvature of surface, non-gradient boundary layers, jets, and wakes. Instability of such flows leads to transitional and turbulent phenomena that have farely simple quasi-regular space structure. Transitional flows usually have coherent structure, and turbulent flows often can have quasi-homogeneous structure (see, for instance, [1, 10]). Quasi-regular flows develop in space and time in such a way that the scale of a typical longitudinal flow structure is significantly smaller then the scale of flow. It is the the reason for adoption of the *local approach* for investigation of non-linear transitional and fully developed turbulent flows of this type.

A number of laminar flows is described with this approach on the basis of investigations of Prandtl problems [16], and the linear theory of hydrodynamic stability for quasi-parallel flows is also founded on *the principle of locality.* This principle can be described in the following way.

Let X_0 be the non-dimensional longitudinal coordinate, counted from some point of a body, and Re be the local Reynolds number, i.e. Reynolds number defined on the basis of the distance from the point of a body to any other point in longitudinal direction. Then the local in X_0 particular solution, which has been obtained in the vicinity of $X_0 = 1$ when $\mathrm{Re} = \mathrm{Re}_1$, can be continued in coordinate X_0 by way of recalculation of the solution when $X_0 = 1$ and $\mathrm{Re} = \mathrm{Re}_2$, where Re_2 corresponds to the choice of another distance.

The validity of the approach is based on continued dependence of a solution on both longitudinal coordinate and local Reynolds number. The peculiarity of the principle is the absence of inflow boundary conditions for laminar problems and both inflow and outflow boundary conditions for the linear theory of hydrodymamic stability. So, the solutions of, respectively, Prandtl problems and the linear problems for disturbed Navier-Stokes equations are *the particular solutions* of differential equations in partial derivatives.

Paper presented at an AGARD FDP Workshop on "High Speed Body Motion in Water", held in Kiev, Ukraine, 1-3 September 1997, and published in R-827.

For investigation of a number of laminar self-similar flows, this principle usually was utilized in an implicit way [16]. In an explicit way, it was applied for examining of coaxial laminar flow over a semi-infinite cylinder in [2]. For investigation of transitional and turbulent quasi-regular flows, the approach leads to the necessity to choose both the model of flow and the mathematical form of the solution that corresponds to the real physical phenomenon.

Various models are suggested for simulation of near-wall flows now. We reffer here to the paper [9], where analysis of existing approaches has been done up to 1994. A new methodology is developed in [12, 13] to provide a successful numerical simulation for the whole process of flow transition in 3D boundary layers. This methodolgy is based on the full Navier-Stokes equations that are solved in the domain with big longitudinal scale. The model boundary conditions are stated at the inflow boundary, and buffer zone is added in outflow domain. A new model also was announced in [4] and described in [8], where transitional flow near a flat plate was examined. This Model of interaction of Slow and Fast disturbances (SFM) is valid for incompressible and compressible 3D quasi-regular flows; it was obtained in a heuristic way, but there is also some regular way of the equation yielding. Here we briefly discuss the SFM and following [5] study in more details the choice of mathematical form of a particular solution.

¿From a practical point of view, 2D flows are not of particular interest, but the main difficulties of modelling are concentrated exactly in 2D problem because of the weak non-homogeneity of quasi-regular flows in longitudinal direction. So we examine here only 2D flow near a flat plate and describe some new numerical results concerning phase speeds of propagation of disturbaces.

2. The Way of Constructing the Model and the Choice of the Form of Solution

One can suppose that the *slow* and *fast* disturbances in longitudinal coordinate are possible in quasi-regular flows [4, 7, 8]. To describe possible process of excitation of disturbances, we consider here the 2D flow over a flat plate.

Let X_0, y, T and x, y, t be nondimensional coordinates and time. They are connected in the following way (see [8]):

$$X_0 = 1 + X, \quad X = \lambda x, \quad T = \lambda t, \quad \lambda = \kappa^2/\mathrm{Re}, \quad \kappa = 1.72078766,$$

where Reynolds number Re is chosen on the basis of the thickness of the boundary layer. We suppose that there is a characteristic size l_d of a typical flow structure, which can be measured with the boundary layer thickness, so we study the flow in the domain

$$\mathcal{D} = \{-l_d/2 \le x \le l_d/2, \quad 0 \le y < \infty\}.$$

Let u, v, p be the non-dimensional components of velocity vector and the pressure. We define the solution

$$\mathbf{F} = \{u, v, p\}(X_0, y, T)$$

of the problem under consideration in the following way

$$\mathbf{F} = \mathbf{F}^P + \mathbf{F}^S + \mathbf{F}^f, \tag{1}$$

where

$$\mathbf{F}^P = \{u^P, v^P, p^P\}(X_0, y), \quad \mathbf{F}^S = \{u^S, v^S, p^S\}(X_0, y, t), \quad \mathbf{F}^f = \{u^f, v^f/\lambda, p^f\}(x, y, t).$$

Here $\mathbf{F}^P, \mathbf{F}^S, \mathbf{F}^f$ are the components describing, respectively, the solution of Prandtl problem, slow, and fast disturbances.

We introduce the x-average in $\mathcal{D}$

$$\overline{\mathbf{G}} = \frac{1}{l_d} \int_{-l_d/2}^{l_d/2} \mathbf{G} dx$$

and suppose that

$$\overline{\mathbf{F}}^f = 0. \tag{2}$$

Fulfilment of the condition (2) puts the restriction on the longitudinal size of flow structure that can be investigated on the basis of SFM. Really, it follows from (1) and (2) that

$$\mathbf{F} = \overline{\mathbf{F}} + \mathbf{F}^f + O(l_d/\mathrm{Re}).$$

So, the value of $(l_d/\mathrm{Re})^2$ must be small.

This local approach leads to coupled equations that are the reduced Navier-Stokes equations [4, 7]. Slow component of flow is controlled by the disturbed Prandtl equations that have an additional term of "mass force". The term is the result of interaction of fast disturbances. Fast component of flow is described by disturbed Navier-Stokes equations that contain slow variables.

For the precise mathematical statement of the problem, the equations need to add the inflow boundary condition for both slow and fast components of flow and the outflow boundary conditions for fast component of flow. These boundary conditions are unknown "in the middle" of the flow, and the interval of changing of slow longitudinal variable is short due to restriction on longitudinal size of examining flow domain. So the model boundary conditions can introduce considerable error in a solution, and the way of obtaining of particular solutions seems to be more preferable.

The terms of the order of l_d/Re can be removed in the equations for fast disturbances, and we can suppose that this component of flow is periodic in x in the transitional area.

The choice of the form of the paticular solution for the slow component of the flow is more difficult. One can suppose that *two types of slow disturbances* are possible in quasi-regular flows [5], so that

$$\mathbf{F}^S = \mathbf{F}^U + \mathbf{F}^D,$$

$$\mathbf{F}^U = \{u^U, v^U, p^U\}(X_0, y, t), \quad \mathbf{F}^D = \{u^D, v^D, p^D\}(X_0, y, t).$$

The first type of slow disturbances, $\mathbf{F}^U$, is generated by non-stationary structures that change fast in longitudinal coordinate. Interaction of such structures excites slow disturbances that *do not decay* down the flow. So interaction of fast disturbances is the permanent source of the excitation of disturbances of quasi-parallel component of the flow.

The second type of slow disturbances, $\mathbf{F}^D$, is connected with peculiarities of the upstream near-wall flow. These disturbances *decay* in longitudinal coordinate [11]. They are

generated at the inflow part of the boundary of the investigated flow domain by stating of the suitable non-stationary boundary conditions. So the second type of slow disturbances is possible with and without the presence of fast disturbances.

Decaying in longitudinal coordinate slow disturbances can be of interest for investigation of "bypass" transition, when the level of free stream turbulence is high; we can ignore the influence of external forces when we examine natural transition and fully developed turbulent flow. If we ignore this influence, we need to answer the following questions. Can the second type of slow disturbances arise sponteneously? Can interaction of fast disturbances be the source of excitation of the second type of slow disturbances? These questions arise because of the indefinitness in the statement of inflow boundary conditions.

First, we suppose that fast disturbances are absent and study the process of self-excitation of slow disturbances.

We will use the principle of locality to explain that self-exciting slow disturbances are impossible in the flow near a flat plate, and corresponding non-linear problem has no non-zero particular solutions steady in time and local in longitudinal coordinate X_0.

Here is some qualitative reasonings that support this conclusion.

1. Both the Blasius solution of the Prandtl equations and particular solution of the examined problem for disturbances depend on Reynolds number *in an implicit way.* So it is sufficient to find both these solutions, when $X_0 = 1$. In accordance with the priciple of locality, the solution of both problems for other values of variable X_0 can be obtained in the way of recalculation of local Reynolds number. Consequently, if local particular non-infinitesimal solution of the Prandtl problem for disturbances exists in the vicinity of $X_0 = 1$, then the sum of this solution and the Blasius solution also is the solution of the Prandtl problem, and this new solution describes fluid flow in the domain which is far enough from the leading edge.

2. If the velocity profile is known at the inflow boundary, then the solution of the non-stationary Prandtl problem is unique [15].

3. Any upstream *slow* disturbances of the Blasius flow decay down the stream far from the place of appearance of the disturbances. This result has been obtained on the basis of investigation of the stationary linearized Prandtl problem for disturbances in [11], but one can suppose that it is valid also for non-infinitesimal disturbances and non-stationary upstream boundary conditions.

If we compare the second and the third statements, we will come to the conclusion that the longer the distance from the inflow boundary condition, the closer the solution of the Prandtl problem is to the Blasius solution. Now the first statement leads to the conclusion that non-zero local in coordinate X_0 steady in time particular solutions of investigating Prandtl problem for disturbances do not exist.

At the same time, an infinite number of modes of infinitesimal disturbances of self-similar solution of the Prandtl problem exist [11]. However, non-linear development in time of such slow self-exciting perturbances leads to the growth of disturbances and their destruction in restricted time interval. This result has been obtained on the basis of DNS of the problem.

The way of discretization in longitudinal direction is described as the following. First, we use the known forms of perturbances for trial function choice:

$$u^S = \sum_{j=0}^{N} U_j(\eta,t)X_0^{-\nu_j}, \quad v^S = \sum_{j=0}^{N} V_j(\eta,t)X_0^{-\nu_j-1/2}, \quad \eta = y/\sqrt{X_0}. \tag{3}$$

In (3) $\nu_0 = 0$; for $j > 0$ power indices ν_j are selected on the basis of exponential damping of vorticity far from the wall, so $\nu_1 = 1, \nu_2 = 1.887, \nu_3 = 2.867, \nu_4 = 3.8$, ... [11]. Then, we use functions $X^k, k = 0, 1$, ... as test functions, expanding the solution in Taylor series in the vicinity of $X_0 = 1$.

The way of discretization in the orthogonal to the wall direction is described in [7, 8].

Simulation was performed for a dynamic system that has 2×31 degrees of freedom (2 functions in longitudinal coordinate and $32 - 1$ functions in orthogonal to the wall coordinate). For integration in time of this system various schemes were applied: the Runge-Kutta method, a semi-imlicit method, and Gear's method. The result of simulation leads to the conclusion that the Cauchy problem has no restricted solution on infinite time interval.

So, both qualitative resonings and numerical simulation lead to the conclusion that we have to exclude the possibility of self-excitation of slow disturbances from physical phenomena accompanying the self-excitation of fast oscillations in the boundary layer.

Now we can also answer the second question. The phenomenon of excitation of slow decaying in longitudinal coordinate disturbances by fast disturbances is also impossible due to the spontaneous arising of such type of slow disturbances on the background of the initiated motion, their growth in time, and the destroying of the simulated flow in restricted time interval. This result was obtained also numerically in [7].

The simplest, but not the only way that leads to the filtration of the solution from $\mathbf{F}^D$ is the following. First, we can represent the solution of slow component of flow in the boundary layer coordinates

$$u^S = U^S(\eta, X_0, t), \quad v^S = V^S(\eta, X_0, t)/\sqrt{X_0}, \quad p^S = P^S(y,t).$$

Then we can drop the dependence of the solution on X_0 in this coordinate system. It seems reasonable to suppose that the slow component of flow is locally self-similar in a small interval of variation of X_0 [6]. This supposition slightly deforms the slow component of the flow but gives the possibility to exclude numerical self-excitation of $\mathbf{F}^D$.

Now we also can remove the terms of the order of l_d/Re in equations for slow disturbances, and the problem under consideration becomes homogeneous in the longitudinal coordinate.

3. Calculation of Phase Speeds, Local DNS, and Some Numerical Results

It is well known that typical structure of a quasi-regular flow propagates down the flow with some phase speed that can be measured experimentally and obtained on the basis of numerical simulation. A simple way of calculation of main phase speed was suggested in [14]. This method is connected with the use of non-inertial coordinate system and based

on calculatoin of phase speed from the condition of minimum of functional that is the scalar product of right-hand parts of the according dynamic system.

We apply the approach described in [14] in the formal way. We can do it, because after separation of X_0, the problem under consideration becomes homogeneous in longitudinal direction.

The Bubnov-Galerkin method was adopted for space discretization of the problem. Fourier series were utilized for discretization in longitudinal coordinate, and exponential polynomials $\mathcal{E}_{n,k}(y)$ [3] were used for discretization in the direction, orthogonal to the wall. Detailes of space and time discretization are described in [7, 8]. The use of moving coordinate system allows us to reduce oscillations in time of longitudinal harmonics and makes it easy to calculate phase speeds in every moment of time.

The value of $l_d = 2\pi/\alpha$ sets the width of examining flow domain. We obtain steady state flow regimes for α and Re that corresponds to transitional phenomenon.

Let $\mathcal{N}$ be the number of degrees of freedom of dynamic system, which is extracted from governing equations, c_0 – phase speed of initial disturbances, t_s – non-dimensional simulation time, c – phase speed of steady state regime of flow, and

$$\tau_w^P = \partial_y u^P, \quad \tau_w^S = \partial_y u^S, \quad \tau_w^f = \partial_y u^f,$$

$$\tau_w = \tau_w^P + \tau_w^S + \tau_w^f,$$

when $X_0 = 1$ and $y = 0$. The results of simulation are adduced in the Table 1 and in Figure 1.

Re	α	$\mathcal{N}$	c_0	t_s	c	τ_w^S
520	0.308	869	0.397	12000	0.58	0.096
550.2	0.308	1031	0.3949	9000	0.59	0.10

Table 1. Paramerers of simulation and characteristics of steady flow.

This result confirms the variant of simulation for $\mathcal{N} = 409$ that was obtained in [8]. The increase in $\mathcal{N}$ or Re leads to a decrease time t_s that is necessary for achieving a steady-state solution.

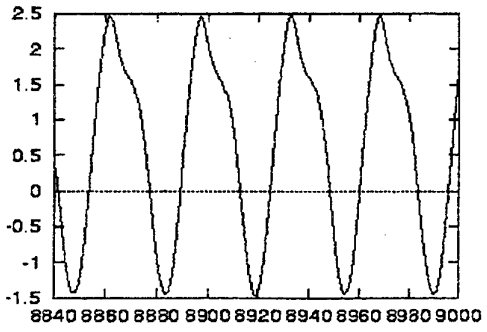


Fig. 1: The dependence τ_w on t for $\mathrm{Re} = 550.2, \alpha = 0.308$

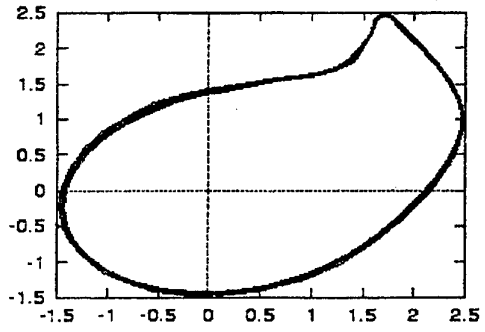


Fig. 2: Phase plot obtained by plotting $\tau_w(t)$ v.s. $\tau_w(t + \Delta t)$

It is of interest that non-linear interaction is strong: the temporal skin friction oscillates in such a way that τ_w changes between the values -1.35 and $+2.38$ in the point $X_0 = 1$ for $\mathrm{Re} = 520$ (see also Figure 1). So the 2D steady flow is an eddy flow. Mean skin friction is greater than in laminar flow, but the recycle zones settle down the surface of a plate, and full skin friction is negative about 1/3 of time in every place of the transitional area. The motion turns out to be close to perodic. The projection of the the attractor on two dimensions using delay coordinates is shown in the Figure 2. The plot is obtained for the second variant of simulation; $8600 \leq t \leq 9140$ and $\Delta t = 30$. The attractor is close to limit cycle; weak background is connected with quasi-periodic component of oscillations.

4. Conclusion

The SFM is valid for local analysis of near-wall flows. The nature of self-excited oscillations in quasi-regular flows leads to the statements of problems that have an indefiniteness in the inflow and outflow boundary conditions. The SFM may not need to use the model both inflow and outflow boundary conditions, but the approach under consideration requires a special choice of the form of solution. This choice is discussed in the present paper.

The SFM can be used for simulation of the development of qusi-regular flows in longitudinal direction. Indeed, big longitudinal scale can be devided onto the parts with suitable sizes, and these parts of flow can be connected by the known local inflow boundary conditions. For such statement of a problem, the choice of the form of the solution requires separate consideration. However, this way of spatial modeling puts the restriction on the length of the wave of disturbance.

Long time simulation is necessary for obtaining the steady-state regime of flow. This regime is found now only for transitional values of parameters. Our numerical experience leads to the conclusion that successful long time local DNS for big Reynolds numbers requires more degrees of freedom than we have used.

5. Acknowledgement

One of the authors (V.S.C.) expresses his gratitude to Prof. D. Knight for the help in international cooperation. The work was supported by an AFOSR grant.

References

[1] Cantwell, B. J. 1981. Organized motion in turbulent flows. *Ann. Rev. Fluid Mech.* 13: 457.

[2] Chelyshkov, V.S. 1986. Applying the method of small parameter for simulation of laminar boundary layer over a cylinder. *Zhurnal vychislitelnoi matematiki i matematicheskoi fiziki.* N 9: 1419. (in Russian)

[3] Chelyshkov, V.S. 1987. Sequences of orthogonal on semi-axis exponential polynomials. *Doklady AN UkSSR.* Ser. A, No 1: 14. (in Russian)

[4] Chelyshkov, V.S. 1994. The model of near-wall flow.*National Academy of Sciences of Ukraine, Institute of Hydromechanics, Annual report for 1993, Kiev*: 54.

[5] Chelyshkov, V.S. 1997. Excitation of slow disturbances in quasi-parallel flows.*National Academy of Sciences of Ukraine, Institute of Hydromechanics, Annual report for 1996, Kiev.*(to be published)

[6] Gertsenshtain, S.Ya, Shtemler, Yu.M. 1976. Disturbances of non-infinitesimal amplitude in the boundary layer. *Izvestia AN USSR, Mekhanika zhidkosti i gaza.* N 1: 150. (in Russian)

[7] Grinchenko, V.T. & Chelyshkov, V.S. 1993. Direct numerical simulation of boundary layer transition. *Near-Wall Turbulent Flows.*, R.M.C.So, C.G. Speziale and B.E.Launder (Editors), Elsevier Science Publishers B.V.: 889.

[8] Grinchenko, V.T. & Chelyshkov, V.S. 1995. Transition in the case of low free stream turbulence. *Progress and Chellenges in CFD Methods and Algorithms.* AGARD-CP-578: 26-1.

[9] Guo, Y.,‹Adams, N.A., Sandham, N.J., Kleiser, L. 1994. Numerical simulation of supersonic boundary layer transition. *Application of Direct and Large Eddy Simulation to Transition and Turbulence.* AGARD-CP-551: 13-1.

[10] Knapp, C.F. & Roach, P.J. 1968. A combined visual and hot-wire anemometer investigation of boundary layer transition. *AIAA J.* Vol. 6, N 1: 29.

[11] Libby, P. & Fox, H. 1963. Some perturbation solutions in boundary layer theory. Part 1. The momentum equation. *J.Fluid Mech.* Vol. 17, N 3: 433.

[12] Liu, C. & Liu, Z. 1995. Multigrid mapping and box relaxation for simulation of the whole process of flow transition in 3D boundary layers. *J. of Computational Physics.* Vol 119: 325.

[13] Liu, Z., Xiong, G. & Liu, C. 1996. Direct numerical simulation for the whole process of transition on 3-D airfoils.*AIAA paper* 96-2081.

[14] Nikitin, N.V. 1994. Spectral-finite-difference method of simulation of turbulent flows of incompressible fluid in tubes and channels. *Zhurnal vychislitelnoi matematiki i matematicheskoi fisiki.* Vol. 34, N 6: 909.

[15] Oleynik, O.A. 1968. Mathematical problems of the theory of the boundary layer. *Uspekhi matematicheskikh nauk.* Vol. 23, N 3 (141): 3. (in Russian)

[16] Schlichting, H. 1979. *Boundary Layer Theory.*, 7th ed., New-York: McGrow-Hill.

A NEW APPROACH TO THE STUDY OF ORGANISED VORTICAL MOTION AFFECTED BY BODY FORCES

Eugene I. Nikiforovich
Department of Thermal and Hydrodynamical Modeling
Institute of Hydromechanics , National Academy of Science
Ul. Zheliabova 8/4, 252057
UKRAINE, Kiev

SUMMARY

Investigations under centrifugal forces transitional boundary layers as well as the spatio-temporal properties of boundary layers vortical structures is one of the major research area of the Department of Thermal and Hydrodynamical Modeling of Hydromechanics Institute of Ukrainian National Academy of Sciences. It has been shown that in case of boundary layer flows under centrifugal forces the small parameter depending on the value of these forces can be introduces. Using methods of matching asymptotical expansions the scenarios of the boundary layers development (including transition processes from 2D to 3D) in terms of space scales of their vortical structures have been proposed. In particular, the knowledge about (i) formation mechanisms of 3D vortical structures in boundary layers; (ii) spatio-temporal properties of 2D and 3D vortical structures depending on basic flow parameters were obtained.

1. INTRODUCTION

The problem of understanding the origin of the transition from laminar to turbulent flow is the most important unsolved problem of fluid mechanics. Usually this transition occurs in shear flows (boundary layers). The widespread case of such flows is a flow over rigid surfaces (generally curved) and natural convection over heated or cooled surfaces. These two types of motion have essentially different nature - the first type deals with external forces; the second one is caused by internal forces of thermodynamical origin i.e. buoyancy forces. Despite the distinctions in the nature of the forces and body geometry the boundary layer development has a set of common specific features characterizing the transition to the fully developed turbulent flow. In particular, intrinsic features of such motions is the existence of (i) a domain of 2D boundary layer which can be described using Prandtl equation in Blasius form and (ii) Tollmien-Schlichting waves and streamwise vortices developing downstream (Ref 7,8,18,19). On the one hand, diversity of such flows can suppose an available single mechanism of this development and on the other hand shows that typical transition stages represent the intrinsic flow feature. So, from this viewpoint we can consider these characteristic stages of the laminar boundary layer development as a result of the transformation one motion kind into an other one (below the "transition" term will mean such a transformation in laminar boundary layers). Recent technological applications deal with the boundary layer control problems ,i.e. the regulation of heat/mass /momentum fluxes near the surface by changing space-time scale characteristics of fluid motion. Practically it implies the possibility to delay/prevent boundary layer separation or transition to turbulence, to reduce drag, to augment heat transfer etc.From the basic viewpoint the optimal solution of the problem should be based on the possibility to generate and maintain a necessary type and scale of fluid motion in a boundary layers for given purposes. In other words, it means the possibility to manipulate with the space-time scales in the mentioned above boundary layer domains using the basic flow parameters (meanflow velocity, fluid viscosity, geometry of body etc.).

Traditionally investigations of transitional boundary layers were carried out in the framework of the stability theory based on the study of the main flow disturbances assumed (or introduced) apriori; Tollmien-Schlichting waves and 3D streamwise vortices generation was considered as a result of meanflow instability .Although

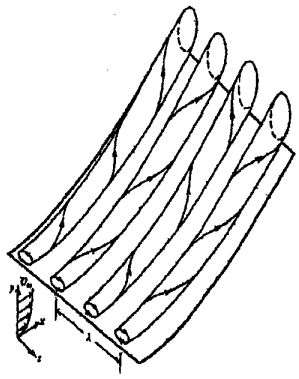


Figure1. Sketch of the Goertler vortices developing on a concave wall (from Swearingen&Blackwelder (1987))

this approach yielded a set of interesting and useful results (Ref 14,15,19,22), it

- does not define space scales of the boundary layer domains (downstream lengths) having different types of the vortex structure (kinds of disturbances – e.g. Tollmien-Schlichting waves, streamwise vortices);

Paper presented at an AGARD FDP Workshop on "High Speed Body Motion in Water", held in Kiev, Ukraine, 1-3 September 1997, and published in R-827.

- does not allow to formulate the transport laws using the basic flow parameters and therefore can not give an optimal method to manage transport processes near a surface;
- can not predict the transition location depending on the basic parameters and therefore does not permit to formulate an approach to the boundary layer control in terms of receptivity ideas.

Therefore the knowledge of mechanisms of the vortical structures formation in laminar boundary layers and their spatio-temporal properties is important both in basic and applied aspects, especially in relation to the idea of optimal boundary layer control. In this connection it is reasonable to study the spatio-temporal properties of boundary layers under centrifugal forces as a prototype problem due to the feasibility of direct applications, mathematical formulation, numerical simulation and available for comparison experimental data obtained in the frame of the traditional stability approach. Such work must bring an insight into the mechanisms of the flows developing in the general case under body forces.

2. GOERTLER PROBLEM

To explain details of the proposed approach let us consider the simplest (from the mathematical viewpoint) case of the boundary layer development under centrifugal forces in open flows - Goertler problem. Consider the flow of homogeneous viscous fluid with meanflow velocity U_0 over a concave surface with constant curvature radius R (Fig.1). Viscosity is supposed to be constant. Continuity and Navier-Stokes equations in a curvilinear coordinate system related to the plate have a form

$$\frac{R}{R-y}\frac{\partial U}{\partial x}+\frac{1}{R-y}\frac{\partial V}{\partial y}+\frac{\partial W}{\partial Z}=0, \quad (1)$$

$$\frac{\partial U}{\partial t}+\vec{U}gradU-\frac{UV}{R-y}=-\frac{R}{R-y}\frac{1}{\rho}\frac{\partial P}{\partial x}+$$

$$\nu\left[\Delta U-\frac{2R}{(R-y)^2}\frac{\partial V}{\partial x}-\frac{U}{(R-y)^2}\right] \quad (2)$$

$$\frac{\partial V}{\partial t}+\vec{U}gradV+\frac{U^2}{R-y}=-\frac{1}{\rho}\frac{\partial P}{\partial y}+$$

$$\nu\left[\Delta V-\frac{2R}{(R-y)^2}\frac{\partial U}{\partial x}-\frac{V}{(R-y)^2}\right], \quad (3) \text{ here}$$

$$\frac{\partial W}{\partial t}+\vec{U}gradW=-\frac{1}{\rho}\frac{\partial P}{\partial z}+\nu\Delta W, \quad (4)$$

$\vec{U}grad$, Δ - convective and Laplace's operators in curvilinear co-ordinate system. All quantities are introduced in a usual way. As usual, let's suppose that a characteristic space scale of the flow parameters variation normally to the surface is much less compare with R. That is we can neglect in the basic equations terms of order δ/R. So, the equation system (1)-(4) transform into

$$\frac{\partial U}{\partial x}+\frac{\partial V}{\partial y}+\frac{\partial W}{\partial Z}=0, \quad (5)$$

$$\frac{\partial U}{\partial t}+\vec{U}gradU=-\frac{1}{\rho}\frac{\partial P}{\partial x}+\nu\Delta U+F_{bx}, \quad (6)$$

$$\frac{\partial V}{\partial t}+\vec{U}gradV=-\frac{1}{\rho}\frac{\partial P}{\partial y}+\nu\Delta V+F_{by}, \quad (7)$$

$$\frac{\partial W}{\partial t}+\vec{U}gradW=-\frac{1}{\rho}\frac{\partial P}{\partial z}+\nu\Delta W+F_{bz}, \quad (8)$$ he

re $\vec{U}grad$, Δ - convective and Laplace's operators in cartesian coordinate system

.The body force $\vec{F}_b$ has a form

$$F_{bx}=\frac{UV}{R}-\nu\left[\frac{2}{R}\frac{\partial V}{\partial x}+\frac{U}{R^2}\right],$$

$$F_{by}=-\frac{U^2}{R}-\nu\left[\frac{2}{R}\frac{\partial U}{\partial x}+\frac{V}{R^2}\right], \quad (10)$$

$$F_{bz}=0$$

This transformation from geometrical viewpoint means the transformation of the curved surface into the flat plate. From mathematical point of view equations system (5)-(8) describe the flow over the flat plate with body forces **F** due to curvature. The availability of body forces essentially changes the boundary layer development compare to Blasius flow. Really, these forces are nonpotential and define the bulk source of vorticity. The intensity of this source explicitly depends on centrifugal forces value. So, there are two different types of vorticity in the considerable problem - bulk source due to centrifugal forces and constant one due to non slip conditions. The laws of their variability in streamwise direction are different. It is clear that the main role in the generation of vorticity in a boundary layer on the initial part of flowing plays the constant source due to viscosity. Their intensity decrease in streamwise direction and there exist the distance where intensities of constant and bulk vorticities become comparable. Just available scales depending on basic parameters define the main difference between boundary layers on flat and curve plates.
The main idea of the present approach consists in the following. The laminar-turbulent transition of the boundary layer over a curved surface is considered as a natural development of the flow under centrifugal forces, i.e. the flow with anisotropy of space scales and their essential dependence on streamwise distance. That is the boundary layer structure is formed under the forces changing along the x axis. So far as the downstream development of viscous and centrifugal forces is different (the first one been defined by the viscosity coefficient and velocity gradient, the second one been defined by the velocity field and curvature) there should be fields in the flow with one of the forces dominant and the fields where the flow structure results from the interaction of two comparable forces. Space

scales of these fields depending on the basic flow parameters are found from the asymptotic analysis of full Navier-Stokes equations.
Goertler problem is characterized only by one nondimensional parameter - Re_R- Reynolds number based on curvature radius which is supposed to be large (or $\varepsilon=Re_R^{-1}$ - small). Case of $\varepsilon=0$ corresponds to the flat plate. Mathematically transition from a curved surface ($\varepsilon \neq 0$) to the flat plate ($\varepsilon=0$) is not regular . Indeed this transition implies the degeneration of space scales of this problem - curvature radius R or viscous length ν/U_0, here ν is the kinematic viscosity and U_0 is a free-stream velocity. And as usual in physical problems the space scale degeneration results in the singular degeneration of the solution. That is, generally speaking, the Blasius solution (or Falkner-Skan in general case) for the flat plate is not valid for the curved surface. From this point of view it is natural to use the stability approach for a flat plate, but that is not evident ,that this approach can be applied in the curved surface case. Therefore modern methods of asymptotic expansions of Navier-Stokes equations can be used for the Goertler problem with ε as a small parameter. Assuming the existence of space scales, which explicitly depends on small parameter, and some kind of expansions for unknown solution, one can get the equations systems for corresponding expansions of an unknown solution valid for certain flow domains. Physically these domains represent flow zones with essentially different dynamic structure and space characteristics. For more details see (Ref 4,21).

2.1. 2D Boundary -layer approximation in the Goertler problem

As mentioned above the limiting case of $\varepsilon=0$ corresponds to the flat plate boundary layer development which is described by Prandtl equations and has self-similar solutions. The influence of centrifugal forces may seem to be taken into account by introducing perturbations proportional to ε into solutions of the Prandtl equations. However the situation appears to be much more complicated. The only nontrivial expansion of Navier-Stokes equations solution in the Goertler problem has a form [Nikiforovich, 1996]]

$$U^*= U_0^*+ \varepsilon^{2/3} U_1^* + \dots$$
$$V^*= \varepsilon^{1/3} V_0^*+ \varepsilon V_1^* + \dots$$
$$p^*= \varepsilon^{2/3} p_0^*+ \varepsilon^{4/3} p_0^* + \dots$$

here nondimensional velocities U^* (streamwise) , V^* (normal) are based on free-stream velocity U_0 and pressure -on dynamical pressure $\rho_0 U_0^2$. The equation system for a 2D boundary layer at zero approximation in ε takes a form of

$$\frac{\partial U_0^*}{\partial x}+\frac{\partial V_0^*}{\partial y}=0,$$
$$U_0^*\frac{\partial U_0^*}{\partial x}+V_0^*\frac{\partial U_0^*}{\partial y}=\frac{\partial^2 U_0^*}{\partial y^2}, \quad (11)$$
$$U_0^*\frac{\partial V_0^*}{\partial x}+V_0^*\frac{\partial V_0^*}{\partial y}=-\frac{\partial p_0^*}{\partial y}+\frac{\partial^2 V_0^*}{\partial y^2}-U_0^{*2}.$$

Available centrifugal forces ($\varepsilon \neq 0$) yield the following space scales $L_x=\varepsilon^{1/3}R=RRe^{-1/3}$ in downstream and $L_y=\varepsilon^{2/3}R=RRe^{-2/3}$ in normal direction respectively. The equations system (11) and existence of space scales $\{L_x; L_y\}$ demonstrates the fundamental distinctions between flat and curved plates: solutions of Prandtl equations are known to be self-similar. It results from the only space scale equal to ν/U_0. For the considered problem the zero approximation for a velocity distribution is congruent to a self-similar solution for a flat plate, however the pressure distribution is not self-similar .This is the result of centrifugal forces (or bulk vorticity source due to the centrifugal forces) influence on a boundary layer structure. The physical meaning of this fact is evident - on initial part proportional to $L_x=R\,Re_R^{-1/3}$ the intensity of the source vorticity due to non-slip conditions (which represents the disturbance of mean flow) is much greater compared to that of the bulk vorticity source due to centrifugal forces. Besides, the self-similar solutions for the flat plate can be interpreted as a result of receptivity of the mean flow (it is not "mean flow" in stability theory!) to disturbances due to non-slip conditions. The first approximation of these expansions has a form of

$$\frac{\partial U_1^*}{\partial x}+\frac{\partial V_1^*}{\partial y}=0$$
$$\frac{\partial U_0^* U_1^*}{\partial x}+V_0^*\frac{\partial U_1^*}{\partial y}+V_1^*\frac{\partial U_0^*}{\partial y}=$$
$$\frac{\partial^2 U_1^*}{\partial y^2}-\frac{\partial p_0^*}{\partial x}+\frac{\partial^2 U_0^*}{\partial x^2}+U_0^* V_0^* \quad (12)$$
$$U_1^*\frac{\partial V_0^*}{\partial x}+U_0^*\frac{\partial V_1^*}{\partial y}+\frac{\partial V_0^* V_1^*}{\partial y}=$$
$$-\frac{\partial p_1^*}{\partial y}+\frac{\partial^2 V_1^*}{\partial y^2}-2U_0^* U_1^*+\frac{\partial^2 V_0^*}{\partial x^2}-\frac{\partial U_0^*}{\partial x}$$

and describes the nonlinear interaction between viscous and centrifugal forces, or in other words, the receptivity of the viscous boundary layer to the disturbances arising due to centrifugal forces. The proposed approach shows the sources of a possible irregularity of the boundary layer solution - one of them is the assumption about the flow two- dimensionality. Really, in the frame of the 2D the zero approximation for velocity distribution does not

depend on centrifugal forces i.e. flow perturbations due to centrifugal forces are small. It results in a natural assumption about invalidity (rather than instability) of the 2D solution for large $x \gg L_x$.

2.2. 3D equations of a boundary layer in the Goertler problem

Vorticity generation in a fluid body is a consequences of the potential energy transition into the kinetic one. This transition may acquire various forms of the vortical motion. But the most widespread one in boundary layers with centrifugal forces is the 3D motion organized as longitudinal vortices. Therefore it can be supposed that their space characteristics and an equation solution have to depend explicitly on a small parameter ε. Using the similar to p. 2.1. asymptotic expansions procedure one can get the following equation system for the 3D boundary layer at zero approximation (Ref 9)

$$\frac{\partial U_0^*}{\partial x}+\frac{\partial V_0^*}{\partial y}+\frac{\partial W_0^*}{\partial z}=0$$

$$U_0^*\frac{\partial U_0^*}{\partial x}+V_0^*\frac{\partial U_0^*}{\partial y}+W_0^*\frac{\partial U_0^*}{\partial z}=\frac{\partial^2 U_0^*}{\partial y^2}+$$

$$+\frac{\partial^2 U_0^*}{\partial z^2},$$

$$U_0^*\frac{\partial V_0^*}{\partial x}+V_0^*\frac{\partial V_0^*}{\partial y}+W_0^*\frac{\partial V_0^*}{\partial z}=-\frac{\partial p_0^*}{\partial y}+ \quad (13)$$

$$+\frac{\partial^2 V_0^*}{\partial y^2}+\frac{\partial^2 V_0^*}{\partial z^2}-U_0^{*2},$$

$$U_0^*\frac{\partial W_0^*}{\partial x}+V_0^*\frac{\partial W_0^*}{\partial y}+W_0^*\frac{\partial W_0^*}{\partial z}=-\frac{\partial p_0^*}{\partial z}$$

$$+\frac{\partial^2 W_0^*}{\partial y^2}+\frac{\partial^2 W_0^*}{\partial z^2},$$

and space scales in downstream, normal and spanwise directions take a form of $L_{3x}=RRe^{-1/3}$; $L_{3y}=L_{3z}=L_0=RRe^{-2/3}$ respectively.

So far as these scales appear due to centrifugal forces responsible for the bulk vorticity sources the obtained scales can be easily interpreted physically : L_{x0}, L_{y0} and L_{z0} represent characteristic space scales along the downstream, normal and spanwise axes of considered vortical structures. It means that here the vortical structure develops because of the nonlinear interaction between viscous and bulk vorticity sources and that it represents vortices elongated downstream. The ratio between their lateral and longitudinal scales have an order of $\varepsilon^{1/3}$. Estimation of corresponding velocities in a boundary layer gives $U_0^* \sim O(1)$, $V_0^* \sim W_0^* \sim \varepsilon^{1/3}$. Perturbations to the zero approximation in ε to the 3D solution can be shown to be of the order of $\varepsilon^{2/3}$ for velocities and of $\varepsilon^{4/3}$ for pressure.

It is necessary to mention principal distinctions between 2D and 3D boundary layers equations. First, in a 3D the zero approximation explicitly depends on ε what is opposite to the 2D case. And secondly - self-similar solutions of 2D boundary layers equation are valid for equation system (13). In other words, these self-similar solutions represent the asymptotic of 3D solutions for small x and the scale $L_{3x}=RRe^{-1/3}$ can be interpreted as a scale where the 3D effects (or the flow perturbations due to centrifugal forces) become comparable with the perturbations of mean flow due to viscosity (non-slip conditions) . In other words the distance X_c where 3D effects can be detected has a form $X_c=A\,L_{3x}=ARRe^{-1/3}$, here A is a constant which can be found from experiments. That value ,certainly, depends on the accuracy of measurement techniques and devices.. For example experiments of Bippes (Ref 21) give A~10-100. On the other hand, X_c value expressed in terms of the basic flow parameters may help to eliminate an arbitrary choice of a downstream location for initial conditions to analyze the stability of Goertler vortices. Thus the considered approach can:

1. explain the transitional processes in boundary layers from the viewpoint of validity of corresponding expansions;
2. join, explain and formalize the validity, stability and receptivity notions in the Goertler problem.

And finally, one of the most significant applied results is the possibility to describe spatio-temporal properties of 2D and 3D boundary layers over curved surfaces in terms of the basic parameters (free-stream velocity, viscosity and curvature).

3. Stability, receptivity and validity of boundary layers' equations. Scenarios of the boundary layers development.

To demonstrate the more general character of the proposed approach to the study of organized vortical motion affected by centrifugal forces let's consider their results in the frame of stability and receptivity theories. The main ideas of the stability theory application to the considered problem are presented in (Ref 19) and further considerations will be based on this article. As known, the main idea of the stability theory consists in the investigation of meanflow disturbances behavior in time or in space. Different types of equations for disturbances can be obtained depending on assumptions about mean flow structure. In any case the problem is reduced to eigenvalue problem with Goertler number

$$G=U_0\Theta/\nu(\Theta/R)^{1/2}, \quad (14)$$

as eigenvalue (Θ–momentum thickness). This problem is correct from the formal viewpoint and this approach yielded a set of useful results. But the transition from full Navier-Stoke equations into the eigenvalue problem consists a set of nonevident assumptions. The main of them is the introduction of Θ (or boundary layer thickness). This parameter could not be introduced in a formal rigorous way despite on it experimental evidence. In the frame of the proposed approach all space scales characterizing the variation of velocities in normal to the surface direction must be proportional to L_0. In particular

$\Theta=f(x)RRe_R^{-2/3}$ (15)

here f(x) - some function of order 1. With regard to (15) Goertler number has a form

$G=f^{3/2}(x)$, (16)

i.e. results of the stability theory have a local character (for fix. x) and don't depend on nonparallel effects. Moreover, it's clear that nonparallel effects are negligible in the stability theory if the meanflow is enough smooth in the streamwise direction. In the proposed approach namely these effects define the longitudinal vortices generation. Using the results of stability theory one can estimate the distance x_0 where longitudinal vortices appear. The linear stability theory give value G=0.6 for longitudinal vortices, i.e. $f(x_0)=(0.6)^{2/3}$. As it was shown above, in zero approximation the boundary layer development over flat and concave surfaces are similar and for rough x_0 estimation the next correlation for Θ can be made

$\Theta=0.664(\nu x/U_0)^{1/2}$. (17)

Taking into account (15) and (17) one can get

$x_0=1.2\ RRe_R^{-1/3}$. (18)

It is evident that (18) is lower estimation for x_0 distance. In other words in reality the longitudinal vortices can be generated on distance more than (18). And of course the correlation (18) is similar to those in p.2.1. The obtained results allow to interpret the stability theory results as follows: in the frame of the proposed approach it was shown that in general case the flows over concave surface are 3D and can be described by equations (13). The 2D Blasius solution is valid for these 3D equations (more exactly Blasius solution is an asymptotic for small x), i.e. assumptions of the stability theory mean that the solution can be presented in form

$\mathbf{U}=\mathbf{U}_{Bl}(\eta)+\varepsilon^{2/3}\mathbf{U}_{3D}(x,y,z)$, (19)

and set of equations for $\mathbf{U}_{3D}(x,y,z)$ will be similar to the stability theory equations at G=1. Than results of stability theory detecting the growing for large x solutions $\mathbf{U}_{3D}(x,y,z)$, define secular terms in expansions (19). The main distinction of the proposed approach from the stability theory is the rigorous definition of space scales, their dependence on basic parameters and clear physical meaning.

Vortex dynamics in transitional boundary layers over concave surfaces can be better understood if the space scales of the 3D vortical motion found from the present analysis are interpreted in terms of the well known stability approach.

To match these two approaches, obtained L_0 and X_c values can be considered in the frame of the Goertler stability diagram (Fig. 2) which allows to judge about the amplification rates of disturbances at growing Reynolds or Goertler numbers. The minimal scale of vortices for a wide range of nondimensional wave numbers is given in the diagram by the nondimensional wave parameter $\Lambda_0=U_0/\nu(\lambda_z^3/R)^{1/2}=30$ found both numerically (Florian, Saric, 1982), and experimentally (Yurchenko et al, 1985, Aihara, 1985), Fig. 3. Numerous results of other experimentalists cited by (Florian, Saric, 1982) display nondimensional scales of longitudinal vortices (of greater values) existing in boundary layers over concave walls

Since all the transverse space scales in this problem are to be proportional to L_0 value, it is evident that $\lambda_z=cL_0$,here c is constant. Substituting λ_z into Λ_0 ,one can find $c\sim 9$. Thus the minimal spanwise scale of longitudinal vortices in the Goertler problem is defined by the basic flow parameters as $\lambda_z=9RRe_R^{-2/3}$.

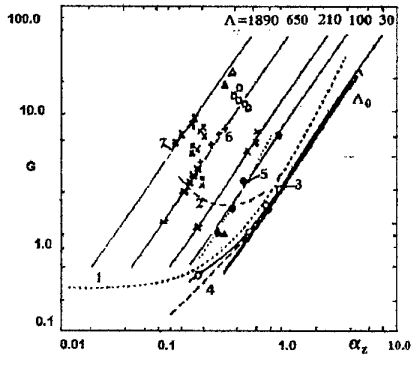


Fig.2. Goertler stability of streamwise vortices in boundary layers: 1, 2 - calculations by Florian & Saric (1982), curves of neutral stability and maximum growth rates respectively; 3 - experimental curves of neutral stability and maximum growth rates respectively by Yurchenko, 1985, 1986; 4 - experimental data for a neutral stability curve (rigid surface) obtained by Aihara (1985); 5 - vortices with maximum growth rates (experiment, Yurchenko, 1985; 6, 7 - experimental results by Blackwelder (1987), Bippes (1972), and Tani (1962) correspondingly.

The obtained results allow to explain the formal meaning of the receptivity concept and to describe possible scenarios of boundary layers development in space scales terms. Let's consider the interaction of the homogeneous meanflow $\mathbf{U}_0=\{1,0,0\}$ with different types of disturbances. It's evident that $\mathbf{U}_0$ is exact solution of full nonstationary zero approximation of ε is 2D and self-similar. So, theoretically the BL development over concave surfaces can be presented as follows: in case of $\varepsilon=0$ we have the flat plate and for this value of basic parameter the BL development is described by Blasius or Folkher-Skan 2D self-similar solutions. From the viewpoint of disturbances

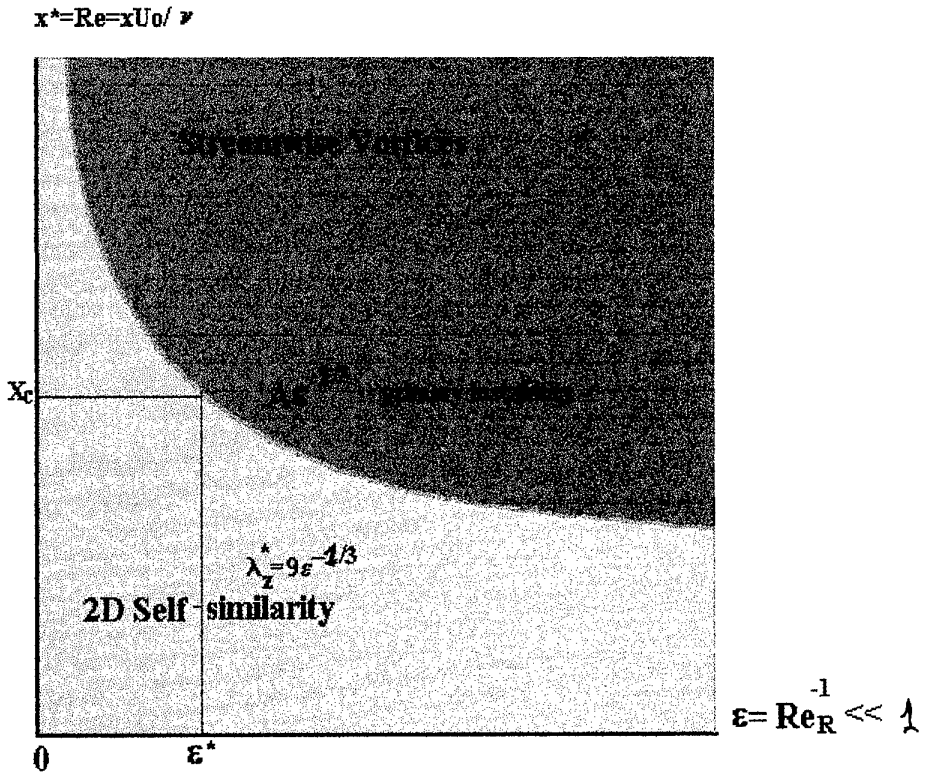


Fig.3 Validity Diagram. Theoretical Scenarios of Boundary Layers Development over Concave Surfaces.
Characteristic lines:
$x^*=\mathrm{Re}=A\mathrm{Re}_R^{2/3}=A\varepsilon^{-2/3}$ – transition point;
$\lambda^*_z=\lambda_z U_0/\nu = 9\,\mathrm{Re}_R^{1/3}=9\,\varepsilon^{-1/3}$ – minimal scale of vortices;

Navier-Stokes equations with corresponding initial and boundary conditions. Fig3 represents the physical interpretation of results obtained in the frame of the proposed approach. The vertical axis is the nondimensional distance from the leading edge of the concave surface based on viscous length; the horizontal axis corresponds to the value of basic parameter of the problem - $\varepsilon=\mathrm{Re}_R^{-1}$. From the physical viewpoint these axes reflect the values of disturbances due to viscous (vertical) and centrifugal (horizontal) forces.
Theoretically it was shown that the flow over concave surface primary has 3D character and the generating vortical structures are elongated in the downstream direction. The main reason of such streamwise vortices appearance is the availability of centrifugal forces. For small x (compare to L_x, not to viscous length) the flow in introducing into meanflow the flat plate represents the disturbance of meanflow due to non slip conditions. The result of these disturbances with meanflow is the Blasius flow. In other words Blasius flow describe the receptivity of the meanflow to disturbances generated by plate. The only one space scale exists in this problem - viscous scale=ν/U_0, connected with the type of disturbances. Namely this circumstance explains the existence of Re_c - critical Reynolds number characterizing the transition to turbulence in case of the flat plate and the existence of self similarity.
And now let's consider the Falkner-Skan flows, which are self similar too. The existence of the self similarity is connected with the special kind of flow far from plate $U\sim x^m$, which can be considered as special kind of disturbances of meanflow $\mathbf{U}_0$. From the physical point of

view there is two types of disturbances - non slip conditions and the special kind of meanflow disturbances. Therefore Falkner-Skan solution describes the nonlinear interactions between two types of disturbances and result in boundary layer with viscous scale ν/U_0.
Both Blasius and Falkner-Skan solutions are valid for large x (compare to viscous length) and describe the nonlinear interaction between meanflow and disturbances induced by nonslip conditions. From the theoretical viewpoint there isn't any reasons for invalidity of 2D self-similarity. The situation is essentially changed in the case of the finite value of ε. For each value ε one can estimate the space scale of quasi 2D BL and minimal scale of the generating 3D vortices. The upper curveline divides the plane onto two parts - the upper part corresponds to the domain of 3D streamwise vortices and the lower part - to quasi 2D BL with the self-similar solutions. The lower curveline defines the minimal scale of generating vortices for given value ε. Thus, this diagram describes the theoretical scenarios of BL development over concave and flat plate and 1) shows the singular degeneration of the problem at the degeneration of the space dimensionality (at $\varepsilon = 0$ we have 2D BL, at finite ε - 3D); 2) that the nature of streamwise vortices is connected with the nonlinear interaction between deterministic viscous and centrifugal disturbances (but not with the instability of meanflow). From this point of view the upper curveline describe the receptivity of viscous BL to "external" disturbances due to centrifugal forces.
It was the theoretical analysis of possible scenarios of BL development under centrifugal forces and this analysis explain some specific features mentioned above. Results of this analysis allow us to understand the physical nature of real flows over concave surfaces. Fig.4 represents the diagram describing the possible scenarios of real BL flows under centrifugal forces in terms of basic parameters. First of all let's consider the case of $\varepsilon=0$ - flat plate. The real flow is characterized by critical Reynolds numbers - $Re_{1,2}$ - nondimensional streamwise distance where the transition to turbulence occurs. This transition reflects the existence of random freestream disturbances and represents the result of nonlinear interaction between such random and deterministic disturbances due to nonslip conditions. In other words freestream disturbances define the quality of real meanflow and surface (from the viewpoint of their correspondence to theoretical initial and boundary conditions). It means that the stability theory describes the interaction between random and deterministic types of disturbances and this theory is natural for the flat plate. That why the stability theory defines well the value of critical Re_c. But the situation is getting quite different in the case of concave surface. As it was shown, streamwise vortices generation is connected with the nonlinear interaction between deterministic viscous and centrifugal disturbances. Therefore the streamwise vortices generation couldn't be described principally by the stability theory.
The real flow over concave surface can be presented as follows: for value $\varepsilon < \varepsilon_2$ the scenario of BL development is defined by interaction of random freestream and deterministic viscous disturbances and is similar to the scenario over the flat plate. Differences will appear in the domain $x^* > Re_1$. In this turbulent region the Goertler vortex structure will have to be appeared due to influence of curvature (this question requests the additional investigations). In the region $\varepsilon > \varepsilon_2$ we have "transition" from 2D self-similar flow into 3D streamwise vortices (like in the previous diagram). Here "transition" means that 3D effects become relatively large and could be detected experimentally. This transition (called the primary instability) is defined by nonlinear interaction of DETERMINISTIC disturbances, but is not the result of meanflow instability. The generating streamwise vortices represent the 3D MEANFLOW for this case. These vortices growth in streamwise direction and the intensity of their vorticity decrease. Finally the freestream disturbances become comparable with disturbances due to vortices. The nonlinear interaction between freestream, viscous and centrifugal disturbances physically defines the breakdown of streamwise vortices and the transition to turbulence. The dependence of points where the primary and secondary instabilities occur on the basic parameter has the same form with different constants A and B. But these constants have a quite different physical meaning - constant A separates the laminar BL regime onto 2D and 3D domains and actually is detected by the experimental investigations accuracy. Constant B has the same nature as critical Re_c for the flat plate and reflects the meanflow and surface quality.

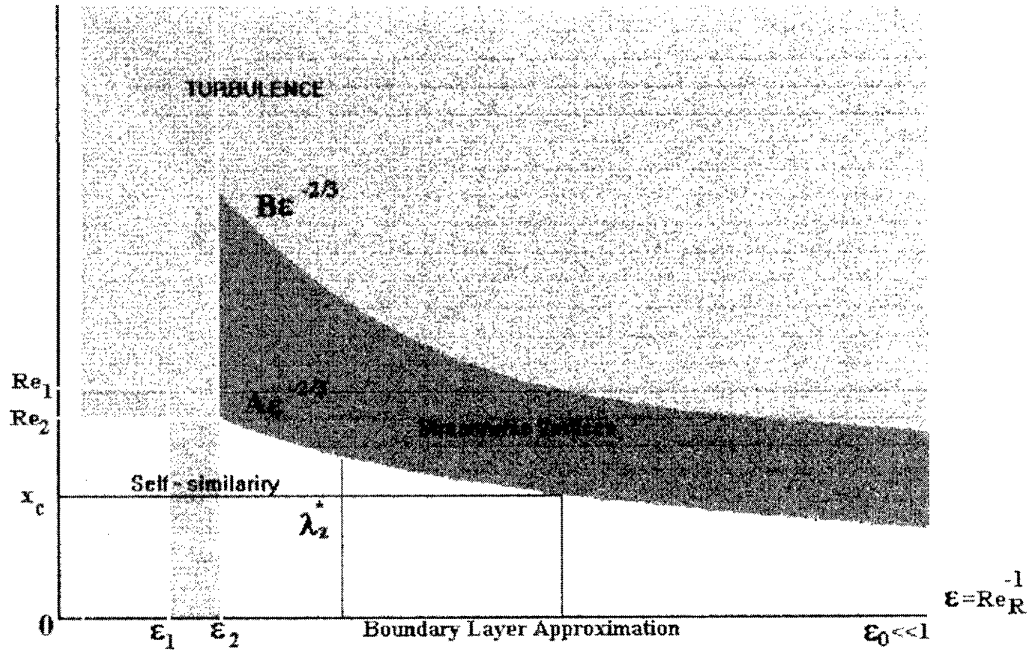


Fig .4 Validity, Stability and Receptivity Diagram
Characteristic lines:
$x^*=A\varepsilon^{-2/3}$ - primary instability; $x^*=B\varepsilon^{-2/3}$ - secondary instability;
$\lambda^*_z=\lambda_z U_0/\nu=9\,\varepsilon^{-1/3}$ - minimal scales of vortices.
$L_{2D}=A\varepsilon^{-2/3}$ - length of 2D BL, $L_{3D}=(B-A)\varepsilon^{-2/3}$ - length of 3D BL (Streamwise vortices),
$Re_{1,2}$ - critical Reynolds numbers for the flat plate, $\varepsilon_{1,2}=(A/Re_{1,2})^{1/2}$.
Boundary Layer Control: ⇔ – control of the bulk vorticity; ⇳ - control of the surface vorticity

This diagram allows to propose some ideas related to optimal BL control methods and shows the possible ways of such control using artificial disturbances. Indeed, the streamwise vortices generation and their minimal space scales are defined by the interaction of surface and bulk sources of vorticity. So, the idea of the optimal BL control consists in the opportunity to balance the viscous and centrifugal (surface and bulk) sources of vorticity. It means 1) the increasing of BL thickness or/and 2) applying of some bulk source of vorticity (from this point of view artificial vortex generators don't generate streamwise vortices by themselves - they make comparable the intensities of bulk and surface sources of vorticity). For each value of basic parameter ε and value of point Xc where it's necessary to generate streamwise vortices, one can show the possible and optimal ways to do this

4 CONCLUSIONS

- The asymptotic analysis of Navier-Stokes equations brought to a deeper insight into the laminar-turbulent transition mechanism and the vortical boundary layer structure developing under centrifugal forces. Longitudinal vortices, as an essential flow structural feature, were shown to originate from the interaction of two vorticity sources (due to viscous and centrifugal forces) when their intensities become comparable at a certain distance. Available centrifugal forces were proved to result in essentially 3D nature of boundary layers.
- streamwise vortices generation is not a result of instability of some unknown meanflow. This is result of nonlinear interaction between DETERMINISTIC viscous and centrifugal disturbances;
- "secondary instability" is really instability of streamwise vortices - result of nonlinear interaction between random freestream and deterministic viscous and centrifugal disturbances.
- Presented analysis allows naturally to join and mathematically explain such notions as validity, stability and receptivity and propose the optimal ways of BL control using basic parameters.

Besides, this approach gives a natural classification of disturbances:

1. Initial and Boundary Conditions; Body Forces - could be described rigorously by thermodynamic and Navier-Stokes equations;
2. Freestream disturbances (random) - reflect the meanflow and surface quality;
3. Artificial generators - vortex generators.

The presented analysis explains the physical mechanism of different types of motion (Blasius and Falkner-Skan flows, Tollmien-Schlicghting waves, longitudinal vortices,

turbulence) generation and existence in boundary layers with centrifugal forces as result of nonlinear interaction between disturbances due to viscosity / centrifugal forces and meanflow. The problem can be characterized by three internal space scales, characterizing the the nonlinear interactions of free, viscous and centrifugal disturbances.
The validity of the used approach follows from the comparison of the results presented in the frame of the Goertler stability diagram, the present approach having the advantage of a more general character. and possible applications dealt with the boundary layer control. It allows to understand the transition to turbulence as a continuous process with the vortex dynamics stipulated by domination or balance of available forces.

References

Conference Proccedings

1. Yurchenko, N.F., Babenko, V.V., Kozlov, L.F. (1985): The influence of generated vortex structures on boundary layer characteristics, Proceedings, 2nd IUTAM Symp. on Lam.-Turb. Transition, Novosibirsk, Russia, 1984, 367-371.
2. Nikiforovich,E.,(1993):Modelling of buoyancy and centrifugal effects on the development of the flow structure. Proceedings of the 8th Couette-Taylor Meeting at Nice,France,April 1993
3. Nikiforovich,E.,(1993):Barocline Mechanism of Vorticity Generation in a Boundary Layer, Proceedings of the of EUROMECH Colloquium 300 "Interaction between vorticity fields and boundaries" at Istanbul,Turkey,September 1993, 74.
4. Nikiforovich,E.,(1994):Boundary layer structure and efficiency of heat transfer,1994, Proceedings of the of EUROMECH-327 "Effects of organized vortex motion on heat and mass transfer" at Kiev,Ukraine, August 1994, 8.
5. Kottke, V. and Gschwind, P, 1994. Regular flow structures in channel with symmetric sinusoidal wavy walls, Proceedings of the EUROMECH Colloquium 327 "Effects of organized vortex motion on heat and mass transfer" at Kiev,Ukraine,
6. Nikiforovich,E.,(1994):Boundary layer structure and efficiency of heat transfer,1994, Proceedings of the of EUROMECH-327 "Effects of organized vortex motion on heat and mass transfer" at Kiev,Ukraine, August 1994, 8.
7. Kottke, V. and Gschwind, P, 1994. Regular flow structures in channel with symmetric sinusoidal wavy walls, Proceedings of the EUROMECH Colloquium 327 "Effects of organized vortex motion on heat and mass transfer" at Kiev,Ukraine,
8. Kottke, V. and Gschwind, P, 1995. Regular flow patterns in Symmetrical sinusoidal wavy channels., Proceedings of the 9-th International Couette-Taylor Workshop at Boulder,Colorado USA
9. Nikiforovich,E.,Rivir,R.,Yurchenko,N. (1995): Kinematic similarity of flows developing under body forces. Proceedings of the 9-th International Couette-Taylor Workshop at Boulder,Colorado USA, August 1995
10. Nikiforovich,E., (1996): Receptivity of 2D boundary layers effected by body forces. Proceedings of the EUROMECH Colloquim 353 "Dynamics of localized disturbances in engineering flows,Karlsruhe GERMANY, April 1996

Periodical Articles

11. Swearingen J.D., AND Blackwelder R.F., The growth and breakdown of streamwise vortices in the presence of a wall, J.Fluid Mech., vol. **182,**pp. 225-290,1987
12. Yurchenko, N.F., Babenko,V.V., Kozlov, L.F. (1986): Experimental study of stability of longitudinal vortical disturbances. Engn-Phys.J., 50, No.2, 201-206 (in Russian, abstract in English).
13. Florian, J.M, Saric, W.S. (1982): Stability of Goertler vortices in boundary layers. AIAA J, v.10, No. 3, p.316-324.
14. Corke,T.C. and Mangano,R.A. 1989. Resonant growth of three-dimensional modes in transitioning Blasius Boundary Layers. J.Fluid Mech., **209**,93
15. Bertolotti,F.P., Herbert,T.and Spalart,P.R. 1992. Linear and nonlinear stability of the Blasius Boundary Layers. J.Fluid Mech., **242**, 441
16. Nikiforovich,E., Yurchenko,N.,(1994): Longitudinal vortical flows - characteristics and analogies. Hydromechanics,No.68,Kiev, 52-67 (in Russian)
17. Saric,W.C., 1994.Low-speed Boundary Layers Transition experiments, In: Transition: Experiments, Theory&Computations, Oxford
18. Reshotko, E. 1994. Boundary Layer instability, transition, and control. AIAA Paper No. 94-0001
19. Saric,W.S. 1994.Gortler vortices. Ann. Rev. Fluid Mech., **26**, 379

Books

21. Fedorovsky,A.,Nikiforovich,E.,Pryhodko,N. (1988):Transport Processes in gas-liquid systems.Kiev.Naukova dumka.256 pp. (in Russian)

Reports

21. Bippes, H. 1978 Experimental study of the laminar-turbulent transition of a concave wall in a parallel flow. NASA TM. 75243.
22. Herbert, T. 1993. Parabolized stability equations. Progress in Transition Modelling, AGARD Report 793,March 1993

Experimental Studies on the Boundary Layer Development in Penguins: Mechanisms of Turbulence Control and their Applicability to Engineering

R. Bannasch
Technische Universität Berlin
FG Bionik & Evolutionstechnik
Ackerstrasse 71-76
D-13355 Berlin
Germany
E-mail: bannasch@fb10.tu-berlin.de

1. SUMMARY

Experimental studies conducted on live penguins as well as measurements with life-sized models of their trunk in a water tank revealed extremely low drag coefficients, although there was some evidence that transition from laminar to turbulent near-wall flow occurred in the most frontal part of their body. At a Reynolds number of $3 \cdot 10^6$ the drag coefficients were 20-35 % lower than those reported for the best turbulent technical bodies. Contrary to fish and dolphins, the penguin's trunk does not contribute to thrust production. Trunk oscillations during a wing beat cycle are moderate. Therefore, the spindle-like penguin trunk may well serve as live example for how energy may be saved by shape optimisation of stiff bodies. The trunk of these birds is relatively short and thick, thus offering a large volume with minimum drag.

Using the arithmetic means of data on body geometry from three medium sized penguin species, an axisymmetric body was constructed. By drag measurements in a water tank, this body of revolution was found to be an excellent low-drag laminar body (e.g. the lowest frontal drag coefficient was c_{wf} = 0,0156, measured at $Re_D = 2{,}331 \cdot 10^5$). When the transition from laminar to turbulent flow was triggered at at 5 % of the body length the surface drag coefficients remained even lower than those of a turbulent flat plate of equal length, and with increasing Reynolds numbers they declined at a higher rate.

Detailed studies on boundary layer development suggested that drag reduction resulted from the multiple curved (wave-like) outlines of the body. Due to alternating concave and convex parts, a stepwise pressure and velocity distribution was developed. Thereby, the thickness of as well as the boundary layer the turbulent velocity fluctuations within the boundary layer could be managed to keep the wall shear stress low. Hypothetically, by this mechanism, the vertical exchange of energy can be managed in a way that the boundary layer receives energy from the outer flow just sufficient to prevent flow separation.

Recently, some numerical approaches have proved the Evolution Strategy to be an appropriate method to achieve optimisation in a parallel way as used by nature. However, based on the calculation methods implemented as yet, multiple curvature effects did simply not occur even in these simulations. Nevertheless, since most of the higher evolved flying and swimming animals show wavy body contours, comparative studies on the curvature development with size progression seem to be promising. At least, a first comparison of three different sized penguin species suggests that there might be some distinct ("harmonic") solutions to that kind of shape adaptation.

However, viscous drag reduction becomes most efficient if shape optimisation can be combined with appropriate drag-reducing surfaces and/or other mechanisms of drag reduction. Using a novel method for flow visualisation with controlled dye ejection underneath of the plumage fundamental insights into the details of the boundary layer development in live penguins swimming at various flow conditions and into its interaction with the vortex system generated by the wings could be obtained. These visualisation experiments confirmed that, in fact, transition occurred in the most frontal part of the bird's body. In most cases, a quite regular pattern of transversal waves running over the compliant surface of the plumage (wave length 2 -3 cm) was observed. Corresponding to the wing circulation changing its direction during each stroke phase, the waves became more pronounced on the dorsal and ventral side during the up-stroke and down-stroke, respectively.

Apart from rather passive mechanisms (multiple curvature effects, compliance and microstructure of the plumage) possibly responsible for keeping boundary layer turbulence at a certain but overall low level, the structure of the near wall flow was managed also by a number of active mechanisms: Tiny adjustments of the body shape (changes in the position of the head, neck, feet and tail) and thereby of the pressure and velocity distribution had a remarkable influence on that flow pattern. Additionally, just after descending, some parts of the body may became covered by a thin film of air that reduces the wall shear stress locally to an absolute minimum. These areas corresponded well to those characterised by a low pressure gradient in the earlier model experiments. The most persistent air bubble was the one in the neck, which was subjected to unsteady oscillation. At this location a vortex seems to be formed which is assumed to underlie the same oscillation. This could be a possible explanation for the mechanism generating the running wave observed further downstream in the boundary layer.

Finally, an extraordinary measure to drastically reduce body drag temporarily could be a sudden ejection of large amounts of air by the bird. Boundary layer saturation with air bubbles could be observed when the animals try to achieve extreme acceleration e.g. during escape reactions or before jumping out of the water.

Paper presented at an AGARD FDP Workshop on "High Speed Body Motion in Water", held in Kiev, Ukraine, 1-3 September 1997, and published in R-827.

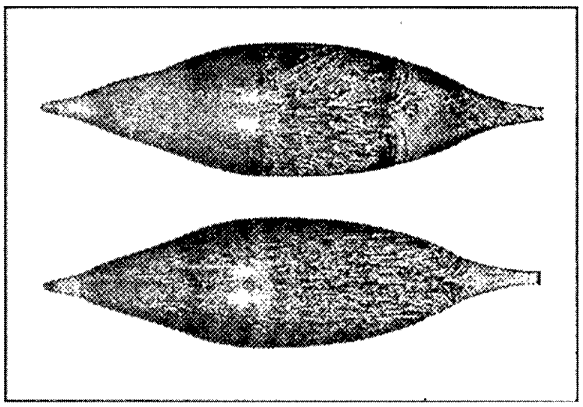


Fig. 7 Paint-flow visualisation without (above) and with turbulence generator (below).

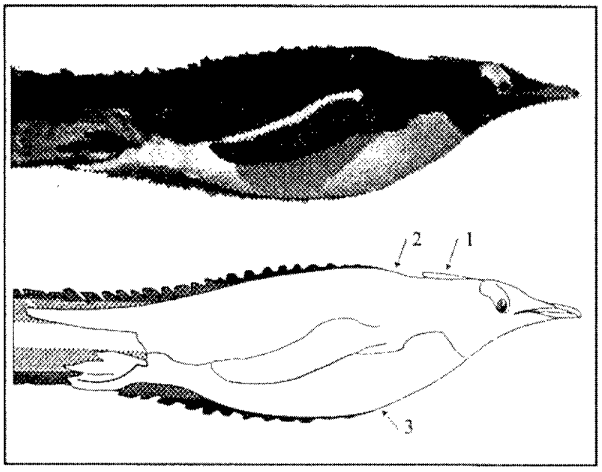


Fig. 10 Boundary layer visualisation in a live Gentoo penguin. Above: a single picture printed out from video records. Below: Scheme obtained from the entire sequence. 1 air bubble, 2 and 3 indicate the places of dye application. Note the quite regular pattern of the intermittent flow.

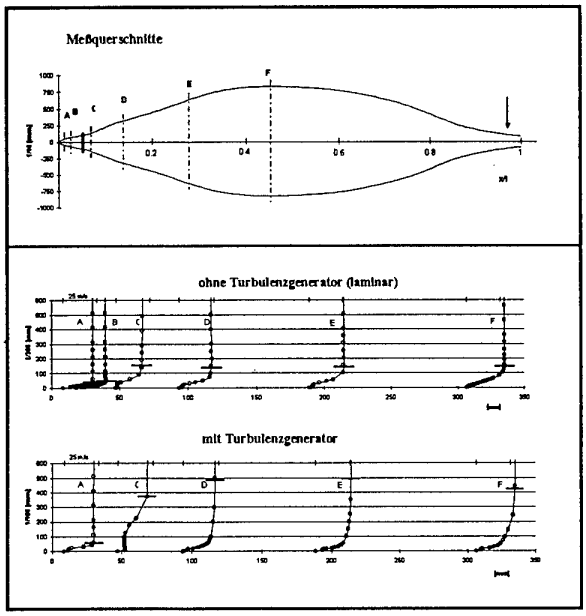


Fig. 8 Velocity profiles in the wavy frontal part of the body measured by hot-wire anemometry. The horizontal lines indicate the boundary layer thickness corresponding to 99% of the velocity of the outer flow.

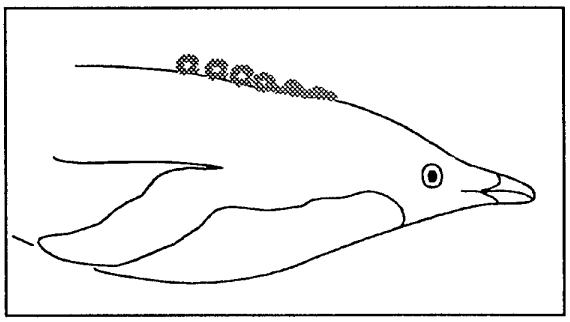


Fig. 11 Schematic graph of a rare high-speed video picture showing the development of ring structures in the boundary layer of an Adelie penguin.

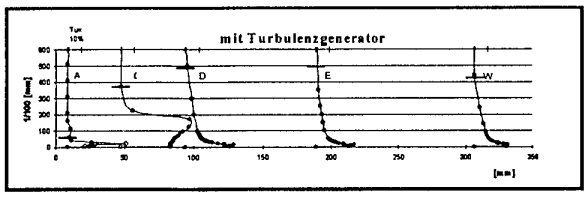


Fig. 9 Turbulence profiles at the same points

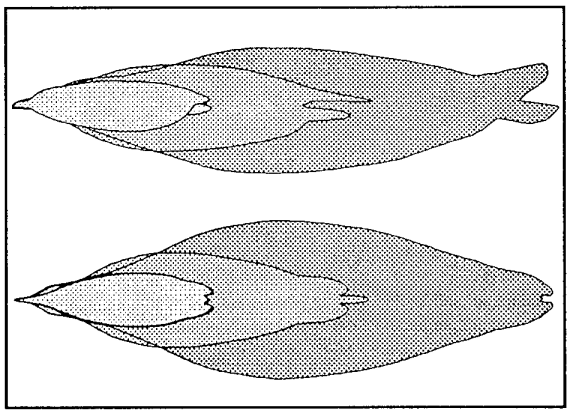


Fig. 11 Comparison of the body contours: Little, Gentoo and Emperor penguin.

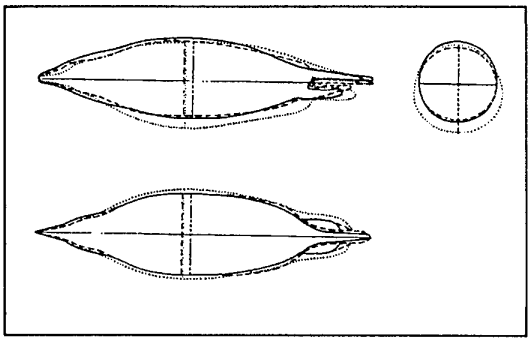


Fig. 1 Geometry of 3 casting penguin models: Adelie (solid line), Chinstrp (dashed line) and Gentoo penguin (dotted line)

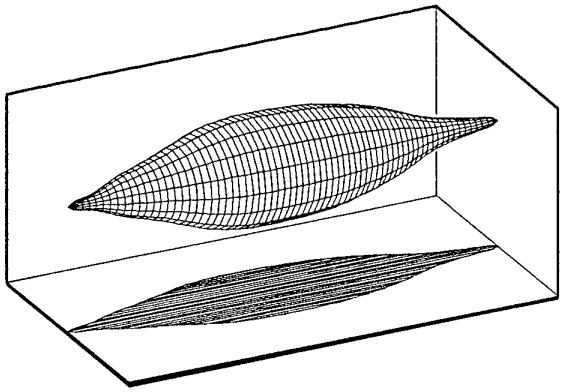


Fig. 2 Body of rotation derived from the penguin data

Table 1. Geometry of penguin bodies. A frontal area (m^2), d diameter of the frontal area (m), l body length (m), x_d abscissa of the maximum thickness (m), l/d length to thickness ratio, x_d/l maximum thickness position.

species	l/d	x_d/l	A	$d=\sqrt{(4A/\pi)}$
P. antarctica	4,54	0,44	0,01959	0,158
P. adeliae	4,35	0,47	0,02083	0,163
P. papua	4,00	0,44	0,02706	0,186
body of revolution	4,237	0,443	0,02147	0,165

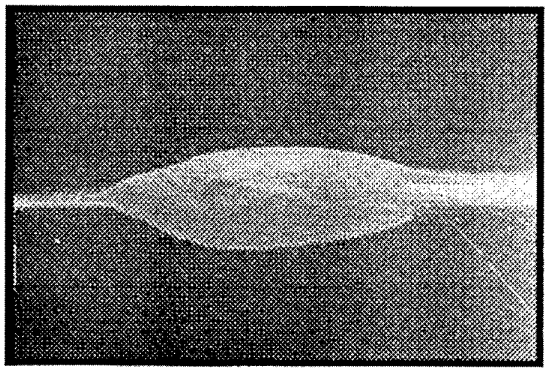


Fig. 3 Model of a Gentoo penguin in the smoke-wind tunnel (steam velocity 11 m/s)

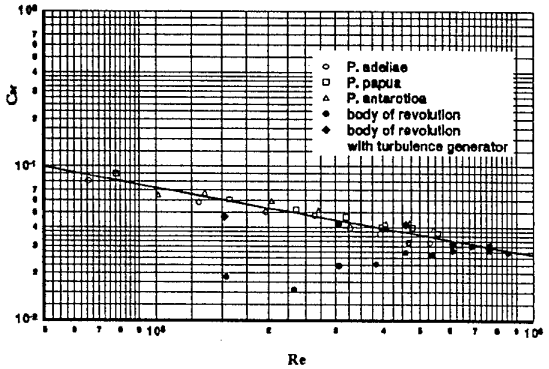


Fig. 4 Frontal drag coefficients plotted against Reynolds numbers. Not that in this graph Re was calculated by using the maximum diameter as reference length.

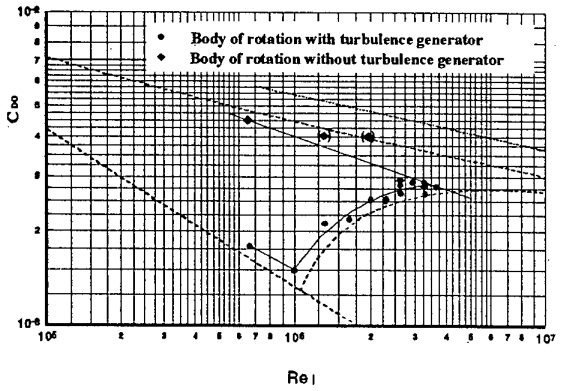


Fig. 5 *Surface drag coefficients of the body of rotation plotted against Reynolds numbers. Note that in this graph Re was calculated by using the body length as reference length. The bracket values contain drag increase due to undesirable Froude numbers and should be ignored. Dotted lines: laminar (below) and turbulent (above) flat plate. Dashed line on top: turbulent bodies with a length to thickness ratio of 4.2 (after Hoerner 1965).*

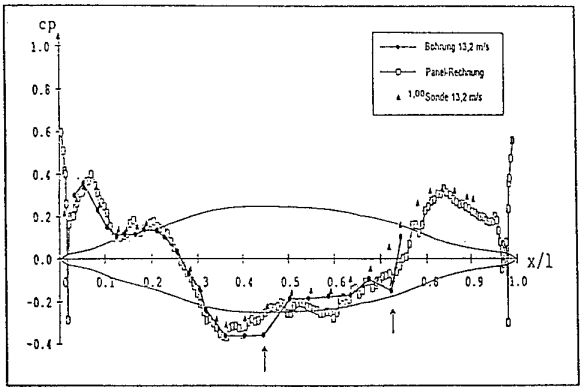


Fig. 6 Pressure distribution, experimental and numerical data.

COMPLIANT COATINGS FOR TRANSITIONAL BOUNDARY LAYER CONTROL

N. Yurchenko
Institute of Hydromechanics
National Academy of Sciences
8/4 Zheliabov St.
252056 Kiev
Ukraine

Summary

Visco-elastic properties of various materials and combinations of their layers were measured, results having been presented by stress-strain characteristics for samples defined by density, porosity, and layer thickness. To estimate the flow-surface interaction and to compare compliant coatings, they were characterized by non-dimensional parameters describing their inertial, visco-elastic, and damping properties.
Boundary-layer vortex dynamics was studied experimentally in a water channel over flat and concave, rigid and compliant surfaces at natural transition to turbulence and under the generation of longitudinal vortices. Compared to the rigid plate case, boundary layers over compliant surfaces were found to have a larger scale vortical structure. Besides, boundary layers over compliant surfaces demonstrated lower receptivity to external disturbances.

Introduction

Propulsion efficiency of moving bodies is known to depend significantly on their surface state. One of the possible surface arrangements which can result in decreased hydraulic losses, deals with the application of compliant coatings. The problem consists of two mutually connected parts: studies of visco-elastic properties of compliant materials and investigation of their interaction with the boundary layer flow.

In this connection, the present work is aimed, first, at mechanical measurements of practically available resin-like materials and, secondly, flow tests of such materials and their combinations.

Mechanical measurements

To define a set of parameters which are essential to characterize materials, they should be considered together with a set of basic flow parameters. Correlation of these two sets of parameters allows to describe the mechanical behavior of compliant materials with their

inertial properties: $M = \rho d / \rho_0 \delta_1$,

ρ, ρ_0 - densities of a compliant material and a flow fluid,
d - thickness of a compliant layer,
δ_1 - displacement thickness;

elastic properties: $C = \rho_0 U_\infty^2 / 2E$,

U_∞ - free-stream velocity,
E - elasticity modulus of a compliant material;

damping properties: $D = K / \sqrt{\langle (p')^2 \rangle} / 0.5 \rho_0 U_\infty^2$

p' - pressure fluctuations in a flow,
K - damping coefficient of a compliant material

Following this scheme, for the first characterization of potential compliant coatings, density values of homogeneous materials with different porosity were measured, the results having been presented in Table 1, Fig. 1.

Compliant coatings for the flow tests were fabricated in a form of one-layer materials of various thickness glued to the Plexiglas basement, as well as multi-layered constructions consisting of the layers of the same or different materials (Table 2). It should be mentioned that the glue layer itself represented a thin membrane. There was also reserved a possibility to heat some of the coatings. A more complicated construction of the compliant coating is proposed in the patent described in (Ref 1).

Elastic properties were measured according to the scheme of Fig. 2 which illustrates two possible cases of a loading state of tested coatings: with a thin rubber membrane glued (a) to the external surface and (b) between the layers of a compliant material.Fig. 3 shows a scheme for investigation of damping properties based on a principle of a falling steel ball and the measurement of its initial height and that of a first bounce. To some extent, it models a local affect of pressure fluctuations on the coating together with the generation of a corresponding frequency spectrum there. The damping coefficient was defined as $K = 1 - h_1/h_0$. This characteristics can be easily expressed in terms of widely used damping parameters, such as a loss angle, $\operatorname{tg} \varphi = E''/E'$, $E^* = E' + iE'' = \sigma/\varepsilon$, or a logarithmic decrement, $\delta = \ln (A_n/A_{n+1}) = \pi \operatorname{tg} \varphi$. Here the values of interest, stress and strain, represent correspondingly $\sigma = \bar{\sigma} \cos \varpi t$ and $\varepsilon = \bar{\varepsilon} \cos(\varpi t - \varphi)$, thus including into consideration the static loading case. Then the loss angle $\operatorname{tg} \varphi$ can be expressed through the damping coefficient K as follows

$$\operatorname{tg} \varphi = 1/\pi \ln (h_0/h_1) = - 1/\pi \ln (1-K).$$

Another method of dynamic measurements of soft materials is described in (Ref 2).

The results of present measurements for certain material samples and fabricated test plates (table 3) are given in a form of the damping coefficient K depending on the excitation energy $P = mg h_0$, where m is a mass of the falling ball (Fig. 4). Here dashed curves 1-7 correspond to homogeneous materials; 8 and 9 represent the results for two superimposed materials No. 4 and No. 5 without gluing them together with respective external layers, No. 4 or No. 5; solid lines correspond to the plates fabricated from the materials

Paper presented at an AGARD FDP Workshop on "High Speed Body Motion in Water", held in Kiev, Ukraine, 1-3 September 1997, and published in R-827.

indicated in brackets. It is seen that, varying a thickness of the layers, types of the materials, and their combinations in plate constructions, one can obtain a variety of damping characteristics of the coating for a given energy range. For instance, simple variation of a coating thickness (curves 5-7) results in different values and character of K(P), the minimum coating thickness of 3.5 mm (curve 5) having displayed the influence of a Plexiglas basement which properties are described with a curve 14. Heating of the compliant plate No. 7 (curve 11) increases the damping compared to the "cool" plate (curve 12). However the effect ("sign") of heating was found to depend on a type of the material.

Figs. 5, 6 show strongly nonlinear stress-strain characteristics of given materials. Therefore the elasticity modulus E can be estimated as a slope of only initial parts of presented stress-strain curves showing the possibility to obtain $E \approx 10^4 - 10^5$. The external rubber membrane appears to increase significantly the elasticity of a system (compare curves Pl. 1 and Pl. 2, Fig. 5); combinations of layers of the same material (Pl. 3, 4, 5) give a range of various E values. The same is also demonstrated in Fig. 6 for the test plates 7, 8, 9 (solid lines) fabricated from various combinations of the materials 1, 3, 5, 6 (dashed lines).

For the flow tests, the plates 7-11 were selected but the main part of experiments in a transitional boundary layer was carried out over the compliant coating No. 10 which represented a one-layer material No. 3 glued to the Plexiglas basement.

Boundary layer measurements

Flow measurements were carried out in an open water channel with free-stream turbulence level of about 0.05% that could be increased up to 10.0%; a test section sketch is given in Fig. 7 (a), the experimental facility and measurement technique having been described in detail in an earlier publication (Ref 3). The boundary layer was investigated on a bottom of the test section with transparent side walls. It provided a possibility to use flow visualization techniques to register a kinematic flow structure. Electrochemical tellurium method was used to get visualized patterns adequate to U(z) velocity distributions, the tellurium wire having been oriented along z axis. Applied pulses of voltage resulted in the ejection of colored lines of colloidal tellurium. Typical visualized time lines propagating downstream of the vortex generators are shown in Fig. 7 (b, c).
The test section bottom surface was either flat or contained a concave part with a curvature radius, R = 1, 4 or 12 m. In each case, a distance from the leading edge to the curved section was 50 cm and a maximum surface sag was 5 cm.

The laminar-turbulent transition was studied over rigid and compliant, flat and concave surfaces, that is taking into account the influence of available centrifugal forces and emphasizing the role of streamwise vortices in the flow. Properties, behavior and control of longitudinal vortices naturally developing during transition to turbulence and those induced with an array of vortex generators were the main purpose of these studies. The special interest to the longitudinal vortical structure is stipulated with the prevalance of this motion type in various flows (Ref 5) and the possibility to describe it in the rigorous mathematical formulation (Ref 6) that together with results of experiments brings to the understanding of basic mechanisms of vortex dynamics.

Vortex generators were mounted on the test surface [4]; the distance between adjacent vortex generators varied in the range of $\lambda_z = 0.4 - 3.2$ cm with 0.2 cm step having defined the scale of generated vortices.

Fig. 8 shows the time lines in xz plane across the boundary layers over flat rigid (left) and compliant (right) surfaces. Analogous flow conditions in both cases resulted in a strongly three-dimensional flow structure in a transitional boundary layer over the rigid plate, while all the processes were delayed and smoothed over a compliant plate (Ref 8). Experiments with the generation of regular vortices displayed a picture similar to that of the natural transition of Fig. 8: intensity and scale of generated vortices had to be greater than on a rigid surface to cause a noticeable response of the boundary layer over a compliant surface to external disturbances. To formalize the investigation of the boundary layer receptivity, it was carried out in terms of Goertler stability. It means that boundary layers over concave rigid and compliant surfaces were analyzed from the viewpoint of the flow ability to support longitudinal vortices of a given scale under given flow conditions. The results are presented in Fig. 9 in a form of neutral and most amplified disturbances. They show a good agreement with the numerically obtained data for the case of a rigid surface having been shifted to the left (larger scales) for the case of a compliant surface.

Conclusions

1. Measurements of compliant materials:
results for various practically available resin-type materials are presented in a form of density values, stress-strain and damping characteristics. They provide the data base for computational and further experimental work, as well as possibilities to estimate and obtain necessary parameters of the coatings for given conditions using multi-layered constructions.

2. Flow measurements:
compared to the rigid surface case, boundary layers over compliant surfaces display

- delayed development of the vortical structure during transition to turbulence,
- enlargement of the vortex space scales both at natural transition, and as a response to external disturbances,
- decreased amplitudes of three-dimensional disturbances.

References

1. Babenko, V.V., Yurchenko, N.F., Damping coatings for solid bodies, Patent (USSR), No. 802672, Bull. No.5, 1981.

2. Babenko, V.V., Kanarsky, M.V., Yurchenko, N.F., A method to determine dynamical visco-elastic characteristics, Patent USSR, No. 1183864, Bull. No.37, Oct.7, 1985.

3. Yurchenko, N.F., One experimental technique to study longitudinal vortices in a boundary layer, "Eng.-Physical J.", *41*, 6, 1981, pp 996-1002.

4. Yurchenko, N.F., Zygmantas, G.P., Generation of longitudinal vortices in boundary layers affected by body forces, "Eng.-Physical J.", *57*, 3, 1989, pp 392-398.

5. Nikiforovich, E.I., Yurchenko, N.F. Vortical flows - properties and analogues, "Hydromechanics", Kiev, Ukraine, *70*, pp 131-154.

6. Nikiforovich, E.I., Yurchenko, N.F. Boundary-layer flows with centrifugal forces. March 1997, "ERCOFTAC Bulletin", *32*, pp 61-65.

7. Babenko, V.V., Kozlov, L.F., Yurchenko, N.F., Development of 3D disturbances over compliant surfaces, in "Engineering Aero-Hydroelasticity", Internat.Conf., Prague, Czechoslovakia, 1989, pp 63-71.

Table 1

sample No.	1	2	3	4	5	6	7
pores/10 cm	17	24	23	25	19	16	3
ρ, kg/m3	42	120	133	173	250	272	1100

Fig. 1 Measurement of inertial properties; density ρ.

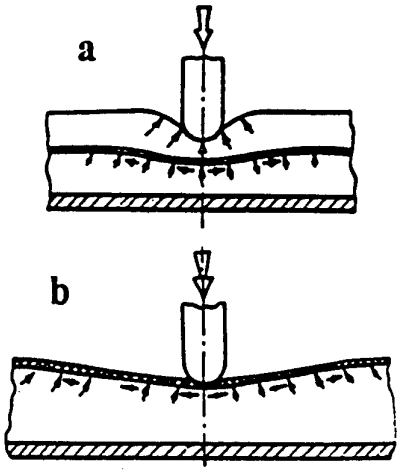


Fig. 2 Measurement of elastic properties under static loading; stress–strain characteristics, $\sigma(\varepsilon)$.

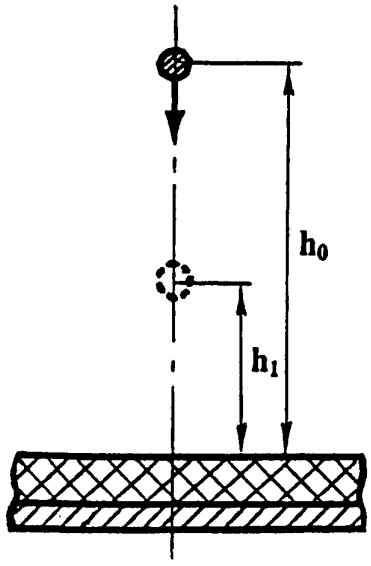


Fig. 3 Measurement of damping properties; damping coefficient depending on the excitation energy, $K(P)$ and loss angles tg φ.

Table 2 Construction of multi–layered compliant plates.

plate No.	1	2	3	4	5	6	7	8	9	10	11
layer types	10mm	10mm	3mm / 2mm	3mm / 6mm	6mm / 3mm	4 / 10mm / 2mm / 5	3 / 5	5 / 5	6 / 1 / 5	3	7 / 5

the same porous material, No. 1

CURVE NO.	SAMPLE TYPE	LOSS ANGLE
1	4	0.7
2	3	0.59
3	5_1*	0.46
4	5_2*	0.28
5	5_1	0.18
6	5_2	0.15
7	5_3	0.15
8	4 + 5_1	0.64
9	5_1 +4	0.47
10	Pl. 10 (3)	0.56
11	Pl.7 (7||5)^	0.51
12	Pl.7 (7||5)	0.44
13	Pl. 8 (5||5)	0.36

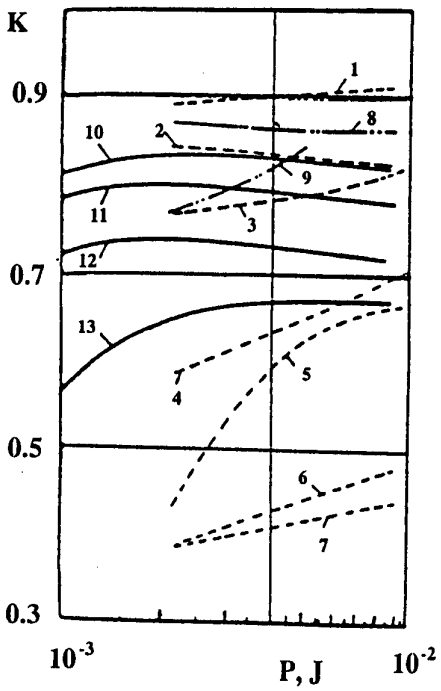


Fig. 4 Damping properties of materials (samples and test plates, thickness d):
Symbols: * – bigger pores, ^ – heating, || – membrane,
Subscripts: $1 - d = 3.5mm$, $2 - d = 7.0mm$, $3 - d = 10.5mm$.

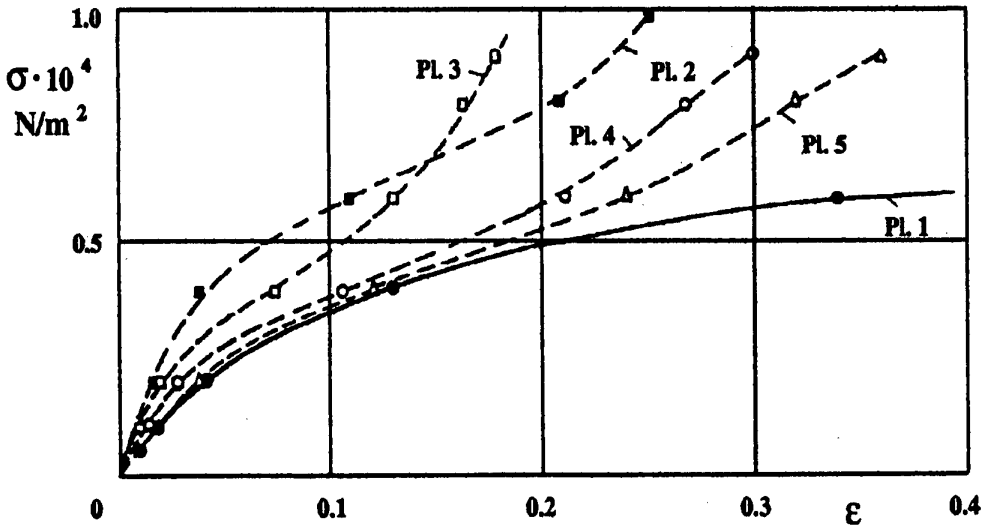


Fig. 5 Stress–strain characteristics of compliant plates fabricated from the porous material No. 1.

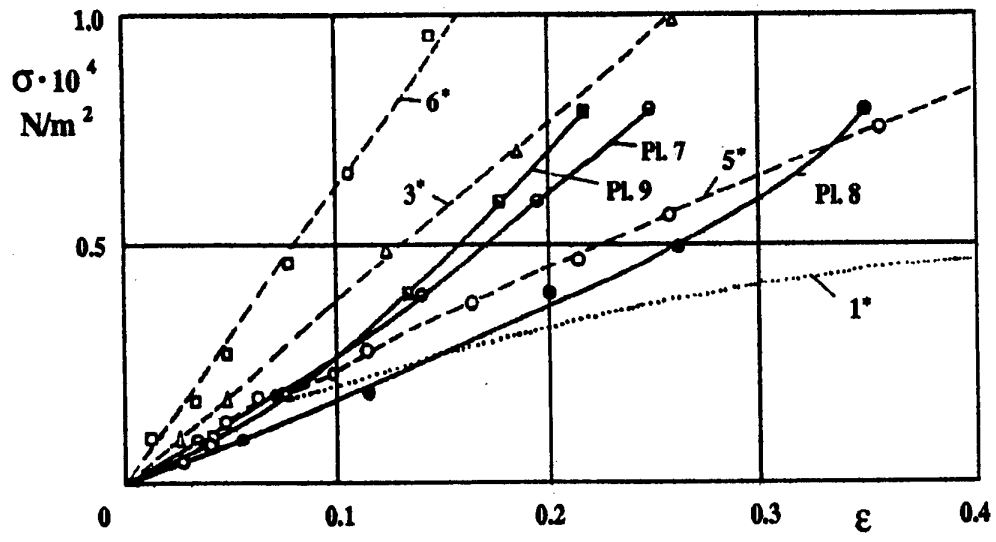
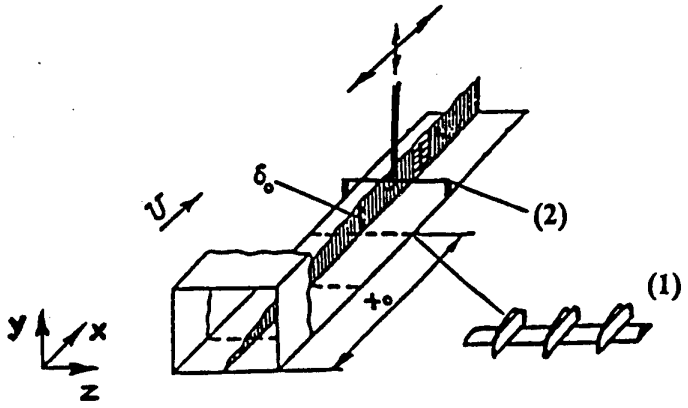
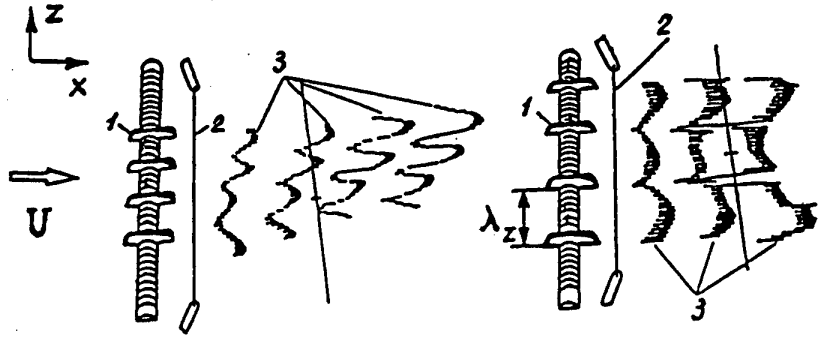


Fig. 6 Stress–strain characteristics of compliant materials 1,3,5,6 (curves marked with asterisks) and multi-layered plates fabricated from them.



a



b c

Fig. 7 (a) Water channel test section, $3.0m \times 0.25m \times 0.1m$, $U_\infty = 0.03 - 0.6$m/s.
(b,c) Flow structure visualization in water channel. 1 – vortex generators
2 – tellurium probe
3 – visualized time-lines

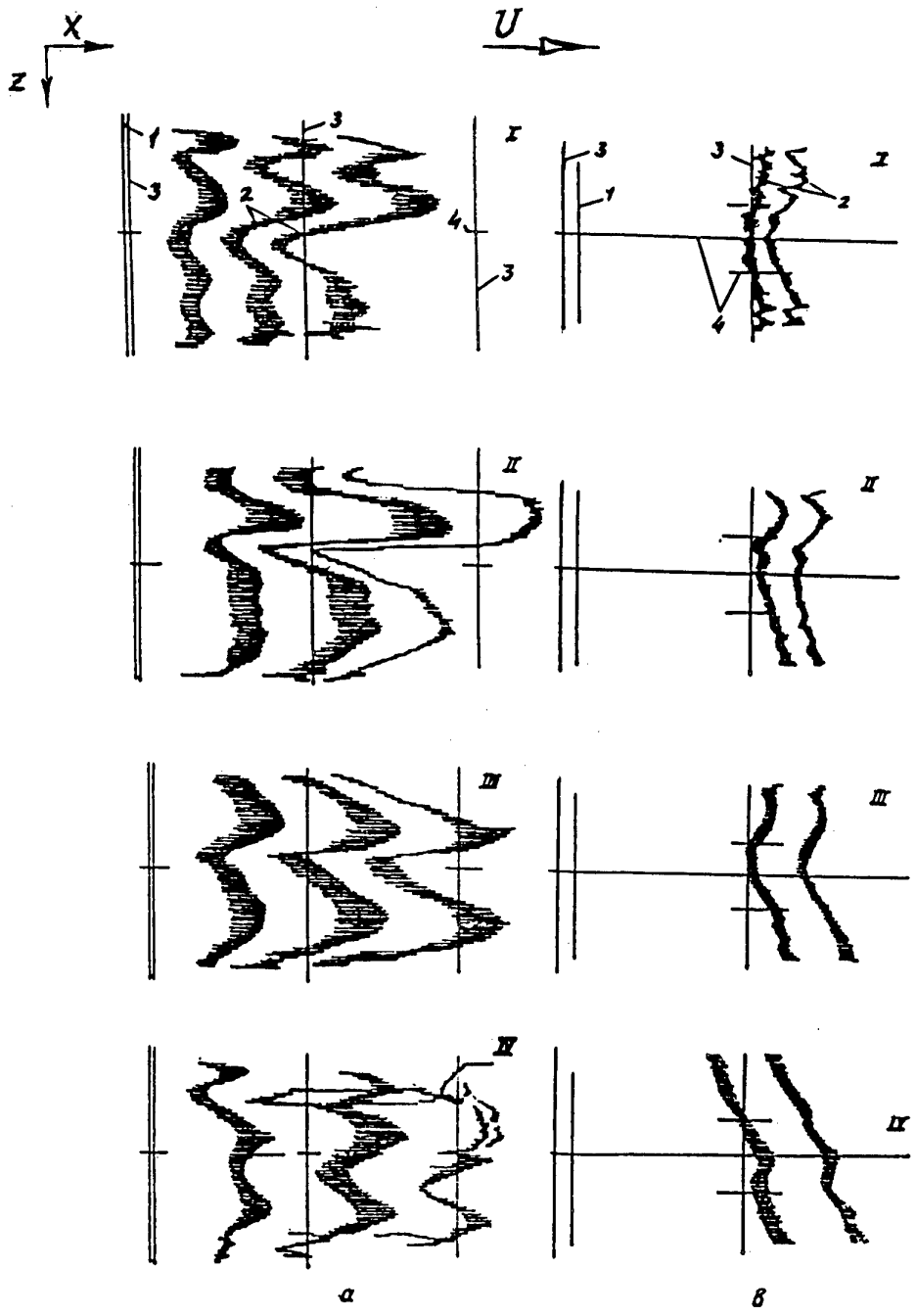


Fig. 8 Visualized flow field (top view) in transitional boundary layers over flat rigid (a) and compliant (b) surfaces:
1 – Tellurium wire, 2 – Tellurium lines, 3 – transverse $10cm$ marks along the bottom, 4 – axis marks;
a: $U_\infty = 6.7cm/s$; $x = 1.1m$; $y = 3mm$ (I), $4mm$ (II), $5mm$ (III), $6mm$ (IV);
b: $U_\infty = 5.0cm/s$; $x = 2.2m$; $y = 2mm$ (I), $4mm$ (II), $6mm$ (III), $8mm$ (IV).

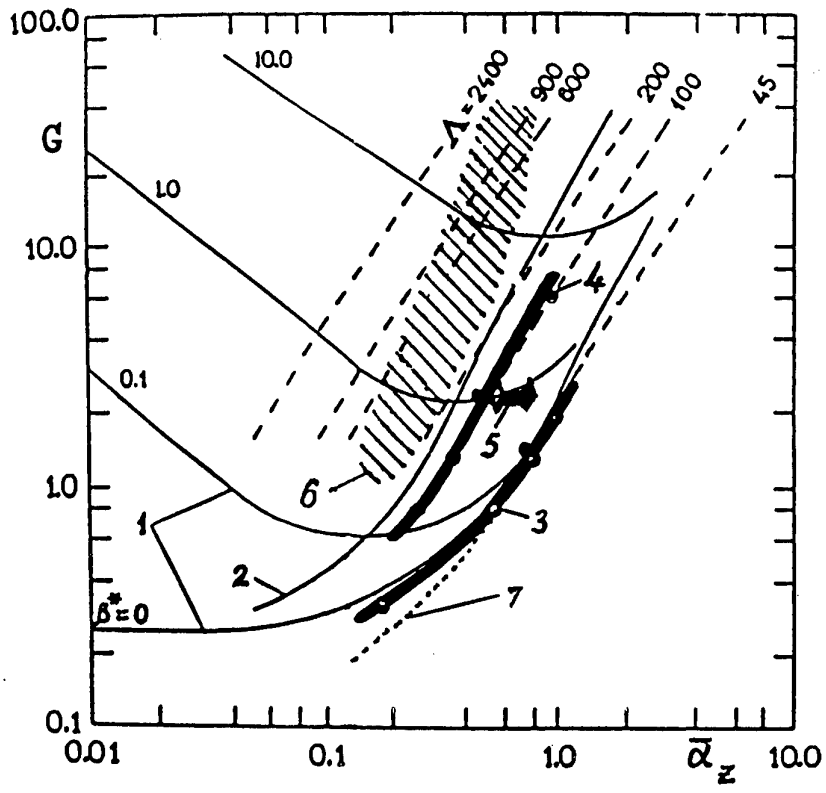


Fig. 9 Stability of streamwise vortices in boundary layers over rigid and compliant surfaces.

1,2 – calculations by Florian & Saric (1982), curves for constant growth rates and maximum amplification respectively;
3,4 – experimental curves of neutral stability and maximum amplification respectively (rigid surface), (1984);
5,6 – experimentally obtained regions for neutrally stable and most amplified disturbances over a compliant surface;
7 – experimental data for neutral Görtler stability curve (rigid surface) obtained by Aihara (1984).

Dynamics of vortices in near-wall flows: eigenfrequencies, resonant properties, algorithms of control

V. Gorban', I. Gorban'
National Academy of Sciences – Institute of Hydromechanics
8/4 Zhelyabov str., Kyiv, 252057
Ukraine

1. SUMMARY

Some ways of control of near-wall flow characteristics are analysed. They are based on generation in the flow of large vortical structures with special dynamic properties. In this connection, dynamics of 2-D stationary vortices located near the flow boundary irregularities are investigated by numerical simulation with using the model of ideal incompressible fluid. Parameters of standing vortices in a cavity, behind a bulge, over a wavy wall, in the wake of a cylinder were calculated and the classification of stationary points for corresponding areas was made. The vortex located in the stationary point was shown has the characteristic eigenfrequency. It leads to resonant interaction of the vortex with external perturbations, when the vortex frequency is similar to that of the perturbation.

To generate the stationary vortices near a body, it is proposed to use special cavities (vortex chambers). Patterns of the flow near the wall with the cavity were obtained by discrete vortex method. The steady standing vortex above a flat ptate was shown can be got in the active control system of pulsed sources with feedback.

2. INTRODUCTION

The control of unsteady fluid flows in near-wall areas and in the wakes of bodies is attracting wide interest in both the fluid mechanics and engineering because of the many potential applications. Drag reduction, lift enhancement, mixing improvement, etc. are some of the many problems where control of near-wall flows can be applied. Because of the flows of fluid in near-wall areas depend considerably on motion and evolution of large vortex structures existing there, knowledge of its dynamic properties is the necessary condition for successful realization of the flow control.

The end aim of the control depends on specific engineering application of the flow. To get the optimal flow characteristics, either formation of large-scale vortices, which are steady to external perturbations, or fast destruction of the large vortices and formation uniformity vorticity field is needed. In particular, reduction of the body hydrodynamic drag can be gotten with transfer from chaotic turbulent flow regime in the near-body area to the regular flow and formation large steady vortices in the wake.

The secondary vortex structures in near-wall area can be formed with the help either of special irregularities of flowed surface (cavities, bulges, steps), or of surface deformations (for example, traveling wave) and vibration of the body. As experimental researches show [5,8,16], the generation of vortices and ensuring of its stability demand large energy costs which may exceed the effect from the local reduction of hydrodynamic drag. Besides, standing vortices are steady in narrow diapason of external flow velocity. The way of control satisfying the requirement of physical validity and utilizing the minimum amount of energy expenditures has to use the information about critical points and other topology features of a flow pattern as well as the knowledge of dynamic properties of the vortices. The modern control schemes are directed on formation the necessary topology of the flow pattern [6, 7, 14]. The last includes the change of the location of flow critical points and their type, that allows to create the stability standing vortices in flow field. Further control uses dynamic properties of the vortices and either supports or destroys those in accordance with the aim of the control.

To develop the algorithms of control of near-wall flow large-scale structure, resonant properties of vortices are also interesting. It is well known that water animals control its flow-around, spending minimum quantity of energy. It has not been real-

Paper presented at an AGARD FDP Workshop on "High Speed Body Motion in Water", held in Kiev, Ukraine, 1-3 September 1997, and published in R-827.

ized in technical equipment using analogous moving manner (for instance, in wavy engine, flopping wing, impuls hydrojet engine). The resonant regime of flow, in which the small disturbance of flowing surface leads to considerable change of the flow pattern and appropriate hydrodynamic load, is one of ways providing such effect.

To realize the strategy of control, as passive algorithms (change of the flowed surface shape, mounting the fixed wings, ribs and other elements) as active those (periodic suction and blowing, mounting the oscillating wings) can be applied. The ways of control with feedback are the most perspective ones. They use monitoring the vortical structure of flow field in virtual time, that allows to direct purposefully the control force either on keeping or on destroying the stationary configuration of large-scale vortices in the flow.

Vortical structure of near-wall flow in real constructions is highly complex and depends on character of flow-around, i.e., Reynolds number, the shape of the boundary, vibration of the design and other factors. Formation of vortices in near-wall flow is the display of viscous interaction forces. Therefore, analysis of generation and dissipation of the vortices demands the development of complex and detailed models based on Navier-Stokes equations. In comparison, stability and dynamic properties of the large vortex structures formed due to vortex sheet instability can be considered in frameworks of ideal fluid. Last years, the approach considering the set of vortices as a dynamic system was developed [2, 7, 10, 17]. The steady vortex in near-wall flow was obtained to have the characteristic eigenfrequency and resonant properties that allows to act on its by means of external periodic perturbation which has the given frequency [10].

In the present work, the theoretical analysis of topology of some near-wall flows and dynamic properties of the vortices located there is made as well as the ways of influence on the behaviour of the vortices and the general structure of the flow are grounded.

3. VORTICES IN RECIRCULATION ZONES FORMED BEHIND BOUNDARY IRREGULARITIES: STATIONARY POINTS AND EIGEN FREQUENCIES

Application of artificial unevenness of the flowed surface (bulges, grooves, ribs, vortex chambers) for improvement of hydrodynamic characteristics of devices was described by P.K. Chang [8], F. Ringleb [15], V.K.Migaj [12] and others. Analysis of experimental and theoretical results shows that reaching the necessary effects (increase of opening angle and reduce of hydrodynamic losses in diffusers, decrease of both the body hydrodynamic drag and the sizes of recirculation zones) are explained not only turbulization of the flow due to unevenness of the wall but also interaction of formed vortices with external flow. Application such systems will make a success if the vortices in near-wall flow are steady ones. Unfortunately, experimental dates [5, 8, 15] are evidence of sensitivity such vortices to external flow perturbations, that reduces efficiency and value considered schemes. In the present work, the nature of excessive sensitivity and non-stability of vortices in near-wall flows is investigated.

Here we consider the flow near the surface with a cavity to demonstrate the characteristic features of near-wall flow. The rolling-up of separated shear layer is modelled by vortex method [3, 4, 9, 11]. The time-dependent circulation of nascent vortex is predicted by an unsteady Kutta condition. To satisfy the boundary condition, the conformal mapping of physical area into the upper half-plane is used. Equations of vortex dynamics are analysed with applying the numerical methods. Since we model the flow with the high Reynolds number, we have to expect the following flow configuration: the flow separation from the entrance edge, the formation of mixing layer above the cavity, the backflow inside the cavity, the flow reattachment near the outlet edge and the movement of large-scale structures in the near-wall area. The complexities of the simulation such processes are connected with the essential non-stationarity of the vortex generation as well as with the necessary to take into account the interaction of the vortical structures of different scales between them's and with the wall.

Some results of calculations are depicted in Fig.1. The vortex sheet shedding from the cavity entrance edge is unsteady one. At an initial stage of its evolution, the vortex sheet breaks down into the separated vortical structures which are like on those generating in the mixing layer (Fig. 1 a, b, c). These structures have the periodic character. The space and temporal periodicity is broken when the shedding layer interacts with the wall near the cavity outlet edge. One part of the vorticity goes into cavity and forms the recirculation zone and another part is carried away in near-wall flow. The formation of both the recirculation zone inside the cavity and the quasistationary flow in near-wall area behing the cavity come over very slowly (when $\tau > 20$, where ($\tau = tU/a$, $2a$ is the cavity chord). In quasistationary flow, the point vortices will occupy

the cavity practically in regular manner, if the cavity is shallow (Fig. 1 *d*). At the same time, those will concentrate near the cavity centre, if the cavity is more depth (Fig.1 *e*). As results of simulation show, the recirculation zone is characterized by nearly periodic pulsations, which are caused by the precession movement of the vorticity centre in the cavity (Fig. 1 f). We will show further that the existence of the eigen periodic motion of the vortex structures leads to selective receptivity of the flow to external periodic perturbations.

Existence of the compact areas with large concentration of the vorticity allows to use the simple model, in which the behaviour of a vortex whose strength is equal to integral intensity of vorticity in the area is considered.

3.1 Model of standing vortices

We are limited by analysis of two-dimensional problem, that permits to use the methods of conformal transform theory. Let a vortex with the coordinates $z_0(x_0, y_0)$ is located in a closed area D whose boundary is $\mathcal{L}$. The free flow in the area is rectilinear and is described by the velocity U_∞. By means of function $\zeta = f(z)$ we realize the conformal mapping of the area into the upper halfplane of auxiliary plane ζ. The complex flow potential describing the free stream with a vortex is the following function from ζ :

$$\Phi(\zeta) = \Phi_0(\zeta) + \frac{\Gamma}{2\pi i} \ln \frac{\zeta - \zeta_0}{\zeta - \bar{\zeta}_0} \qquad (1)$$

$$\zeta = f(z).$$

Here Φ_0 is the complex potential corresponding to the external flow, Γ is the strength of the vortex, ζ_0 is the complex coordinate of the vortex in ζ–plane, the overbar denotes a complex conjugate and $i^2 = -1$.

The equation describing the movement of vortex in the area D can be obtained from (1):

$$\overline{V_0} = V_{0x} - iV_{0y} = \frac{dx_0}{dt} - i\frac{dy_0}{dt} =$$

$$= \left(\frac{d\Phi_0}{d\zeta}\Big|_{\zeta=\zeta_0} + \frac{\Gamma}{4\pi\eta_0}\right)\frac{d\zeta}{dz}\Big|_{z=z_0} + \frac{\Gamma}{4\pi i}\left(\frac{d^2\zeta}{dz^2}\Big/\frac{d\zeta}{dz}\right)\Big|_{z=z_0} \qquad (2)$$

The position of a stationary vortex $z_0^*(x_0^*, y_0^*)$ is determined from the condition:

$$\overline{V_0}\Big|_{z=z_0^*} = 0 \ , \qquad (3)$$

It can be presented in the following form :

$$\left(\frac{d\Phi_0}{d\zeta}\Big|_{\zeta=\zeta_0^*} + \frac{\Gamma}{4\pi\eta_0}\right)\left[\left(\frac{d\zeta}{dz}\right)^2\Big/\frac{d^2\zeta}{dz^2}\right]\Big|_{z=z_0^*} - \frac{i\Gamma}{4\pi} = 0 \qquad (4)$$

Extracting the real part from (4) under the condition $Real\left[\frac{d\Phi_0}{d\zeta}\right] = 0$, one derives the equation for determining the stationary vortex position :

$$Real\left[\left(\frac{d\zeta}{dz}\right)^2\Big/\frac{d^2\zeta}{dz^2}\right]\Big|_{z=z_0^*} = 0. \qquad (5)$$

To find the strength Γ_0 of the standing vortex, the image part (4) is used. The condition (3) is not sufficient one. To determine the parameters of the standing vortex in full, Kutta condition has to be used when the flow boundary has sharp edges. Otherwise, experimental data may be attracted.

The motion of the vortex in the neighbourhood of stationary point can be as stable as unstable with respect to perturbations of free stream velocity, strength of the vortex and shape of the flow boundary. The behaviour of the vortex in the neighbourhood of stationary point $z_0^*(x_0^*, y_0^*)$, in the presence of perturbations is investigated by analysis of the following linear equations :

$$\begin{aligned} \frac{d\Delta x}{d\tau} &= a_{11}\Delta x + a_{12}\Delta y \\ \frac{d\Delta y}{d\tau} &= a_{21}\Delta x + a_{22}\Delta y \end{aligned} \qquad (6)$$

$$\Delta x = x_0 - x_0^* \qquad \Delta y = y_0 - y_0^*,$$

The coefficients a_{ij} are the components of Jacobi matrix for equation (2):

$$a_{11} = \left(\frac{\partial V_x}{\partial x_0}\right)_* , \quad a_{12} = \left(\frac{\partial V_x}{\partial y_0}\right)_* ,$$

$$a_{21} = \left(\frac{\partial V_y}{\partial x_0}\right)_* , \quad a_{22} = \left(\frac{\partial V_y}{\partial y_0}\right)_* .$$

The asterisk means that derivatives correspond to the stationary point $z_0^*(x_0^*, y_0^*)$.

The solution of system (5) may be derived as :

$$\Delta x = X\exp(\lambda\tau), \qquad \Delta y = Y\exp(\lambda\tau)$$

The eigennumber λ is determined from the following equation :

$$\lambda^2 - (a_{11} + a_{22})\lambda + (a_{11}a_{22} - a_{21}a_{12}) = 0. \quad (7)$$

The set of equations (2) describing the dynamics of a vortex is Hamiltonian one. Similarly [17], its Hamiltonian is given by the expression :

$$H[x_0, y_0] = \eta_0 + \frac{\overline{\Gamma}}{8\pi} \ln\left(\eta_0^2 \left|\frac{d\zeta}{dz}\Big|_{z=z_0}\right|^2\right) \quad (8)$$

It is known , that in Hamiltonian systems, the coefficient with λ (divergence) in eq. (7) is equal to zero : $\Delta = a_{11} + a_{22} = 0$. The stationary point can be either elliptical or hyperbolic. Its type depends on the sign of the Jacobian $J = a_{11}a_{22} - a_{21}a_{12}$. Under the condition $J > 0$ one has the steady stationary point and the vortex revolving on its stationary point with the characteristic eigen frequency $\omega_0 = \sqrt{a_{11}a_{22} - a_{21}a_{12}}$.

3.2 Standing vortex in a cavity

In connection with development of approach using the vortex chambers for control of flow, we shall consider the topology of the flow in a cavity. The depth of the cavity is supposed to be much larger than the thickness of boundary layer formed on the wall. The necessary conformal mapping is carried out by the following function

$$\zeta = a_0\gamma \frac{1 + \left(\frac{z-a}{z+a}\right)^\gamma}{1 - \left(\frac{z-a}{z+a}\right)^\gamma}, \qquad \gamma = \frac{\beta}{\pi - \beta} \quad (9)$$

where $2a_0$ is the chord of the cavity, the angle β defines the cavity depth ($\beta < 0$). All linear sizes will be divided by half-hord of the cavity a_0, $\overline{\Gamma} = \Gamma / U_\infty a_0$.

The equations characterizing the movement of vortex (2) as well as those used for determining the coordinates and the circulation of standing vortex are difficult enough. To solve those, the numerical procedure was used (the fourth-order Runge-Kutta method in combination with the iteration scheme for solution of transcendental algebraic equations). As follows from results of calculations, in a cavity, there is the vortex which is stationary and satisfies the Kutta condition in both sharp edges. It is important peculiarity of the considered flow configuration, which shows that stabilization of vortex in a cavity may be achieved without additional admission of energy. The locus of fixed point against the angle β characterizing the cavity depth is obtained. In each such point, the vortex is stationary and satisfies the Kutta condition, and its circulation Γ_0 is shown in Fig. 2 (curve 1).

A linear stability analysis shows that the eigenvalues of the system are complex conjugates with zero real parts. It means, the fixed points of the flow are centers and if a vortex is located in such point (it is standing), it will have eigenfrequency ω_0 (Fig. 2, curve 2). To give a complete characterization of the dynamics of the system, we plot the phase portrait of the trajectories of the vortex (Fig. 3). These trajectories are obtained for constant vortex circulation. There are four types of vortex trajectories delimited by separatrixes and three critical points. These are the center disposed on cavity axis and two unstable saddle points near edges. Phase portrait features will play the important role in analysis of the dynamic properties and evolution of standing vortex in the field of perturbations.

3.3 Standing vortices in the wake of a cylinder

The stationary flow with two symmetrical vortices in the wake of circular cylinder is observed experimentally at small Reynolds numbers (Foppl vortices [13, 19]). The corresponding theoretical solution is adduced in Milne-Thomson's monograph [13]. It is based on the model of single vortex moving in ideal incompressible fluid. To define the flow potential and the velocity of the vortex, the theorem about the circle was used there. The solution consists the expressions for coordinates and circulation of stationary vortices. The similar results for parameters of standing vortex were obtained numerically in the present study. The conformal transformation (9) was employed. Under the condition $\beta = \pi/2$ it maps the area with half-cylinder lying on the wall into the upper half-plane. The curves defining the positions of standing vortices and the dependence of vortex circulation Γ_0 (Fig. 4) on the radius-vector R coincide accurately with appropriate analytical solutions. The novelty of the present research consists in determination of eigenfrequency ω_0 of stationary vortices (Fig. 4). Due to this, the most suitable regimes needed to affect on the vortices with the help of periodic perturbations of external flow may be found.

3.4 Standing vortices above a wavy surface

Some dynamic properties of standing vortices located above a wavy surface will be considered. This problem initiates the interest in connection with practical realization some effects of the traveling wave. Results of simulation are important to obtain detailed understanding of the nature of vortex stability in wave troughs as well as study the influence of external perturbation introduced by the boundary shape on vortices.

The wall profile is a relation in y and x and is

given by the following equation :

$$y = \ln\left(a\cos\frac{2\pi}{\lambda}x + \sqrt{b^2 - a^2\sin^2\frac{2\pi}{\lambda}x}\right) \quad (10)$$

where λ is the length of the wave; a, b are the parameters connected with the wavy amplitude h by the following relationships :

$$a = (1 - e^{2h})/2\ , \quad b = (1 + e^{2h})/2\,.$$

The flow configuration in physical plane z is the channel of the width L. One wall of this channel is given by the equation (10).
The flow area may be reflected into the upper half-plane by means of two consecutive transformations:

$$w = -\frac{i}{\omega}\ln\frac{e^{i\omega z} - m}{n - ce^{i\omega z}} \quad (11)$$

$$\omega = \frac{2\pi}{\lambda}, \quad m = a + bc\,, \quad n = b + ac$$

$$c = \frac{e^{-2L} - a^2 - b^2}{2ab} + \sqrt{\frac{e^{-2L} - a^2 - b^2}{2ab} - 1}$$

$$L' = \ln\frac{e^{-L} - m}{n - ce^{L}}$$

$$\zeta = \exp(\frac{\pi}{L'}w) \quad (12)$$

The rectilinear flow in physical plane z with the velocity U_∞ corresponds to the source located on the centre of coordinates of the auxiliary plane ζ. Its power is $Q = U_\infty L'$. Thus the complex velocity potential characterizing the external flow above the wavy surface is given by :

$$\Phi_0(\zeta) = \frac{U_\infty L'}{4\pi}\ln\zeta \quad (13)$$

All linear sizes will be divided by wavy amplitude h , $\overline{\Gamma} = \Gamma/U_\infty h$ (further the overbar will be omitted).
The vortex $z_0(x_0,\ y_0)$ placed above a flat wall is known to move in parallel with the wall. The direction of its movement depends on relationship between the freestream velocity U_∞ and the self-excited velocity $\Gamma/4\pi y_0$. If the vortex moves above a wavy surface, its trajectory will be defined by the value of the vortex circulation Γ. Dependences of circulation Γ_0 and eigenfrequency ω_0 of the standing vortex in wave trough on wave parameters and vertical coordinate of the vortex are adduced in Fig. 5. To avoid resonant interaction of the disturbances introduced by a traveling wave with standing vortex, one has to take into account frequency characteristics of the vortex when selecting parameters of the wave.
When the system of two vortices moves above a wavy surface, the resonance another type was discovered by us. If the length of own oscillating motion of the vortex pair is like to that of the wave, the motion become most regular. As a result, the velocity of vorticity transfer decreases considerably in comparison with the cases when the pair moves either above a flat wall or before and beyond the resonance. This situation is reflected in Fig. 8. Here curve 1 is the graph of the vorticity transfer velocity above a wavy surface, dotted line 2 corresponds to its average value and curve 3 shows the average value of the velocity when the pair moves above a flat wall. Because of the hydrodynamic drag of surface is proportional to velocity of vorticity transfer along the surface, this type of motion is very interesting. To form a travelling wave, active control system of pulsed sources may be used that enlarges possibilities of flow control.

4. RESONANT PROPERTIES OF STANDING VORTICES AND THEIR BEHAVIOUR IN PRESENCE OF EXTERNAL PERTURBATIONS

Knowledge about the eigen frequency of standing vortices becomes especially important, when the external periodic perturbations is present in the flow. These perturbations can be either artificial, i.e., be introduced in the flow with the express purpose to control the necessary parameters, or natural. We shall consider the influence of periodic perturbation of the free stream velocity U_∞ on dynamics of standing vortex located in a cross groove (cavity) and in the wake of circular cylinder. Let the free stream velocity is changed according to the following expression :

$$U_\infty = U_*\,(1 + a\sin\Omega\tau)\ , \quad U_* = const\,, \quad a \ll 1 \quad (14)$$

Here a, Ω are the amplitude and the frequency of the perturbation accordingly.
To determine the trajectory of vortex, the equations (2) characterizing the movement of vortex near the curved boundaries are used. The numerical integration of those is based on fourth–order Runge–Kutta method. At an initial instance $t = 0$, the vortex with circulation Γ_0 is supposed to locate in the stationary point. It means that in unperturbed flow, the vortex rotates with the eigenfrequency ω_0 along the infinitely small trajectory.

The trajectory of the vortex is changed considerably under the action of the external perturbation containing the small periodic component. Its character depends on the frequency of external perturbation Ω. If the value of external frequency is far from that of the eigenfrequency ω_0 or her subharmonics $\omega_0/2$, $2\omega_0$, the vortex will move periodically on a closed trajectory in the small neighbourhood of stationary point. The size of the neighbourhood is proportional to the amplitude of the perturbation a.

The trajectory of vortex will be highly changed, if the external frequency Ω comes nearer to the eigenfrequency of the vortex ω_0 (or her subharmonics). The motion of vortex is characterized by its deviation from stationary point:

$$R(\tau) = \sqrt{\left[x_0(\tau) - x_0^*\right]^2 + \left[y_0(\tau) - y_0^*\right]^2},$$

where x_0^*, y_0^* are the coordinates of stationary point, $x_0(\tau)$, $y_0(\tau)$ are the coordinates of the vortex at considering time step.

The movement of vortex is multiperiodic one. The small external perturbation being to generate the low-frequency oscillations of the vortex with large amplitudes. This property follows from the nonlinear nature of the equations defining the dynamics of vortex in near–wall area.

The resonant curves are plotted versus the nondimensional frequency of perturbation Ω/ω_0 in Fig. 5. They characterize the dependence of maximum deviation of the vortex R_{max} on the stationary point. Dependence of the value of resonant peaks on the amplitude of perturbation, displacement of the resonance to more high frequencies $\Omega/\omega_0 > 1$ as well as availability of secondary peaks at $\Omega/\omega_0 \approx 0.5$ and $\Omega/\omega_0 \approx 2$ are characteristic features of the curves. When the cavity sizes are reduced, the height of resonant and subresonant peaks as well as the width of resonant zone increase. Therefore, one may suppose that the vortex becomes less mobile due to growth of the hollow depth. It means that its reaction on the perturbation fades.

As results of calculations show, the resonant peak may become infinitely large. In Fig. 6, such trajectory of standing vortex is depicted. In this case, the vortex goes away from the cavity by the external flow. It means, the vortex crosses the line separating the trajectories of various types on the phase portrait.

The similar resonant effects will be observed, if the standing vortex is located in the wake of a body (Fig. 7). The dependence $R_{max}(\Omega/\omega_0)$ dealing with the vortex behind the cylinder is different from that as the vortex is located in a cavity. In particular, the main resonance peak shifts to lesser frequencies and gets under the condition $\Omega/\omega_0 < 1$. If the frequency of perturbation Ω increases to ω_0, the value R_{max} defining the amplitude of vortex precession will grow spasmodicly. It means that we have the nonlinear system with "rigid" excitation. In accordance with presented results, the stationary vortices in the wakes are less steady to the external perturbation than those in the inner flows (for example, in grooves). In particular, the vortex behind the cylinder reacts considerably on perturbation which are characterized by very small amplitudes.

When the system of two vortices moves above a wavy surface, the resonance another type was discovered by us. If the length of own oscillating motion of the vortex pair is like to that of the wave, the motion become most regular. As a result, the velocity of vorticity transfer decreases considerably in comparison with the cases when the pair moves either above a flat wall or before and beyond the resonance. This situation is reflected in Fig. 8. Here curve 1 is the graph of the vorticity transfer velocity above a wavy surface, dotted line 2 corresponds to its average value and curve 3 shows the average value of the velocity when the pair moves above a flat wall. Because of the hydrodynamic drag of surface is proportional to velocity of vorticity transfer along the surface, this type of motion is very interesting. To form a travelling wave, active control system of pulsed sources may be used that enlarges possibilities of flow control.

Summing up, the resonant perturbation of flow intensifies essentially the fluid mixing in near–wall areas. It changes also the appropriate characteristics of thermal, acoustic and other hydrophisic fields.

5. GENERATION OF STANDING VORTEX AT THE BEND OF FLOW AND ITS INFLUENCE ON DECREASING SEPARATED ZONE SIZES

Use of standing vortices for control of near-wall flow parameters near angle is considered. In this area, one has the flow with large positive pressure gradients and, as a result, global separation of the flow and formation of vast recirculation zone [5, 11, 17]. Theoretical analysis of the flow topology shows that there are no steady stationary points near angle. To form those, we propose to change the boundary shape, disposing the cross cavity (vortex chamber) at the bend (Fig. 9). Parameters of the standing

vortex (coordinates and circulation) and the shape of the cavity (angles α, β and center of circle) are determined from the condition of stationarity (3) and two Kutta conditions satisfied at the sharp edges. The last does not allow generation of vorticity at the edges. As results of calculations show, this problem has the solution with broad diapason of cavity parameters. Dependence of the angle β characterizing opening the cavity on angle α is linear. The circulation Γ_0 and eigenfrequency ω_0 of the standing vortex versus angle α are plotted in Fig. 10.

The present research allows to evaluate the strength of recirculation zone in the vortex chamber, which should prevent the global separation of the flow at boundary bend. Calculations with using the discrete vortex method show that the vortex generated in the chamber has the lesser strength than Γ_0 demands. As a result, the separation zone near the boundary bend does not disappear completely, but its sizes are reduced considerably. Nonseparation flow at the bend can be provided if the vortex having the necessary circulation and coordinates is created specially in the chamber. The passive schemes, when energy is extracted from the external flow can be used (for example, wings). To reach the necessary strength of the vortex, the active schemes with admission of energy are effective also.

6. STANDING VORTEX IN THE SYSTEM BODY-CONTROL PLATE

Experimental researches show [5, 14] that mounting control plate either before or beyond a bluff body reduces considerably the drag such system. Selection of geometrical parameters (the height of plate, the distance between the plate and the body) and the shape of plate is very important when working the systems. The present model confirms that improvement of hydrodynamic characteristics is achieved due to generation of standing vortex between the control plate and the body and allows to state the value of the system parameters. The standing vortex satisfying the Kutta condition in both the plate end and the body edge were found and its parameters (coordinates, circulation, eigenfrequencies) were obtained. Existence such vortices results in reducing the vortex shedding intensity near body edges. The total drag of the body plus plate is decreased relative to the configuration without plate [5, 14]. Flow patterns with the standing vortex between two plates and in the system control plate-body are plotted in Figs. 11,12. Analysis of eigenfrequencies and resonant properties of the standing vortices explaines the high sensivity of this system to turbulent pulsations of external flow and shows the ways how to improve the vitality of the vortices.

7. ACTIVE CONTROL OF VORTEX STRUCTURES IN NEAR-WALL FLOWS

Control of near-wall flow with admission of energy (for example, blowing and suction of fluid) allows to change topology of flow. In the work [6] it has been showed that there is the steady standing vortex providing the Kutta condition at the edge of flat plate, if the special source is mounted in the flow. We obtained analogous results for standing vortex near the angle (bend of the flow boundary). It must be noted such schemes demand large energy costs for suction or blowing of fluid.

The lesser energy expeditures are needed in active control schemes, when the stationary vortex exists in the flow but it is unstable, for example saddle or unstable foci. Such flow cannot be realized owing to its instability. This situation is changed with using active control scheme with feedback. We shall consider the work such system, when unstable vortex is located above a flat surface. The system consists of two pulsed sources and sensing element ensuring shadowing the vortex. The power of source is changed in proportion to deviation of the vortex from its stationary position. The type of the stationary point is changed, it becomes the steady foci. It is important that the vortex has the characteristic eigenfrequency. As a result, the efficiency of this control system depends on frequency characteristics of perturbations in near-wall flow. Calculations show that accidental deviation of the vortex from its stationary point is suppressed quickly at high frequency of external perturbations, on the contrary, at low frequency of perturbations the vortex deviation can be increased.

8. CONCLUSIONS

Control of near-wall flow vortical structure will be effective, if it takes into account topology properties of the flow: type of critical points, existence of steady standing vortices, correlation between the eigenfrequency of the vortex system and spectral properties of external perturbations. Perturbations with frequencies which are similar to eigenfrequency of the vortex system lead to considerable change of the flow pattern. Obtained results show ways for improvement of hydrodynamic characteristic of devices through organization in near-wall flow large vortical structures with special properties.

REFERENCES

1. Acton E., Dhanak M.R. "The motion and stability of a vortex array above a pulsed surface." **Journal of Fluid Mechanics**, v. 247, (1993): 231-246.

2. Aref H. "Integrable, chaotic and turbulent vortex motion in two-dimensional flows." **Ann. Rev. Fluid Mech.**, 15 (1983): 345-389.

3.Belotsercovskij S.M., Nisht M.I. **Separated and unseparated flows behind thin wings in ideal fluid**. Moscow, Nauka, 1978, 352 p. (in Russian).

4.Belotsercovskij S.M., Ginevsky A.S. **Turbulent jets and wakes simulation using the metod of diskrete vortices** . Moscow, Nauka, 1995, 366 p. (in Russian).

5.Belov I.A. **Interaction of nonregular flows with obstacles** . Moscow, Mashinostroenie, 1983, 166 p. (in Russian).

6.Cortelelezzi L." Nonlinear feedback control of the wake past a plate with a suction point on the downstream wall " **Journal of Fluid Mechanics**, v. 327,(1996):303-324.

7.Cortelelezzi L.,Leonard A.,Doyle J.C. " An example of active circulation control of the unsteady separated flow past a semi-infinite plate" **Journal of Fluid Mechanics**, v. 260,(1994):127-154.

8. Ghang P.K. **Control of Flow Separation**, Hemisphere Publ. Corp., 1976.

9. Gorban' I., Gorban' V.,Saltanov N. "Numerical simulations of separated flows in near–wall areas." **Dopovidy AN of Ukraine**, Ser.A, No 2 (1989): 26–30 (in Russian).

10.Gorban' V., Gorban' I. " Resonant properties of vortices behind boundary irregulariti " **Dopovidy AN of Ukraine**, Ser.A, No 2 (1996): 44–47 (in Ukrainian).

11.Gorban' I. **Investigations of vortex flows in near–wall areas**, Ph.D.thesis, Institute of hydromechanics, Kiev, 1994, 235 p. (in Russian).

12.Migaj V.K. "The research of diffusers with ribs." **Teploenergetika**, No 10 (1962): 55–59 (in Russian).

13.Milne–Tomson L.M. **Theoretical Hydrodynamics**. St. Martin's Press, London, 1960, 656 p.

14.Monkewitz P.A. " A note on vortex shedding from axisymetric bluff bodies." **Journal of Fluid Mechanics**, v. 192, (1988): 561-575.

15.Ringleb F.O. "Two–Dimensional Flow with standing Vortexes in Ducts and Diffusers." **Trans. of the ASME, J. of Basic Engineering**, No 10 (1960): 921–927.

16.Roos F.W., Kegelman J.T. "Control of coherent structures in reattaching laminar and turbulent shear layers." **AIAA Journal**, No 12 (1986): 1956–1963.

17. Saltanov N.V.,Gorban' V. **Vortex structures in fluid: Analitical and numerical solutions**. Kiev, Naukova Dumka, 1993, 241 p. (in Russian).

18.Sarpkaya T. "Computational Methods with Vortices. - The 1988 Freeman Scholar Lecture." **Journal of Fluid Engineering**, No 1 (1989): 5–60.

19.Shlichting G. **Theory of boundary layer**. Moscow, 1974, 711 p (in Russian)

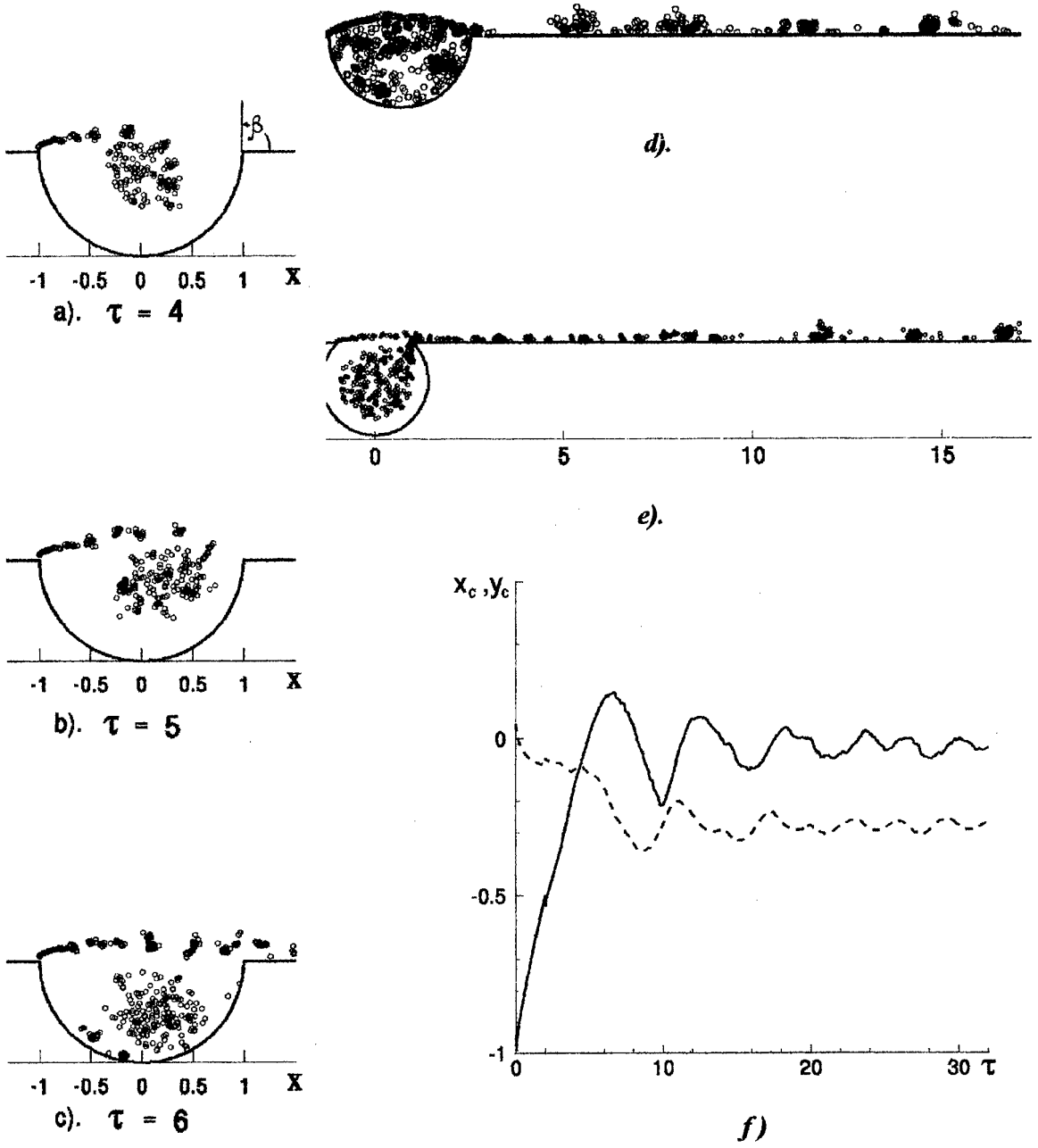


Fig. 1. Generation of the vortical structures in the flow behind cavity ***(a-e)*** and vorticity center precession in the cavity ***(f)***

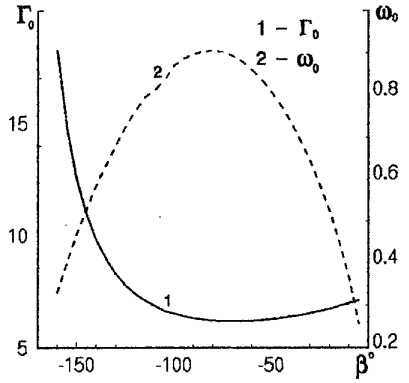


Fig. 2. Circulation Γ_0 and eigenfrequency ω_0 of the standing vortex in a cavity versus angle β characrerizing the cavity depth

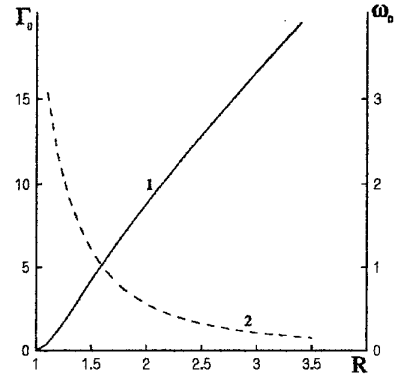


Fig. 4. Dependence of circulation Γ_0 (curve 1) and eigenfrequency ω_0 (curve 2) of standing vortex in the wake of cylinder against its locus

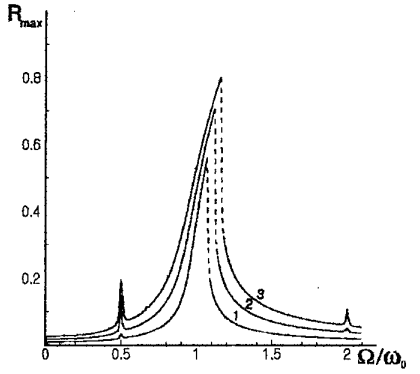


Fig. 5. Resonant curves characterising the dependence of vortex maximum deviation from the stationary point in a cavity $1-a=0.025$, $2-a=0.05$, $3-a=0.075$

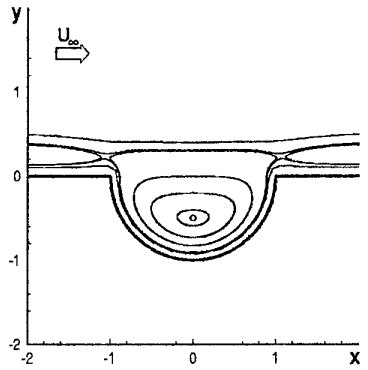


Fig. 3. Phase portrait of vortex trajectories in a cavity

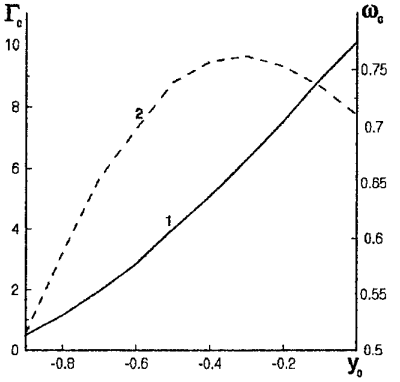


Fig . 5. Standing vortex above a wavy wall: dependence of circulation Γ_0 (curve 1) and eigenfrequency ω_0 (curve 2) of vortex on its vertical coordinate y_0 ($\lambda=4$, $h=1$)

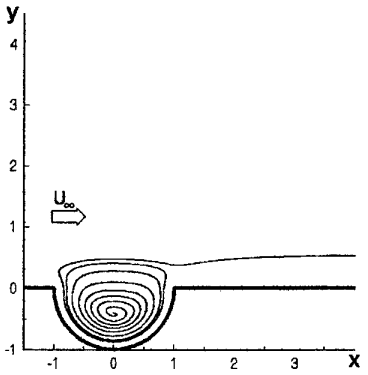


Fig. 6. Trajectory of the standing vortex behind a cavity at flow resonant perturbations

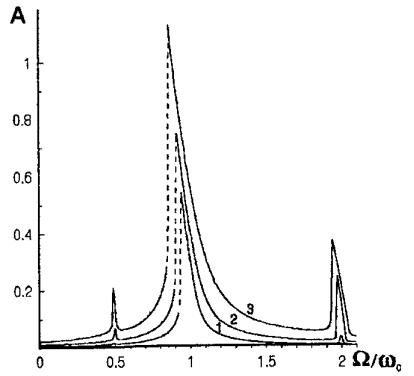


Fig.7. Resonant curves characterizing the dependence of vortex maximum deviation from the stationary point behind cylinder

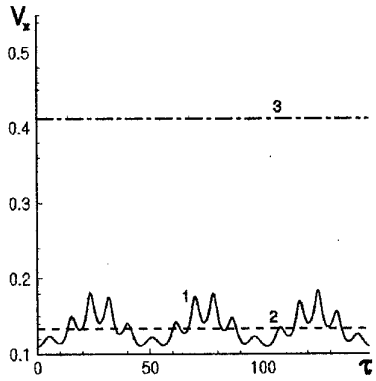


Fig . 8. Velocity of vortex pair vorticity center above a wavy wall in resonant regime

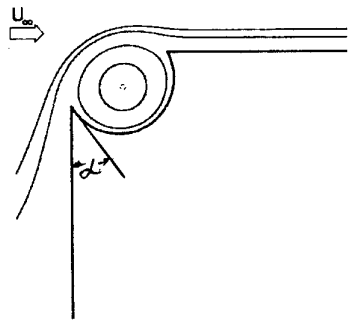


Fig. 9. Flow pattern near bend of the boundary with vortex chamber

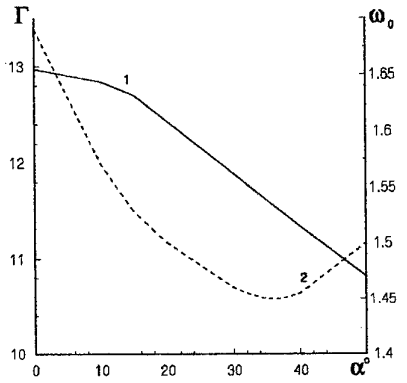


Fig. 10. Circulation Γ_0 and eigenfrequency ω_0 of the standing vortex in a vortex chamber versus angle α characterizing the chamber shape

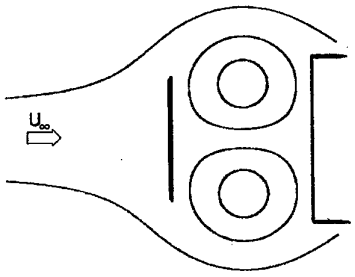


Fig. 11. Flow pattern with the standing vortex in the system control plate-bluff body

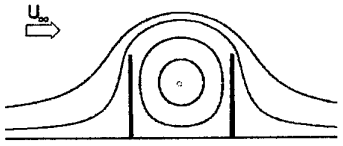


Fig. 12. Flow pattern with the standing vortex in the system two plates

A Simple Model for the Aero–Hydrodynamics of Ekranoplans

U.P. Bulgarelli, M. Greco, M. Landrini, C. Lugni
INSEAN, Italian Ship Model Basin
Via di Vallerano 139, 00128 Roma – Italy

SUMMARY

The problem of a wing–shaped body moving close to the air–water interface is addressed in term of an inviscid–rotational model in which the aerodynamic problem is coupled to the water flow by means of suitable interface conditions. A numerical procedure to solve the nonlinear unsteady problem is described. Numerical examples are given for some linearized cases. In particular the steady flow generated by a flat plate at incidence in forward motion over calm water is studied at first. The linearized wave–wing interaction is then analized in the frequency domain.

List of symbols

A	amplitude of incident wave
AR	aspect ratio
a_{kj}	added mass coefficients
b_{kj}	damping coefficients
c	characteristich chord length
C_D, C_L	drag and lift coefficients
$\boldsymbol{g}$	gravity acceleration
G	free space Green function
h	clearence
$\boldsymbol{U}_\infty$	stream velocity
$\boldsymbol{w}$	interface velocity
$\boldsymbol{x}$	vector position in the moving frame
X_k	exciting force
α	angle of attack
γ	vorticity strength
μ	dipole strength
ρ_l	air (l=1) and water (l=2) density
σ	source strength
φ_l	air (l=1) and water (l=2) perturbation potential
$\varphi_{l,j}$	air (l=1) and water (l=2) radiation potentials
$\varphi_{l,0}$	air (l=1) and water (l=2) incident potential
$\varphi_{l,7}$	air (l=1) and water (l=2) scattering potential
ω_0	frequency of incident wave
ω, $\boldsymbol{k}$	frequency of encounter and wave number vector
Ω_l	air (l=1) and water (l=2) domain
$\partial\Omega_B$	wing
$\partial\Omega_{\overline{B}}$	mean wing position
$\partial\Omega_{\mathcal{IF}}$	interface
$\partial\Omega_{\mathcal{W}}$	wake

1. Introduction

In order to make medium range sea–transportation competitive with respect to other means, a continously increasing effort is devoted to the development of high speed marine vehicles.

Among these, the russian 'ekranoplan' concept, a vehicle designed to operate in close proximity of underlying surface, has been recently recovered and proposed as 'Wing in Surface Effect Ships' (WISES) (see [1] for a discussion of the basic concepts and a hystoric perspective).

As the air–water density ratio is very small, the usual assumption in describing WISES–fluid dynamics is to neglect completely the free surface deformation and to consider the behaviour of the vehicle in ground effect. A deep analysis of these flow conditions can be found in [2] and in the literature cited therein. In particular, it is evidenced the strong three–dimensional character of the aerodynamic field and the dramatic role of endplates in determining the efficiency of the entire lifting system. More specifically, the lift–to–induced drag ratio increases as the clearance h decreases and it has been consistently pointed out in [3] that the new WISES generation will be characterized by an extremely reduced clearance with respect to the chord c of the main lifting device and a range $h/c \simeq 0.05 - 0.1$ has been suggested. In these flow–conditions the aerodynamic field and the wavy motion of the free surface are more strongly coupled and possible interactions with incoming waves could significantly alter the dynamic behaviour of the vehicle. In this case the relevant mathematical approaches are closely related to those considered for studying the wave propagation along sharp density interface. In the case of ship hydrodynamics a thorough analysis of ship generated internal waves can be found in [4],[5] and, even more related to the problem at hand, in [6] where the two–dimensional steady flow generated by a flat plate beneath an interface is discussed.

In this paper, we discuss a model to study the three-dimensional air–water flowfields generated by a lifting body when running in close proximity of the interface. Some physical assumptions are introduced. In particular, by assuming to deal with wing–shaped body and high Reynolds number attached flows, an inviscid–rotational model can be adopted to described the 'aerodynamic' part of the problem. Namely the viscous diffusion is neglected, the vortical regions are modelled by means of zero thickness vortex layers shed from the tips and the trailing edge of the wing, and a velocity potential exists almost everywhere. Also the effect of air–compressibility is neglected. The non–uniform pressure field created by the wing generates, or alters, the underlying wave field and, indeed, the motion of the air is coupled to that of the water. In describing the interface motion, viscous effects (i.e. the boundary layer on the two sides of the interface) are neglected and a velocity potential in the water–domain can be also introduced. Boundary conditions at the interface are deduced, which link the potentials existing in the two fluid domains.

On this physical ground, in §2. a mathematical model is introduced for dealing with the general unsteady case. The resulting problem is clearly highly nonlinear because of the free and moving boundaries (the interface, the wake and the wing surface). An iterative procedure to solve numerically the two coupled aerodynamic and hydrodynamic flowfields is described.

In order to gain confidence with physical and numerical aspects of the problem at hand, we limit ourself to solve some linearized cases (cfr. §3.). Namely the steady flow generated by a wing running above an initially calm interface is firstly considered. And, secondly, the interaction of the lifting device with an incoming wave systems is analyzed in the frequency domain, i.e. by assuming the time-dependance of the solution to be harmonic. For these problems, the solution can be easily identified as the problem of a wing on a porous soil coupled to the special free surface flows for which the Fourier-integral representation of the solution exists. As a result the numerical solution is greatly simplified. Although we developed the present theory indipendently, the use of

Paper presented at an AGARD FDP Workshop on "High Speed Body Motion in Water", held in Kiev, Ukraine, 1-3 September 1997, and published in R-827.

the Fourier representation of the steady solution for solving the complete (linearized) problem is apparently anticipated in [2].

Some consideration about the properties of the solution (see also the two–dimensional theory in [7]) can be inferred starting from the properties of the two separate problems. This issue and the numerical aspects concerning the solution of the unsteady nonlinear problem are under development and will be reported elsewhere.

2. Problem definition

In the following, we define the initial value problem describing the flow about a wing–shaped body $\partial\Omega_B$ moving close to an interface $\partial\Omega_{I\!F}$ which separates two inviscid incompressible fluids with densities ρ_1 (upper fluid) and $\rho_2 > \rho_1$. A frame of reference fixed with respect to an observer moving with the mean velocity $-U_\infty$ of the wing is adopted. We introduce the potentials φ_1, φ_2 harmonic in the corresponding domains,

$$\nabla^2\varphi_i = 0 \qquad \forall \boldsymbol{P} \in \Omega_i \,, \tag{1}$$

such that $\boldsymbol{u}_i = \boldsymbol{U}_\infty + \nabla\varphi_i$ are the fluid velocities in the upper, $i = 1$, and lower, $i = 2$, domains, respectively.

Interface boundary conditions The interface is defined by the kinematic property that the fluids do not cross it. Hence the displacement velocity w_n of the interface points $\boldsymbol{P} \in \partial\Omega_{I\!F}$ equals the normal velocity of the fluid on the two adiacent sides, namely $\boldsymbol{w}\cdot\boldsymbol{n} = \boldsymbol{u}_1\cdot\boldsymbol{n} = \boldsymbol{u}_2\cdot\boldsymbol{n}$. Moreover, when viscous and surface tension effects are neglected, the local momentum balance requires the continuity of the pressure p across the interface. From the above kinematic and dynamic conditions, it is possible to deduce different sets of (equivalent) evolution equations for $\partial\Omega_{I\!F}$. In particular, by choosing the velocity of the points $\boldsymbol{P} \in \partial\Omega_{I\!F}$ as

$$\boldsymbol{w} = \frac{1}{2}(\boldsymbol{u}_1 + \boldsymbol{u}_2) = \frac{1}{2}(\nabla\varphi_1 + \nabla\varphi_2) + \boldsymbol{U}_\infty \,, \tag{2}$$

the geometric evolution of the interface is obtained by following the motion of its geometric points. Moreover, once the pressure on the two sides of $\partial\Omega_{I\!F}$ is expressed by means of the Bernoulli equation, from the dynamic condition it is possible to relate the evolution of the two potentials φ_i at the interface. Eventually, the kinematics and the dynamics of the interface can be described by means of

$$\begin{cases} \dfrac{D_{I\!F}\boldsymbol{P}}{Dt} = \dfrac{1}{2}(\boldsymbol{u}_1 + \boldsymbol{u}_2) \\ \dfrac{D_{I\!F}\varphi_2}{Dt} = -g\eta + \dfrac{\rho_1}{\rho_2}\left\{\dfrac{D_{I\!F}\varphi_1}{Dt} + g\eta\right\} \\ \qquad\qquad + \dfrac{1}{\rho_2}\left\{(\rho_1 - \rho_2)\dfrac{\nabla\varphi_1\cdot\nabla\varphi_2}{2}\right. \\ \qquad\qquad \left. + \boldsymbol{U}_\infty\cdot[\rho_1\nabla\varphi_1 - \rho_2\nabla\varphi_2]\right\} \end{cases} \tag{3}$$

where the total derivative

$$\frac{D_{I\!F}}{Dt} := \frac{\partial}{\partial t} + \boldsymbol{w}\cdot\nabla \tag{4}$$

following the interface points has been introduced.

Body and wake boundary conditions On the wing boundary $\partial\Omega_B$ the standard impermeability constraint applies

$$\frac{\partial\varphi_1}{\partial n} = -\boldsymbol{U}_\infty\cdot\boldsymbol{n} \qquad \forall \boldsymbol{P} \in \partial\Omega_B \,. \tag{5}$$

Moreover, as for the case of the interface model, it is expedient to describe the evolution of the wake in terms of particle evolution equations. This can be accomplished by exploiting the mass and momentum conservation which require the continuity both of the normal velocity component and of the pressure across $\partial\Omega_W$, [8]. In particular, once the velocity $\boldsymbol{v}$ of the wake points is defined as the mean value $\frac{1}{2}(\boldsymbol{u}_1^+ + \boldsymbol{u}_1^-)$ of the fluid velocity on the two sides '+' and '−' of $\partial\Omega_W$, the kinematic and dynamic evolution of the wake is ruled by

$$\begin{cases} \dfrac{D_W\boldsymbol{P}}{Dt} = \dfrac{1}{2}(\boldsymbol{u}_1^+ + \boldsymbol{u}_1^-) \\ \dfrac{D_W\Delta\varphi_1}{Dt} = 0 \end{cases} , \tag{6}$$

where $\frac{D_W}{Dt} := \frac{\partial}{\partial t} + \boldsymbol{v}\cdot\nabla$ and the constancy of the potential jump $\Delta\varphi_1 := \varphi_1^+ - \varphi_1^-$ follows from the Bernoulli equation when written on the two sides of the wake.

An iterative method of solution The flow about a wing close to an interface can be described as two problems for the Laplace equation coupled *via* the interface conditions (3). The potential φ_1 in the fluid surrounding the wing must also satisfy the body boundary condition (5) and the wake equations (6). A procedure is now described to solve the unsteady nonlinear problem. Suppose that for $t = t_0$ the interface and wake geometries are known, as well as the distribution of $\Delta\varphi_1$ on $\partial\Omega_W$. Then

1. starting from the known boundary data $\frac{\partial\varphi_2}{\partial n}$ on the interface and $\frac{\partial\varphi_1}{\partial n}$ on the body we can solve the problem

$$\begin{cases} \nabla^2\varphi_1 = 0 & \forall \boldsymbol{P} \in \Omega_1 \\ \dfrac{\partial\varphi_1}{\partial n} = g_1 & \forall \boldsymbol{P} \in \partial\Omega_B \\ \dfrac{\partial\varphi_1}{\partial n} = g_2 & \forall \boldsymbol{P} \in \partial\Omega_{I\!F} \end{cases}$$

   where the Neuman boundary condition at the interface follows from the kinematic condition $\boldsymbol{u}_1\cdot\boldsymbol{n} = \boldsymbol{u}_2\cdot\boldsymbol{n}$ discussed above.

2. Once the field φ_1 is known at the interface, the right hand side of the dynamic equations in (3) can be evaluated and stepwise integrated to obtain a new guess for the boundary data φ_2 on $\partial\Omega_{I\!F}$.

3. The problem

$$\begin{cases} \nabla^2\varphi_2 = 0 & \forall \boldsymbol{P} \in \Omega_2 \\ \varphi_2 = f & \forall \boldsymbol{P} \in \partial\Omega_{I\!F} \end{cases}$$

   in the lower domain is then solved, and a new distribution of $\frac{\partial\varphi_2}{\partial n}$ on $\partial\Omega_{I\!F}$ can be evaluated.

4. Steps 1–3 are repeated until convergence is reached, after that

5. The geometry of the interface and the wake are updated in time.

6. Go to step 1 for a new time–step.

When dealing with free boundary flows, it is expedient to recast the problem in term of boundary integral equations; this can be accomplished both for free surface problems [9] and for the inviscid–rotational aerodynamics [10]. On this ground, the two boundary value problems (step 1 and 3 above) can be solved by introducing suitable integral representations for the potentials φ_i. It is to be stressed that the presence of moving boundaries, $\partial\Omega_{\mathcal{IF}}$ and $\partial\Omega_{\mathcal{W}}$ and $\partial\Omega_{\mathcal{B}}$, gives to the problem a strong nonlinear character which, in turn, implies a huge computational effort to solve the relevant boundary integral equations at each time step. In the present paper, we have decided to solve some linearized test cases to preliminary verify the effectiveness of the proposed iterative procedure and to gain some confidence with the physical problem. Therefore, in the following sections the nonlinear problem is simplified by assuming small wave heights and by transfering the interface boundary conditions on the $z = 0$ plane. This allows for solving the two boundary value problems once and for all.

2.1 The linearized steady problem

The fully nonlinear problem can be simplified by following a standard procedure and assuming steady flow conditions. In this case, the flow is described by the aerodynamic problem

$$\begin{cases} \nabla^2\varphi_1 = 0 & \forall \boldsymbol{P} \in \Omega_1 \\ \dfrac{\partial\varphi_1}{\partial n} = -\boldsymbol{U}_\infty \cdot \boldsymbol{n} & \forall \boldsymbol{P} \in \partial\Omega_{\mathcal{B}} \\ \text{Wake \& Kutta Conditions} & \\ \dfrac{\partial\varphi_1}{\partial n} = \dfrac{\partial\varphi_2}{\partial n} & \forall \boldsymbol{P} \in \partial\Omega_{\mathcal{IF}} \end{cases}$$

coupled to the hydrodynamic one

$$\begin{cases} \nabla^2\varphi_2 = 0 & \forall \boldsymbol{P} \in \Omega_2 \\ \dfrac{\partial^2\varphi_2}{\partial x^2} + \dfrac{g}{U_\infty^2}\dfrac{\partial\varphi_2}{\partial z} = \dfrac{\rho_1}{\rho_2}\left\{\dfrac{\partial^2\varphi_1}{\partial x^2} + \dfrac{g}{U_\infty^2}\dfrac{\partial\varphi_1}{\partial z}\right\} & \forall \boldsymbol{P} \in \partial\Omega_{\mathcal{IF}} \end{cases}$$

It is interesting to note that the first boundary value problem describes the flow of a wing moving close to a porous soil with flux $\frac{\partial\varphi_2}{\partial n}$. The motion of the body alters the pressure distribution acting on the interface and, in fact, the hydrodynamic problem can be seen as the linearized steady wave resistance problem of a pressure disturbance advancing with velocity $-\boldsymbol{U}_\infty$ on a free surface. For this problem, a Fourier-Stjeltes representation of the solution is given, for example, in [11]. Therefore, only the aerodynamic problem has to be solved numerically and the iterative procedure is greatly simplified. More specifically, once a tentative solution for φ_1 is known, the right hand side of the Neumann–Kelvin condition can be computed and a new guess φ_2 is explicitely evaluated. In a refined scheme, an iterative procedure for taking into account the nonlinearities due to the wake is easily introduced (see for example [12], [13] for details). The convergence of the whole procedure is usually obtained in few iterations and some sample results are given below.

2.2 The linearized time–harmonic problem

Here we introduce the governing equations for the case when the wing is free to oscillate under the exciting action of an incident regular wave with frequency ω_0 and amplitude A. The problem is linearized under the hypothesis of small wave amplitude and small body motions. Further, neglecting the initial transient, a time harmonic dependance of the solution is assumed. Hence the total potentials in the two flow domains ($l = 1, 2$) can be expressed in the form

$$\varphi_l(\boldsymbol{P}, t) = \Re\left\{ e^{\mathrm{i}\,\omega\,t}\left[A\,(\varphi_{l_0} + \varphi_{l_7}) + \sum_{j=1}^{6}\xi_j\,\varphi_{l_j}\right]\right\}$$

where φ_{l_0} is the potential of the incident wave and φ_{l_7} is the scattering potential generated when the wing is restrained to move. In the absence of incident wave, $\xi_j\varphi_{l_j}$ is the radiation potential due to the body oscillation in the j–th degree of freedom with amplitude ξ_j. So far, it is possible to define a *radiation problem*

$$\begin{cases} \nabla^2\varphi_{1_j} = 0 & \forall \boldsymbol{P} \in \Omega_1 \\ \dfrac{\partial\varphi_{1_j}}{\partial n} = \mathrm{i}\omega n_j + m_j & \forall \boldsymbol{P} \in \partial\Omega_{\mathcal{B}} \\ \text{Wake \& Kutta Conditions} & \\ \dfrac{\partial\varphi_{1_j}}{\partial n} = \dfrac{\partial\varphi_{2_j}}{\partial n} & \forall \boldsymbol{P} \in \partial\Omega_{\mathcal{IF}} \end{cases}$$

$$\begin{cases} \nabla^2\varphi_{2_j} = 0 & \forall \boldsymbol{P} \in \Omega_2 \\ (\mathrm{i}\omega + \boldsymbol{U}_\infty \cdot \nabla)^2\varphi_{2_j} + g\dfrac{\partial\varphi_{2_j}}{\partial z} = \dfrac{\rho_1}{\rho_2}\mathcal{NK}_\omega(\varphi_{1_j}) & \forall \boldsymbol{P} \in \partial\Omega_{\mathcal{IF}} \end{cases}$$

where j is equal 1...6, and a *diffraction problem*

$$\begin{cases} \nabla^2\varphi_{1_7} = 0 & \forall \boldsymbol{P} \in \Omega_1 \\ \dfrac{\partial\varphi_{1_7}}{\partial n} = -\dfrac{\partial\varphi_{1_0}}{\partial n} & \forall \boldsymbol{P} \in \partial\Omega_{\mathcal{B}} \\ \text{Wake \& Kutta Conditions} & \\ \dfrac{\partial\varphi_{1_7}}{\partial n} = \dfrac{\partial\varphi_{2_7}}{\partial n} & \forall \boldsymbol{P} \in \partial\Omega_{\mathcal{IF}} \end{cases}$$

$$\begin{cases} \nabla^2\varphi_{2_7} = 0 & \forall \boldsymbol{P} \in \Omega_2 \\ (\mathrm{i}\omega + \boldsymbol{U}_\infty \cdot \nabla)^2\varphi_{2_7} + g\dfrac{\partial\varphi_{2_7}}{\partial z} = \dfrac{\rho_1}{\rho_2}\mathcal{NK}_\omega(\varphi_{1_7}) & \forall \boldsymbol{P} \in \partial\Omega_{\mathcal{IF}} \end{cases}$$

where

$$\begin{cases} \varphi_{l_0} = \mp\dfrac{\mathrm{i}\,\omega\,A}{|\boldsymbol{k}|}\,e^{\mp|\boldsymbol{k}|\,z}\,e^{\mathrm{i}\,\boldsymbol{k}\cdot\boldsymbol{x}}, \quad l = 1, 2 \\ |\boldsymbol{k}| = \dfrac{\omega^2}{g}\left(\dfrac{\rho_2 - \rho_1}{\rho_1 + \rho_2}\right) \end{cases}$$

is the potential of the incident interfacial wave and $\mathcal{NK}_\omega := (\mathrm{i}\omega + \boldsymbol{U}_\infty \cdot \nabla)^2 + g\frac{\partial}{\partial z}$. In the radiation problem the generalized n_j components and the celebrated m_j are introduced

following [14]. Each one of the above problems can be seen as an aerodynamic problem coupled to a hydrodynamic one in which the wavy motion of the free surface is forced by an oscillating pressure disturbance acting on $\partial\Omega_{\mathcal{IF}}$. Also in this case, a Fourier representation of the solution of the hydrodynamic problem [11] can be used in the iterative solution of the problem, thus significantly reducing the computational effort.

3. Numerical results

3.1 Integral representation of the solution

The velocity potential in the upper domain is represented as

$$\varphi_1 = \int_{\partial\Omega_B} \sigma G dS + \int_{\partial\Omega_{\mathcal{IF}}} \sigma G dS + \int_{\partial\Omega_W} \mu \frac{\partial G}{\partial n} dS \quad (7)$$

that is as a sum of simple layer potentials generated by a source distribution on $\partial\Omega_B \cup \partial\Omega_{\mathcal{IF}}$ and a dipole sheet which mimics the rotational wake $\partial\Omega_W$. In solving the aerodynamic problem the velocity field

$$\begin{aligned} \nabla\varphi_1 &= \nabla \int_{\partial\Omega_B} \sigma G \, dS + \nabla \int_{\partial\Omega_{\mathcal{IF}}} \sigma G \, dS \\ &+ \nabla \times \int_{\partial\Omega_W} \gamma G \, dS \end{aligned} \quad (8)$$

is also required. In particular, in (8) the velocity induced by the wake is re-expressed in the form of a Biot–Savart integral which enables the use of a simple vortex–lattice technique [10] for discretizing the wake. A standard zero–order panel method [15] has been employed for the source integrals.

In the framework of the described iterative solution, formulas (7,8) are used to solve the aerodynamic problem in term of boundary integral equations. Namely, a first integral equation is obtained by taking the normal projection of (8) written for the points belonging to the wing, where the normal velocity component is known from the impermeability constraint. A second integral equation is obtained for $\boldsymbol{P} \in \partial\Omega_{\mathcal{IF}}$, where $\frac{\partial\varphi_2}{\partial n}$ is given.

For the linearized problems discussed in the following, the system of algebraic equations obtained by discretizing the integral equations are solved once and for all at the beginning of the iterative procedure. In the computations a typical number of panels per wavelength is 80, the wing is usually discretized by a network of 12×6 panels and simmetry with respect to the stream direction is enforced. Usually the discretized free surface in the streamwise direction is of the order of the wavelength, while the lateral extension is of several chord–lengths. Typical computational domains can be qualitatively appreciated in the wave–pattern contours shown below.

3.2 The linearized steady problem

In the following we discuss some results concerning the flow generated by a flat plate at incidence α flying at an altitude h above the undisturbed mean water level $z = 0$. In all the cases presented below a unity span–to–chord ratio of the wing is considered. The vortex shedding is modeled both from the trailing edge and from the tips. No attempt to model more effective lifting devices (tapered swept back wing, endplates or canard configurations) is discussed, and this type of analysis is left to a future activity.

As a first problem we consider the case of forward motion with constant velocity over initially calm water.

The wave patter generated for $Fr = U_\infty/\sqrt{gc} = 5.$ can be seen in figure 2, where the wing planform is also indicated by the thin square for a better understanding. As it can be expected, the wave system is highly swept back; along the x–axis, just past the wing, a narrow depression can be detected which is accompained, on the two sides, by two larger humps. Starting from the central depression, the water level rises gently forming a V-shaped pattern which is downstream followed by a positive wave elevation. Although a relatively small portion of the entire flowfield is contained in the computational domain, some convergence tests (not reported) obtained by increasing the domain length ensure that both the wave pattern and the forces acting on the plate are well converged.

The latter are discussud by considering the figures 3-4. The first one shows the effect of varying the clearance h/c on the lift C_L and on the drag C_D coefficients for different angles of attack α of the flat plate. In particular, as h/c decreases the lift increases as well as the drag coefficient does. Actually the efficiency of the wing (lift to drag ratio) does not increases significantly: this is consistent with the analysis in [2], where it is shown that only the inclusion of endplates significantly enhances the performances.

Morever, at least within the context of the present linearized analysis, the free surface effects appears to be negligeable. The figure 4, in fact, shows that the aerodynamic forces acting on the plate in ground effect (dashed lines) are undistinguisheable from the ones obtained by including the effect of the free surface (symbols).

3.3 The linearized time–harmonic problem

For obvious safety reasons, the seakeeping performances of a marine vehicles is of main concern. Although we cannot discuss the dynamic behaviour of a WISES (a more realistic arragement of lifting surfaces should be considered), it seems of some interest to analyze the influence of incoming waves on the aerodynamic loading, which in turn is relevant for the design of control system. According to what discussed in §2.2, the problem is linearized by assuming small motions and it is assumed that the phenomenon has reached a steady harmonic regime. In this case the forced motion of a wing running over a calm water can be studied separately from problem of the interaction of incoming waves with a wing in steady forward motion.

We consider the case of a flat plate running at a mean altitude $h/c = 0.15$, with nondimensional velocity $Fr = 5.0$. For simplicity, a zero mean angle of attack is assumed and only the motion in head sea is considered.

Figure 5 shows the wave patterns. More precisely in the upper and center plots the wave systems as generated during heave and pitch oscillations is reported, while in the third plot the scattering wave system, that is the contribution to the wave heigth related to φ_{l_7}, is shown.

The corresponding aerodynamic loads are described in the following figures. In particular, as it is customary in naval hydrodyamics, the load due to the forced motions of the wing is expressed in term of its real and imaginary parts

$$a_{kj} = -\frac{\rho_1}{\omega^2} \Re \left\{ \int_{\partial\Omega_{\overline{B}}} [i\omega + \boldsymbol{U}_\infty \cdot \nabla] \varphi_j \, n_k \, dS \right\}$$

$$b_{kj} = \frac{\rho_1}{\omega} \Im \left\{ \int_{\partial\Omega_{\overline{B}}} [i\omega + \boldsymbol{U}_\infty \cdot \nabla] \varphi_j \, n_k \, dS \right\}$$

where $k, j = 1...6$, that is by means of the added mass and

the damping coefficients. For the considered Froude number, the behaviour of the force coefficients when varying the frequency of oscillation is shown in figure 6.

Finally, the amplitude and the phase of the exciting force

$$X_k = -\rho_1 A \int_{\partial\Omega_B} [i\omega + \boldsymbol{U}_\infty \cdot \nabla](\varphi_0 + \varphi_7)\, n_i\, dS$$

induced in the two considered degrees of freedom ($k = 3, 5$) are plotted in figure 7.

4. Conclusions

In this paper a mathematical model to describe the unsteady flow about a wing moving in proximity of the air–water interface is presented. When viscous effects in water and air are neglected, as well as the air compressibility, velocity potentials in the two fluid can be introduced. In the general case, the flow is described in term of two initial boundary value problems for the Laplace equation coupled through the conditions at the interface. An interative provedure to solve the resulting nonlinear problem is proposed.

Preliminary numerical results are given for some simplyfied special cases. The steady flow generated by a flat plate running over initially calm water is studied at first. Results for moderately high Froude numbers show the limited role of free surface in affecting the aerodynamic forces which, ultimately, coincide with those predicted by considering a pure ground effect. The results qualitatively agree with previously developed analysis.

The interaction of the wing with a system of regular waves is then addressed by assuming a time harmonic behaviour of the solution for the linearized problem. Wave patterns and force coefficients are presented but, to our knowledge, reference results are not available. On this very preliminary ground, a marginal role of wave effects seems to emerge also in this case.

An obvious explanation is in the small radiation properties of a wing at high speed. It is also to be stressed that only linearized problems have been presently solved and significant nonlinear corrections could appear when considering the fully nonlinear problem. In particular, during transient regimes, very small clearances and relatively reduced speeds could be possible and a fully nonlinear analysis, presently under development, is of concern.

Acknowledgements

The research was supported by Ministry of Transport and Navigation through INSEAN Research Program 1994–96.

References

[1] ROZHDESTVENSKY K. State of the art and perspectives of development of Ekranoplans in Russia. *Proceedings of FAST '93*. 1993

[2] STANDINGFORD D.W. & TUCK E.O. Lifting surfaces in ground effect *Workshop proceedings of Ekranoplans & Very Fast Craft*, Sydney, 5-6 December 1996.

[3] ROZHDESTVENSKY K. Nonlinear aerodynamics of Ekranoplans in strong ground effect *Proceedings of FAST '95*. 1995

[4] MILOH T., TULIN M.P., A theory od dead water phenomena. *Proc. of the 17th Symp. on Nav. Hydro.*, 1988.

[5] TULIN M.P.,MILOH T., Ship internal waves in ashallow termocline: the supersonic case. *Proc. of the 18th Symp. on Nav. Hydro.*, 1990.

[6] WU G.X.,MILOH T., *J. of Ship Res.*, 1997.

[7] GRUNDY I.H. Airfoils moving in air close to a dynamic water surface *J. Austral. Math. Soc. Ser. B* 27, 1986.

[8] FRIEDRICHS, K. O. Special Topics in Fluid Mechanics New York, Gordon and Breach, 1966.

[9] BASSANINI P., BULGARELLI U., CAMPANA E., LALLI F., The Wave Resistance Problem in a Boundary Integral Formulation, *Surv. Math. Ind.*, 4, 151–194, 1994.

[10] ROM J., *High angle of attack Aerodynamics* Springer Verlag, New York, 1992.

[11] WEHAUSEN, J.V., AND LAITONE, E.V. , Surface Waves. In *Handbuck der Physik*, n. 9, 1960.

[12] LANDRINI M., CASCIOLA C.M., COPPOLA C., A Nonlinear Hydrodynamic Model for Ship Maneuverability, *Proceedings of International Conference on Marine Simulation and Ship Manoeuvrability (MARSIM '93)*, St. John's (Newfoundland–Canada), 1993.

[13] LANDRINI M., CAMPANA E.F., Steady waves and forces about a yawing flat plate. *J. of Ship Res.*, Vol. 40, No. 3, 1996.

[14] TIMMAN, R, AND NEWMAN, J.N. , The coupled damping coefficients of symmetric ships. *J. of Ship Res.*, n. 5, 1962.

[15] HESS J.L., SMITH A., Calculation of Potential Flows around Arbitrary Bodies, *Prog. Aer. Sci.*, n.8, 1966.

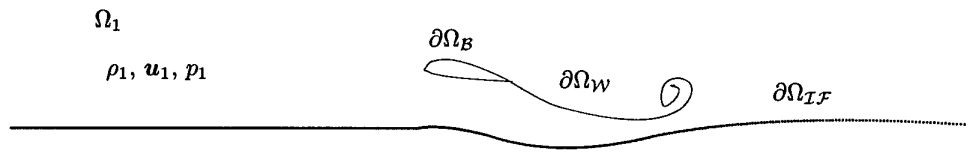


Figure 1: Sketch of the problem and of the relevant nomenclature

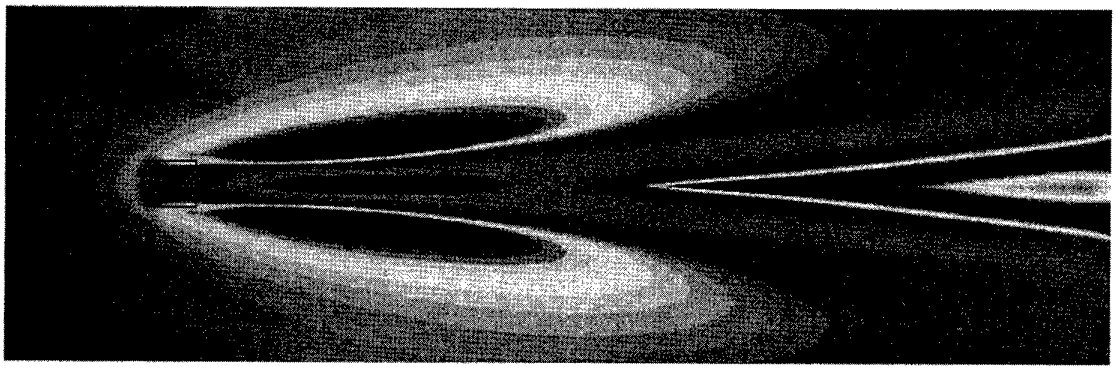


Figure 2: Wave pattern generated by a flat plate in steady forward motion. $AR = 1.0$, $Fr = 5.0$, $h/c = 0.15$ and $\alpha = 5$ degrees

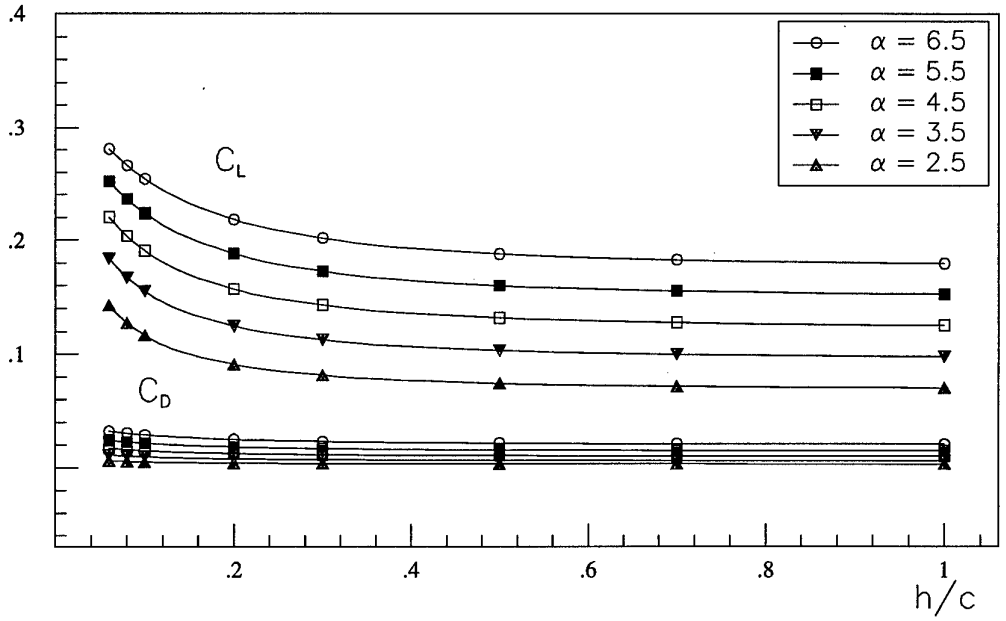


Figure 3: Lift and drag coefficients for a flat plate (AR=1) in steady forward motion ($Fr = 0.5$): effect of the incidence α and of the distance h/c from the water surface.

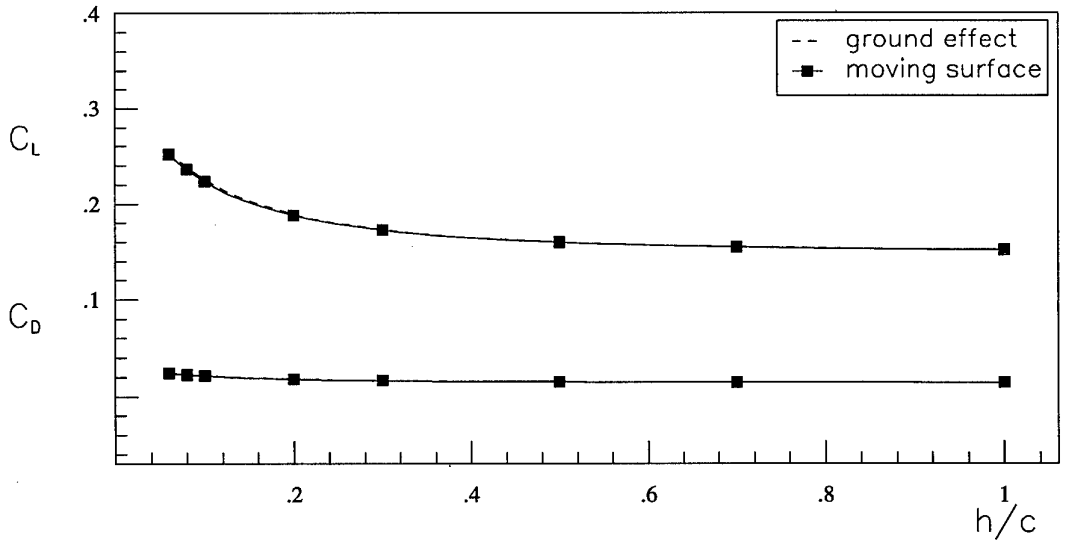


Figure 4: Comparison of lift and drag coefficients for a flat plate (AR=1) in steady forward motion ($Fr = 0.5$, $\alpha = 5$) in surface effect (symbols) and in ground effect (dashed lines).

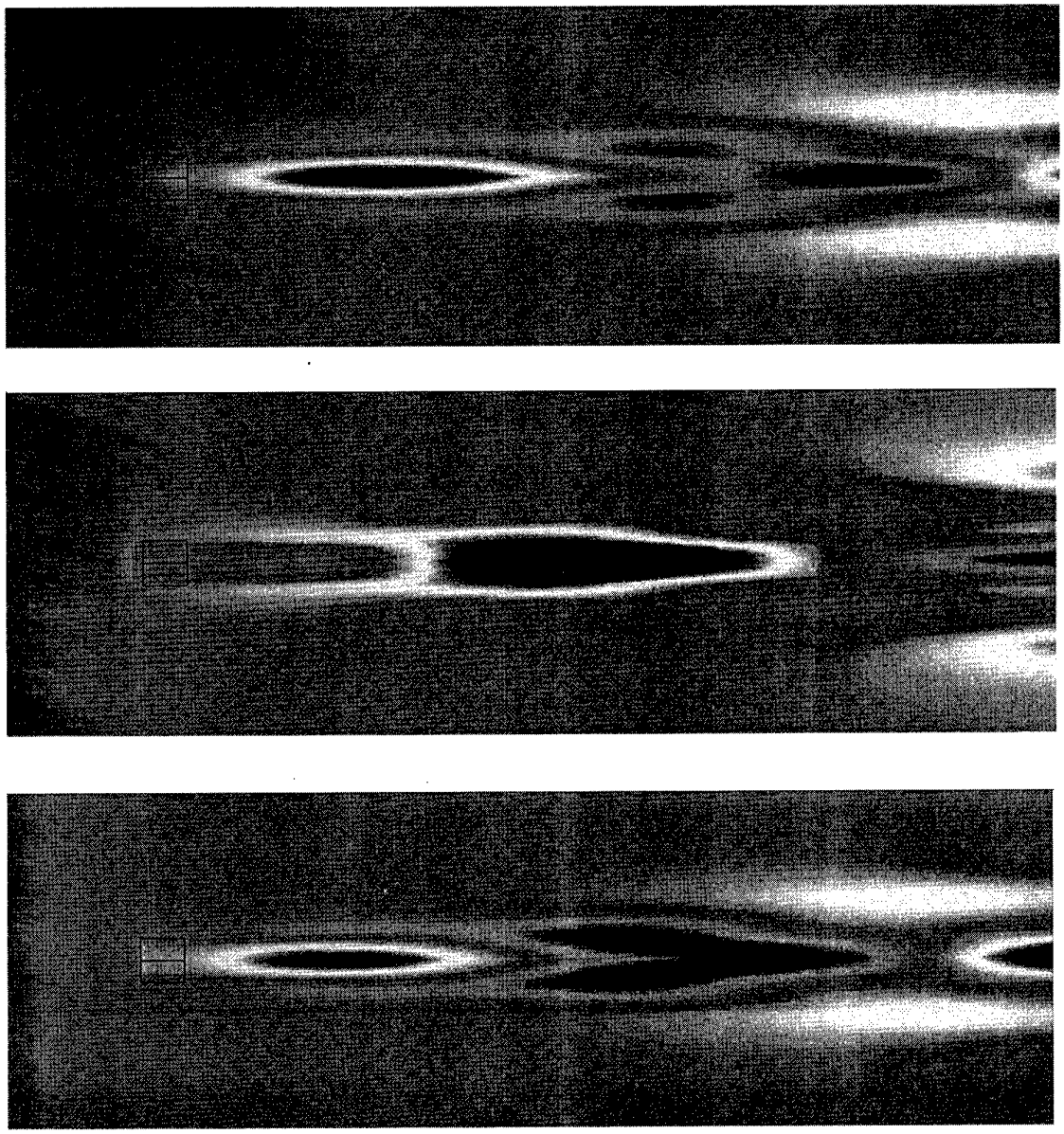


Figure 5: Wave pattern generated by a flat plate, $AR = 1$, in heave motion (top figure) in pitch motion (center plot) and scattering wave pattern (bottom figure) in head waves, $\omega_0/\sqrt{g/c} = 0.547$ ($Fr = 5.0$, $h/c = 0.15$).

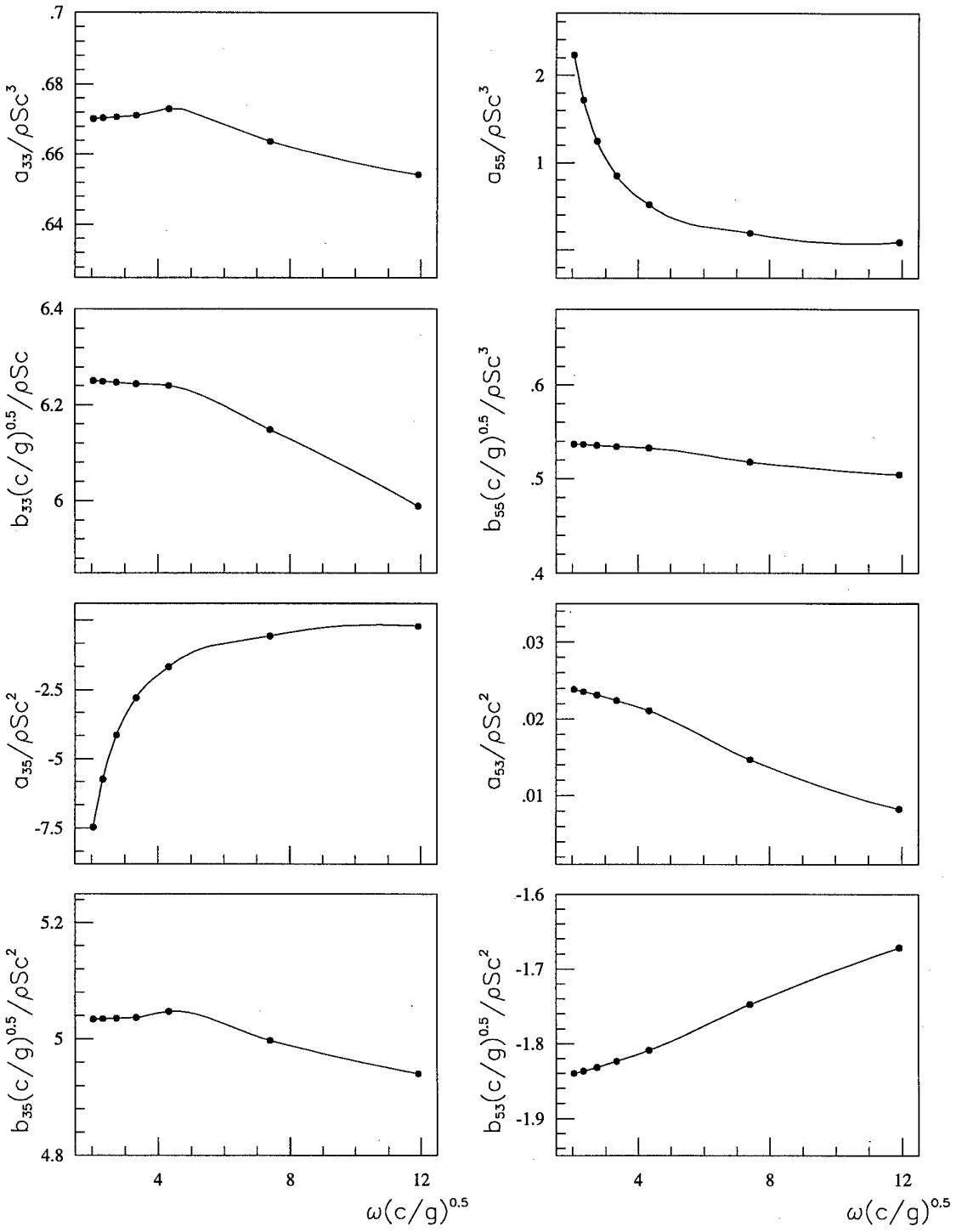


Figure 6: Added mass, a_{ij}, and damping, b_{ij}, coefficients for heave ($i, j = 3$) and pitch ($i, j = 5$) as a function of the frequency ω.

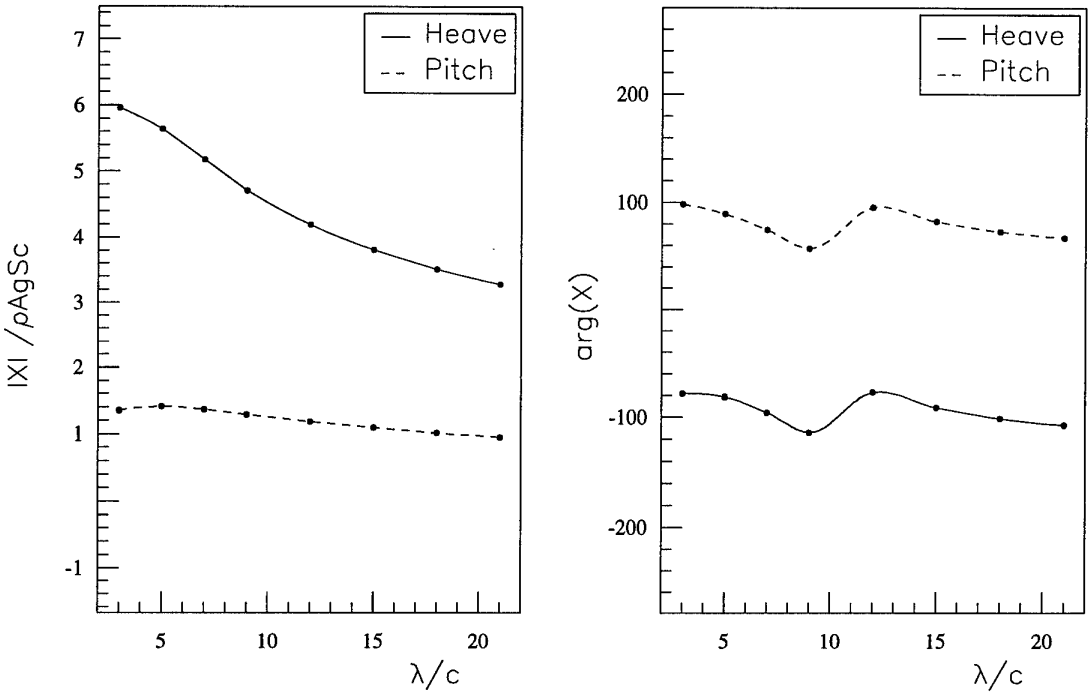


Figure 7: Amplitude and phase of the exciting force acting on a flat plate in steady forward motion in head waves.

ABOUT MOVEMENT OF A WING ABOVE WAVY SURFACE OF WATER

V.G. Belynsky

Institute of a Hydromechanics
8/4 Zheliabov Street, Kiev, 252057 Ukraine

SUMMARY

In work the outcomes of an experimental research hydrodynamical characteristics of a wing driven above wavy screen are represented the description of experimental installation and techniques of realization of experiment is given. The instantaneous significances of a lift coefficient for wings of the rectangular form in the plan, various elongations driven with various angles of attack on various distances from a flat screen and a screen, consisting of waves of sinusoidal structure of various length and height, are determined. The dependence of a lift coefficient of a wing form Strouhal number for movement above a wave screen is established. Is shown, that there is additional, not known earlier, a gain of lift of a wing stipulated by the wavy form of a surface of water. The efficiency of a flap near to a screen is appreciated.

LIST of SYMBOLS

C_y - lift coefficient of wing
$C_y\beta$ - lift coefficient of wing with flap
K - coefficient of hydrodynamic quality
b - chord of wing
ℓ - span of wing
λ - elongation of wing
Θ - angle of attack of wing in degrees
β - angle of deviation of flap in degrees
v - velocity of wing
h - distance from trailing edge of wing up to screen
λ_b - wavelength of wave screen
H_b - height of wave of wavy screen
ω - circular frequency of wave of screen
P^* - Strouhal number
φ - phase angle of wave of screen
a_k и b_k - coefficients of Fourier series
ζ_y - efficiency of flap on lift

1. INTRODUCTION

Per the last decades the interest to creation of large transport ships engaging an intermediate position between airplanes and high-speed ships, driven above surface of water, was worldwide exhibited. It, so-called, "wing-in-surface effect craft" (ekranoplane) , intended for movement with a large velocity in air medium in immediate proximity from a water surface and using positive influence of this proximity to lift of the bearing surfaces. The plenty theoretical and experimental researches devoted development of various aspects of creation ekranoplanes was lately conducted. Numerous experimental samples ekranoplanes also were created, which tests in full-scale conditions have confirmed, in general, determined viability of idea of creation of such means of transport.
Broad application in practice all of them have not received yet, the interest to their creation periodically is exhibited again and again. The good review of work& on this problem is contained in work& [1,2]. In the present work the experimental outcomes relating the least investigated part a problems - to definitionof influence of performances of disturbance of a water surface (of a wave screen) are represented, above which is gone ekranoplane, on aerodynamic performances it of bearing surfaces - wings. One experimental work on movement of a wing above a wave screen [3] is known only to us. However, in this work one special case of movement of a wing above waves only one length and height is investigated only, that has not allowed to receive informations about influence of rather broad spectrum of performances of a wave screen on hydrodynamic characteristics of a wing, driven above a him. In the given work this defect in some measure is filled.

Paper presented at an AGARD FDP Workshop on "High Speed Body Motion in Water", held in Kiev, Ukraine, 1-3 September 1997, and published in R-827.

2. TECHNIQUE of EXPEREMENT

Experimentally aerodynamic characteristics of a wing near to a screen are usually investigated in aerodynamic tunnels in conditions of conversion movement, when a fixed wing meet a stream of air. Such condition of experiment stipulate the certain violation of boundary conditions in relation to horizontal velocities on a screen, that results in appropriate errors.

The violation of boundary conditions has an effect for a surface of a screen especially for want of movement of a wing on small distance from a flat screen and for want of movement above a wave screen, that represents the special interest in the present work. The given research was conducted in conditions of direct movement, when the wing moved above a fixed screen in a fixed medium, that has allowed to execute boundary conditions on a screen and has supplied a rather low degree of a turbulence filling on a wing of a stream. Besides the movement of a wing in an air medium was replaced by movement of a wing in a water medium, and liquid flat or wave screen, above which is gone full-scale ekranoplane is replaced in experiment by a rigid flat and wave screen. By other words, was applied hydrodynamic method of a research of problems of aerodynamics [4]. A replacement of an air medium in experiment by a water medium is possible, as in conditions of the given research the effects of a compressibility can be neglected.

Such replacement is expedient, as allows in experiments to receive rather large forces which are being a subject to a measurement, that increases an exactitude of measurements, and to reach rather large Reynold's numbers(order 2 10^6) for want of rather small velocities of towage of wings (order 5 ÷ 6 м/сек). The replacement of a liquid screen rigid is in this case possible, as tests of wings be ordered for want of large Froude numbers (order 4,0), which for want of perturbations called by movement of a wing, the surfaces of a screen on considerable a distance behind a wing reach and outcomes of experiment do not influence.

3. EXPERIMENTAL INSTALLATION

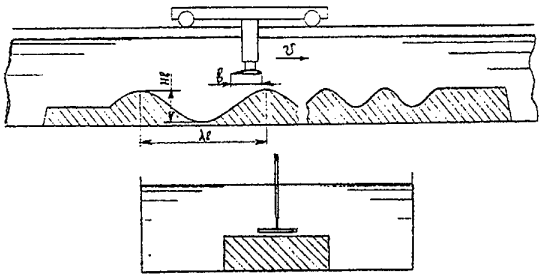


Fig. 1

The experimental installation (Fig. 1) consist from hydrodynamic channel suffices large length (140,0 m), which at the bottom was builded a underwater rigid screen consisting of two plots flat and five plots of the wavy form. The wavy plots consist of separate groups of sinusoidal waves of various length and height. The wave plots were located so, that the crests of all waves were oriented perpendicularly axeses of the channel and were at one horizontal level. Before wavy screen at a level of centerline of the first group of waves located the first flat screen, and in an extremity of a wave screen at a level of crests of waves the second flat screen was located. Above the channel moved the towing carriage supplied with a vertical hydrodynamic knife of variable height, with the tested wing fastened to his extremity. A screen and wing placed in the channel on sufficient depth so, that the influence of a free surface of water was excluded. All tested wings were of the rectangular form in the plan and had an identical structure with a relative thickness 6 % and chord b = 250 mm. The wings of various elongations were tested $\lambda = \ell / b$ from λ = 0,5 up to λ = 5,0, where ℓ span of wing. Length of flat plots of a screen made 24 b, and length of waves of a wave screen λ_b was changed in limits from λ_b =20 b up to $\lambda_b = b$. Height of waves of a screen H_b on different wave plots was equal from $H_b = \lambda_b /20$

for rather long waves up to $H_b = \lambda_b$ for rather short waves. The position of a wing concerning a screen was characterized relative distance $\bar{h} = h/b$, where h - distance from a back edge of a wing up to a screen. Thus, the constructed screen, which general length 70 м, represented a peculiar polygon, on which, driven above a him from a constant velocity and at given height, the wing runing by the towing carriage passed sequentially above two flat plots located at different height, and above a number of groups of waves, each of which had distinct from other characteristics. Besides for each want of the towing carriage on plots of the channel before a screen and after it the wing moved actually in conditions of a boundless liquid, that allowed effectively to inspect outcomes of experiment. For want of passing of a wing above a wave screen the range of Strouhal numbers was enveloped

$$P^* = \frac{\omega \cdot b}{v} = \frac{2\pi \cdot b}{\lambda_b} = 0{,}314 \div 6{,}28$$

Where ω - circular frequency of waves of a screen, v - a velocity of a wing. For want of tests the instantaneous significances of a body force of a wing, resistance and longitudinal moment of a wing concerning it of a leading edge were measured. The results were represented as appropriate dimensionless coefficients C_y, C_x, C_{mz} in the standard form.

4. TEST of WINGS ABOVE FLAT SCREEN

In the given work are represented in main results for a wing above a wave screen. However, first two Figures concern to movement of a wing above a flat screen. First from them (Fig. 2) gives general submission about obtained results as the settlement diagram " $\bar{K} - \bar{C}_y$ " for a wing with lengthening(elongation) $\lambda = 3$, driven above a flat screen. The diagram is constructed in coordinates

$$\bar{C}_y = \frac{C_{y\bar{h}}}{C_{y\infty}} \quad , \bar{K} = \frac{K_{\bar{h}}}{K_\infty}$$

Where $C_{y\bar{h}}$ and $C_{y\infty}$ - accordingly lift coefficients near to a screen on distance $\bar{h}$ and in a boundless liquid; K_∞ and $K_{\bar{h}}$ - accordingly factors of hydrodynamic quality in a boundless liquid and near to a screen on distance h. On the diagram a series of a curve constant of significances relative distance from a screen $\bar{h}$ = const (solid lines) and series of a curve constant of significances of angles of attack of a wing Θ = const (dashed lines) is put. Under this diagram on known significances $C_{y\infty}$ And K_∞ it is possible to determine $C_{y\bar{h}}$ and $K_{\bar{h}}$ for the tested wing (precisely) and for a wing, close on the form, that elongation (approximately) for specific significances $\bar{h}$ and Θ.

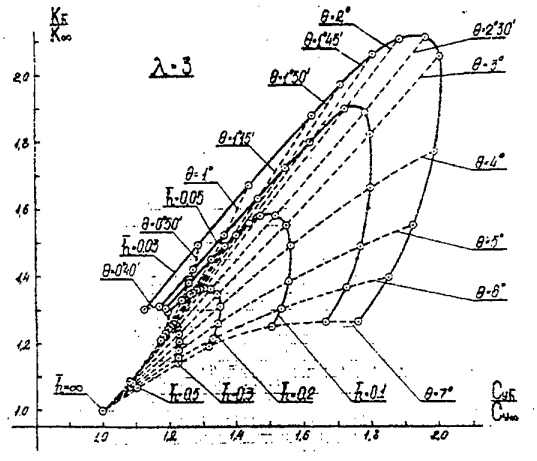


Fig. 2

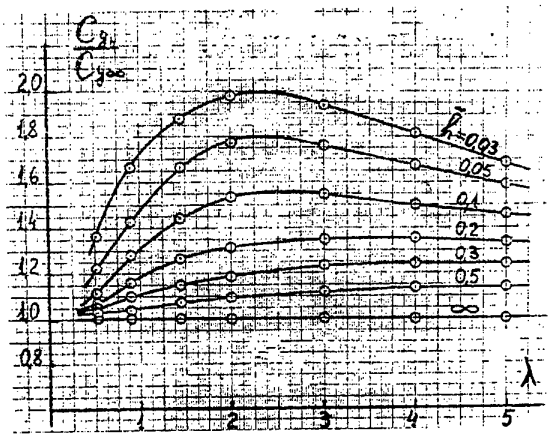


Fig. 3

The similar diagrams are constructed for wings of other elongations from $\lambda = 0{,}5$ up to $\lambda = 5{,}0$, however in this work they are not represented. On the other graph relating to flat screen (Fig. 3), are put curve $\bar{C}_y = C_{y\bar{h}} / C_{y\infty}$ depending on elongation of a wing λ for a constant of significances relative distance from a screen $\bar{h}$ for want of fixed angle of attack. This graph contains that interesting result, that for want on small distance from a screen ($\bar{h} < 0{,}2$) magnitudes $\bar{C}_y$ has the maxima between significances $\lambda = 2$ and $\lambda = 3$. Therefore, from the point of view of the greatest lift perspective for application on ekranoplanes the wings with elongations $\lambda = 2 \div 3$ are.

Taking into account this circumstance, the main information content about movement of a wing above a wavescreen in the present work was obtained for wings with elongation $\lambda = 2$ and $\lambda = 3$. The wings with other elongations within the limits of $\lambda = 0{,}5 \div 5{,}0$ above a wave screen also were tested, but under the reduced program.

5. TEST of WINGS ABOVE a WAWY SCREEN

5.1 For want of consideration of results of experiments about movement of a wing above a wave screen the main attention in this work is given to a lift coefficient of a wing, as by major it to performance. The datas on drag coefficients and longitudinal moment here are not considered. Some submission about them can be received from work& [5,6,7].

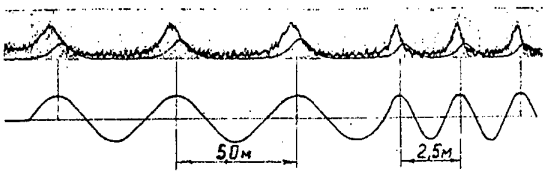


Fig. 4
On Fig. 4 the typical fragments of an oscillogram of a continuous entry in time of lift originating on a wing, driven on small distance above crests of waves of various length are represented. Appropriate plots of a wave screen are represented below. Each point curve on an oscillogram meets to instantaneous significance of lift in that moment, when the leading edge of a wing is above a point, appropriate on a vertical, of a wave screen. The analysis of oscillograms shows, that the sinusoidal form of a wave screen is answered with a unsinusoidal character of a time history of lift of a wing. The maximas of a curve of lift occur earlier, than the leading edge of a wing will pass above a peak level of a crest of a wave, and curves of lift are nonsymmetric concerning verticals which are taking place through their maximas. And, the left branch of a curve appropriate to an approximation of a wing to a crest of a wave, is more full on a comparison with the right branch appropriate to deleting of a wing from a crest of a wave. The marked regularities are fair in all cases, when the chord of a wing is less than a wavelength of a screen.

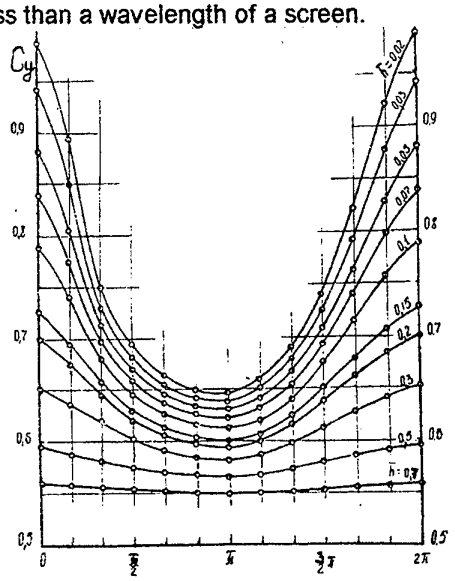


Fig. 5
5.2 All curves, obtained in experiment, of instantaneous significances of lift in a dimensionless kind were subjected to a Fourier analysis with selection average for period of significance of a lift coefficient and coefficients for first six harmonic of Fourier serieses

$$C_y(\varphi) \cong \frac{a_0}{2} + \sum_{K=1}^{6} a_k \cos K\varphi + \sum_{K=1}^{6} b_k \cdot \sin K\varphi$$

Where: φ - phase angle of a curve lift, $\frac{a_0}{2}$ - average for period significance of coefficient

C_y, C_y and b_k - coefficients of a Fourier series, which were determined under the Bessel formulas for an approximate Fourier analysis

. In a fig. 5 the curves of instantaneous significances of a lift coefficient for a wing with elongation λ = 3, driven above a wave screen with an angle of attack Θ = 7 ¨ for want of to wavelength of a screen λ_b = 6·b are represented, for an example. The curves are constructed for various distance from crests of waves depending on a phase angle φ for want of passing by a wing of a path from one crest (φ = 0) up to other (φ =π·2). In a fig. 6 the results of a Fourier analysis of these curve are represented, on which under the above indicated formula the curve of instantaneous significances C_y for anyone distance from a screen, only for datas of significances λ , Θ and λ_b can be restored.

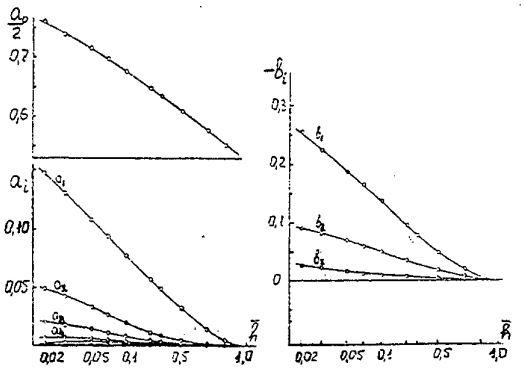


Fig. 6

5.3. We shall consider some features describing lift of a wing above a wave screen. In a fig. 7

the dependence is representedrelative lift coefficient $\bar{C}_{y\bar{h}} = \frac{C_{y\bar{h}}}{C_{y\infty}}$ from relative

distance up to crests of waves for a wing λ = 2 for want of angle of attack Θ = 3 ¨ 35 ' and wavelength of a scree λ_b= 20 · b. The following interesting results follow from consideration of these curve. Instantaneous significances $\bar{C}_{y\,\bar{h}}$ above crests of waves (curve " 1 ") exceed $\bar{C}_{y\,\bar{h}}$ significances, appropriate to them, for want of movement of a wing above a flat screen at a level of crests of waves (curve "2"). Characteristic just the incongruity of curves " 1 "and" 2 " here is, that is a corollary purely of dynamic effect connected to influence of a wavelength of a screen on lift of a wing. For want of more short waves, than in this case, the instantaneous significances above crests of waves can be of smaller significances, appropriate to them, of a wing above a simple screen at a level of crests of waves, that will be shown further. The special interest represents that detected experimentally fact, that average for period of significance of coefficient $\bar{C}_{y\,\bar{h}}$(curve "3") exceed significances, appropriate to them, of a wing above a flat screen at a level of centerline of waves of a screen (curve "4"). This remarkable fact with reference to ekranoplane means, that for want of flight at some small height above the wawy surface of the sea some increment of lift on a comparison with flight at same height, but above a undisturbed surface of the sea will be derivated.

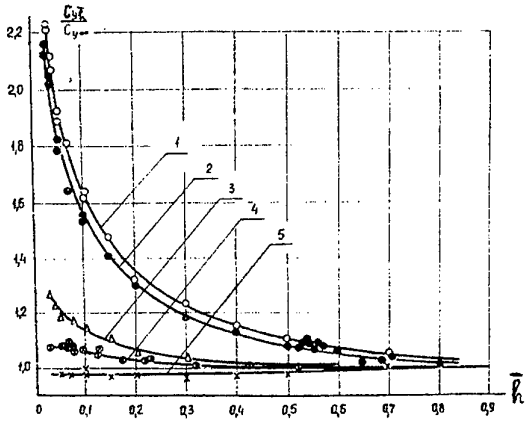


Fig. 7

Significances of coefficient $\bar{C}_{y\,\bar{h}}$ above a wave hollow (the curve " 5 ") in this case differs from unit a little. It is connected that height of a wave on magnitude was equal the given experiment to a chord of a wing and, therefore, relative отстояние from a trailing edge of a wing up to a wave hollow was more unit, that equivalently to movement in a boundless liquid, for want of which $\bar{C}_{y\,\bar{h}}$ = 1. In case of movement above waves with smaller height, when relative distance from a trailing edge of a wing up to a wave hollow will be less unit, the curve "5"

can place above than significances equal to unit.

5.4. The large interest represents a research of influence of length and height of a wave of a wave screen on lift of a wing, driven above him. Obviously, that the lift of a wing should depend on a ratio between length of a chord of a wing, on the one hand, both length and height of a wave of a screen, on the other hand. As two extreme cases of such movement it is possible to present, for example, movement of a wing above a rather long wave, when chord of wing makes only small part of a wavelength of a screen, and the movement of a wing above rather short waves, when on length of a chord of a wing is equal to some lengths of waves of a screen.
Criterions of such movement are Strouhal Number and relative height of a wave

$$P^* = \frac{2\pi \cdot b}{\lambda_b} \quad , \quad \bar{H}_b = \frac{H_b}{\lambda_b}$$

Let's mark some characteristic cases from a range of Strouhal Numbers from zero to infinite, using Fig. 8, on which on an axes abscissas the Strouhal Numbers, and on an ordinate axis relative are placed lift coefficient, equal to the relation of a lift coefficient above a crest of a wave to a lift coefficient above a flat screen at a level of crests of waves

$$\bar{\bar{C}}_{y\bar{h}} = \frac{C_{yw}}{C_{yfl}}$$

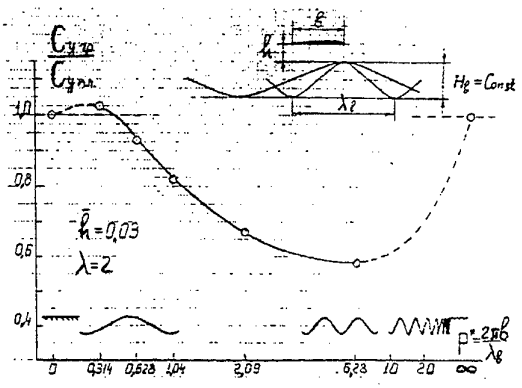


Fig.8

The case $P^* = 0$ corresponds to a wavelength of a screen equal to infinity, that it is possible to treat as a flat screen at a level of crests of waves. The case $P^* = 2\pi$ corresponds to a wavelength of a screen to an equal chord of a wing. For all of $P^* < 2\pi$ the chord of a wing is less than a wavelength of a screen, and for all of $P^* > 2\pi$ the chord of a wing is more than a wavelength of a screen. The deleted point on an axes of abscissas($P^* \to \infty$) corresponds to an oscillating screen with an indefinitely small wavelength, that is possible also to treat as a flat screen located at a level of crests of waves. On Fig. 8 the datas for a wing $\lambda = 2$, driven with an angle of attack $\Theta = 3^\circ 49'$ on relative distance from a level of crests of waves $\bar{h} = 0,03$, are indicated. For want of it to trace influence to lift of a wing of a wavelength of a screen in the pure state, were selected datas relating to waves of various length, but identical height equal to length of a chord of a wing $H_b = b$ in put on the graph only. The consideration of an obtained curve gives the following submission about influence of a wavelength of a screen to lift of a wing. For want of rather long waves ($P^* < 0,5$) lift of a wing above crests of waves is close on magnitude to lift of a wing above a flat screen at a level of crests of waves and can a little exceed this significance. However, for want of magnification of Strouhal Number from $P^* \cong 0,5$ up to $P^* \cong 2\pi$, that corresponds to a diminution of a wavelength of a screen up to magnitude to an equal approximately chord of a screen, the lift of a wing above crests of waves continuously decreases and for want of $P^* \cong 2\pi$ reaches significance approximately equal 0,6 from the significance above a flat screen at a level of crests of waves. For want of further diminution of a wavelength of a screen, when under a chord of a wing places more, than one ripple of a wave, lift, probably, is increased and for want of $P^* \to \infty$ the significance $\bar{\bar{C}}_{y\bar{h}} = 1$, as above a flat screen at a level of crests of waves should be restored. On the graph the prospective disposition of a curve for want of is designated by a dashed line. Physically such behaviour of a curve of lift above

crests of waves depending on Strouhal Number becomes clear of consideration of the sketch in a top Fig. 8. If the wavelength of a screen is more than length of a chord of a wing, with magnification of Strouhal Number the lift of a wing above a crest should decrease, because the average distance from a surface of a wing up to a surface of a screen is increased. If the wavelength of a screen is less than length of a chord of a wing, with magnification of Strouhal Number the lift of a wing above crests of waves should be increased, as the average distance from a surface ,of a wing up to a surface of a screen decreases.

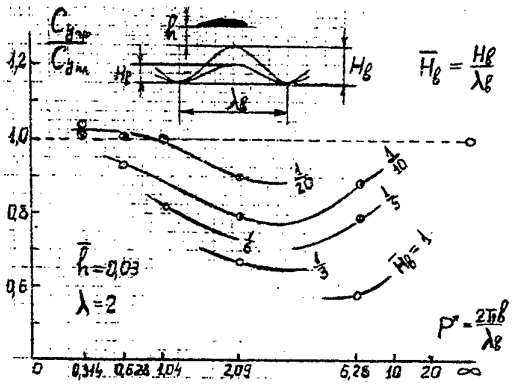


Fig. 9
About influence of height of a wave of a screen to lift of a wing above a crest

the waves are possible to made by submission, analyzing datas indicated on Fig. 9. On this graph the relation of a lift coefficient of a wing above a crest of a wave to a lift coefficient of a wing above a flat screen at a level of crests of waves $\bar{\bar{C}}_{y\bar{h}}$ is given depending on Strouhal Number for various significances of relative height of a

wave of a screen $\bar{H}_b = \frac{H_b}{\lambda_b}$

In experiment it was possible to envelop a range of a modification of relative height of waves of a screen in limits

$$\bar{H}_b = 1 \div \frac{1}{20}$$

As the general character is visible from the graph, curves $\bar{\bar{C}}_{y\bar{h}} = f(P^*)$ for want of $\bar{H}_b = \text{Const}$ is similar considered in a Fig. 8 for the same wing, but for want of $H_b = b$. Here tendecy $C_{yw} \rightarrow C_{yfl}$ for want of rather long waves of a screen ($P^* \rightarrow 0$) and for want of very short waves ($P^* \rightarrow \infty$) also is observed. However, in all a range, enveloped by experiment, of a modification of Strouhal Numbers the essential dependence of lift of a wing above crests of waves from relative height of a wave $\bar{H}_b$ is observed. This dependence expresss that the lift of a wing above crests of waves essentially decreases with magnification of relative height of waves. For want of diminution of relative height of waves of a screen and tendecy it to zero, the lift of a wing above crests of waves, naturally, tends to the significance above a flat screen at a level of crests of waves.

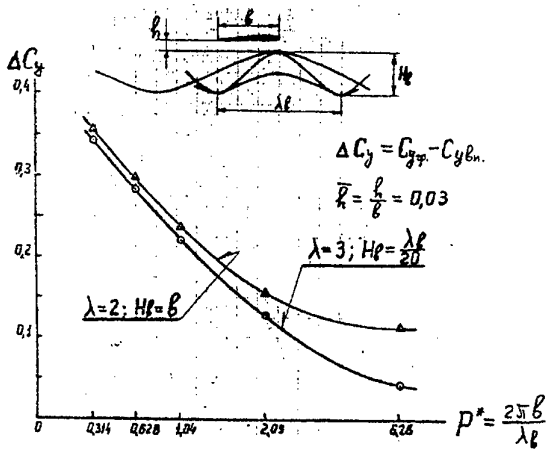


Fig. 10

It is possible to judge influence of Strouhal Number on magnitude of oscillation frequency of a curve lift above a wave screen by results of, represented in a Fig. 10. On this graph the dependence on Strouhal Number of a difference between instantaneous significances of lift coefficient of a wing for want of passing it above a crest and above a middle of a hollow of a wave of a screen is given. On the graph two curves are given. One for a wing with elongation $\lambda = 2$ above a wave screen, at which the waves of all lengths had identical

height equal to a chord of a wing $H_b = b$. Other curve corresponds to movement of a wing with elongation $\lambda = 3$ above a wave screen, at which height of each wave was equal to the one twentieth part of its length $H_b = \frac{\lambda_b}{20}$. An angle of attack of wings and relative distance from crests of waves in both cases were identical. Both in first, and in the second case oscillation frequency of lift above a wave screen essentially decreases with magnification of Strouhal Number.

5.5 Is higher, for want of discussion of results, represented in a Fig. 7 already, it was mentioned, that for want of movement of a wing above a wave screen average for the period of significance of a lift coefficient is exceeded by significances lift coefficient for want of movement of a wing above a flat screen at a level of centerline of a wave. In a Fig. 11 this " the effect of exceeding " is reflected as dependence on Strouhal Number of magnitude

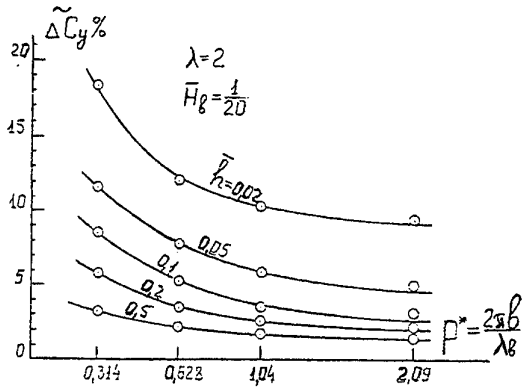


Fig. 11

$$\Delta \tilde{C}_y = \frac{C_{y\tilde{av}} - C_{y\bar{av}}}{C_{y\bar{av}}} \cdot 100\ \%$$

Where: $C_{y\tilde{av}}$ - average for period significance of a lift coefficient of a wing above a wave screen; $C_{y\bar{av}}$ - lift coefficient for want of movement of a wing above a flat screen at a level of centerline of a wave. From the graph it is visible, that " the effect of exceeding " for want of small Strouhal Numbers can reach 15 % and more, but it decreases with magnification of Strouhal Number and with magnification relative distance of a wing from crests of waves.

6. WING WITH A FLAP NEAR TO A SCREEN

The interesting results were obtained for want of tests above flat and wave screen of a wing with deviating flap [8]. Was investigated problem of influence of a screen to efficiency of a flap. Efficiency of a flap on lift far from a screen we shall take as the relation of a gain of a body force of a wing stipulated by a deviation of a flap to lift of a wing with undeflected flap.

$$\zeta_y = \frac{C_{y\beta} - C_{y\beta=0}}{C_{y\beta=0}}$$

Where: β - angle of a deviationof a flap, $C_{y\beta}$ - lift coefficient wing with deviating flap; $C_{y\beta=0}$ - lift coefficient of a wing with undeflected flap. For case of movement near to a screen efficiency of a flap on lift we shall express by a similar ratio

$$\zeta_{y\bar{h}} = \frac{C_{y\bar{h}\beta} - C_{y\bar{h}\beta=0}}{C_{y\bar{h}\beta=0}}$$

Where: $\bar{h}$ - relative отстояние from a trailing edge of a flap up to a screen. Influence of a screen to efficiency of a flap on lift we shall be to characterize by relative efficiency of a flap on lift

$$\bar{\zeta}_y = \frac{\zeta_{y\bar{h}}}{\zeta_y}$$

In a Fig. 12 the graph of relative efficiency of a flap is represented on lift depending on relative distance from a trailing edge of a flap up to a screen.

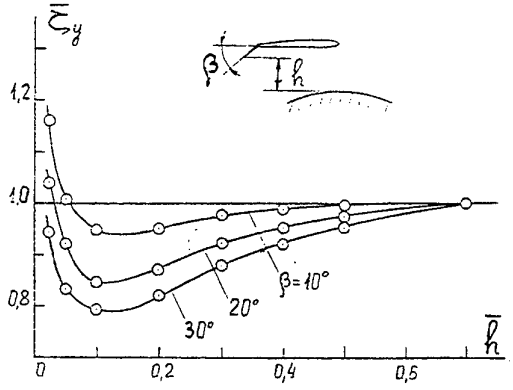


Fig. 12

A flap was located on the whole range of a wing λ =2, driven with an angle of attack $\Theta = 2^{\circ} 30'$. The chord of a flap has made the one tenth part of a chord of a wing. A flap deviated sequentially on angles β = 10°, 20° и 30°. As it is visible from the schedule, for want of approximation of a wing with deviating flap to a screen the relative efficiency it on lift in the beginning is reduced and the more, than greater angle of a deviation of a flap. It is possible to explain it by effect of straightener of a screen on a stream, deviating by the flap. However on extreme small distance from a screen for want of $\bar{h} < 0,1$ relative efficiency of a flap begin to increase, that it is possible to explain by a blocking effect of a stream by a flap near to a screen.

7. CONCLUSION

In Institute of a Hydromechanics UNAS the unique experimental installation for a research of movement of a wing near to the boundaries of the complicated form was created. On this installation large volume of a new information about influence of a flat and wave screen to hydrodynamic performances of a wing, driven above a him, is obtained. The obtained results can be used for want of designing of ekranoplanes and for want of analysis of their movement above the quiet and wavy surface of the sea. Some from these results are represented in the present work.

LITERATURE

1. Stephan F. Hooker. " A review of current technical Knowledge Necessary to develop large scale wing-in- surface effect craft ". Intersociety advanced marine Vehicles conference., Arlington, VA / June 5 - 7, 1989, pp 367 - 429.

2. Ollila R.G. "Historical Review of WJG Vehicles". J. of Hydronantics, 1980, v.14, N3, pp 65-77.

3. Гребешов Э.П. и др. "Аэродинамические характеристики профиля крыла вблизи плоского и волнового экрана". Труды ЦАГИ, вып. 1725, 1976.

4. Эпштейн Л.А."Гидродинамические методы исследования задач аэродинамики". Труды ЦАГИ, вып. 2035, 1980.

5. Белинский В.Г., Зинчук П.И. и др."Максимальные исредние значения гидродинамических характеристик крыла, движущегося над неплоским экраном". Сб. Гидромеханика, 1974, вып.29

6. Белинский В.Г., Зинчук П.И. и др. "Влияние формы неплоского экрана на гидродинамические характеристики движущегося над ним крыла". Сб.Гидромеханика, 1975, вып.31.

7.Белинский В.Г., Зинчук П.И. и др."О влиянии числа Струхаля на характеристики крыла вблизи волнового экрана". Сб.Гидромеханика, 1975,вып.31.

8. Белинский В.Г., Оришичев В.А." Об эффективности закрылка вблизи твердой стенки". Сб.Гидромеханика,1985, вып.52.

Some Problems of Supercavitating Flows

G.V.Logvinovich
State SRC TzAGI
18 Radio str., Moscow, 107005
Russia

1. SUMMARY

Now, at immense successes of the computer hydrodynamic it is useful to consider some fundamental physical statements. The types of cavitating flows, reentrant jets, energy conservation principles, cavity pulsation at cavitation are presented below.

2. SOME TYPES OF CAVITATING FLOWS

A fully developed cavity in weightless fluid is defined by cavitation number $\sigma = \frac{\Delta p}{\rho \frac{V^2}{2}}$, where Δp is the pressure difference in undisturbed fluid p_∞ and in a cavity p_k; V is the relative velocity: ρ is the density. A closed cavity with certain area of the mid-section $S_k \sim \frac{W}{\Delta p}$, which is proportional to the cavitator drag W, is derived at $\sigma > 0$ (Fig. 1, II). Obviously, S_k exists at any $\Delta p > 0$, and in this point the cross section area $S(x)$ satisfies the condition $\frac{\delta S}{\delta x} = 0$. It is clear that this cavity develops on large distances $r \to \infty$ as a dipole, and the absolute velocity of fluid V is proportional to $1/r^3$.

The case, when $\Delta p = 0$ and $\sigma = 0$, (Fig. 1, I) corresponds to the infinite cavity. Its cross section $S(x)$ has no maximum. Hence, this cavity corresponds to an infinite chain of sources. In spite of the cavity contour $S(x)$ near the cavitator at small $\sigma \to 0$ asymptotically coincides with the cavity at $\sigma = 0$, these two flows are principally different, and this is necessary to take into account. So, for example, if the cavitator is flowed by jet with diameter $d \ll d_H$, then on the large distances the cavity is degenerated into a cone jet of angle $\theta \sim \frac{d_H}{d}\sqrt{c_x}$.

3. REENTRANT JETS AT CAVITATION

Theoretically, a steady cavity at $\sigma > 0$ is formed that a spray jet of section F_c with relative velocity $V_k = V\sqrt{1+\sigma}$ and absolute velocity $V + V_k$ is directed from its back part forward. At small σ, $V + V_k \sim 2V$ and the cavitator drag $W \sim 2\rho F_c V^2$. If the jet was colliding with the bottom part of the cavitator and then was dissipating perpendicularly to the motion direction, its pressure on the bottom, which is directed forward, would be $\rho F_c V^2$ or, approximately $\frac{1}{2}W$. The jet turn on the cavitator bottom completely compensates the cavitator drag. It is theoretical. Practically, in the stationary cavity the jet is destroyed and carried over with supplied gas to the wake. However, in some cases (Fig. 1, III) the power jets directed up and to within the cavity are formed at the cavity closure during vertical water entry with high velocity. The internal jet collides with the bottom of the body, and this effect is considerable. In the experiment we observed the total destruction of instrumentation located in the body's bottom part by namely such jet (Fig. 1, III).

4. ENERGY CONSERVATION PRINCIPLE

At stationary motion the force overcoming the drag W performs work per second $WV = \frac{dE}{dt}$, and the energy E remains in the wake. Along the cavity length l the energy in the wake $Wl \sim \Delta p S_k l$. Since, the energy density must be the same for each part of the wake length l at the enough distance from the cavitator, it is natural to suppose that a sum of the kinetic energy T and potential energy U is equal to energy E for overcoming the cavitator drag. Then $\frac{\delta}{\delta h}(I + U + E) = 0$, where h is the cavitaor center trajectory. For stationary cavity at $\sigma \to 0$ we obtain $T \sim \Delta p(S_k l - O_k)$, where O_k is the cavity volume. Spreading the previous equation on the unsteady motion along the curvilinear trajectories is the mathematical formulation of "principle of independence of the cavity section expansion". For an ellipsoid $O_k = \frac{2}{3}S_k l$. As is known the stationary cavity is close to an ellipsoid.

5. PRINCIPPLE OF INDEPENDENCE OF CAVITY SECTION EXPANSION

The approximate "principle of independence of the cavity expansion" was formulated in 1960 - 1961. It was subjected to the careful experimental testing to apply in practice.

Comparisons of calculations with results of the corresponding experiments are shown in Fig. 2. A snake-shaped cavity is formed past a disk at cross oscillations of a bar with disk. An analysis of this cavity's frames at fixed velocity and supply before

Paper presented at an AGARD FDP Workshop on "High Speed Body Motion in Water", held in Kiev, Ukraine, 1-3 September 1997, and published in R-827.

the oscillation beginning, at oscillations and again without the oscillations has shown the total identity of the contour. At vertical water entry with high speed the body moves with deceleration, and the cavity is obtained wider. In photograph the calculated points are plotted on a basis of the "independence principle". They coincide with the experimental contour.

The known M.I. Gurevich's work has shown that the additional mass at impact of the plate with *Kirhgoff* cavity past it is more only on 8 % that the additional mass of the plate swimming on the flat water surface. The photograph (Fig.) shows the test where the weight gliding along the bar is impacting against the disk after the cavity formation past it. In the impact moment the cavity separation is formed, and a new cavity begins to be formed, while the "old" cavity is being developed practically independently on the impact. A detailed analysis has shown that the "impact" additional mass of the disk is less approximately in two times than "cavitationally" developing one at moderate accelerations.

An application of the "independence principle" permitted the acoustic radiation of the cavities to evaluate. It is of interest from point of view of information connection.

5. CAVITY PULSATIONS

In many experiments the cavity pulsations are being observed when wave-shaped appendages and hollows run along the cavity. A long time this effect had no strict explanation. It was not clear how may it be controlled. The explanation and theory of this effect are obtained in fundamental work by *E. V. Parishev.* He has been using the "independence principle" and has shown that the cavity behaviour can be described by equations with lagging argument. The basic results of *E. V. Parishev's* work are shown in Fig. 3.

An analysis of the equations has shown that the cavity is stable only for the lagging argument range $0 < \tau_0 < \pi\sqrt{2}$, where $\tau_0 = \sqrt{\frac{12}{\gamma}\frac{Eu}{\sigma} - 1}$. Here, Eu is *Euler* number, γ is the politropic exponent of gas within the cavity. It means physically that the ventilated cavity is stable about the vapor cavitation at $p_k/p_\infty < 0.7$, if $\gamma = 1.4$ (see Fig. 3). If $\tau_0 > \pi\sqrt{2}$, then waves arise. The number of them $N \sim \frac{\tau_0}{2\pi}$ is close to integer numbers. I want to emphasise that before *Parishev's* works this phenomenon nature was not clear. *Parishev's* equation, its solution illustration and a comparison with experiments are shown in Fig. 3.

7. PRINCIPLE OF INDEPENDENCE OF PLANE SECTIONS

The principle of plane sections, which is generally the same principle of independence, was used in the numerous works by *Yu.F.Zhuravlev* (Moscow) and *V.N. Buyvol* (Kyiv). They have studied in detail the deformation of cavity cross sections. Really, for equation deduction we consider not cylindrical expansion of the cross layer extending to infinity but the motion in stream pipe based on the cavity length units where the kinetic energy is finite.

8. OTHER CASE OF INDEPENDENCE PRINCIPLE APPLICATIONS

The "Independence Principle" can be treated in wider sence not only for cavities. In all the cases when a wake remains past a body where disturbed velocities of fluid along the trajectory are small in comparison with velocities normal to the trajectory we can with known approximation state that the wake length part moves independently on the following motion of the body. In particular, for hydroplane the wake is formed past the first step at the moment t, it reaches to the second step for time interval $\tau = l/V$. During time τ the wake is deformed existing independently. The force acting on the first step at the moment $t_1 = t + \tau$ is approximately independent on the wake, but the force depending both on the hydroplane kinematic parameters at the moment t_1 and on the wake containing "history" of it formation at the moment $t_1 - \tau = t$ and deformation for time τ acts to the second step. It is clear that a system of differential equations of the hydroplane motion should contain terms with lagging argument. At some combinations of parameters instability arises.

9. CONCLUSION

Repeating some known statements, it is useful to emphasize that it is appropriate to make preliminary physical evaluations of a situation and to separate the "possible" from "impossible" at composing the computer programs.

REFERENCES

1. Eng. J., AN SSSR, 1, 1961, Moscow.
2. Eng. J., AN SSSR, 5, 1965, Moscow.
3. J.: Trudy TzAGI, 1797, 1976, pp 3–17.
4. J.: Trudy TzAGI, 1907, 1978, pp 17–40.
5. J.: Trudy TzAGI, 2272, 1985, pp 29 – 35.
6. J.: Trudy TzAGI, 2595, 1995.

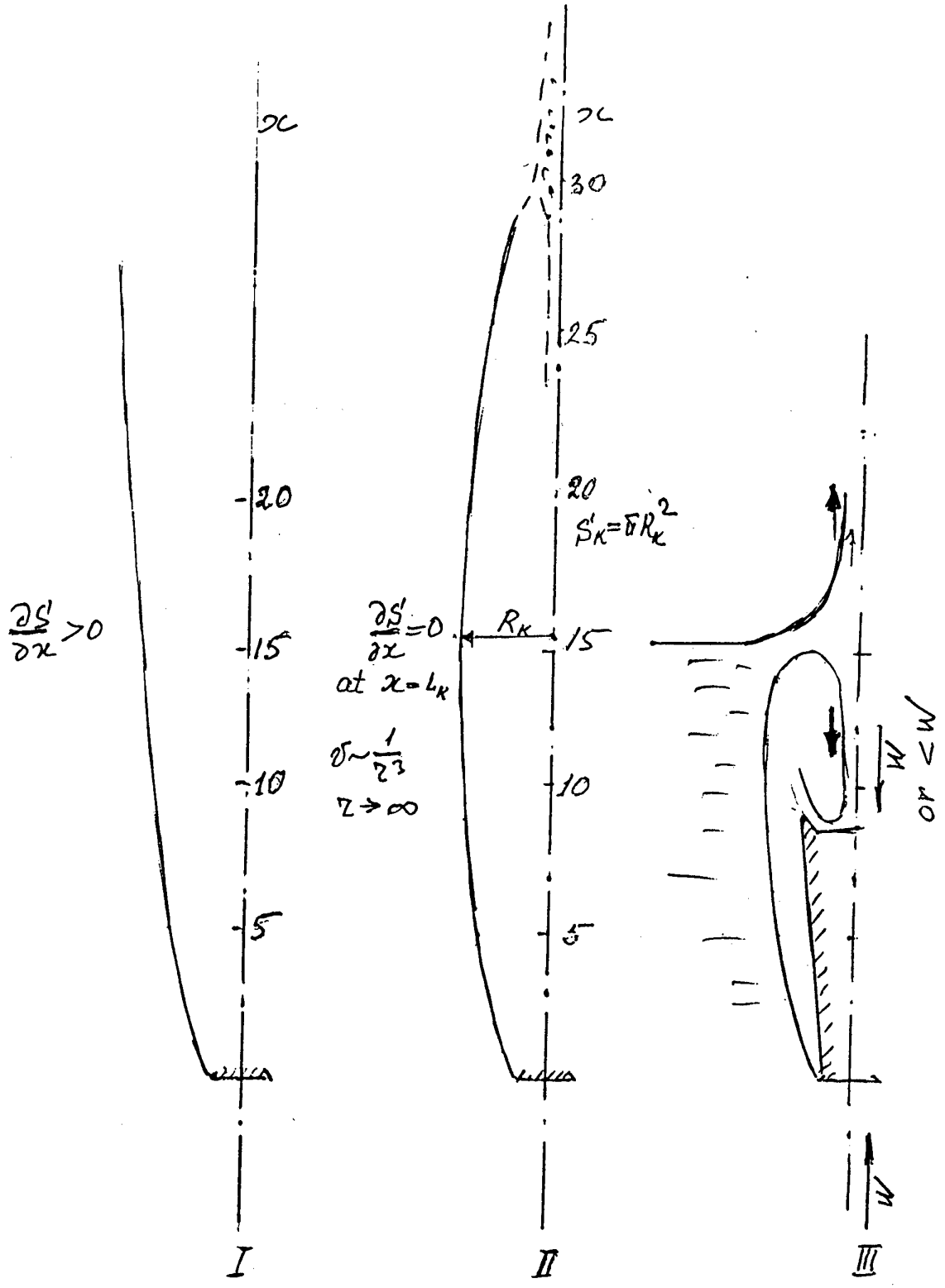

x
20
15
10
5
$\frac{\partial S'}{\partial x} > 0$
I
x
30
25
20
15
10
5
$S'_K = \pi R_K^2$
$\frac{\partial S'}{\partial x} = 0$
at $x = L_K$
R_K
$\sigma \sim \frac{1}{z^3}$
$z \to \infty$
II
W
$M > 40$
W
III

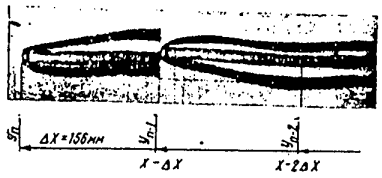
Fig. 1

$$\frac{\partial}{\partial h}(T+U+E)=0, \quad W=-\frac{\partial E}{\partial h}$$

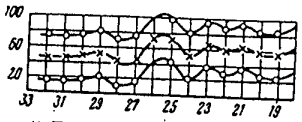
$$stat.cav. \quad T\cong\Delta p(S_c l-O_c)\cong\frac{k}{2}\Delta p O_c; \quad O_c=\int_0^l S\,dl; \quad k<2$$

Photographs of cavities

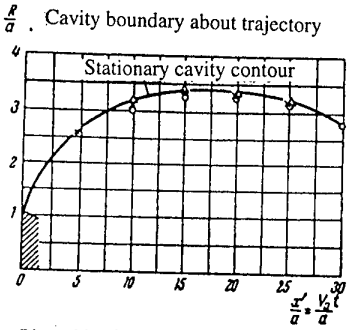
Frame #24 Frame #23 $2a=18.8, \quad V_0=5m/sec; \quad h=350mm$



Trajectory of disk center and cavity boundaries



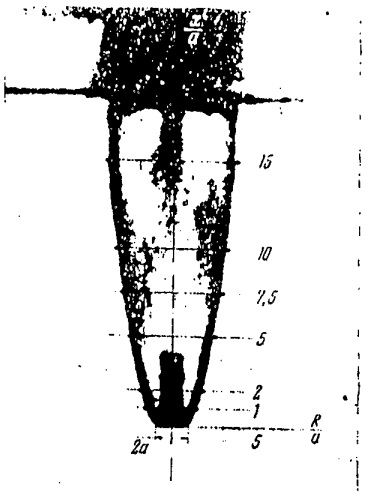
× Trajectory of disk center ∘ Points on boundaries for Δx = const



Plotted by frames ## 23; 24; 29; 30; 33

$2c' \cong h$

$$\frac{\partial^2 S(h,t)}{\partial^2 t}=-\frac{k}{\rho}\Delta p=\frac{k}{\rho}\left[P_\infty(h,t)-P_c(h,t)\right]$$



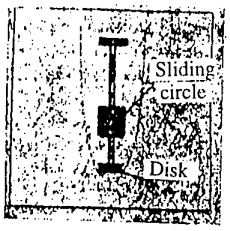
• Calculation

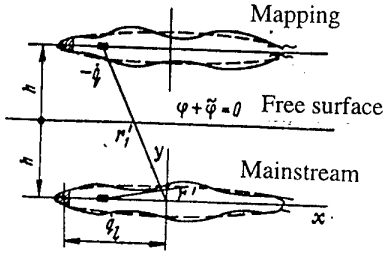
$$\frac{\partial\varphi}{\partial t}+\frac{v^2}{2}+\frac{p}{\rho}=const$$

$$R\dot{R}\sim\sqrt{\frac{W(\Delta p\to 0)}{\pi\rho\,(\ln R+A)}}$$

$$m_0^*\sim\frac{4}{3}\rho\,R^3; \quad m_c^*\sim 2.52\,\rho\,R^3$$

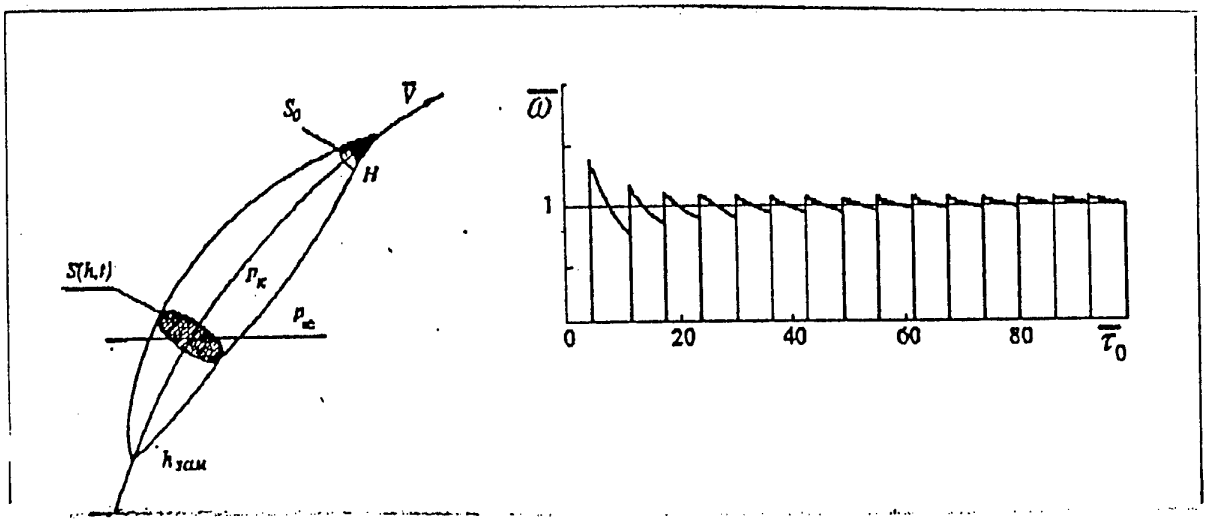






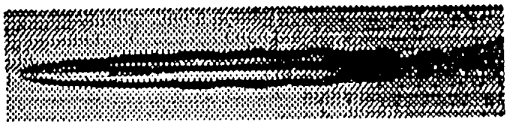
$$N\sim\frac{\pi L_c^2}{(\ln 1/\delta)^2}\frac{P_m^2}{\rho C}; \omega\sim\frac{6\gamma P_c}{\rho R_c^2}\frac{1}{\ln 1/\delta}$$

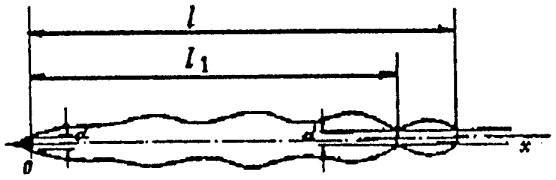
Fig. 2

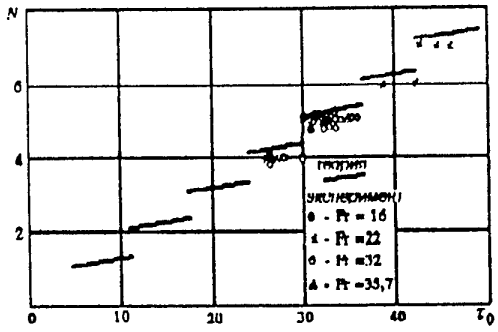


$$P_c''' (t) + P_c' (t) + P_c' (t - \tau_0) - \frac{2}{\tau_0} P_c(t) + \frac{2}{\tau_0}(t - \tau_0) = 0$$

$$S''(h,t) = -k\frac{\Delta p}{\rho}$$







$$0 < \tau_0 < \pi\sqrt{2}; \quad \tau_0 = \sqrt{\frac{12}{\gamma}\left(\frac{Eu}{\sigma} - 1\right)}$$

$$0.7 \sim \frac{1}{\frac{6}{\pi\gamma} + 1} > \frac{P_c}{P_0}, \quad \gamma = 1.4$$

Fig. 3

Cavity Shapes in Three Dimensions

M. P. Tulin

Director, Ocean Engineering Laboratory
University of California, 6740 Cortoona Drive
Santa Barbara CA 93106-1080, USA

Key words: Supercavitation, Cavities, Cavity Shapes, High Speed Hydrodynamics

1. Introduction

Cavitating and ventilated bodies produce trailing cavities of a length and volume out of all proportion to the dimensions of the body itself. The shape and dimensions of these cavities have attracted research interest which is intensified by the engineering of high speed bodies enveloped by their cavities in order to reduce their resistance.

In his introductory work on the linearized, or thin body, theory of planar supercavitating flows, the present author obtained asymptotic results defining the cavity shape, Tulin (1953). It was shown that the trailing planar cavity behind a head form was asymptotic in shape to a slender elliptic cylinder whose length, ℓ, and thickness, T, depend in a simple way on the body drag coefficient, C_D, and cavitation number, $\sigma \ll 1$:

$$\begin{aligned} \ell/t &\cong (8/\pi)C_D/\sigma^2 \\ T/t &\cong (4/\pi)C_D/\sigma \end{aligned} \tag{1}$$

where, t is a characteristic length of the body. Later, Tulin (1956), it was shown that in the case of a lifting foil, only the symmetric part of the flow field (i.e. strut-like) entered into the determination of the drag and cavity length.

A few years later, Garabedian (1956) obtained corresponding results for axisymmetric bodies like cones:

$$\begin{aligned} (\ell/d)^2 &\cong C_D \frac{1}{\sigma^2} \ell n \frac{1}{\sigma} \\ (T/d)^2 &\cong C_D/\sigma \end{aligned} \tag{2}$$

where d is the diameter of the base of the cone forebody and C_D is non-dimensionalized with the base area. The shape of the trailing cavity is essentially spheroidal.

Paper presented at an AGARD FDP Workshop on "High Speed Body Motion in Water", held in Kiev, Ukraine, 1-3 September 1997, and published in R-827.

Here we derive a generalization of (1) and (2) to the case of genuinely three dimensional headforms. It is clear that all possible head shapes are unlikely to shed cavities of the same general characteristics. For example, delta wings produce cavities with the appearance of a re-entrant jet along the top axis of symmetry, Tulin (1955), while rectanglular wings produce smooth trailing cavities with the addition of strong cavitating tip vortices. As a prototype headform we consider a wing of elliptical shape, span W and midchord C,see figure 1 at the top; the aspect ratio, AR, of the wing is W/C. This headform seems likely to produce a trailing cavity of basically ellipsoidal shape.

2. Regimes of Cavity Shape(Quasi-Planar; Long-Flat; Spheroidal)

The cavity length, ℓ, and thickness, T, increase with increasing speed, q_o, or decreasing cavitation number, σ. With increasing speed the shape of the three dimensional cavity changes, too, as shown in figure 1; the speed is increasing from top to bottom. We identify three distinct regimes.

For a wing of sufficiently high aspect ratio, the cavity has at first a width, B, equal to the wing span, but of much shorter length; the flow about the wing is thus *quasi-planar* (I). With increase in speed, the cavity length too becomes as large as the wing span; this results in the thin cavity labeled "discus" in figure 1.

The discus is a transition between the quasi-planar regime (I) and the *long-flat* regime (II). In the latter, the cavity length exceeds the wing span, but the latter is larger than the cavity thickness; the cavity width remains fixed in size, equal to the wing span.

Eventually the cavity thickness equals its width, and the *spheroidal* regime (III) is initiated. Thereafter, with increase in flow speed, the cavity remains spheroidal and thin, with the diameter exceeding the wing span.

We note that in each of these regimes the cavity width is specified, leaving its length and thickness (or diameter in III) to be determined. In the spheroidal regime, the requisite asymptotic relationships have already been given by Garabedian (1956), eqn. (2). This leaves regimes I and II to be treated.

3. Thin Ellipsoids as Cavities

Thin ellipsoids aligned with a uniform flow are known to have a pressure, P_c, over most of their smooth sides which is almost uniform and

reduced from the ambient pressure, P_o. We imagine headforms like the elliptic wing in a flow at a low cavitation number σ, trailing cavities which are essentially thin ellipsoids, where now:

$$\sigma = \frac{P_o - P_c}{1/2\rho q_o^2} \tag{3}$$

The flowspeed is q_o.

The added mass of this thin ellipsoid (length ℓ, thickness T, width B, is given by $\rho k_1 V$, where V is the ellipsoid volume and k_1 the horizontal added mass coefficient. It is well known that the latter is directly related to the speed, q_c, on the smooth sides of the thin ellipsoid, which can be shown to be,

$$q_c \cong (1 + k_1) q_o \tag{4}$$

and, therefore, using Bernoulli's equation relating q_c and P_c, and (3),

$$\sigma = (1 + k_1)^2 - 1 \cong 2k_1 \tag{5}$$

4. The Added Mass Coefficient

The added mass coefficient k_1, and therefore σ is dependent on the shape of the thin ellipsoid,

$$k_1 = \frac{\sigma}{2} = (T/\ell) f(\ell/B) \tag{6}$$

For example in the two dimensional and axi-symmetric cases where B disappears as an independent variable, $\sigma = 2(T/\ell)$ for slender elliptic cylinders and $\sigma = (T/\ell)^2 ln(T/\ell)^2$ for slender spheroids.

In the general three dimensional case, k_1 for ellipsoids is known in terms of complete elliptic integrals of the first, F, and second, E, kinds, Munk (1934). In application to supercavitating flows, $T/L \ll 1$, we find for each of the two regimes in figure 1;

$$Regime I (B > \ell): \qquad k_1 \ell/T = f_1(\ell/B) \tag{7}$$

$$Regimes II and III (\ell > B): \qquad k_1 \ell/T = f_2(B/\ell) \tag{8}$$

where,

$$f_1(\ell/B) = \left[1 - (\ell/B)^2\right]^{-1} \left[E(\mu_1) - (\ell/B)^2 F(\mu_1)\right]$$

$$\mu_1 = \left[1 - (\ell/B)^2\right]^{1/2} \tag{9}$$

$$f_2(B/\ell) = B/\ell \left[1 - (B/\ell)^2\right]^{-1} [F(\mu_2) - E(\mu_2)]$$

$$\mu_2 = \left[1 - (B/\ell)^2\right]^{1/2} \tag{10}$$

These relationships (7) and (8) must now be supplemented by another which provides a relationship between the headform drag and the cavity dimensions. These together give a general three dimensional solution equivalent to (1) and (2) for the limiting cases of two-dimensional and axi-symmetric flow.

5. Energy Flux and Drag

The headform, with drag D, moving in a quiescent fluid with the speed u_o in the x direction does work on the fluid at the rate $D \cdot u_o$. This corresponds to a kinetic energy flux from the headform of the same magnitude, which is absorbed at the tail at some nominal time τ later. This transit time, τ, must scale with the time of passage of the body-cavity past a fixed point, ℓ/u_o.

This kinetic energy flux thus provides in time τ the kinetic energy, KE, which is distributed throughout the flow field around the body, especially in its close vicinity:

$$KE\ flux \cdot Transit\ Time \propto Flowfield\ KE \tag{11}$$

The RHS above is proportional to $(\rho u_o^2/2) \cdot k_1 \cdot lBT$. Therefore, after substitutions and cancellations, (11) can be written:

$$D = \gamma \cdot (\rho u_o^2/2) \cdot k_1 \cdot BT \tag{12}$$

where γ is a factor to be determined. After using (5), this result is of the same form as a theorem found by Garabedian (1956) for supercavitating cones by scaling arguments, and leading to (2) lower. It is also of the same form found by Tulin (1953) for planar bodies ($B = 1$), equation (1) lower. In both cases, planar and axisymmetric, (12) is identical to (1) and (2) lower, for $\gamma = 2/\pi$. It is quite remarkable that the same value of γ suffices here for both planar and axisymmetric cases. This fact provides the rationale for our use of (12) with $\gamma = 2/\pi$ in the general three dimensional case. Finally, we note that this derivation provides some physical insight into the nature of the mathematical laws of Garabedian and Tulin.

Our general three dimensional law, (12), can be given the form:

$$BT/A_n = (4/\pi)C_D/\sigma \tag{13}$$

where A_n is the reference area of the forebody used in forming C_D. In the case of the elliptic wing, $A_n = (\pi/4)WC = W\bar{C}$. Equation (13) is the three dimensional generalization of (1) and (2) lower.

The cavity thickness, T, may be removed from (13) by using (7) or (8) leading to relationships for the cavity length.

Finally, after some substitutions, we find for the elliptic wing:
Regimes I, II.

$$T/\bar{C} = (4/\pi)C_D/\sigma \tag{14}$$

$$\ell/\bar{C} = (8/\pi)C_D/\sigma^2 \cdot f_{1,2}\,[\ell/W] \tag{15}$$

Where:

$$\ell/W = \ell/\bar{C} \cdot \pi/4 \cdot 1/AR \tag{16}$$

and $f_{1,2}$ is given by (9) and (10), $B = W$. In the planar case, $t = \bar{c}$, $f_1 \equiv 1$.
Regime III (spheroidal).

$$(T/C)^2 = (C_D \cdot AR)/\sigma \tag{17}$$

$$\ell/T = \frac{2}{\sigma} f_2(T/\ell) \tag{18}$$

$$\ell/T \gg 1 \qquad \sigma \cong (T/\ell)^2 ln(\ell/T)^2 \tag{19}$$

which can be approximated after some minipulation, again for very slender cavities,

$$(\ell/T)^2 = \frac{1}{\sigma} \ell n \frac{1}{\sigma} \tag{20}$$

Multiplying (17) and (20) the general law for elliptic wings in regime III becomes

$$(\ell/C)^2 = \frac{C_D \cdot AR}{\sigma^2} \ell n \frac{1}{\sigma} \tag{21}$$

In the axisymmetric case, $AR = 1$, $C = d$ and (21) yields Garabedian's law, equation (2) upper.

6. Concluding Remarks

The theory given here is hueristic in nature; it is not exact. It needs to be supported by experiments and additional theory. In addition, unconventional headforms may lead to unconventional cavities, with deviation from ellipsoidal shape. These need their own special consideration.

Among the results which can be easily derived from the present theory are the boundaries between Regime I and II, and II and III. On the former the cavity is a discus, as shown in figure 1; on the latter it first assumes spheroidal shape. These two transition boundaries are given by the following laws, respectively:

$$\sigma^{\star} = \left[\pi/2 \frac{C_D}{AR}\right]^{1/2} \tag{22}$$

$$\sigma^{\star\star} = [C_D/AR] \tag{23}$$

see figure 2.

It is hoped that these laws will prove useful in design.

Acknowledgement. This work has been partially supported by the Ocean Technology Program of the Office of Naval Research, Dr. Thomas Swean, Program Director.

7. References

1. Garabedian, P.R., 1956. "Calculation of Axially Symmetric Cavities and Jets," *Pacific Journal of Mathematics*, Vol. 6, p. 611.

2. Munk, M., 1934. Fluid Mechanics, Part II. In *Aerodynamic Theory*, Vol. I, W.F. Durand, ed., p. 301. Durand Reprinting Committee.

3. Tulin, M.P., 1953, Steady Two-Dimensional Cavity Flows About Slenderbodies. David Taylor Model Basin, Rept. No. 834, Navy Dept., Washington, D.C.

4. Tulin, M.P., 1955. Supercavitating Flow Past Slender Delta Wings. *Journal Ship Research*, Vol. 3, No. 3, pp. 17-22.

5. Tulin, M.P., 1956. Supercavitating Flow Past Foils and Struts. In *NPL Symposium on Cavitation in Hydrodynamics*. London. Her Majesties Stationery Office, pp. 16.1-16.19. Also: Philosophical Library, 1957.

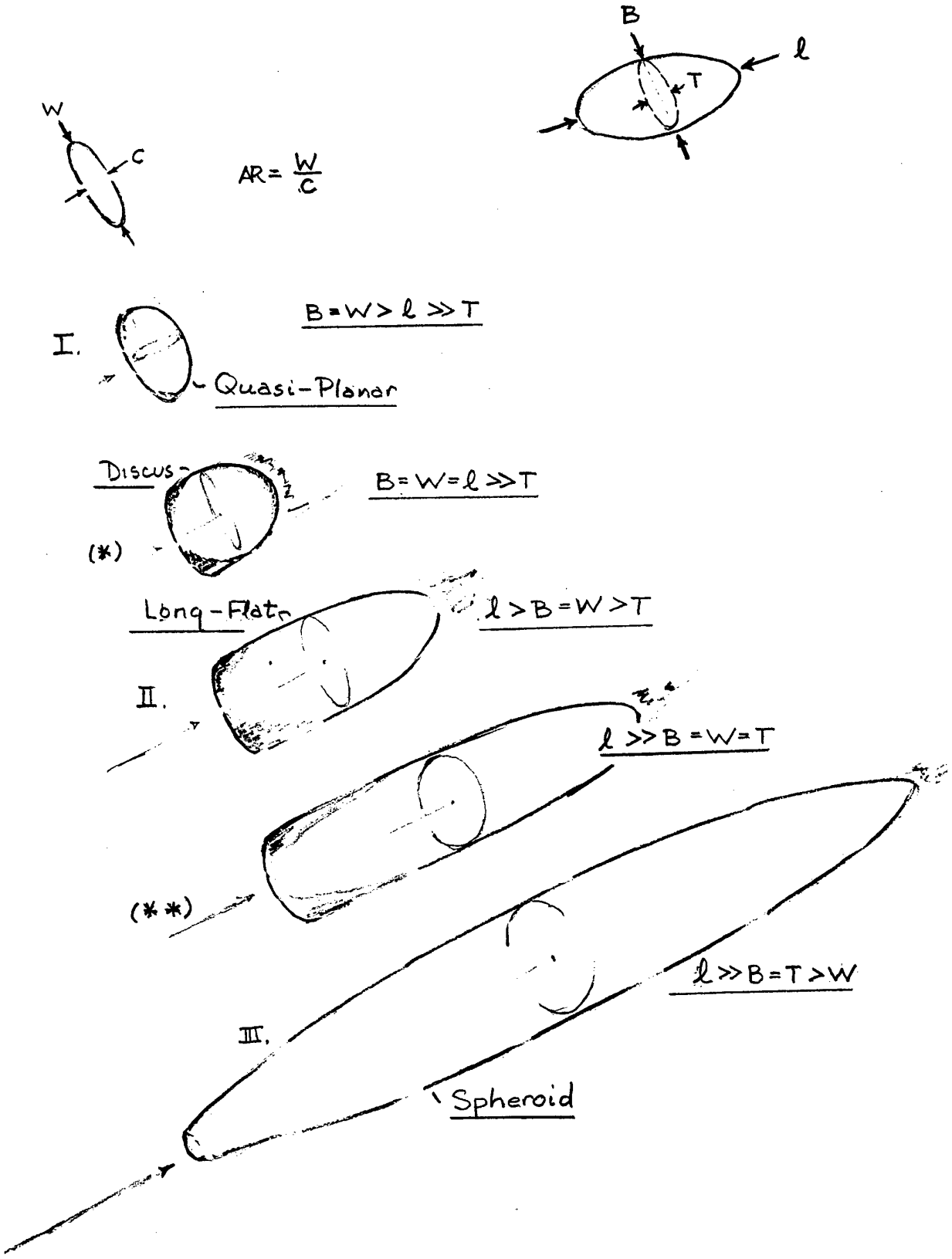


Figure 1: Supercavitating Regimes

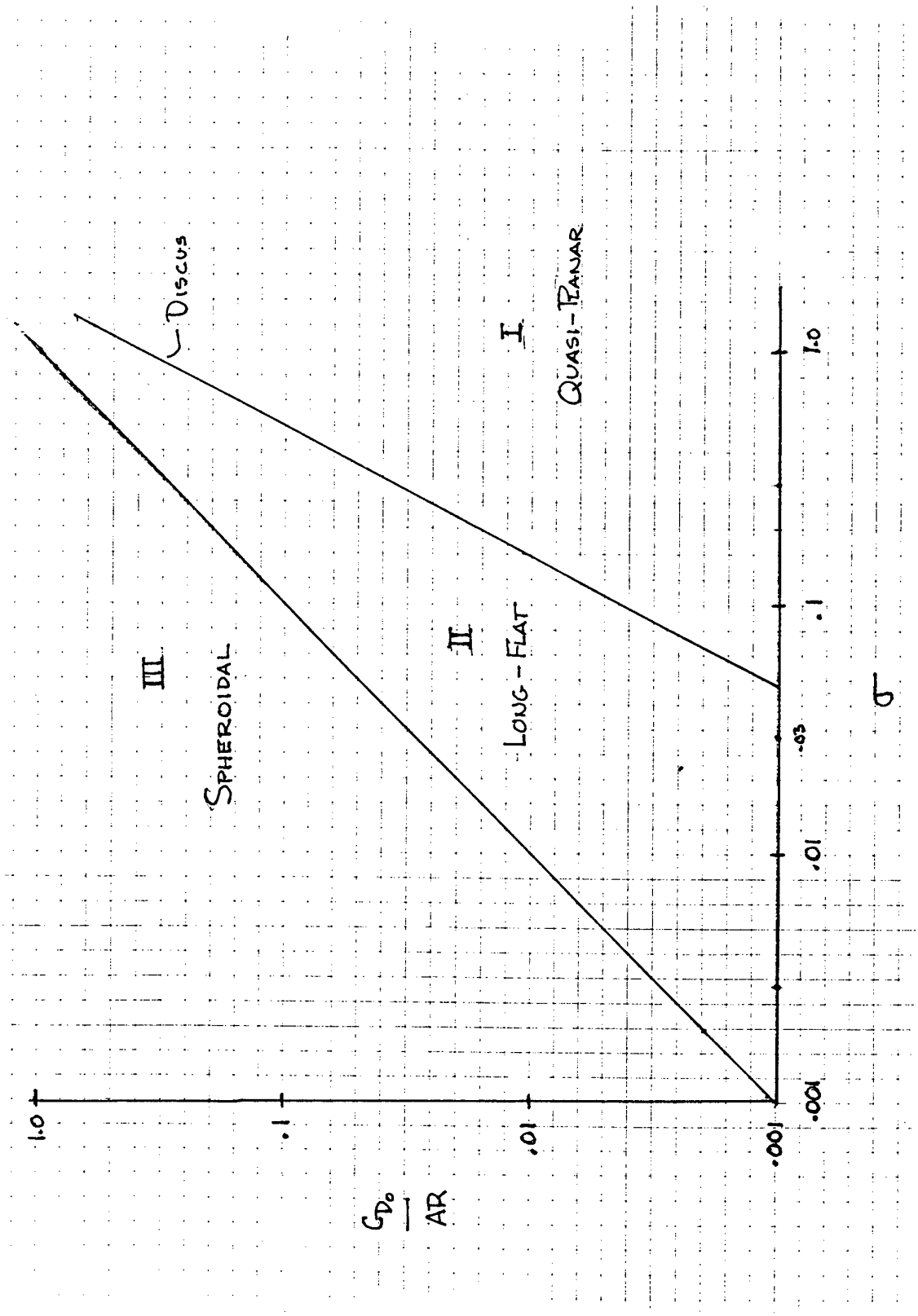


Figure 2: Regimes of Three Dimensional Cavity Shapes

Investigation of High-Speed Supercavitating Underwater Motion of Bodies

Yu.N.Savchenko
National Academy of Sciences - Institute of Hydromechanics
8 / 4 Zhelyabov str., Kiev, 252057
Ukraine

1. SUMMARY

The main hardware of the institute of Hydromechanics of UNAS for research of high-speed supercavitating motion in water are presented. These are the 35 m launching tank with electrochemical catapult, the vertical tank to investigate water entry, the hydrodynamic tunnel of open type. Cinegrams of supercavity obtained at underwater motion of supercavitating models for speeds up to 1360 m/s (0.93 M) are demonstrated.

The hydrodynamic effects connected with supercavitating motion of objects and their stability are discussed.

2. INTRODUCTION

Experience of development of experimental high-speed hydrodynamics shows that it is convenient for velocities up to 30 m /s to use the inverted motion, which is realized due to hydrodynamic tunnels [14]. IHM has two hydrodynamic tunnels.

The small hydrodynamic tunnel. Its working section is 0.34x0.34 m, the working part length is 2m, the mainstream velocity is 9 m/s. It is a tunnel of open type with opened working part. Pumps inject water to the upper tank, where free level is sustained constant. The water arrives under constant pressure of water column equal to 4.5 m to the working part.

The big hydrodynamic tunnel. Its working section is 0.5 x 0.5 m, the working part length is 4 m. It is a tunnel of open type with opened working part with maximal admissible velocity up to 30 m/s.

It is convenient for velocity range $30 \div 200$ m/s to use the models moving on wires. The 30 m flume with the vapor catapult is used to realize this. The catapult can launch models up to 5 kg with velocity 130 m/s.

The launching tanks with free motion of models are used for velocities about 1000 m/s [14]. At the IHM the supplying part of big hydrodynamic tunnel is used as a launching tank. The launching tank has 10 pairs of looking windows and is supplied by an electrochemical catapult using the electrolysis gas energy after decomposition of water. The maximal achieved velocity on this tank is equal to 1360 m/s (0.93 M).

The object is partially or completely placed in the supercavity (Fig. 1) formed by nose part – cavitator according to the hydrodynamic scheme of supercavitating flow [1 – 6]. The object can not have points of contact with a cavity boundary (Fig. 1, c) at use of the jet cavitator.

It is seen from formulae of hydrodynamic drag for bodies at continuous and cavitation flow schemes

$$X = C_x(\mathrm{Re})\,\frac{\rho V^2}{2} S\ , X_c = C_c(\sigma)\frac{\rho V^2}{2} S_c \qquad (1)$$

that X_c does not depend on the viscosity. Here $\mathrm{Re} = VL/\nu$ is Reynolds number, $\sigma = (P - P_0)/\frac{\rho V^2}{2}$ is the cavitation number, S and S_c are the wetted surfaces of body at continuous and cavitation flow regimes, ρ and ν are the density and viscosity of water.

The cavitation flow scheme has also one important and surprising property. Calculations show that the cavitation scheme of flow around the body in water can ensure the lower drag than at motion with the same velocity in air.

Moving in the vapor or gas cavity, the cavitating object loses the main advantage of motion in fluid (the Archimedean buoyancy force) and needs dynamic means of its weigh maintenance inside the cavity [14].

The classical condition of the object motion stability in continuous medium (location of the object mass center ahead of center of external force application) is violated by the most adverse way in the supercavitating flow scheme: the center of external hydrodynamic force application is on the extreme forward point of the object far ahead of the mass center (Fig. 2). Moving in the cavity with subsonic velocity relatively to water ($V_a = 1430$ m/s), the

Paper presented at an AGARD FDP Workshop on "High Speed Body Motion in Water", held in Kiev, Ukraine, 1-3 September 1997, and published in R-827.

object executes the supersonic ($V = 4$ M) motion relatively to the steam filling the cavity as at height 34 km above the sea level.

We should note that the problem on cavity closure including the cases of closure on the object body is a big independent theme having applications in realization of artificial supercavities and touching the problem of further drag reduction to values less than X_c .

It is possible with account of mentioned features of the supercavitating flow scheme to generalize that the realization of supercavitation flow scheme is possible only at successful solving the problem of maintenance of object motion stability in the cavity. Therefore, the spherical body was more often used in the experiments on water entry of bodies and formation of cavities [12, 14]. The cavity covers only the body part for the scheme of flow around moving objects, and the tail part was wetted to save the object motion stability (see Fig. 1, *a*). Blades of ship screws and pumps are the most widespread object of supercavitation in engineering.

The supercavity gives the perfect possibility to protect the part of design located in the cavity from contact with water. This phenomenon is basis of creation of a new class of two-medium foils of wings and blades intended to use in alternate mediums (water – air). The special shape of the foil [11] promotes the supercavity formation and the foil protection against overloads on the lift (side force) in water. Such foil permits the constant lift to save at change of the medium water – air (Fig. 3).

To calculate two-medium foils we have developed the special computer program enabling to design the foil with given characteristics and to determine the range of allowable angles of attack in the supercavity.

3. SUPERCAVITY SHAPE

The supercavity parameters in the velocity ranges up to 1360 m/s were investigated at the IHM UNAS on the special launching tank with length 35 m and section 2.2 x 2.2 m [7]. Models were started due to the gas catapult, where the energy of burning the electrolysis gas was used according to known reaction of the compound of hydrogen with oxygen $2H_2 + O_2 = 2H_2O + 136.6$ Kkal. The parameters of cavitating flow were registered by a high-speed camera.

The supercavity shape for the model having a conic shape and a disk cavitator [1, 3] is shown in Figs. 4 and 5. The photo of cavity is obtained by splice of consecutive frames made through the window of the launching tank. The obtained cinegrams give picture of evolution of the cavity section fixed in the absolute coordinate system. This permits the shape and dimensions of the stationary cavity to determine according to the principle of independence of the cavity section expansion [4] at cavitation number value corresponding to instant velocity of passing by cavitator through given section.

Froude number $\mathrm{Fr} = V_0/\sqrt{2gR_n}$ was varying in range $3 \cdot 10^4 \ldots 10^5$ in the experiment. Then the disturbed influence of gravity force field on their shape are absent in spite of large aspect ratio of the cavity $\lambda = L_c/R_c = 90 \div 200$. Mach number M $= V_0/a$, where $a = 1430$ m/s is the sound velocity in water, was varying in range $0.3 - 0.93$.

Researches have shown that the stable and steady vapor cavities with clearly discernible boundaries along their length are formed behind the models with disk cavitator for mentioned ranges of numbers M, Fr, σ. The contour of registered supercavities remains close to ellipsoidal calculated by universal law of expansion of the cavity section of [3] at neglect of the cavitator dimension.

$$\left(\frac{R}{L_c}\right)^2 = \frac{1}{\lambda^2}\,\frac{x}{L_c}\left(2 - \frac{x}{L_c}\right), \qquad (2)$$

where $\lambda = L_c/R_c$; $x = V_0 t$; L_c is the cavity half-length; t is the time; V_0 is the motion velocity. It is shown by curve line in Fig. 5. The contour of the frontal part of the slender cavity can be determined by asymptotic law of free streamline expansion [3] at M = 0:

$$\overline{R}^2 = 2\sqrt{C_{x0}(M)}\,\frac{\overline{x}}{\sqrt{\ln \overline{x}}}\left[1 - \frac{\ln\ln \overline{x}}{4\ln \overline{x}}\right] + \cdots \qquad (3)$$

The main dimensions of the supercavity (the mid-section radius R_c, the half-length L_c, the aspect ratio $\lambda = L_c/R_c$) can be calculated with precision 2 - 4 % by asymptotic formulae

$$\begin{aligned} \overline{R}_c &= \frac{R_c}{R} = \sqrt{\frac{C_x}{\varkappa\sigma}}\,, \\ \overline{L}_c &= \frac{L_c}{R} = \frac{1}{\sigma}\sqrt{C_x \ln\frac{1}{\sigma}}\,, \\ \lambda &= \frac{L_c}{R_c} = \sqrt{\frac{1}{\sigma}\ln\frac{1}{\sigma}}\,. \end{aligned} \qquad (4)$$

4. INFLUENCE OF WATER COMPRESSIBILITY

4.1. Accounts of compressibility influence in frameworks of linear theory (Prandtl – Glauert analogy)

The flow potential of an ideal compressible fluid satisfies equation [15, 16]:

$$\beta^2 \varphi_{xx} + \varphi_{yy} + \varphi_{zz} = 0, \qquad (5)$$

where $\beta = \sqrt{1-M^2}$, at precision accepted by the theory of small perturbations.
The transformation of coordinates:

$$x = \beta\xi; \quad y = \eta; \quad z = \zeta \tag{6}$$

transfers the Eq. (5) into Laplace equation

$$\varphi_{\xi\xi} + \varphi_{\eta\eta} + \varphi_{\zeta\zeta} = 0 \tag{7}$$

Therefore, the transformation (6) establishes the conformity between a compressible fluid flow in space x, y, z and some flow of an incompressible fluid in space ξ, η, ζ.
Thus, the cross dimensions of bodies and velocity perturbations φ_y and φ_z are saved. The longitudinal dimensions of bodies are increased proportionally to β^{-1}.

$$V'_\infty = V_\infty/\beta,$$

$$\sigma' = \beta^2\sigma \tag{8}$$

Thus, we obtain the following sequence of the calculation:
- the angle $\delta' = \delta\beta$ is determined;
- the number of cavitation $\sigma' = \beta^2\sigma$ is determined;
- dimensions of bogus cavity R'_c and L'_c are calculated;
- the dimensions of the cavity to be calculated $R_c = R'_c$; $L_c = L'_c\beta$ are determined.

The radius of the bogus cavity is calculated by formula

$$R'_c = R_n\sqrt{\frac{C'_x(1+\sigma')}{k\sigma'}}$$

where C'_x is the drag coefficient of a cone with angle at top $2\delta'$.

$$L'_c = R'_c\lambda'$$

The results of calculations are shown in Fig 6. It is seen that in frameworks of given theory the compressibility account results in increase of the cavity dimensions.

4.2. Applications of the theory of slender body

The question about compressibility influence on a cavity shape at subsonic and supersonic velocities is considered in [9, 13, 17]. These works use asymptotic methods of slender body theory.

A.D.Vasin has delivered the simple relations enabling to calculate the cavity shape and dimensions at subsonic and supersonic velocities, if the cavitator drag is known at given Mach number.

For subsonic velocities they are

$$\sigma = \frac{2}{\lambda^2}\ln\left[\lambda/(\sqrt{e}\sqrt{1-M^2})\right] \tag{9}$$

and

$$R^2(x) = \varepsilon^2\left\{(1-x^2) + \frac{x^2\ln 4 - \ln\left[(1+x)^{(1+x)}(1-x)^{(1-x)}\right]}{2\ln\lambda}\right\} \tag{10}$$

where σ is the cavitation number;
$\lambda = \frac{L_c}{R_c}$ is the cavity aspect ratio;
$\varepsilon = \frac{1}{\lambda}$;
e is a basis of natural logarithms;
x is a distance from the cavity mid-section with respect to its half-length L_c;
For supersonic velocities they are:

$$\sigma = \frac{2}{\lambda^2}\ln\frac{\lambda}{\sqrt{e}\sqrt{M^2-1}}$$

$$R^2(x) = \varepsilon^2\left\{(1-x^2) + \frac{x^2\ln 4\ln\left[(1+x)^{(x^2-x-2)}(1-x)^{(x-x^2)}\right]}{2\ln\lambda}\right\}$$

Thus, the compressibility influence is displayed in changing the cavitator drag and the cavity aspect ratio.

In a compressible fluid the cavity frontal part is seen to be more slender than in an incompressible fluid. The main contribution into change of dimensions and form of a cavity introduces The change of C_{x0} of the cavitator has main effect on change of the cavity shape and dimensions.

In a compressible fluid the cavity has the same greatest diameter at the same C_{x0} of the cavitator, but it longer than in an incompressible fluid. Therefore, its frontal part is more slender (Fig. 6).

These calculations have shown that in an incompressible fluid the cavity dimensions can be more than in an incompressible fluid. The cavity radius increases due to increase of the cavitator drag. The cavity aspect ratio grows, if number M is more than $\sqrt{2}$.

This conclusion is not agreed with results of direct calculations adduced in [18]: there the cavity frontal part radius considerably decreases at increase of M.

The calculation results by various approximate theories are not always agreed among themselves and with results obtained by numerical solving total equations of the compressible fluid motion. The reliable data about cavitation drag of bodies are absent at subsonic and supersonic velocities.

Thus, the compressibility influence on the cavity shape and dimensions is investigated insufficiently.

This influence cannot be considerable owing to small water compressibility and small values of induced velocities on the cavity surface.

4.3. Next approach for supercavity shape

However, existing theories do not take considerations low water strength due to action of tension forces. Appearance of the water discontinuities in zones of negative pressure near the cavitator and fluid layer separations near the cavity surface are really possible.

The pressure and velocity fields past the supercaviting wedge in compressible fluid were calculated by Godunov method at the IHM. We supposed the flow separation in points of the flow, where the local pressure is $p \leq 0$. As a result of calculation of secondary cavitating process we obtained thin layer of separated fluid moving to the center of supercavity past the wedge. The line 2 of Fig. 6 is typical shape of this separated layer in supercavity that very confines the useful volume of supercavity.

From practical point of view the search of exact value of the cavity boundaries has the limit, which is determined by natural destruction of the free boundary. We should refer to natural perturbations of the cavity boundary first of all the perturbations obtained at flow around the cavitator due to the secondary cavitation and hydrodynamic perturbations in the boundary layer.

It is possible to refer to natural perturbations also the presence of gas boundary layer in the clearance between the object body and the free boundary of the cavity, "ebullition" of the free boundary owing to nonequilibrum processes of evaporation from the fluid surface.

Investigations of the spray drag carried out in the laboratories of the IHM UNAS have shown that notwithstanding the small spray concentration in the wall layer $C_F \approx 10^3$, the hydrodynamic drag coefficient C_x can have the same order as the drag coefficient at continuous flow [10]. Thus, the film thickness z_0 of fluid on the wall can be comparable with thickness δ^{**} of the turbulent boundary layer

$$\frac{z_0}{\delta^{**}} = 27.8\, C_F \mathrm{Re}_h^{0,2} \mathrm{tg}\alpha \ . \qquad (11)$$

5. SUPERCAVITY CONTROL

It is convenient to control the cavity by varying the value of gas-supply to the cavity [4] for artificial cavitation regimes at varying the body motion depth and velocity.

$$\overline{Q} = \frac{Q}{Vd^2} = F(\sigma, \mathrm{Fr}, \mathrm{Re}, \mathrm{We}) \ . \qquad (12)$$

In the region of considerable influence of gravity the formula for supply value has the form [4]

$$\overline{Q} = \frac{0.27}{\sigma[\sigma^2 \mathrm{Fr}^4 - 2]} \ . \qquad (13)$$

In the region of regimes close to vapor ones the structure of the dependence (12) changes:

$$\overline{Q} = kVS\left(\frac{\sigma_v}{\sigma} - 1\right). \qquad (14)$$

The control of supply in the artificial cavitation regime is restricted by values $\sigma_{min} = gD_c/V_0^2$ and occurrence of vapor cavitation at

$$\sigma \leq \sigma_v = \frac{2(P - P_v)}{\rho V^2} \ . \qquad (15)$$

In the vapor cavitation regime it is possible to control the cavity by varying the cavitator drag C_{x0} according to dependencies

$$\overline{R_c} = \sqrt{\frac{C_{x0}(1+\sigma)}{k\sigma}} \ , \ \overline{L_c} = \frac{1}{\sigma}\sqrt{C_{x0}(1+\sigma)\ln\frac{1}{\sigma}} \ . \qquad (16)$$

The cavity control at use of cavitator with channel [8] is possible also to be realized by varying the fluid rate through the cavitator.

The dependence of the cavity part length formed by jet on the velocity of jet directed against the flow is submitted in Fig. 7. A supercavity formed by water jet in working part of the hydrodynamic tunnel designed at the IHM UNAS is presented in Fig. 8. We note that the cavity separation from the nozzle does not correspond to the scheme of jet collision against the critical point, where $\rho V_\infty^2 = \rho V_0^2$. $V_0 = 0.75 V_\infty$ according to the experiments. This corresponds to the scheme of jet collision with formation of critical region without points of braking. Thus, V_0 is close to the value determined from ratio $\rho V_\infty^2 = 2\rho V_0^2$; $V_0 = 0.705 V_\infty$.

The cavity boundary shape calculated by computer program CAVAR is submitted in Fig. 9. The program permits the axisymmetric cavity shape for the body with channel to calculate in dependence on the fluid rate through the channel [8].

6. MOTION OF BODIES IN SUPERCAVITATING FLOW REGIME

Thus, the body locating in the cavity can suffer not only the hydrodynamic force applied to the cavitator and also aerodynamic and spray forces of interaction with vapor filling the cavity and sprays near the cavity boundary. Equations of the body motion in the cavity in the general case have the form

$$m\left(\frac{dV_x}{dt} + w_y V_z - w_z V_y\right) =$$

$$= (C_{x_0} S_c + C_{xp} S_p + C_s S_s)\,\frac{\rho V^2}{2} +$$

$$+C_{xv}\frac{\rho_v V^2}{2}S_{suf}\ ,$$

$$m\left(\frac{dV_y}{dt}+w_zV_x-w_xV_z\right)=$$

$$=(C_yS_c+C_{yp}S_p+C_sS_s)\frac{\rho V^2}{2}+$$

$$+C_{yv}\frac{\rho_v V^2}{2}S_{suf}\ ,$$

$$m\left(\frac{dV_z}{dt}+w_xV_y-w_yV_x\right)=$$

$$=(C_yS_c+C_{yp}S_p+C_sS_s)\frac{\rho V^2}{2}+$$

$$+C_{yv}\frac{\rho_v V^2}{2}S_{suf}\ ,$$

$$I_y\frac{dw_y}{dt}+w_xw_z(I_x-I_z)=$$

$$=(C_mS_cL_c+C_{mp}S_pL_p+C_{ms}S_sL_s)\frac{\rho V^2}{2}+$$

$$+C_{my}\frac{\rho_v V^2}{2}S_{suf}L_{suf}\ , \qquad (17)$$

$$I_z\frac{dw_z}{dt}+w_xw_y(I_y-I_x)=$$

$$(C_{mz}S_cL_c+C_{mp}S_pL_p+C_{ms}S_sL_s)\frac{\rho V^2}{2}+$$

$$+C_{my}\frac{\rho_v V^2}{2}S_{suf}L_{suf}\ .$$

Here V_x, V_y, V_z and w_x, w_y, w_z – are projections of the velocity V and the angular velocity w onto the axes of the connected system of coordinates X, Y, Z; I_x, I_y, I_z are the moments of inertia about corresponding axes; and indexes "v", "s", "p" refer respectively to parameters of vapor, spray and planning interactions.

Using these equations, we have worked out the program STABILITY for computer simulation of the supercavitating body dynamics. This program allows the motion stability to investigate at given model shape, its mass, the initial motion conditions and also under action of external perturbations. The software STABILITY consists of the following program modules:

"Inputdata" is the module of interactive input of model shape and initial parameters of motion;
"Dynamic" is the module of integration of a system of ordinary differential equations with respect to coordinates, velocity components, the angular velocity and pitch angle of the model [12];
"Cavity" is the module to compute current cavity shape;
"Force" is the module to calculate forces of vapor, spray and planing interactions acting to the model;
"Plot" is the module to plot on the PC-screen current location of the model, cavity boundaries, as well as graphs of varying parameters with respect to time.

The software STABILITY permits due to computer experiment the model motion stability to check under effect of various perturbations. The fragment of PC screen copy during work of program STABILITY on simulation of influence of sine wave oscillations of the body of revolution in the cavity on its boundary shape is shown in Fig. 13.

The result of numerical simulation of influence of the external pressure impulse on supercavity boundary shape is submitted in Fig. 14.
The complexity of the body dynamics calculation in the cavity consists that the coefficients of hydrodynamic, aerodynamic and spray forces should be defined previously for a particular body and a cavity. Thereto all the coefficients of forces and moments (except for forces on the cavitator) are lag time functions with respect to the instant angle of the object deviation. The value of delay is determined by velocity of perturbation distribution along the cavity V_∞ and distance L from the cavitator to location of their effects on the object body: $t_3 = L/V$.

Nevertheless, we have proved experimentally that the stable motion of supercavitating models is possible with all velocities from $\sim$ 70 m/s up to the sound velocity in water a = 1460 m/s [1]. The analysis has shown that the four different mechanisms of motion stabilization sequentially act at the motion velocity increase.

6.1. Two-cavity flow scheme (Fig. 10a), $V \sim 70$ m/s.

In this case the hydrodynamic drag center is placed behind the mass center, and stabilizing moment of the force L_2 acts to the model. It means that the classical condition of the motion stability is fulfilled.

6.2. Stationary hydroplaning along the cavity internal surface (Fig. 10b), $V \sim 50 \div 200$ m/s.

In this case the model tail hydroplanes along the lower internal cavity surface to compensate the buoyancy losses. As a result the motion is also stable as a whole, but the low-frequency oscillations of the model in the vertical plane and stability loss are possible. The finite velocity of the perturbation spreading from cavitator along the cavity boundary

is the cause of that.

6.3. Impact interaction with cavity boundaries (Fig. 10c), $V \sim 300 \div 900$ m/s.

The initial perturbations of the model attack angle and its angular velocity cause to the impact of the model tail against the internal boundary of supercavity. The numerical simulation has shown that the model can perform steady or damped oscillation after this impact. These oscillations are accompanied by periodic impacts of the model tail alternately against the upper and lower cavity walls. Then the motion can remain stable as a whole.

An example of calculated dependence of the model pitch angle ψ and the vertical component of the inertia center velocity of the body V_{yg} on the dimensionless path s is presented in Fig. 11a. The frame of the experimental cinegram is shown in Fig. 12. It demonstrates the cavity disturbed shape at motion of similar type (the model moves from right to left, $V = 890$ m/s). Three-dimensional spiral oscillation of the model in the cavity about its mass center is possible as well.

6.4. Aerodynamic interaction with vapor–spray medium of cavity (Fig. 10d), $V \sim 1000$ m/s and higher.

The aerodynamic forces due to the model interaction with vapor filling the cavity and spray stream near the cavity boundaries affect on the body motion with very high velocities. The clearance between the body surface and the cavity boundary is usually small compared to the cavity radius. That is why, we use the known methods of near-wall aerodynamics to estimate arising forces. The analysis testifies to favourable influence of the internal cavity boundaries on the body motion stability.

6.5. Statically stable cavitators.

We have shown theoretically that the model self-stabilization in a supercavity is possible due to the specially so called statically stable shape of the cavitator [19]. Fig. 15 demonstrates a stable region for concave wedges having a semiangle $\beta > 90°$. Concave wedges belong to the self-stabilizing cavitators because

$$\frac{C_y}{C_x} > tan\alpha \qquad \text{for } \beta > 90°.$$

It means that the returning momentum M appears every time at $\alpha \neq 0$ and tends to turn the cavitator back to the initial position, when $\alpha = 0$. This stabilization mechanism can be effective at small initial perturbations of the model motion (see Fig. 11b).

REFERENCES

1. Savchenko, Yu.N., Semenenko, V.N., Serebryakov, V.V., "Experimental Investigation of Developed Cavitating Flows at Subsonic Flow Velocities", Dopovidi AN Ukrainy, 2, 1993, pp 64–69 (in Russian)

2. Savchenko, Yu.N., "Hydrodynamics of Separated Flows" in "Applied Hydrodynamics", Kiev, USSR, 1989, pp 169–191. (in Russian)

3.Savchenko, Yu.N., Semenenko, V.N., Serebryakov, V.V., "Experimental Check of Asymptotic Formulae for Axisymmetric Cavities at $\sigma \rightarrow 0$" in "Problems of high-speed hydrodynamics", Cheboksary, Russia, 1993, pp 117 – 122. (in Russian)

4. Logvinovich, G.V., "Hydrodynamics of Flows with Free Boundaries", Kiev, USSR, Naukova dumka, 1969, 208 P. (in Russian)

5. Savchenko, Yu.N., "On Motion in Water in Supercavitating Flow Regime", Hydromechanics, 70, 1996, pp 105 – 115. (in Russian)

6. Savchenko, Yu.N., Savchenko, V.T., "Unsteady Motion of Disk at Collapsing Cavity Presence", Hydromechanics, 34, 1976, pp 35–38. (in Russian)

7. Deynekin, Yu.P., "Shotting Body by Vapor-Gas Catapult", Hydromechanics, 66, 1993, pp 40–44. (in Russian)

8. Deynekin, Yu.P., "Cavitating Flow around Bodies with Channel", Hydromechanics, 68, 1993, pp 156–165. (in Russian)

9. Yakimov, Yu.L., "Slender Cavity in Compressible Fluid" in "Problems of modern mechanics", Moscow, USSR, 1983, pp 66–73. (in Russian)

10. Savchenko, Yu.N., "Some Special Cases of Flows Over Bodies", Fluid Mechanics – Soviet Research, **21**, 1, 1992, pp 131–136.

11. A.c. 1710445 USSR, ICI 5**B54C** 3/14 Aerofoil / Yu.N., Savchenko, S.I., Putilin, V.T., Savchenko. – Publ. 07.02.92, N5.

12. May, A., "Vertical Entry of Missiles into Water", J. Appl. Phys., **23**, 2, 1952, pp 1362–1372.

13. Varghese, I.S., Uhlman, I.S., Kirschner, I.N., "Axisymmetric Slender Body Analysis of Supercavitating High-speed Bodies in Subsonic Flow", Papers of Third International Symposium on Performance Enhancement for Marine Applications. – Newport RI, USA, 6 – 8 May 1997.

14. Cnapp, R.T., Daily, J.W., Hammitt, F.G. "Cavitation", New York, USA, Mograw–Hill Book C^o, 1970, 687 P.

15. Bielotzerkovsky, S.M., " Slender Lifting Surface

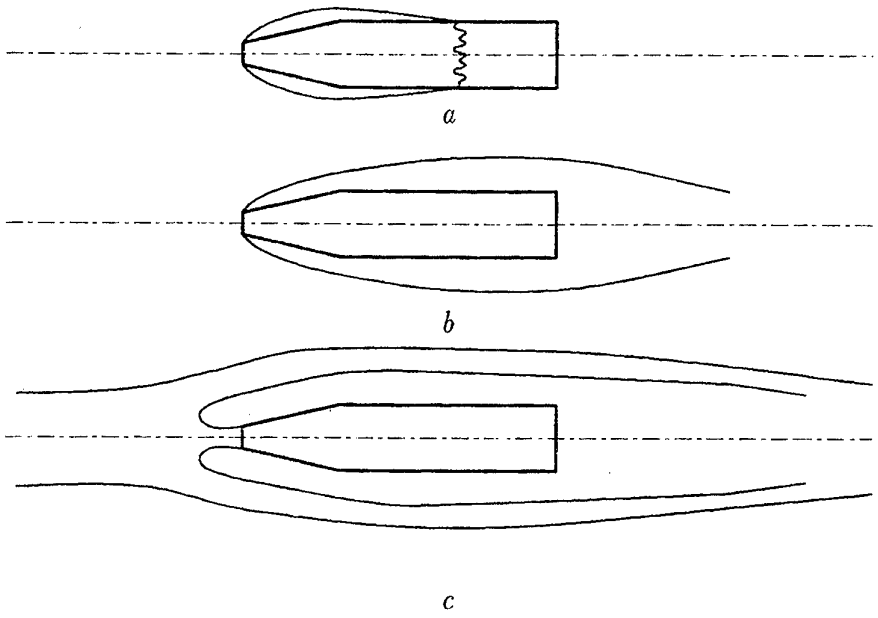
in Subsonic Gas Flow", Moscow, USSR, Nauka, Glavnaya redaktziya fiziko-matamaticheskoy literatury, 1968, 511 P. (in Russian)

16. Loytzyansky, L.G., "Mechanics of fluid and gas", Moscow, USSR, Nauka, Glavnaya redaktziya fiziko-matematicheskoy literatury, 1970, 904 P. (in Russian)

17. Vasin, A.D., "Slender Axisymmetric Cavities in Sub- and Supersonic Flows of Compressible Fluid" in "Proceedings of Third Workshop on High-Speed Hydrodynamics", Krasnoyarsk, Publ. of Krasnoyarsk polytechnical institute, 1987, pp 58–62. (in Russian)

18. Aliev, G.A., "Breaking Flow Around the Circular Cone by Transonic Water Stream", Izvestiya AN SSSR, Mechanics of fluid and gas, 2, 1982, pp 152–154. (in Russian)

19. Savchenko, Y., Semenenko, V., Naumova, Y., Varghese, A., Uhlman, J., Kirschner, I., "Hydrodynamic Characteristics of Polygonal Contours in Supercavitating Flow", Papers of Third International Symposium on Performance Enhancement for Marine Applications.–Newport RI, USA, 6-8 May 1997.

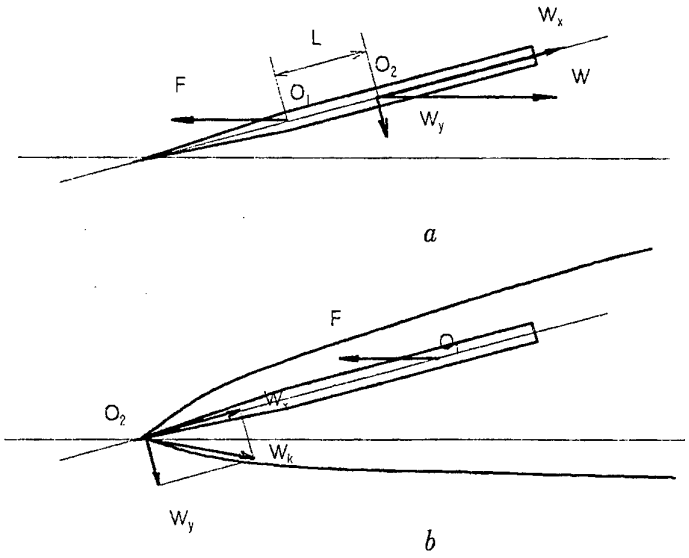


a

b

c

Fig. 1. Schemes of supercavitating flow around bodies: *a* – with partial wash off the body ; *b* – with nose cavitator and free location of a body in a cavity; *c* – with jet cavitator without contact points of a body and a free cavity boundary.



a

b

Fig. 2. Action of forces to a body of revolution: *a* a regime of continuous flow with formation of the stabilizing moment $M_z = LW \sin\alpha$; *b* a regime of cavitating flow with formation of destabilizing moment $M_z = LW \sin\alpha$.

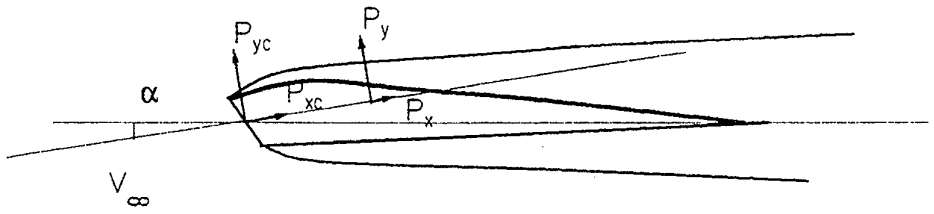


Fig. 3. Scheme of flow around a two-medium wing [11] in supercavitating regime; P_{xc}, P_{yc} are components of the hydrodynamic force vector; P_x, P_y are components of the aerodynamic force vector.



Fig. 4. Photograph of supercavity past a model having cone shape with disk cavitator: $V = 1000$ m/s; $L_c = 12$ m; $D_n = 3$ mm; $\sigma = 10^4$.

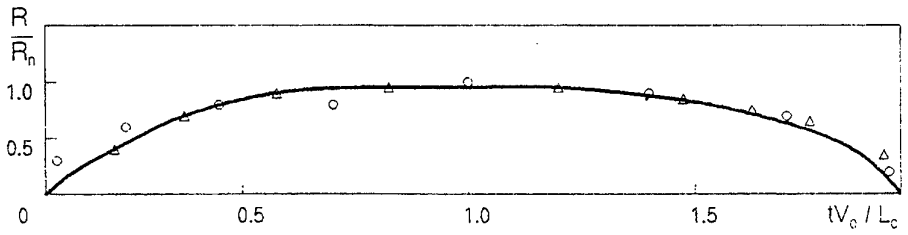
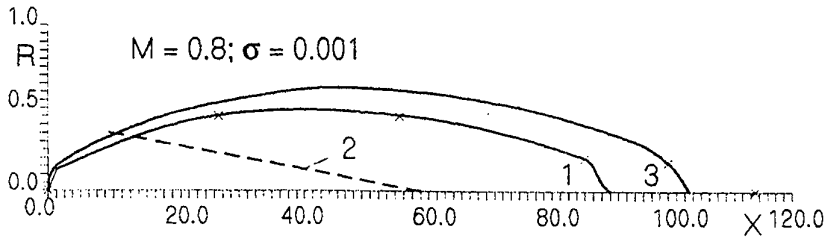


Fig. 5. An elliptic cavity shape: experimental points at $\sigma = 10^{-4}$, Fr $= = 10^4 \div 10^5$, M $= 0.3 \div 0.93$; a curve is the asymptotic contour of jet spreading [3].



1 - Compressible fluid; cone characteristics were recalculated by Prandtl Glauert law;

2 - Boundary of separated layer due to tension force appearance

3 - Incompressible fluid.

Fig. 6

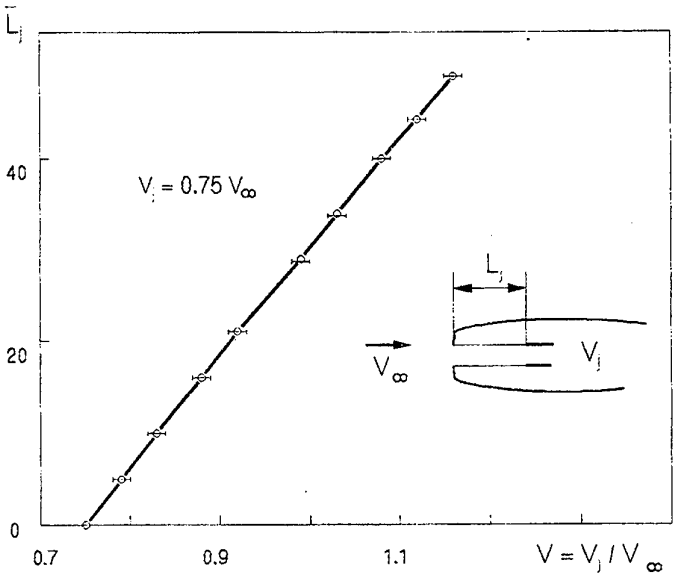


Fig. 7. Experimental dependence of the jet part length of a cavity $\overline{L}_j$ on jet velocity $V = V_j/V_\infty$; $L_0 = 0$ at $V_j = V_0 = 0.75V_\infty$.



Fig. 8. Supercavity formed by water jet coming from the opposite direction.

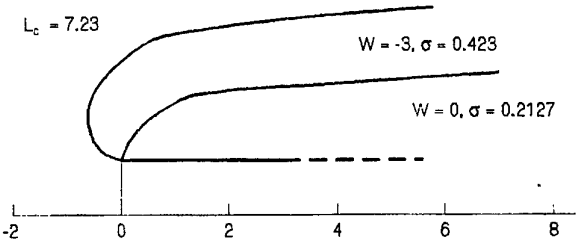


Fig. 9. Cavity shape formed by jet cavitator for two values of the rate W.

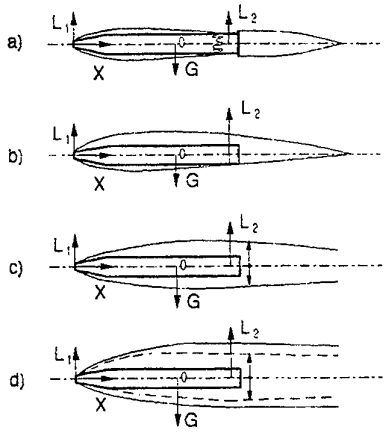


Fig. 10

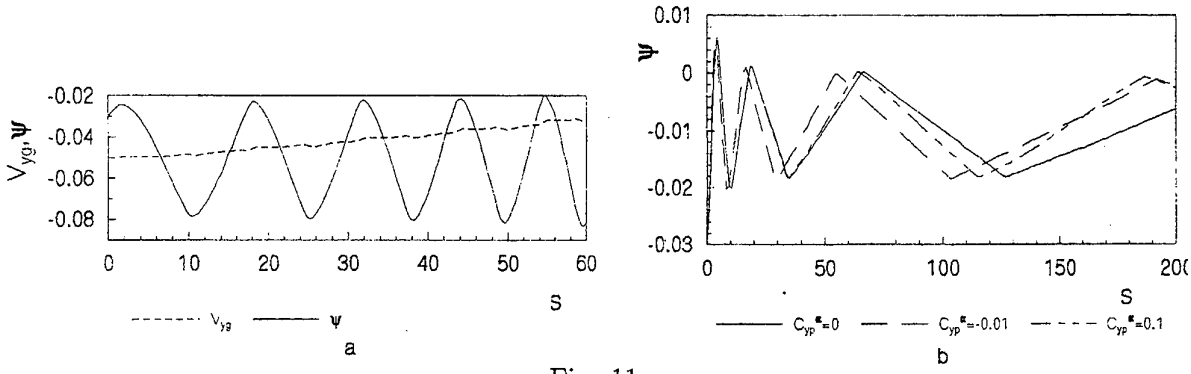


Fig. 11

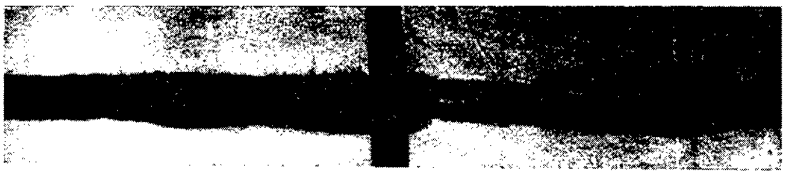


Fig. 12

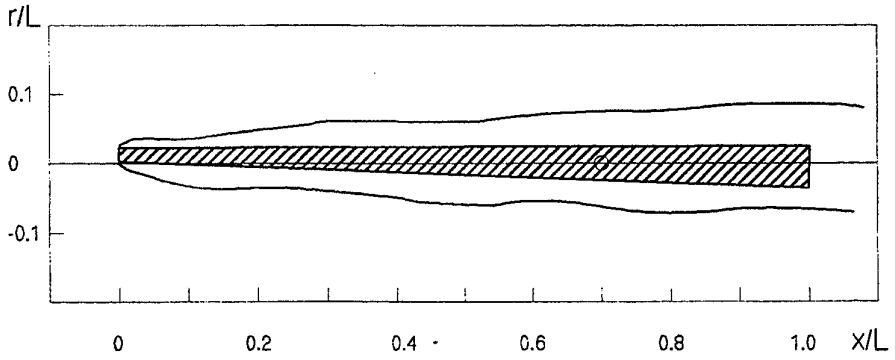


Fig. 13. Result of numerical simulation of influence of sine oscillations on a cavity shape.

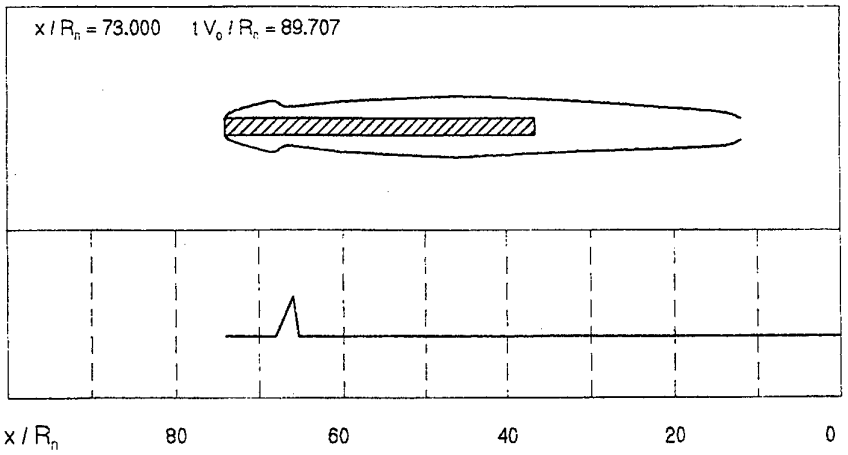


Fig. 14. Result of numerical simulation of influence of the external pressure impulse on a cavity boundary shape, current coordinates $x/R_n = 73.0$, $tV_0/R_n = 89.707$.

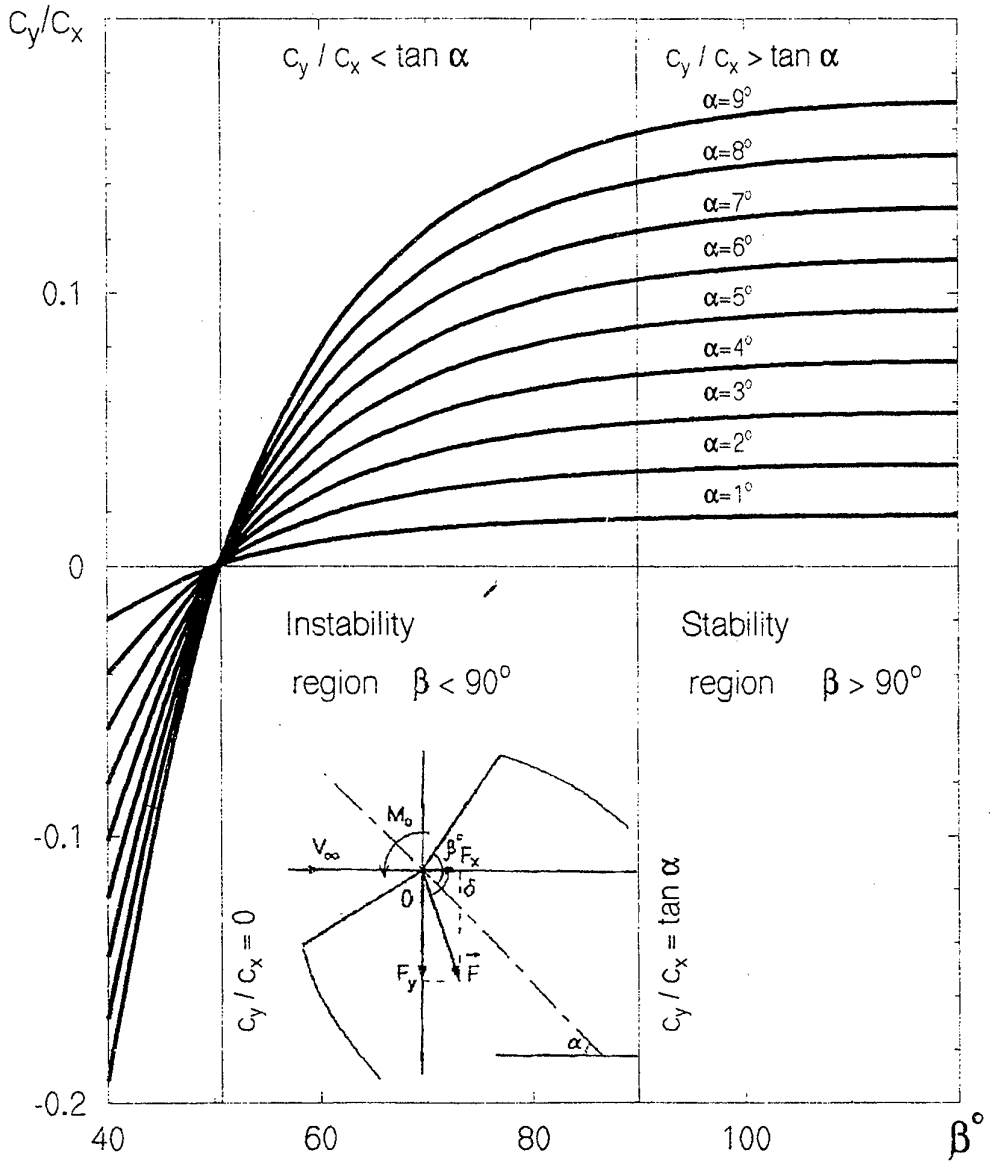

c_y/c_x
$c_y / c_x < \tan\alpha$
$c_y / c_x > \tan\alpha$
α=9°
α=8°
α=7°
α=6°
α=5°
α=4°
α=3°
α=2°
α=1°
0.1
0
-0.1
-0.2
Instability
region β < 90°
Stability
region β > 90°
M_o
V_∞
β°
F_x
δ
0
F_y
$\vec{F}$
α
$c_y / c_x = 0$
$c_y / c_x = \tan\alpha$
40
60
80
100
β°

Fig.15.

Supercavitating Flows at Supersonic Speed in Compressible Water

A.D.Vasin
State SRC TsAGI
18 Radio str., Moscow, 107005
Russia

In the beginning I notice basic results obtained in the theory of supercavities in compressible fluid, then I notice the features of supersonic flow.

Since 1980 in the USSR interest has arisen to supercavities in compressible fluid. On the basis of the slender body theory works have been made, these are *Yakimov's* works [1, 2], mine [3, 4] and *Serebryakov's* works [5, 6]. On the basis of the early numerical method Al'ev [7] has calculated cavity past a thin cone. The recent development of numerical methods and the widespread use of computers has made it possible to calculate compressible cavitation flows efficiently. It should be noted works have been made recently: *Kiselev's* [8] and mine [9, 10].

Now I stop on some my results. On the basis of the slender body theory axisymmetric supercavities in subsonic and supersonic flow of compressible fluid have been considered [3, 4]. *Riabouchinsky* scheme was applied and the condition that the cavitator is very small in comparison with the cavity was used. The cavity shape was defined and the relationship between the cavity aspect ratio and the cavitation and *Mach* numbers was derived. Basic result concludes that an ellipsoid of revolution is the first approximation of cavity shape (how in the incompressible fluid). However, application of the slender body theory to the supersonic cavitation flows has some features. I'll speak about that below. It should be noted that for blunt cavitators, such as a disk, a blunt cone, slender body theory gives no way of obtaining the complete data for the cavitation flow, for example, the cavity shape immediately downstream of the cavitator and the cavitation drag. Moreover, the linear equation for the potential of compressible fluid flow past slender axisymmetric bodies is inapplicable on the transonic velocity range.

I have designed a numerical method of calculating compressible subsonic and supersonic flow over a wide range of cavitation numbers. Scheme of method is shown in Fig. 1. As the main equation we use the equation of continuity. We take the density - velocity relationship from *Bernoulli* equation. *Riabouchinsky* scheme was applied, in this scheme the cavity is closed by a disk of the same dimensions as the cavitator disk. In view of the flow symmetry, we will examine the flow in a meridional plane. The problem consists in determining the shape of the boundary MN satisfying the constant velocity and impermeability conditions for a given cavity length Lk (Fig. 1, where AM is the cavitator disk, NB in the closing disk, $CFED$ is the external boundary).

We assume the flow to be potential. In the case of supersonic flow the shock waves appear, line 1 is the head shock wave arising in front of the disk, line 2 is the back shock wave going away from the edge of closing disk. However, the appearance of shock waves does not break the condition that the flow is potential. In water over a wide range of pressures a shock adiabat agrees with static one, expressing by *Tate* equation. The analysis has shown that we can assume the shock waves as isentropic and the flow as potential when *Mach* numbers are less than 2.2.

We apply a finite-difference method to solve continuity equation. To make the formulation of the boundary conditions at the cavity surface more convenient, it makes sense to map the computational domain onto a unit square in ξ, η coordinates. As distinct from the subsonic flow we apply the artificial viscosity in order to the difference scheme will be stable in the supersonic area. The artificial viscosity is introduced as modification of density expression.

The nonlinear system of equations, obtained as a result of the discretization, was solved using the iteration method with approximate factorization. Before proceeding to the calculations, the first approximation for the cavity shape between the points M and N was preassigned and the computational network corresponding to the given cavity was constructed in the x, r plane using an algebraic

Paper presented at an AGARD FDP Workshop on "High Speed Body Motion in Water", held in Kiev, Ukraine, 1-3 September 1997, and published in R-827.

mapping technique. The velocity Vk on the cavity surface was determined in each iteration stage using the values of potential Φ_N, Φ_M at the points N and M, Sn is the arclength between these points. The iteration procedure turned out to be convergent; the discrepancy diminished and the potential increment vanished as the number of iteration cycles increased. However, in general, the solution thus obtained did not satisfy the impermeability condition on the cavity surface. The cavity shape was varied using the differential equations which corresponding the condition of equality of the normal velocity $\partial\Phi/\partial n$ to zero. For the subsonic flow the first order differential equation was used, for the supersonic flow the second order one was used. The cavity shape thus obtained satisfied both the constant velocity condition and the impermeability condition.

Calculation of supercavities downstream of a disk within the range of *Mach* numbers $0 \leq M \leq 1.4$ has been performed. The numerical analysis was performed for cavity constant length, corresponding to cavitation number 0.02 for incompressible fluid. As a result of the analysis for different *Mach* numbers, the following was defined: cavitation number, cavitation drag ratio, mid-section radius, cavity shape, distance of shock wave from a disk (for supersonic flow).

Let us consider the basic results. For the subsonic flow the cavity shape in the vicinity of the disk is shown in Fig. 2. The continuous curve represents the *Guzevsky's* calculations [11] for incompressible fluid ($M = 0$). My results are shown by points for the different *Mach* numbers. In Fig. 3 we compare the cavity profiles in compressible and incompressible fluids for the same cavitation number $\sigma = 0.0235$. The continuous curve corresponds to the cavity profile in a compressible fluid calculated by the numerical method for $M = 0.8$; dotted line curve corresponds to the cavity in an incompressible fluid calculated by Logvinovich's formula [12]. For the subsonic flow the numerical results agree well with my results of slender body theory [3].

For the supersonic flow the cavity shape in the vicinity of the disk is shown in Fig. 4. It can be seen that for the supersonic flow the cavity in the initial region is narrower than for the incompressible flow. I'll speak about reason of this effect below. In Fig. 5 we compare the cavity profile in the supersonic flow and incompressible fluid for the same cavitation number $\sigma = 0.0308$. The continuous curve corresponds to the cavity profile in a compressible fluid calculated by the numerical method for $M = 1.2$; dotted line curve corresponds to the cavity in an incompressible fluid. The positions of head shock wave and the sound line (on which $M = 0$) were defined in the numerical calculation. As an example, in Fig. 6 the position of head shock wave is shown for *Mach* number equal 1.1. Line 1 corresponds to the head shock wave; line 2 corresponds to the sound line; line 3 corresponds to the profile of head part of the cavity. *Mach*-number-dependence of the cavitation drag coefficient of the disk is shown side by side.

It should be noted that the results of the numerical calculation were checked on the satisfaction of the mass and impulse conservation laws. The test showed a good accordance. For the supersonic flow the cavity shape defined by the numerical calculation is close to an ellipsoid of revolution. It agrees to my results of slender body theory [4]. However, results of nonsymmetry of shape (mid-section displacement relatively middle of cavity) do not agree. Probably the slender body theory is not applicable to the second approximation for the cavity shape. Really, the first approximation (ellipsoid of revolution) is not the slender body in the head part, where the shock wave arises. The shock wave is not described by the small disturbance theory. This is the first feature of application of the slender body theory to the supersonic cavitation flows, which I wish to note.

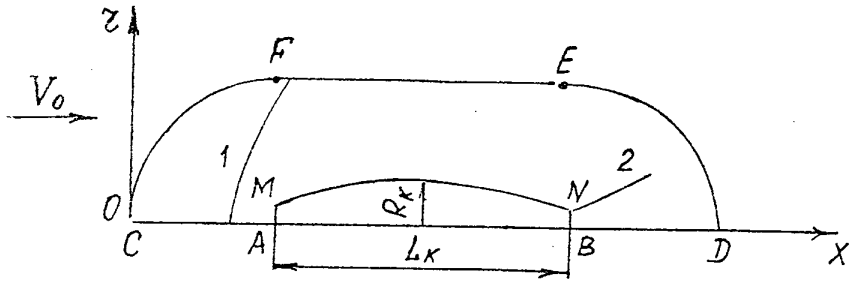
Let us consider axisymmetric cavitation flow past the thin cones in compressible fluid. We apply the slender body theory and *Riabouchinsky* scheme. We can deduce an integral-differential equation for the cavity profile. We can solve this equation using the method of expansion into asymptotic rows. For the cone with semiangle equal 6^o results of solution are shown in Fig. 7. Subsonic flow is shown in upper picture, supersonic flow is shown in under picture. Dotted line curve corresponds to the first approximation for the cavity shape, the continuous curve corresponds to the second one. It can be seen that the slender body theory is applicable for the subsonic flow, as the second members of asymptotic row are smaller than the first ones. However, for the supersonic flow such correlation is broken. The second approximation essentially differs from the first one.

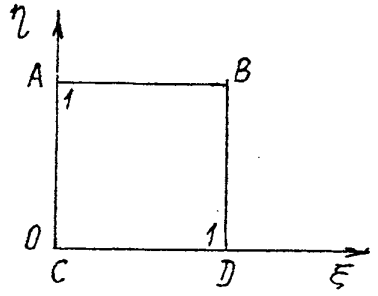
The analysis of this effect has shown, that the slender body theory does not agree the flow at the edge of cone. In the supersonic flow the *Prandtl-Meyer* stream arises at the edge. The stream must turn away by the angle dependent on pressure in the cavity or cavitation number. The incline of free stream line is fewer than the semiangle of cone. It agrees with my results of numerical calculation of cavity past a disk, which have shown some narrowing of cavity in the head part. The second feature of application of the slender body theory consists in discrepancy to the stream at the edge in the supersonic flow.

In my report I have spoken about my basic results obtained in the theory of supercavities in the compressible fluid. Also I have noted some features of application of the slender body theory to the supersonic cavitation flows.

REFERENCES

1. Yakimov, Yu.L., "Asymptotic laws of degeneration of thin cavity shapes", Isv.Akad.Nauk SSSR, Mekh.Zhidk.Gaza, No 3, 1981, pp 3–10.
2. Yakimov, Yu.L., "Thin cavitation cavity in a compressible fluid", in "Problems of Contemporary Mechanics, Pt1", Moscow University Press, Moscow, 1983, pp 66–73.
3. Vasin, A.D., "Thin axisymmetric cavities in subsonic compressible flow", Izv. Akad. Nauk SSSR, Mekh.Zhidk.Gasa, No 5, 1987, pp 174–177.
4. Vasin, A.D., "Thin axisymmetric cavities in supersonic flow", Izv. Akad. Nauk SSSR, Mekh. Zhidk. Gasa, No 1, 1989, pp 179–181.
5. Serebryakov, V.V., "Asymptotic solutions of problems of axisymmetrical supercavitation flow in slender body approximation", in "Hydrodynamics of High Speeds", Chuvash. University Press, Cheboksari, 1990, pp 99–111.
6. Serebryakov, V.V., "Asymptotic solutions of axisymmetrical problems of subsonic and supersonic separated water flows with zero numbers of cavitation", Dokl. Akad. Nauk Ukrainy, No 9, 1992, pp 66–71.
7. Al'ev, G.A., "Separated transonic water flow past a circular cone", Izv. Akad. Nauk SSSR, Mekh. Zhidk. Gaza, No 2, 1983, pp 152–154.
8. Zigangareeva, L.M., Kiselev, O.M., "Calculation of the compressible subsonic cavitation flow past a circular cone", Prikl.Mat.Mekh., 58, No 4, 1994, pp 93–107.
9. Vasin, A.D., "Calculation of axisymmetric cavities downstream of a disk in subsonic compressible fluid flow", Izv.Rus.Akad.Nauk, Mekh. Zhidk.Gaza, No 2, 1996, pp 94–103.
10. Vasin, A.D., "Calculation of axisymmetric cavities downstream of a disk in supersonic flow", Izv.Rus.Akad.Nauk, Mekh.Zhidk.Gaza, No 4, 1997, pp 55–63.
11. Guzevsky, L.G., "Numerical analysis of cavitation flows", Institute of Thermal Physics, Siberian Branch of the USSR Academy of Sciences, Preprint No 40–79, Novosibirsk, 1979.
12. Logvinovich, G.V., "Hydrodynamics of flows with free boundaries", Naukova Dumka, Kiev, 1969.





$$\frac{\partial}{\partial x}(\rho U_x z) + \frac{\partial}{\partial z}(\rho U_z z) = 0 \; ; \quad \rho = \left[1 + \frac{(n-1)M^2}{2}\left(1 - U_x^2 - U_z^2\right)\right]^{\frac{1}{n-1}}$$

$$\rho^*_{j+1/2,i} = (1-\nu)\rho_{j+1/2,i} + \nu\rho_{j-1/2,i} \; , \quad \nu = c\left(M^2_{j,i} - 1\right)$$

$$V_K = (\Phi_N - \Phi_M)/S_N \; ; \quad \Phi(S) = V_K S + \Phi_M$$

$$\frac{\partial \Phi}{\partial n} = \frac{\partial \varphi}{\partial n} + \frac{\partial x}{\partial n} \; ; \quad \frac{\partial z}{\partial S} = \frac{\partial x}{\partial n} \rightarrow \frac{\partial z}{\partial S} = -\frac{\partial \varphi}{\partial n} \; , \quad \frac{\partial x}{\partial S} = \left(1 - \left(\frac{\partial z}{\partial S}\right)^2\right)^{1/2}$$

$$\frac{\partial^2 z}{\partial S^2} = -\frac{\partial}{\partial S}\left(\frac{\partial \varphi}{\partial n}\right), \quad \frac{\partial^2 x}{\partial S^2} = \frac{\partial}{\partial S}\left(\left(1 - \left(\frac{\partial z}{\partial S}\right)^2\right)^{1/2}\right)$$

$$S = 0 : \; x = 0, \; z = 1 \; ; \quad S = S_N : \; x = L_K \, , \; z = 1$$

Fig. 1

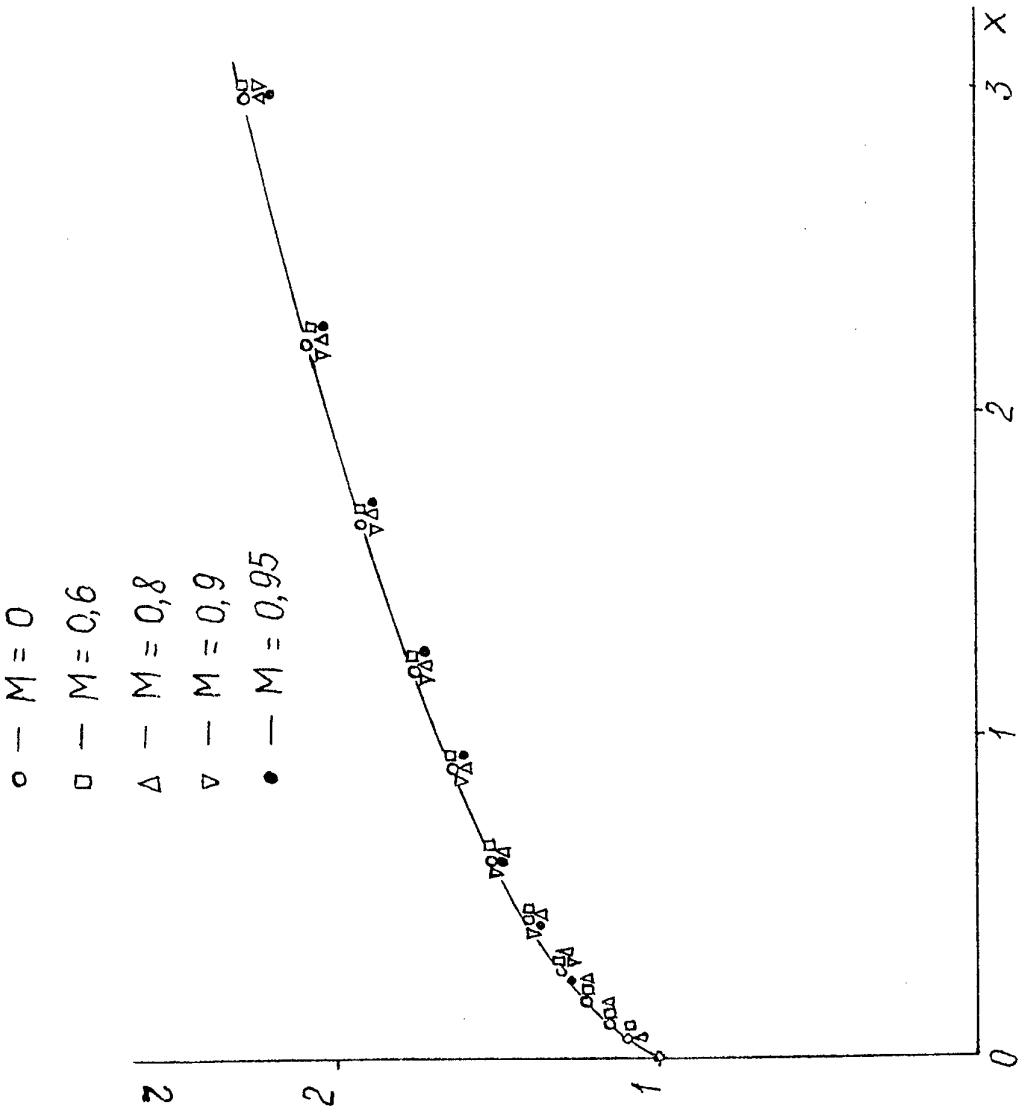


Fig. 2

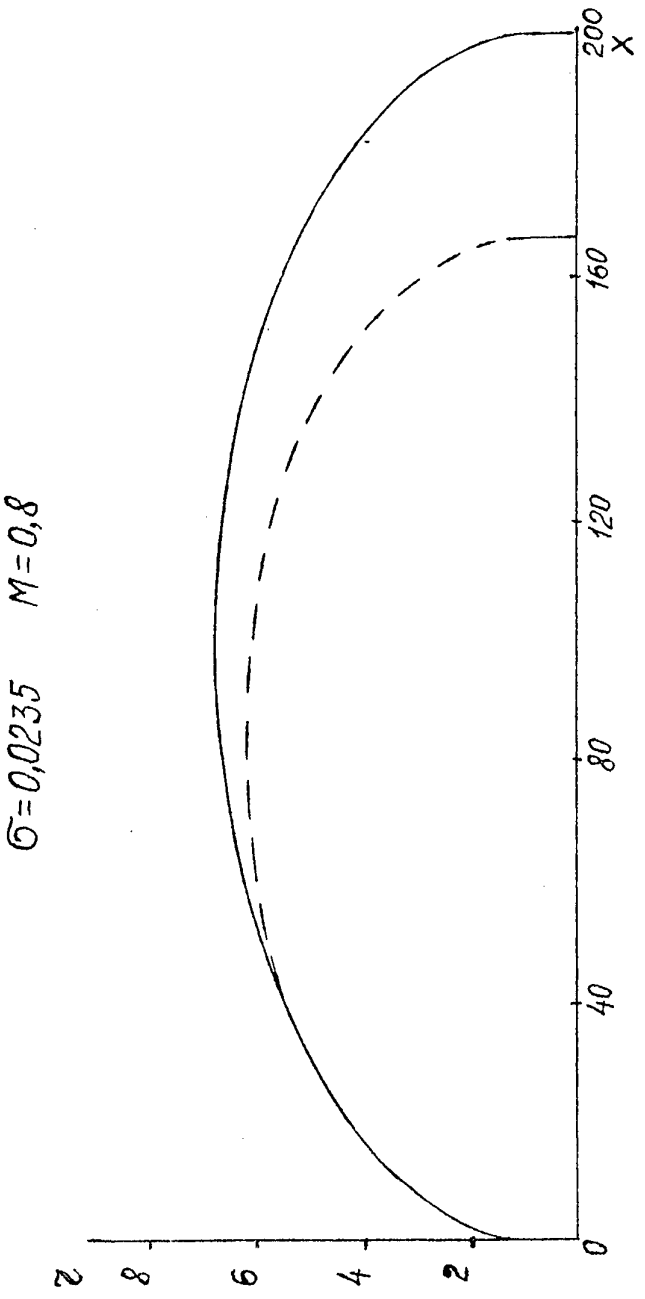


Fig. 3

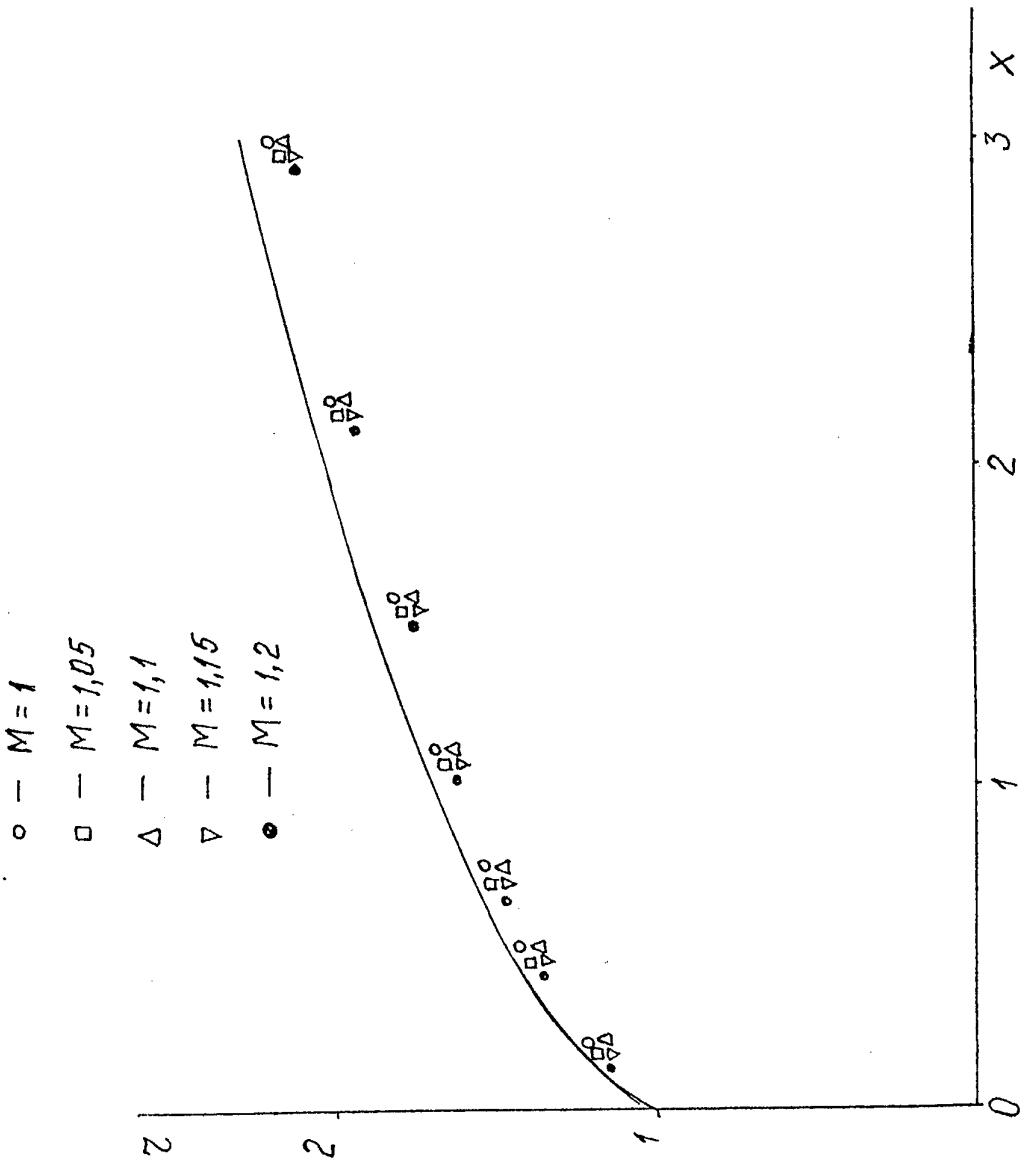


Fig.4

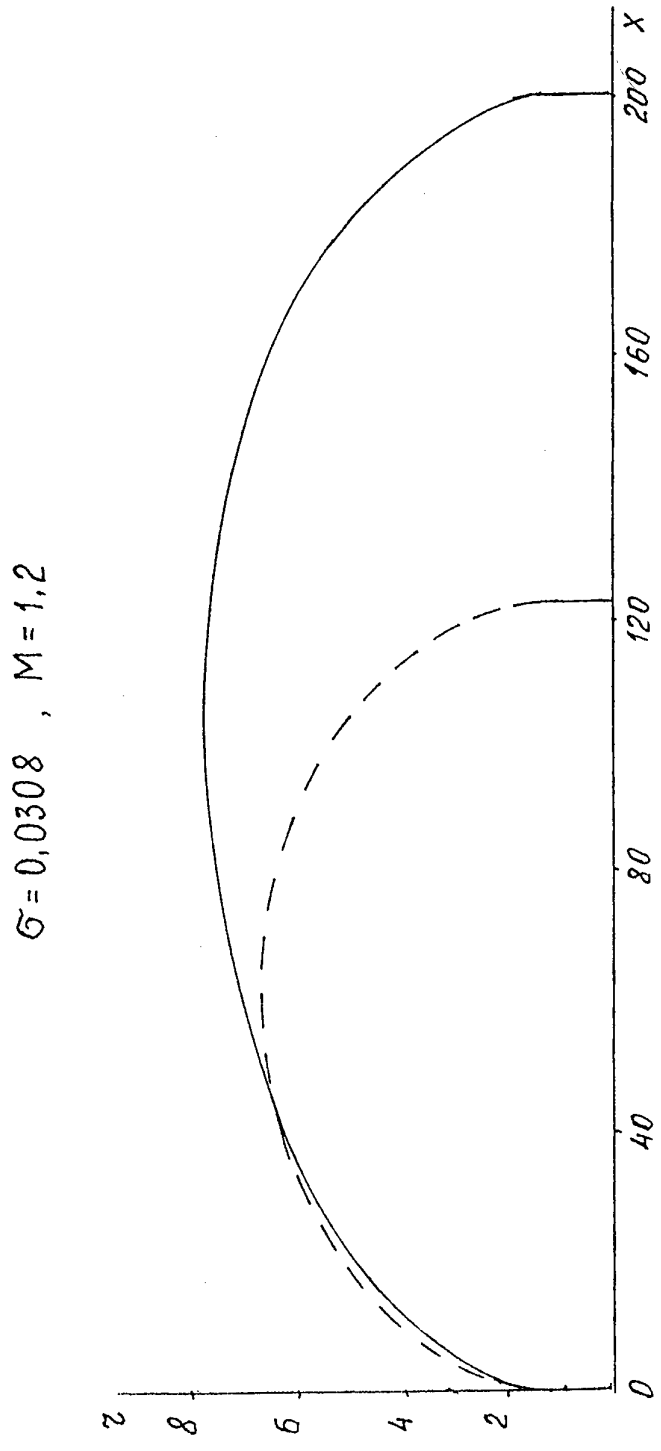
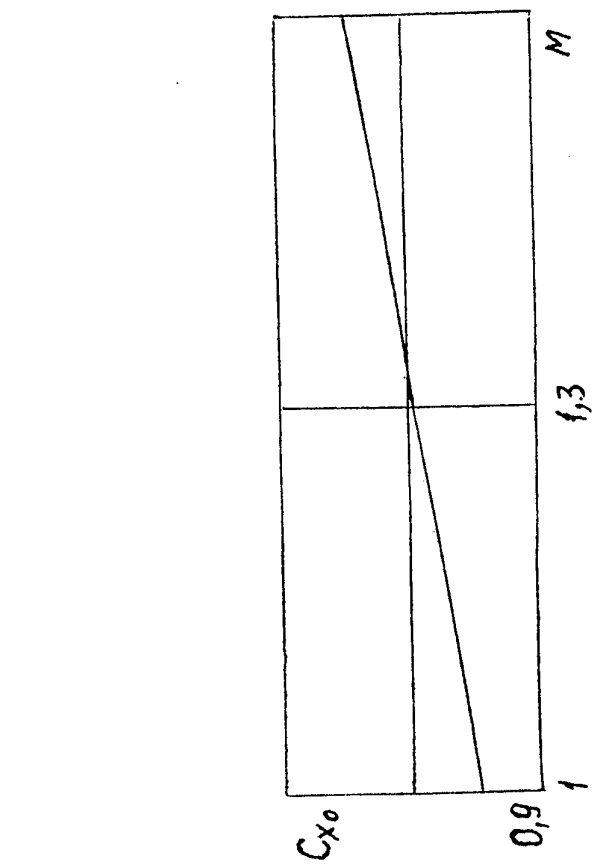


Fig. 5



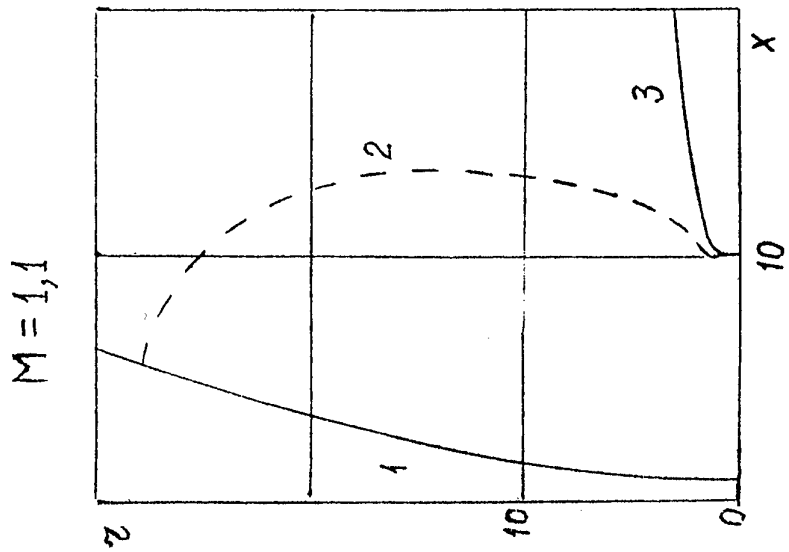
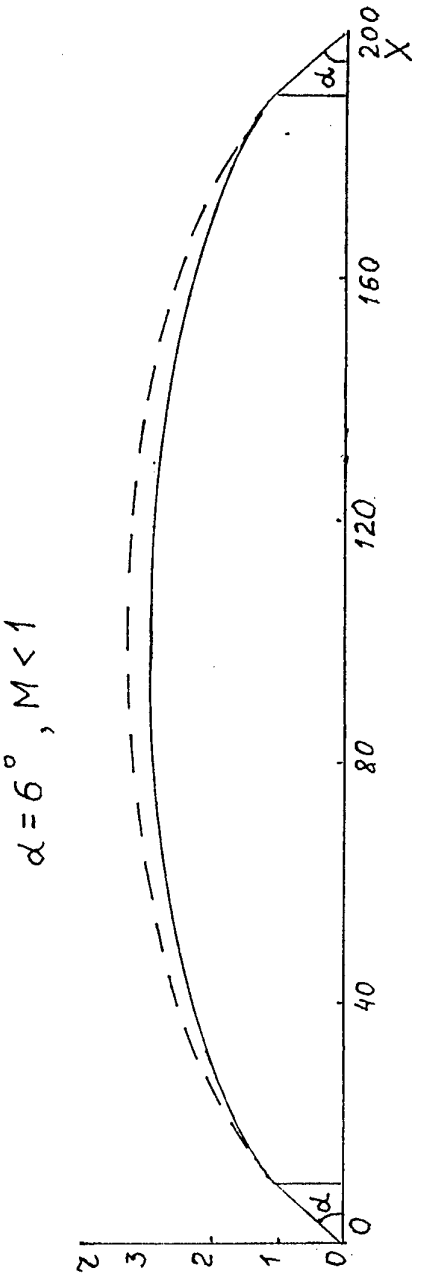


Fig. 6


α = 6°, M < 1
0
40
80
120
160
200
X
α
0
1
2
3
2

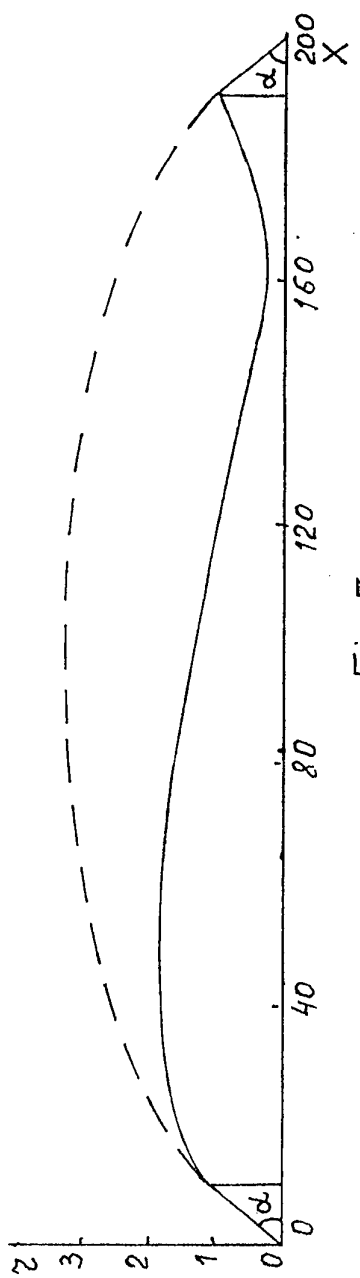

α = 6°, M > 1
0
40
80
120
160
200
X
α
0
1
2
3
2

Fig. 7

Computer Simulation of Unsteady Supercavitating Flows

V.N.Semenenko
National Academy of Sciences – Institute of Hydromechanics
8/4 Zhelyabov str., Kyiv, 252057.
Ukraine

1. SUMMARY

A mathematical model of unsteady axisymmetrical supercavity and an algorithm of numerical solution as well as corresponding computer programs are described. Examples of computer simulation of the unsteady supercavitating flows are presented.

2. INTRODUCTION

The unsteady supercavitating flows are distinguished by complexity of physical processes and difficulty of mathematical descriptions. We use a complex approach to investigate these flows. It is a combination of the physical experiment with a high–speed shooting of unsteady cavities and their computer simulation.

We solve the following three problems by computer simulation: 1) test of hypothesis about actions of various physical causes on the unsteady process; 2) more precise definition of both the mathematical model of the process and the calculation algorithm; 3) statement of the "computer experiment" with a visualization of the unsteady process on a PC–screen.

The computer simulation have played a positive role for the work out of problems on the high–speed underwater model design and the right arrangement of the water entry. As a result, we have attained experimentally the speed of the model motion in water upwards of 1300 m/s [1].

3. MATHEMATICAL MODEL

The necessary condition for a development of programs for computer simulation is the use of rather simple mathematical models and "fast" computation algorithms. We use the approximate equation of the expansion of axisymmetrical cavity sections based on the independence principle by *G.V.Logvinovich* [2, 3] (in dimensionless form):

$$\frac{\partial^2 S(\tau,t)}{\partial t^2} = -\frac{k_1}{2}\left[\overline{p}_\infty(\xi) - \overline{p}_c(t) + \overline{p}_1(t)\right]. \quad (1)$$

Here, $x-l(t) \le \xi \le x$, S is the area of the section ξ, $\tau \le t$ is time of the section ξ formation, k_1 is the empirical constant, $\overline{p}_c$ is the cavity pressure, $\overline{p}_1$ is the external water pressure perturbation, x is the cavitator coordinate, l is the cavity length (see Fig.1).

The Eq. (1) should be integrated for $t > \tau$ with initial conditions:

$$S(\tau,\tau) = \frac{\pi D_n^2}{4}, \qquad \frac{\partial S(\tau,\tau)}{\partial t} = \dot{S}(0), \quad (2)$$

where D_n is the cavitator diameter, $\dot{S}(0)$ is the initial velocity of the cavity section expansion, which is defined by the cavitator shape and the instant model velocity V, but does not depend on the cavitation number. We choose the constant k_1 and $\dot{S}(t,t)$ so that the known asymptotic expressions for both the cavity mid–section diameter D_c and the cavity length by *P.R.Garabedian* [4] are fulfilled:

$$D_c = D_n\sqrt{\frac{c_x}{\sigma}}, \qquad l = \frac{D_n}{\sigma}\sqrt{c_x \ln\frac{1}{\sigma}}, \qquad \sigma \to 0. \quad (3)$$

Here, c_x is the cavitation drag coefficient, $\sigma = 2(p_\infty - p_c)/\rho V^2$ is the cavitation number. We have confirmed experimentally the validity of asymptotic formulae (3) for models with disc cavitators, moving with velocities $300 \div 1300$ m/s [1].

The Eq. (1) describes the main part of the prolate cavity. It is incorrect for the upper end of cavity part with a length of several cavitator diameters. We set the shape of the upper end of cavity by empirical exponential function [2] for the better correspondence with experiment:

$$\frac{2R}{D_n} = \left(1 + \frac{6x}{D_n}\right)^{\frac{1}{3}}, \qquad \frac{x}{D_n} < 1 \div 2. \quad (4)$$

The cavity shape given by expressions (1), (4) should be matched at $x \approx D_n$.

The independence principle of the expansion of axisymmetrical cavity sections was repeatedly tested by means of comparison with experiment. It was shown that the approximate equation (1) adequately describes the unsteady supercavitating processes for various conditions. We have made an experiment on passing of supercavitating model through the thin steel sheet with the velocity about

Paper presented at an AGARD FDP Workshop on "High Speed Body Motion in Water", held in Kiev, Ukraine, 1-3 September 1997, and published in R-827.

900 m/s. High–speed shooting shows that the obstacle does not influence on a cavity shape. This result gives us the experimental substantiation of the independence principle in the case of very high–speed motion.

Besides the main Eq. (1), the mathematical model can include the mass of gas in the cavity balance equation during its isothermal expansion:

$$\frac{d}{dt}\left[\,(\beta-\overline{\sigma}(t))\;Q(t)\,\right]=\beta\left[\,\dot{q}_{in}-\dot{q}_{out}(t)\,\right]. \qquad (5)$$

Here, $\beta = Eu\,/\,\sigma_0$, $\overline{\sigma}(t) = \sigma(t)\,/\,\sigma_0$, $Eu = 2p_\infty/\rho V^2$ is the *Euler* number, σ_0 is the initial cavitation number, Q is the cavity volume, $\dot{q}_{in}$ and $\dot{q}_{out}(t)$ are the based on free–stream pressure volumetric air–supply rate into the cavity and air–leakage rate from the cavity (for ventilated cavities).

We also use the equation of supercavitating body motion on inertia:

$$\frac{dV}{dt}=\frac{1}{Fr^2}-\frac{\rho\pi D_n^3 c_{x0}}{8m}\left[V^2+\overline{p}_{atm}+\frac{2H(t)}{Fr^2}-\overline{p}_c(t)\right]. \qquad (6)$$

Here, $Fr = V/\sqrt{gD_n}$ is the *Froude* number, g is the gravity acceleration, m is the body mass, c_{x0} is the cavitation drag coefficient at $\sigma = 0$, $\overline{p}_{atm}$ is the atmospheric pressure, $H = const$ when the motion is horizontal, $H = x(t)$ when the motion is vertical.

4. NUMERICAL ALGORITHM AND COMPUTER PROGRAMS

We develop two types of the computer programs:

1) The programs enable to compute quickly the cavity shape and all necessary flow parameters for various combinations of the parameters. In this case, the convenience of data input with PC–keyboard is considerable. The computation result must be quickly display in the graphic form comfortable for perception. Our program SUPERCAVITY is an example of such program.

2) The programs enable to carry out "the computer experiment" with dynamic display of the non–stationary cavity shape and another necessary information at the program run–time. Our programs ENTRY, STABILITY, PULSE, DIVE are examples of such programs.

Our programs could be used on widespread desktop computers with moderate capacity. They have a comfortable user's interface including the menu system, the window system of data input from PC–keyboard, the graphic output of results on a PC–screen too.

We construct the numerical solution of the system of Eqs. (1), (5), (6) at sequential points of trajectory $x^{(n)} = x^{(n-1)} + h$, $n = 2, 3, \ldots$. The initial conditions are $x^{(1)} = 0$, $V^{(1)} = 1$, $\sigma^{(1)} = \sigma_0$, $l^{(1)} = l_0$. Computations at n–th step (*i.e.* at $x = nh$) are proceeded in following order:

1) The body velocity $V^{(n)}$ is computed by Eq. (6). The elapsed time $t^{(n)}$ is computed by equation:

$$t=\int_0^x \frac{ds}{V(s)}.$$

2) The areas of cross–sections $\overline{S}_i^{(n)}$ (when $i = 2, 3, \ldots$) are computed by Eq. (1) until the inequality $\overline{S}_i^{(n)} \le 0$ fails. The subscript value $i = 1$ corresponds to the cavity nose point. In this time moment, the position of the cavity tail point $l^{(n)} = ih$ is determined. Then it is corrected by linear interpolation.

3) The cavity volume $\overline{Q}^{(n)}$ is computed by numerical integration of $\overline{S}_i^{(n)}$ along the cavity.

4) The $\overline{\sigma}^{(n)} \to \overline{\sigma}_1^{(n)}$ is computed by Eq. (5). A few iterations are fulfilled, if it is necessary.

We assume that a separation of the cavity part and a jump of the function $l(t)$ take place at the moment of confounding the upper and lower boundaries of the cavity contour. Just such behaviour of cavity is observed in the experiments. The return with one step h occurs when detecting the jump of the function $l(t)$. Then the moment of separation is determined more exactly with reduced step $h_1 \ll h$. However, the cavity pressure $p_c(t)$ varies continuously in this time. The total precision of the numerical algorithm is equal to $O(h_1)$.

The contours of cavity and model are erased and put again on the PC–screen in each several steps. As a result, the run–time animation of process is presented. Simultaneously, the graphs of the velocity, the external pressure $\overline{p}_1(t)$, the cavity pressure $\overline{p}_c(t)$, *etc.*, are plotted on the PC–screen. We can compare this graphical information with the high–speed movies of experiments.

5. EXAMPLES OF COMPUTER SIMULATION

We present below some examples of the computer simulation of the unsteady supercavitating flows for different conditions.

5.1 High–speed motion of bodies in water

In experiments on high–speed motion of bodies in water [2], the shape of the model must satisfy the following requirements:

1) the model must continually be inside the natural vapor supercavity;

2) the supercavitating motion regime must be structurally stable.

In this case, the process is described by two Eqs.

(1), (6). We have developed the SUPERCAVITY program for the automation of the calculations when designing the models. In program, the comfortable user's interface was realized. The following characteristics are calculated for given model shape and mass m, initial velocity V_0 and the motion depth H:
1) the impact load P_{max} affecting the model;
2) the parameters of motion and the cavity shape for any mark of the trajectory x;
3) the distribution of width of the circular clearance between the model surface and the cavity boundaries.
For example, two fragments of the PC–screen copies when the SUPERCAVITY program run–time are shown in Figs. 2, 3.

5.2 Supercavity formation at high–speed water entry

The unsteady processes of the supercavity formation at the water entry with the velocities of the order of 1000 m/s continue parts of millisecond. However, these processes exert the main influence on the following motion. Shooting of the water entry in a number of experiments has shown that the process of the supercavity formation usually passes through the stage of cavity closure on the model or behind it. If both the motion stability loss and the model deformation do not happen in this case, then the normal cavity formation continues.

We have assumed that the cause of cavity closure after the water entry is the impulse increase of the water pressure because of the model penetration and the catapult gas action. Then Eq. (1) can be used to compute the cavity evolution when imposing the external pressure impulse $\overline{p}_1(t)$. The impulse shape should be calculated or taken from experiment.

To calculate the pressure field in water near the cavity we suppose the validity of the principle of freezing of free boundaries: in every moment of penetrating the cavity can be replaced by solid body with the same shape.

5.2.1 Water entry through a rigid wall

We consider the problem on the penetration of a body of revolution through the round perforation in a flat undeformable wall into the half–space filled by ideal incompressible weigthless fluid. We construct a solution in the stationary cylindrical coordinate system (see Fig.4). The kinematic part of problem consists of determination of the stream function satisfying the boundary conditions at each moment of time (for dimension variables):

$$\psi = \frac{VR^2}{2} \quad on\ the\ body, \quad \psi = \frac{VR_w^2}{2} \quad on\ the\ wall, \tag{7}$$

where $R(x,t)$ is the body radius, $R_w(t)$ is the wall perforation radius.

Let the penetration velocity V_0 is constant, h is the step of the pushing of a body forward. We distribute the ring sources with intensities q_j, radii r_j, and center x–coordinates $x_j = x_n - jh/2$, $j = 1, 2, \ldots, N$ along the body surface (Fig.4). Here, N is the number of steps that are made, $x_n = Nh$ is the current x–coordinate of the body nose point. The stream function is determined by numerical integration:

$$\overline{\psi} = \int_0^r r \frac{\partial \overline{\varphi}}{\partial x} dr + const, \tag{8}$$

where $\overline{\varphi}(x_j, r_j; x, r)$ is the sum of the potentials of a ring source and its mirror reflection from the wall. These potentials are expressed by total elliptic integrals of the first kind [5]. The arbitrary constant in the Eq. (8) is chosen from the condition of equality of the total rate of sources to the velocity of increase of the washed part of a body volume $Q_b(t)$:

$$2\pi \sum_{j=1}^{N} q_j = \frac{dQ_b}{dt}. \tag{9}$$

Thus, the problem at N–th step is reduced to the determination of the intensities of the ring sources from the system of linear equations (in dimensionless form):

$$\sum_{j=1}^{N} q_j \overline{\psi}(x_j, R_j; x_i, R_i) = \frac{R_i^2}{2}, \quad i = 1, 2, \ldots, N. \tag{10}$$

The dynamic part of the problem consists of determination of the water pressure by *Cauchy - Lagrange* equation. The graphs of the pressure on the body nose point $(x_n, 0)$ for a sphere and paraboloids of revolution $r = a\sqrt{x_n - x}$ are shown in Fig.5.

The described method of calculation was generalized for the case of variable body velocity $V(t)$. We use the calculated dependence $p_1(t)$ as initial data for the Eq. (1) in the ENTRY program. The computer simulation has shown that the arising of the water pressure when penetrating the model causes the local cavity closure and the annular washing of the model. A fragment of the PC–screen copy at the program ENTRY run–time is shown in Fig.6. Here, x, R_n are the cavitator coordinate and radius, V_0 is the initial velocity of the water entry. The model shape is plotted by thin lines, the cavity shape is plotted by bold lines. For comparison, the cavity contour is shown by dotted lines at absence of the pressure perturbations.

5.2.2 Water entry from within a gas–bubble

We assume now that the model enters the water through the free boundary of gas–bubble previously formed in water (see Fig.7). It is possible to calculate exactly the water pressure in this case [6]:

$$\frac{p-p_\infty}{\rho} = \frac{2R\dot{R}^2 + R^2\ddot{R}}{r} - \frac{R^4\dot{R}^2}{2r^4}. \qquad (11)$$

Here, $R(t)$ is the bubble radius, $r > R(t)$ is the current radial coordinate. Let the bubble pressure is being supported as constant for some time. Then substituting the $r = R$ into the Eq. (11), we determine the equation of bubble expansion:

$$\frac{3}{2}\dot{R}^2 + R\ddot{R} = \frac{p_j - p_\infty}{\rho}, \qquad (12)$$

$$R(0) = R_0; \qquad \dot{R}(0) = 0.$$

On the other hand, if we know the function of bubble expansion $R = R(t)$, for example from experiment, it is possible to calculate the water pressure for adoption in ENTRY program.

A fragment of the PC–screen copy showing the cavity deformation when penetrating the model into water from within the gas–bubble is shown in Fig.8. It is assumed that the model velocity is considerably greater than the bubble expansion velocity: $V_0 \gg \dot{R}$. The cavity pressure is supposed to be equal to the bubble pressure for initial stage of penetration: $p_c = p_j$. A comparison with experimental high–speed shooting shows the good agreement of the calculated and experimental cavity shape histories.

5.3 Cavity deformations due to internal and external perturbations

Simplified Eq. (1) allows us to calculate the unsteady axisymmetrical deformation of the cavity. Using the methods of the theory of cavity perturbations [2, 7] we also can calculate three–dimensional cavity shapes in cases of nonsymmetric perturbations that can be induced with gravity when a body moves horizontally, or the presence of an angle of attack of a cavitator.

The result of computer simulation of the influence of the model angular oscillation about the center of mass on the cavity shape is shown in Fig.9 (STABILITY program). A fragment of the PC–screen copy showing the effect of the external pressure impulse on the cavity shape is shown in Fig.10 (the underwater explosion simulation). The maximal impulse pressure is attained at $\bar{t} = 80$. In this case the cavity closure with the washing of the model occurs at a sufficient value of the pressure impulse amplitude.

Earlier we have researched experimentally the effect of water pressure impulse on artificial cavities. In those tests, the water pressure impulse was created by an air shot of a pneumatic catapult. The similar kind of pattern of cavity deformations was observed.

5.4 Self–induced and forced oscillation of ventilated cavities

The gas–filled supercavities have properties of the dynamic oscillation system with distributed lag time. First the phenomenon of self–excited pulsation of two–dimensional ventilated cavities was discovered and investigated experimentally [8, 9]. In the paper [10] this phenomenon was explained theoretically according to the linear theory of stability on the basis of approximate Eqs. (1), (5). We have exactly solved a problem on instability of the two–dimensional supercavity [11]. We have shown theoretically that two–dimensional and axisymmetrical cavities have similar of kind dynamical properties. The obtained in [11] results are good agreed with the experimental data [8].

If the mass of gas in cavity is constant the axisymmetrical cavity has the following fundamental reduced frequencies:

$$k_n = 2\pi n \quad at \quad \beta_n = 1 + \frac{(\pi n)^2}{6}, \quad n = 1, 2, \ldots \qquad (13)$$

Here, $k = \omega l_0 / V_\infty$, ω is the circular frequency. The cavity is unstable when $\beta > 2.645$. Kinematic waves arise on the cavity boundary as a result of the cavity pressure pulsation. They spread along the cavity with a velocity about V_∞. In this case $l_c/\lambda_n = k_n/2\pi = n$ waves pack on the cavity length.

We used the quasi–stationary semiempirical law for the air–supply rate to the cavity and the air–leakage rate from the cavity [2] in the Eq. (5). This law was obtained in the case of weak action of gravity:

$$\dot{q}_{in} = \gamma S_c \left(\frac{\sigma_v}{\sigma_0} - 1 \right), \qquad (14)$$

$$\dot{q}_{out}(t) = \gamma S_c(t) \left(\frac{\beta}{\overline{\sigma}(t)} - 1 \right).$$

Here, $\gamma = 0.01 \div 0.02$ is the empirical constant, S_c is a mid–section area of the stationary cavity, $\sigma_v \approx Eu$ is the cavitation number for the vapor cavity.

The PULSE program package was developed for the numerical solving of the system of the nonlinear Eqs. (1), (5) and the statistical analysis of the results. There are detailed description of the numerical algorithm and analysis of the computation result in our paper [12]. Calculations have shown that oscillations are developed in the dynamic system (1), (5) if the values of the parameters γ, β_0 belong to the linear instability region. As

a result, the stationary regime (mode) of periodic or quasi–periodic self–induced oscillations is established with disconnected dependence $l(t)$. Power spectral density (PSD), normalized autocorrelation function and other statistical characteristics are calculated for the time series $\overline{\sigma}^{(n)} = \overline{\sigma}(t^{(n)})$, $l^{(n)} = l(t^{(n)})$. It is shown, that new frequencies and their linear combinations are appeared in the spectrum $\overline{p}_c$, when the bifurcational parameter $q_0 = \beta_0 \dot{q}_{in}$ increases. This corresponds to attainment of higher modes of the cavity pulsation. The spectrum $\overline{p}_c$ becomes more complicated for every mode, but the main harmonic is varying weakly. The linear theory [10, 11] gives the same behaviour of the cavity pressure.

The estimation of limits of the self–induced oscillation modes according to the linear theory is shown in Fig.11. In this case $\gamma = 0$, *i.e.* the mass of gas in cavity is constant. The results of computer simulation are also plotted by circles. The PC–screen copy is shown in Fig.12 at the program PULSE run–time. The transformation of spectrum of the cavity pressure oscillations $\overline{p}_c = \beta - \overline{\sigma}$ is shown in Fig.13, when the bifurcation parameter q_0 increases ($\gamma = 0$). When $0 < q_0 < 1.2$, periodic oscillations (mode I or the limiting cycle) with a disconnected dependence $l(t)$ is established (Fig.13,a). Corresponding phase portrait $\overline{\sigma}(l)$ is shown in Fig.14,a. When $q_0 \approx 1.2$, the mode II of composite quasi–periodic self–induced oscillations arises spasmodically. As a result, the main harmonic is approximately doubled (Fig.13,b). The spectrum in Fig.13,c corresponds to the mode III.

When the mode II replaces the mode I, the oscillation energy is abruptly removed to the low frequencies in the spectrum $l(t)$. Then the cavity length oscillations become like chaotic. Influence of parameter γ on the cavity pulsation consists in some decreasing the amplitude and the phase lag between the cavity pressure oscillation and the cavity length oscillation. The phase portraits $\overline{\sigma}(l)$ for the increasing values of γ are shown in Fig.14 ($q_0 = 0.4$, mode I).

The PULSE program also simulates the effect of the external pressure $\overline{p}_1(t)$ oscillation on the gas–filled cavity pulsation. Fig.15 shows an example of acting the forced oscillations $\overline{p}_1(t) = \kappa \sin k_f t$ with various frequencies to the self–induced cavity oscillation ($\gamma = 0$, $q_0 = 0.8$, $\kappa = 0.1$). Corresponding spectrum $p_c(t)$ at absence of the external perturbation is shown in Fig.13,a. The modulation for $\tilde{k}_f \ll \tilde{k}_I$ (a), the synchronization for $\tilde{k}_f \approx \tilde{k}_I$ (b), or the "chaotisation " for $\tilde{k}_f > \tilde{k}_I$) (c) of the periodic mode are observed in dependence on relation between the forced frequency $\tilde{k}_f$ and the cavity self–induced oscillation frequency $\tilde{k}_I$. Here, the reduced frequencies are referred to the cavity average length l_m.

5.5 Vertical water entry through the free water surface

It is known that in the case of vertical water penetration, the surface closure or the depth closure of a cavity takes place in dependence on the initial entry conditions [13]. It is shown in experimental work [14] that both the drag coefficient and the cavity shape near the cavitator cease to vary after the depth equal to $1.5 \div 2$ of cavitator diameters at high–speed water entry. Thus, the influence of the free water surface on the cavity shape spreads only on the depth of cavitator diameter. This result gives us the experimental justification to use the simplified calculation model (1) — (6) for a computer simulation of water entry of models through the free surface.

5.5.1 Wave formation on cavity

Earlier we have experimentally discovered the phenomenon of wave formation on the cavity during the vertical water penetration of bodies [15]. The experiments are made in the water tank $2.0 \times 1.0 \times 0.6$ m. The cylindrical models of different diameter D and angle of conic head α were thrown down in the tank. The velocity of water entry V_0 was $5 \div 10$ m/s in different experiments. The process was recorded by shooting.

The analysis of pictures has shown that $1 \div 5$ waves usually appear on cavities at once after the cavity depth closure. The wave number and the wave intensity depend on each of the parameters $Fr_0 = V_0/\sqrt{gD}$, α (*i.e.* c_x), $Eu_0 = 2p_{atm}/\rho V_0^2$, also on the severity of cavity blocking up by the model.

We have applied the results of linear theory of the gas–filled cavity stability to explain this phenomenon. We have shown that its cause is the excitation of a fundamentalal oscillation of cavities filled by atmospheric air. We have obtained a simple *a priori* estimation of a wave number N in the case of sufficiently great both the body mass and the *Froude* number Fr_0:

$$N \approx \frac{1}{\pi}\sqrt{\frac{2Eu_0 Fr_0}{B}}, \qquad B = \sqrt{\sqrt{c_x}}. \qquad (15)$$

The calculation model of this process includes all three Eqs. (1), (5), (6). Their solution is calculated for each time step by the use of the *Steffensen* iterative process (DIVE program). Results of computer simulation of the cavity transformation at vertical dive of a disk and cones give a good agreement with both high–speed shooting the experiments and the *a priori* estimation (15). The dependence of the cavity length l and the cavity pressure p_c on the cavitator depth x are shown in Fig.16. The dotted line corresponds to the $l(x)$ computed without

taking into account the elasticity of the air filling the cavity. A comparison of the calculated and the experimental cavity shapes is shown in Fig.17 at sequential times.

5.5.2 Near–surface closure of cavity

We have experimentally shown that the near–surface closure of the cavity behind the body occurs for the water entry velocity about 100 m/s. It is caused by the impulse increase of the water pressure. It is important that mechanism of this closure differs fundamentally from the known surface closure of cavities, which is caused by the pressure reduction in the cavity throat due to flowing of atmospheric air into cavity [13]. This phenomenon develops especially brightly in experiments on high–speed entry of models into the bounded water volume. A comparison of the calculated and experimental cavity shapes is shown in Fig.18, when $D_n = 16$ mm, $V = 84$ m/s. The waves are not formed on the cavity during the further dive. Such behaviour is predicted correctly by the *a priori* estimation (15). The DIVE program also simulates this process.

6. CONCLUSIONS

Our computation experience and the comparison of obtained results with experimental data show that the approximate Eqs. (1) — (6) correctly predict the unsteady supercavitating flows for various conditions. We use all accumulated computation experience for development of the STABILITY software for computer simulation of the supercavitating model dynamics. In this program, we have taken into account the interaction of the model body with both the internal cavity walls and the gas–vapor–spray medium filling the cavity.

The computer simulation has shown that the model can execute the steady or damped oscillations in cavity after the impact its tail against the internal cavity wall. In this case the motion can be stable "as a whole". Also the aerodynamic forces due to model interaction with both the vapor filling the cavity and the spray stream near the cavity walls can affect on the motion with very high speed, if the clearance between the body surface and the cavity walls is sufficiently small. We have shown theoretically that the model self–stabilization in supercavity is possible also due to specially so called "statically stable" shape of the cavitator [16].

The STABILITY software investigates the stability of the supercavitating model motion "as a whole" for given cavitator and body shape, model mass, initial conditions of motion (*i.e.* the pitch angle and the angular velocity), and also when acting external perturbations.

REFERENCES

1. Savchenko, Yu.N., Semenenko, V.N., Serebryakov, V.V., " Experimental Study of the Supercavitation Flows at Subsonic Flow Velocities", Doklady AN Ukrainy, 2, 1992, pp 64–69 (in Russian).
2. Logvinovich, G.V., "Hydrodynamics of Flow with Free Boundaries", Kiev, USSR, Naukova Dumka, 1969 (in Russian).
3. Logvinovich, G.V., "Questions of Theory of Slender Axisymmetric Cavities", Trudy TzAGI, 1797, 1976, pp 3–17 (in Russian).
4. Garabedian, P.R., "Calculation of Axially Symmetric Cavities and Jets" Pac. J. Math, 4, 6, 1956, pp 611–684.
5. Kuhemann, D., Weber, J., "Aerodynamics of Propulsion", New York, 1953.
6. Landau, L.D., Lifshitz, Ye.M., " Hydrodynamics", Moscow, USSR, Nauka, 1986 (in Russian).
7. Buyvol, V.N.. "Slender Cavities in Flows with Disturbances", Kiev, USSR, Naukova Dumka, 1980 (in Russian).
8. Silberman, E., Song, C.S,., "Instability of Ventilated Cavities", J. Ship Res., 1, 5, 1961, pp 13–33.
9. Michel, J.–M. "Ventilated cavities. A contribution to the study of pulsation mechanism", in "Non-steady flow of water at high speeds. Proceedings of the IUTAM symposium held in Leningrad, 1971". Nauka, Moskow, 1973, pp 343–360.
10. Parishev, E.V., "Theoretical Investigations of Stability and Pulsation of Axisymmetric Cavities", Trudy TzAGI, 1907, 1978, pp 17–40 (in Russian).
11. Semenenko, V.N., "Instability of Two-dimensional Gas-filled Supercavity in Unbounded Flow", Hydromechanics, 69, 1995, pp 56–64 (in Russian).
12. Semenenko, V.N., "Computer Simulation of the Ventilated Cavity Pulsations", Hydromechanics, 71, 1997, pp 110–118 (in Russian).
13. Knapp, R.T., Daily, I.W., Hammitt, F.G., "Cavitation", McGraw - Hill Book Co., 1970.
14. Bivin, Yu.K., Gluhov, Yu.M., Permyakov, Yu.V., "Vertical Water Entry of Solid Bodies", Izvestiya AN SSSR, MZhG, 6, 1985, pp 3–9 (in Russian).
15. Savchenko, Yu.N., Semenenko, V.N., "Wave Formation on Cavity Boundaries at Water Entry of Disk and Cones", in "Problemy hidrodinamiki bolshykh skorostei". Cheboksary, USSR, Publ. of Chyvashian Univ., 1993, pp 231–239 (in Russian).
16. Savchenko, Y.N, Semenenko V.N., Naumova Y.I., Varghese A.N., Uhlman J.S., Kirschner I.N., " Hydrodynamic Characteristics of Polygonal Contours in Supercavitating Flow", in "Third International Symposium on Performance Enhancement for Marine Applications". Newport, 1997.

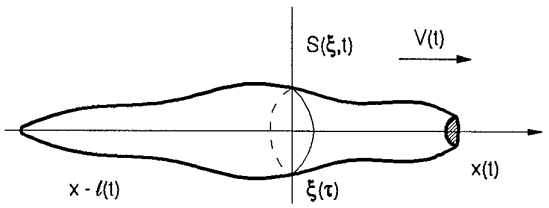


Fig.1. Calculation scheme of axisymmetrical supercavity.

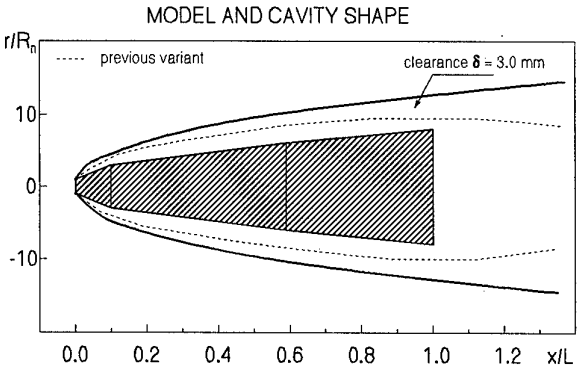


Fig.2. Computation of the cavity shape (SUPERCAVITY).

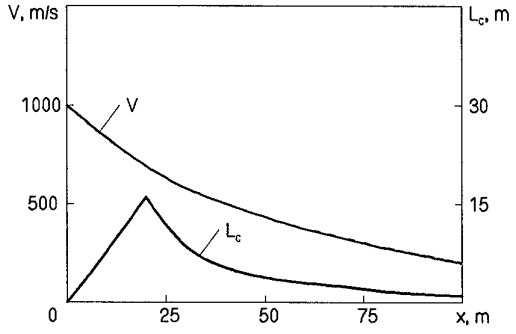


Fig.3. Histories of cavity length and model speed (SUPERCAVITY).

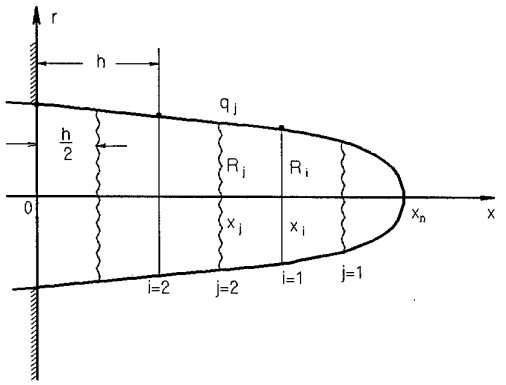


Fig.4. Calculation scheme of water penetration through the rigid wall.

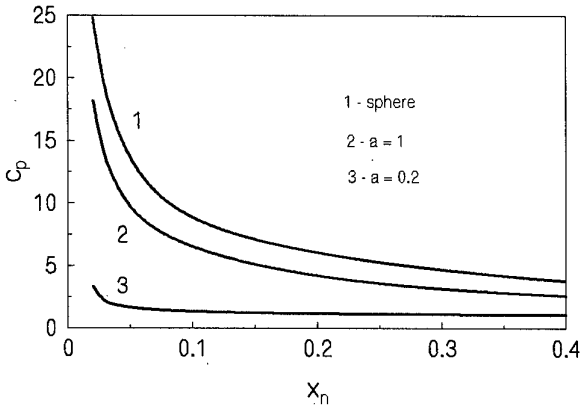


Fig.5. History of pressure in the body nose point.

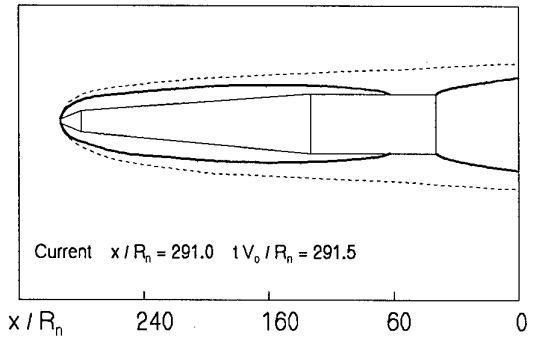


Fig.6. Computer simulation of water entry through the rigid wall (ENTRY).

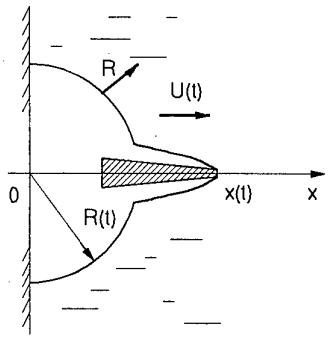


Fig.7. Scheme of water penetration from within the gas bubble.

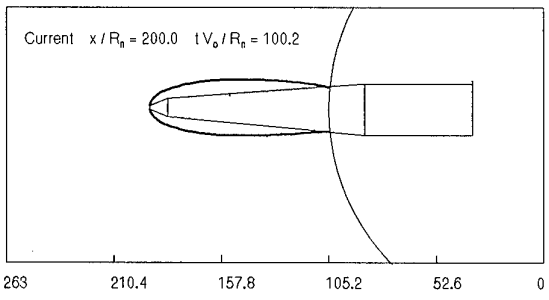


Fig.8. Computer simulation of water penetration from within the gas bubble (ENTRY).

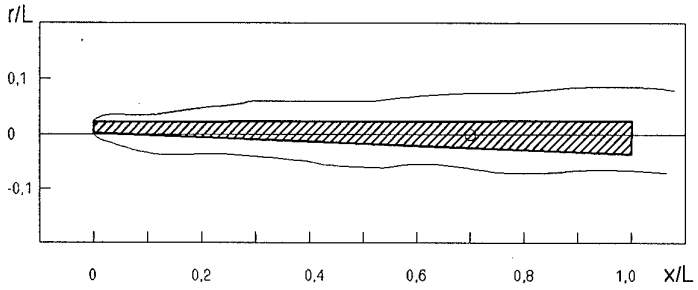


Fig.9. Action of the model angular oscillation (STABILITY).

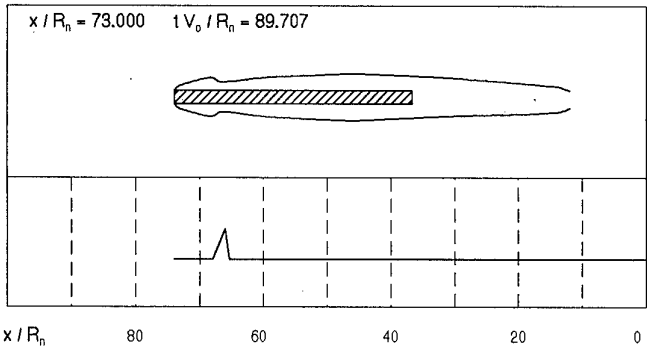


Fig.10. Action of the external pressure perturbation (ENTRY).

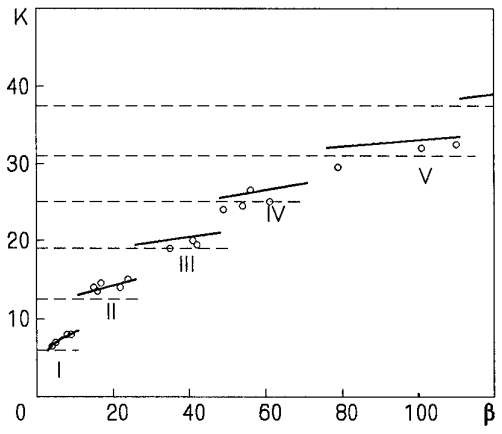


Fig.11. Self–induced oscillation modes of ventilated cavity at $\gamma = 0$.

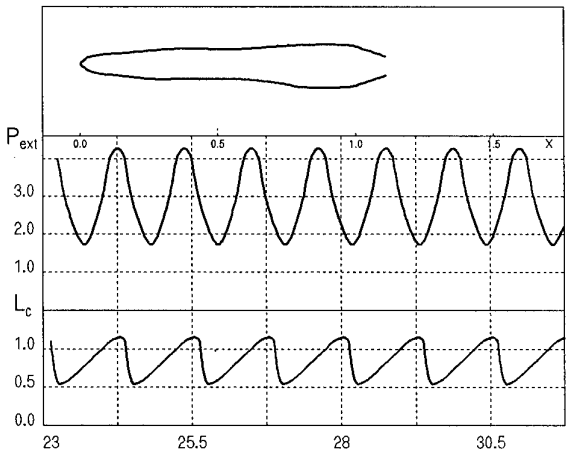


Fig.12. Computer simulation of the ventilated cavity self–induced oscillations (PULSE).

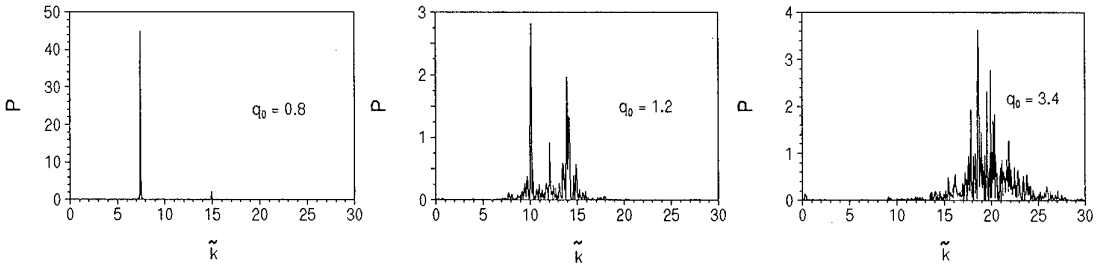


Fig.13. Power spectral density of $p_c(t)$ at self–induced oscillations.

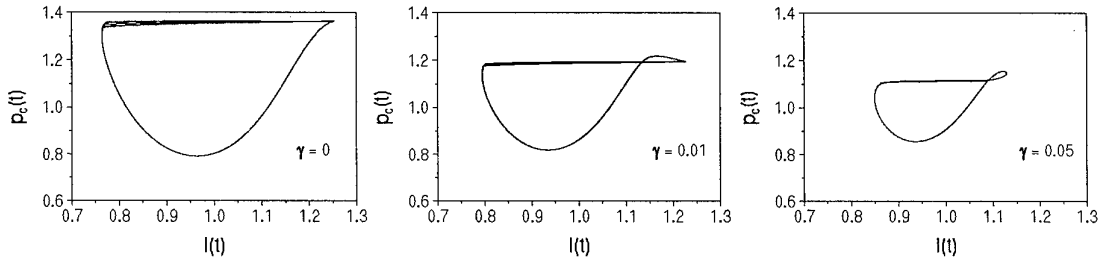


Fig.14. Phase portraits $p_c(I)$ at the varying γ.

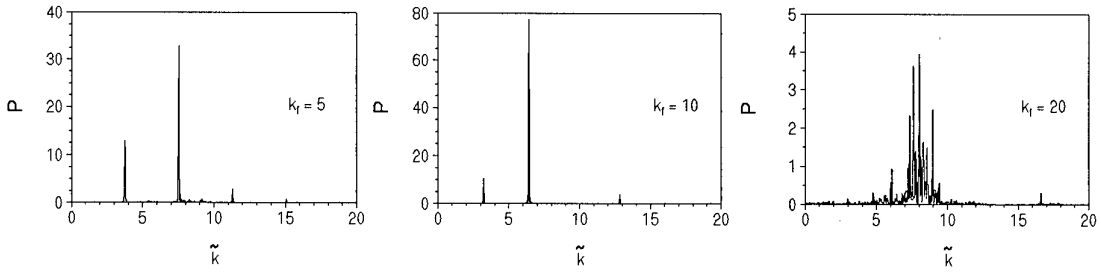


Fig.15. Power spectral density of $p_c(t)$ at forced oscillations.

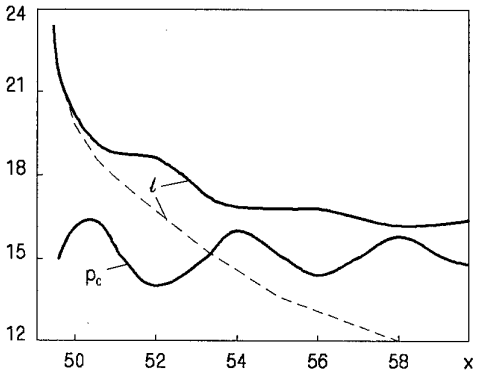


Fig.16. Histories of cavity length and pressure during vertical water penetration at $V_0 = 9$ m/s (DIVE).

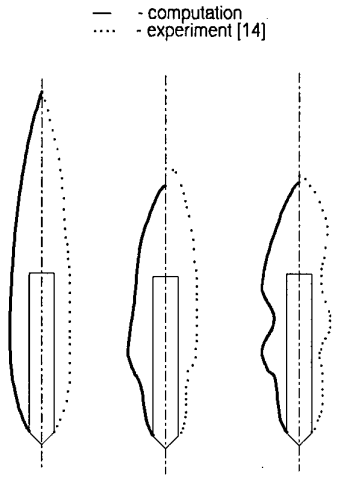


Fig.17. Comparison of computed and experimental cavity shape at $V_0 =$ 9 m/s (DIVE).

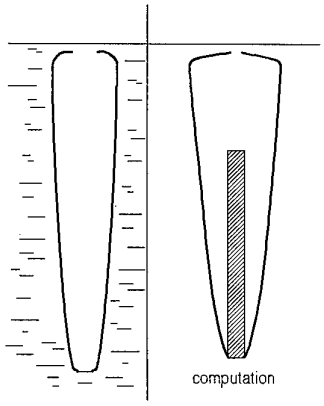


Fig.18. The same at $V_0 = 84$ m/s.

SOME PROBLEMS OF THE SUPERCAVITATION THEORY FOR SUB OR SUPERSONIC MOTION IN WATER

V.V. Serebryakov
Institute of Hydromechanics of NASU
8/4, Zhellabov Str., Kyiv, 252057, Ukraine

SUMMARY

Main concepts, results and methods of the linearized Theory of axisymmetric supercavitation are presented on the basis of the Slender Body approximation in incompressible fluid. Because of considerable increase of possible velocities of motion in water up to values comparable with the sonic velocity, an effort is made to apply the developed here approach to the analysis of supercavitation flows taking into account basic effects of compressibility.

LIST OF SYMBOLS

r, x	cylindrical frame of coordinates
$r = R(x)$	axisymmetric cavity form
$r = \eta(x)$	axisymmetric cavitator form
$R_m, (R_k)$	maximal cavity radius
L_c	cavity length
ℓ, x_o, R_n	cavitator length, coordinate of streamlines separation section and cavitator radius at this section
$L = \ell + L_c$	length of the system cavitator-cavity
R_k, L_k, λ -	maximal radius, semi- length, aspect ratio of slender cavity behind small cavitator (in particular disk for σ = const)
k	coefficient in formula for R_k
U, U_∞	prolong speeds in free flow and at infinity
u, v	axial and radial components of speeds perturbations
ϕ	speeds potential
φ	perturbation of speeds potential
a, a_∞	sonic speed in flow and at infinity
$M_\infty = U_\infty / a_\infty$	Mach Number
$\beta^2 = 1 - M^2$	
$B^2 = M^2 - 1$	
P, P_∞, P_k	pressure in flow, at infinity and in cavity
$\Delta P = P - P_k$	pressure difference in flow and in cavity on a cavity surface
ρ, ρ_∞	mass density in flow and at infinity
$\sigma = \dfrac{\Delta P}{\rho U_\infty^2 / 2}$	cavitation Number
D	cavitator drag
c_d, c_{do} -	cavitator drag coefficients for σ = const , $\sigma = 0$
C_D, C_{Do} -	cavitational drag coefficients for cavity middle section and for ahead cavity part for $\sigma = 0$
ε	cavitator slenderness parameter (for cone with semi-angle γ, $\varepsilon = tg\gamma$
$\delta \sim 1/\lambda$	cavity slenderness parameters what can be given by different ways
e - 2,718	
SBT	Slender Body Theory
MAEM	Matched Asymptotic Expansion Method

1. INTRODUCTION

Applying of supercavitation allows, while isolating a body surface from water, to avoid viscous losses and to decrease resistance considerably. *The least values of the cavitational drag coefficient* C_D for a cavity middle section (of a body compactly enough inscribed in the cavity) *are reached just for slender cavities:*

$$C_D \sim \sigma \sim \frac{2\ln\lambda}{\lambda^2} \qquad (1.1),$$

where $\sigma = \dfrac{P_\infty - P_k}{\rho U_\infty^2/2}$ - the cavitation Number,

$\Delta P = (P_\infty - P_k)$ - the difference of pressures in a free flow at infinity and in the cavity, ρ - the fluid mass density, U_∞ - the undisturbed free flow velocity at infinity, λ - the cavity aspect ratio.

Obtained at the present by experiments super-high velocities in water have helped to realize the *fact that the drag in water at high velocities can be very small and even the comparable with its values in air*. Super-high velocities are reached in experiments by launching of small elongated bodies of mass about 0.1-0.3 kg. During next instances the body moves practically straightforward by inertia at a slow velocity decrease, and thanks to small cavitational drag the launched body *can overcome considerable distances. Cavities at that are enough close to stationary ones and they are very slender rather resembling needles.*

Classical supercavitation is based on a model of incompressible fluid and supercavitation is apparently one of the best area for this model to be applied. Further growth of velocities up to the values, comparable with the sonic velocity in water $a_\infty \sim 1500$ m/sec leads to appearance of considerable compressibility effects . Important here is the Mach Number $M = U_\infty/a_\infty$, and such effects as shocks, wave drag, transonic phenomena that requires, correspondingly, further development of the theory.

The main problem of supercavitation is to determine cavitator drag, sizes and form of the cavity. The problem of determining the principal sizes and form of the cavity in incompressible fluid has here been solved just after appearance of the theory on the basis of the integral lows of conservity and was carefully checked experimentally. However the process of developing a more exact asymptotic theory of slender cavities and a numerical nonlinear theory was very long. Nowadays, with regard to available publications, analogous difficulties seems also will have place when developing the theory taking into account compressibility.

The paper contains an attempt to generalize and develop linearized theory based on the Slender Body theory and integral lows of conservation. The main advantage of asymptotic solutions is that they give correct results in any extreme situation, for example in case of super-slender cavities. The first part of the paper characterize possibilities of the linearized theory in case of slender axisymmetric cavities in incompressible fluid: approach, methods, results. In the second part an attempt is made to analyze possibilities and applications of analogous

Paper presented at an AGARD FDP Workshop on "High Speed Body Motion in Water", held in Kiev, Ukraine, 1-3 September 1997, and published in R-827.

approach taking into account the principal effects of compressibility, in the most interesting range of $M \sim 0+2$. The most attention is paid to clarify whole picture of flow properties understanding for motion with slender cavities for $M=0$ and its generalization with account main compressibility effects.

2. SUPERCAVITATION IN INCOMPRESSIBLE FLUID

2.1 Principal equations. The most characteristic is statement of a stationary problem fig. 2.1 for a potential free flow of ideal incompressible fluid using the cavity closure by the Rjabushinsky scheme. On a given surface of a cavitator $r = r_1(x)$ (and the end closure correspondingly) there is given a condition of impenetrability, on an unknown earlier surface of the cavity - conditions of penetrability and given pressure ΔP; disturbances on infinity are decreasing to 0. For simplicity a separation streamlines cross-section is assumed to be fixed:

$$\frac{\partial^2\varphi}{\partial r^2} + \frac{1}{r}\frac{\partial\varphi}{\partial r} + \frac{\partial^2\varphi}{\partial x^2} = 0, \quad (2.1)$$

(1) (1) $\delta^2 \ln 1/\delta$

$$\left[\frac{\partial\varphi}{\partial r} = U_\infty \frac{dr_1}{dx} + \frac{\partial\varphi}{\partial x}\frac{dr_1}{dx}\right]_{r=r_1(x)}, \quad \left[\frac{\partial\varphi}{\partial r} = U_\infty \frac{dR}{dx} + \frac{\partial\varphi}{\partial x}\frac{dR}{dx}\right]_{r=R(x)} \quad (2.2)$$

(1) (1) $(\delta^2 \ln 1/\delta)$ (1) (1) $(\delta^2 \ln 1/\delta)$

$$r = r_1(x) \quad \left[\frac{1}{2}\left(\frac{\partial\varphi}{\partial r}\right)^2 + \frac{1}{2}\left(\frac{\partial\varphi}{\partial x}\right)^2 + U_\infty \frac{\partial\varphi}{\partial x} = \frac{\Delta P}{\rho}\right]_{r=R(x)} \quad (2.3)$$

$(\ln 1/\delta)^{-1}$ $(\delta^2 \ln 1/\delta)$ (1) (1)

$$\varphi\big|_{r,x\to\infty} \to 0 \quad (2.4)$$

$$\left[R = r_1\right]_{x=x_*} \qquad \left[\frac{dR}{dx} = \frac{dr_1}{dx}\right]_{x=x_*} \quad (2.5)$$

Here r, x are the axis's of cylindrical system of coordinates, φ is the potential of disturbances. (2.1-2.5) should be completed also conditions cavity end closure. If considering the system cavitator-cavity as the surface of some slender body with the slenderness parameter $\delta = 1/\lambda$ the equations of the problem (2.1 - 2.5) with the accuracy to small values $\delta^2 \ln 1/\delta$ may be significantly simplified. Orders of smallness of the values at $\delta \to 0, L = (01)$ (L is the characteristic length of the system) in the problem (2.1 -2.5) are indicated under each of the terms of the equations. Using the known Slender Body Theory expansion:

$$\varphi = -\frac{1}{4\pi}\int_0^L \frac{f(x_1)dx_1}{\sqrt{(x-x_1)^2 + r^2}} \qquad f = U_\infty \frac{dR^2}{dx} \quad (2.6)$$

the problem (2.1-2.5) is simplified with the accuracy to

$$\varphi \approx \frac{f(x)}{2\pi}\ln r + \frac{f(x)}{4\pi}\ln\frac{1}{4x(L-x)} - \frac{1}{4\pi}\int_0^L \frac{f(x_1) - f(x)}{|x - x_1|}dx_1 + O\left(r^2 \ln r\right)$$

$r \to 0$

small values $\delta^2 \ln 1/\delta$ and is reduced to the following problem of integer-differential equation for a slender axisymmetric cavity behind a slender cavitator:

$$\frac{1}{4R^2}\left(\frac{dR^2}{dx}\right)^2 + \frac{1}{2}\frac{d^2R^2}{dx^2}\ln\frac{R^2}{4x(L-x)} - \frac{1}{2}\int_0^{x_1} \frac{\frac{d^2r_1^2}{dx^2}\big|_{x=x_1} - \frac{d^2R^2}{dx^2}}{|x_1 - x|}dx_1 -$$

$(\ln 1/\delta)^{-1}$ (1) $(\ln 1/\delta)^{-1}$

$$-\frac{1}{2}\int_{x_1}^L \frac{\frac{d^2R^2}{dx^2}\big|_{x=x_1} - \frac{d^2R^2}{dx^2}}{|x_1 - x|}dx_1 - \frac{1}{2}\frac{\frac{dr_1^2}{dx}\big|_{x=0}}{x} + \frac{1}{2}\frac{\frac{dR^2}{dx}\big|_{x=L}}{L-x} = \sigma, \quad (2.7)$$

$(\ln 1/\delta)^{-1}$ $(\ln 1/\delta)^{-1}$ $(\ln 1/\delta)^{-1}$ (1)

$$\left[R^2 = r_1^2(x)\right]_{x=x_*} \qquad \left[\frac{dR^2}{dx} = \frac{dr_1^2}{dx}\right]_{x=x_*} \quad (2.8) \qquad \left[R^2 = 0\right]_{x=L} \quad (2.9)$$

Here the linearized variant of the closing conditions (2.9) supposes an automatic closing of the cavity on some small body with the accuracy to small values $\sim \delta^2\sqrt{\ln 1/\delta}$.

2.2 General Notions. In the case of the slender cavities a disk-like cavitator sizes are little and its drag is practically independent on the cavity form, and the cavity form is independent on the cavitator form and is determined only by its drag. Equation (2.7) may be interpreted on the basis of the following simple model [5, 32] of slender cavity formation fig. 2.2. A moving cavitator pushes motionless fluid apart and the work of its drag is transformed into kinetic energy of the practically radial flow generated in the region $r < \psi$ in each of passing through by it motionless cross-sections of fluid. Further, under the action of the pressure difference ΔP in the flow and in the cavity, a independent motion of radial flow in each section, generated by the passing cavitator, takes place together with the expansion of the cavity cross-section.

2.3 Dynamics and experience of investiga-tions. The first stage is years 40-50th. Here thank to using heuristic models and integral conservation lows the ellipsoid form of a cavity and its basic sizes were determined and in particular the known formula for the maximal radius of cavity R_k:

$$R_k = R_n\sqrt{\frac{c_d}{k\sigma}} \quad (2.10)$$

where R_n is the radius of the cavitator, c_d is its drag coefficient, $k = 0{,}96 - 1$ and a practical independence of the cavity cross-sections expansion was realized. These were investigations by H. Reichardt, G. Birkhoff...and as well as G. Logvinovich who has formulated idea of independence of cavity cross-section expansion the most clearly in the form of the known principle " independence of the cavity expansion" [19]. Here the known formula by P. Garabedian has been obtained too:

$$\lambda^2 = \frac{\ln 1/\sigma}{\sigma} \quad (2.11),$$

as well as the known two-term asymptote of the streams expansion at infinity by M. Gyrevich - N. Levinson:

$$R^2 = 2\sqrt{c_{do}}\frac{x}{(\ln x)^{0.5}}\left[1 - \frac{1}{4}\frac{\ln\ln x}{\ln x} + \cdots\right] + O\frac{1}{(\ln x)^{1.5}} \quad (2.12)$$

Creation of the known linear theory of two-dimensional supercavitation by M. Tulin has considerably stimulated development of the analogous linearized theory of axisymmetric flows. However, in order to complete it till 1980 years, it took more than 30 years. From one side, the solutions of the problems analogous to (2.7 - 2.9) were found on the basis of numeric-analytical methods [7, 23, 25, 50] ... . From the other side, as the most effective was to use methods of the perturbations theory [14, 20, 23-25, 28, 31-41, 53]... . Here on the first stages they have met considerable difficulties and obtained a series of insufficiently correct solutions in consequence of that the extremely complicated structure of solutions had been understood not at once. Because of a very complicated structure of solutions analogous difficulties nearby separation cross-section and a series of insufficiently correct solutions were took place also when developing the numerical nonlinear theory which was also finished considerably later in 80th. Some of the works in this area are given in the reference list .

2.4 Matched Asymptotic Expansions Method , application. Base of this approach in the slender cavity theory was developed start from [20, 31, 36-38]. When considering the surfaces of a cavitator and a cavity as the surface of some whole slender body it is necessary to take into account that the surface in reality consists of two independent parts. For instance, in case if a cavity behind cone we can independently vary its semi-angle γ and the cavitation Number σ . In further it is convenient to consider a scheme of two small parameters of slenderness: for cavitator- ε , for a cavity - δ , (for a cone $\varepsilon = tg\gamma$), for a cavity $\delta = 1/\lambda \sim \delta(\sigma)$. Let $\varepsilon, \delta \to 0$, supposing the length of the complex $L = O(1)$ with reference to the problem (2.7 -2.9). More general cases of the nonstationary problem [34-37] of unfixed separation cross-section are considered as analogous. The result of limiting transition at $\delta, \varepsilon \to 0$ depends on the way of their tending to 0. But as the most preferable, certainly, would be a result applicable for any relationship between ε, and δ . There are here two characteristic cases:

1) the case of regular perturbations fig. (2.3a)

$$\delta/\varepsilon = O(1),\ (\sigma = O(\varepsilon^2 \ln 1/\varepsilon)),\ L = O(1) \quad (2.13)$$

2) the case of singular perturbations fig. (2.3b):

$$\delta/\varepsilon \to 0,\quad (\sigma << \varepsilon^2 \ln 1/\varepsilon)\quad L = O(1) \quad (2.14)$$

1) $\delta/\varepsilon = O(1)$; here taking into account conditions (2.13) the problem (2.7 - 2.9) in a limit is the problem for a differential equation. The lengths of the cavitator ℓ and the cavity L_c cannot be strongly different $\ell/L_c = O(1)$, Physically we have an ellipsoidal cavity and we may equate the incline angles of the cavitator and the cavity in a separation streamlines cross-section. From the point of view of the theory of perturbations the whole solution is situated in the area of *outer solution only and the boundary conditions in the separation cross-section are not lost* and we can apply them.

2) $\delta/\varepsilon \to 0$. Here at $\delta/\varepsilon \to 0$ taking into account conditions (2.14) the cavitator tends to become infinitely small in comparison with the cavity $\ell = O\left(\varepsilon^2 \sqrt{\ln 1/\delta}\right)$. In the limit we have an ellipsoidal cavity again, however, we cannot satisfy the boundary conditions at the separation cross-section - they are lost. The most important particular case here is a slender cavity behind a notslender disk-like cavitator. The solution at $\delta/\varepsilon \to 0$ has a rather complicated asymptotical structure consisting of 3 parts [20, 31, 37, 38], fig. (2.3b). This is inner - nearby the cavitator solution, depending on the cavitator shape (for a disk the solution is nonlinear), intermediate solution is asymptotic (2.12), external - for the middle part - perturbation of ellipsoidal cavity. Asymptotic are sought in each of the area in series:

$1/(\ln 1/\delta)$; $1/(\ln 1/\varepsilon)$. Initial conditions are satisfied in the inner area and the inner solution is complete. The constants of the intermediate solution are determined by matching with the inner solution, the constants of the outer solution - by matching with the intermediate solution. Further, the additive rule [45] is used and the uniformly applicable solution, applicable for the whole area, is constructed.

Asymptotic solutions for both cases $\delta/\varepsilon = O(1)$, $\delta/\varepsilon \to 0$ are valid in different regions of δ, ε relation and complement one another.:

- solutions at $\delta/\varepsilon = O(1)$ are valid when the cavitator is not too small;

- solutions at $\delta/\varepsilon \to 0$ are valid when the cavitator is small enough.

These solutions have between them a certain boundary zone, where they may give some near results, however, more than likely they don't have any region of overlap. For the solution in both cases various methods to specify δ may be used, the most important of which are:

$$\delta^2 = \frac{1}{\lambda^2}, \qquad \delta^2 = \varepsilon^2 \qquad (2.15)$$

a) b)

$$\delta^2 = \frac{\sigma}{\ln 1/\sigma}, \qquad \sigma = \delta^2 \ln \frac{1}{\delta^2}$$

c) d)

It should here be noted that asymptotic solutions are built in the form of rather weak **Ln** series ($1/\ln 10 \sim 0.43$, $1/\ln 100 \sim 0.22$ ...) and the first approximations sometimes can hardly be considered as solution in general, for example, as in case of an ellipsoidal cavity when we equate the incline angles of a slender cavitator and the cavity in the separation cross-section. There are two principal ways to improve this solutions:

a) improvement of the first approximation with the help of a more optimal choice of small parameters or by some another methods;

b) obtaining of solutions of the second order approximation (two terms of a series as a rule).

Therefore in further under the asymptotic structure we will understands the first term of a series, determining the general properties of the solution, but the accuracy of the solution and its chances to be used are not determined.

2.5 Regular Solutions $\delta/\varepsilon = O(1)$. Two approaches of asymptotic solutions are developed here [20, 33, 38, 39]:

1) direct - ε, σ are given and the asymptotic solution of the problem is found in series on $1/\ln(1/\delta)$ for the shape and sizes of a cavity.

2) "semi-reverse" the length of a cavity is given and the asymptotic solution of the problem is found for the shape of a cavity and the cavitation Number .

The asymptotic two-term solution of the problem at $\delta/\varepsilon = O(1)$ in direct statement in the case of a slender cone ($x = 0$ is in the separation cross-section, $\ell = 1$) has the form:

$$R^2 = \frac{\sigma}{\ln(1/\delta^2)}\left\{\frac{\varepsilon^2\ln(1/\delta^2)}{\sigma} + 2\frac{\varepsilon^2\ln(1/\delta^2)}{\sigma}x - x^2\right\} +$$
$$+ \frac{2\sigma}{(\ln(1/\delta^2))^2}\left\{\frac{L_e}{4}\left[(x-L_\xi)\ln\left|\frac{x-L_\xi}{L_\xi}\right| - x + (x-x_\xi)\ln\left|\frac{x-x_\xi}{x_\xi}\right| - x\right] + \right.$$
$$+ \frac{1}{4}\left(1 + \frac{\varepsilon^2\ln(1/\delta^2)}{\sigma}\right)x^2\ln\frac{x^2}{e^3} -$$
$$- \frac{\varepsilon^2\ln(1/\delta^2)}{\sigma}\left[\frac{1}{4}\left((x+1)^2\ln\frac{(x+1)^2}{e^3} - \ln\frac{1}{e^3}\right) + x\right] - \qquad (2.16)$$
$$- \left[\frac{1}{4}\left((x-x_\xi)^2\ln\frac{(x-x_\xi)^2}{e^3} - x_\xi^2\ln\frac{x_\xi^2}{e^3}\right) + x_\xi x\ln\frac{|x_\xi|}{e}\right] -$$
$$\left. - \frac{1}{2}\left[1 + \ln(1/\delta^2) + \ln\frac{\sigma}{4\ln(1/\delta^2)}\right]x^2\right\}$$

where $e \sim 2{,}718$, the parameters of the limit ellipsoid L_ξ, x_ξ, L_e are determined by the following dependencies:

$$L_\xi = \frac{\varepsilon^2\ln(1/\delta^2)}{\sigma}\left[1 + \sqrt{1 + \frac{\sigma}{\varepsilon^2\ln(1/\delta^2)}}\right]$$
$$x_\xi = \frac{\varepsilon^2\ln(1/\delta^2)}{\sigma}\left[1 - \sqrt{1 + \frac{\sigma}{\varepsilon^2\ln(1/\delta^2)}}\right] \qquad (2.17)$$
$$\frac{1}{2}L_e = \frac{\varepsilon^2\ln(1/\delta^2)}{\sigma}\sqrt{1 + \frac{\sigma}{\varepsilon^2\ln(1/\delta^2)}}$$

In particular, at $\delta = \varepsilon$, (2.17 - 2.18) becomes applicable nearby the cavitator at $\sigma = 0$ too.

$$R^2 = \varepsilon^2\left\{(1+2x) + \frac{1}{\ln(1/\varepsilon^2)}\left[\frac{1+2x}{2}\ln(1+2x) + \right.\right.$$
$$\left.\left. x^2\ln x - (1+x)^2\ln(1+x)\right]\right\} \qquad (2.18)$$

2.6 Outer Solutions at $\delta/\varepsilon \to 0$. An outer solution describes the most part of a cavity and it is sufficient to know the solution in the majority of cases. To determine the constants of the solution instead of matching the integral conservation laws [45] may be applied, in particular the formula for R_k (2.10). For the solution one may neglect the sizes of a cavitator ($O\delta^2\sqrt{\ln 1/\delta}$) and may apply two possible variants of "semi-reverse" approach:

assuming the half-length of the cavity L_k and its aspect ratio λ to be given we seek the solution for its shape and the cavitation Number in the form of series on $\ln\lambda$;

- assuming L_k and λ to be given we seek the solution for its shape and the cavitation Number in the form of series on $\ln 1/\delta$ taking into account opportunities of (2.15).

The solution in the first case is found in the form of series [31] on the basis of the problem (x = 0 in cavity middle section, $L_k = 1$):

$$\frac{1}{4R^2}\left(\frac{dR^2}{dx}\right)^2 + \frac{1}{2}\frac{d^2R^2}{dx^2}\ln\frac{R^2}{4(1+x)(1-x)} \cdot$$
$$(\ln 1/\delta)^{-1} \qquad (1) \qquad (2.19)$$
$$-\frac{1}{2}\int_{-1}^{+1}\frac{\frac{d^2R^2}{dx^2}|_{x=x_1} - \frac{d^2R^2}{dx^2}}{|x_1 - x|}dx_1 - \frac{1}{2}\frac{\frac{dR^2}{dx}|_{x=-1}}{1+x} + \frac{1}{2}\frac{\frac{dR^2}{dx}|_{x=+1}}{1-x} = \sigma,$$
$$(\ln 1/\delta)^{-1} \qquad (\ln 1/\delta)^{-1} \quad (\ln 1/\delta)^{-1} \quad (1)$$

$$\left[R^2(x) = 0\right]_{x=-1},\ \left[R^2(x) = \delta^2\right]_{x=0},\ \left[R^2(x) = 0\right]_{x=+1}$$

in the form of series:

$$R^2 = \delta^2\left[R_0^2 + R_{-1}^2(\ln 1/\delta^2)^{-1} + R_{-2}^2(\ln 1/\delta^2) + \ldots\right] \qquad (2.20)$$
$$\sigma = \delta^2\left[\sigma_1(\ln 1/\delta^2) + \sigma_0 + \sigma_{-1}(\ln 1/\delta^2)^{-1} + \ldots\right] \qquad (2.21)$$

and for σ = const is:

$$R^2 = R_k^2\left[(1-x^2) + \frac{x^2\ln 4 - \ln(1+x)^{(1-x)} \cdot \ln(1-x)^{(1-x)}}{2\ln\lambda}\right] \qquad (2.22)$$
$$\sigma = \frac{2}{\lambda^2}\ln\frac{\lambda}{\sqrt{e}} \qquad (2.23)$$

Taking into account the opportunities of (2.15), asymptotic equivalent expansions (2.23) has the form:

$$\lambda^2 = \frac{1}{\sigma}\ln\frac{\ln 1/\sigma}{e\sigma} \approx \frac{1}{\sigma}\ln\frac{1{,}5}{\sigma};$$
$$\text{a)} \qquad \text{b)} \qquad (2.24)$$
$$\lambda^2 = \frac{1}{\sigma}2\ln\frac{1}{\delta\sqrt{e}},\ \sigma = \delta^2\ln\frac{1}{\delta^2}$$
$$\text{c)} \qquad \text{d)}$$

Solutions (2.22 -2 .24) are essentially the solution of the second approximation. At that each of the variants of dependencies (2.23-2.24) has its own advantages. Fig. 2.4 illustrates dependencies (2.23, 2.24 b)) in comparison with the data of nonlinear numerical calculations [16].

2.7 Improving of the first approximation equations. The main idea here is to improve the small parameter so that one of the two-term (2.22 - 2.23) expansions would be transformed into an one-term one. It is convenient at that to introduce the value μ -- the inertial coefficient. For example, basing on (2.23):

$$\mu = \ln\frac{\lambda}{\sqrt{e}} \qquad (2.25)$$

It give possible to define kinetic energy of radial flow in the form:

$$E_k = \frac{\pi\mu\rho}{4}U_\infty^2\left(\frac{dR^2}{dx}\right)^2 \qquad (2.26)$$

At that instead of integer-differential equation (2.7) we obtain simplest differential equation. Obtaining one of the initial conditions using the energy conservation law with account (2.26), equations for defining of the slender cavity shape behind small cavitator are [20, 32]:

$$\mu\frac{d^2R^2}{dx^2} + \frac{\Delta P(x)}{\rho U_\infty^2/2} = 0$$
$$R^2\Big|_{x=0} = 0,\ \frac{dR^2}{dx}\Big|_{x=0} = 2\sqrt{\frac{D}{k\pi\mu\rho U_\infty^2}} \qquad (2.27)$$

For σ = const solution of (2.27) defines ellipsoidal cavity and the known dependence for R_k (2.10):

$$R^2 = R_n\sqrt{\frac{2c_d}{k\mu}}\cdot x - \frac{\sigma}{2\mu}x^2$$

$$R_k = R_n\sqrt{\frac{c_d}{k\sigma}}, \qquad (2.28)$$

$$L_k = R_n\frac{\sqrt{2\mu c_d/k}}{\sigma}, \qquad \lambda = \sqrt{\frac{2\mu}{\sigma}}$$

At that the dependence for defining μ (2.24b) is the most convenient:

$$\mu \approx \frac{1}{2}\ln\frac{1{,}5}{\sigma} \qquad (2.29)$$

2.7 Equation for Calculations of Nonstationary Cavities of Variable Pressure. Here one applies the system of coordinates connected with motionless fluid. Coming from the nonstationary integral-differential equation [34] (what is like (2.7)), simplifying it and applying the energy conservation law in the initial moment $t = t_k(x)$ when a cavitator passes the cross-section x and has at that the drag $D(x)$, the shape of the middle part of a slender nonstationary cavity behind small cavitator is determined by the equations [20, 32]:

$$\mu\frac{\partial^2 R^2}{\partial t^2} + 2\frac{\Delta P}{\rho} = 0 \qquad (2.30)$$

$$R^2\Big|_{t=t_k(x)} = 0, \quad \frac{\partial R^2}{\partial t}\Big|_{t=t_k(x)} = 2\sqrt{\frac{D(x)}{k\pi\mu\rho}}$$

Here $k \sim 0{,}96-1$ - is the correction alike as in (2.10), Equations (2.30) are the simplest expression of heuristic model fig. 2.2 and the principles of the "independence of the cavity expansion" [19]. At the stationary flow they determine the ellipsoidal cavity (2.28) and are more general with compared to equation developed in [5]. The value of the inertial coefficient μ in the equations is usually as taken in the form of some universal const $\mu \sim 2$ or on the basis of the solution for the stationary cavities (2.25 ,2.29). Fig. 2.5 illustrate the values of μ for various ways its defining. Comparison of the value of $\sigma\lambda^2/2 = \mu$ with date of nonlinear numerical calculation [16] illustrating expediency of introducing this value is also presented.
These equations are useful in calculations of the cavities differing considerably from nonstationary ones. They were repeatedly verified and their correctness lies within 5 - 7 %. Nowadays they are the most convenient way of estimating shapes of nonstationary cavities. At that a small part of nonlinear solution nearby the disk conserving its form for most part of possible case of flow is easily built over in the final stage of calculation. These equations give the possible for the first time to calculate a number of the nonstationary cavities of variable pressure and they are used in the theory of cavity pulsation and in the theory of the cavities with gas injection.

2.9 Asymptotic Structure of Solutions (cavitator length $l = 1$, for cone $n = 1$):

$\delta/\varepsilon = O(1)$

$$R^2 = \varepsilon^2\left[1 + 2n(x-1) - \frac{\sigma}{\varepsilon^2\ln 1/\delta^2}(x-1)\right] \sim x \qquad x\to\infty \qquad (2.31)$$

$\delta/\varepsilon \to 0$

$$R^2 = \varepsilon^2\left\{\left[2n\left(\frac{\ln 1/\varepsilon^2}{\ln x/\varepsilon^2}\right)^{0.5}x + (1-2n)\right] - \frac{\sigma}{\varepsilon^2\ln 1/\delta^2}(x-1)^2\right\} \sim \frac{x}{(\ln x)^{0.5}} \qquad \to\infty \qquad (2.32)$$

Lets also write down a simplified variant of dependence for a sufficient distance from the cavitator (basing only on the intermediate and outer solution,) what determines asymptotic structure of the solutions in case of notslender cavitators of disk type $R_n = 1$.:

$$R^2 = \frac{2\sqrt{c_d}}{(\ln x)^{0.5}}x - \frac{\sigma}{\ln 1/\delta^2}x^2 \to \frac{2\sqrt{c_{do}}}{(\ln x)^{0.5}} \qquad (2.33)$$
$$x\to\infty$$

Proceeding from (2.31 - 2.32) it is obviously that the solutions at $\delta/\varepsilon = O(1)$ of the type (2.16 -2.17) have incomplete asymptotic structure without intermediate part (2.12) and become unsuitable for essential large $L_c \to \infty$, where become suitable the solutions at $\delta/\varepsilon \to 0$.

2.10 Intermediate Solution. In order to develop at $\delta/\varepsilon \to 0$ the second order theory two terms (2.12) are not enough . Intermediate expansion was extracted from (2.6) and it defines for $\sigma = 0$ differential intermediate equation : [36,53] instead of integer-differential equation (2.7):

$$\frac{1}{4}\frac{1}{R^2}\left(\frac{dR^2}{dx}\right)^2 + \frac{1}{2}\frac{d^2R^2}{dx^2}\ln\frac{R^2}{4x^2} - \frac{1}{2x}\frac{dR^2}{dx} = 0 \qquad (234)$$

and its 3 terms expansions at $x\to\infty$ [36]:

$$R^2 = \frac{2\sqrt{c_{do}}}{(\ln x)^{0.5}}\left[1 - \frac{1}{4}\frac{\ln\ln x}{\ln x} + \frac{1}{2}\frac{\ln\frac{e}{2}\sqrt{c_{do}}}{\ln x}\right] \qquad (2.35)$$

2.10 Main Points of the Theory at $\delta/\varepsilon \to 0$. On the basis of (2.35) at $\delta/\varepsilon \to 0$ the second order theory was developed and a number of the most interesting asymptotic solution of the problems [36-39] was obtained. The central point here is the determination of the two-term dependence for R_k by way of matching outer solution of the second order (2.21) with asymptotic (2.35):

$$\frac{R_k}{R_n\sqrt{c_d}} = \frac{1}{\sqrt{\sigma}}\left[1 + \frac{\ln 2/\sqrt{c}}{\ln 1/\delta^2}\right] \qquad (2.36)$$

This structure for R_k fully coincides with the structure of expansion of R_k, obtained by way of applying the variation approach [28] on the basis of solution (2.22).
. On the basis of the second order theory we have the complete solution of the main problem of supercavitation in the second approximation. In particular, principal sizes of the cavity are determined here for R_k - (2.36) using the convenient series of δ (2.15 a, c, d) and accordingly one of the convenient dependencies for λ (2.23 - 2.24). There are in incompressible fluid several basic opportunities to realize the main supercavitarion problem - defining of main cavity sizes:

1) In case of notslender disk-like cavitators - we can find with the help of the impulse conservation law const of the intermediate solution (asymptotic at $x \to \infty$) and to find R_k having matched the asymptotic with the outer solution ;
- we can apply the theorem of impulse directly to the outer solution and to determine R_k.
2) In case of slender cavitators we can also find the inner solution and to determine R_k by successive matching the inner solution with the intermediate and outer ones.
It should however be noted that determination of R_k *in such a manner (asymptotic theory at* $\delta/\varepsilon \to 0$ *in general case of slender cavitators) is possible only in the case of cavities slender enough.* In particular, for the cone $\gamma \sim 10°$ this becomes real for the cavities with the aspect ratio not less than $\lambda \sim 15 \div 20$. At velocities low enough this way for determining R_k seems to be in general of theoretical interest. However, this way may turn out to be significant at super-high velocities of motion.
3) As important here is the moment that the known expansion SBT (2.6) as well contains at $M = 0$ an intermediate asymptotic for potential φ. This was proved by the identity of asymptotic structures for R_k, obtained by various ways.

2.11 Effective Method of Calculation of Slender Cavities. Inner nearby a disk-like cavitator solution is universal substantially and is a constituent part of a wide class of stationary and not stationary cavities. The area of this solution is critically nonlinear but one may here find a simple effective although insufficiently rigorous solution. Assuming here the flow over to be close enough to the stream about a paraboloid the left part of intermediate equation (2.34) by means of coordinate transformation turns into exact expression for the pressure distribution on the surface of a paraboloid. At that equations for the inner part turn out simultaneously to be the common equation for the inner and the intermediate part with the accuracy up to three terms of asymptotic. Using for the outer area improved equation of the first approach (2.27) based on the first-order matching , we obtain:

$$\frac{dR^2}{dx} = \frac{2\sqrt{c_q}\,R_n}{\sqrt{\ln\dfrac{4(x+\Delta)^2}{R^2}}} - \frac{\sigma}{\mu}x \to \frac{2\sqrt{c_b}}{(\ln x)^{0.5}}, \qquad x \to \infty \quad (2.37)$$

$$R^2|_{x=0} = R_n^2;\ \Delta = \frac{R_n}{2}\left(\sqrt{c_b} + \frac{1}{\sqrt{c_b}}\right).$$

Equation (2.38) are a rough preliminary variant. There are now more perfect ones including nonstationary variants of the method. These equations allow to calculate the majority of stationary and nonstationary cavities in various reasonable enough cases of flow over, avoiding at that application of the complicated methods of nonlinear numerical calculations. Fig 2.6 illustrates calculation results — based on equations (2.37) in the case of disk for $\sigma = 0.04$ in comparison with nonlinear numerical calculation Δ [16].

3. INFLUENCE OF COMPRESSIBILITY

3.1 Principal Equations Within the scope of the model of ideal incompressible fluid supposing isentropic condition, Laplace equation (2.1) in the problem (2.1-2.5) is replaced with the known system of two equations

$$\left(1 - \frac{v^2}{a^2}\right)\frac{\partial^2\phi}{\partial r^2} + \frac{v}{r} + \left(1 - \frac{U^2}{a^2}\right)\frac{\partial^2\phi}{\partial x^2} + \frac{2Uv}{a^2}\frac{\partial^2\phi}{\partial x \partial y} = 0 \quad (3.1)$$

$$a^2 = a_\infty^2 - \frac{n-1}{2}\left(2U_\infty u + u^2 + v^2\right) \quad (3.2)$$

where a is the sonic velocity if water. Condition (2.3) as also changed on the basis of Bernoulli equation:

$$\frac{n}{n-1}\frac{P+B}{\rho} + \frac{U^2+v^2}{2} = \frac{n}{n-1}\frac{P_\infty + B}{\rho_\infty} + \frac{U_\infty^2}{2} \quad (3.3)$$

The base for equations (3.2 - 3.3) accounting the water state equation in form of Tet adiabatic curve [8]:

$$\frac{P+B}{\rho^n} = \frac{P_\infty + B}{\rho_\infty^n} \quad (3.4)$$

where B, n are the constants: $B = 3045\ kg/cm^2$, $n = 7{,}15$. For comparison in the case of air the analogous (3.2) equation is [13]:

$$a^2 = a_\infty^2 - \frac{\gamma-1}{2}\left(2U_\infty u + u^2 + v^2\right) \quad (3.5)$$

In the case of small flow perturbations for $M < 1$ and $M > 1$ equations (3.1-3.3) in the SBT approximation are simplified and Laplace equation (2.1) in the problem (2.1 - 2.5) are replaced by Prandtl-Glauert equation $M < 1, M > 1$:

$$\frac{\partial^2\varphi}{\partial r^2} + \frac{1}{r}\frac{\partial\varphi}{\partial r} + \left(1 - M^2\right)\frac{\partial^2\varphi}{\partial x^2} = 0 \quad (3.6)$$

In order to describe flow in transonic area $M \sim 1$ equation (3.6) is replaced by more accuracy transonic Karman-Guderley equation:

$$\frac{\partial^2\varphi}{\partial r^2} + \frac{1}{r}\frac{\partial\varphi}{\partial r} + \left[\left(1 - M_\infty^2\right) - \frac{(n+1)M_\infty^2}{U_\infty}\frac{\partial\varphi}{\partial x}\right]\frac{\partial^2\varphi}{\partial x^2} = 0 \quad (3.7)$$

Analogously (2.7) equation (3.6) on the base of SBT approximation can be reduced to integer-differential equations:

$M < 1 \quad \beta^2 = 1 - M^2$

$$\underset{(\ln 1/\delta)^{-1}}{\frac{1}{4R^2}\left(\frac{dR^2}{dx}\right)^2} + \underset{(1)}{\frac{1}{2}\frac{d^2R^2}{dx^2}\ln\frac{\beta^2 R^2}{4x(L-x)}} - \underset{(\ln 1/\delta)^{-1}}{\frac{1}{2}\int_0^{x_1}\frac{\frac{d^2r_1^2}{dx^2}|_{x=x_1} - \frac{d^2R^2}{dx^2}}{|x_1 - x|}dx_1} -$$

$$- \underset{(\ln 1/\delta)^{-1}}{\frac{1}{2}\int_{x_1}^{L}\frac{\frac{d^2R^2}{dx^2}|_{x=x_1} - \frac{d^2R^2}{dx^2}}{|x_1 - x|}dx_1} - \underset{(\ln 1/\delta)^{-1}}{\frac{1}{2}\frac{\frac{dr_1^2}{dx}|_{x=0}}{x}} + \underset{(\ln 1/\delta)^{-1}}{\frac{1}{2}\frac{\frac{dR^2}{dx}|_{x=L}}{L-x}} = \sigma \quad (3.8)$$

$M > 1 \quad B^2 = M^2 - 1$

$$\underset{(\ln 1/\delta)^{-1}}{\frac{1}{4R^2}\left(\frac{dR^2}{dx}\right)^2} + \underset{(1)}{\frac{1}{2}\frac{d^2R^2}{dx^2}\ln\frac{B^2R^2}{4x^2}} - \underset{(\ln 1/\delta)^{-1}}{\int_0^{x_1}\frac{\frac{d^2r_1^2}{dx^2}|_{x=x_1} - \frac{d^2R^2}{dx^2}}{|x_1 - x|}dx_1} -$$

$$- \underset{(\ln 1/\delta)^{-1}}{\int_{x_1}^{x}\frac{\frac{d^2R^2}{dx^2}|_{x=x_1} - \frac{d^2R^2}{dx^2}}{|x_1 - x|}dx_1} - \underset{(\ln 1/\delta)^{-1}}{\frac{\frac{dr_1^2}{dx}|_{x=0}}{x}} = \sigma\,. \quad (3.9)$$

at the initial conditions and the closure condition:

$$[R = \eta(x)]_{x=x_1} \qquad \left[\frac{dR^2}{dx} = \frac{d\eta^2}{dx}\right]_{x=x_1} \qquad \left[R^2 = 0\right]_{x=L} \qquad (3.10)$$

3.2 General Analysis. As it follow from (3.1 -3.3), (3.5) the equations in the nonlinear statement practically coincide for water and air with a slight difference for the condition on a cavity surface because of some difference of state equation for water (3.4) as compared to analogous adiabatic curve for air. Moreover the equations of small disturbed flows for sub and supersonic (3.6, 3.8, 3.9) are based on the acoustics equations and are absolutely the same for water and air. Transonic equations (3.7) for water and air are different only by the magnitude of const n, γ ! This means that sub and supersonic effects have to be the same with the accuracy up to the isentropic condition in water and air. However the area of appearance of the effects and applicability of equations (3.6, 3.8, 3.9) as well as the range of M with essential transonic effects will be considerably different due to the difference between the values $n \sim 7{,}15$ and $\gamma \sim 1{,}4$.

Water in the range $M \sim 1 \div 2$ very well satisfy the model of ideal, isoentopic compressible fluid. Static and dynamic adiabatic curves for water really coincide here, viscosity influence is negligible. However, even in such ideal medium at slight disturbances in flow under the motion of slender bodies, as it follows from the equations of acoustic approach (3.6, 3.9), a significant wave drag appears. At that summary transition of impulse through side control surfaces are not small. This effect investigated by T. von Karman lies in the base of considerable part of the classical supersonic aerodynamics [13]. In view of a complete identity of equations (3.6, 3.9) for water and air this effect has also unavoidably to be manifested for supercavitation and in a lager degree for less slender cavitators, however, in the area of applicability equation (39) just for water!

Equations (38, 39) have similar asymptotic structures, hence:

- in case of slender cavities in compressible fluid analogously $M = 0$ cavitator drag for $M < 1$ slightly depends on and for $M > 1$ is independent on cavity shape and the cavity shape really do not depend on cavitator form;
- expressions for pressure on slender body with account of compressibility are different from case $M = 0$ in outer area only with second order terms. This mean that cavity shape in outer area $M < 1$, $M > 1$, $M \sim 1$ taking into account also (3.6,3.7) will be near to ellipsoidal form.
- the terms defining wave effects for $M > 1$ are small values of the second order in the outer area and we can expect essential wave effects only for $\delta/\varepsilon \to 0$. in inner and intermediate areas.
- sizes of the inner area near the cavitator for $\delta/\varepsilon \to 0$ (where in case of a disk nonlinear consideration is necessary with using state fluid equation (3.4)) analogously as for $M = 0$ are small :

$$M = 0, M < 1: \quad R_n = O\left[\delta^2(\ln 1/\delta)^{0.5}\right]$$
$$M < 1: \quad R_n = O\left[\delta^2(\ln 1/\delta)^{1.5}\right] \qquad (3.10a)$$

and rather they are small as well as for $M \sim 1$.

Some details of nature flow in nonlinear area can give estimation of values of flow at breaking point. Results this estimations in dependence on M, neglecting of hydrostatic pressure, are presented in fig. 3.1.

$\rho_\infty, P_\infty, c_{x^*}, T^\circ_*$ are the values of mass density, pressure, pressure coefficient, temperature in degrees centigrade at the breaking point. ΔP_{*s} - the pressure in normal shock on axis. As following from fig 3.1 at Mach range under consideration changing of mass density, pressure coefficient and temperature are not essential, pressure at the shock is not large. But pressure at breaking point and in particular in case of disk cavitator can reach yield points for strongest steels.

The most important from the point of view of applying here all the opportunities of the approach at $M = 0$ are the following problems:

1. Is there a principal possibility to apply equations (38, 39) and in particular (39) :
a) in the outer region?
b) in the intermediate area - that is does the expansion SBT for φ , in particular at $M > 1$, analogously to $M = 0$, contains an intermediate component of expansion? Or SBT expansion at $M > 1$ is only outer?
c) in the inner region in case of slender cavotators?
2. Is the condition of angle equality in streamlines separation cross-section (2.8) correct enough at $M > 1$ as this problem is noted in [17]?
3. Which is the area of applicability of equations (38, 39) just for the case of water?

The following details may prove to be here considerable:

1. 6) For $M = 0$ we use SBT expansion for φ with sources on the axis which in some cases may exactly describe flows even in nonlinear regions. In the same time the sources at $M < 1$, $M > 1$ are suitable only for description of small disturbed flows.
2. In case of a fixed separation cross-section nearby this region a rather different change of pressure takes place when comparing with its magnitude on the cavitator up to small magnitude on the cavity .

Although some uncertainty we, for the possibility of preliminary consideration will assume that the situation concerning questions (1-3) is the same as at $M = 0$.

Accounting absence of an analogous integer -differential equation for $M \sim 1$ we will try to estimate the situation on the left of $M < 1$ and on the right of $M > 1$ as well as main tendencies of changing the situation when transiting to intermediate between them transonic zone. At that however, it should be noted , that if $\delta/\varepsilon = O(1)$ whole solution lies in the outer region, better explored in aerodynamics, while for $\delta/\varepsilon \to 0$, main from the point of view of wave effects are inner and intermediate regions what can be more problematic for the theory.

3.3 Asymptotic solutions for $\delta/\varepsilon = O(1)$ are defined here by the methods, analogous as for $M = 0$, but basing on one of the equations (3.8, 3.9) for conditions (3.10). Solutions for $M < 1$ is obtained if in solution for $M = 0$ (2.16, 2.17) we will use small parameter $\beta\delta$ instead of δ . At present there is here a numerical solution of the problem for $M < 1$ on the base of equation (3.8) [46]. Asymptotic solution for $M > 1$ on base equation (3.9) is found analogously to (2.16, 2.17) for $M = 0$. At that the first order solution (2.16) and values (2.17) here are the same both $M = 0, M < 1, M > 1$. Solutions for $M = 0, M < 1, M > 1$ are differed only by second order small values . In particular for $M > 1$ solutions in case of cone ($x = 0$ is at separation section , $l = 1$,) are sought on the base of problem (3.9, 3.10) for $\delta/\varepsilon = O(1)$ in the form of expansion:

$$R^2 = \frac{\sigma}{\ln(1/\delta^2)}\left[\tilde{R}_0^2 + \tilde{R}_{-1}^2\frac{1}{\ln 1/\delta^2} + \ldots\right] \qquad (3.11)$$

and are reduced to series of boundary problems, after that 2 terms of expansion are obtained:

$$R^2 = \frac{\sigma}{\ln(1/\delta^2)}\left\{\left[\frac{\varepsilon^2\ln(1/\delta^2)}{\sigma} + 2\frac{\varepsilon^2\ln(1/\delta^2)}{\sigma}x - x^2\right] + \frac{2}{\ln(1/\delta^2)}\left[\int_0^x \left.\frac{d^2\tilde{R}_1^2}{dx^2}\right|_{x=z}(x-z)dz\right]\right\} \qquad (3.12)$$

In particular the expression of $\frac{d^2\tilde{R}_1}{dx^2}$ is easily obtained on the base of the second order problem for equation (3.9). In ready solution it is possible to apply one of the convenient dependencies of δ (2.15). In particular for $\delta = \varepsilon$ solution (3.12) is applicable also for $\sigma = 0$ near cavitator and for $M > 1$, $\sigma = 0$ is:

$$R^2 = \varepsilon^2\left\{[2x+1] + \frac{1}{\ln 1/\varepsilon^2}\left[x + (x+1/2)(\ln 2x+1) + 2x^2\ln(x) - 2(1+x)^2\ln(1+x)\right]\right\} \qquad (3.13)$$

Its asymptotic for $x \to \infty$:

$$R^2 \sim 2\varepsilon^2 x + \frac{\varepsilon^2}{\ln 1/\varepsilon^2}[x\ln 2/e - 3x\ln x] \qquad (3.14)$$

For comparison we write down also asymptotic (2.18) for $M < 1, x \to \infty$:

$$R^2 \sim 2\varepsilon^2 x + \frac{\varepsilon^2}{\ln 1/\varepsilon^2}[x\ln 2/e - x\ln x] \qquad (3.15)$$

Conclusions. As follows from comparison of solutions for $\delta/\varepsilon = O(1)$ $M = 0, M < 1$ (2.16, 2.17, 3.15), $M > 1$ (3.11 - 3.14) : for $M < 1$ compressibility influence is determined by the second order values, it is insufficient and is not increased if it is increased cavity length with compared to cavitator length for transition from case $\delta/\varepsilon = O(1)$ to- $\delta/\varepsilon \to 0$. For $M > 1$ and condition $\delta/\varepsilon = O(1)$ compressibility influence is defined by second order small values but it is quickly increased if cavity length is increased for transition from $\delta/\varepsilon = O(1)$ to $\delta/\varepsilon \to 0$. At that cavity sizes for $M > 1$ can be essential smaller with compared to $M = 0, M < 1$ and this fact can be explained by energy wave losses . At that applicability range of relation δ/ε for increasing relative cavity length can be essential smaller for $M > 1$ with compared to solutions for $M = 0, M < 1$. We can see it in particular when comparing last terms of asymptotics (3.14, 3.15)!

3.4 Outer solution for $\delta/\varepsilon \to 0$ with account compressibility [47] after the manner (2.19-2.23) [31] is defined enough small influence of M, contained in integer-differential equations in form of $|1 - M^2|$. Dependence of (2.23) with account M is:

$$\sigma = \frac{2}{\lambda^2}\ln\frac{\lambda}{\sqrt{e|1-M^2|}} \qquad (3.16)$$

Analogously with account M it can be obtained all possible asymptotically the same variants of dependence (2.23), but the most convenient is:

$$\lambda^2 \approx \frac{1}{\sigma}\ln\frac{1{,}5}{\sigma|1-M^2|} \qquad (3.17)$$

Singularities of influence M on cavity aspect ratio λ $M < 1, M > 1$ are illustrated in fig. 2.4.

3.5 General Pattern of M Influence for supercavotation is first of all represented by the influence of M on the cavitator drag which determines R_k and the cavity aspect ratio λ . Fig. 3.2 illustrate singularities of the M influence for $M < 1, M > 1$ on the drag coefficient of slender cavitators (cone) in according to with dependencies (3.34,3.35) and the cavity aspect ratio λ - (3.17). For a disk-like cavitator the dependence drag on M is mainly determined by a simple dependence for the pressure in the braking point. Further we will try also to clarify singularities of influence on drag and cavity of wave effects for $M > 1$ and transonic effects in intermediate range of $M \sim 1$ between $M < 1$ and $M > 1$.

.3.6 Intermediate expansions Intermediate equations is extracted from integer-differential equations (3.8,3.9) and their asymptotic for $x \to \infty$ are [39-41]:

$M < 1$ $\beta^2 = 1 - M^2$

$$\frac{1}{4}\frac{1}{R^2}\left(\frac{dR^2}{dx}\right)^2 + \frac{1}{2}\frac{d^2R^2}{dx^2} - \ln\frac{\beta^2R^2}{4x^2} - \frac{1}{2x}\frac{dR^2}{dx} = 0 \qquad (3.18)$$

$$R^2 = \frac{2\sqrt{c_{cb}}}{(\ln x)^{0.5}}\left[1 - \frac{1}{4}\frac{\ln\ln x}{\ln x} + \frac{1}{2}\frac{\ln\sqrt{c_{cb}}\,\varphi^2/2}{\ln x}\right] \sim \frac{x}{(\ln x)^{0.5}} \qquad (3.19)$$

$M > 1$ $B^2 = M^2 - 1$

$$\frac{1}{4}\frac{1}{R^2}\left(\frac{dR^2}{dx}\right)^2 + \frac{1}{2}\frac{d^2R^2}{dx^2} - \ln\frac{B^2R^2}{4x^2} - \frac{1}{x}\frac{dR^2}{dx} = 0 \qquad (3.20)$$

$$R^2 = \frac{K_S}{(\ln x)^{1.5}}\left[1 - \frac{9}{4}\frac{\ln\ln x}{\ln x} + \frac{3}{2}\frac{\ln K_S B^2/4}{\ln x}\right] \sim \frac{x}{(\ln x)^{1.5}} \qquad (3.21)$$

Nature of asymptotic for $M = 0, M < 1$ at $x \to \infty$ is following - they define cavity as wake with constant contain of energy in its each sections [19]. Comparing of (3.19, 3.21) shows more narrow at $x \to \infty$ asymptotic for $M > 1$ and hence on possibility of essential wave losses by ahead part of cavities in this case.

3.7 A Cavity Behind a Slender Cavitator at $\sigma = 0$. Solutions, obtained earlier (2.18,3.13) for a cavity behind a slender cone at $\sigma = 0$ are inner solutions. Uniformly suitable second order solutions for cavity behind slender cone on base problems of (3.8-3.10) for $\sigma = 0$ are ($l = 1$):

$M < 1$,

$$R^2 = \varepsilon^2\left\{\left[\frac{2x}{\sqrt{\tilde{s}}} - 1\right] + \frac{1}{\ln(1/\varepsilon^2)}\left[\left(\frac{2x-1}{2}(\ln 2x - 1) + (x-1)^2(\ln x - 1) - x^2\ln x\right) + \left(\frac{\left(\ln 4/\varepsilon^2\beta^2\right)x}{\sqrt{\tilde{s}}} - \frac{1}{2}\frac{x\ln\tilde{s}}{\tilde{s}\sqrt{\tilde{s}}} + \frac{x\ln\beta^2e/2}{\tilde{s}\sqrt{\tilde{s}}}\right) - \left(x\ln\frac{2}{e} - x\ln x\right)\right\} \qquad (3.22)$$

$M > 1$,

$$R^2 = \varepsilon^2\left\{\left[\frac{2x}{\tilde{s}\sqrt{\tilde{s}}} - 1\right] + \frac{1}{\ln(1/\varepsilon^2)}\left[\left((x-1) + \frac{2x-1}{2}(\ln 2x - 1) + 2(x-1)^2(\ln x - 1) - 2x^2\ln x\right) + \left(\frac{\left(3\ln 2/B^2 + \ln 2/e\right)x}{\tilde{s}\sqrt{\tilde{s}}} - \frac{9}{2}\frac{x\ln\tilde{s}}{\tilde{s}^2\sqrt{\tilde{s}}} + 3\frac{x\ln B^2/2}{\tilde{s}^2\sqrt{\tilde{s}}}\right) - \left(x\ln\frac{2}{e} - 3x\ln x\right)\right]\right\} \qquad (3.23)$$

where:

$$\tilde{S} = \frac{\ln(x/\varepsilon^2)}{\ln(1/\varepsilon^2)}$$

Solution (3.23) at $x \to \infty$ defines also value K_s for cone:

$$K_S = 2\varepsilon\left[\ln\left(\frac{2}{e}\right)^{1/3}\frac{2}{B^2\varepsilon^2}\right]^{.5} \sim 2\varepsilon\left(\ln\frac{1}{\varepsilon^2}\right)^{.5} \quad (3.24)$$

Fig. 3.3 illustrates the results of calculation in agreement with dependencies (3.22, 3.23): —— calculation, ---- calculation at $M = 0$; $\lambda_n = x/R$ at $M = 0$; x – nonlinear numerical solution [3]. The results of calculation shows small compressibility influence on the front parts of cavities at $M < 1$. At $M > 1$, however, this influence can be considerable: the front parts of cavities at $M > 1$ can be essentially narrower as compared to cavities for $M = 0$ and $M < 1$.

3.8 Asymptotic Structures of Dependencies at $\delta/\varepsilon \to 0$. Uniformly suitable first order solutions behind a slender cavitator are universal and independent of cavitator shapes ($l = 1$):

$M < 1$

$$R^2 = \varepsilon^2\left[2n\left(\frac{\ln(1/\beta^2\varepsilon^2)}{\ln(x/\beta^2\varepsilon^2)}\right)^{0.5} x + (1 - 2n)\right] -$$

$$- \frac{\sigma}{\ln 1/\beta^2\delta^2}(x-1)^2 \sim \frac{x}{(\ln x)^{0.5}}; \quad (3.25)$$

$M > 1$

$$R^2 = \varepsilon^2\left[2n\left(\frac{\ln(1/\beta^2\varepsilon^2)}{\ln(x/\beta^2\varepsilon^2)}\right)^{1.5} x + (1 - 2n)\right] -$$

$$- \frac{\sigma}{\ln(1/B^2\delta^2)}(x-1)^2 \sim \frac{x}{(\ln x)^{1.5}}; \quad (3.26)$$

Solutions, containing only the intermediate and the outer part (as applied in particular to disk-like cavitators):

$$M < 0 \quad R^2 = \frac{2\sqrt{c_{do}}}{(\ln x)^{0.5}} x - \frac{\sigma}{\ln 1/\beta^2\delta^2} x^2 \quad (3.27)$$

$$M > 0 \quad R^2 = \frac{K_s}{(\ln x)^{1.5}} x - \frac{\sigma}{\ln 1/B^2\delta^2} x^2 \quad (3.28)$$

3.9 Finite Cavities Here for $\delta/\varepsilon \to 0$ $M < 1, M > 1$ on the basis of equations (3.8,3.9) enough complete the second order theory is developed. Taking into account that the shape of the most part of cavity (in the outer area) rather close to ellipsoid, defining dependence for R_k here is principal. The dependence for R_k for $M < 1$ has turned out to be dependent on M only in the drag coefficient. For $M > 1$ dependence for R_k, obtained by matching of the intermediate and the outer solutions is:

$$\frac{R_k}{R_n} = \frac{1}{\sqrt{\sigma}}\frac{K_s/2}{\ln 2e/B^2\delta^2} \quad (3.29)$$

where any convenient dependence for δ (15 a,c,d) can be used. Here magnitude of K_s in asymptotic for $M > 1$ (3.21) in case like disk cavitators are some value $K_s = O(1)$. In case of slender cavitators this value can be defined by matching of the inner and the intermediate solutions. In particular for the cone value K_s on base second order solutions (3.23) is defined by dependence (3.24). As follows from (3.29) dependence for R_k for $M > 1$ can be expressed in view of (2.10) however dependence for k account from (3.29), has following structure:

for like-disk cavitators

$$k \sim c(\ln\lambda^2/B^2)^2 \to \infty$$

$$c = O(1),, \quad \delta \sim 1/\lambda \to 0 \quad (3.30)$$

for slender cavitators

$$k \sim \left(\frac{\ln\lambda^2/B^2}{\ln 1/B^2\varepsilon^2}\right)^2 \to \infty$$

$$\delta/\varepsilon \to 0 \quad (3.31)$$

And as distinct from $M = 0, M < 1$ $k \sim 0{,}96 + 1$ (2.36) the value k for $M > 1$ can be essentially by more than 1.

With account of a small compressibility influence in the outer part of solutions simple equations (2.27 -2.30) are applicable as well here. In the case of a slender cavitators analogous to (2.27) equations are:

$$\frac{d^2R^2}{dx^2} + \frac{\sigma}{\mu} = 0$$

$$R^2\Big|_{x=0} = R_n^2, \quad \frac{dR^2}{dx}\Big|_{x=0} = \sqrt{\frac{2(c_d - \sigma)}{k_d\mu}} \quad (3.32)$$

At that in equations (2.27,2.30, 3.32) it is the most convenient to apply value μ on the base of (2.29), but with account of M:

$$\mu = \frac{1}{2}\ln\frac{1{,}5}{|1 - M^2|\sigma} \quad (3.32a)$$

and it is need account that values of k for $M > 1$ can be essential more than 1.

M influence on μ is illustrated in fig. 2.5

Fig. 3.4 illustrates calculation results for slender axisymmetric cavity behind slender cone for $M > 1$ using equations (3.32) where k is defined on the base (3.24, 3.29). For c_d defining dependencies (3.35,3.37) are applied.

For the approach within the scope of the theory being developed the value R_k may be determined only on the basis of matching. Proceeding from this it should be reminded about the restrictions of the theory which are analogous as at $M = 0, M < 1$ (see p. 2.11), the applicability of the theory in the case of slender cavitators is only for enough slender cavities(small σ). Comparing of the cavitator sizes (3.10a), we can see, that at $M > 1$ the cavitators can be considerably larger and that can make range of the theory applicability less large and can demand still more less σ. Besides, it should be noted a considerably more worse convergence of the series in asymptotic (3.21) at $M > 1$ as compared to (3.19) and remind notes of p.3.2. Proceeding from the above dependence (3.29) may be applicable only for preliminary rough estimations. *Nevertheless it express a very important regularity - an essential and can be able also a considerable decrease of the main cavity sizes (and hence the lengths)* of supersonic cavities in comparison with the cavities at $M = 0, M < 1$ at the same values of the cavitators drag. At $M > 1$ the cavitator drag ceases to be such an universal value as at $M > 1$ which determines the sizes of cavities in a unique fashion. At $M > 1$ significant wave losses appear depending in a definite manner on the

cavitator shape and the cavitators having the same drag at $M > 1$ can produce cavities of considerably differing sizes.

3.10 Cavitational Drag . Drag coefficient of disk-like cavitators taking into account the closeness of flow to an isentropical one and small losses on a normal chock, the coefficient c_{do} for $\sigma = 0$ can be obtained accurately enough on the basis of the pressure coefficient in the breaking point: In particular for disk it may be written:

$$c_{do} \approx 0{,}82 c_{x*}|_{M=0} = 0.82$$

$$c_{x*} = \frac{2B}{M^2 pa^2}\left[\left(1+\frac{(n-1)\,M^2 pa^2}{n\quad 2B_*}\right)^{\frac{n}{n-1}} - 1\right] \quad (3.33),$$

where B, n are the same as in (3.4).

Drag coefficients for slender cavitators are obtained in works [11,19, 24, 29, 35-39]... .For $\sigma = 0$ at $M > 1, M > 1$ they have similar structures. In particular in case of cone for

$M < 1$:

$$c_{do} = 2e^2 \ln \frac{2}{e}\frac{1}{\beta\varepsilon} \quad (3.34)$$

$M > 1$ [11]:

$$c_{do} = 2e^2 \ln \frac{2}{\sqrt{e}}\frac{1}{\beta\varepsilon} \quad (3.35)$$

Number cavitation influence is defined by the known dependencies.

For $\delta/e \to 0 \quad M < 1$:

$$c_d = c_{do}(1+\sigma) \quad (3.36)$$

for $\delta/\varepsilon = O(1) \quad M < 1$:

$$c_d = c_{do} + \sigma \quad (3.37)$$

dependence (3.37) is, however, rather rough because the cavity influence on the distribution of hydrodynamic pressures on the cavitator and this influence, although being determined by small values of the second order, may be significant [35,39]. However, at $M > 1$ the reverse influence of the cavity is absent and dependence (3.39) is here both exact and applicable in the two cases $\delta/\varepsilon = O(1)$, $\delta/\varepsilon \to 0$.

Cavitational drag coefficients for middle cavity section and for some section $x = L_o$ with radius R_o of its forward part for $\sigma = 0$ in apply to motion in ahead part of cavity are some indexes cavitation effectiveness. Second order asymptotic dependencies $\delta/e \to 0 \quad M < 1$ [38-41] in case of motion in ahead cavity part $\sigma = 0$ is:

$$C_{Do} = \frac{\delta_o^2}{4}\ln\frac{4}{e\beta^2\delta_o^2} \sim \frac{1}{8}\frac{\ln\lambda_o/\beta}{\lambda_o^2}$$

$$\delta_o = 1/\lambda_o = 2R_o/L_o \quad (3.38)$$

Second order expansion in additional to known dependence of drag coefficient for middle section $C_D = \sigma$ are:

$$C_D = \frac{c_d R_n^2}{R_n^2} = \sigma\left[1 - \frac{2\ln 2/\sqrt{e}}{\ln 1/\beta^2\delta^2}\right] \sim \frac{2\ln\alpha/\beta}{\lambda^2} \sim \sigma \quad (3.39)$$

Asymptotic structures for C_{D_i}, C_D on the base of (3.21, 3.29) also are:

$$C_{D_i} \sim \frac{1}{8}\left(\frac{\ln\lambda_o/B}{\ln 1/B\varepsilon}\right)\frac{\ln\lambda_o/B}{\lambda_o^2} \quad (3.40)$$

$$C_D \sim \left(\frac{\ln\lambda/B}{\ln 1/B\varepsilon}\right)^2 \frac{2\ln\lambda/B}{\lambda^2} \sim \left(\frac{\ln\lambda/B}{\ln 1/B\varepsilon}\right)^2 \sigma \quad (3.41)$$

The results of calculations in agreement with dependencies (3.38, 3.39) are shown in fig. 3.5 and allow to draw the following conclusions.

- The motion in a cavity is the more effective the more it is slender. The principal limitation at velocities high enough is achievable in practice body aspect ratio.
- The motion in the ahead part of a cavity provide the most small drag coefficients that considerably smaller than in case of a finite cavity. From this point of view the influence of pressure is essential factor to decrease the effectiveness of motion with supercavitation in spite of a certain possibility of the energy regeneration in the end part of the cavity.

At $M > 1$ as it follows from (3.40, 3.41) we have the tendency of considerable decrease of effectiveness of applying cavitation due to wave losses. In case of slender cavitators this effect is increased for increasing of cavitator slenderness (cone semi-angle).

3.11. Transonic effects. The transonic region $M \sim 1$ is intermediate between $M < 1, M > 1$. The main problem here is to understand what properties of the flow are conserved here the same as for $M = 0, M < 1$ and what ones are changed abruptly enough when transiting through the transonic region, as well as characteristic scales of the intensity of transonic effects and the extension of this region. Let us note some peculiarities of the flow in this case using also results of the known investigations for air [10, 13, ...].

The sizes of nonlinear zone near by a disk-like cavitator may be assumed to be also small, a slender cavity will be similar to ellipsoidal one and the disk-like cavitator drag may be determined basing on the pressure coefficient in the breaking point (3.33).

In the region of small disturbed flow equation (3.7) is here valid. Lets write separately expression for the coefficients of (3.7) differing this equation from acoustic one for M<1, M>1.

$M < 1$

$$+\left[\left(1-M_\infty^2\right) - \frac{(n+1)M_\infty^2}{U_\infty}\frac{\partial\varphi}{\partial x}\right] \quad (3.42)$$

$M > 1$

$$-\left[\left(M_\infty^2 - 1\right) + \frac{(n+1)M_\infty^2}{U_\infty}\frac{\partial\varphi}{\partial x}\right] \quad (3.43)$$

- Depending on the sign of $\frac{\partial\varphi}{\partial x}$ influence of the second transonic term either favors change of, for example, elliptic type of equation to hyperbolic one, or retards it. In particular, the influence of a slender cone-like cavitator will be decelerate this process and the influence of a cavity, quite the reverse, will be accelerate one. When transiting along the M axis from an entirely subsonic flow to an entirely supersonic one the flow is usually mixed, consisting of separate regions of sub- and supersonic flows.

-The knows investigations found also at M~1 a considerable increase of transverse sizes of the outer region (region of disturbed flow) to $O(1/\delta)$.

- On account of the considerably more great adiabatic curve index for water n~7.15 in comparison to air, sizes of the transonic region in water are to be considerably more wide than that in air. At that the singularity at $M \sim 1$ may be assumed to be considerably more smooth, and transverse sizes of the disturbed flow region will be considerably more narrow than that in air.

As it follows from the estimate results at $1 - M^2 = O(1)$ the value of the second term in (3.42-3.43) is essential small. Hence, an influence of the second term will be the less the more narrow will be the transonic region and the sharper will be the peak in the singularity region if the more slender will be the cavitator and the cavity. At that due to the features of the structure of dependencies for the drag of slender cavitators and the cavity aspect ratio ,transonic influence on the drag of slender cavitators has to be more significant than on cavity aspect ratio.

- As it follows from the comparison (fig.(3.2)) of the slender cone drag coefficient with the data of nonlinear numerical calculations [2], extent of the transonic range reaches here $M \sim 0{,}7+1{,}5$ for the case of water . For aspect ratios in the case of disk $\sigma \sim 0{,}03$ this region as M>1 also seems to be considerable because values , determined by nonlinear calculations [49] are different up to 20% from the calculations in agreement with dependence (3.16-3.17) at $M \sim 1{,}2$.

- At $\delta/\varepsilon \to 0$ it seems quite possible for a region close to the cavitator to be essentially transonic and the outer region of a slender enough cavity at $\sigma \to 0$ to be supersonic. Two main moments are here principal:
1) The cavity aspect ratio is fully determined by the outer solution and all the dependencies for (3.16,3.17) will be valid here . But the value of wave losses and also what fraction of the cavitator drag will be transformed into the energy of radial flow and, consequently, R_k , is determined namely by the transonic part of flow. As it follows from the investigations of the transonic flows in air [10, 13, 43] when transiting from M<1 to M>1 no abrupt changes in the pressure distribution over the body surface take place and the flow is reformed rather smoothly when changing M in the transonic region. The wave part of resistance at the front parts of bodies appears smoothly too. Analogous, but the more smooth process can be expected in the case of supercavitation flow in water. This has some confirmation in the dynamics of growing k included in dependencies (2.10-3.29) with growing $M.> 1$ on the basis of the numerical calculation data at $(\sigma \sim 0.025 - 0{,}03)$ [49]:

M	0	1	1,05	1,1	1,15	1,20
$\sigma\sim$	0.026	0.026	0.027	0.029	0.03	0.031
k	0,934	1,003	1,016	1,047	1,115	1,198
k/k_o	1	1,07	1,09	1,12	1,19	1,28

for $k_o \sim 0.934$.

4. MOTION PROBLEMS.

Flow over stabilizers - the theory of sub, trans, and supersonic planing of a unit plate and of a system of plates. Here a rather complete theory is developed taking into account compressibility and a considerable appearance of transonic effects and an actual smoothing the peak maximum is revealed for the lift force in this region [21].

The penetration problems here are connected with appearance of considerable but short-time acting pressures in the instant of impact which exceed considerably the pressures at the motion with a constant velocity and may actually reach values up to $(5-10)\times10^4 kg/cm^2$. The linearized theory of penetration is developed here taking into account plastic deformations. Plastic deformation for speed comparable with sonic speed are considerable even for strongest steels and quickly increase if penetration speed is increased.

Motion theory. The linearised theory of longitudinal and transverse motion of elongated bodies is here developed. The transverse motion under the action of initial disturbances has at that an obviously expressed oscillatory nature. On the basis of the theory the models of the decrease of the trajectory side disturbances and the maximal increase of the length of the supercavitation part of trajectory are developed [42].

Hydroelasticity problems. At the elongated body motion with the values M high enough they becomes similar to the branches of a young tree. As a result of bending the angle of attack of the end stabilizing surfaces is significantly different from its values on the basis of the ideal rigid body theory, which in the most real cases proves to be applicable at $-M < 0{,}3$. only. A linearized theory of motion are developed with account hydroelastic effects and the nature frequencies oscillations of bodies as well as of compelling forces are obtained.

5. CONCLUSIONS

- The linearized theory of axisymmetric cavitation in an incompressible fluid is nowadays complete enough. Developed here rather simple methods really allow to calculate stationary and nonstationary cavities at a given pressure on the majority of real cases of flow without applying very complicated techniques of nonlinear numerical calculations.

- In the case of the compressibility flow application of the developed earlier for $M = 0$, methods of linearized theory on the SBT basis together with the integral lows of conservation is effective enough. Many features of supercavitation flows for $M = 0$ hold also true in compressible fluids but new serious problems appear. Calculation methods of the linearized theory are effective enough as applied to compressible fluids and here a number of solution is obtained. However, the quantity of theoretical and experimental investigations as well as opportunities of experiments are at present rather limited in the given area and the main problem here is the problem of verification. As the most topical and the least investigated and the most complicated from the point of wiev of the theory of small disturbed flows is here development of the transonic suparcavitation flow theory appearing in water in a considerably more extended range of M as compared with air. Correspondingly, the questions of reliable obtaining principal sizes of cavities and decrease of cavitation drag in this range of M are of large interest too.

6. REFERENCES

1. Abelson H. A "Prediction of Water Entry Cavity Shape" , "Pa. Amer. Soc. Eng." N WA/FE- 8, 1970 , pp 3.
2. Aleve G. A. "Separated flow over circle cone by transsonic water flow " Izvestia of AS of USSR, Mechanics of fluid and gas, N 2 , 1983, pp 152 - 154. (Russ)

3. Aleve G. A. "Subsonic separated flow of water around circular cone with finite length " Dynamics of continuum medium - Chebocsary, publ. of Chuvash. state Univ , 1984, pp 3 - 7. (Russ.).
4. Billet M. L., Holl J.W. Weir D.S. "Correlations of thermodynamics effects for developed cavitation" Trans ASME J. Fluids Eng, , 103, 4, 1981 pp 534-542.
5. Birkhoff G., Zarantonello E. " Jets, wakes and cavities", New York, USA ,1957.
6. Brennen C. "A numerical solution of axisymmetric cavity flows" J. Fluid Mech,37, 4, 1969, pp 671-688.
7. Chou C. "Axisymmetric cavities flows past bodies of revolution "J. of Hydronautics, 8, 1, 1974, pp 13 - 18.
8. Cole R. "Underwater explorations", Izd-vo inostr. Literat., 1950, (Russ., translated from Engl.)
9. Cole J. "Perturbation methods in applied mathematics" Waltham, Massachussets, London-Toronto, Blaisel Publ. Comp. A division of Ginn and Comp. , 1968.
10. Cole J. , Cook L. "Transonic aerodynamics" Moscow ,Mir, 1989. (Russ, transl from Engl.)
11. Frankl F., Karpovich E. "Slender Bodies Gasdynamics" Moscow-Leningrad, GosTechIzdat publ., 1948, 175p. (Russ.)
12. Garabedian P.R. "Calculation of axially symmetric cavities and jets " Pac. J. Math, 1956, 6, 4, pp 611 - 684.
13. "General Theory of High Speed Aerodynamics" editor W. Sears, Prinston, New Jersey, Prinston University Press , pp 9-33, 112-264.
14. Grigoryan S. "Approximation solution of problem of separated flow over axisymmetrical body" Appl. Math. and Mech., 1959, 23, 5, pp 951 - 953. (Russ.).
15. Gurevitch M. "Theory of jets in ideal fluid" New York-London, 1965. (transl. from Russ.)
16. Guthevsky L. "Numerical analysis of supercavitation flow" -Novosibirsk, 1979, (preprint. Siberian department of AS of USSR, Inst. of Thermophysics, N 40 - 79), 36pp (Russ.).
17. Kirschner I. "Approximations at high Mach Number" - ARPA/ ONR review of supercavitation high speed bodies, 11-13 April 1995 University of Rhode Island, USA.
18. Levinson N. "On the asymptotic shape of the cavity behind an axially symmetric nose moving through an ideal fluid " Ann. Math. 47, 1946, pp 707 - 731.
19. Logvinovich G. "Hydrodynamics of flow with free boundaries" Kyiv, publ. "Naukova dumka", 1969. pp 216 (Russ.).
20. Logvinovich G. , Serebryakov V. "On methods of calculation of of slender axisymmetric cavities shape" Hydromechanics, 32, Kyiv, 1975, pp 47-54. (Russ.)
21. Miboroda A. " Hydrodynamics perfomances planing vessel for high speed of motion" International conference Modelling and investigations of system stability, Kyiv, May 1997, pp.78 . (Russ)
22. Michel J.M. "Ventilated cavities . A Contriibution to the Study of Pulsation Mechanism" Procedings of the IUTAM Symposium held in Leningrad "Nauka" Publishing House Moscow ,1973, pp 343-360.
23. Nakatani H., Nakatani Y., Miyai Y. " A finite cavity flow about a slender body of revolution in a tube" Bull. JSME, 22, 170, 1979 , pp 1092-1098.
24. Nesteruk I. "Some problems of axisymmetric cavitational flows " Izvestia AS of USSR Mechanic of Fluid and Gas, 1, 1982, pp 28-34(Russ.)
25. Nishiyama T., Kobayshi H. "Finite cavity flow of axial symmetry " Technol. Rept. Tohoku Univ, 34, 1, 1969, pp 173 - 178.
26. Nishiyama T. and Khan O. "Compressibility effects upon cavitation in high-speed liquid flow (Transonic and supersonic liquid flows) "Bulletin of the Japanese Society of Mechanical Engineers 24, 190, 1981.
27. Parishev E. "Systems nonlinear differencial equations with delay argument described dynamics of unsteady axisymmetrical cavities " Proceeding of TSAHI, N 1907, 1978, pp 48. (Russ.).
28. Petrov A. "Asymptotic expansions for slender axisymmetric cavities" Appl. Mech. and Techn. physics 5 (159), 1986 pp 45 - 49.(Russ.)
29. Sagomonyan A. "Penetration" Moscow , Publ. of Mosc. Univ., 1974, pp 300 (Russ.)
30. Savchenko J., Semenenko V., Serebryakov V. "The experimental investigation of supercavitation in subsonic flow" DAN of Ukraine, 2 , 1993, 64 - 68. (Russ.)
31. 31.Serebryakov V. "Asymptotic solution of the problem on slender axisymmetric cavity" DAN of Ukraine SSR, ser. A , 12, 1973 pp 1119 - 1122. (Russ.).
32. Serebryakov V. "Rings model for calculation of axisymmetrical flows with supercavitation " Hydromechanics , 27, Kyi v, 1974, pp 25 - 29 (Russ.)
33. Serebryakov V. "Asymptotic solution for slender axisymmetric cavity form behind slender body" Kyiv, Hydromechanics, 34, 1976, pp 48-52.(Russ.)
34. Serebryakov V. "On statement of linearized problems of axisymmetrical supercavitation in unsteady flows" Mathematical methods of hydrodynamics flows investigations, Kyiv publ. Naukova Dumka, 1978, pp 58-62. (Russ)
35. Serebryakov V. "Calculation of slender axisymmetric cavity forms in unsteady flow for a number of characteristic cases" Kiev, Hydromechanics, 44, 1981, pp86-94.(Russ.).
36. Serebryakov V. "Dependencies to limit of Slender Body Theory for unsteady axisymmetric flows" Bionics, Kiev, 20, 1986, pp 22 - 32 (Russ.)
37. Serebryakov V. "On limit equations of slender axisymmetric cavity in unsteady flow" Kiev, Bionics, 23, 1989 , pp18-33.(Russ.)
38. Serebryakov V. "Asymptotic solutions of the supercavitation problems by the Slender Body Theory approximation " High speed Hydrodynamics - Chebocsary, Publ. of Chuvashian state Univ., 1990, pp 99 - 111 (Russ.).
39. Serebryakov V. "Asymptotic dependencies for axisymmeytic cavities and cavitational drag on slender body approximation" Kiev, Hydromechanics, Kiev, 66, 1993, pp 103-108. (Russ.)
40. Serebryakov V. "Asymptotic solutions of axisymmetric problems for sub and supersonic separated water flows with zero number of cavitation" DAN of Ukraine, 9, 1992, pp 66-71 (Russ.).
41. Serebryakov V. "Asymptotic solutions of the supercavitation problems on basis the Slender Body Theory approximation " Hydromechanics, Kiev, 68, 1994, pp 62 - 74 (Paper to USSR Mechanics congress in Moscow, 1991)(Russian).
42. Serebryakov V. "Investigation sub and supersonic body motion in fluid under inertia" Proceding of 2-d scientific school Impulse processes in Mechanic of continuos medium , Nikolaev, 1996, pp 50-51. (Russ)
43. Spreiter J. "Aerodynamics of wing and bodies at transonic speeds" J. Of the Aero/Space Sciences, 26, 8, 1959, pp 465-486.
44. Tulin M. "Supercavitating flows - small perturbation theory " J. Ship Res., 7, 3, 1964. pp16 - 37.

45. Van Dyke M. "Perturbation methods in Fluid Mechanics" New York - London ,Academic Press , 1964.
46. Vargnese A., Uhlman J., Kirschner I. Axisymmetric slender-body analysis of supercavitation high-speed bodies in subsonic flow , Procedings of conference in Rhode Island 1997 , pp 185-200.
47. Vasin A. "Slender axisymmetric cavities in sub- and supersonic flow of compressible fluid " Transactions of 3 scientific school for hydrodynamics of high speeds, Krasnoiarsk, Publ. of Krasnoiarsk polytechnic inst., 1987, pp58-62.(Russ.)
48. Vasin A. "Calculation of axisymmetric cavities behind a disk in subsonic flow of compressible fluid" Izvestia As of Russia, Mech. of Fluid and Gas, №2, 1996, pp 94 - 103(In Russ.).
49. Vasin A. "Calculation axisymmetric cavities behind disk in supersonic flow"Izvestia As of Russia, Mech of fluid and gas , 4 , 1997, pp 54-62
50. Vorus W. "Ambient supercavitaties of slender bodies of revolution " 3, N3, J. Ship Res., 1986, 215-219.
51. Vorus W. "A flat cylinder theory for vessel impact and steady planing resistance"J. Ship Research, 1996, 40, 2, pp. 89-106.
52. Ward G "Linearized theory of steady high-speed flow", Cambridge Univ. Press, London- New York, 1955.
53. Yakimov J. " On energy integral for motion with small supercavitation number and cavity shapes to limit" Izvestia AS of USSR , Mech Fluid and Gas, 3, 1983, pp 67-70 (Russ.).
54. Yakimov J. "Slender cavity in compressible fluid" Problems of modern mechanics in 2 parts - Publ. of Moscow state Univ., 1983- part.1, pp 66-73.(Russ.).
55. Terentev A. Chechnev A. "Penetration of plate and disk into compressible fluid " Izvestia of AS of USSR, Mech. Fluid and Gas, 3, 1989, pp 147-149. (Russ.)

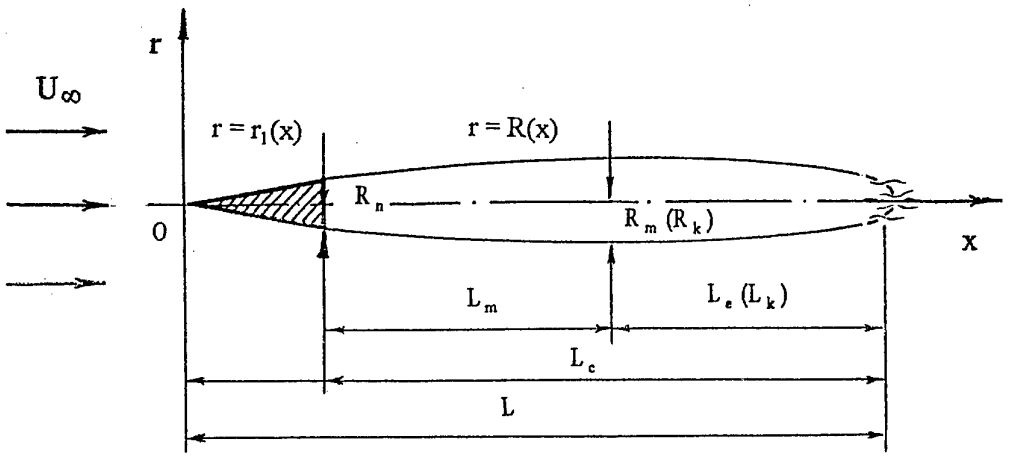

r
U∞
r = r1(x)
r = R(x)
Rn
Rm (Rk)
0
x
Lm
Le (Lk)
Le
L

Fig. 2.1

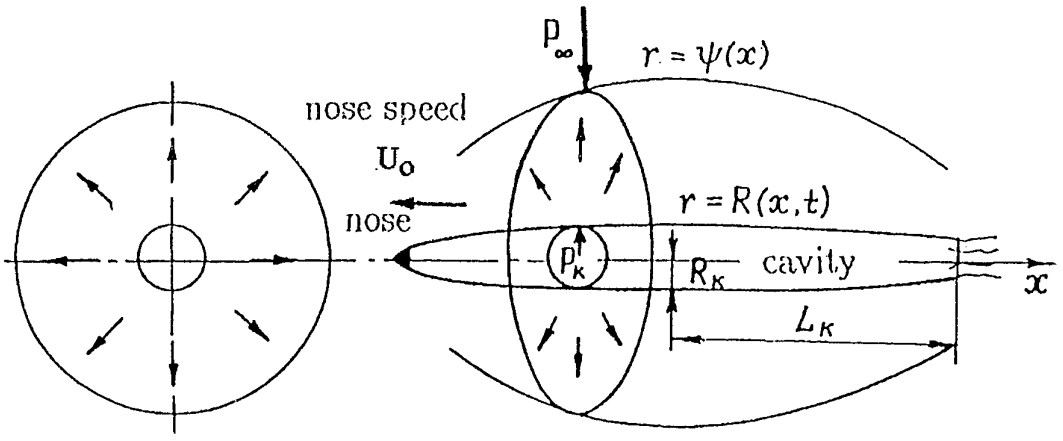
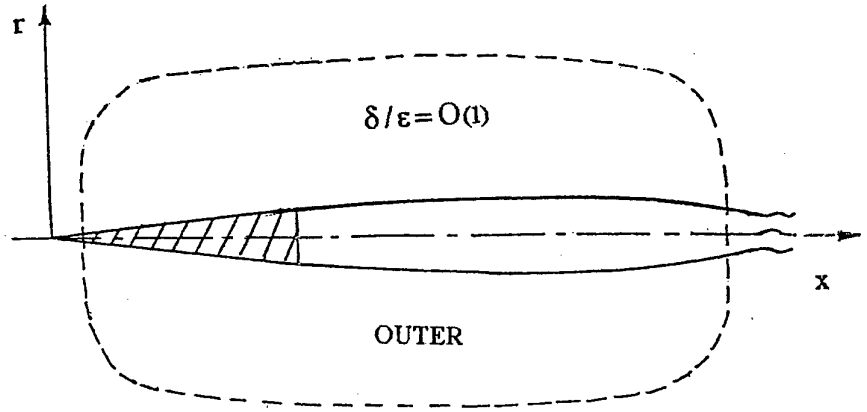
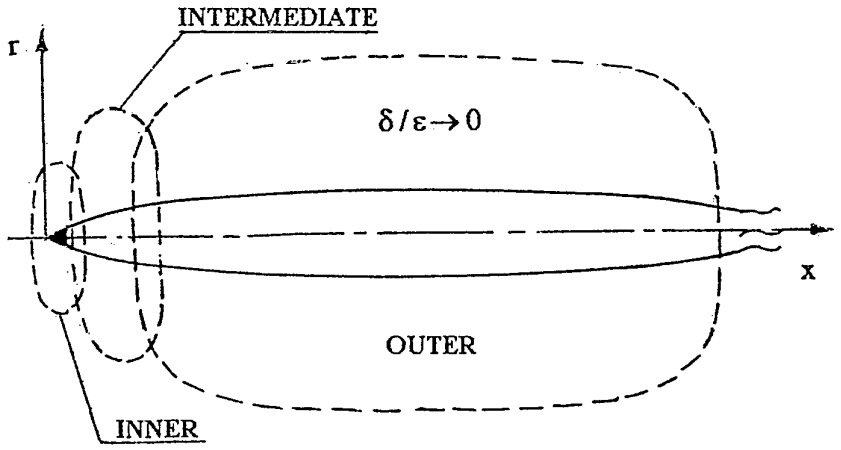

p∞
r = ψ(x)
nose speed
U0
nose
r = R(x,t)
pk
Rk
cavity
x
Lk

Fig. 2.2

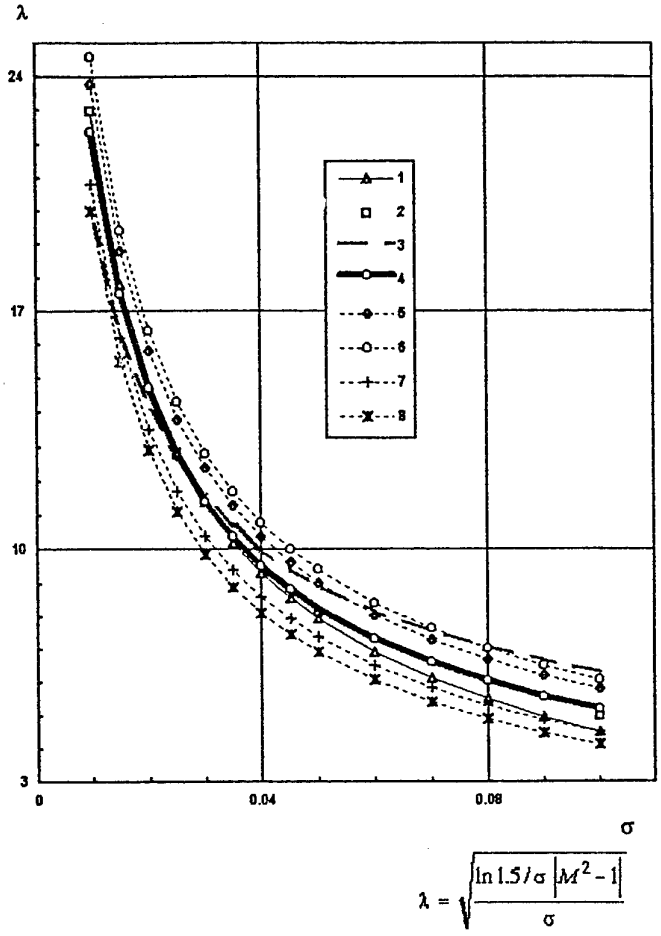


a)



b)

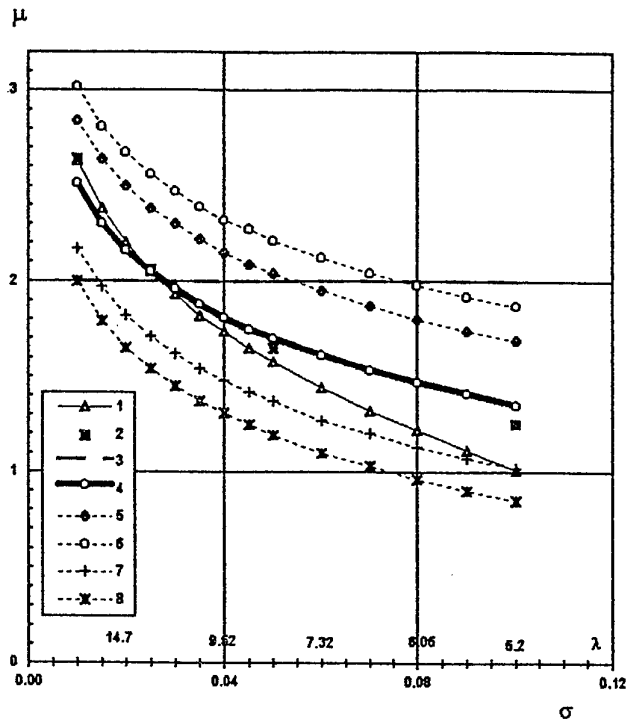
Fig. 2.3



$$\lambda = \sqrt{\frac{\ln 1.5/\sigma \left|M^2 - 1\right|}{\sigma}}$$

1. $M = 0, \sigma = \frac{2}{\lambda^2} \ln \frac{\lambda}{\sqrt{e}}$
2. $M = 0$ [16]
3. – $\mu = 2$
4. $M = 0$ $(M = 1{,}414)$
5. $M = 0{,}7$ $(M = 1{,}23)$
6. $M = 0{,}8$ $(M = 1{,}17)$
7. $M = 1{,}72$ (–)
8. $M = 1.93$ (–)

Fig. 2. 4



$$\mu = \frac{1}{2}\ln\frac{1{,}5}{|M^2-1|\sigma}$$

1. $M = 0$, $\mu = \ln\lambda / \sqrt{e}$.
2. $M = 0$, $\mu = \sigma\lambda^2/2$ [16].
3. - $\mu = 2$.
4. $M = 0$ ($M = 1{,}414$)
5. $M = 0.7$ ($M = 1{,}23$)
6. $M = 0{,}8$ ($M = 1{,}17$)
7. $M = 1{,}72$ (-)
8. $M = 1{,}93$ (-)

Fig. 2.5

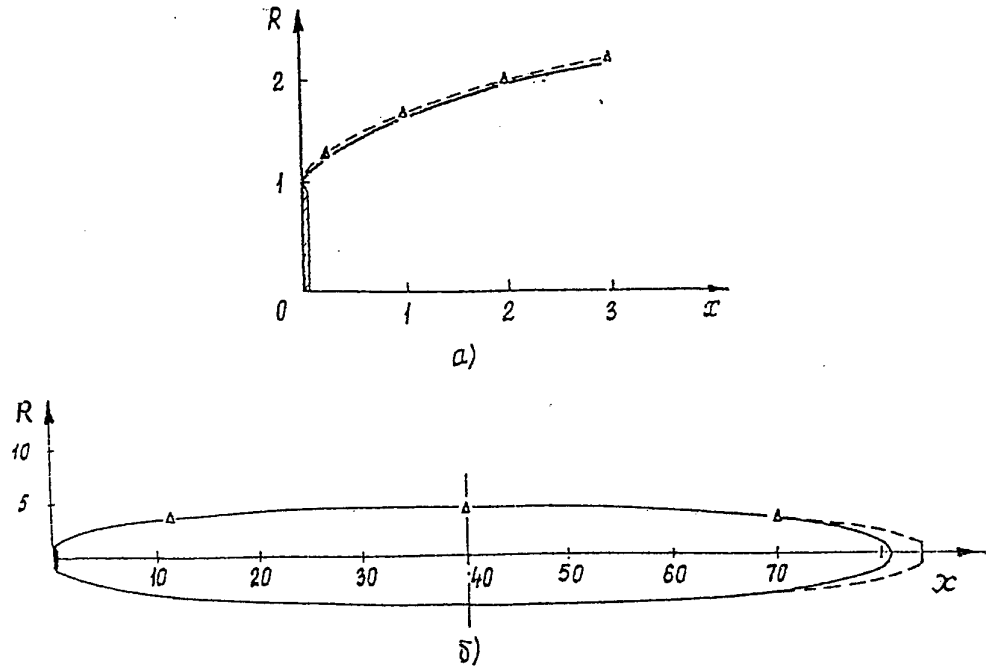


Fig. 2.6

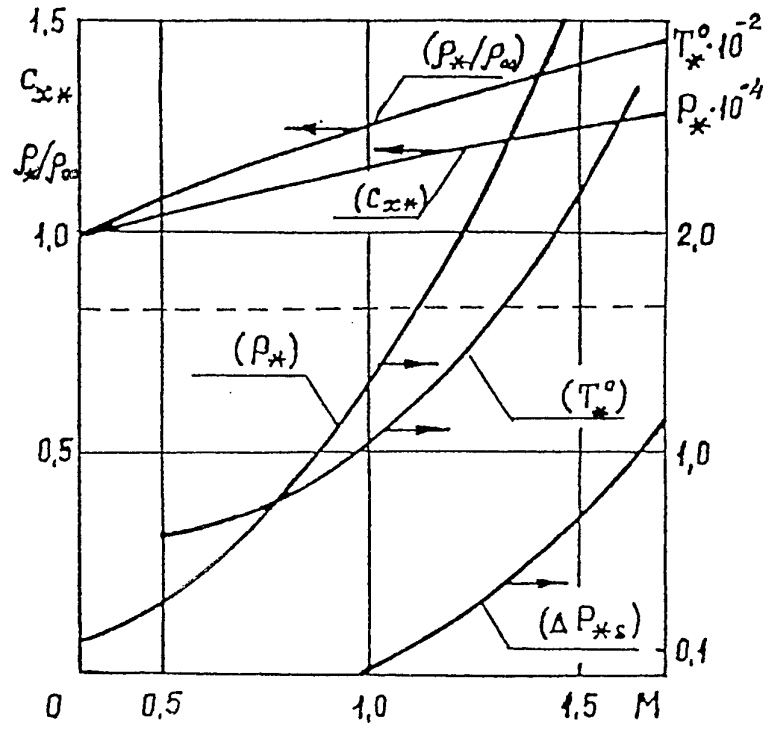
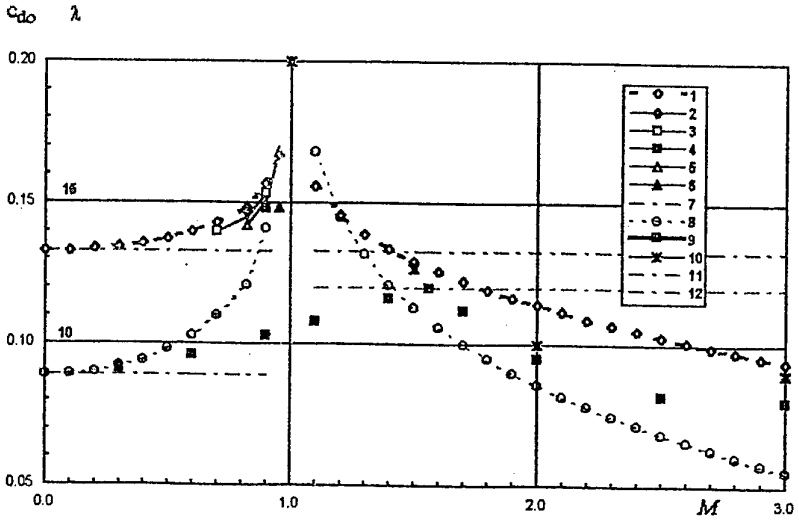


Fig. 3.1



λ $(\delta/\varepsilon \to 0)$

1. σ = 0,0235, (3.17)
2. – [48]
3. σ = 0,0245, (3.17)
4. – [48]
5. σ = 0,0252, (3.17)
6. – [48]
7. $M = 0$; $M = 1.414$ (3.17)

c_{do}, $(\gamma = 10°)$

8. $M < 1$ (3.34), $M > 1$ (3.35)
9. [2]
10. M)1 [11] nonlinear - air
11. $M = 0$ (3.34)
12. $M = 1{,}414$ (3.35)

Fig. 3.2

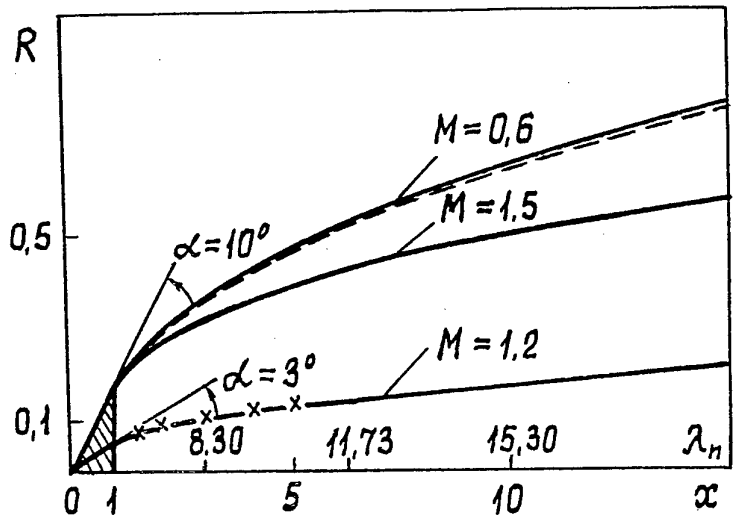
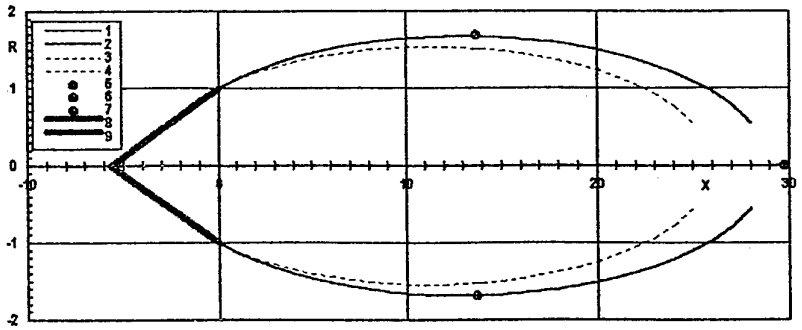


Fig. 3.3



$\gamma = 10°$, $\sigma = 0{,}04$

1. r_1; R $M = 0$
2. r_1; R $M = 0$
3. R $M = 1{,}4$
4. R $M = 1{,}4$
5. R_m $M = 0$
6. R_m $M = 0$
7. L_c $M = 0$
8., 9. - cone

Fig. 3.4

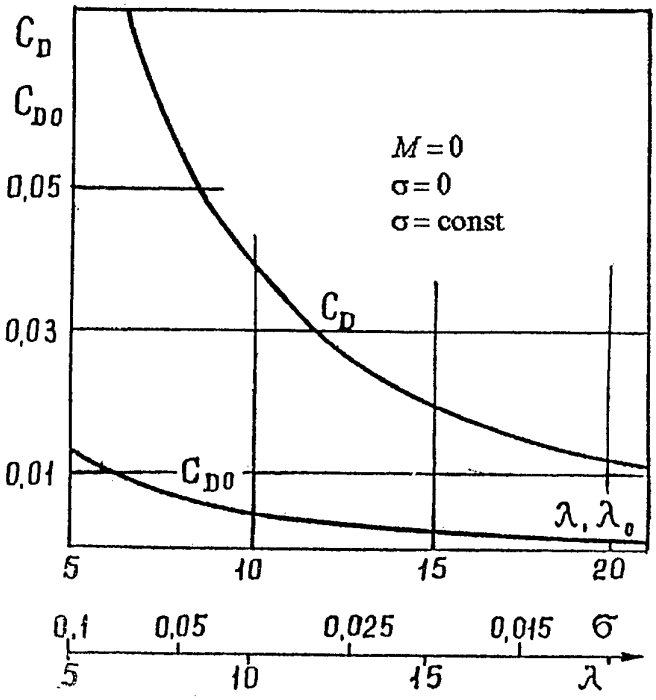

C_D
C_{D0}
0,05
0,03
0,01
$M = 0$
$\sigma = 0$
$\sigma = \text{const}$
C_D
C_{D0}
λ, λ_0
5
10
15
20
0,1
0,05
0,025
0,015
σ
5
10
15
λ

Fig. 3.5

WATER ENTRY OF SHIP SECTIONS AND AXISYMMETRIC BODIES

Odd Faltinsen
Department of Marine Hydrodynamics
Norwegian University of Science and Technology
7034 Trondheim, Norway

Rong Zhao
MARINTEK, P.O.Box 4125 Valentinlyst
Trondheim, Norway

SUMMARY

Theoretical methods for water entry of two-dimensional and axisymmetric bodies are presented. When the local angle between the water surface and the body surface is very small, hydroelasticity must be considered. The presented slamming analysis assumes the structure is rigid. Two 2-D numerical methods are discussed. One of the methods simplifies the dynamic free surface condition and details of the jet flow. Flow separation from sharp corners are incorporated. The simplified method is generalized to 3-D axisymmetric flow without flow separation. In order to verify the 3-D method, water entry of axisymmetric bodies with small local deadrise angles are studied analytically by means of matched asymptotic expansions. A composite solution for the pressure is presented. The numerical method is verified by comparing with the asymptotic method and validated by comparing with experiments for cones and spheres. It is demonstrated that satisfaction of exact body boundary condition is more important than satisfaction of exact free surface conditions. The effect of local rise up of the water is significant.

1. INTRODUCTION

Impact between the water and a ship, i.e. slamming, can cause important local and global loads on a vessel. Different physical effects may have an influence. When the local angle between the water surface and the body surface is very small at the impact position, an air cushion may be formed between the body surface and the water surface. Compressibility of the air influences the air flow. The air flow interacts with the water flow, which is influenced by the compressibility of the water. When the air cushion collapses, air bubbles are formed. The large loads that can occur during impact between a nearly horizontal body and a water surface, can cause important dynamic hydroelastic effects. This can lead to subsequent cavitation and ventilation. These physical effects have different time scales. The important time scale from a structural point of view is when maximum stresses occur. This scale is the highest wet natural period for the local structure. The effect of compressibility and the formation and collapse of an air cushion are significant initially and normally in a time scale much smaller than the time scale of when maximum stresses occur. This may occur for wetdeck slamming. By wetdeck is meant the structural part connecting the side hulls of a multihull vessel. Compressibility and air cushion formation will then have a smaller effect on maximum local stresses relative to dynamic hydroelastic effects. The largest impact pressures occur initially and will have a minor effect on the maximum stresses. It is an initial force impulse that matters. The reasons are that the largest pressures have a short duration relative to highest natural period for the local structure and have a small spacial extent at a given time instant. Theoretical and experimental studies of wave impact on horizontal elastic plates of steel are presented in refs. [1], [2], [3] and [4]. Ref. [5] studied also aluminium plates. The effect on plates with a small angle is discussed in refs. [3] and [6]. It is demonstrated that dynamic hydroelastic effects are significant. Ref. [7] studied slamming against elastic wedges penetrating an initially calm water surface.

When the local angle between the water surface and the body surface is not small at the impact position, local hydroelastic effects are not important for slamming on ship cross-sections. The slamming pressures can then be used in a static structural response analysis to find local slamming induced stresses. The air flow is unimportant and the water can be assumed incompressible and the flow irrotational. Since water impact is associated with high fluid accelerations, gravity does not matter. The local rise-up of the water has a significant effect. The spray by itself is not important for slamming. The pressure inside the spray is close to atmospheric. But the generation of spray is associated with high pressure gradients on the hull. This is more dominant, the smaller the local angle between the water surface and the body surface is at the impact position. The water entry loads on a ship cross-section with bowflare will introduce global hydroelastic effects (whipping) of the ship. Flow separation from knuckles should then be accounted for. Two numerical methods for water entry of ship cross-sections will be reported. They have been validated by comparisons with model tests. One of the methods is exact within potential theory. The other represents a simplification and is more robust for engineering use. The theoretical and experimental studies show that common engineering methods to predict water entry loads on ship cross sections give too low maximum force and wrong time history of the force.

Generalizations of the two-dimensional methods to three-dimensional flow are needed. An asymptotic theory for water entry of an axisymmetric body with small local deadrise angles is presented. This represents a valuable tool for verification of three-dimensional methods. It is demonstrated that local rise up of the water at the impacting body is also significant for three-dimensional flow.

Paper presented at an AGARD FDP Workshop on "High Speed Body Motion in Water", held in Kiev, Ukraine, 1-3 September 1997, and published in R-827.

The simplified numerical method derived for 2-D flow is generalized to water entry of axisymmetric bodies. The method is verified by comparing with the asymptotic method and validated by comparing with experiments for spheres and cones. It is demonstrated that satisfaction of exact body boundary conditions is more important than satisfaction of exact free surface conditions. It is possible to further develop the method and study water entry of a general 3-D structure.

2. SLAMMING LOADS ON SHIP CROSS-SECTIONS

Slamming on ship hulls is often categorized as bottom slamming and bow flare slamming. The physics of bottom slamming has similarities with wetdeck slamming. When a bow flare section of a ship enters the water, the local loads around the flare are not significantly influenced by hydroelasticity. The pressure distribution can for instance be estimated by the nonlinear boundary element method developed by Zhao and Faltinsen [8]. This method accounts for the local rise-up of the water and the spray generation during entry. The fine details of the spray are neglected, but this is believed to be unimportant for slamming pressures and integrated water entry loads. A reason is that the pressure is close to atmospheric pressure in the spray. Gravity is neglected since fluid accelerations are initially dominating relative to gravitational acceleration. Gravity may play a role at a later stage of the water entry. However, it is a priori believed that introduction of gravity in the numerical model will not cause any problems. The numerical method solves the two-dimensional Laplace equation for the velocity potential as an initial value problem. The exact free surface conditions without gravity and the exact body boundary condition are satisfied at each time instant. An important feature is how the intersection between the water surface and the body surface is handled. Since the fine details of the spray are not studied and the pressure can be approximated as atmospheric in the spray, the spray is excluded in the boundary element formulation. A control surface normal to the body surface is drawn through the spray root. This surface can be handled in a similar way as a free surface. The advantage of doing this is that the intersection between the water and the body at the free surface can be handled in a more robust way. Following the details of the jet flow associated with the spray could cause a small intersection angle between the free surface and the body surface. Small numerical errors would cause large errors in the prediction of the intersection points. This can then destroy the numerical solution. This is a more severe problem the more blunt the body is. Since the free surface will have a high curvature close to the body surface during water entry of a blunt body, the free surface shape was described in ref. [8] by a higher order description. If straight line elements are used, artificial mass may be generated and destroy the accuracy.

Very good agreement with similarity solutions for wedges with deadrise angles between 4^o and 81^o and with asymptotic solutions for small deadrise angles were documented in ref. [8]. The water entry velocity is constant. There is a peak in the pressure distribution at the spray root close to the free surface when the deadrise angle is less than approximately 30^o. This pressure peak is what is often referred to as the slamming pressure. When the deadrise angle is less than 20^o the pressure distribution becomes more and more peaked and concentrated close to the spray root and sensitive to the deadrise angle. A consequence of this is that rolling could have an important effect on the slamming loads. Faltinsen [9] validated the method by comparing with drop tests of a bowflare section with a constant heel angle of 22.5^o.

The original method does not include flow separation from knuckles or convex surfaces. Zhao, Faltinsen and Aarsnes [10] have extended the original method to include separation from knuckles. A Kutta condition implying tangential velocity and continuity in the pressure at a separation point is satisfied. The pressure becomes more uniformly distributed in space after flow separation. The magnitude of the pressure is still significant. Predicting flow separation from convex surfaces have not been studied. This is a harder problem because the separation point is a priori unknown. An iteration procedure is needed. The flow separation cannot be determined by a viscous flow analysis. The duration of the water entry is too short to develop velocity profiles with zero shear stress at a point on the surface. The latter is the normal criterion for flow separation due to viscous effects. The situation is believed to be more similar to cavity flow past a blunt body like a circle in cross-flow.

Even if hydroelasticity does not affect the local loads during water entry of a ship cross section, it may play an important role in a global analysis. By considering the ship hull as an elastic beam, the integrated water-entry force on for instance a bow flare section causes transient hydroelastic response (whipping) of the ship. The commonly used methods to predict whipping due to water entry of ship cross-sections do not account for the local rise-up of the water. Ref. [10] demonstrated that local rise-up of the water is important for water entry forces on bow flare sections. Its importance will increase with increasing relative vertical velocities between a ship cross-section and the water. The smaller this relative velocity is, the more important is Froude-Kriloff and hydrostatic forces. By Froude-Kriloff forces is meant the pressure loads due to the incident waves only. Ref. [10] also showed that the hydrodynamic water entry force is not negligible when the flow has separated from the knuckles. The peak in the vertical force occurs when the spray root is at the knuckle.

If the hydrodynamic vertical water entry forces are expressed in terms of the time derivative of infinite frequency added mass as a function of submergence relative to undisturbed free surface, the force part after flow separation from the knuckles will be negligible. This is common to do. An approach like this will also give too low maximum force and a wrong time history of the force. The reason is that an important part of the force is associated with the rate of change with time of the wetted area. The local rise up of the water implies a larger rate of change of the wetted area.

At a late stage of the water entry, it is of interest to compare the numerical results of vertical force with theoretical drag coefficients for steady symmetric cavity flow past a blunt body. These values are a function of the cavitation number.

Knapp et al. [11] defines the cavitation number as $K=(p_0-p_B)/0.5\rho V^2$ for water entry. Here V is the velocity of the body, p_0 is pressure in undisturbed fluid at the depth of the nose of the entering body , p_B is the cavity pressure. The cavity pressure is the same as atmospheric pressure in our case. Further ρ is the mass density of water. According to ref. [11], C_D is 0.745 for two-dimensional symmetric steady supercavitating flow (K=0) past a wedge with interior angle 120° at the nose. C_D is defined as $C_D=F/(0.5\rho V^2 B)$. Here F is the total force and B is the maximum breadth of the section. This body shape was studied in ref. [10]. Since gravity is neglected in the numerical computations, the water entry force on the wedge should approach the results for supercavitating flow when the submergence goes to infinity and the drop velocity is constant. The results show that the unsteady force part reduces slowly after a rapid decrease just after flow separation from the knuckles. The results were plotted as a function of the inverse of the submergence of the wedge. This makes it easier to estimate asymptotic values when Vt goes to infinity. Here t is the time variable. The results indicated that the computed C_D-value for a wedge with deadrise angle 30^o approaches an asymptotic value close to 0.745 when the submergence goes to infinity. The numerical simulations should ideally have been continued for larger submergences, but numerical difficulties were encountered. The computations indicated that the cavity becomes infinitely long when the submergence goes to infinity. It is expected that the cavity will be finite if gravity is included. The deceleration of the section will also affect the solution.

The presented method does not solve secondary impact problem. An example on this is water entry of a cross-section with a sonar dome. The jet flow separating from the sonar dome can cause secondary impact on the hull. The same may occur due to flow separation from the bottom of a heeled structure entering the water.

A simplified solution for water entry of a two-dimensional body was presented by Zhao, Faltinsen and Aarsnes [10]. The solution is more numerically robust and faster than the original method in ref. [8]. The quality of the predictions is believed to be satisfactory for engineering applications. The method is a generalization of Wagner's method. Wagner [12] developed an asymptotic solution for water entry of two-dimensional bodies with small local deadrise angles. The flow was studied in two fluid domains. The inner flow domain contains a jet flow at the intersection between the body and the free surface. In the outer flow domain the body boundary condition and the dynamic free surface condition $\phi=0$ where transformed to a horizontal line. The kinematic free-surface condition was used to determine the intersection between the free surface and the body in the outer flow domain. Satisfaction of the kinematic free surface condition implies that the displaced fluid mass by the body is properly accounted for as rise up of the water. This is not true for a von Karman approach that does not account for the local rise up of the water.

In the generalization of Wagner's solution to larger local deadrise angles only the outer flow domain solution is analyzed. A main difference from the Wagner theory is that the exact body boundary condition is satisfied at each time instant. The wetted body surface is found by integrating in time the vertical velocities of fluid particles on the free surface and finding when the particles intersect the body surface. Wagner did also that, but he could use analytical solutions due to the simplified boundary conditions. The dynamic free-surface condition is the same as Wagner used. This is a simplification relative to the more complete method presented in ref. [8]. The pressure is calculated by the complete Bernoulli's equation without gravity. It has not been possible to find an inner flow solution near the spray roots that matches the outer flow solution for finite deadrise angles. This would have made it possible to exclude in a rational way the large negative pressures that occur at the intersection points in the outer flow solution. The procedure is simply to neglect the negative pressures. The theory was verified by comparing with the fully nonlinear solution and validated by comparisons with model tests. The simplified theory shows the importance to satisfy the exact body boundary condition and include the local water elevation at the hull. The exact dynamic free-surface condition is less important.

The simplified nonlinear analysis in ref. [10] was extended by Zhao, Faltinsen and Haslum [13] to include flow separation from fixed separation points. This is done by an iterative process. A shape of the separated free-surface is assumed and the kinematic free-surface condition is satisfied on the assumed free surface. The functional form of the separated free-surface is found by an analytical solution close to the separation point. The shape of the separated free surface is iterated until the difference between the pressure on the separated free-surface and atmospheric pressure is minimized. A Kutta condition is satisfied at the separation points. The solution was verified by comparing with the fully nonlinear solution in ref. [10] for water entry of wedges with knuckles. The method was also validated by comparing with experiments from drop tests of a wedge and a bow flare section with knuckles.

3. ASYMPTOTIC THEORY FOR WATER ENTRY OF AN AXISYMMETRIC BODY

In order to generalize the two-dimensional numerical methods to three-dimensional methods for water entry of ships or other structures, analytic solutions are important as verification tools. This is a motivation for studying an asymptotic theory for water entry of an axisymmetric body with small local deadrise angles.

The theory of Wagner [12] for water entry of a two-dimensional body will be generalized to an axisymmetric body. It will be shown that an axisymmetric outer flow solution matches Wagner's inner two-dimensional jet flow solution and that a composite solution for the pressure distribution on the body can be constructed. The matching is similar as Cointe [14] did in two dimensions. Chuang [15] and Shiffman and Spencer [16] studied also the outer flow solution during water entry of an axisymmetric body. Chuang's solution is approximate and leads to different results than ours.

The body shape and definition of coordinate system are shown in Fig. 1. The water entry velocity V is assumed

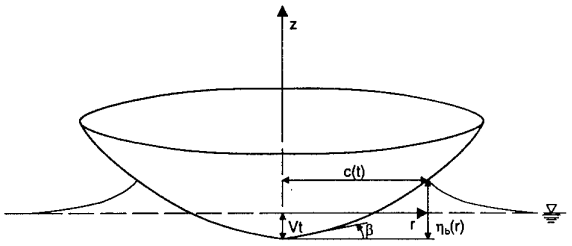


Fig. 1 Water entry of axisymmetric body. Definition of coordinate system.

constant. The instantaneous draft relative to calm water is Vt where t is the time variable. The vertical distance from the lowest point of the structure to the intersection between the free surface and the body shape is $\eta_b(r)$ in the outer flow description. The corresponding radial coordinate r is c(t). β is a local deadrise angle and assumed to be small in the fluid domain. The fluid is assumed incompressible and the flow irrotational. Boundary conditions in the outer flow are shown in Fig. 2. Since β is assumed small, the body boundary conditions are transferred to the lower part of a circular disc with radius c(t). The dynamic free surface condition $\phi=0$ is satisfied on a horizontal plane as shown in Fig. 2. The kinematic free surface condition is used to find c(t).

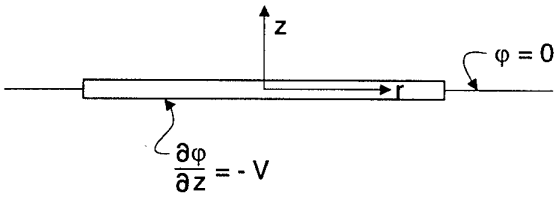


Fig. 2 Boundary conditions in the outer flow domain used in the analysis of water entry of a blunt axisymmetric body.

We need the velocity potential ϕ on $z=0^-$, r<c. We use the solution in Milne-Thomson [17] on p.499-501. The velocity potential is given by

$$\phi = -\frac{2V}{\pi}\sqrt{c^2-r^2} \qquad (1)$$

The solution agrees with Chuang's [15] solution. When we want to find the vertical velocity w at z=0 for r>c, it is convenient to start out with the stream function ψ. It follows that

$$w = \frac{2V}{\pi}\left\{\left((\frac{r}{c})^2-1\right)^{-1/2}-\sin^{-1}\left(\frac{c}{r}\right)\right\} \qquad (2)$$

When r/c → ∞, w ~ $2Vc^3/(3\pi r^3)$. The behavior is as expected like the flow due to a vertical dipole with singularity at r=0 and z=0. We should note that the dominant term when r → c agrees with ref. [15], but not the complete expression given by Eq. (2). When r → ∞, his solution for w behaves like r^{-2} and does not have the proper behavior.

We now want to find the intersection line between the body surface and the free surface like Wagner [12] did in the outer flow problem in two dimensions (see also Faltinsen [18]). The free surface elevation at the body and relative to the bottom of the structure can be found by integrating w in time and adding Vt. This has to be equal to $\eta_b(r)$ which is the vertical coordinate of a point on the structure relative to the bottom (see Fig. 1). We can write

$$\eta_b(r) = \int_0^r\left[\frac{2}{\pi}\left\{\left((\frac{r}{c})^2-1\right)^{-1/2}-\sin^{-1}\left(\frac{c}{r}\right)\right\}+1\right]\mu(c)dc \qquad (3)$$

where

$$\mu(c) = Vdt/dc \qquad (4)$$

Eq. (3) is an integral equation for $\mu(c)$. When $\mu(c)$ is found, we use Eq. (4) to find c(t). We write $u(c) = \Sigma A_n c^n$. We will in practice be interested in n=0 and 1. It follows that Eq. (3) can be written

$$\eta_b(r) = A_0\frac{4}{\pi}r + A_1\frac{3}{4}r^2 \qquad (5)$$

Case I Cone

We can write $\eta_b(r)=r\tan\beta$ where β is the deadrise angle. It follows from Eq. (5) that $A_1=0$ and $A_0=\pi/4\tan\beta$. The solution of Eq. (4) is

$$c(t)=\frac{4\ Vt}{\pi\tan\beta} = 1.27\frac{Vt}{\tan\beta} \qquad (6)$$

This does not agree with Chuang [15], who gets $c=1.36\,Vt/\tan\beta$. But the result agrees with Shiffman and Spencer [16]. The 2-D result for a wedge is $(\pi/2)Vt/\tan\beta$. This means that the rise of water is higher for a wedge than a cone with the same β at the same time. In calm water we have $Vt/\tan\beta$.

Case II Sphere (small submergences)

We can write $\eta_B=0.5\,r^2/R$ where R is radius of the sphere. It follows from Eq. (5) that $A_0=0$ and $A_1=2/(3R)$. Integration of Eq. (4) gives

$$c(t) = \sqrt{3RVt} \qquad (7)$$

for a sphere at small submergences. In calm water we have $\sqrt{2RVt}$. Wagner's method for a circular cylinder gives $2\sqrt{RVt}$. So our result is between a von Karman approach, i.e. no local rise of the water, and a Wagner approach for a circular cylinder. We note that dc/dt → ∞ when t → 0. This is similar as for a circular cylinder and indicates that compressibility of the water is important initially.

The ratio C_w between the vertical coordinate η_b corresponding to Eq. 7 and the submergence of the sphere with no local rise up of the water is time independent and equal to 1.5. This agrees with Ref. [16]. If the flow separates above η_b, C_w has a physical meaning as a wetting factor. This may not be so for a cone. A thin jet flow above the intersection line corresponding to Eq. (6) may stay attached to the cone. This case will be analyzed after the following matching.

Matching

We will match the inner 2-D jet flow solution by Wagner with our outer 3-D solution for axisymmetric flow. It follows from Eq. (1) that an inner expansion of the outer solution near r=c is

$$\phi \approx -\frac{2V}{\pi}\sqrt{2c}\sqrt{c-r} \qquad (8)$$

for r < c. The outer expansion of the inner expansion follows from earlier 2-D analysis in refs. [8] and [14] and is

$$-4\frac{dc}{dt}\sqrt{\frac{\delta}{\pi}}\sqrt{c-r} \qquad (9)$$

where δ is the jet thickness (see Fig. 3). Since Eq. (8) and (9) should be equal, it follows that

$$\delta = \frac{V^2}{2\pi}c\left(\frac{dc}{dt}\right)^{-2} \qquad (10)$$

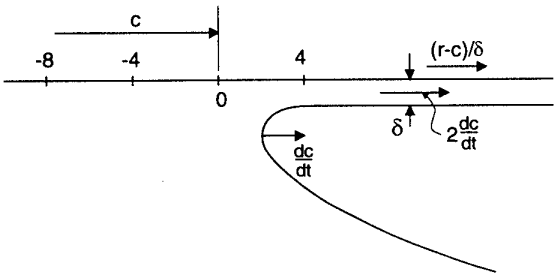


Fig. 3 2-D inner flow domain at the spray root during water entry of blunt axisymmetric body.

For a cone we get (see Eq. 6)

$$\delta_{cone} = \frac{1}{8}\tan\beta(Vt) \qquad (11)$$

The 2-D result for a wedge is twice the expression for a cone. For a sphere at small entrances we get

$$\delta_{sphere} = \frac{2}{\pi\sqrt{3}}\frac{(Vt)^{3/2}}{\sqrt{R}} \qquad (12)$$

Wagner's inner flow solution assumes that the jet flow has semi-infinite extent with thickness δ. In reality this is not so. Cointe [14] analyzed the details of the jet part of the flow for a 2-D wedge and matched with the inner flow by Wagner. Cointe assumed the jet stayed attached to the wedge. We will do similar for a cone. The detailed jet flow has a triangular form in the r-z plane with a length ℓVt and an intersection angle α between the cone surface and the free surface (see Fig. 4) The volume $Vol(t)$ of the detailed part of the jet flow around the cone is

$$Vol(t)=2\pi\alpha\{\frac{1}{2}(c+\ell Vt\cos\beta)(\ell Vt)^2 - \frac{1}{3}\cos\beta(\ell Vt)^3\}$$

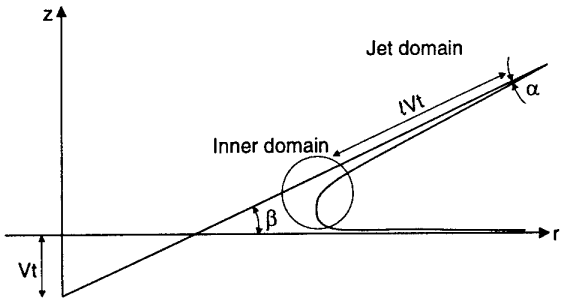


Fig. 4 Attached jet flow during water entry of blunt axisymmetric body.

It follows by using fluid mass continuity that $\rho dVol(t)/dt$ is equal to $\rho(dc/dt)\delta\, 2\pi c$, which is the fluid mass flux into the detailed part of the jet flow. This gives $\ell V=dc/dt$ and

$$\alpha=\frac{\delta}{\ell Vt}=\tan^2\beta \cdot \pi/32$$

The α-value for a wedge with the same β is 16 times as large. The wetting facta C_w for a cone with attached jet flow is then $4(1+1/\cos\beta)/\pi$ which for small angles β is approximately 2.5. A similar 2-D analysis for a wedge gives $C_w=\pi-1$.

Composite solution for the pressure

We will construct a solution for the pressure on the body that is valid both for the inner and outer flow. If only the outer flow description was used, it would lead to infinite pressures at r=c. The composite solution gives finite values for the pressure when t>0. We will construct the composite solution in the same way as Zhao and Faltinsen [8] did for the 2-D water entry problem. It follows from Eq. (1) and Bernoulli's equation that the leading order pressure in the outer domain on the body is

$$p_{out}-p_a=\frac{\rho 2V}{\pi}c\frac{dc}{dt}(c^2-r^2)^{-1/2}$$

p_a means atmospheric pressure and ρ is the mass density of water. The pressure in the inner domain follows from Eq. (4.2) in ref. [8] and is given by

$$p_{in}-p_a=2\rho[dc/dt]^2|\pi|^{1/2}(1+|\tau|^{1/2})^{-2} \qquad (13)$$

where $|\tau|$ is related to r by

$$r-c=(\delta/\pi)(-\ln|\tau|-4|\tau|^{1/2}-|\tau|+5) \qquad (14)$$

(see Eq. (4.3) in ref. [8]). δ is given by Eq. (10). The composite solution for the pressure on the body for $0\le r\le c(t)$ is then (compare with Eq. (4.5) in ref. [8]).

$$p-p_a = \rho\frac{2V}{\pi}c\frac{dc}{dt}\left((c^2-r^2)^{-1/2}-(2c(c-r))^{-1/2}\right) + 2\rho[dc/dt]^2|\tau|^{1/2}(1+|\tau|^{1/2})^{-2} \qquad (15)$$

When $r>c(t)$, Eq. (14) is used. $c(t)$ is given by Eq. (6) for a cone and by Eq. (7) for a sphere. $|\tau|$ is related to r by Eq. (15) and δ is given by Eq. (11) for a cone and by Eq. (12) for a sphere.

The theory is an asymptotic theory valid for small local deadrise angles. The maximum pressure is $0.5\rho(dc/dt)^2+p_a$ and occurs at $r=c(t)$. The maximum pressure on a cone is then

$$(p_{\max})_{cone}-p_a=\rho\frac{8V^2}{\pi^2\tan^2\beta} \qquad (16)$$

Chuang predicts higher maximum value. The dominant pressure term in his expression for small β is $\rho 9.2V^2/\pi^2\beta^2$. This is consistent with that Chuang predicts higher values for dc/dt than us. The ratio between the maximum pressure on a cone and a wedge with the same value of β is with our analysis

$$\frac{(p_{\max})_{cone}-p_a}{(p_{\max})_{wedge}-p_a} = \frac{64}{\pi^2} = 0.66 \qquad (17)$$

Wagner's solution has been used for the wedge. Chuang [15] finds that this ratio is 0.75. This is based on Pierson's [19] analysis for a wedge. Takemoto [20] has compared Chuang's theory with Chuang and Milne's [21] experiments for a cone. He corrected for that the pressure gauge has a finite diameter and that the large pressures around maximum pressure have a small spacial extent. The latter becomes more and more pronounced the smaller β is. He presented comparisons for $\beta = 1^o, 3^o, 6^o, 10^o$ and 15^o. In all these cases the finite size of the pressure gauge represented an important correction. Further Takemoto corrected for the velocity of the cone is smaller when the pressure gauge comes into the water and maximum pressure occurs. Takemoto [20] documented good agreement with Chuang's theory except possibly for $\beta = 1^o$. Air cushion effects may then matter. Making similar corrections with our theory give also good agreement with the experiments. Actually the agreement is better except for $\beta = 6^o$ where it is difficult to say which theory agrees best. At the nose of the cone ($r=0$) our analysis gives $(p_{nose})_{cone}-p_a = \rho 8V^2/(\pi^2\tan\beta)$. As long as $\beta<45^o$, this is lower than $(p_{\max})_{cone}$. This result is consistent since $\beta=45^o$ can hardly be called a small angle. The ratio between the pressure at the nose of a cone and a wedge is $[(p_{nose})_{cone}-p_a]/[p_{nose})_{wedge}-p_a] = 16/\pi^3 = 0.51$.

The maximum pressure on a sphere is time dependent while it is not for a cone with a constant water entry velocity. Actually when $t=0$ the pressure on a sphere is infinite based on the preceding analysis. Other physical effect like airflow and compressibility of the water will make the pressure finite at the initial time. Hydroelasticity will also matter. If we want to find the resulting local maximum structural stresses, this may be the most important part (Faltinsen [3]).

Vertical force

The vertical force F_3 can be obtained by properly integrating the composite solution for the pressure. An alternative approximate way is to use the outer solution. It follows that

$$F_3=\rho\frac{2V}{\pi}c\frac{dc}{dt}\int_0^c\frac{2\pi r\,dr}{\sqrt{c^2-r^2}} = \rho 4Vc^2\frac{dc}{dt} \qquad (18)$$

This is based on constant entry velocity V. If V changes, the added mass force $A_{33}dV/dt$ has to be added. By using Eq. (1) and the definition of added mass it follows that

$$A_{33}=\frac{2}{\pi}\rho\int_0^c\sqrt{c^2-r^2}\,2\pi r\,dr = \frac{4}{3}\rho c^3 \qquad (19)$$

The total water entry force can then be written

$$F_3 = \frac{d}{dt}(A_{33}V) \qquad (20)$$

Eq. [18] can be shown to be asymptotically correct to lowest order by using conservation of momentum as the fluid. The momentum flux into the jet flow is then higher order. It is also possible to show Eq. [18] by energy arguments. The hydrodynamic work done on the body is F_3V. This is equal to the sum of the flux of kinetic energy out into the jet and the rate of change with time of the kinetic energy in the fluid. The kinetic energy flux out into the jet is

$$\rho\frac{1}{2}(2\frac{dc}{dt})^2\delta 2\pi c\frac{dc}{dt}$$

By using Eq. (10) this can be written $\rho 2V^2c^2dc/dt$. The time derivative of the kinetic energy in the fluid is

$$\frac{d}{dt}(\frac{1}{2}A_{33}V^2) = 2\rho c^2\frac{dc}{dt}V^2$$

This follows by Eq. (19) and using that the kinetic energy can be related to the added mass. This proves Eq. (18) by energy arguments. Ref. [22] used similar arguments for 2-D flow.

By assuming V is constant and using Eq. (6) it follows that the force on a cone is

$$F_3 = 4(4/\pi)^3(Vt)^2\rho V^2/\tan^3\beta \qquad (21)$$

By using Eq. (7) it follows that the slamming force coefficient for a sphere at small submergences is

$$C_s = \frac{F_3}{0.5\rho\pi R^2 V^2} = \frac{12\sqrt{3}}{\pi}\left(\frac{Vt}{R}\right)^{1/2} \qquad (22)$$

A similar result has been derived in refs. [23] and [24]. Eq. (22) shows that the initial C_s-value is zero and increases with time. This is opposite of the behavior of the impact of horizontal circular cylinder which starts initially with a finite C_s-value with a Wagner type of analysis.

Miloh [25] has studied theoretically the impact of a sphere. His analysis did not incorporate the local rise up of the water. However, he satisfied the exact body boundary conditions for any submergence. Miloh [25] predicts a maximum value of C_s=0.96 at $Vt/R \approx 0.2$, which means a local deadrise angle β of 37^o at the intersection between the undisturbed free surface and the body. An asymptotic theory would be questionable at so large β-values. Miloh's analysis for small values of Vt/R could be compared with an asymptotic analysis with a von Karman approach. This give a slamming coefficient of $(8\sqrt{2}/\pi)\ (Vt/R)^{1/2}$. Miloh [26] studied in details the asymptotic behavior for small values of Vt/R based on the solution in ref. [25]. Terms of $0((Vt/R)^{3/2})$ were included. He discussed the influence of wetting corrections. If he used C_w= 1.5 like in the asymptotic method presented in this chapter, he got

$$C_s = (12\sqrt{3}/\pi)\tau^{1/2} - 5.36\tau - 5.76\tau^{3/2} \qquad (23)$$

where $\tau = Vt/R$. The leading order term agrees with Eq. (22). He found by using his computational value C_w=1.327 that

$$C_s = 5.5\tau^{1/2} - 4.19\tau - 4.26\tau^{3/2} \qquad (24)$$

This agrees satisfactory with the experimental data in ref. [27] for $\sim 0.08 < \tau^{1/2} < \sim 0.53$. The maximum value of C_s based on Eq. (24) is 1.26 and occurs when Vt/R=0.164.

4. THREE-DIMENSIONAL NUMERICAL METHOD

The simplified 2-D water entry theory described in ref. [10] will be generalized to 3-D flow with an axisymmetric body. A coordinate system rz_1 which follows the vertical motion of the body is used (see Fig. 5). The problem is solved as an initial value problem. Green's second identity is used to represent the velocity potential ϕ as a distribution of Rankine sources and dipoles over the body surface and a horizontal plane outside the body that starts at the intersection line between the body and the free surface (see Fig. 5). The dynamic free surface condition ϕ=0 is satisfied. ϕ is represented in the far-field as a vertical dipole. The dynamic free surface condition implies that fluid particles on the free surface have only vertical velocities. Fig. 5 illustrates the free surface l_i and l_{i+1} at two time instances t_i and t_{i+1}. The free-surface condition is satisfied on the horizontal planes L_i and L_{i+1} at t_i and t_{i+1}. An integral equation is used at each time step t_i to find the velocity potential on the body surface and the vertical

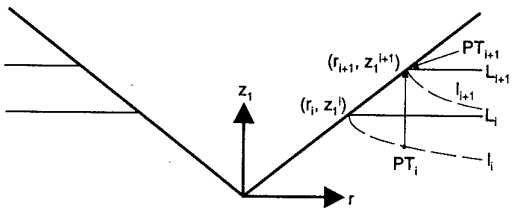


Fig. 5 The coordinate system (r, z_1), the real free surface ℓ and the horizontal lines L used in the numerical simulation for time steps t_i and t_{i+1} in the simplified solution of water entry of an axisymmetric body.

velocities at L_i. It is assumed that the vertical velocity on L_i for a given r-value is the same as the vertical velocity on l_i. The solution can be stepped from $t = t_i$ to $t = t_{i+1}$ in the following way. The procedure is first to decide the intersection line (r_{i+1}, z_1^{i+1}) at time t_{i+1} and then find what $\Delta t = t_{i+1} - t_i$ must be. One can write

$$\Delta P = \int_{t_i}^{t_{i+1}} W(c(t), r_{i+1})\,dt \qquad (25)$$

where $\Delta P = PT_{i+1} - PT_i$ (see Fig. 5) and W is the relative vertical velocity of a point between PT_i and PT_{i+1} with r-coordinate r_{i+1}. W depends on c(t) which is the r-coordinate of the intersection line between the free surface and the body surface at time t. Eq. (25) can be written

$$\Delta P = \int_{r_i}^{r_{i+1}} W(c(t), r_{i+1})\frac{dt}{dc}\,dc \qquad (26)$$

This is evaluated numerically by using an average value $(dt/dc)_m$ for dt/dc. W is expressed in terms of a local solution. Here a local polar coordinate system (R_2, θ_2) is used (see Fig. 6). W can be written as

$$W = -(D/(2-\gamma/\pi))R_2^{(2-\gamma/\pi)^{-1}-1} \qquad (27)$$

where R_2 is $(r_{i+1} - c(t))$. γ is defined in Fig. 6 and is assumed constant from t_i to t_{i+1}. D is found from the global solution. An average value D_m for the two time instances t_i and t_{i+1} is used. Eq. (26) can now be analytically integrated. It follows that

$$\left(\frac{dt}{dc}\right)_m = -\frac{\Delta P}{D_m(r_{i+1} - r_i)^{(2-\gamma/\pi)^{-1}}} \qquad (28)$$

Δt is now determined as $(dt/dc)_m(r_{i+1} - r_i)$.

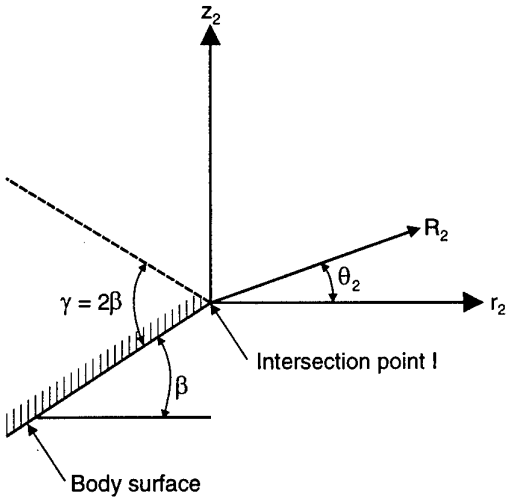


Fig. 6 Local polar coordinate system (R_2, θ_2) and local Cartesian coordinate system (r_2, z_2). I is intersection between the body and the free surface β=local deadrise angle. Free surface condition is satisfied on the r_2-axis.

After the velocity potential on the body surface has been determined, the pressure distribution on the body can be found from Bernoulli's equation. Special care is shown near the intersection between the body and the free surface. Since the velocity is infinite there, the velocity square term in Bernoulli's equation will be negative infinite. It can be shown that the $-\rho\partial\phi/\partial t$-term is positive infinite at the intersection point, and that the velocity square term is more singular than the $-\rho\partial\phi/\partial t$-term. Therefore the total pressure is negative infinite. But this is an integrable singularity. Let us define the integrated vertical force for the part with negative pressure as F_N, and from the part with positive pressure as F_P. It can be shown that F_N/F_P goes to zero when the deadrise angle goes to zero. For small deadrise angles, the maximum pressure (positive) is obtained near the intersection point.

4.1 Verification and validation

It was documented in chapter 3 that maximum pressures predicted by the asymptotic method on cones with deadrise angles β between 3^o and 15^o are in good agreement with experimental values. Fig. 7 shows the pressure distribution on a cone with $\beta=10^o$. The agreement between the numerical method and the asymptotic method given by Eq. (15) is good. Similar comparisons were made for β between 5^o and 30^o. The smaller β is, the better the agreement is. Results for $\beta=30^o$ are shown in Fig. 8. The asymptotic method shows a small nearly non-noticeable kink in the pressure distribution around maximum pressure. This is an indication that β is too large for the asymptotic theory to be

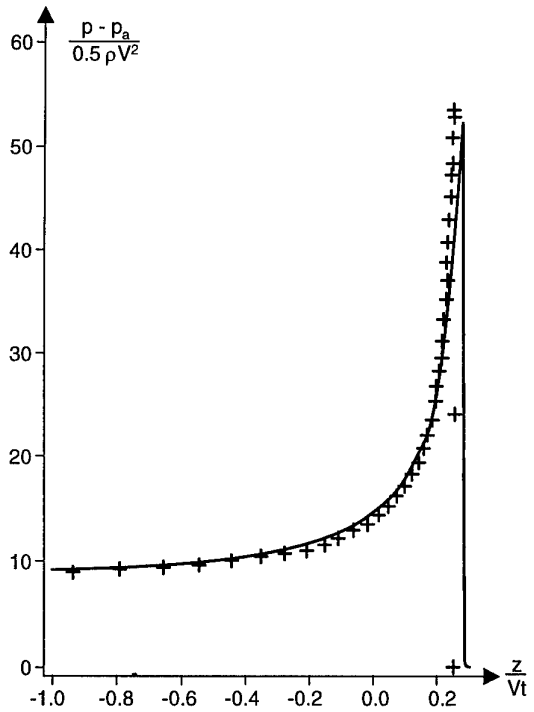


Fig. 7 Prediction of the pressure distribution during water entry of a cone with constant downwards velocity V. Deadrise angle $\beta=10^o$, ++++, numerical method; ——, asymptotic solution.

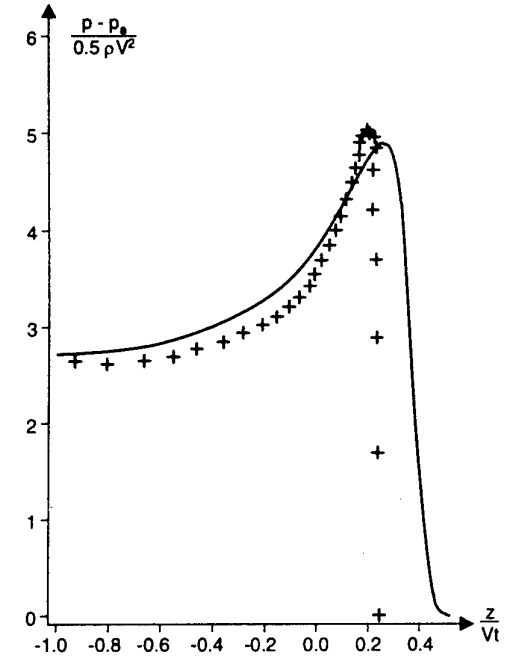


Fig. 8 Predictions of the pressure distribution during water entry of a cone with constant downwards velocity V, Deadrise angle $\beta=30^o$. ++++, numerical method; ——, asymptotic solution.

valid. We note that the magnitudes of the predicted pressures are similar, but the numerical method predicts less rise up of the water than the asymptotic method. This is also evident from Fig. 9 where the wetting factor $C_w=\eta_b/(Vt)$ (see Fig. 1) is presented versus β. The vertical force as a function of

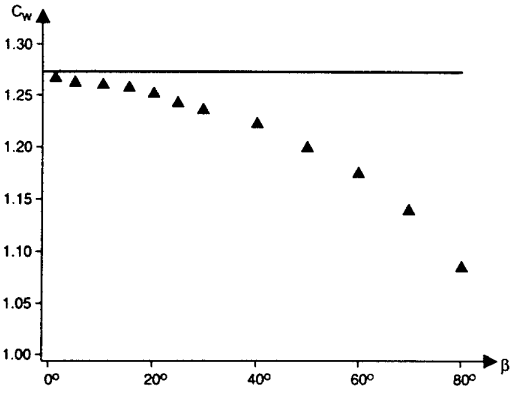


Fig. 9 Wetting factor C_w during water entry of a cone with constant downwards velocity. Presented as a function of deadrise angle β. ▲▲▲▲, numerical method; ——, asymptotic solution.

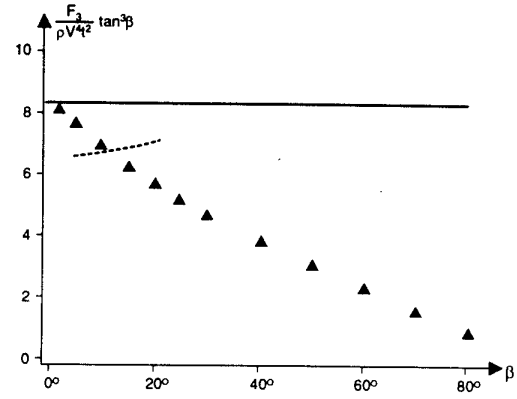


Fig. 10 Non-dimensionalized vertical force F_3 during water entry of a cone with constant downwards velocity V. Presented as a function of deadrise angle β. ▲▲▲▲, numerical method; ——, asymptotic solution; ----- experiments (Watanabe [28]).

β is shown in Fig. 10. The force calculated by the numerical method is obtained by pressure integration, while the asymptotic method is based on Eq. (21). The force has been non-dimensionalized so that the asymptotic method predicts a constant non-dimensionalized value as a function β. The numerical method predicts a decreasing non-dimensionalized force with increasing β-value. This is consistent with the wetting factor in Fig. 9 and that the two different methods predict similar magnitudes of pressures for $\beta \leq 30^o$. The two methods agree when $\beta \to 0$. Experimental values by Watanabe [28] are also presented in Fig. 10. Watanabe performed drop tests for β between 5^o and 20^o. An empirical force formula that depends on the structural mass M of the dropped object was presented. The results in Fig. 10 are obtained by letting $M \to \infty$. The agreement between the numerical method and the experiments is good except that the experimental non-dimensional values show a small increase with increasing β.

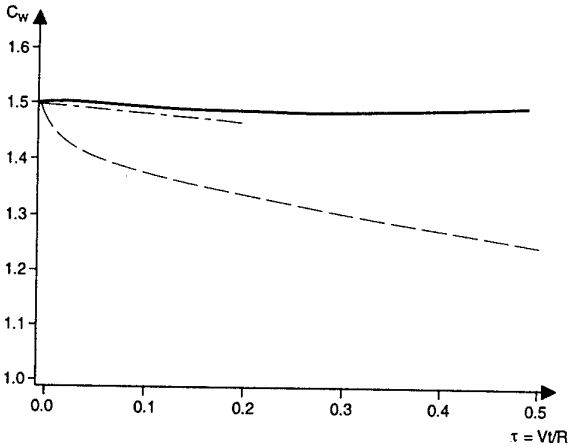


Fig. 11 Wetting factor C_w during water entry of a sphere with constant downwards velocity V versus dimensionless time. ——, numerical method; - - - - - - - -, experiments (Cooper [29]);— — —, experiments (Shiffman and Spencer [23]).

Fig. 11 shows the wetting factor as a function of $\tau=Vt/R$ during water entry of a sphere with constant downwards velocity V. Experimental results by Cooper [29] for $0<\tau<0.2$ and by Shiffman and Spencer [23] for $0.2<\tau<0.8$ are presented together with results by the numerical method. The asymptotic method predicts $C_w=1.5$ which is in good agreement with the numerical method and the experimental results in ref. [29]. The agreement with ref. [23] is less good.

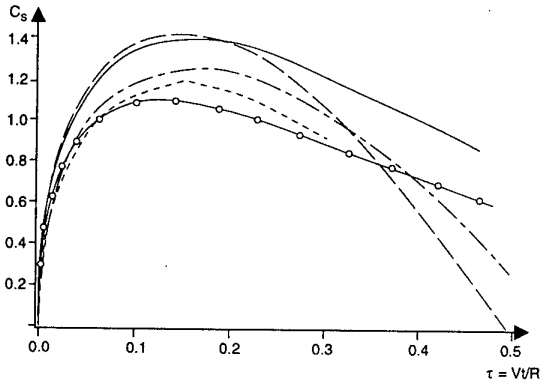


Fig. 12 Slamming coefficient C_s during water entry of sphere with constant downwards velocity V versus dimensionless time.—∘—∘—, numerical method and pressure integration; —— numerical method and VdA_{33}/dt; ———, Eq. (23) (Miloh [26]); ————, Eq. (24) (Miloh [26]); ---------, experiments (Moghisi and Squire [27]).

Fig. 12 shows the slamming force coefficient C_s defined by Eq. (22) as a function of τ. Eqs. [23] and [24] proposed by Miloh (26) are plotted together with results by the numerical method and the experimental results by Moghisi and Squire [27]. The force calculated by the numerical method is obtained by pressure integration. The quantity VdA_{33}/dt where A_{33} is our calculated infinite frequency added mass in heave as a function of submergence, is also plotted in Fig. 12. When $\tau \to 0$ (see the discussion in chapter 3), VdA_{33}/dt is the vertical force based on conservation of momentum in the fluid. The derivation requires that the pressure is atmospheric on the free surface. When τ is finite, the condition of atmospheric pressure on the free surface is not satisfactorily satisfied with the "ϕ=0 condition" on the free surface. The quadratic velocity term in the Bernoulli's equation for the pressure cannot be neglected. This is why VdA_{33}/dt for finite τ does not agree with the force obtained by pressure integration. The experimental results for $\tau<0.16$ are based on the empirical relation found by regression analysis in ref. (27). The results for $0.16<\tau<0.3$ are based on own judgement of the experimental results. We note that both Eq. (24) and the numerical method based on pressure integration agree quite well with the experimental results. When $\tau \to 0$, the numerical method agrees with the asymptotic results given by Eqs. (22) and (23), but not with Eq. (24). When $\tau > \sim 0.25$, the numerical method and Eqs (23) and (24) have a different trend. The reason is that Eqs. (23) and (24) are based on τ being small. Eq. (23) agrees quite well with our calculations of VdA_{33}/dt up to $\tau \sim 0.25$. The reason is that Miloh's derivation of Eq. (23) is consistent with using VdA_{33}/dt as the vertical force together with a wetting factor of 1.5. Our results show that it is better to use pressure integration than calculating the force as VdA_{33}/dt.

These verification and validation tests document that the numerical method is a valuable tool for studying water entry of three-dimensional bodies. However, since the atmospheric pressure condition is not satisfactorily satisfied on the free surface for finite values of the local deadrise angles, it is recommended in the future to generalize the more complete 2-D method presented in ref. [8] to 3-D flow.

5. CONCLUSIONS

Theoretical methods for water entry of two-dimensional and axisymmetric bodies are discussed. When the local angle between the water surface and the body surface is very small, hydroelasticity should be considered. The presented analysis of water entry loads assumes that the local angle between the water surface and the free surface is not very small. The structure can be considered rigid and compressibility effects can be neglected. Two 2-D numerical methods are discussed. Both methods satisfy the exact body boundary condition and account for the local rise up of the water. One of the methods satisfies the exact free surface condition without gravity. The studies show that it is more appropriate to approximate the free surface conditions than the body boundary condition. Flow separation from sharp corners has been incorporated. Gravity has been neglected, but should be incorporated after flow separation occurs. The loads after flow separation have been found to be non-negligible. The simplified method has been generalized to 3-D axisymmetric flow without flow separation. In order to verify the 3-D method, water entry of axisymmetric bodies with small local deadrise angles are studied analytically. An inner domain solution for the jet flow is matched to an outer solution and a composite solution for the pressure is presented. Verification and validation tests for spheres and cones are reported. It is demonstrated that the local rise-up of the water is also important during water entry of a blunt 3-D structure. A common formula for the impact force in terms of the time derivative of added mass is discussed. It is only recommended to use this formula as long as the local deadrise angle is small.

REFERENCES

1. Kvålsvold, J., Faltinsen, O., "Hydroelastic Modelling of Wetdeck Slamming on Multihull Vessels", J. Ship Res., September 1995, Vol. 39, No. 3, pp. 225-239.

2. Kvålsvold J., "Hydroelastic Modelling of Wetdeck Slamming on Multihull Vessels". Dr.ing.thesis, Department of Marine Hydrodynamics, Norwegian Institute of Technology, 1994, MTA-Report 1994:100.

3. Faltinsen, O., "The Effect of Hydroelasticity on Slamming", Phil. Trans. R. Soc. Lond. A, 1997, 355, pp. 575-591.

4 Faltinsen, O., Kvålsvold, J., Aarsnes, J.V., "Wave Impact on a Horizontal Elastic Plate, J. Marine Science and Technology, 1997, Vol. 2, No. 2.

5 Kvålsvold, J., Faltinsen, O., Aarsnes, J.V., "Effect of Structural Elasticity on Slamming Against Wetdecks of Multihull Vessels", Proc. PRADS'95, Korea, The Society of Naval Architects of Korea, 1995, pp. 1.684-1.699. Also to be published in Journal of Ship and Ocean Technology.

6. Haugen, E.M., Faltinsen, O., Aarsnes, J.V., "Application of Theoretical and Experimental Studies of Wave Impact Wetdeck Slamming", Proc. FAST'97, Sydney, Australia, 1997.

7. Meyerhoff, W.K., "Die Berechnung Hydroelastischer Stösse", Schiffstechnik, 1965, 12, 60.

8. Zhao, R., Faltinisen, O., "Water Entry of Two-Dimensional Bodies", J. Fluid Mech., 1993, Vol. 246, pp. 593-612.

9. Faltinsen, O., "On Seakeeping of Conventional and High-Speed Vessels", 15th Georg Weinblum Memorial Lecture, J. Ship Res., Vol. 37, No2, June 1993, pp. 87-101.

10. Zhao, R., Faltinsen, O., Aarsnes, J.V., "Water Entry of Arbitrary Two-Dimensional Sections With and Without Flow Separation", Proc. 21st Symp. on Naval Hydrodynamics, Trondheim, Norway, National Academy Press, Washington DC, 1996.

11. Knapp, R., Daily, J.W., Hammitt, H.F.G., "Cavitation", Mc-Graw-Hill Book Company, 1970.

12. Wagner, H., "Über Stoss- und Gleitvorgänge and der Oberflache von Flüssigkeiten", Zeitschr. f. Angew. Math. und Mech., 1932, Vol. 12, No. 4, pp. 193-235.

13. Zhao, R., Faltinsen, O., Haslum, H., "A Simplified Nonlinear Analysis of a High-Speed Planing Craft in Calm Water", Proc. FAST'97, Sydney, Australia, 1997.

14. Cointe, R., "Free Surface Flows Close to a Surface-Piercing Body", In Mathematical Approaches in Hydrodynamics (ed. T. Miloh), Soc. Ind. Appl. Maths., Philadelphia, USA, 1991, pp. 319-334.

15. Chuang, S.L. "Theoretical Investigations on Slamming of Cone-Shaped Bodies", J. Ship Res., Vol. 13, No.4, December 1969, pp. 276-283.

16. Shiffman, Spencer, D.C., "The Force of Impact on a Cone Striking a Water Surface (Vertical Entry)", Communications Pure and Applied Mathematics, Vol. 4, No. 4, 1951, pp. 379-417.

17. Milne-Thomson, L.M., "Theoretical Hydrodyna-mics", Dover Publications, 1996.

18. Faltinsen, O., "Sea Loads on Ships and Offshore Structures", Cambridge University Press, 1990.

19. Pierson, J.D., "On the Pressure Distribution for a Wedge Penetrating a Fluid Surface", Institute of Aeronautical Sciences, Sherman M. Fairchild Publication Fund Paper Preprint 167, June 1948.

20. Takemoto, H., "Some Considerations on Water Impact Pressure", J. Soc. Naval Arch. Japan 156, 1984, pp. 314-322.

21. Chuang, S.L., Milne, D.T., "Drop Test of Cones to Investigate the Three-Dimensional Effects of Slamming", NSRDC Report 3543, April 1971.

22. Molin, B., Cointe, R., Fontaine, E., "On Energy Arguments Applied to the Slamming Force", 11th Int. Workshop on Water Waves and Floating Bodies, Hamburg, Germany, 1996.

23 Shiffman, M., Spencer, D.C., The Force of Impact on a Sphere Striking a Water Surface", AMP Rep. 42 2B, AMG-NYU, No. 133, 1945.

24. Pukhnachov, V.V., Korobkin, A.A., "Initial Asymptotics in Problem of Blunt Body Entrance into Liquid", Proc. 3rd International Conf. Num. Ship Hydrodynamics, Paris 1981, pp. 579-581.

25. Miloh, T., "Wave Slam on a Sphere Penetrating a Free Surface", J.Eng. Math., Vol. 15, No. 3, July 1981, pp. 221-240.

26. Miloh, T., "On the Initial-Stage Slamming of a Rigid Sphere in a Vertical Entry", Applied Ocean Research, 1991, Vol. 13, No. 1, pp. 43-48.

27. Moghisi, M., Squire, P.T., "An Experimental Investigation of the Initial Force of Impact on a Sphere Striking a Liquid Surface", J. Fluid Mech. 1981, 198, pp. 133-146.

28. Watanabe, S., "Resistance of Impact on Water Surface, Part I-Cone and Part II-Cone (Continued)", Institute of Physical and Chemical Research, Tokyo, (Scientific Papers), Vol. 12, 1929, pp. 251-267, and Vol. 14, 1930, pp. 153-168.

29. Cooper, E.P. "Splash Contours on Water Entry. Normal Entry of Spheres and Cones", NOTS Rep. Inyokern Cal., 1950.

Asymptotics Theories of Incompressible Water Entry

E. Fontaine
Ecole Centrale de Nantes,
1 rue de la Noë,
44072 Nantes Cedex, France.

R. Cointe
Ministère de l'Environnement,
20 av. de Ségur, Paris 07 SP, France.

SUMMARY

The problem of a two-dimensional body impacting a free surface is studied using potential theory. When the angle (or its tangent) between the body and the free surface is very small, i.e. when the free surface and the body are almost parallel, the method of matched asymptotic expansions provides a first order composite solution. This solution includes three subdomains: the far-field, the spray root and the jet domains. This asymptotic solution appears to be a good approximation of the nonlinear solution, even for large values of the small parameter. In this paper, the asymptotic expansion for a wedge with small deadrise angle is extended up to second order for the far-field problem. This allows the jet volume to be taken into account within the composite solution. Then, a direct time domain simulation of the problem is performed using a mixte eulerian-lagrangian method. In order to overcome the numerical difficulties that arise at the body-free surface intersection, a special numerical treatment is introduced, based on the asymptotic solution describing the jet. This treatment allows the influence of the jet to be accounted for without having to actually compute the flow in the jet.

1. INTRODUCTION

The water entry problem has led to numerous study since the early thirties and the pioneering work of Von-Kàrmàn [13] and Wagner [14]. As a model, the two-dimensional water entry of a wedge at constant vertical speed into a free surface initially at rest will be discussed here. The wedge is supposed to be rigid, the fluid perfect and the flow irrotationnal. This problem is one of the simplest example of the violent deformation of the free surface in the vicinity of a moving surface piercing body. It is nevertheless strongly nonlinear because of the free surface boundary conditions which not only include quadratic terms but also are written on an a priori unknown boundary.

For a numerical resolution of the problem, the Mixted Eulerian-Lagrangian method (MEL) appears particulary well suited for the study of free surface potential flows (e.g. Cointe [2]). However, the use of this method is not straightforward here because of the jet that develops at the intersection between the free surface and the impacting body. The existence of this jet, the thickness of which is small compared to the characteristic length of the structure, leads to a large increase of the computationnal time. This stems from the fact that the spatial discretisation needs to be fine enough to capture the jet and that the numerical time-step needs to fit both the spatial discretisation and the time evolution of the jet. The jet can not be ignored, however, if one wishes to estimate quantities such as the force imposed on the body. Molin, Cointe and Fontaine [10] show that at the beginning of the impact, half the energy given to the fluid corresponds to kinetic energy of the jet. A way to overcome these difficulties and to achieve the numerical resolution of the problem is to simulate most of the flow using the MEL method and to introduce a local model in order to take account of the influence of the jet on the flow. This approach will be used here, using asymptotic methods to study the local flow.

2. ASYMPTOTICS SOLUTIONS

2.1 Self-similar flow

Dimensional analysis allows to express the potential as (see fig. 1 and 2 for notations):

$$\phi = V^2 t\, f_1(\frac{x}{Vt}, \frac{y}{Vt}, \frac{g\,t}{V}; \theta)$$

For very small time or for very large impacting speeds, i.e. when $gt/V \ll 1$, gravity effects can be neglected. The only length scale in the problem is then the immersion Vt of the wedge. The flow is therefore self-similar and the number of independant variables can be reduced from three -x, y, t- to two:

$$\phi = V^2 t\, f_2(\frac{x}{Vt}, \frac{y}{Vt}; \theta)$$

Paper presented at an AGARD FDP Workshop on "High Speed Body Motion in Water", held in Kiev, Ukraine, 1-3 September 1997, and published in R-827.

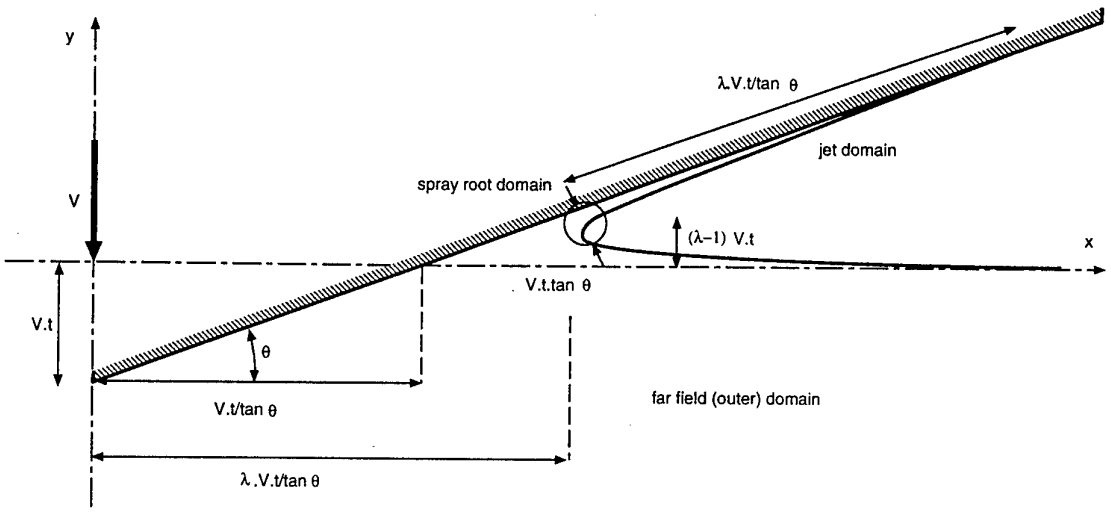


Figure 1: Illustration of the different subdomains of the composite solution.

The self-similar nature of the problem allows a mathematical study of this strongly nonlinear flow. Wagner [14] demonstrated an arc length conservation property along the free surface. This means that the free surface deformation is similar to that of a sheet of paper. Wagner used this property to introduce a mapping allowing to map the unknown and unbounded fluid domain to a domain bounded by straight lines. Dobrovol'skaya [3] reduced the problem to the resolution of an integral equation. It is only very recently, however, that Fraenkel and McLeod [6] produced an existence and uniqueness proof. When the free surface and the body are initially almost parallel ($\tan\theta \ll 1$), Fraenkel and McLeod [6] obtained an asymptotic expansion of the exact solution expresssed in terms of the small parameter $\tan\theta$.

2.2 First order composite solution

In the same configuration, a more heuristic approach based on the matched asymptotic expansions can be used. A first order composite solution (e.g. Cointe [1], Howison, Ockendon et Wilson [7]) can be obtained taking $\tan\theta$ as small parameter. This method leads to defining three different zones in which three asymptotic expansions are performed (see fig.1):

- The far field (or outer) flow is defined on a length scale equal to the wedge wetted width $\lambda Vt/\tan\theta$. This flow is given by the flow without free surface around a flat plate of width the wetted width.
- The spray root (inner flow) is defined on a length scale equal to $\lambda Vt\tan\theta$. The flow is given in this zone by a steady free surface flow with jet. The inner solution depends on two parameters: the thickness of the jet and the position of the stagnation point.
- The jet itself is defined on a length scale equal to the wedge wetted width but on a thickness scale equal to the thickness of the jet in the spray root. The flow in the jet is governed by shallow water equations.

Matching these three solutions allows the determination of the jet thickness and of the wetted width. The resulting composite solution is in very good agreement with the expansion of the exact solution performed by Fraenkel and McLeod [6]. In particular, in the limit where θ goes to zero, the arc length conservation property is satisfied and the value of the intersection angle between the jet and the wedge is correctly estimated:

$$\beta = \frac{\theta^2}{2\pi}$$

2.3 Pressure distribution

Different composite solutions for the pressure distribution are proposed by Wagner [14], Cointe [1] and Zhao & Faltinsen [15]. The inner and outer solutions are the same in these three references, even different notations are used. Nevertheless, the composite solutions for the pressure distribution differ since different matching procedure are used to match outer and inner solutions. Wagner [14] and Zhao & Faltinsen [15] used classical matching procedure as describe in ref. [12] and [8]. In that case, the position of the stagnation point remains undetermined at first order. From a theoretical point of view, this parameter should be determined by matching the inner solution and the second order outer solution. Cointe [1] proposed to fix this parameter by matching inner and outer solutions for the maximum pressure. Even being not completly coherent, this matching enables one to account for second order effects in a very simple and practical way as will be demonstrated below.

The pressure distribution can be characterised (see fig.2) by the maximum pressure coefficient Cp_{max}, the location y_{max} on the wedge of the pressure pic, the width ΔS of the pressure pic at half height, and the vertical force F_y, i.e., the area of the pressure distribution.

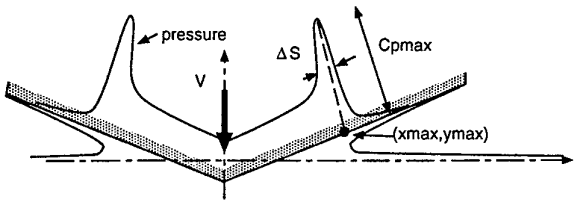


Figure 2: Characteristic parameters describing the pressure distribution.

All these quantities are ploted in figure 3 to 6. Good agreement is observed, even for relatively large values of θ, when comparing with the numerical solution obtained by Zhao & Faltinsen [15] using Dobrovol'skaya's approach [3].

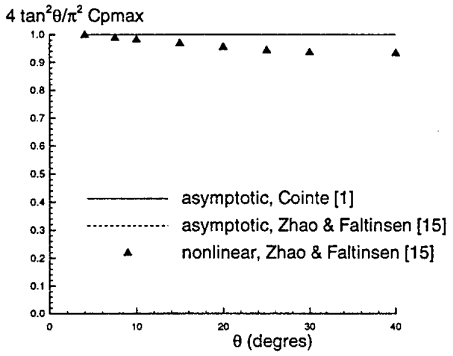


Figure 3: Non-dimensionalized maximum pressure coefficient during water entry of a wedge with constant downward velocity V. Presented as a function of the deadrise angle θ.

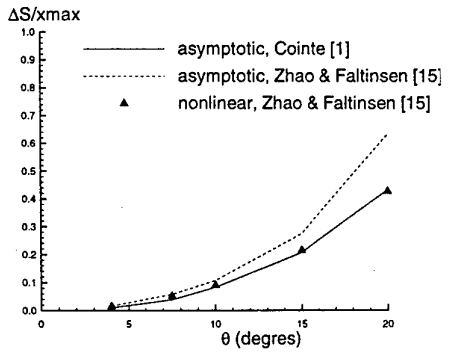


Figure 4: Non-dimensionalized width ΔS of pressure pic at half height during water entry of a wedge with constant downward velocity V. Presented as a function of the deadrise angle θ.

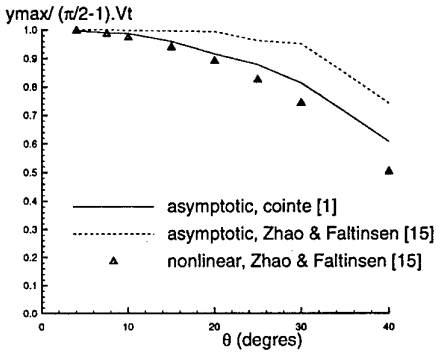


Figure 5: Non-dimensionalized position y_{max} of pressure pic during water entry of a wedge with constant downward velocity V. Presented as a function of the deadrise angle θ.

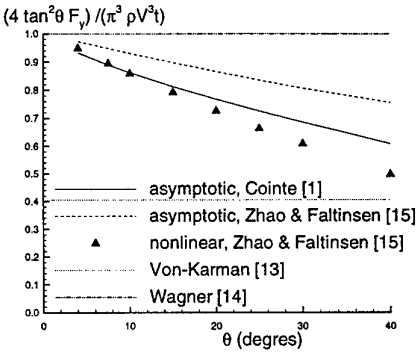


Figure 6: Non-dimensionalized vertical force F_y during water entry of a wedge with constant downward velocity V. Presented as a function of the deadrise angle θ.

The vertical force is obtained by numerical integration of the composite pressure distribution. This enables to account for second order effects since the spray root domain is taken into account. However, an exact second order estimation of the force would need the second order outer solution to be matched with the spray root solution. Figures 7 and 8 show a comparison between numerical results and experiments by Zhao, Faltinsen and Aarsnes [16] for the water entry of a wedge with deadrises angle $\theta = 30°$. Good agreement is obtained for the prediction of vertical force and pressure coefficient. The mesured vertical velocity is used to perform the simulation but Magee & Fontaine [9] present a coupled approach where the force and the motion are computed simultaneously. The differences that appear between the numerical and experimental results at this end of the simulation come from the fact that the flow separates and the jets develop in the air instead of along the wedge.

The asymptotic solution can also be extented to the case of blunt bodies of arbitrary shape and/or for curved but flat free surface (Cointe, [1]). From a practical point of view, the numerical integration

of the composite pressure distribution by Cointe [1] leads to a robust and easy way to estimate impact loads.

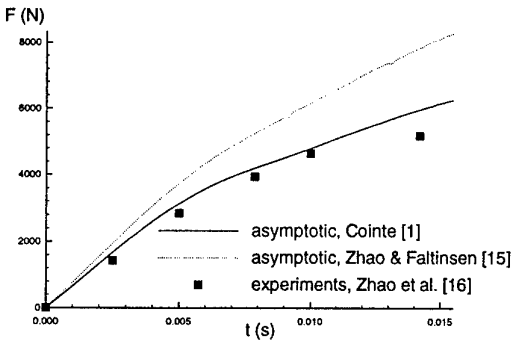


Figure 7: vertical force F_y during water entry of a wedge with deadrise angle $\theta = 30°$.

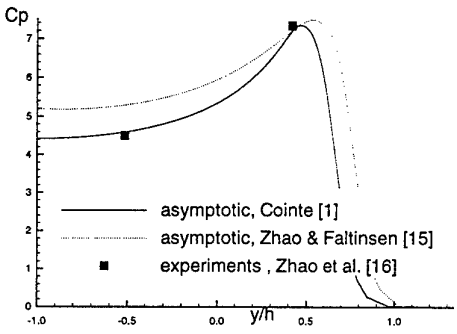


Figure 8: Coefficient pressure, along a wedge with deadrise angle $\theta = 30°$, immersed at h at the beginning of the impact (t=0.00435s).

3. SECOND ORDER OUTER SOLUTION

However, the composite first order solution described below satisfy only volume conservation at order $(Vt)^2/\tan\theta$. The jet volume, of order $(Vt)^2$, is neglected. In order to take it into account, it is necessary to solve the outer problem at second order.

3.1 Outer flow

The first order outer solution is given by the flow without free surface around a flat plate [14]. This solution is singular near the edges of the plate, i.e. at the intersection between the outer expansion of the free surface and the wedge. This singularity leads to the formation of a jet in the vicinity of this intersection point $\left(\lambda Vt/\tan\theta, (1-\lambda)Vt\right)$. In order to express the second-order problem, a change of variable is performed. This allows the singularity to be locate at the point of coordinate $(1,0)$. The new variables are thus given by:

$$\hat{x} = \frac{x\tan\theta}{\lambda Vt}, \quad \hat{y} = \frac{y\tan\theta}{\lambda Vt} - \tan\theta\,(1-\frac{1}{\lambda}),$$

$$\hat{\phi} = \frac{\phi\tan\theta}{\lambda V^2 t}, \quad \hat{\eta} = \frac{\eta\tan\theta}{\lambda Vt} - \tan\theta\,(1-\frac{1}{\lambda}),$$

and $\hat{t} = t/T$, where T is the time scale. The potential $\hat{\phi}$ must satisfy Laplace equation in the fluid domain and the following boundary conditions:

- on the free surface $(\hat{y} = \hat{\eta}(\hat{x}),\ \hat{x} > 1)$

$$\hat{\phi} + \hat{t}\,\hat{\phi}_{\hat{t}} - \hat{x}\,\hat{\phi}_{\hat{x}} - \left[\hat{y} + \tan\theta\,(1-\frac{1}{\lambda})\right]\hat{\phi}_{\hat{y}}$$
$$+\frac{\tan\theta}{2\lambda}\hat{\nabla}\hat{\phi}\cdot\hat{\nabla}\hat{\phi} + \frac{gT}{V}\,\hat{t}\left[\hat{\eta} + \tan\theta\,(1-\frac{1}{\lambda})\right] = 0$$

$$\hat{\eta} + \hat{t}\,\hat{\eta}_{\hat{t}} + \tan\theta(1-\frac{1}{\lambda}) - \hat{x}\,\hat{\eta}_{\hat{x}} \qquad (1)$$
$$+\frac{\tan\theta}{\lambda}\left(\hat{\eta}_{\hat{x}}\,\hat{\phi}_{\hat{x}} - \hat{\phi}_{\hat{y}}\right) = 0,$$

- on the wedge $(\hat{y} = \tan\theta(\hat{x}-1),\ 0 < \hat{x} < 1)$

$$\hat{\phi}_{\hat{x}}\tan\theta - \hat{\phi}_{\hat{y}} = 1$$

- and on the axis of symmetry $(\hat{x} = 0, \hat{y} < \tan\theta)$

$$\hat{\phi}_{\hat{x}} = 0$$

When gT/V is much smaller than 1, gravity can be neglected. One can look for a solution independant of $\hat{t}$. This is just the self-similar solution.

3.2 First order outer solution

The following asymptotic expansions are assumed:

$$\hat{\phi} = \hat{\phi}_0 + o(1), \quad \hat{\eta} = \tan\theta\,\hat{\eta}_1 + o(\tan\theta),$$
$$\lambda = \lambda_0 + o(1)$$

At first order, the harmonic potential $\hat{\phi}_0$ must satisfy the following boundary conditions:

$$\begin{aligned}
\hat{\phi}_{0\hat{y}} &= -1, & \hat{y} &= 0, & 0 < \hat{x} < 1\\
\hat{\phi}_0 &= 0, & \hat{y} &= 0, & \hat{x} > 1\\
\hat{\phi}_{0\hat{x}} &= 0, & \hat{x} &= 0, & \hat{y} < 0
\end{aligned}$$

This is a classical problem, corresponding to the flow without free surface around a flat plate of unit width. The complex potential corresponding to this flow is given by:

$$\hat{\phi}_0 + i\hat{\psi}_0 = -i\sqrt{z^2-1} + iz,$$

where $z = \hat{x} + i\hat{y}$. The free surface elevation is obtained by integrating the free surface kinematic boundary condition (1) that can be written at first order for $\hat{y} = 0$ and $\hat{x} > 1$:

$$\frac{d}{d\hat{x}}\left(\frac{\hat{\eta}_1 - \hat{\eta}_{1\infty}}{\hat{x}}\right) = -\frac{1}{\hat{x}^2}\left(\frac{\hat{\phi}_{0\hat{y}}}{\lambda_0}\right),$$

where $\hat{\eta}_{1\infty} = -(1-1/\lambda_0)$. Since $(\hat{\eta}_1 - \hat{\eta}_{1\infty})$ vanishes at infini, this leads to:

$$\hat{\eta}_1 - \hat{\eta}_{1\infty} = \frac{1}{\lambda_0}(-1 + \hat{x}\,\arcsin\frac{1}{\hat{x}})$$

In order to determine the value of the parameter λ_0, it is necessary to use the volume conservation. Eventhong volume conservation is automatically satisfied since Laplace equation is solved, the self-similar nature of the flow does not allow initial conditions, and in particular initial volume, to be remenbered. At first order, only the outer solution has to be taken into account and volume conservation leads to:

$$\frac{(Vt)^2}{2\tan\theta} = (\lambda-1)^2\frac{(Vt)^2}{2\tan\theta} + \int_{\frac{\lambda Vt}{\tan\theta}}^{\infty}\eta(x,t)\,dx\,,$$

This can also be written using non-dimensionnal variables:

$$(\lambda_0-1)^2 + 2\int_1^{\infty}(\hat\eta_1-\hat\eta_{1\infty})\,d\hat x = 1$$

Solving this equation leads to $\lambda_0 = \pi/2$. This indeed corresponds to the classical first order solution ([14], [1] and [7]). The free surface and the wedge intersects in $\hat x = \lambda_0$. The solution is however singular at this point because the fluid velocity and the slope of the free surface are unbounded in its vicinity.

3.3 Second order outer solution

The following asymptotic expansions are assumed:

$$\begin{aligned}\hat\phi &= \hat\phi_0 + \tan\theta\,\hat\phi_1 + o(\tan\theta),\\ \hat\eta &= \tan\theta\,\hat\eta_1 + \tan^2\theta\,\hat\eta_2 + o(\tan^2\theta),\\ \lambda &= \lambda_0 + \tan\theta\,\lambda_1 + o(\tan\theta)\end{aligned}$$

The linearized second order problem is obtained through a Taylor expansion of the potential and the free surface elevation (these functions being assumed regular enough in the vicinity of the wedge and the free surface). The harmonic potential $\hat\phi_1$ has to satisfy the following boundary conditions:

- on the free surface ($\hat y = 0$, $\hat x > 1$):

$$\frac{d}{d\hat x}\Big(\frac{\hat\phi_1}{\hat x}\Big) = -\frac{1}{\hat x^2}\Big(\hat x\hat\eta_1\hat\phi_{0\hat x\hat y} - \frac{1}{2\lambda_0}\hat o^2_{0\hat y} + \frac{\lambda_0-1}{\lambda_0}\hat\phi_{0\hat y}\Big) \tag{2}$$

$$\frac{d}{d\hat x}\Big(\frac{\hat\eta_2-\hat\eta_{2\infty}}{\hat x}\Big) = -\frac{1}{\hat x^2}\Big[\frac{1}{\lambda_0}(\hat\phi_{1\hat y}+\hat\eta_1\hat\phi_{0\hat x\hat y}) - \frac{\lambda_1}{\lambda_0^2}\hat\phi_{0\hat y}\Big], \tag{3}$$

- on the wedge ($\hat y = 0$, $0 < \hat x < 1$):

$$\hat\phi_{1\hat y} = \hat\phi_{0\hat x} - (\hat x - 1)\hat o_{0\hat y\hat y},$$

- and on the axis of symmetry ($\hat y = 0$, $\hat x > 1$):

$$\hat\phi_{1\hat x} = 0,$$

where $\eta_{2\infty} = -\lambda_1/\lambda_0^2$.
As for λ_0, the value of the parameter λ_1 is obtained by writting volume conservation for the composite solution. At second order, the jet volume has to be taken into account:

$$\begin{aligned}\frac{(Vt)^2}{2\tan\theta} &= (\lambda-1)^2\frac{(Vt)^2}{2\tan\theta}\\ &\quad + \int_{\frac{\lambda Vt}{\tan\theta}}^{\infty}\eta(x,t)\,dx + e\lambda\frac{(Vt)^2}{2}\end{aligned}$$

where $e = \pi/8\lambda_0$ is the jet thickness in the spray root [14]. Solving this equation for λ_1 leads to:

$$\lambda_1 = -\lambda_0^2\int_1^{\infty}(\eta_2-\eta_{2\infty})d\hat x - \frac{\pi}{16}$$

The problem for $\hat\phi_1$ and $\hat\eta_2$ is solved numerically. The free surface dynamic boundary condition (2) is integrated, starting from "infinity". The asymptotic behaviour of the solution is used to set the initial value of the potential. The integration is then performed using a classical 4^{th} order Runge-Kutta algorithm. Once the boundary conditions for the potential and its normal derivatives are known, Laplace equation is solved numerically using a classical boundary integral method (see §4, eq. (7)). The free surface elevation $\hat\eta_2$ is then obtained by integrating the free surface kinematic boundary condition (3) starting from "infinity" and using the asymptotic behaviour of $(\hat\eta_2 - \hat\eta_{2\infty})$. This is however only possible if the value of λ_1 is known. Equations (3) and (4) are thus solved iteratively until the convergence of the solution procedure is reached. The convergence of the resolution procedure has been checked by comparing numerical and theoretical results obtained at first order.

Asymptotics solutions at first order and second order for a deadrise angle $\theta = \pi/20$ are schown in figure 9. The free surface elevation at second order in the outer domain is slightly smaller than that at first order. This stems from the fact that by hypothesis, the volume between the two curves is just equal to the volume of the jet. The second order correction is small, but significant in the vicinity of the wedge. The numerical value obtained for λ_1 is very small ($\lambda_1/\lambda_0 \simeq 10^{-2}$) so that there is almost no second order correction to the wetted width. These two asymptotic solutions can be compared to the second order approximation presented by Fraenkel & McLeod [6]. If all solutions have a similar behaviour, a precise comparison is made difficult by the fact that the solution [6] satisfies the boundary conditions on an approximate geometry (at second order) while the exact geometry (but approximated equations) are taken into account for the asymptotic solutions. A more precise comparison could be obtained on the pressure and the second order impact force, but this would necessitate to perform matching between the outer and inner solution at second order. This work is currently under progress.

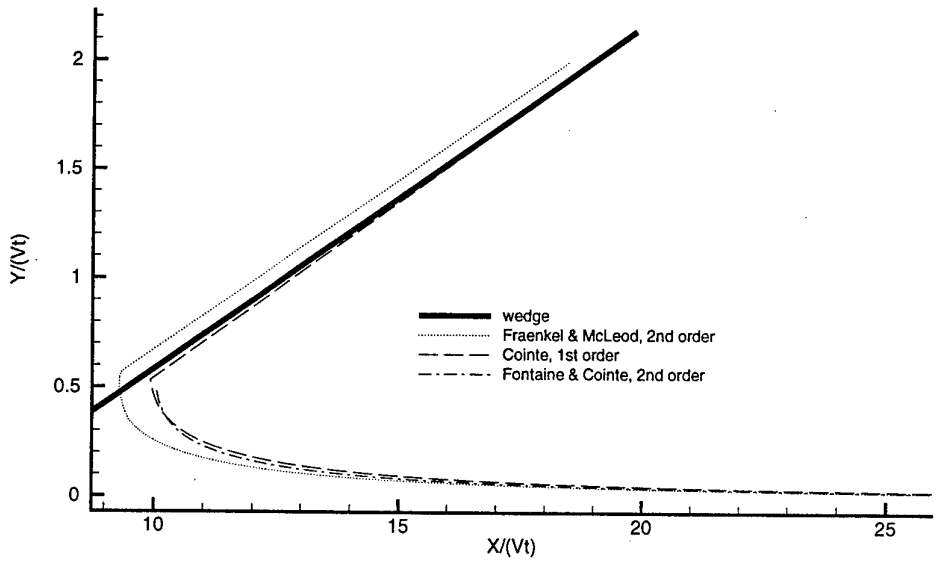


Figure 9: Comparison of the different asymptotic solutions for $\theta = \pi/20$.

4. TIME DOMAIN SIMULATION

4.1 Description of the MEL method

The direct time domain simulation of the flow is performed using the Mixed Eulerian-Lagrangian method. Markers are located on the free surface and followed in their motion. This lagrangian approach allows the free surface boundary conditions to be easily taken into account. The velocity field is computed efficiently using a boundary integral approach (eulerian description of the flow).

The lagrangian formulation of the free surface conditions leads to:

$$\frac{D\phi}{Dt} = -g\,y + \frac{1}{2}\left[\left(\frac{\partial\phi}{\partial s}\right)^2 + \left(\frac{\partial\phi}{\partial n}\right)^2\right] \qquad (4)$$

$$\frac{D\vec{X}}{Dt} = \frac{\partial\phi}{\partial s}\,\vec{s} + \frac{\partial\phi}{\partial n}\,\vec{n}, \qquad (5)$$

where $\vec{X} = (x, y) \in \Gamma_d(t)$ is the position of a marker on the free surface and ϕ is the associated potential. D/Dt is used for the material derivative and $\vec{s}$ and $\vec{n}$ are unit vectors tangent and normal to the free surface.

Boundary conditions on the body and on the axis of symmetry leads to Neumann boundary condition for the potential on these borders (Γ_n).

Far away from the body, the first order outer asymptotic solution enables to conclude that the potential behaves like those generated by a two dimensional vertical dipole placed at origin:

$$\phi \simeq A(t)\frac{y}{x^2 + y^2} \qquad (6)$$

In order to take into account properly the behaviour at infinity of the solution (see Fontaine, [4]), the fluid domain is bounded by a circular control surface Γ_r on which a Fourier boundary condition is imposed:

$$\phi + r\,\frac{\partial\phi}{\partial n} = 0$$

where $r = \sqrt{x^2 + y^2}$.

As the potential has to satisfy Laplace equation $\Delta\phi = 0$ together with the boundary conditions on Γ_n and Γ_r, the problem can be reduced to a set of evolution equations (4)-(5) for $(\phi, \vec{X})$. This stems from the fact that if at a given instant ϕ and $\partial\phi/\partial n$ are known along Γ_d and Γ_n, respectively, the right hand sides of equations (4)-(5) can be calculated. For that purpose, the following boundary integral equation is used:

$$\theta(M)\,\phi(M) = \int_\Sigma \phi(P)\,\frac{\partial G}{\partial n_P}(M,P)\,ds_P - \int_\Sigma \frac{\partial\phi}{\partial n_P}(P)\,G(M,P)\,ds_P \qquad (7)$$

where M is a point on the border $\Sigma = \Gamma_n + \Gamma_d + \Gamma_r$, $G = \ln\|\vec{MP}\|$, is the Green function for a simple source, $\theta(M)$ is the angle between the two tangents to the boundary at M ($\theta(M) = \pi$ if the boundary is regular) and s is a curvilinear abscissa along Σ. Equation (7) is discretised using a standart collocation method. The boundary of the domain is approximed by straight lines elements along which ϕ and $\partial\phi/\partial n$ are assumed to vary linearly. This allows the Green function, its normal derivative G_n and their products by the curvilinear abscissa to be

integrated analytically. Computations are therefore simple, accurate, and can easily be vectorised on a paralell computer. Using the previous hypothesis, the discretised form of equation (7) is:

$$[A_{ij}]\{\phi_i\} = [B_{ij}]\{\phi_{ni}\} \qquad (8)$$

where the influence coefficients A_{ij} and B_{ij} are only dependent of the geometry of the problem and are given by the classical expressions:

$$\begin{aligned} A_{ij} &= A_{1\,ij} + A_{2\,ij} - \theta_i\,\delta_{ij} \\ A_{1\,ij} &= \frac{1}{s_j - s_{j-1}} \int_{s_{j-1}}^{s_j} s\,G_n\,ds - \frac{s_{j-1}}{s_j - s_{j-1}} \int_{s_{j-1}}^{s_j} G_n\,ds \\ A_{2\,ij} &= \frac{s_{j+1}}{s_{j+1} - sj} \int_{s_j}^{s_{j+1}} G_n\,ds - \frac{1}{s_{j+1} - s_j} \int_{s_j}^{s_{j+1}} s\,G_n\,ds \end{aligned}$$

and

$$\begin{aligned} B_{ij} &= B_{1\,ij} + B_{2\,ij} \\ B_{1\,ij} &= \frac{1}{s_j - s_{j-1}} \int_{s_{j-1}}^{s_j} s\,G\,ds - \frac{s_{j-1}}{s_j - s_{j-1}} \int_{s_{j-1}}^{s_j} G\,ds \\ B_{2\,ij} &= \frac{s_{j+1}}{s_{j+1} - sj} \int_{s_j}^{s_{j+1}} G\,ds - \frac{1}{s_{j+1} - s_j} \int_{s_j}^{s_{j+1}} s\,G\,ds \end{aligned}$$

Equations (8) can be rearranged so that the unknowns (potential on Γ_n and Γ_r. and its normal derivative on Γ_d) are put in left hand side $\{X\}$ while known quantities are moved to right hand side $\{bb\}$. The linear matricial system that results from collocation has the form:

$$[AA]\{X\} = \{bb\} \qquad (9)$$

and is solved by the GMRes iterative scheme (see [11]), using the solution at the preceding time-step as initial guess. A finite centered difference scheme is used to evaluate the tangential derivative of the potential $\partial\phi/\partial s$ along the boundary and the evolution equations (4)-(5) are integrated numerically using the 4^{th} order Adams-Bashforth-Moulton method.

The MEL method has been tested and thoroughfully validated for numerous applications related to wave generation and seakeeping (e.g. Cointe [2]). Its application to water entry problem is still delicate, however, because of the strongly non-linear character of this problem. The flow is almost undisturbed, except in the close vicinity of the body where the jet is created. Difficulties to correctly model the flow are related to the numerical treatment of the flow in the vicinity of the intersection point. This is, actually, the difficult point in most numerical resolution of free surface potential flows. When a jet is present, difficulties are made worse because of the strong nonlinearities that exist close to this intersection.

4.2 Special treatment for the jet flow

The asymptotic analysis described above suggest that the jet flow is described by shallow water equations without gravity. For a straight body boundary, the fluid contained in the jet has a solid body motion. This asymptotic solution has been used in order to develop a local model allowing the influence of the jet on the remaining part of the flow to be accounted for. The jet is truncated normally to the

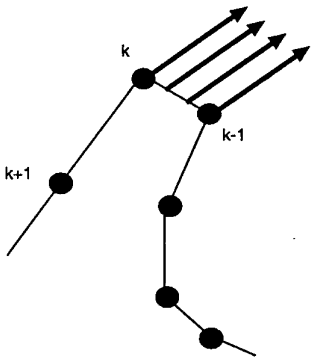


Figure 10: local flow within the jet.

body boundary as soon as its thichness becomes of the order of magnitude of a segment of the grid (fig. 10). A new segment is then introduced to bound the fluid domain. Along this segment, the normal derivative of the potential is imposed constant, equal to the tangential velocity on the body boundary. The fluid tangential velocity across the jet is therefore constant, equal to its value on the body boundary. The tangential derivative of the potential along the segment cutting the jet is also assumed to be constant, but not necessarilly equal to its value on the body boundary. This leaves an extra degree of freedom to the solution. This approximations are used in the calculation of the influence coefficients. This leads to (see Fontaine, [4]):

$$\begin{aligned} A_{i,k-1} &= -\theta_i\delta_{ik} + A_{1\,ik} + A_{2\,ik} \\ B_{i,k-1} &= B_{2\,i,k-1} \\ A_{ik} &= -\theta_i\delta_{ik} + A_{1\,ik} + A_{2\,ik} - \frac{1}{s_{k+1} - s_k} \int_{s_{k-1}}^{s_k} G\,ds \\ B_{i,k} &= B_{1\,i,k} \\ A_{i,k+1} &= -\theta_i\delta_{ik} + A_{1\,ik} + A_{2\,ik} + \frac{1}{s_{k+1} - s_k} \int_{s_{k-1}}^{s_k} G\,ds \\ B_{i,k+1} &= B_{1\,i,k+1} + B_{2\,i,k+1} \end{aligned}$$

During the simulation, a new segment cutting the jet is introduced as soon as the jet thickness becomes to small (as compared to the length of a grid segment). This algorithm revealed robust (fig. 11). It led to a good agreement with the solution computed by Zhao & Faltinsen [15] using Dobrovol'skaya's method [3]. It can also be notice on figure 12 that the first order outer expansion of the free surface elevation is in good agreement with the nonlinear solution, even the value of θ is relatively large.

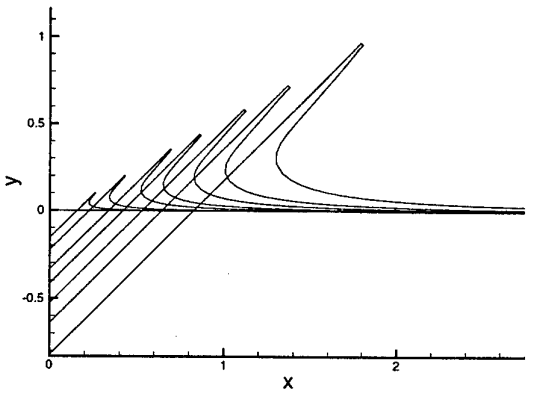


Figure 11: Temporal evolution of the free surface in the vicinity of the wedge ($\theta = \pi/4$).

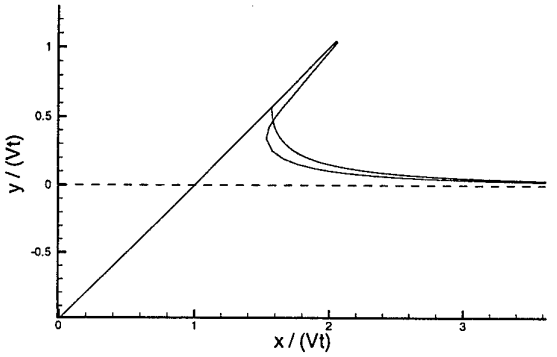


Figure 12: Comparison between the numerical self-similar solution and the first order outer expansion of the free surface ($\theta = \pi/4$).

5. CONCLUSIONS

Practical ways to compute impact loads using asymptotic theories are discussed. The numerical integration of the first order composite solution for the pressure distribution presented by Cointe [1] revealed to be an easy, robust and accurate method. Results were also obtained that show that water entry can be simulated using the Mixte Eulerian Lagrangian method and a local model describing the influence of the jet on the remaining part of the flow. This local model is the result of an asymptotic analysis of the problem. At first order, the jet flow is described by shallow water equations without gravity. The hyperbolic nature of these equations allows the influence of the jet to be accounted for without having to actually compute the flow in the jet. The analysis that was described in the case of a wedge can be extended to arbitrary geometries as long as the angle between the tangent to the body and to the free surface remains small ([1], [7]). Work is underway to extend these numerical results to water entry for a body of arbitrary shape.

One of the authors (E. Fontaine) wishes to express his gratitude to the French Departement of Defense, DRET, for supporting this study. By the way, a partial french traduction of this paper is given in ref. [5].

REFERENCES

[1] Cointe, R., 1989, "Two-Dimensional Water-Solid Impact", *J. Offshore Mechanics and Artic Engineering, Vol. 111, pp. 237-243.*

[2] Cointe, R., 1989, "Quelques aspects de la simulation numérique d'un canal à houle", *Thèse de Doctorat de l'école Nationale des Ponts et Chaussées, Paris.*

[3] Dobrovol'skaya, Z.N., 1969, "On some problems of similarity flow of fluid with a free surface", *J. Fluid Mech., Vol. 36, pp. 805-829.*

[4] Fontaine, E., 1996, "Simulation de l'écoulement potentiel engendré par un corps élancé perçant la surface libre à forts nombres de Froude", *Thèse de Doctorat de l'Ecole Nationale des Ponts et Chaussées, Paris.*

[5] Fontaine, E. & Cointe, R., 1997, "Quelques résultats récents sur l'étude asymptotique de l'impact hydrodynamique", *Symposium Saint Venant, Ecole Nationale des Ponts et Chaussées, Paris.*

[6] Fraenkel L.E. & McLeod, J.B., 1997, "Some results for the Entry of a Blunt Wedge into Water", *Phil. Trans. R. Soc. London A, Vol. 355, pp 523-537.*

[7] Howison, S.D., Ockendon, J.R., Wilson, S.K., 1991, "Incompressible water-entry problems at small deadrise angle", *J. Fluid Mech., Vol. 222, pp. 215-230.*

[8] Kevorkian, J. and Cole,J.D., 1981, "Perturbation Method in Applied Mathematics", *Applied Mathematical Sciences, Vol. 34, Springer-Verlag New York Inc.*

[9] Magee, A. & Fontaine, E., 1998, "A Coupled Approach for Evaluation of Slamming Loads on Ships", *to be published in PRADS 98.*

[10] Molin, B., Cointe, R. and Fontaine, E., 1996, "On energy arguments applied to the slamming force", 11^{th} *International Workshop on Water Waves and Floating Bodies, Hamburg.*

[11] Saad, Y., Schultz, M. H., 1986, "GMRes : A Generalized Minimal Residual Algorithm for Solving Nonsymetric Linear System", *Siam J. Sci. Stat. Compt., Vol. 7, No. 3.*

[12] Van dyke, M., 1975, "Perturbation Method in Fluid Mechanics", *The Parabolic Press, Standford, California.*

[13] Von Kàrmàn, Th., 1929, "The Impact on Seaplane Floats During Landing", *NACA 321.*

[14] Wagner, H., 1932, "Über Stoβ und Gleitvorgänge an der Oberfläche von Flüssigkeiten.", *ZAMM, Vol. 12,pp. 193-215.*

[15] Zhao, R. & Faltinsen O., 1993, "Water Entry of Two-Dimensional Bodies", *J. Fluid Mech., Vol. 246, pp. 593-612.*

[16] Zhao, R., Faltinsen, O., Aarsnes, J.V.,1996, "Water entry of arbitrary two-dimensional sections with and without fow separation", *Proceedings 21th Symposium on Naval Hydrodynamics, Trondheim, Norway.*

STABILITY OF SUPERCAVITATING SLENDER BODY DURING WATER ENTRY AND UNDERWATER MOTION

S.I.Putilin
National Academy of Sciences – Institute of Hydromechanics
8/4 Zhelyabov str., Kiev, 252057
Ukraine

1. SUMMARY

This paper describes main results of experimental and theoretical investigations of slender body motion stability when it enters water and moves underwater in supercavitation conditions, being made in Institute of Hydromechanics. Experimental investigations allowed to study flows, occurred in the situation considered and get data for developing mathematical models of flows. Previously known theoretical relations for forces, acting the body are defined more exactly and new ones are derived. Mathematical model of body motion in supercavitating regime is delivered.

2. INTRODUCTION

There was a grate interest to problems of a slender body motion when it enters water at high speed or moves underwater at supercavitating regime from 60 – s till to beginning of 90 – s years. Results of these investigations were published in works of Logvinovich G.V., Parishev E.V. [8,9], Juravlev Yu.F. [3,4], Guzevsky L.G.[2], Moran J.P. [20], Kazite Tikao [21], A.May [24] and others.

A complex of theoretical and experimental works concerning stability of slender body motion under situation considered were conducted at the Institute of Hydromechanics then.

Experimental investigations included experiments with freely moving models, being launched by device, that was put above water surface, and experiments with models, installed in a water flow at water tunnel.

The main aim of the first kind experiments was investigation of processes, that went when a body entered the water, and influence of different body features on these processes. Experiments at water tunnel enabled to study flow near body and some its elements in details and to obtain data necessary to develop mathematical models of motion.

The main aim of theoretical investigations, conducted at the Institute of hydrodynamics, was to take into account some new factors, that had not been considered previously. Influence of elements, intersecting a cavity surface, interaction of two bodies, that moved one behind another, effect of side forces, appearing at body head on the motion stability was investigated. Influence of inner cavity medium was studied also. Some theoretical solutions that relate hydrodynamic and aerodynamic forces to cinematic parameters of motion.

Mathematical models of body motion, based on results of the said theoretical and experimental results were constructed and programs to calculate body trajectory were elaborated.

3. EXPERIMENTS WITH FREELY MOVING MODELS

Special aims of experiments with freely moving models were:
– to investigate conditions of stable water entrance;
– to investigate process that take place when body divides into parts in water;
– to investigate conditions of rapid speed brake and transition to smooth flow;
– to investigate process of air transport at underwater trajectory after water entrance.

3.1. Equipment

Equipment, used for experiments, was created during work.
Pneumatic launching device (catapult) was created to launch models. It was installed above hydraulic water tunnel with glass side walls. It was possible to change inclination of its barrel and an angle between the barrel axes and the model axes. So it was possible to change an angle between the model velocity and horizon and between the model velocity and the model axis and to investigate the model motion under different trajectory inclination and different model incidence.

A special installation was created later. It consisted of cylindrical tank, that could be installed under different angles to horizon (Fig. 1). There was a catapult, windows and device to capture

Paper presented at an AGARD FDP Workshop on "High Speed Body Motion in Water", held in Kiev, Ukraine, 1-3 September 1997, and published in R-827.

models on the tank. It was thought, that there would be a system of pressure control and a system of underwater launch on the installation.

Some difficulties appeared when models tested at very low inclinations of trajectory. Essence of these difficulties arose from very low position of catapult, otherwise a model path in an air was too long. As a result an entrance points of models with little difference in parameters (say, the same model with ring nozzle 2 and 4 mm wide) were significantly different. Two ways were proposed to overcome the difficulty: to use water tunnel and to use high speed towing tank (hydrostand).

We refused from first way as the water surface at the pipe was too bad.

The second way consisted of model being hanged under the towing tank carriage and, after the carriage had reached full velocity, being dropped at desired path point. Camera shot down the following model motion.

Maximum velocity of the carriage is over 20 m/s. This velocity is comparable to model velocity, achieved at most of installations of conventional type.

There are some advantages of the method. It makes it possible to use grate models, to shoot by camera, that moves with a model velocity, to investigate a model entrance through a wavy surface. Very small drop height corresponding to low trajectory inclination angle is the main disadvantage.

3.2. Water entry

After model touch a water surface its motion can change itself significantly. Some typical forms of motion are distinguished [3,9,13,16,21,23]. The main features of them are:
- the model motion changes little after water entry;
- the model reflects from water surface and moves in nearly previous position in air;
- the model touches water surface and begin to rotate about transverse horizontal axis;
- the model enters water but changes its motion significantly (it deflects toward water surface and leaves water; moves in previous direction under water surface; rotates bow down and begin to move down or in direction, opposite to initial).

Real model motion can consist in consequence of said forms. For instance, a model can reach water surface at low angle, reflect from it, reach it for the second time at greater angle and enter water or begin to rotate about transversal axis.

Specific motion form depend on body itself and on its motion before it reaches water.

It is known that good body motion when it enters water is achieved at bodies with flat or concave for surface. Motion of pointed bodies can be enhanced by different types of ring nozzles [21]. Models with such nozzles were tested in this work, dimensions and position of nozzles being varied.

Motion of some models is showed at Figs. 2 – 4.

At Fig. 2 model does not enter water. It touches water surface, makes long enough hollow, turns over and moves father, the stern end being in front. It is seen, that overturn does not take place in the plane of initial motion.

Two shoots at Fig. 3 correspond to the same model, the same nozzle being put at different distance from model head. So clearances between the head and the nozzle are different, and this influenced cavity dimensions.

Fig. 4 shows waves on the cavity surface.

3.3 Some features of body immersion

Special models consisting of two parts – fore and stern – were constructed to investigate underwater division of a body into two parts. Aft part of the model contain a spring device that ensures division of the model parts some time after model leaves carriage of the catapult. Velocity of for part increases during division, velocity of stern part – decreases.

Aft part of a model usually was in a cavity after division and its resistance was little. Resistance of for part was great and its velocity diminished quickly. If incidence was small, it overtook for part quickly. If incidence was not small, stern part deflected from the cavity axis and reached its boundary. Resistance of stern part became great and this prevented model parts from collision.

Investigation of model brake was similar to said investigation but trajectory inclination range and constructions of devises used were another. Small diameter cavitators put before model and towing disks were tested. Devices of the first kind created small cavity. It collapsed at the model body. This ensures rapid transition to nonseparating flow with great resistance.

Braking disk was towed at some distance behind the model body. It interacted with cavity boundaries, created additional resistance and divided inner cavity part from atmosphere. The latter promoted cavity to collapse quickly.

Investigation of cavity gas transport was conducted at new closed test stand. There are some niches at the stands tank upper side. Air from the collapsed cavity came to these niches, and its amount was measured.

Models with great and small cavitators and models with cavitators of complex forms were tested. Air amount at cavities created by disc cavitators proved to be nearly proportional to the third degree of the cavitator diameter. Towed brake can influence the air amount in the cavity significantly. This influence is different for cavitators of different types.

4. EXPERIMENTS AT WATER TUNNEL

Experiments at water tunnel permits to investigate structure of flow, and to get data to calculate a body free motion trajectory.

Experiments at water tunnel of IHM can be divided into three types:
- experiments with a full model;
- experiments with a fore part of a model;
- experiments with a stern part of a model.

Experiments of the first two kinds were conducted with conventional stern struts, experiments of the third kind were condacted with bow struts (Fig. 5).

Note experiments with complex cavitators and experiments with some types of stern parts.

Special device was constracted to test cavitators. It gave opportunity to rotate cavitator about two axis: longitudinal and transverse. The device was connected to dynamometer, mounted at strut. Dynamometer could measure three components of hydrodynamic force: R_x, R_y and R_z.

Plane and conical cavitators with appendages that permitted to influence cavitator lift, round cavitators with spherical and cylindrical for surface were tested.

Fig. 6 shows cavity formed by star - formed cavitator. Complex form of fore cavity part is seen.

Stern parts of models were tested with fore struts. Theory of cavitator, being put at such strut, was derived in [14]. Construction of the device gave

an opportunity to change model incidence in wide limits and to move the model relative the cavitator in longitudinal and transverse direction.

Conical and fan - shaped, i.e. sectioned, body stern parts were tested among others.

5. THEORETICAL INVESTIGSTIONS

5.1 Principal relations

Theoretical investigation of a body motion was conducted by numerical solution of Cauchy problem for simultaneous equations of the motion.

The equations include three equations for centre of inertia velocity components and for angular velocity (Fig. 7). They are filled up by relations that connect force and moment coefficients to kinematical parameters of motion and by relations that connect cavity dimension and form to said cinematical parameters of motion.

Equation for transverse velocity component is reduced to equation for incidence angle [7, 10, 11]. So non dimensional equations are:

$$\frac{dv_x}{dS} = -\frac{\rho S_0 L_0}{2m}\left[c_{xp}\bar{S}_p + c_{xG} + \overline{\rho_a} c_{xa}\right] \quad (1)$$

$$\frac{d\alpha}{dS} - \omega = \frac{gL_0}{v^2} - \frac{\rho S_0 L_0}{2m}\left[c_{yp}\overline{S_p} + c_{yG} + \overline{\rho_a} c_{ya}\right] \quad (2)$$

$$\frac{d\omega}{dS} = -\frac{\rho S_0 L_0^3}{2mR_i^2}\left[m_{zp}\overline{S}_p^{3/2} + m_{zG} + \bar{\rho}_a m_{za}\right] \quad (3)$$

where
S – nondimensional body path;
v, v_x, v_y – body velocity and its components;
α – incidence at the centre of inertia;
ω – nondimensional angular velocity;
ρ – fluid density;
ρ_a – density of inner media of the cavity;
L_0 – reference length;
S_0 – reference area;
V_0 – reference velocity;
m – body mass;
$\bar{S}_p$ – nondimensional cavitator area;
R_i – body radius of inertia;
c_x, c_y, m_z – coefficients of force components and moment;
indexes p, G и a note force and moment components due to cavitator, side body surface – cavity boundary interaction and side body surface – inner cavity media interaction.

It is convenient to use body length, body stern part section area and initial body velocity as reference values.

Equations (1 – 3) include nondimensional parameters:

$$\mu = \frac{\rho S_0 L_0}{m}$$

$$G = \frac{gL_0}{V_0^2}$$

$$i = \frac{mR_i^2}{\rho S_0 L_0^3} = \mu r_i^2$$

μ may be treated as a relation of the fluid density to the body density;
G, may be treated as Froud number;

i – is the body nondimensional moment of inertia.

Force and moment coefficients in right – hand part of equations depend on nondimensional motion parameters, – incidence and angular velocity, – and on body and cavity mutual position.

The latter causes some features of calculations. The body position is determined by body motion equations, the cavity position – by its deformation laws. At one body motion calculating cavity position depends on the same body motion after all. At two bodies motion calculating, one being behind another, mutual position of the back body and the cavity depends on motion of both bodies.

5.2 Influence of side forces, appearing at cavitator, on body motion

There will be considered side forces acting on cavitator, and their influence on a body motion.

Constant body velocity will be considered, so equations (2) and (3) describe the motion.

Acting on cavitator force components and moment depend on the angle between the cavitator axis and oncoming the cavitatir flow velocity α_p. The latter is connected to incidence at the center of inertia of the body α and its angular velocity by

$$\alpha_p = \alpha - \omega l_p. \tag{4}$$

If α_p is small, linear relation of side force coefficient c_{py} and moment coefficient m_{zp} on α_p may be used:

$$c_{py} = c_p^\alpha \alpha_p; \quad m_{zp} = m_{zp}^\alpha \alpha_p \tag{5}$$

A motion period when body do not interacts with cavity boundary is considered.

If we use relation, similar to (5) for c_a and m_{za} and designate

$$\begin{gathered} c_y^\alpha = c_p^\alpha \overline{S}_p + \overline{\rho}_a c_y^\alpha \\ m_z^\alpha = \overline{\rho}_a m_{za}^\alpha + (c_p^\alpha l_p + m_{zp}^\alpha)\overline{S_p} \\ c_y^\omega = \overline{\rho_a} c_{ya}^\omega - c_p^\alpha l_p \overline{S}_p \\ m_z^\omega = \overline{\rho}_a m_{za}^\omega - \overline{S_p}(c_p^\alpha l_p^2 - m_{zp}^\alpha l_p) \end{gathered} \tag{6}$$

then equations (1 – 3) became similar to equations of leteral motion of an airplane. Their characteristic equation is

$$\lambda^2 + 2P\lambda + Q = 0, \tag{7}$$

where

$$\begin{gathered} P = \frac{1}{4\mu}[c_y^\alpha - \frac{1}{r_i^2} m_z^\omega] \\ Q = \frac{1}{2\mu r_i^2}\frac{1}{2\mu}[c_y^\alpha m_z^\omega - m_z^\alpha \bar{c}_y^\omega] \\ \bar{c}_y^\omega = c_y^\omega - 2\mu \end{gathered} \tag{8}$$

If (6) are inserted into (8) and aerodynamic terms are omitted, then

$$Q = -\frac{1}{2\mu r_i^2}(c_{yp}^\alpha + m_{zy}^\alpha S_p^{3/2}$$

$$P = \frac{1}{4\mu}\left[c_p^\alpha S_p \left(1 + \frac{l_p^2}{r_i^2}\right) + m_{zp}^\alpha \frac{l_p}{r_i^2} S_p^{3/2}\right]$$

Roots of characteristic equation (7) are

$$\lambda_{1,2} = -P \pm \sqrt{P^2 - Q} \tag{9}$$

Then for positive values of c_{py}^α and m_{pz}^α roots are real, one being positive, hence initial perturbation rise by exponential law. This is a result of the body static instability.

For negative values of c_{py}^α and m_{pz}^α roots are either real, one being positive, either complex, but both have positive real parts. Hence motion is unstable due to luck of demping.

Calculations by full motion equations show, that there is some difference in motion of a body with positive and negative c_{py}^α (Figs. 8,9). Fig. 8 shows examples of trajectories, Fig. 9 – inclination angle versus path for bodies with different c_{py}^α.

At Fig. 8 motion of the body with positive c_{py}^α is unstable, motion of bodies with zero and negative c_{py}^α is stable.

At fig. 9 body having positive c_{py}^α reached nonoscillating regime of motion, the pitch angle ψ and vertical component of velocity v_{yg} rising slowly. If c_{py}^α were less, body would oscillate, the oscillation frequency being less, then oscillation frequency of the body with neutral cavitator. The body with negative c_{py}^α also reached oscillation regime, but its frequency is greater, than oscillation frequensy of the body with neutral cavitator.

5.3. Models of inner medium

Interaction of a body and inner cavity medium can influence the body motion stability.

Inner cavity medium consists of water vapour, gas, water drops and sprays. Mathematical description of such medium is a complex problem, so it is necessary to employ some simplified schemes. Some possible models are:

1. A model of rare gas.

2. A model of continuous media (gas).
3. A model of multilayer fluid.
4. A model of multicomponent fluid.
The first three will be considered.

1. Model of rare gas permits to estimate influence of water drops and sprays. It is thought, that drops and sprays moves at the velocity of outer flow and do not interact each other. When they reach the body surface, they transfer to the latter part of their momentum. The normal component is transferred completely, tangential – partly.

If transferred to body part of tangential momentum component is small, a theory of rare gas [6] may be used. This theory gives simple enough relations for calculating of forces, acting at the body.

2. If inner cavity medium is treated as homogeneous continuous medium, the problem is reduced to the problem of a body in a gas flow, but the gas density must be defined in so way, that affect of drops and sprays be accounted for. Then usual aerodynamic methods may be used.

Note, that hydrodynamic coefficients depend on cavity radius and body position about cavity, because a space between the cavity and the body is restricted. Date, necessary for calculating are published in [5] and other works. Methods used to correct results of experiments at aerodynamic tunnels should be employed with care, because they may be valid for small body in grate channel only.

3. Sprays and drops are distributed nonuniformly through the cavity section. Their concentration is the greatest near the cavity boundary and diminishes toward its axis. In addition the cavity boundary is not a smooth surface: it is a consequence of hollows and hills.

This conception of cavity inner medium makes it possible to use multilayer scheme: inner cavity space is divided into some layers, each having constant density, varying from one layer to another.

Figs. 10 and 11 show influence of medium density on a body motion.

6. CONCLUSION

Experimental investigations of flows occurred when models with additional devises and compound models enter water were conducted. Previously known theoretical solutions concerning interaction of slender body and cavity boundary are specified and some new ones are obtained.

Mathematical models of body motion in supercavitating conditions accounting for effect of appendages and inner cavity medium are elaborated. Mathematical model of motion of compound body separated part is constructed also. Programs for calculating body motion accounting for said factors were created.

7. REFERENCES

1. Vasin, A.D., " Nonstationary planning of axisymmetric bodies upon fluid surface" – Tr. TzAGI, M.: 1993, numb. 2496. — p.p. 28 – 35. (in Russian).
2. Guzevsky, L.G., 1979, "Numerical Analysis of Cavitating Flow." Novosibirsk (Preprint of Institute of Thermophysics SD of AS of USSR); 40 -79, 36 P. (in Russian).
3. Jyuravlev, Yu.F., "Immersion of disk into fluid at angle to free surface", Collection of works on hydrodynamics. BCI TzAGI, M.: 1959, p. 227 – 232. (in Russian).
4. Jyuravlev, Yu.F.. "Depth cavity collapse at vertical disk entry into water" – Tr. TzAGI, M.: 1966, numb. 1006. (in Russian).
5. Kapankin, E.N., "Blow of circular cylinder in fluid with outer rigid or free boundary in form of circle. Accounting for influence of flow boundaries at wind tunnels." Tr. TzAGI — 1969 — Num. 1154 — 24 p.p. (in Russian).
6. Krasnov, N.G., " Aerodynamics" — Moscow:, Higher school, 1971. — 630 p. (in Russian).
7. Lyebyedyev , A.A., Chyernobrovkin, L.S., "Dynamics of flight of nonpiloted aircrafts" — M., Mashinostroyenie (Enginebuilding), 1973. — 616 p. (in Russian).
8. Logvinovich, G.V., 1969, "Hydrodynamics of Flow with Free Boundaries." Kiev, Naukova Dumka, 208 P. (in Russian).
9. Logvinivich, G.V., "Some problems of planning" Tr. TzAGI — 1980. — Num.. 2052 — P. 3 – 15. (in Russian).
10. Lucomski, Yu.A., Chugunov, V.S., "Control of sea moveable objects" — L.: Sudostroyeniye (Shipbuilding), 1988. — 272 p. (in Russian).
11. Pantov, Ye.N., Mahin, N.N., Sheremetov, V.V.. "Fundamentals of theory of underwater apparatus motion" — L.: Sudostroyeniye (Shipbuilding), 1971. — 211 p.p. (in Russian).
12. Petrov, K.P., "Aerodynamics of elements of aircrafts" — M., Mashinostroyenie (Enginebuilding), — 1985 — 272 p.p. (in Russian).
13. Stryekalov, V.V., "Ricochet when entering into water of disk, plane of which is nearly vertical" Scientific transactions of TzAGI, 1977, v. 8 num. 5, p. 66-73. (in Russian).
14. Logvinovich, G.V., Buyvol, V.N., Dudko, A.S., Putilin, S.I., Shevchuk, Yu.R., "Flows with free boundaries" – Kiev: Naukova Dumka (1985) - 296 p. (in Russian).

15. Shorigin, O.P., "Immersion into fluid of axisymmetric bodies of simplest forms at an angle to free surface" Non-steady flow of water at high speeds. Proceeding of the IUTAM symposium held in Leningrad, 1971, pp. 397 – 403. (in Russian).
16. Shorigin, O.P., Shulman, N.A., "Entrance into water of a disk at an incidence angle" , Scientific transactions of TzAGI, 1977, v. 8 num. 1, p.p. 12 – 21. (in Russian).
17. Epshtein, L.A., 1970, "Methods of Theory of Dimensionality and Similarity in Problems of Ship Hydromechanics" , L.: Sudostroenie. 207 P. (in Russian).
18. Epshtein, L.A., Blyumin, V.I., Fadyushin, A.P., "Experimental investigation of gas leakage and cavity length behind cones", – Tr. TzAGI, M.: 1968, numb. 1100. (in Russian).
19. Alexander B. Stavovy, Sheng – Lung Chuang, "Analytical determination of Slamming Pressures for High – Speed Vehicles in Waves", – J. of Ship Res., December 1976, v. 20, N 4, p.p. 190 – 198.
20. John P. Moran, "The vertical water exit and Entry of Slender Symmetric Bodies", – J. of the aerospace sciences, 1961, October, v. 28 N.10, p.p. 803 – 812.
21. Kazite Tikao, "Motion of projectile, striking a water surface at arbitrary angle", – J.Sci. Hiroshima University, 1955, July, ser. A vol.19, N 1. part 1 – p.p. 137 – 149; part 2 – p.p. 151 – 159.
22. Shin – Kien Chow, Arthur J. Hou, Lonis Landweber, "Hydrodynamic coefficients of an Alongated body, Rapidly Approaching a Free surface" — J. of Hydronautics, 1976, April, v. 10, N 2, p.p.46-54.
23. W., Jonson, S.R., Reid, "Ricochet of Spheres off Water", J. of Mechanical Engineering Science. 1975, v. 17 N 2. p.p. 71-81.
24. May, A., "Vertical Entry of Missiles into Water", J. of Appl. Phys., 23, 1952, p.p. 1262 – 1272.

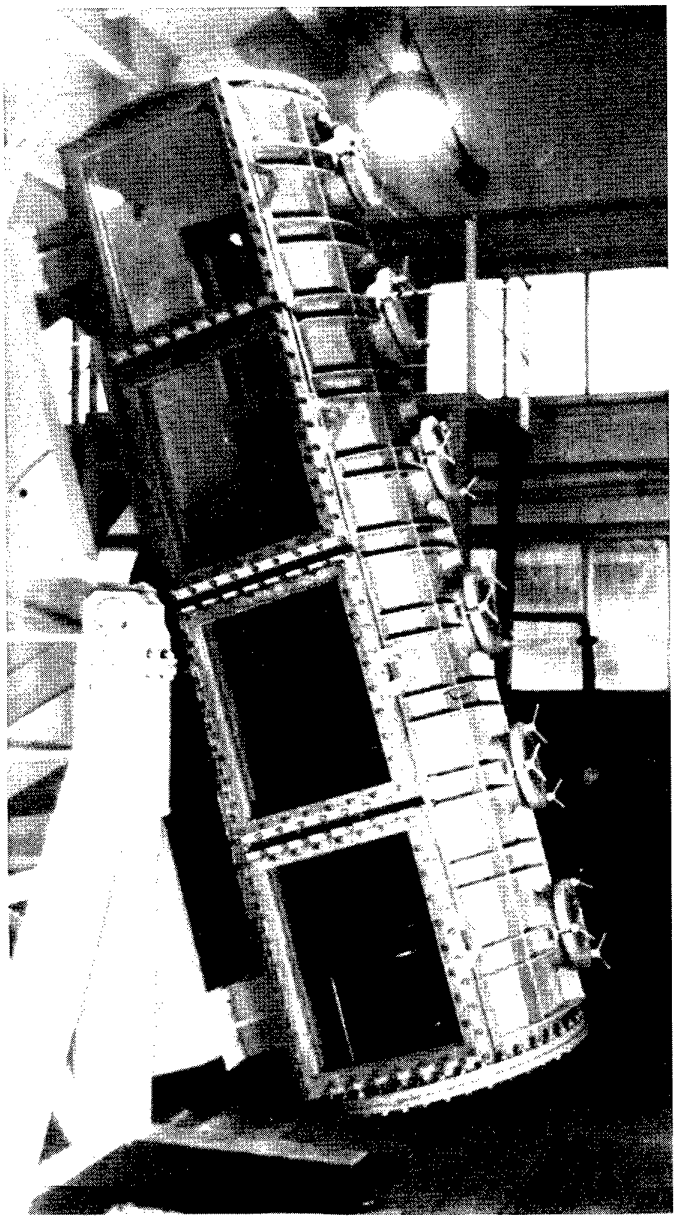


Fig. 1. Stand with varying tank inclination.

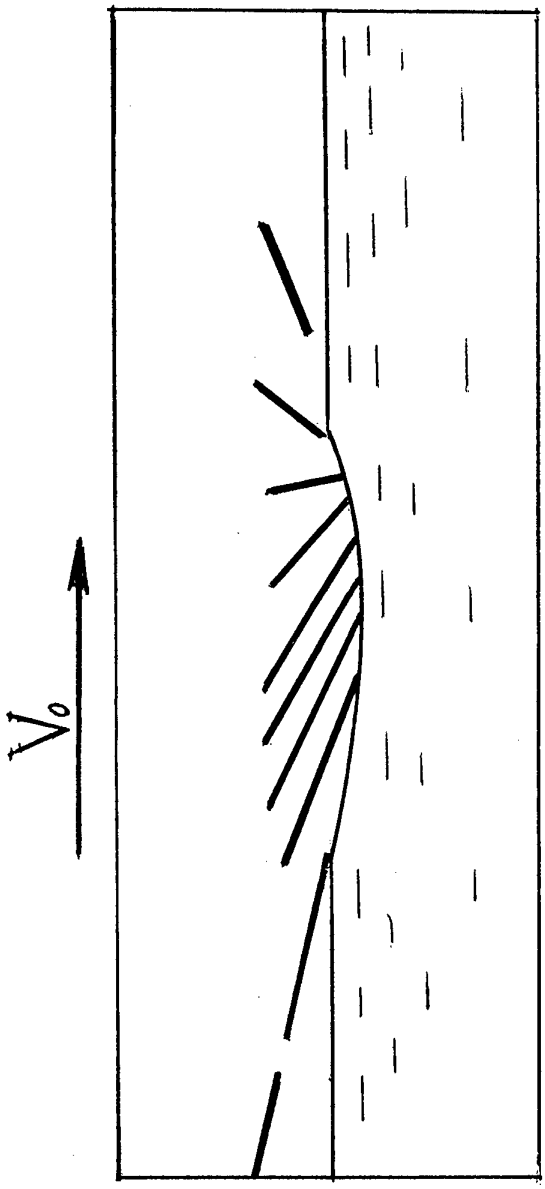


Fig. 2. Ricochet of a body with nozzle.

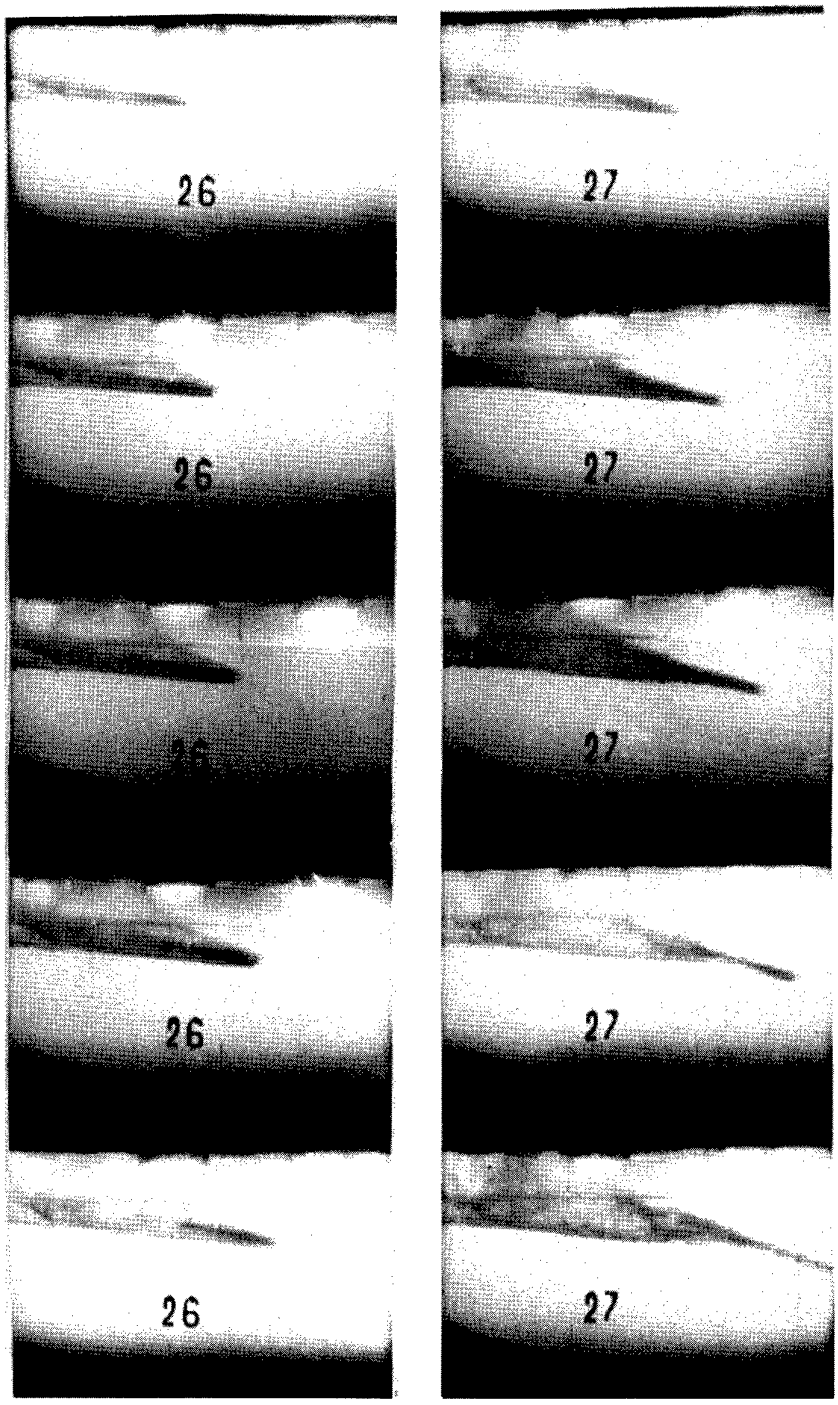


Fig. 3. Influence of a body – nozzle gap:
left — small gap; right — great gap.

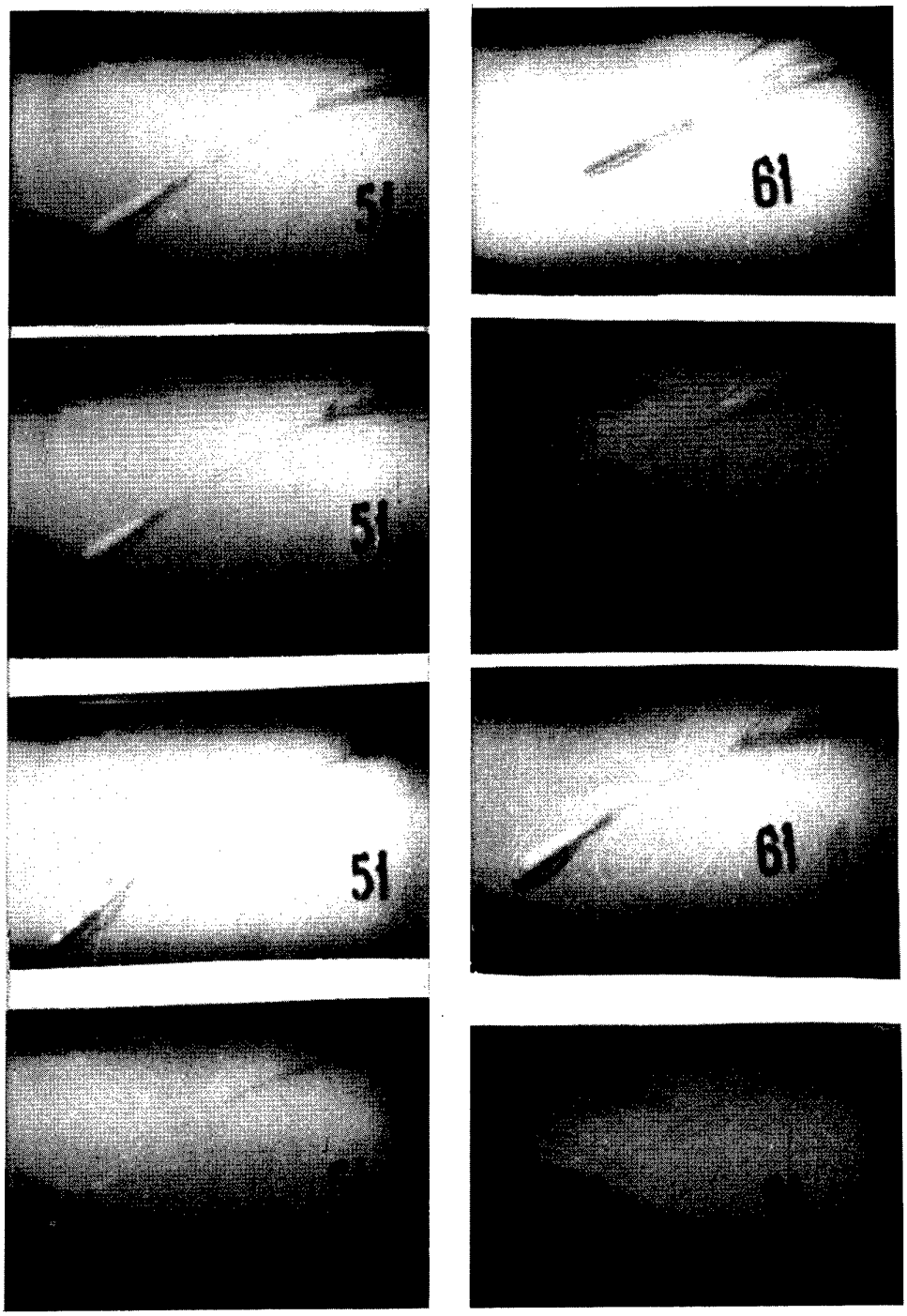


Fig. 4. Wave shaped cavity deformation.

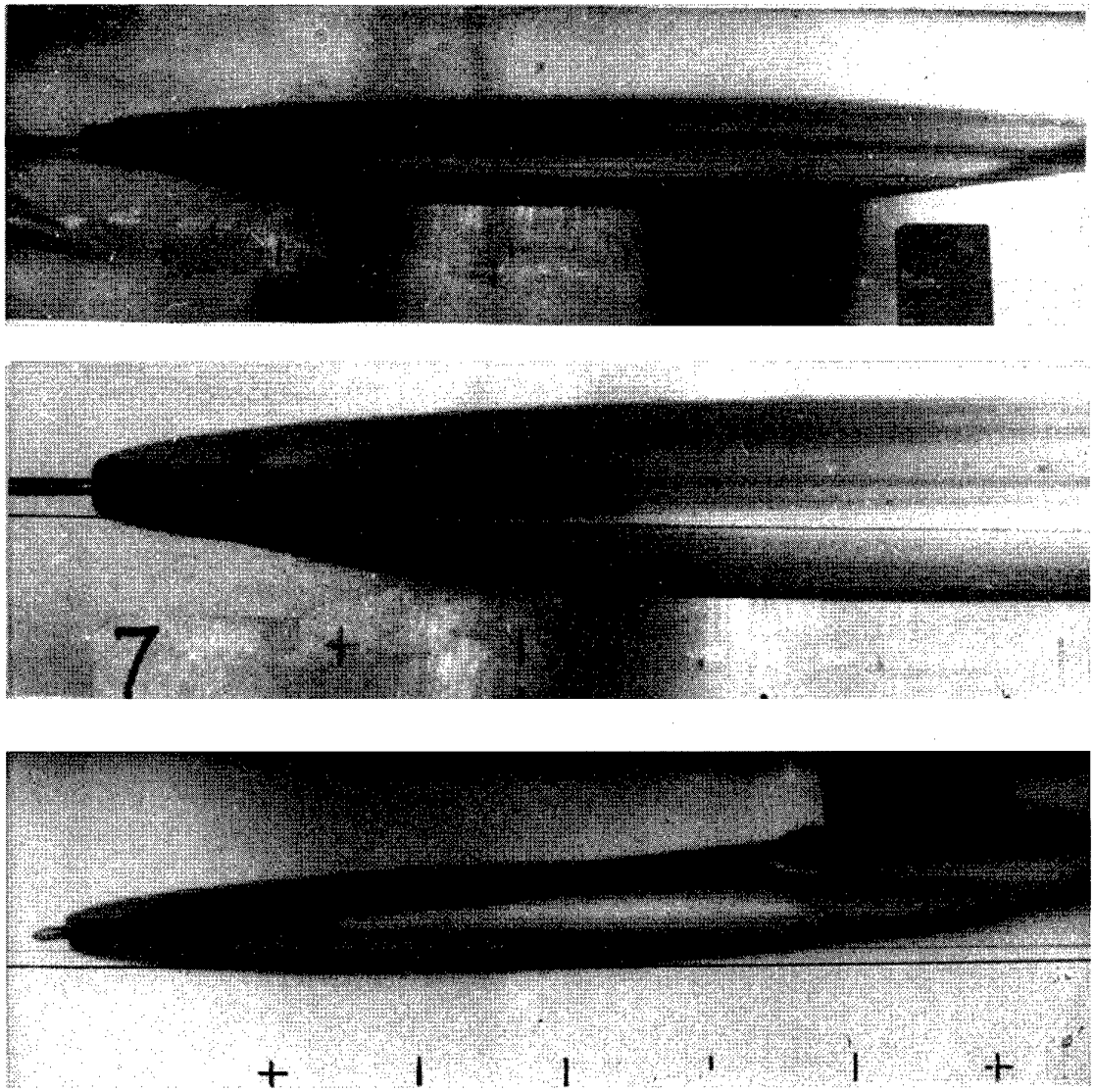


Fig. 5. Cavity in water tunnel.

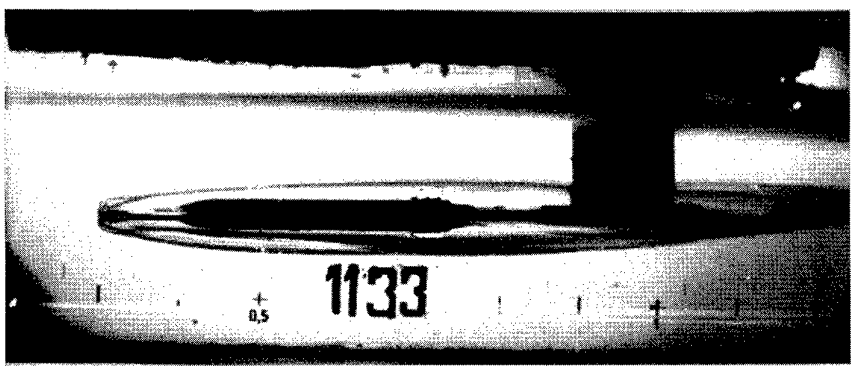


Fig. 6. Cavity behind star – shaped cavitator.

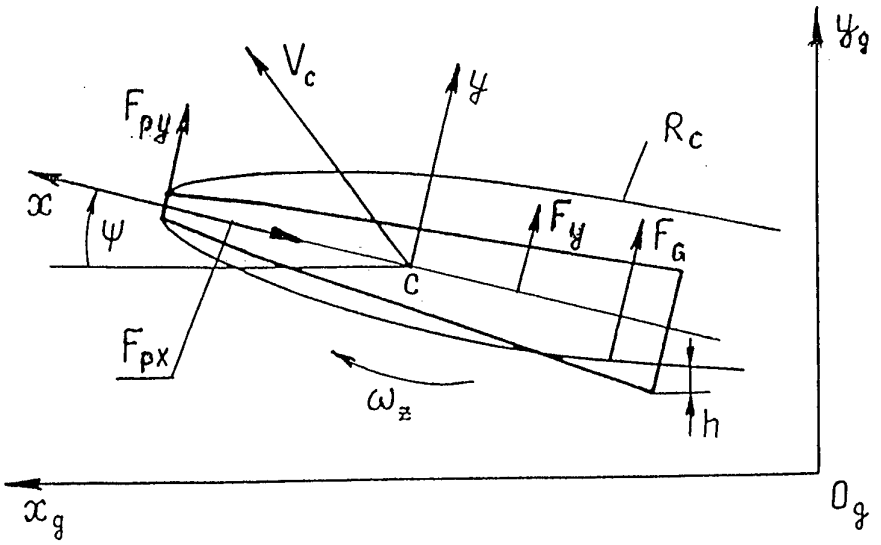


Fig. 7. Supercavitating body

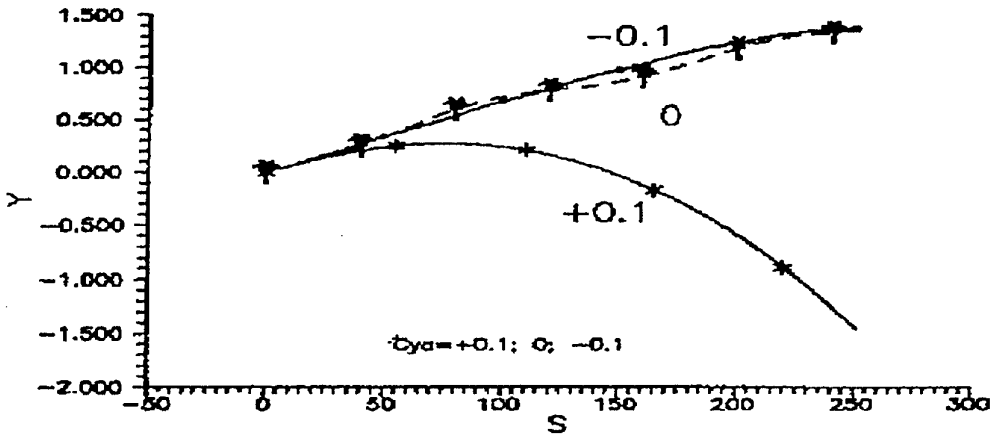


Fig. 8. Influence of C_{py}^{α} on body motion – trajectory

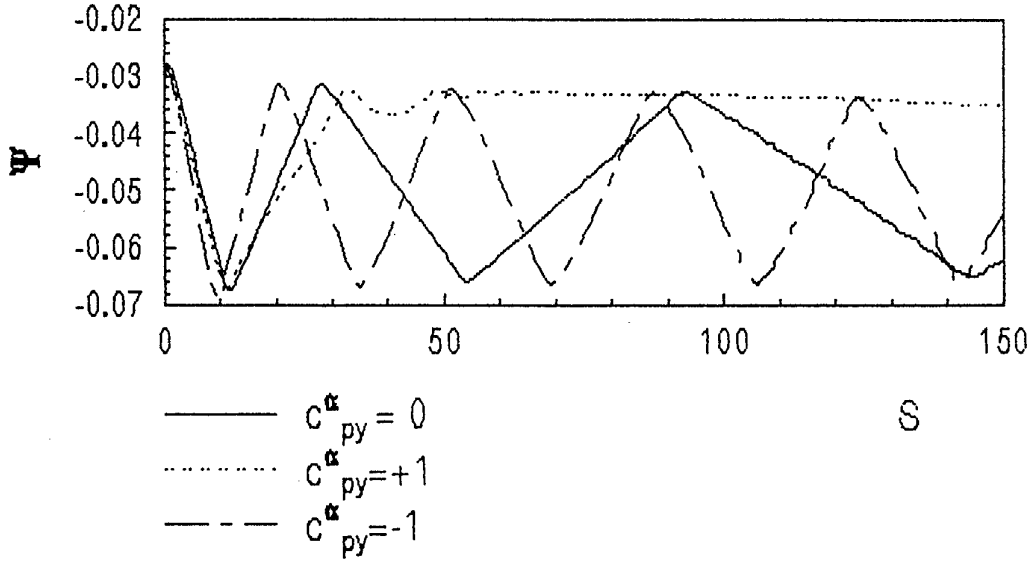


Fig. 9. Influence of C^{α}_{py} on body motion – dependence of pitch angle on body path

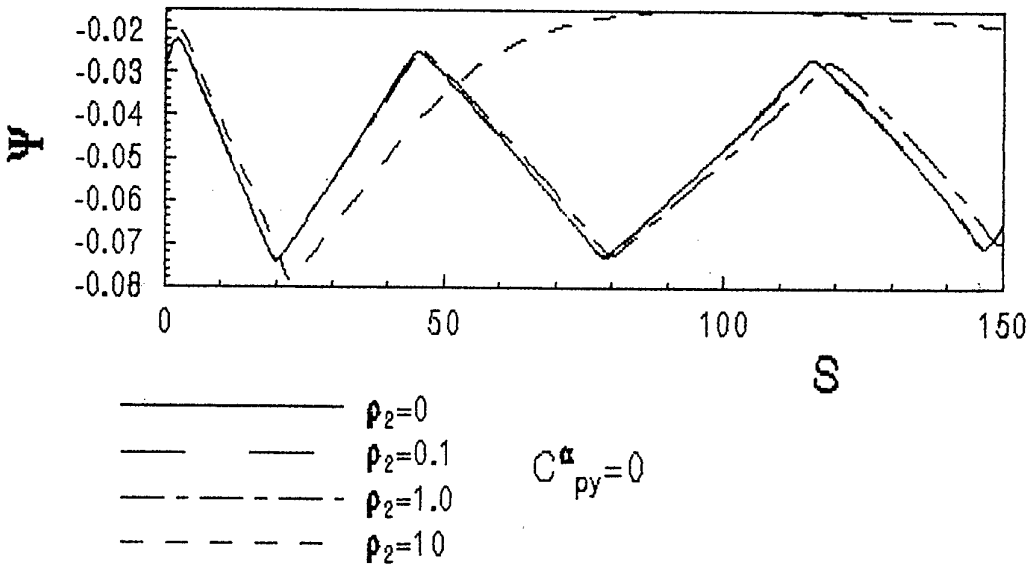


Fig. 10. Influence of inner medium density on body motion. Neutral body head

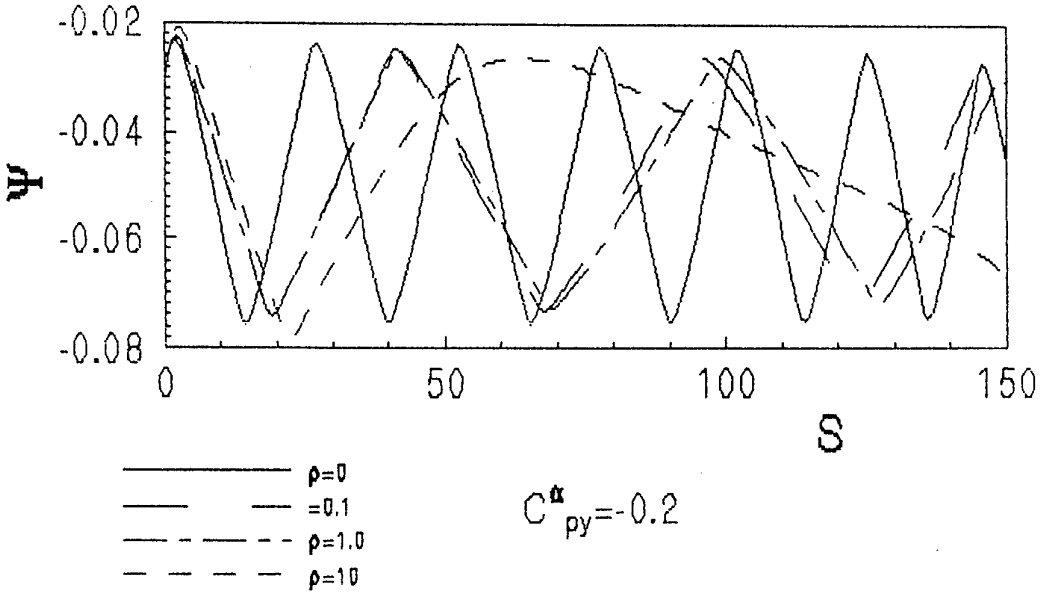


Fig. 11. Influence of inner medium density on body motion. Statically stable body head

EMERGENCE OF CAVITATING PROFILE

M. ARNAUD, L. DIEVAL

Centre Technique des Systèmes Navals
B.P. 28, 83800 Toulon Naval, France.

Abstract

The paper presents a numerical method for unsteady cavitation simulation around engines moving with large vertical velocity. The numerical modelling of the creation and the development of the cavitating flow zones attached to the profile, as well as the free surface deformation, is done using an interface tracking method of « Volume of Fluid » type, inserted into a Navier-Stokes code.

Results show that the model is well adapted to simulate this complex physical phenomena.

LIST OF SYMBOLS

(u, v)	the Cartesian velocity components.
$(\tilde{u}, \tilde{v})$	the contravariant velocity components.
(x, y)	the Cartesian co-ordinates.
(ξ, η)	the curvilinear co-ordinates.
(n_x, n_y)	the components of the normal vector.
$(\vec{e}_x, \vec{e}_y)$	the components of the unit vector.
$\vec{\nabla}$	nabla vector.
ρ	the constant density of the liquid.
$\tilde{\rho}$	the fictitious density.
ρ_{ref}	the density of reference.
$\vec{\tau}$	the stress viscid tensor.
p	the pressure.
p_{ref}	the pressure of reference.
σ	the surface tension coefficient.
σ_i	the cavitation number.
r	the free surface curvature or the position of the particle. in the fluid.
R	the position of the interface.
R_0	the position initial of the bubble.
g	the gravity acceleration.
J	the jacobien of the coordinates transformation.
μ	the molecular viscosity coefficient.
U_0	the constant.
U_1	the constant.
χ	the constant.
$\tilde{W}$	the fictitious vector.
L	the length of the profile
L_{max}	the maximal length of the cavity non dimensional
l	the width of the profile
l_{max}	the maximal thickness of the cavity non dimensional

1. INTRODUCTION

The problem is the emergence of an engine from the water with a high vertical velocity. When approaching the free surface, the surrounding pressure decrease, cavitation regions appears on the fore of the profile and the crossing of free surface could be affected by the presence of gas regions close to the body surface. We are interested here in the modelling of cavitation bubbles evolution on the profile, as well as in the free surface deformation.

The study of unsteady cavitation bubble may be done using different types of methods :

- The potential method e.g. Molin[1], De Lange[2].
- The two phase method e.g. A. Kubota[3], Y. Ventikos[4], and Y. Delannoy[5].
- The interface tracking method e.g. L. Diéval[6].

The aim of this study is to demonstrate the capacity of the VOF method to simulate the unsteady cavitation phenomena, especially the creation processes, re-generation, tracking and bubble cracking . This method consists in defining, in a fixed mesh, the interface from the volume fraction of two phases (liquid and gas) e.g. Hirt[7]. Its advantage over purely two phase method is a true tracking interface method without numerical diffusion and it has not the mathematics stiffness of compressible flow treatment when the sound velocity is very high compared to the flow velocity .

The liquid flow equations are computed by a finite volume method on curvilinear grids, with solve the Navier-Stoke equations. The evolution of liquid-gas interface of bubble is calculated by VOF method, linked to the flow equation solver by an explicit algorithm, described in subsequent paragraphs.

2. NUMERICAL MODEL

2.1 Equations

The unsteady Navier-Stokes equations for incompressible bidimensional flows are written in the following semi-conservative form, in curvilinear co-ordinates (ξ, η) :

$$\frac{1}{J}\frac{\partial W}{\partial t} + \frac{\partial G}{\partial \xi} + \frac{\partial H}{\partial \eta} = \frac{1}{J}(R + T) \qquad (1)$$

with

$$W = \begin{bmatrix} 0 \\ \rho u \\ \rho v \end{bmatrix}; \quad R = \begin{bmatrix} 0 \\ 0 \\ -\rho g \end{bmatrix}; \quad T = \begin{bmatrix} 0 \\ \frac{\sigma}{r} n_x \\ \frac{\sigma}{r} n_y \end{bmatrix}$$

Paper presented at an AGARD FDP Workshop on "High Speed Body Motion in Water", held in Kiev, Ukraine, 1-3 September 1997, and published in R-827.

$$G=\frac{1}{J}\begin{bmatrix}\rho\tilde{u}\\ \rho\tilde{u}u+\xi_x p-\vec{\nabla}(\xi).\vec{\tau}_x\\ \rho\tilde{u}v+\xi_y p-\vec{\nabla}(\xi).\vec{\tau}_y\end{bmatrix};\quad H=\frac{1}{J}\begin{bmatrix}\rho\tilde{v}\\ \rho\tilde{v}u+\eta_y p-\vec{\nabla}(\eta).\vec{\tau}_x\\ \rho\tilde{v}v+\eta_y p-\vec{\nabla}(\eta).\vec{\tau}_y\end{bmatrix}$$

$$\tilde{u}=\xi_x u+\xi_y v \qquad \tilde{v}=\eta_x u+\eta_y v \qquad J=\frac{\partial(\xi,\eta)}{\partial(x,y)}$$

$$\vec{\tau}_x=\vec{\vec{\tau}}.\vec{e}_x \qquad \vec{\tau}_y=\vec{\vec{\tau}}.\vec{e}_y \qquad \vec{\vec{\tau}}=\mu\left(\vec{\nabla}.\vec{U}+{}^t\vec{\nabla}.\vec{U}\right)$$

2.2 Pseudo-compressibility method

Time discretization is ensured using a fully implicit second order scheme. The solution of the non-linear system for the unknown values of the time step $n+1$ is based on the pseudo-compressibility technique, e.g. De Jouette[8]. We will simply remind the reader of the principle of this approach, referring to the above reference for a detailed presentation and the justification of the pseudo-unsteady formulation selected.

Considering the semi-discretized equations at the time level $n+1$ and introducing a time-like variable τ, called pseudo-time, one adds pseudo-unsteady terms which are derivatives of the unknowns at time level $n+1$ with respect to τ:

$$\frac{1}{J}\frac{\partial\tilde{W}^{n+1}}{\partial\tau}+\frac{3W^{n+1}-4W^{n}+W^{n-1}}{2\Delta t}+\left(\frac{\partial G}{\partial\xi}\right)^{n+1}+\left(\frac{\partial H}{\partial\eta}\right)^{n+1}=\frac{1}{J}(R+T) \qquad (2)$$

with: $\tilde{W}=\begin{bmatrix}\tilde{\rho}\\ \tilde{\rho}u_x\\ \tilde{\rho}u_r\end{bmatrix}^{n+1}$

The pseudo-unsteady terms involve a new unknown variable $\tilde{\rho}$ called pseudo-density and subject to remain positive. The pressure is calculated as a function of $\tilde{\rho}$ through an additional equation which is identified with a pseudo-law of state. This numerical relation can be selected in different ways, as discussed in De Jouette[8]. The choice retained is the following:

$$p=\rho\left(U_0^2+\chi U_1^2\right)\ln\frac{\tilde{\rho}}{\rho_{ref}}+P_{ref} \qquad (3)$$

where U_0, U_1, P_{ref} et ρ_{ref} are constants.

The system (2,3) is integrated step-by-step in pseudo-time until convergence towards a solution independent of τ which is then the numerical solution of the instant t^{n+1}

The system is hyperbolic with respect to τ and - this is one of the reasons that has led to the choice of this system - it is formally very close to Navier-Stokes equations in compressible flow (without the equation of energy), due to the presence of the same $\tilde{\rho}$ factor in the terms of derivatives in τ. This property makes it possible to directly apply existing and efficient algorithms, have been developed for compressible flows, to the solution of this system. Which we have used an adaptation of the finite volume method with artificial viscosity, originally developed by Jameson[9] for compressible flows.

Discretization in space is of the centred type. The variables $\tilde{\rho}$, $\tilde{u}$, $\tilde{v}$, p being defined at the centres of the cells, the fluxes at an interface are obtained from the averages of values at the centres of the two adjacent cells. Artificial viscosity, which is necessary in the case of a centred scheme to ensure stability and convergence and prevent the uncoupling of the even/odd nodes, includes second order derivatives and fourth order derivatives and is adjustable using coefficients.

The scheme used in pseudo-time is the explicit 5 step Runge-Kutta scheme, associated with an implicit residual smoothing technique Jameson[9]. The basic Runge-Kutta scheme is explicit, but one introduces an implicit treatment of the unsteady source term $\partial W/\partial t$, which reinforces stability while leaving the calculation effectively explicit. The maximum value of the pseudo-time step $\Delta\tau$ is fixed by the local Courant-Friedrichs-Lewy stability criterion. For each cell, one uses the maximum local value (local time step technique). The method is unconditionally stable with respect to the physical time step.

2.3 V.O.F method

Water-air interfaces constitute moving discontinuity surfaces the positions of which, at time level $n+1$, are part of the unknowns of the problem.

In the VOF method, the flow problem is discretized in a fixed grid and the free surface is known only through a scalar variable F defined in each cell as the fraction of the volume of the cell occupied by the fluid. This variable F therefore has values between 0 and 1, limits included, and the free surface is located in the cells where $0<F<1$. The evolution of the variable F in a given curvilinear cell Ω is ruled by the mass conservation equation which can be written for this cell as:

$$V\frac{dF}{dt}+\int_{\partial\Omega}\frac{1}{J}f\vec{\tilde{U}}.\vec{n}dS=0 \qquad (4)$$

where V is the volume of the cell, $\partial\Omega$ its boundary, $\vec{\tilde{U}}(\tilde{u},\tilde{v})$ the velocity vector at the interface and where f is a function defined at all points which can have only two values : 1 at a point occupied by the fluid, and 0 otherwise; one notices that :

$$VF=\int_{\Omega}fdV$$

The integration of (4) for the calculation of F from the time level n to the time level $n+1$ raises difficulties in the case when the cell Ω is a partial cell, i.e. such that $0<F<1$, since then the distribution of f on $\partial\Omega$ cannot be exactly recovered from the knowledge of F in Ω and in neighbouring cells. The originality and interest of the VOF method is that it provides an approximate - but conservative - evaluation of the mass flux through $\partial\Omega$ only from the knowledge of F in Ω and in surrounding cells.

Consider two adjacent cells, which therefore have a common interface. The normal velocity component at the interface makes it possible to distinguish between the donor cell (upstream) and the acceptor cell (downstream). The flux of mass through the interface is then determined according to a complex algorithm which distinguishes a certain number of possible situations depending on the value of F and the orientation of the free surface in the donor cell and in the acceptor cell, (Hirt[7]).

The calculation algorithm for F is explicit in time ; the stability of this algorithm limits the time step to a value which corresponds to a displacement of the free surface of one cell at the most. In practice, this means that a cell full of fluid cannot become empty (or inversely) in a single time step.

2.4 Numerical treatment at the boundaries

Boundary conditions on the free surface concern partial cells i.e. cells, for which $0<F<1$. The pressure in a partial cell is taken equal to the pressure imposed at the interface itself. At the free surface of the tank, the pressure is the atmospheric pressure. The pressure of the gas in the cavitation bubbles is the vapour pressure. The velocity in a partial cell is determined by extrapolation from neighbouring cells, and more precisely as the weighted average of the velocities in the 8 neighbouring cells, the weight of a cell being chosen equal to the fifth power of the value of F in that cell.

2.5 Coupling of flow and free surface calculation methods

The pseudo-compressibility method and the VOF method can be coupled together by updating the position of the free surface at each step in physical time even though the flow calculation is operated at each Runge-Kutta step of pseudo-time iterations. The general algorithm of the free model consists in the following main steps :

1 . Physical time iteration.
   a. Pseudo-time iteration.
      i. Sweep of Runge-Kutta steps.
         - Calculation of fluxes and of residuals for the liquid cells (VOF = 1).
         - Smoothing of the residuals.
         - Up-dated values of velocity and pseudo-density.
         - Boundary conditions for the partial cells of interfaces (0<VOF<1).
         - Boundary conditions for outer boundaries.
      ii. End of Runge-Kutta steps.
   b. End of pseudo-time iteration.
   c. Updating of the VOF field.
2 . End of physical time iteration.

2.6 Cavitation criterion

When the profile approaches the free surface, the surrounding pressure decreases. The passage of subcavitating flow to cavitating flow is realised when the pressure around the profile reaches a critic threshold corresponding to the vapour pressure. In these conditions, the cavitation bubble is initialised the cells of the mesh which verify the vaporising criterion with a VOF value equal to 0 and the vapour pressure.

The interface velocity is equal to the normal velocity of the liquid phase with the velocity mass transfer between the phases added. This velocity may generally be neglected and the evolution of the interface is calculated by the VOF method which considers the local velocity field. At each time step, a cavitation criterion permits to localise possible new liquid cells where the pressure is lower than the vapour pressure, which are then imposed at VOF = 0 and at the limiting vapour pressure. This semi-empirical mass transfer criterion between liquid and gas on the interface into consideration which allows vapour creation dependant on the flow dynamics conditions.

3. NUMERICAL APPLICATION

3.1 Implosion of Rayleigh bubble

3.1.1 Time and pressure

One points out only the equation of momentum which comes from the equation established by Rayleigh-Plesset. For more details, one can see for example Franc[10]

$$\ddot{R}\frac{R^2}{r^2}+2\dot{R}^2\frac{R}{r^2}-2\dot{R}^2\frac{R^4}{r^5}=-\frac{1}{\rho}\frac{\partial p}{\partial r} \tag{5}$$

with :

- r : Particle position in the liquid flow

The integration of the equation (5) gives the time of implosion of the Rayleigh bubble :

$$\tau=\sqrt{\frac{3}{2}\frac{\rho}{p_\infty-p_v}}\int_{R_0}^{0}\frac{dR}{\sqrt{\left(\frac{R_0}{R}\right)^3-1}} \tag{6}$$

and the field of pressure in the liquid flow :

$$\frac{p-p_\infty}{p_\infty-p_v}=\frac{R}{3r}\left(\left(\frac{R_0}{R}\right)^3-4\right)-\frac{1}{3}\left(\left(\frac{R_0}{R}\right)^3-1\right) \tag{7}$$

3.1.2 Calculation domain

The simulation of the implosion of the Rayleigh bubble is carried out by the Euler equations coupled with method VOF developed above. By taking into account all symmetries of the problem, the field of calculation is reduced to a sector of circle. The field of calculation is thus composed of 200 nodes with a minimum step of 0.0001 meters. See figure 1.

The design criteria on the borders of the field are the following ones :

- On the right : Pressure = 10^5 Pascals and velocity = 0
- On the bottom : Axisymmetric condition
- On the top : Symmetric plane
- On the left : free boundary

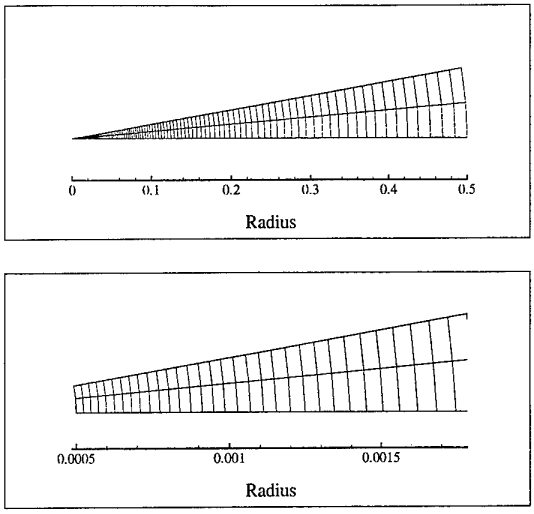


Figure 1 : Bubble mesh

3.1.3 Results

The method of pseudo-compressibility coupled with the method of fluid fraction of volume (VOF) makes it possible to find the distribution and the peaks of pressure in the liquid part of the fluid (see figure 5) in the various positions of the interface. Compared to the distribution of pressure in the liquid given by the equation (7), until after the peak of pressure, one can observe a rather weak fall of the pressure compared to (7). The field velocity in the liquid part of the flow is correctly represented.

The error rate between the analytical results obtained by Rayleigh-Plesset and this code computer is the following ones:

- Rayleigh time : $\left|\frac{\tau - \tau_{cal}}{\tau}\right| \times 100 = \Delta\tau = 2{,}89\%$
- Pressure : 6,0%
- Velocity : 5,03%

see figure 5 for the pressure and see figure 6.for the velocity

3.2 Emergence of cavitating profile

We consider a cavitating flow around a submerged engine of L m height and l m width, and with various values of vertical velocity. The profile is supposed to be fixed in the grid, only the free surface goes down. The grid for the two profiles considered (spherical head and conical head) is composed of 141x51 nodes (See figures 2 and 3).

The velocity of the flow with respect to the engine velocity is imposed to the bottom boundary on the domain (the computation is done in the reference frame attached to the engine). On the free surface, one imposes the atmospheric pressure and in the pocket of cavitation the saturated vapour tension. Finally on the profile considered, we impose the conditions of adherence. (The equations of Naviers-Stokes are solved in streamline flow.). See figure 7.

The cavity is created when the pressure in the liquid flow next to the profile is lower than the vapour pressure. The cavity grows, a retrant-jet establishes and it cuts the cavity. See figure 4. The cavity grows again and so on... When the profile emerges, the cavity implode in the liquid flow except for a velocity of 40 m/s. This situation corresponds to the supercavitation. For the different profiles, we can write the following data :

For a conical profile

Velocity m/s	σ_i	L_{max}	$l_{max}\ 10^{-2}$
20	0,98	0,448	5,167
30	0,65	0,687	5,833
40	0,49	1,180	10,83

For a spherical profile

Velocity m/s	σ_i	L_{max}	$l_{max}\ 10^{-2}$
20	0,97	0,348	3,333

with :

- $L_{max} = \frac{\text{lengh of the cavity}}{L}$
- $l_{max} = \frac{\text{width of the cavity}}{l}$

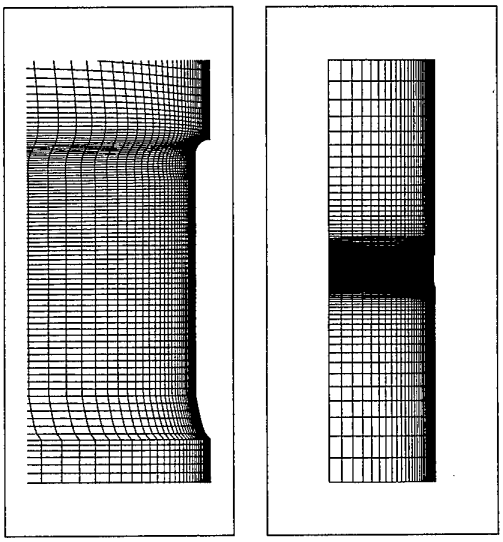


Figure 2 : Mesh of the calculation domain associated a profile having a spherical head

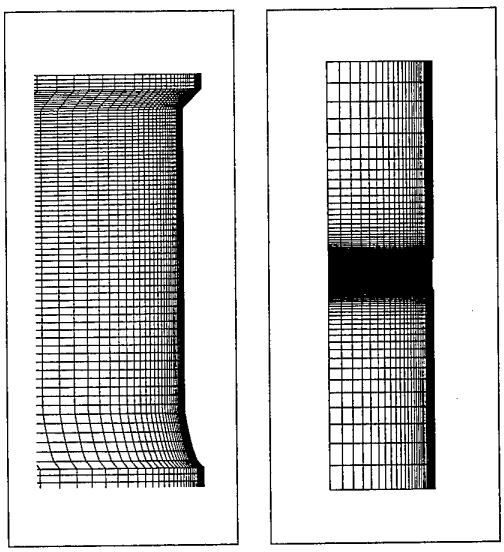


Figure 3 : Mesh of the calculation domain associated Grid of a field for a profile having a conical head

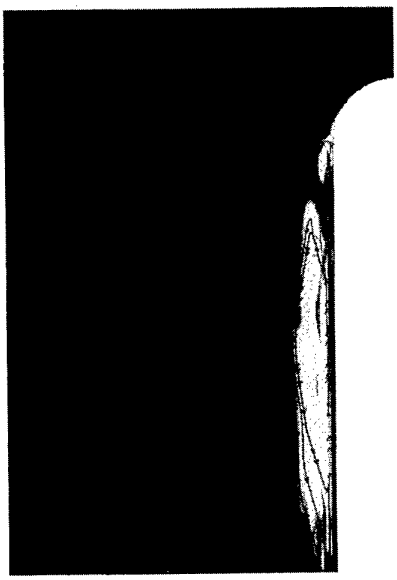


Figure 4 : Retrant jet

4. CONCLUSIONS AND PERSPECTIVES

A free surface tracking model of VOF type has been developed to simulate emergence of cavitating profile. First results show the high potential of the VOF method to treat these complex physical phenomena.

The future extension of the method concerns the development of the coupling between the gas flow in the cavitation bubble and the liquid flow. The aim is to simulate particular physical mechanisms of the cavitation such as mass transfer between liquid and gas on the interfaces and re-compression zone of the gas in the wake of the cavitation bubble.

5. REFERENCES

1. B. Molin, L. Diéval, R. Marcer and M. Arnaud, *Modélisation instationnaire de poches de cavitation par la méthode potentielle et par la méthode VOF*, 6e Journées de l'Hydrodynamique, 24-26 février 1996, Nantes, France.

2. D.F. De Lange, G.J. De Bruin and L. Van Wijngaarden, *Numerical modelling of unsteady 2D sheet cavitation,* 3èmes journées Cavitation, 13 - 14 nov. 1996, Grenoble, France.

3. A. Kubato, H. Kato and H. Yamaguchi, *Finite difference analysis of unsteady cavitation on a two dimensional hydrofoil*, 5th International Conference on Numerical Ship Hydrodynamics, Hiroshima, Japan, 1989.

4. Y. Ventikos, G. Tzabiras, *A numerical study of the steady and unsteady cavitation phenomenon around hydrofoils,* International Symposium on Cavitation, Cav'95, 2-5 may Deauville, France, 1995.

5. Y. Delannoy, *Modélisation d'écoulements instationnaires et cavitants,* thèse de l'Institut National Polytechnique de Grenoble, 1989.

6. L. Diéval, R. Marcer et M. Arnaud, *Modélisation de poches de cavitation par une méthode de suivi d'interfaces de type VOF*, 3e Journées Cavitation, SHF, Grenoble, 13-14 novembre 1996.

7. Hirt C.W. et. Nichols B.D, *Volume Of Fluid (VOF) Method for the Dynamics of Free Boundaries*, J. of Comp. Physics, Volumes 39, pages 201-255, 1981.

8. De Jouette C., "Développement d'une méthode de pseudo-compressibilité pour le calcul des écoulements de fluide incompressible - Applications aux écoulements instationnaires en présence d'une surface libre", Thèse de l'Université de Nice - Sophia Antipolis, 1994.

9. Jameson A., Schmidt A., Turkel E., *Numerical Solutions for the Euler Equations by finite volumes methods using Runge-Kutta Time-Marching Schemes*, AIAA-81-1259, AIAA 14th Fluid and Plasma Dyn., Conf. Palo Alto, California, June 1981.

10. Franc J.P, and al., *La Cavitation Mécanismes physiques et aspects industriuels*, Collection Grenoble Sciences, 1995.

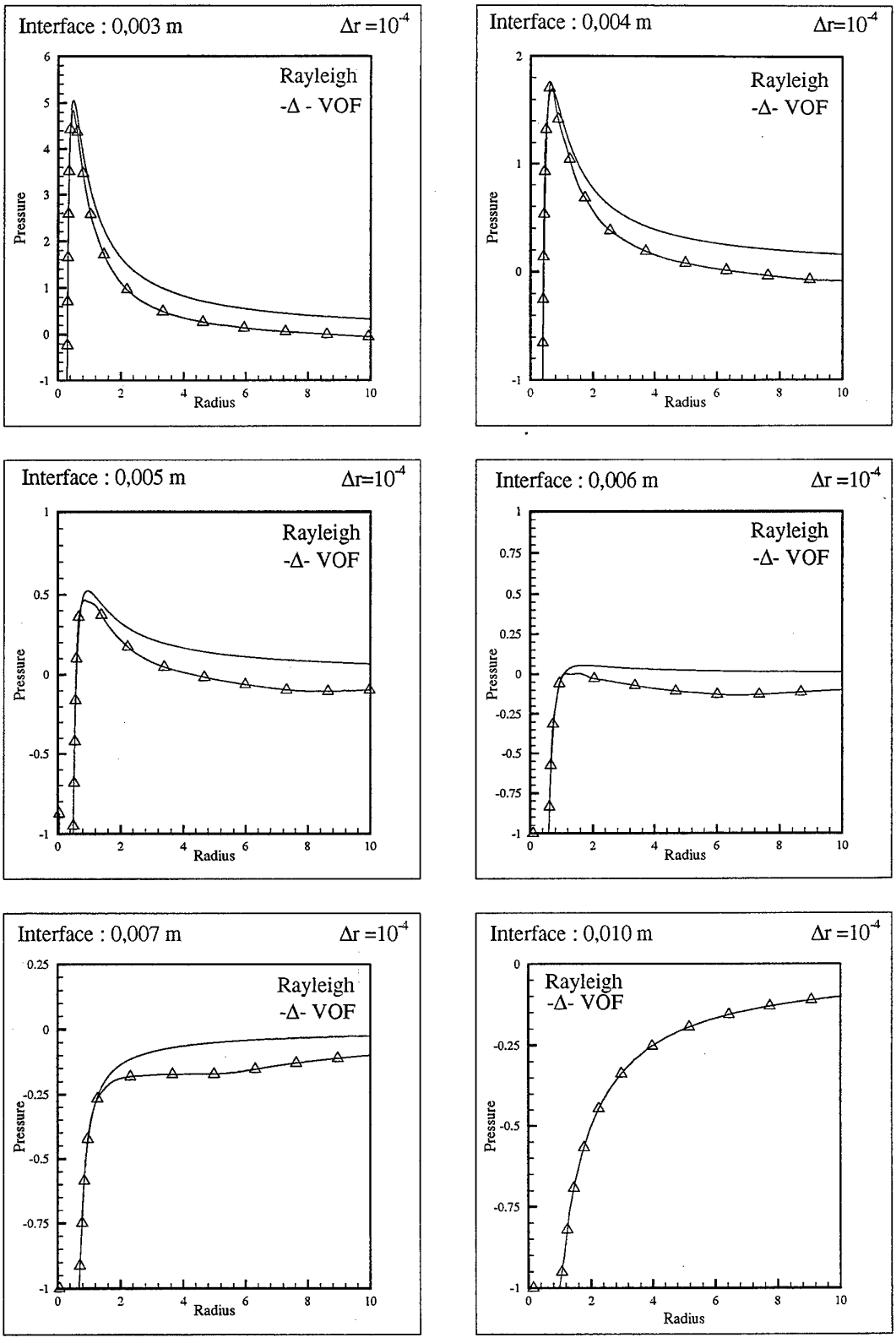


Figure 5 : Pressure

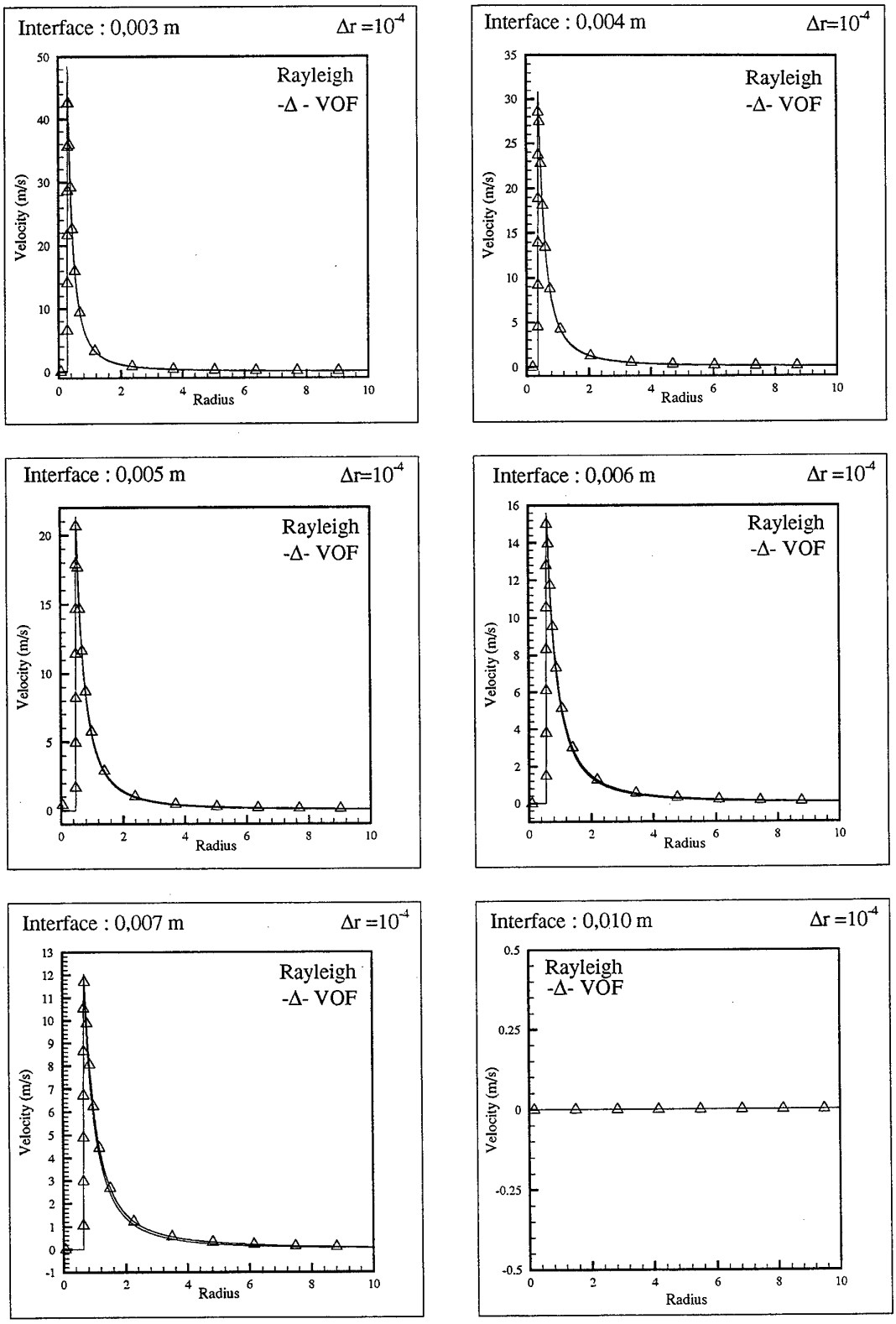


Figure 6 : Velocity

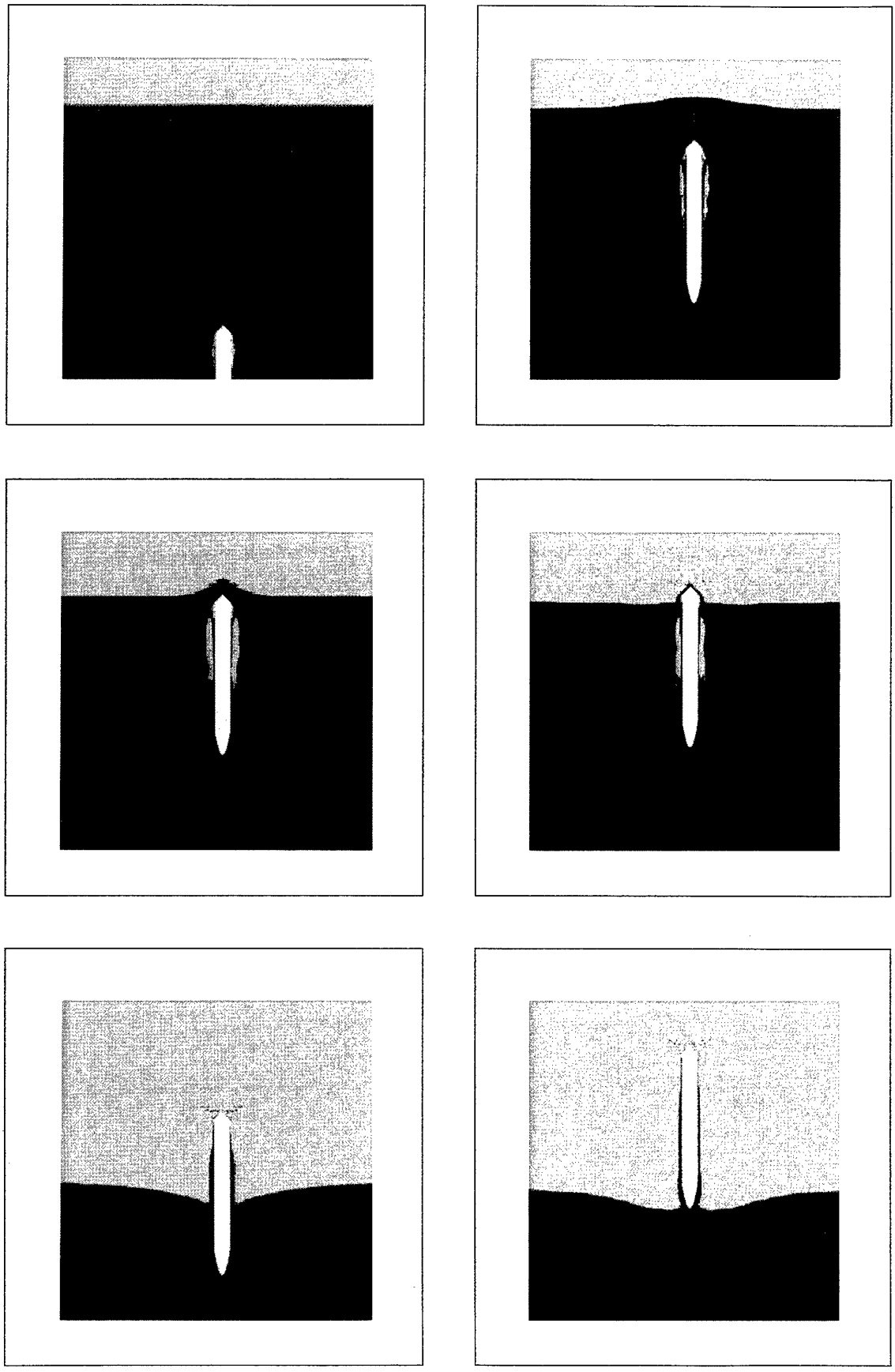


Figure 7 : Emergence of cavitating profile

REDUCTION OF OVERLOAD ON A BODY ENTERING WATER AT HIGH SPEED.

V.T. Savchenko
National Academy of Sciences-Institute of Mathematical Machines and Systems Problems. Kyiv, Ukraine.

SUMMARY

An object on a high speed entering water experiences significant overloads caused by sharp increase in density of the environment. At present paper we are considering two angles - the entrance angle θ between a trajectory of body gravity center and a free surface; the attack angle α between body's axis and direction of a motion. So a whole hydrodynamic force F can be presented as a drag (axial) force X and a significant lift (lateral) force Y. Surrounding an object by supercavity allows us to solve the series of problems, including the following:

reduce hydrodynamic drag;

reduce or eliminate destructive lift(lateral) loads for the object's appendage elements (ledges);

damp(restrain) impact loads concentrated primarily on a cavitator.

Presented research offers based upon the results of experiments technical design for the new series of two-medium foils. Such foils provide the protection of stabilizers and a rudders of two-medium apparatuses from destructive hydrodynamic forces.

LIST OF SYMBOLS

X	drag(axial) force
Y	lift(lateral) force
Cx	drag force coefficient
Cy	lift force coefficient
ρw	water density
ρa	air density
θ	angle of body entrance in water
α	attack angle
d	diameter of disk (cavitator)
Vo	entering speed of body
V	speed of body motion
a	sound speed in water
M	Mach number
σ	cavitation number
h	depth of foil immersing
bo	profile cord
to	profile thick
b	foil sharpness
t	size of cavitating element (leading edge sharpness of foil).

1.INTRODUCTION.

The scientific problem: how objects under water can reach the speed close to the sound velocity, has been solved by creating the supercavity flow [1]. This scientific achievement laid basis for treating certain technical problems in the fields of marine, space, and other investigations. High-speed processes computer modelling allows us to predict various effects in about- and supersonic regimes in the water [2,3]. Space capsules' water-landing, stabilizers' and rudders' protection, support for two-medium devices (machines, apparatuses) and pump blades can serve as examples of practical application for the discussed technical approach. In all the cases we deal with an object's high-speed entry into water connected with formation supercavity around it on its underwater trajectory. Once an object gets in contact with water it undergoes impact hydrodynamic overloads caused by increase in the environment's density $\rho w/\rho a=800$. This causes the attack angles α to create destructive axial forces acting upon the ledges of an object. Impact of these forces needs to be reduced.

2.DISCRIPTION OF PHYSICAL PROCESSES

Examples mentioned earlier use hydrodynamic drag reduction effect. This effect can be achieved by creating supercavity along the object. Supercavity is filled by water vapour (steam) the density of which ρs is a hundred times less than the air density ρa [1]. The required cavity's size is reached with the aid of a cavitating element located on the object's frontal part. Aspect ratio for the object's body is calculated so that object dimensions do not step out beyond the cavity's size. Object's (or appendage elements') gliding on the cavity's

Paper presented at an AGARD FDP Workshop on "High Speed Body Motion in Water", held in Kiev, Ukraine, 1-3 September 1997, and published in R-827.

surface and cavitator's asymmetry jointly provide necessary curve for the underwater trajectory. As marked before, an object experiences impact hydrodynamic overloads once it gets in contact with water. Maximum longitudinal overloads occur in case of disk's right-angle impact entry into the water (θ=90°) [4].

$$F = \frac{\pi d^2 \rho_w}{4} V_0 a (1 + 2M). \quad (1)$$

Where M=Vo/a - Mach number, a≈1440m/s-sound speed in water. From (1) we obtain the estimated value for the maximum drag coefficient:

$$C_x^{max} = \frac{8F}{\rho_w V_0^2 \pi d^2} = \frac{2}{M} + 4. \quad (2)$$

In reality the acting forces are always less than in (2), even in case of the direct impact entry. As a result of modeling experiments on high-speed disk's entry into the fluid-environment for M<0,7 we obtained empirical dependence [5]:

$$C_x^{max} = 1.87 + \frac{2.13}{M}. \quad (3)$$

In case of the incline disk's entry an object's speed has horizontal as well as vertical components(partials) and the acting forces are significantly less. Works of O. Shorygin, N. Shulman, V. Yerohin offer us semi-empirical dependence for the maximum drag coefficient, including adjustments for water compression which occurs in case of the very high-speed entry [6,7].

$$C_x^{max} \approx 0.8 Cos\alpha \left[1 + \frac{Sin\theta}{Cos(\theta - \alpha - 0.35M)}\right]. (4)$$

These results conform well with the experimental data on the matter of angles diapasons -30°<α<+30° and 60°<θ<90°. Experimental formulas (3) and (4) presently are considered to be the most reliable calculations for the direct and inclined high-speed object's entry into water. They can be used for estimating overloads an object, entering water has to undergo.

Fig.1 shows experimental flat-sheared cylinder's drag coefficient's dependence upon sizeless time τ=VoT/d for four values of entry angles when the entry speed is about 100m/sec. When a cavitator penetrates into water impact loads can exceed significantly the cavity resistance force. However their action is limited by the period of time during which an object goes down 2-3 times cavitator's diameter. First of all these forces act along the object's rotation axis. An object possesses the maximal firmness reserve in this direction, so we can suppress(restrain) these loads by elastic spacer for the cavitator.

However if the attack angles of an object, entering water, are significant, we have to solve another challenging problem - how to protect the ledges (appendage elements) from the lateral loads.

As this problem's solution we offer the new different foil's configuration. It is based upon the process of advanced cavitation flow and is capable to work for two mediums. Presented foil is supplied with the cavitating element (nose truncation with cavity creating).

Advanced cavity formation surrounding the rest portion of an object creates fundamental opportunity for protection the foil against destructive hydrodynamic forces. Along with this however it is necessary to solve the problem, how to preserve controllability of the foil, when the whole system works in a different regime. This foil holds a patent [8].

3.TEST RESULTS .

While creating and investigating two-medium supercavitating foils we conducted series of tests using foils with the following parameters:

- 40x200mm plate; cord and thick at the cross section bo=40mm and to=6mm (Fig.2).
- the leading profiles parameter t (cavitating element's size) was been varied in the range of 1/6≤t/to≤5/6;
- the body sharpness b was being changed as b/bo=4/8;3/8;2/8.

The plate was being dipped into a water stream, moving at 10m/sec speed. The plate could turn around α=0° reaching +10°,-10° with the step 2°.

The change of a depth of foil immersing h permitted to change the cavitation number within the range of $0.08 \le \sigma \le 0.02$.

Two forces acting upon the foil were measured. These were the forces in directions Y and X corresponding to the lift (lateral) force and drag (axial) force.

The main foil's characteristic is a polar - dependence between the lift force coefficient

Cy and the drag force coefficient Cx. Our task is
to achieve such a range for the attack angles which makes the value of Cy less than the value of Cy', where Cy' is according to allowable loads on the foil.
Fig.3 illustrates the way to the offered profile of two-medium foils: polares of a NACA profile, a wedge profile and a two-medium profile.
Decrease in Cy value depends upon increase in Cx value. However the drag force is not so dangerous since it is directed towards the maximum firmness of the foil. More than 1'000 tests were conducted on the discussed matter. Their results are displayed on fig. 4-8.
Fig. 4 demonstrates the experimental dependence of Cy value upon attack angles and the leading edge sharpness t ,while b/bo=const. The main outcome: the range of attack angles, guaranteeing Cy=0, increases with increase t. But when t/to>0.5 such increase is insignificant.
Experimental measurements of the drag coefficient Cx as a function of attack angles α and leading edge sharpness t are presented on fig.5. The main outcome: when t/to>0.5, we have significant increase Cx and insignificant expansion of the diapason for Cy=0.
Fig.6 and 7 show dependence of hydrodynamic coefficients Cy, Cx as a function of attack angles and a body sharpness b. Here we have increase of the diapason for Cy=0 with increase of the body sharpness.
The total conclusion: the optimum configuration of foil we have, when t/to=0.5 and b/bo>0.5.
Fig.8 illustrates lift-drag characteristics as a function of attack angles and the leading edge sharpness. Final foil configuration choice should be made according to the technical requirements for two-medium foils and for the attack angles diapason, where Cy=0 or $Cy \leq Cy'$.
Feasible attack angles range is determined by cavity's shape and foil's configuration. It is limited by two extreme foil's locations inside the cavity, in which it touches upper or lower cavity's edge.
Developing of underwater cavitating foils can be conducted with the aid of a special computer program. This program allows to calculate the attack angles range for the given foil's shape and the cavitation number. It also calculates hydrodynamic forces coefficients for continuous and supercavity flow regimes.
Fig. 9,10 demonstrate the typical examples of these calculations. Allowing (~2°) for an error we observe quite consistent conformity of experimental data with the calculations.

The most important forces of two-medium foils in water concentrate on the cavitator. Design of a special cavitator shape (leading edge sharpness) will permit to reserve the lift-control function of two-medium foils in water.

4.CONCLUSION.

The supercavitation reduces destructive forces significantly.
Design of the new type foil, which operates effectively in two medium is possible. The initial design complete-shape has been tested. The results of experimental and calculation researches and so optimization of such foils are submitted.
Improved lift-control shapes proposed for future testing.

5.REFERENCES.

1. Savchenko,Yu. N., "About movement in water at supercavitation flow regimes." J.Hydromecanics,70,1996,pp105-115. (in Russian).
2. Vasin,A.D.,"Slender Axisymmetric Cavities in Sub- and Supersonic Flows of Compressible Fluid", in "Proceedings of Third Workshop on High-Speed Hydrodynamics", Krasnoyarsk, 1987, pp 58-62. (in Russian).
3. Semenenko,V.N, "Computer simulation of the ventilated cavity pulsation", J. Hydromechanics, 71,1997,pp 110-118. (in Russian).
4. Sagomonijan,A.Ya, "Shock and Penetrate of Bodies into Water", Moscow, Moscow University, 1986. 17p. (in Russian).
5. Shashin,V.M., "Hydromechanics", Moscow: Higher school.,1990, 384p. (in Russian).
6. Shorygin,O.P., Shulman,N.A., "Penetrate in water the disc with attack angle",J. Scientific notes of CAGI, 8, 1, 1977, pp 12-21 (in Russian).
7. Yerohin,V.A., "Penetrate of disk into compressible liquid with angle to a free surface". J. News Academy of Sciences. Mechanics fluid and gas.,2, 1983, pp 142-144. (in Russian).
8. Savchenko,V.T., Putilin,S.I.,Savchenko,Y.N. "Two-medium profile". A.S.1710445, Inform. Bull.,5, 1992. (in Russian).

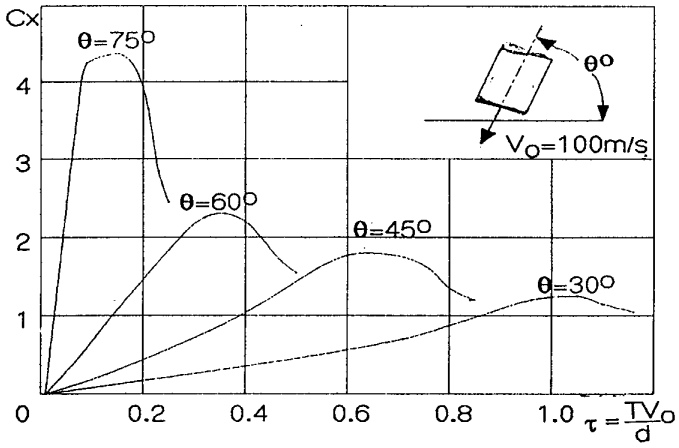


Fig.1. DRAG COEFFICIENT OF A FLAT CUTTING CYLINDER (EXPERIMENTAL RESULTS)

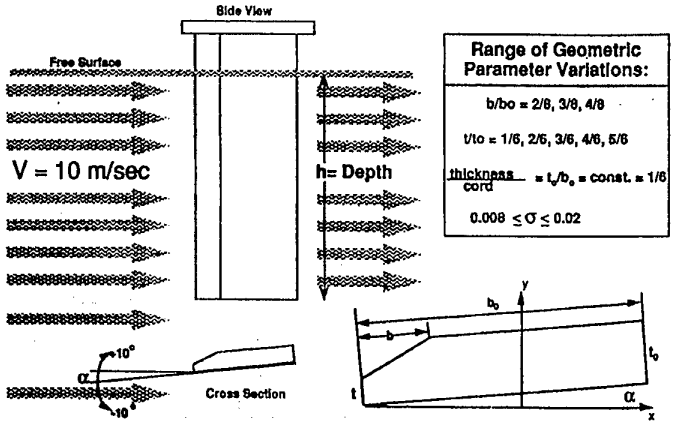


Fig.2. EXPERIMENTAL GEOMETRY

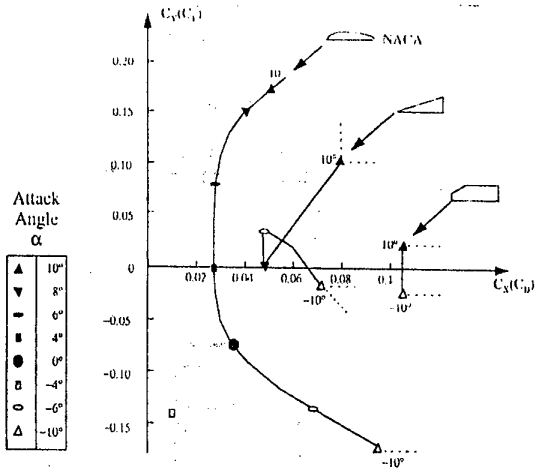


Fig.3. LIFT-TO-DRAG CHARACTERISTICS

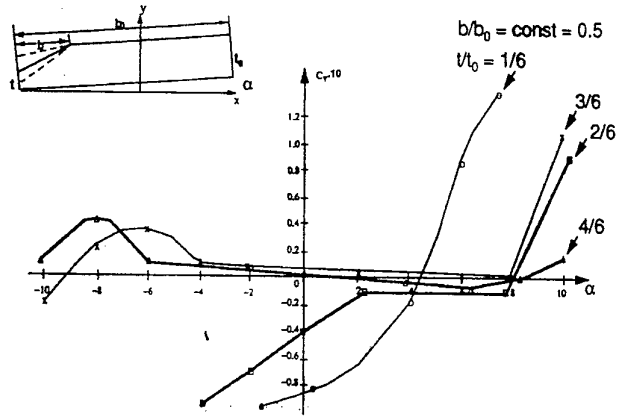


Fig.4. EXPERIMENTAL MEASUREMENTS OF LIFT COEFFICIENT AS A FUNCTION OF ATTACK ANGLE AND LEADING EDGE SHARPNESS

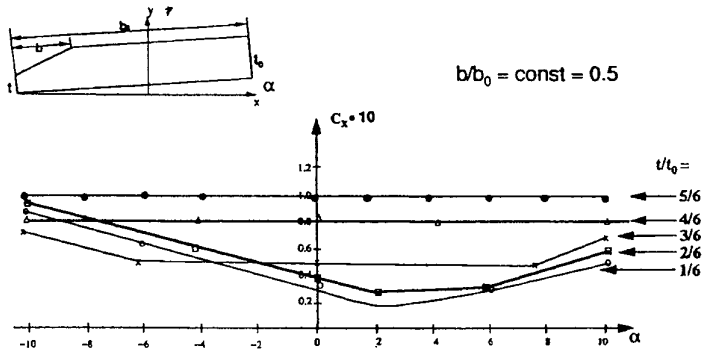


Fig.5. EXPERIMENTAL MEASUREMENTS OF DRAG COEFFICIENT AS A FUNCTION OF ATTACK ANGLE AND LEADING EDGE SHARPNESS

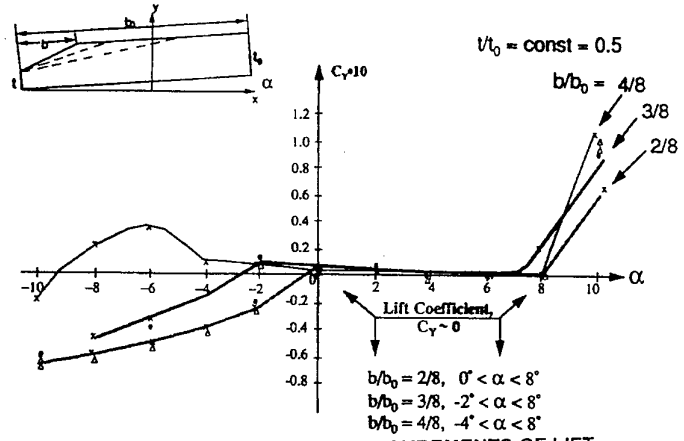


Fig.6. EXPERIMENTAL MEASUREMENTS OF LIFT COEFFICIENT AS A FUNCTION OF ATTACK ANGLE AND BODY SHARPNESS

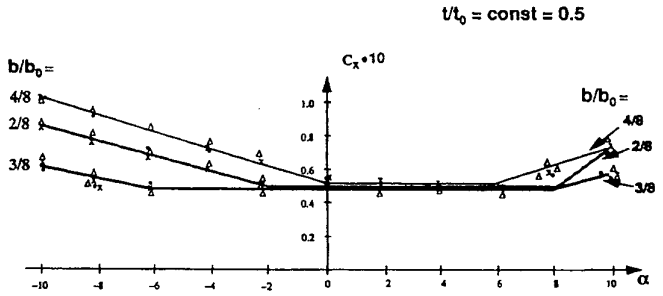


Fig.7. EXPERIMENTAL MEASUREMENTS OF DRAG COEFFICIENT AS A FUNCTION OF ATTACK ANGLE AND BODY SHARPNESS

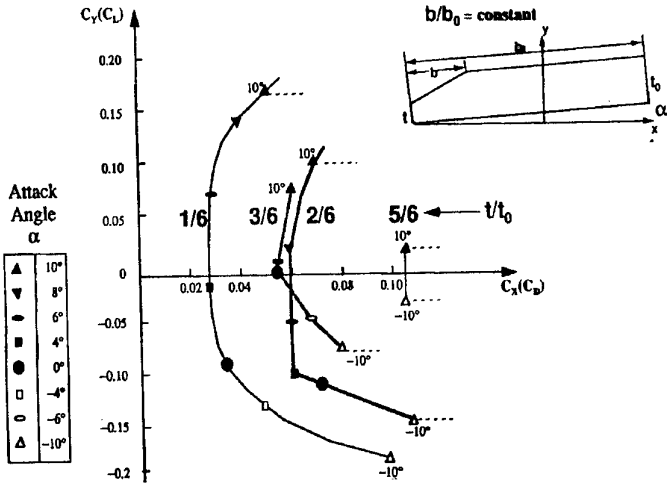
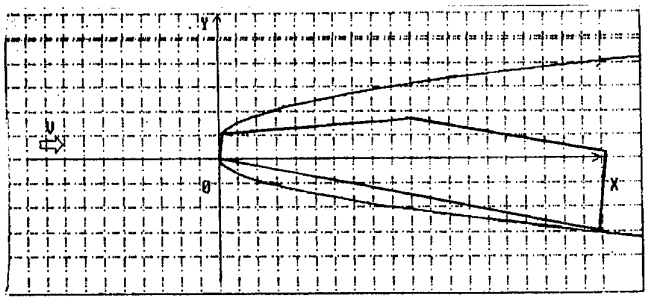


Fig.8. LEFT-DRAG CHARACTERISTICS AS A FUNCTION OF ATTACK ANGLE AND LEADING EDGE SHARPNESS

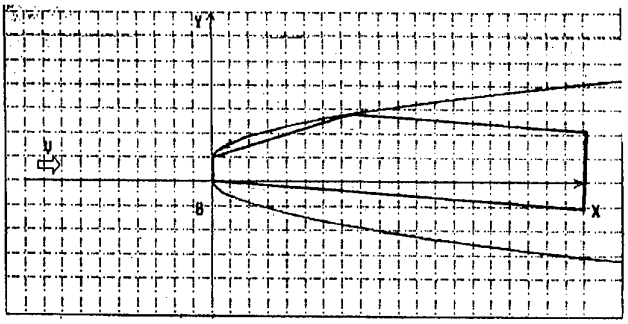


Angle of Attack: -8.5°

C_x = 0.865, C_y = 0.129, K = 0.149

XA(2) = 0.000, YA(2) = 2.000, XA(3) = 20.000, YA(3) = 6.400

Fig.9. LIMITING CASES FOR FITTING FOILS TO CAVITY SHAPES DERIVED FROM MODEL



Angle of Attack: -3.0°

C_x = 0.878, C_y = -0.046, K = -0.052

XA(2) = 0.000, YA(2) =2.000, XA(3) = 15.000, YA(3) = 6.400

Fig.10. LIMITING CASES FOR FITTING FOILS TO CAVITY SHAPES DERIVED FROM MODEL

CAVITATION SCALE EFFECTS

A REPRESENTATION OF ITS VISUAL APPEARANCE AND EMPIRICALLY FOUND RELATIONS

by

Andreas P. Keller
Munich University of Technology
Germany

SUMMARY

Incipient cavitation was measured on four rotational symmetric test body families and a NACA 16020 profile at four different angles of attack, varying the size of the test bodies, the free stream velocity, the viscosity, and the free stream turbulence level. By these experiments, it was determined that all four parameters have strong effect on the cavitation inception of submerged bodies. The dependencies of the cavitation number on these parameters are called scale effects.

As a prerequisite, the normally covering effect of the water quality, concerning its cavitation susceptibility, had to be got under control. This was achieved by measuring the tensile strength of the test water by means of vortex nozzle instrument.

The relations deduced from the experimental results lead to empirical scaling relations of stunning simplicity.

LIST OF SYMBOLS

C		constant, defined in text
Cp_{min}		min. pressure coefficient
K		characteristic cavitation index free of scale effects
K_0		basic value of K for turbulence level 0 %
L	(m)	characteristic length
P_∞	(N/m^2)	reference pressure
P_{crit}	(N/m^2)	critical pressure
P_V	(N/m^2)	vapor pressure
P_{ts}	(N/m^2)	tensile strength of test liquid
S	(m/s)	standard deviation of the free stream velocity
Tu	(%)	turbulence level S/V
V_∞	(m/s)	reference velocity
V_0	(m/s)	basic velocity of 12m/s
ρ	(kg/m^3)	mass density of liquid
σ		cavitation number
σ'		modified cav. number
σ_0		basic cavitation number of a test body for $V_\infty = 0$
σ_i		cav. inception number
σ_i'		mod. cav. incept. number
$\Delta\sigma_{ts}$		effect of tensile strength on cavitation number
$\Delta\sigma_T$		effect of turbulence on cavitation number
ν	(cSt)	kin. viscosity of liquid
ν_0	(cSt)	kin. viscosity of water at 20° Celsius

1. INTRODUCTION

This report strives to represent the problem of scaling cavitation phenomena and its technical relevance, and contains new experimental results in the field of cavitation inception research. Its focus is on the problems encountered when model tests are used to determine the cavitation behavior of a prototype. There are numerous examples where the model was observed to be cavitation free at design operating conditions, however, the prototype suffered extensive cavitation to severe damage under similar conditions.

The cavitation phenomenon has received widespread attention and intense investigation in many fields of engineering, ranging from aerospace to civil engineering, from ship building to turbine and pump industry. Although the occurrence of scale effects with model tests has long been well known and was already mentioned 1930 by Ackeret, it can be stated, that there is no generally accepted similarity law, neither for the transfer of model test results to the prototype, nor even for test results of identical or similar model bodies investigated in different test facilities. As early as 1963 the Cavitation Committee of the ITTC initiated a comparative test program related to cavitation inception on head forms. The results were widely scattered in that an increase of velocity lead to decreasing, constant or increasing cavitation indices (Lindgren, Johnsson, 1966).
Later, extensive comparative tests in the 70-ies on hydrofoils were initiated by the ITTC. The aim of the test program was to determine inception of different types of cavitation as a function of tunnel water speed and gas content ratio. Again the data showed large differences between the various tunnels and observers (ITTC, 1978). Fig. 1 shows the dilemma of incomparability of test results. It is one example of

Paper presented at an AGARD FDP Workshop on "High Speed Body Motion in Water", held in Kiev, Ukraine, 1-3 September 1997, and published in R-827.

many that can be found in the literature. Large differences in inception number and its velocity dependency are found between the tunnels involved.

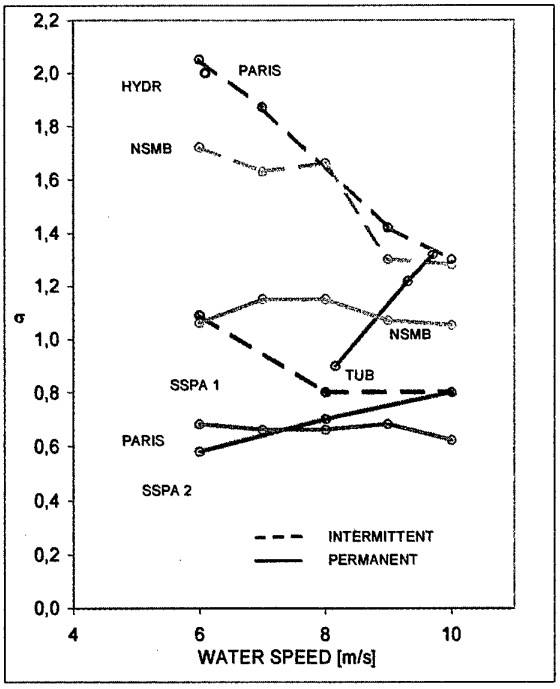


Fig. 1: Experiments on tip vortex cavitation on a hydrofoil circulated to several laboratories, as an example of the dilemma of uncomparativity of even the best test results available (ITTC, 1978).

Many summaries of this problem are available in the literature, and it is not the intent of this paper to provide yet another review. However, an attempt will be made to document the complexity of the scale effects, and to show the state of development of scaling laws, which were evaluated from long series of cavitation tests on different test body families at the hydraulic laboratory in Obernach.

2. VISUAL APPEARANCE OF THE SCALE EFFECTS FOR THE DIFFERENT PARAMETERS OF INFLUENCE FOR THE CAVITATION PHENOMENON

The classical cavitation index

For estimation of the danger of cavitation of hydraulic machines, such as pumps and turbines, elements of ships, or hydraulic structures in civil engineering, the beginning and subsequent development of cavitation phenomena are evaluated experimentally. The submerged parts are investigated as models in a test facility, and by means of e.g. the Thoma number its cavitation behavior is judged. The key parameter, which is used usually, is the dimensionless cavitation index

$$\sigma = 2\,(P_\infty - P_V) / \rho\, V_\infty^2 \qquad (1)$$

wherein P_∞ and V_∞ are a characteristic pressure and velocity of the flow upstream of the body, ρ and P_V represent the density and vapor pressure of the liquid, respectively. This classical relation (1) is deduced from the dimensionless minimum pressure coefficient, Cp_{min}, where it is assumed that the minimum pressure corresponds to the vapor pressure of the liquid.

The cavitation theory assumes, that the cavitation phenomena at the model and the prototype for geometrically similar bodies are identical at equal σ-values, irrespective of variations in physical parameters like body size, flow velocity, temperature, type of the liquid, etc. One particularly important value of σ is the value at which cavitation is first observed, for this cavitation condition is definable the most precisely. All conditions beyond this must be denoted as developed cavitation, and are not repeatable precisely for another observer. The difficulty of reproducing cavitation inception at one test body in different test facilities, is pointed out by the wide scatter of comparable results in the literature.

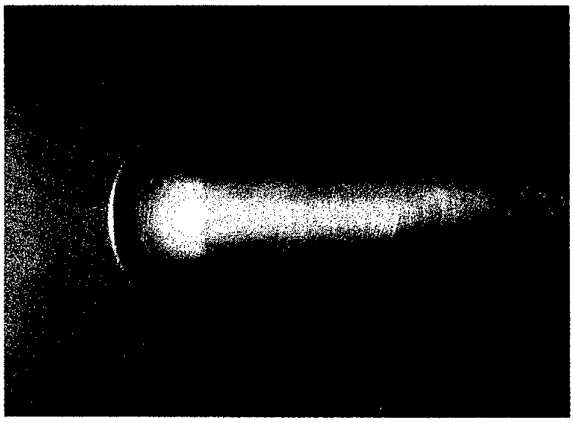
From systematic investigations and experience in practice it is well known, that the classical cavitation relation allows no sufficiently precise transfer of test results from the model to the prototype. At a submerged part of a prototype fully developed cavitation is visible, whilst at its model at identical cavitation number no or just beginning cavitation can be observed. Also, at identical test bodies, differently marked cavitation is observable if they are exposed to different velocities at equal σ-values. Differences in the viscosity of the fluid and the turbulence level of the flow have possibly additional strong effects on the extension of cavitation . These differences in the cavitation phenomena at model and prototype, or at one test body at equal σ but different flow parameters, are summarized under the term "scale effects".

Water Quality Effect

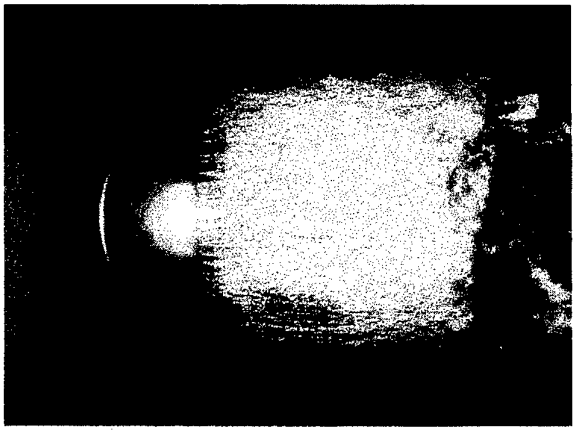
Basic supposition with cavitation investigations is, that the rupture of liquids begins when the pressure in the flow around a submerged body reaches vapor pressure, P_V, as equation (1) implies. The fact that cavitation tests at identical test bodies, or even the same test body, carried out in different test facilities lead to totally different results (e.g. Lindgren Johnson, 1966; ITTC, 1978) proves this assumption to be valid only as the exception. This wide range of experimental results can be attributed primarily to different tensile strength, P_{ts}, of the test liquid, i.e. to different water quality concerning its cavitation susceptibility.

The following photo series illustrate this fact. Photo series 1 shows the effect of tensile strength of the test water on the hemispherical test body. In the first photo,

no cavitation is observable due to high tensile strength of the test water, whilst at the second photo, at equal cavitation number (σ = 0.43) and equal flow velocity (V_∞ = 11.00 m/s) violent cavitation is registered after the capability of the water to withstand a tension is destroyed.



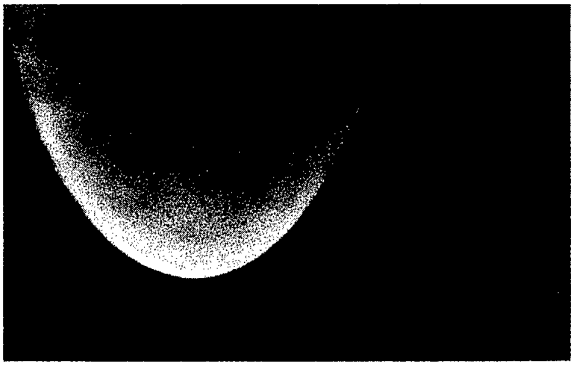
a) No cavitation, at high tensile strength of the test water; V_∞ = 11,00 m/s, σ = 0,43



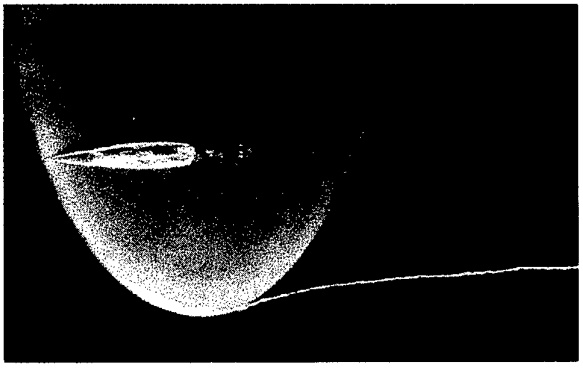
b) Developed cavitation after tensile strength of the test water is removed; V_∞= 11,00 m/s σ = 0,43

Photo series 1: Effect of tensile strength of the test water on the cavitation appearance, for the example of a hemispherical body (body diameter 60 mm)

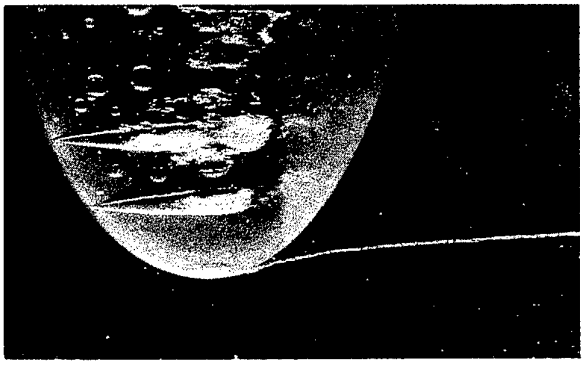
In photo series 2 the cavitation phenomena at the tip of a profile (NACA 16 020, angle of attack 6°) are shown, for three different water qualities at equal cavitation number (σ = 0.69) and equal flow velocity (V_∞ = 9.5 m/s). In the first photo no cavitation is visible at high tensile strength of the test water. In the second photo, for a water quality of zero tensile strength (definition see below), beginning tip vortex cavitation can be recognized. A fixed cavity, caused by a surface irregularity is also visible. For negative tensile strength of the test water, a fully developed tip vortex cavitation and single bubble cavitation at the profile is registered.



a) High tensile strength of the test water; no cavitation; V_∞= 9,50 m/s σ = 0,69



b) Zero tensile strength of the test water; beginning tip vortex cavitation;V_∞= 9,50 m/s, σ = 0,69



c) Negative tensile strength of the test water; travelling bubble and developed tip vortex cavitation; V_∞= 9,50 m/s, σ = 0,69

Photo series 2: Effect of the water quality on the cavitation appearance for the example of a NACA 16020 profile (chord 200mm, α = 6°)

The classical relationship (1) assumes that the critical pressure for the rupture of a liquid corresponds to its vapor pressure. However, the factual critical pressure, i.e. the tensile strength P_{ts} of a liquid, depends strongly on its gas content, its content of so-called cavitation nuclei, and its prehistory. Unquiescented water with high gas content can carry big bubbles in high concentration, so that this water quality cannot bear any

tensile strength. To the contrary, the bubbles grow in zones of low pressure even before reaching vapor pressure, and thus feign cavitation.. This water quality is denoted as negative tensile strength, and the corresponding cavitation phenomenon is called pseudo cavitation. On the other hand clean, degassed and quiescented water can attain high tensile strength, so that bubbles or cavities can develop only after the liquid is ruptured at pressures more or less far below vapor pressure. Thus the critical pressure of a liquid at cavitation inception can deviate to both sides from vapor pressure.

The number for beginning cavitation, σ_i, can be made free of water quality effects, by replacing vapor pressure, P_V, by the actual critical pressure for rupture of the liquid, $P_{crit} = P_V - P_{ts}$:

$$\sigma_i` = 2\,(P_\infty - P_{crit}) / \rho\, V_\infty^2$$
$$= 2\,[P_\infty - (P_v - P_{ts})] / \rho\, V_\infty^2 \qquad (2)$$

This modified cavitation number for inception, $\sigma_i`$ , can also be written in the form $\sigma_i` = \sigma_i + \Delta\sigma_{ts}$, with

$$\Delta\sigma_{ts} = 2\, P_{ts} / \rho\, V_\infty^2 \qquad (3)$$

As shown in Figure 2 schematically, the effect of the tensile strength, P_{ts}, of a liquid for cavitation tests can be essential. Whereas $\Delta\sigma$ for a given P_{ts} is relatively small for high velocities, it grows rapidly with decreasing velocity, and tends theoretically towards infinity when approaching zero velocity. With increasing velocity the curves asymptotically approach the curve for zero tensile strength, and then follow the velocity scaling law, i.e. increasing σ_i with increasing flow velocity (for definition of the velocity scaling law see later).

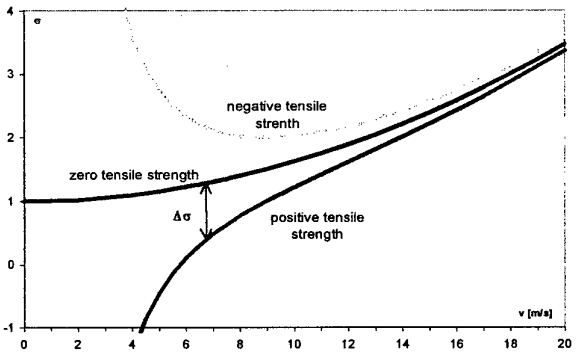


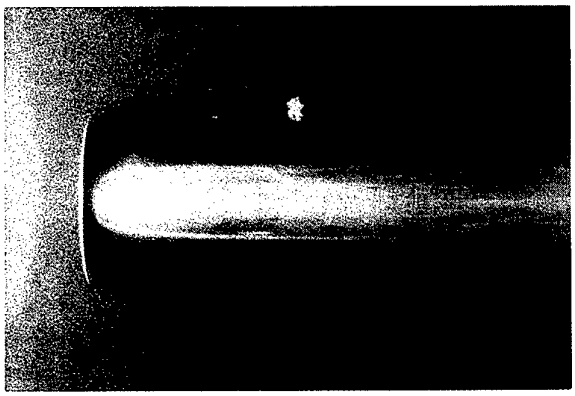
Fig. 2: Schematically represented test results for cavitation inception, with and without tensile strength of the test liquid (chosen tensile strength $P_{ts} = 0.2$ bar).

The results shown in the photo series, as well as the test results with different water qualities imply that cavitation phenomena react extremely sensitively to water quality. This explains the tremendous scatter of the results in comparable tests. Even small differences in water quality can lead to big differences in cavitation inception number. Thus water quality effects can lead to confusing results at cavitation tests, and this effect can outweigh real scale effects in cavitation tests, thus leading to totally wrong conclusions concerning the process for rationally extrapolating model data to estimates of prototype cavitation behavior of any given facility.

Therefore a measurement technique to determine the tensile strength of the test liquid was developed to its routinely applicable form, and used throughout the test program for the evaluation of the real scale effects. Details of this technique (Vortex Nozzle Chamber, VNC) as a cavitation susceptibility meter are already published, and will not be dealt with here (e.g. Keller, 1981,1984).

Velocity Scale Effect

The following photo series 3 gives an example of the velocity scale effect, meaning the appearance of cavitation at a submerged body at constant cavitation number σ for different flow velocities. The water quality concerning its cavitation susceptibility was held constant at zero tensile strength throughout the tests. Whilst at the respective lowest flow velocities just beginning cavitation can be recognized, at higher velocities distinctly further developed cavitation is observable at constant σ.



Cavitation inception at $\sigma = 0.41$, $V_\infty = 8.0$ m/s

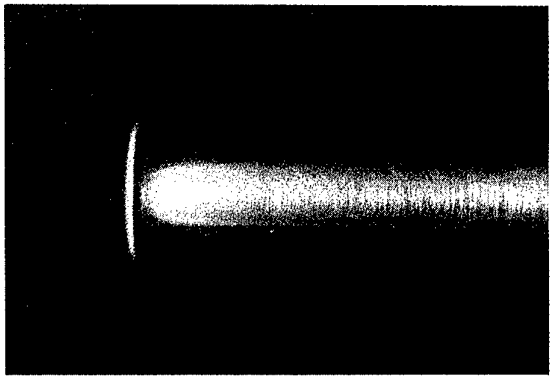


Developed cavitation at $\sigma = 0.41$, $V_\infty = 14.0$ m/s

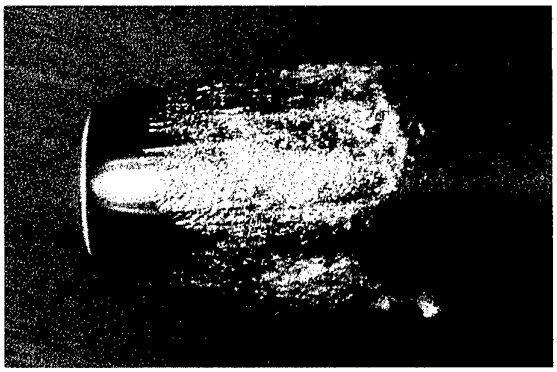
Photo series 3: Velocity scale effect for cavitation at the Schiebe body of 60 mm diameter

Size Scale Effect

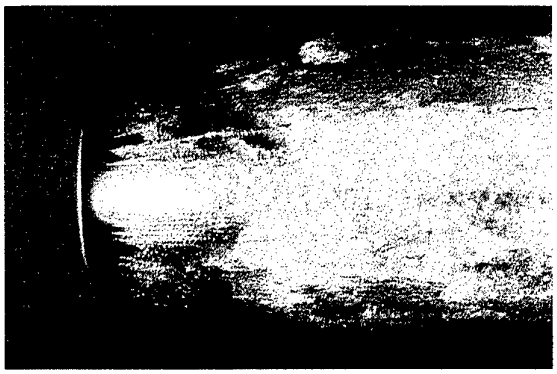
The photo series 4 gives an example of the size scale effect, i.e. the appearance of cavitation at three model bodies of identical form but of different size. Again the test conditions are equal cavitation number, and this time even equal flow velocity. Whilst at the respective smallest model just beginning cavitation can be recognized, with increasing body size distinctly further developed cavitation is visible.



a) body size: 15 mm, $\sigma = 0.26$, $V_\infty = 11.0$ m/s
beginning cavitation



b) body size: 30 mm, $\sigma = 0.26$, $V_\infty = 11.0$m/s
somewhat developed cavitation

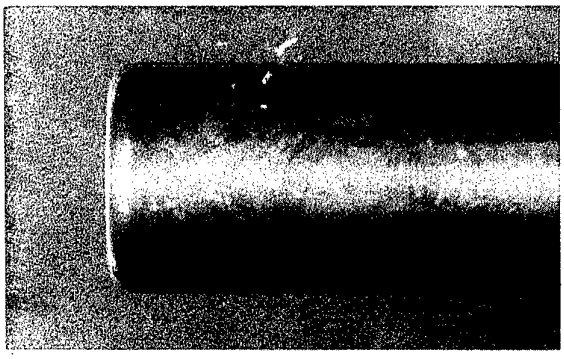


c) body size: 60 mm, $\sigma = 0.26$, $V_\infty = 11.0$ m/s,
fully developed cavitation

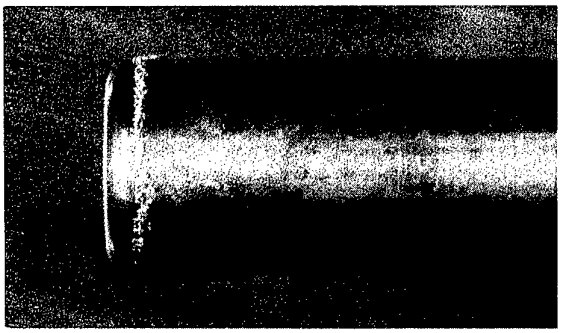
Photo series 4: Size scale effect for cavitation at the Schiebe body, for σ and V_∞ corresponding to cavitation inception at the smallest body size.

Turbulence Scale Effect

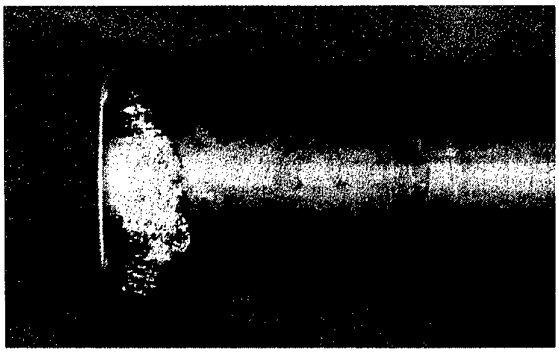
Most recent investigations reveal, that the turbulence level of the free flow also has an influence on the beginning and the development of cavitation at submerged bodies (Keller, 1996, 1997). At otherwise equal flow parameters, the cavitation inception number increases, or cavitation develops further at constant σ, with increasing flow turbulence. The photo series 5 illustrates these facts. For σ-values at cavitation inception and a natural turbulence level of the cavitation tunnel of ca. 1 %, the cavitation appearance develops just by increasing the flow turbulence.



a) cavitation inception, S = 0.08 m/s (Tu =1%),
σ = 1.78, V_∞ = 8.0 m/s, L = 30 mm



b) developed cavitation, S = 0.56 m/s (Tu = 7%),
σ = 1.78, V_∞ = 8.0 m/s, L = 30 mm



c) fully developed cavitation, S = 0.96 m/s (Tu =12%),
σ = 1.78, V_∞ = 8.0 m/s, L = 30 mm

Photo series 5: Turbulence scale effect for cavitation by example of the 1/8 caliber ogive body, at σ and V_∞ corresponding to cavitation inception at S = 0.08 m/s

Viscosity Scale Effect

With the application of the classical cavitation parameter σ (1) it is further assumed, that the cavitation conditions for model and prototype for geometrically similar bodies are identical also irrespective of the type of the liquid, i.e. irrespective of its viscosity. To investigate this parameter, extensive cavitation tests were conducted in glycerin- water mixtures.

These investigations revealed that the viscosity of a liquid has an tremendous effect on the cavitation occurrence at submerged bodies. The results are published elsewhere in detail (Keller, Kuzman-Anton, 1992; Keller, 1992, 1994). Unfortunately the viscosity scale effect was not documented in photo series.

3. THE EMPIRCALLY EVALUATED RELATIONS FOR THE SCALE EFFECTS

None of the parameters of influence represented above is taken into consideration in the classical relationship for cavitation (1). In the past years these parameters and their scale effects were investigated in long lasting test series in Obernach. By focusing on the parameter of influence generally blurring experimental results, i.e. the tensile strength of the liquid, clear dependencies for size, velocity, viscosity and turbulence scale effects were revealed, and it was proven, that cavitation tests performed without consideration of the "water quality" on cavitation susceptibility do not lead to useful and comparable results. Experimental results obtained with water quality considered, show a surprisingly clear regularity with regard to the real scale effects.

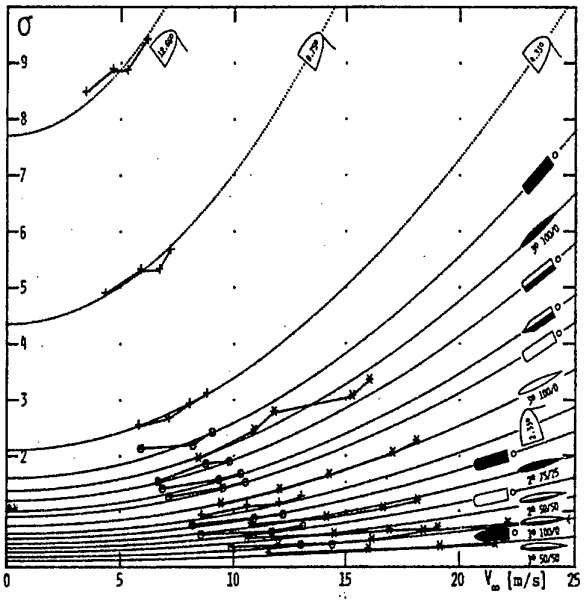


Fig. 3: Cavitation number - velocity relation for cavitation inception for all body types in liquids of zero tensile strength

As a summary, a representative selection of the results of all previously tested bodies are displayed in Fig. 3. The classical cavitation number σ for incipient cavitation is plotted versus the flow velocity V_∞ irrespective of shape, size, and liquid viscosity, the data points for all test bodies, connected by curves, show a steady increase of the σ-number with increasing velocity. The curves start from a basic σ-value, σ_0, for the reference velocity $V_\infty = 0$. Altogether there appears a striking regularity in the set of curves.

Velocity Scaling Relation

To show the evaluation of the velocity scaling relation for beginning cavitation, the same selection of test results as in Fig.3 is plotted in the most basic form, i.e. pressure P_∞ versus flow velocity V_∞ in Fig. 4. Again a regular set of curves appears, which converges as the velocity tends to zero. Since the water quality for all test series was kept to zero tensile strength, the point of convergence must correspond to vapor pressure (P_V = 2 kPa), as the visual check confirms.

A polynom of 4th power proved to be the most suitable relation to fit the test data in Fig. 4:

$$P_\infty = P_{crit} + c_1 V_\infty^2 + c_2 V_\infty^4 \qquad (4)$$

After some modifications of equation (4), the relation for the velocity scale effect presents itself as follows (for detailed deduction see Eickmann, 1992, Keller 1994):

$$\sigma_i = \sigma_0 (1 + V_\infty^2) / V_0^2) \qquad (5)$$

The basic value σ_0 is thus a characteristic parameter of a distinct body, from which the σ–value for each velocity can be calculated. The constant V_0 has proved to be a generally valid basic velocity (V_0 = 12,7 m/s), irrespective of the body shape, size, and type of fluid. At this velocity the σ number is twice the σ_0-value.

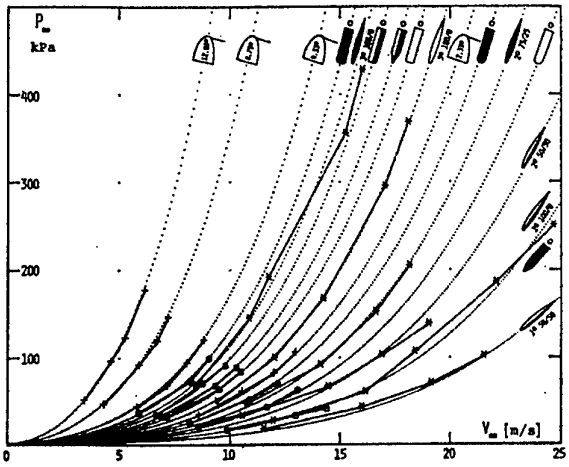


Fig. 4: Pressure - velocity relation for cav. inception for all body types in liquids of zero tensile strength

Size Scaling Relation

However, σ_0 is still dependent on the size of a geometrically similar body. The analysis of the test results concerning this parameter revealed, that the size scaling follows the square root of a characteristic dimension, L. A plot of σ_0 of a selection of test body families versus L (Fig. 5) confirms this; the data points can be very well approximated by parabolas, i.e

$$\sigma_0 = k\, L^{1/2} \qquad (6)$$

where the quantity k is now a characteristic factor which determines the cavitation behavior of a body shape.

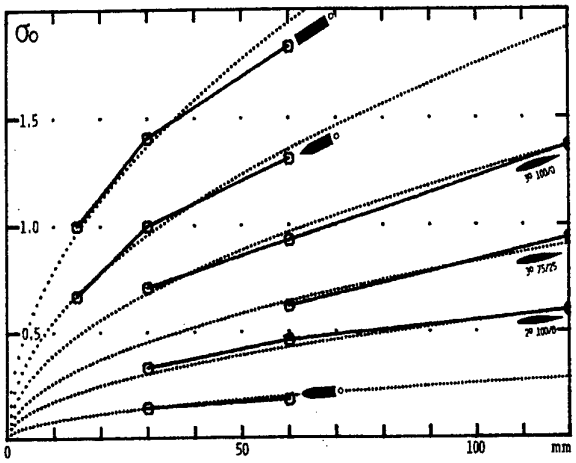


Fig. 5: Plot of basic cavitation number σ_0 versus size L of submerged bodies; rotational symmetric bodies and NACA 65 006 foils

The supposition, that σ_0 becomes zero irrespective of body shape, when the size of the test body converges to zero, is physically explainable, if one considers the fact, that at that point there is no difference anymore between the body shapes, no boundary layer can develop in the flow, etc.

Viscosity Scaling Relation

For model tests in water, and the transfer of the result to the prototype in water of approximately the same temperature and thus the same viscosity, this factor k would be applicable. However, if viscosity plays a role, then viscosity scale effects must be taken into consideration. In Fig. 6 the k-values of NACA 65 006 profiles, tested in water and water-glycerin mixtures are plotted versus the relation of the kinematic viscosity of water at 20° C, ν_0, to the kinematic viscosity of the liquid, ν , to the power 0.25.

The mean k-values for one angle of attack lie approximately on straight lines. The scatter of the results and the deviations from the regression lines must be considered under the aspect of very difficult achievement of zero tensile strength in the test liquids during the test series. Thus the viscosity scaling follows the law:

$$k = K\,(\nu_0/\nu)^{1/4} \qquad (7)$$

where K is a cavitation-related shape factor, now independent of flow velocity, size, and viscosity of the fluid.

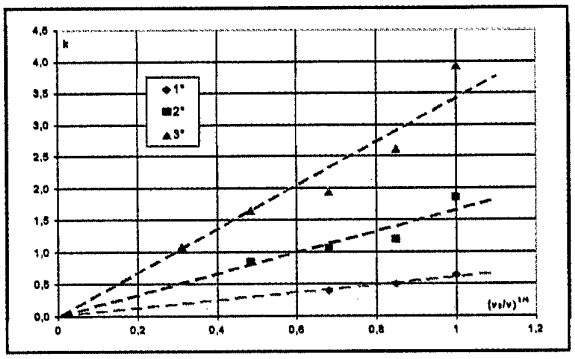


Fig. 6: k-value - viscosity relation, evaluated from test results at NACA 65 006 profiles of different size and angles of attack in water and water-glycerin mixtures of zero tensile strength.

Turbulence Scaling Relation

Finally, most recent investigations on the influence of the flow turbulence on cavitation reveal, that cavitation number σ increases with the turbulence intensity of the free flow (Keller, 1996, 1997). In Fig. 7 the connection between cavitation inception and flow turbulence is represented by example of the blunt test body family. A considerable growth of the classical cavitation number σ with the turbulence level Tu is ascertained. Besides this turbulence effect, the before mentioned scale effects for velocity and size are also evident.

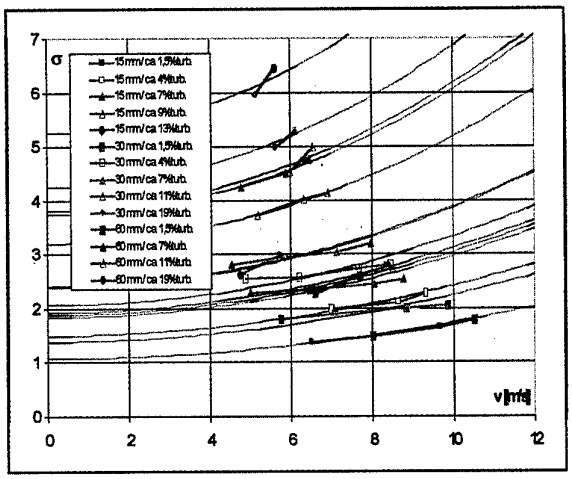


Fig. 7: Cavitation inception at the blunt test body family, in the conventional plot σ–value versus flow velocity, for turbulence levels of the free flow from natural up to ca. 20 %

In order to show the effect of the flow turbulence without the superimposed effects for velocity and size, in Fig. 8 the K-values of the blunt body family are plotted versus the standard deviation of the flow velocity, together with the regression line through the test data. In Fig. 9 the regression lines evaluated from the cavitation test data at four rotational symmetric bodies and a NACA profile at various angles of attack are plotted versus the standard deviation S, of the flow.

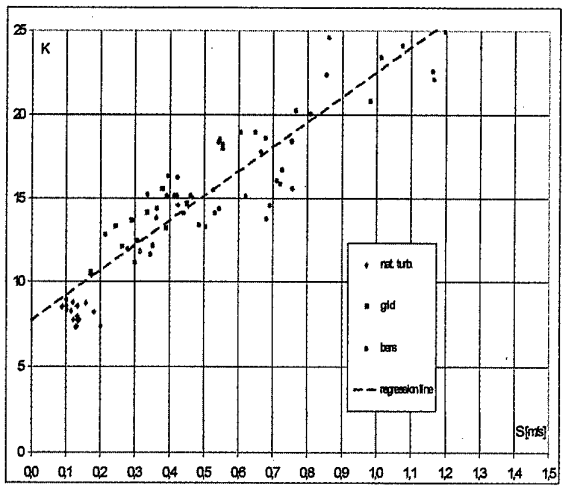


Fig. 8: New characteristic number K for cavitation inception at the blunt test body family, versus the standard deviation S of the free flow velocity, together with the regression line through the data points

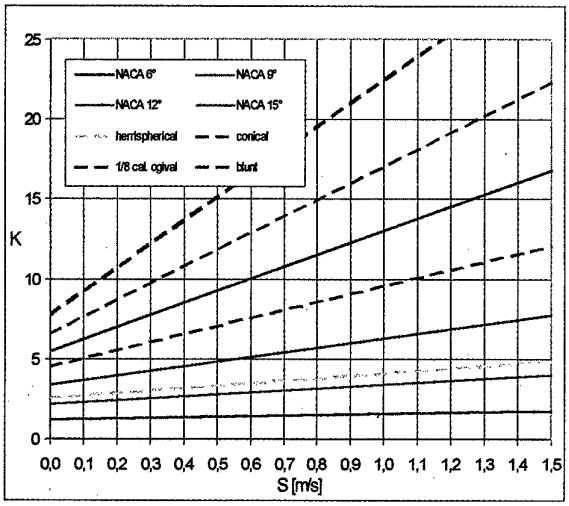


Fig. 9: Combination of the regression lines for the investigated rotational symmetric test bodies of different shape and a NACA profile at various angles of attack, versus the standard deviation of the free flow velocity

The dependency of the new characteristic parameters K on the standard deviation, S, of the velocity of the free flow can be approximated by the relation

$$K = K_0 (1 + K_0 S / 4) \qquad (8)$$

where K_0 represents a basic value of the new characteristic cavitation number K at a turbulence level of 0 %, S represents the standard deviation of the free flow. K_0 must be derived experimentally. The K_0-values evaluated so far are listed in Table 1.

Table 1: K_0-values of the investigated bodies

Testbody	K_0	Testbody	K_0
hemispherical	2.5	NACA, 6°	1.2
conical	4.5	NACA, 9°	2.2
1/8 cal. ogive	6.5	NACA, 12°	3.4
blunt	7.7	NACA, 15°	5.5

4. DISCUSSION

After removing the main factor for confusing and blurring test results, i.e. the liquid quality effects with regard to its tensile strength, and after carrying out extensive test series, where only one parameter of relevance was varied while all the others were kept constant, strikingly simple and clear relations for scale effects appear. Starting with equation (5) for the velocity scaling, and using the relations (6), (7) and (8), one gets the complete and purely empirical relation for all the investigated scale effects:

$$\sigma_i = K_0 L^{1/2} (\nu_0 / \nu)^{1/4} [1 + (V_\infty / V_0)^2] (1 + K_0 S / 4) \qquad (9)$$

Knowing K_0 for a certain body contour, the σ-number for cavitation inception at that type of body, for every size, flow velocity, viscosity of the fluid and turbulence level of the flow should be predictable. In principle the shape factor K_0 can be evaluated experimentally through a single cavitation experiment, by evaluating σ_i with the help of equation (2), for a certain model body of known size, flow velocity and its standard deviation, and known viscosity of the liquid. However, it must be ensured that the liquid quality, concerning its cavitation susceptibility, P_{ts}, is determined as precisely as possible.

All the shown results make it evident that there are deviations from the classical relation (1), which is based on the assumptions that all pressure differences in the flow are proportional to $0.5\ \rho V_\infty^2$, i.e. that no other forces than inertia forces are effective, and that the critical pressure for cavitation occurrence is the vapor pressure. This assumption also implies that σ_i should equal the minimum pressure coefficient Cp_{min}.

The reason for the departures from the classical theory must be looked for in viscous forces and bubble dynamics effects. The actual flow around a body and its pressure depart from the ideal flow, because of the boundary layer creating turbulent pressure fluctuations and other effects acting on cavitation nuclei carried in the flow. Thereby it is obvious that the cavitation phenomena respond as sensitive to the water quality as they respond to pressure fluctuations in the flow caused by viscous effects.

The similarity law for the departures caused by viscous effects is expressed by the Reynolds number. To maintain a constant ratio of inertia to viscous forces the Reynolds number, Re, must be kept constant.

$$Re = VL / \nu = const$$

Therefore often the cavitation number σ is correlated to the Re-number, or a certain power of it, respectively. If the classical similarity relation would hold, σ_i would be independent of Re, and if the scale effects are solely caused by viscous forces, there should be a clear dependency of σ_i on Re.

To demonstrate that this is not true, the above relations for size, velocity and viscosity are plotted in the σ-Re diagram. By applying equation (9) for the example of the hemispherical body (K_0 = 2.5), and starting at the point for the body size of 30 mm diameter, 10 m/s flow velocity, a turbulence level of ca. 1% and a cinematic viscosity for water at 20°C, i.e. Re = 298800, the σ_i-values are plotted versus Re, changing Re by varying the three Re-parameters, V_∞, L, and ν separately.

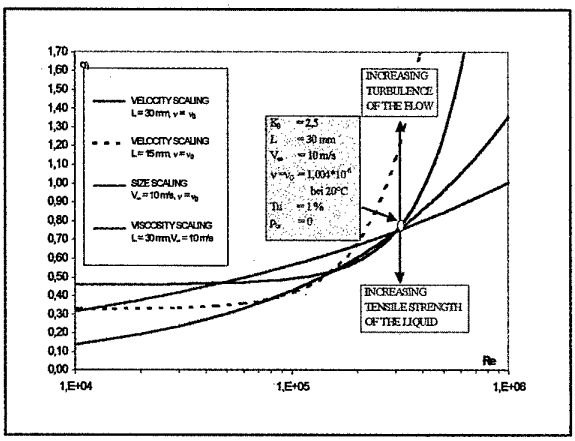


Fig. 10: Variations of σ_i with Reynolds number, by changing V_∞, L and ν separately.

In general, increasing the Re-number by increasing the flow velocity (V_∞), the body size (L), or decreasing the viscosity (ν), respectively, causes the σ_i-number to increase, however, the rate of increase is totally different, so that different σ_i-values result at equal Re--numbers even for the same body, depending on the Re-parameter changed .

The variations of σ_i with the turbulence level of the flow and the tensile strength of the liquid at constant Re-number are indicated by vertical arrows.

There is no indication at any of the presented results that an increase of the Re-number through size, velocity, or viscosity causes a decrease in the cavitation number, as is reported from several results in the literature. The decrease in σ_i with e.g. increasing velocity or size, can thus be only explained by an uncontrolled and unknown change of the water quality during the experiments.

Although the understanding of the physical mechanisms remains shallow, and analytical /numerical prediction methods are nonexistent, the reported findings leave hope that the pessimistic views listed in the introduction can be turned into more optimistic prospects. It seems that there is a universal kind of cavitation and a single scaling law will suffice. However, to find out the correct physical model for cavitation onset, more and sophisticated experiments are necessary.

5. CONCLUSIONS

The prediction, or better, the avoidance of cavitation, is the aim for the design of hydraulic machines and structures. Model tests are necessary because cavitation still evades exact theoretical prediction. With the transfer of model test results to the prototype, discrepancies arise from the expected cavitation behavior. These discrepancies are called scale effects.

The complexity and the number of the scale effects let account for the fundamental questions still open with the transfer of cavitation tests. Innumerable examples can be found, where a model was observed to be cavitation free at the design σ, and under similar conditions the prototype suffered extensive cavitation, which led possibly within short time to massive damages.

Through extensive experimental work the scale effects on hydrodynamic cavitation of flow velocity, body size, viscosity of the liquid, and flow turbulence were evaluated, after the covering effect of water quality, concerning its cavitation susceptibility, was got under control. Relations for the scale effects were evaluated, which altogether lead to the following overall relation:

$$\sigma_i = K_0 L^{1/2} (\nu_0 / \nu)^{1/4} [1 + (V_\infty / V_0)^2] (1 + K_0 S / 4)$$

This relation proved to be valid for all investigated body types. Only one basic characteristic parameter, K_0, for a distinct body shape is necessary to evaluate cavitation inception of this body at any size, flow velocity, viscosity of the liquid, and flow turbulence. The shape factor, K_0, must be evaluated experimentally by a cavitation test, under strict control of the water quality.

These purely empirical scaling relations are of stunning simplicity, and the general validity is astonishing. However, the relations should be checked by other observers in all kinds of facilities. But only if a standard water quality measuring instrument, respectively a critical pressure definition method is routinely used for the cavitation inception experiments, comparable test results can be expected.

The cavitation phenomenon proves to be as one of the

most difficult problems, with which an engineer in the area of hydromechanics is confronted. It is believed that the obtained findings about the influence of the different parameters on the cavitation appearance, and the derived empirical relations will provide a step forward in the efforts towards a better understanding of the extremely complicated cavitation phenomenon. It still remains a big need of further theoretical and experimental research in order to reveal the very process of cavitation inception and the scale effects.

6. LITERATURE

Ackeret, J.: "Experimentelle und theoretische Untersuchungen über Hohlraumbildung (Kavitation) im Wasser", Technische Mechanik und Thermodynamik, Monatliche Beihefte zur VDI-Zeitschrift, Berlin, Bd. 1, Nr. 1 und 2,1930

Arndt, R.E.A., Daily, J.W.: "Cavitation in Turbulent Boundary Layers", Prc. of the Symp. on Cavitation State of Knowledge, AS ME, Evanston, 1969

Eickmann G. :"Maßstabsgesetze der beginnenden Kavitation", Dissertation, Munich University of Technology, Rep. No.69 of the Hydraulic Laboratory Obernach, 1992

ITTC, Report of the Cavitation Committee, Appendix A, 1978

Keller, A.P.: "Tensile Strength of Liquids", Proc. of the 5th Intern. Symp. on Water Column Separation, IAHR Work Group, Obernach 1981

Keller, A.P.: "Maßstabseffekte bei der Anfangskavitation unter Berücksichtigung der Zugspannungsfestigkeit der Flüssigkeit", Pumpentagung Karlsruhe, 1984

Keller, A.P., Kuzman-Anton, A.F.: "Scaling of cavitation inception in liquids of higher viscosity than water, under consideration of the tensile strength of the liquids", 2eme Journees Cavitation, Societe Hydrotechniques de France, Paris, 1992

Keller, A.P.: "Cavitation Inception - new scaling laws, developed by consideration of a parameter of influence generally blurring experimental results", International Conference on Cavitation, Proceedings of the Institution of Mechanical Engineers, Cambridge, 1992

Keller, A.P.: "New Scaling Laws for Hydrodynamic Cavitation Inception", The Second International Symposium on Cavitation, Tokyo, Japan, 1994

Keller, A.P.: "Der Einfluß der Turbulenz der Anströmung auf den Kavitationsbeginn", Pumpentagung Karlsruhe, 1996

Keller, A.P.: "The Effect of Flow Turbulence on Cavitation Inception", ASME Fluids Engineering Division Summer Meeting, Vancouver, June 1997

Lindgren, H:, Johnsoson, C.-A.: "Cavitation Inception on Head Forms, ITTC Comparative Experiments", Report of Cavitation Committee, Proc. 11th ITTC, Tokyo, 1966

TIP VORTEX ROLL-UP AND CAVITATION IN WATER AND POLYMER SOLUTIONS

Daniel H. Fruman[1] and **Jean-Yves Billard**[2]

[1] Groupe Phénomènes d'Interface

Ecole Nationale Supérieure de TECHNIQUES AVANCEES

75739 Paris Cedex 15, France

[2] Laboratoire d'Hydrodynamique

Ecole navale

29240 Brest naval, France

SUMMARY

Results of experiments performed by ejecting semi-dilute drag reducing polymer solutions from an orifice situated at the tip of an elliptical hydrofoil are reported. It is demonstrated that the conditions for tip vortex cavitation occurrence are substantially modified by the ejection of very small flow rates of the polymer solutions while non appreciable alteration occurred when pure water is ejected. In order to investigate the causes of the cavitation inhibition effect, axial and tangential velocity profiles along the tip vortex in the very near region, comprised between the tip and one maximum chord downstream, were measured using Laser Doppler Anemometry. Statistical information on the moments and cross moments of the velocity fluctuations were also obtained. The ejection of the polymer solution results in the widening of the viscous core of the tip vortex, where the tangential velocities are reduced as compared to the pure water situation and the axial velocities display a marked wake effect. Changes are also apparent on the root mean square and skewness of the velocity fluctuations and on the cross moment of the axial and tangential velocity fluctuations. Analysis of the data indicates that the velocity modifications may be associated to the swelling of the polymer solution when issuing from the orifice. The changes of the velocity fluctuation and cross moments shows that they are essentially caused by the spatial bias introduced by the finite dimension of the measuring volume and the wandering of the vortex; "true" turbulence being a relatively small additional effect. By simulating the spatial bias effect it is shown that the ejection of the polymer solution results in a nearly complete suppression of the "true" turbulence in the core region.

1. INTRODUCTION

Since tip vortex cavitation is generally the earliest form of cavitation to occur, much attention has been devoted to investigate the conditions of inception and desinence on propellers and hydrofoils.

We recall that on a finite span wing, for specific conditions of reference pressure, mean velocity and angle of attack, the pressure at the tip vortex axis decreases below the vapour pressure and cavitation occurs along the vortex path. Thus, onset of cavitation can be predicted from the minimum pressure coefficient on the vortex axis, $C_{P\min}$, function of the local vortex intensity Γ, hence the lift coefficient C_l, and the viscous core size a. McCormick [1] hypothesized that the tip vortex core radius can be related to the foil boundary layer thickness and thus expressed as a function of the Reynolds number, Re, to a power n. Billet and Holl [2] have shown that the minimum pressure coefficient on the axis of a Rankine type vortex will be given, for fully turbulent boundary layer conditions prevailing on the foil surface, by :

$$C_{P\min} = k\, C_l^2\, Re^{0.4} = \sigma_{i,d} \qquad (1)$$

where k is a constant, function of the foil characteristics (planform, cross section). If cavitation occurs when the local pressure on the vortex axis is equal to the vapour pressure, the critical cavitation number for inception, σ_i, or desinence, σ_d, should be equal to $-C_{P\min}$.

Up to a very recent past, most of the results showed that the experimentally predicted $C_{P\min}$ (with sign changed) was generally higher than the critical cavitation number. Some authors (see Arndt and Keller, [3] and Green, [4]) assumed that either extraneous effects, such as pressure fluctuations due to turbulence, or water quality ("strong" or "weak" water) were responsible of the above mentioned disagreement. Moreover, the tangential velocity profiles used to estimate the core pressure were ill selected (situated too far downstream from the position were the minimum occurred), measured with a very poor spatial definition or without taking into account the bias measuring effect due to the vortex wandering. Under these circumstances, the possibility of equating the critical cavitation number to the minimum pressure coefficient computed numerically using a Navier-Stokes code (in the event the said code incorporates the proper turbulence model for intense rotating flows) and of validating expression (1), essential to be able to

Paper presented at an AGARD FDP Workshop on "High Speed Body Motion in Water", held in Kiev, Ukraine, 1-3 September 1997, and published in R-827.

accurately extrapolate the results obtained in small cavitation tunnels to prototype operating conditions, was subject to criticism. Moreover, no appropriate methodology to distinguish the contribution of pressure fluctuations, measuring bias and water quality was offered.

In order to respond to these interrogations, a detailed investigation of tip vortex roll-up and cavitation inception (desinence) has been conducted in a variety of cavitation tunnels with the sponsorship of the Direction des Recherches et de la Technologie (DRET) Ministry of Defence, France, under the Action Concertée Cavitation Program [5]. The foil geometry - cross section and planform -, the flow conditions (Reynolds number, background turbulence and boundary layer transition promotion), the water quality, as well as the consequence of drag-reducing polymer solution ejection from the tip of the foils were some of the many parameters whose impact was to be determined. The procedure developed by the participants to the ACC was to conduct detailed measurements of axial and tangential velocities in the very near region (less than a chord downstream the tip), allowing to establish the evolution of the local intensity, the local core radius and the minimum pressure coefficient on the axis of the tip vortex. In the majority of the test conditions the minimum of the pressure coefficient on the vortex axis compares very favourably to the critical cavitation numbers.

The objective of this paper is to present the results of a research conducted to investigate the effect of the ejection of solutions of a drag reducing polymer on tip vortex cavitation. Earlier investigations, Aflalo [6] and Fruman and Aflalo [7], demonstrated that ejection of these solutions at very low flow rates at the tip of an elliptical hydrofoil was an effective way of delaying cavitation occurrence. By performing some limited tangential velocity measurements at a single station far from the foil tip, Aflalo [6] was able to show that the main effect of the polymer ejection was to increase the diameter of the vortex (viscous) core and thus to decrease the maximum tangential velocity without modifying, in any significant way, the tip vortex intensity (circulation). Thus, the pressure at the axis is increased as compared with the no ejection situation. Equal mass ejection rates of water and water plus glycerine solutions were shown not to alter the tip vortex occurrence conditions. The cavitation inhibition was thus associated to the viscoelastic properties of the polymer solutions. It was speculated that the jet coming out from the ejection orifice swells in such a way that the roll-up of the potential flow occurs over a fictitious rounded tip. The promising results shown by Aflalo [6] and Fruman and Aflalo [7] with an elliptical foil at very low ($\approx 0.2 \times 10^6$) Reynolds numbers have been confirmed by Chahine *et al.* [8] in the case of polymer ejected through appropriate orifices at the tip of the blades of a 29 cm diameter propeller. With a polymer concentration of 3000 ppm and a flow rate of about 1.3 cm^3/s they were able to achieve critical cavitation number reductions of about 35%. In this presentation we concentrate on results obtained with a foil twice as large as the one employed by Aflalo [6] and at larger flow velocities, thus much larger Reynolds numbers [9]. Also, detailed axial and tangential velocities and velocity fluctuations measurements in the very near region allow to provide more information on basic aspects of tip-vortex roll-up and turbulence development in the very near region [10].

2. EXPERIMENTAL

2.1 Experimental facility

Experiments were conducted in the Ecole Navale Cavitation Tunnel (ENCT) with a 3.8 area ratio elliptical hydrofoil having a NACA 16020 cross section and a maximum chord length of 80 mm. The lift coefficient for the base foil in pure water with and without the ejection port have been given in Fruman *et al.* [9, 11]. The wing was mounted horizontally on one of the vertical walls of the test section, as described by Fruman *et al.* [12]. Lift and drag forces were measured using a three component strain gauge balance. Axial and tangential velocities were measured using a two component Dantec Laser Doppler Velocimetry (LDV) system operating in the back-scattering mode. For the optical configuration selected, the measuring volume is 0.5 mm long and 0.04 mm wide. The circulating water and the ejected fluid were seeded with Iriodine in order to increase the data rate.

The ejection port was situated just at the foil tip and has a diameter of 1 mm, as the one used by Aflalo [6]. Ejection tests were conducted with aqueous solutions of Poly(ethylene) oxide POLYOX WSR 301 (provided by Union Carbide), a very effective drag-reducing polymer conferring to the solvent marked viscoelastic properties. A master solution of 1000 ppm was fabricated 24 hours prior to the tunnel tests in order to assure a well homogenized solution. The polymer solution contained in a 0.1 m^3 reservoir is pressure driven through a rotameter into the ejection port. This rotameter was calibrated prior the tests by measuring the volume discharged during a given time. Ejection rates selected for the tests were 4.7 or 3.4 cm^3/s for the polymer solutions and 5.5 cm^3/s for water.

2.2 Experimental procedures

Tip vortex cavitation inception and desinence were obtained from direct visual observation of the test section, improved using a stroboscopic light source. In order to guarantee the best tests conditions, a specific procedure was implemented. For a given free stream velocity and no ejection, the reference pressure was decreased until incipient conditions were reached. The pressure was then further reduced in order to develop a cavity within the tip vortex. Then, the desinent condition was determined by increasing the pressure. At this point the polymer ejection flow rate was set and the pressure was varied down and up as for the no ejection tests. The incidence angle was then changed and the whole procedure repeated. Only the data obtained for a given set of no-ejection/ejection tests are compared.

During all this procedure, the hydrodynamic forces were checked in order to assess any change due to the increase of the polymer concentration in the circulating water. The final homogeneous polymer concentration built up in the tunnel at the end of the ejection tests did not exceed one ppm, well below the levels ($\approx$10 ppm) for which Fruman and Aflalo [7] have reported significant lift changes in homogeneous polymer solutions.

For LDV measurements, with or without ejection, the centre

of the vortex is first approached by making the point of crossing of the laser beams to coincide with the cavities convected in the vortex path for a cavitation number slightly below the critical one. Then, the precise location of the axis is determined by velocity measurements within a short distance around this approached position, as described in Fruman *et al.* [11]. The velocity profiles are measured along a direction, y, parallel to the span, positive outboard and passing through the vortex axis. The downstream distance, x, is referred to the tip of the foil, taken as the origin. Measurements were conducted for x/c_{max}, where c_{max} is the maximum chord, of 0.125, 0.25, 0.5 and 1.0. The rough signal from the LDV is treated by two Burst Spectrum Analyser (BSA) from Dantec [13] giving the mean,

$$U = \frac{1}{N}\sum_i U_i \tag{2}$$

of each velocity component, the root mean square,

$$\mathrm{RMS} = \left[\frac{1}{N}\sum_i (U_i - \overline{U})^2\right]^{1/2} \tag{3}$$

and the skewness,

$$\mathrm{Sk} = \frac{1}{\mathrm{RMS}^3\, N}\sum_i (U_i - \overline{U})^3 \tag{4}$$

of the velocity fluctuations, as well as the product of the axial (index a) and tangential (index t) fluctuations,

$$V_t' V_a' = \frac{1}{N}\sum_i (U_i - \overline{U})(V_i - \overline{V}) \tag{5}$$

These values are recorded on a hard disk for off-line treatment. In these expressions U_i is an instantaneous measurement of the velocity depending both on the time an on the position of the detected particle in the measuring volume even if, in the treatment, the position information is ignored.

The relative error of the lift coefficient is estimated to be less than ±2%, taking into account the uncertainties associated with the lift force measurement and the free stream velocity, respectively ±0.5% and ±0.75%. The uncertainty associated with the cavitation number is less than the standard deviation, ±2.5%, of experimental data issued from repeated tests conducted at a given angle of attack and free stream velocity. The LDV measurements are associated with a random uncertainty estimated to be less than ±1.5% which is issued from the electronic and numerical treatment of the Doppler signal giving the instantaneous velocity. For large enough samples, it can be expected that the error on the mean value is much less than 1.5%. The mean velocity values are the mean of about 2500 readings for each position. The ejection rate uncertainty is about ±3%.

3. RESULTS

3.1 Critical cavitation numbers

The cavitation number is defined as,

$$\sigma = 2\frac{P_\infty - P_v}{\rho V_\infty^2} \tag{6}$$

where P_v and ρ are respectively the vapour pressure and the specific mass at the temperature of the circulating water, and P_∞ and V_∞, the reference pressure and the free stream velocity measured at the entrance of the test section. The inception and desinent cavitation numbers without polymer ejection (σ_i and σ_d respectively) are plotted in Figure 1 together with the results for an ejection of a 1000 ppm polymer solution (σ_{ie} and σ_{de} respectively) at a flow rate of 4.7 cm^3/s as a function of the angle of attack for two free stream velocities corresponding to Reynolds numbers of 0.62×10^6 and 10^6. In both cases, ejection results in a decrease of over 20% of the cavitation numbers.

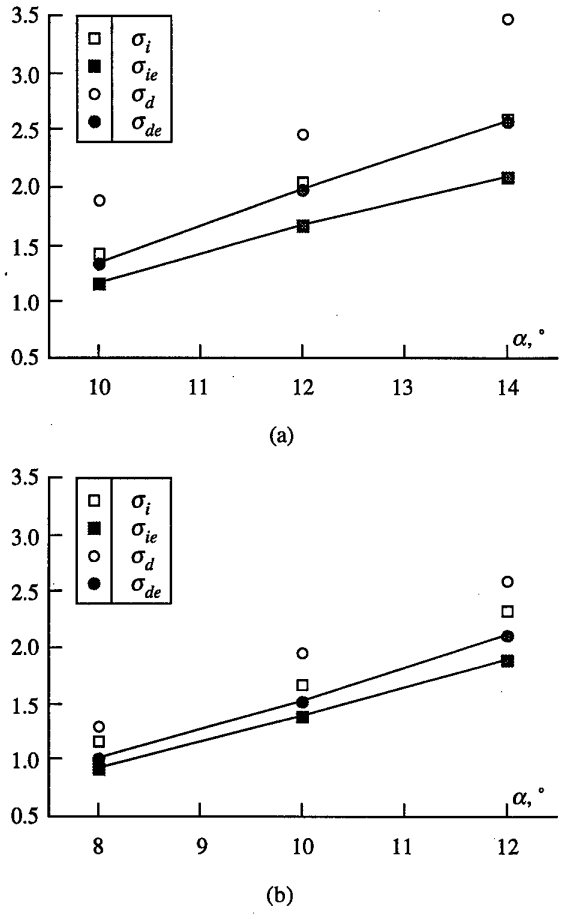


Fig. 1 : Critical cavitation numbers as a function of the angle of attack for (a), $Re = 0.62 \times 10^6$ and (b), $Re = 10^6$. (polymer concentration : 1000 ppm, ejection rate : 4.7 cm^3/s).

Figure 2 shows that the desinent cavitation numbers obtained during the ejection of polymer solutions with concentrations of 1000 and 500 ppm and an ejection rate of 4.7 cm^3/s are within the experimental errors. A 30% reduction of the ejection flow rate, from 4.7 to 3.4 cm^3/s, do not causes either a significant modification of the cavitation conditions, Figure 3.

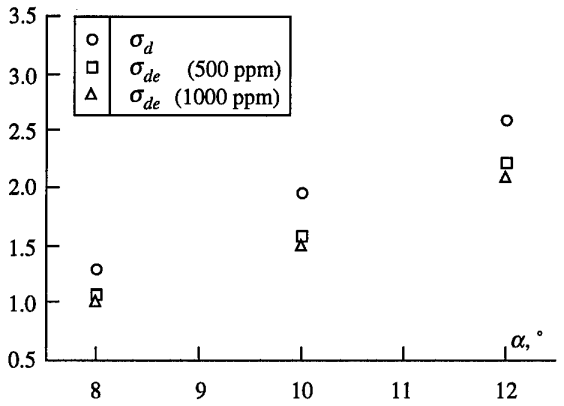


Fig. 2 : Desinent cavitation number as a function of the angle of attack for two injected polymer concentrations; ($Re = 10^6$; ejection rate: 4.7 cm^3/s).

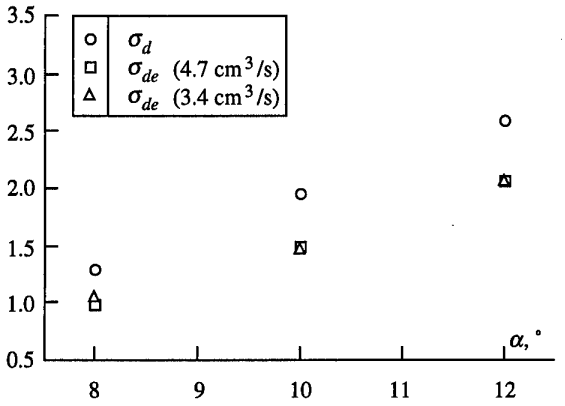


Fig. 3 : Desinent cavitation number as a function of the angle of attack for two injection rates ($Re = 10^6$, polymer concentration : 1000 ppm).

3.2 LDV measurements

Figure 4 shows the profiles of the non dimensional axial, V_a / V_∞, and tangential, V_t / V_∞, velocity components at four stations within one chord from the tip, for an angle of attack of 10°, a free stream velocity of 12.5 m/s ($Re = 10^6$) and three conditions : no ejection, ejection of a 1000 ppm polymer solution at a rate of 4.7 cm^3/s and ejection of water at 5.5 cm^3/s (for only two stations). Positive values of y / c_{max} correspond to the outboard positions.

The tangential velocities display in all cases a solid body rotation region, where velocities increase linearly with distance to the vortex axis, an intermediate transition region and a potential region, where velocities are inversely proportional to the distance to the vortex axis. Only minor modifications of the tangential velocity profiles occur during water ejection. However, the ejection of the polymer solution causes a significant reduction of the maximum velocity and an appreciable increase of the size of the viscous core, while the potential region remains unchanged. These results are qualitatively analogous to those obtained by Aflalo [6] in his early investigation. It should be pointed out, however, that the present results offer a much detailed spatial resolution and a unique view of the effects taking place in the very near region downstream the vortex.

Without mass ejection from the tip, the axial velocities are nearly constant everywhere. Mass ejection of water or polymer solution causes a reduction of the velocities in the viscous core region. At the station closest to the tip, the effects of the polymer solution are significantly larger than those of water. When the distance increases, the difference between water and polymer solution ejection fades away, but the velocity defect persists.

Figure 5 shows, for the pure water and the polymer solution ejection situations and at one maximum chord downstream the tip, the root mean square (RMS) and skewness (Sk) of the velocity fluctuation of the tangential and axial components.

As compared to the pure water situation, the changes due to the polymer ejection can be summarized as follows :

i) the maximum tangential velocity fluctuation is much reduced,

ii) the axial velocity fluctuation is increased and develops a saddle type behaviour in the core region, the minimum coincides with the centre of the vortex, the maximum on each side are at the same position that the extreme of the tangential velocity,

iii) the skewness of the tangential velocity component has its maximum and the slope in the core region reduced and the scatter in the potential region increased,

iv) the skewness of the axial velocity components becomes more organized in the core region and with limited scatter in the potential region.

The cross moment, Figure 6, develops a positive contribution as large as the negative one ; the latter being smaller than in pure water. More details about the RMS, Sk and cross moment distributions are given below.

RMS

Whatever the station, the tangential velocity fluctuations in pure water are nearly symmetrical with respect to the maximum, centred on the vortex axis, affected by a very limited scatter and show practically the same maximum. For the polymer solution ejection and the station closest to the tip, the scatter is significant and the maximum, smaller than in the case of pure water, is on the onboard side of the vortex. Moving downstream, the maximum decreases slightly and the symmetry is recovered at distances larger than half a maximum chord. For the axial velocity fluctuations the major change is associated with the occurrence of a saddle type behaviour everywhere but particularly marked, in amplitude and extent, at the first station.

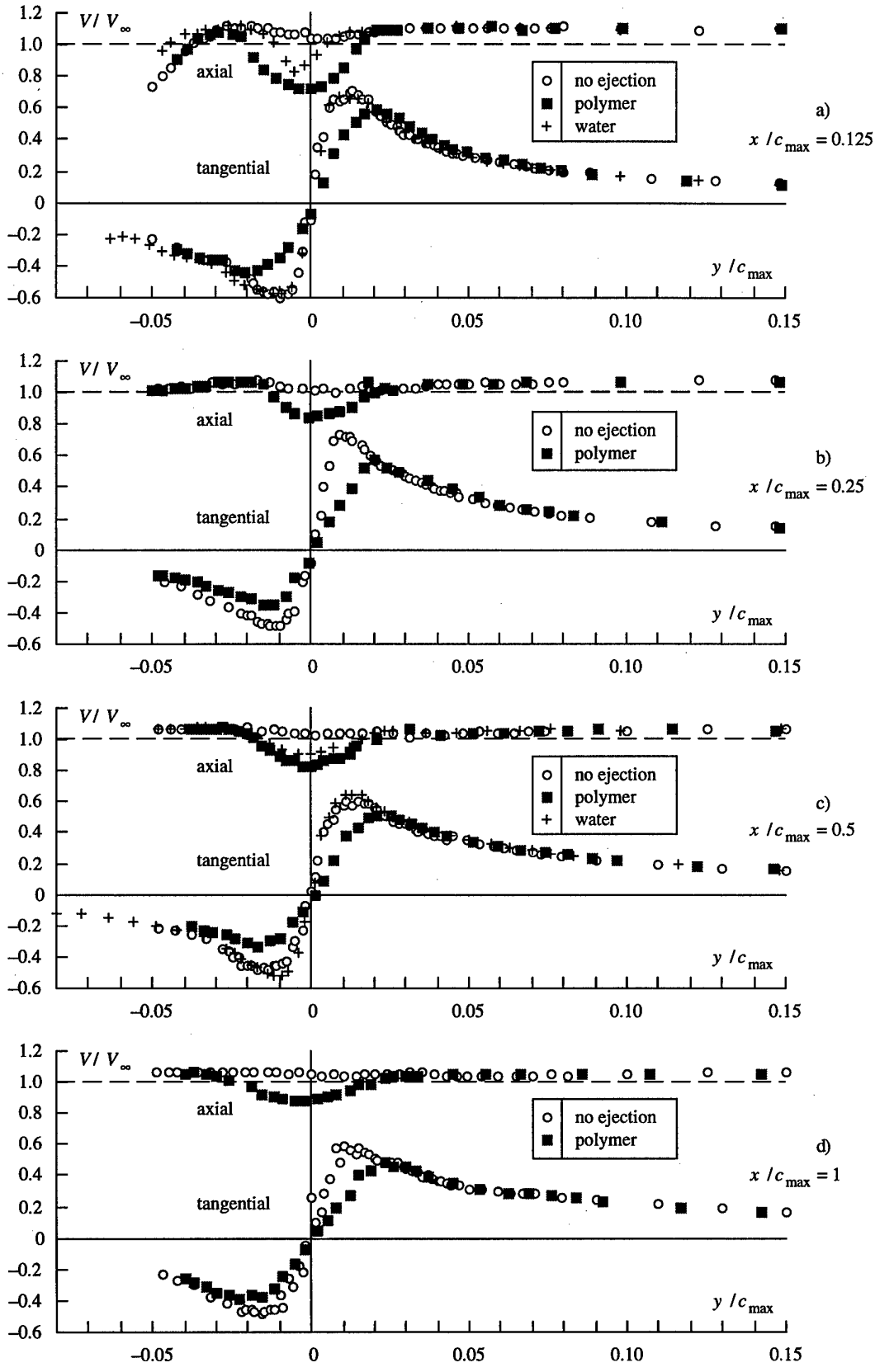


Figure 4a-d : Non-dimensional tangential and axial velocities as a function of distance to the vortex axis for different axial stations ($\alpha = 10°$, $Re = 10^6$, polymer concentration : 1000 ppm)

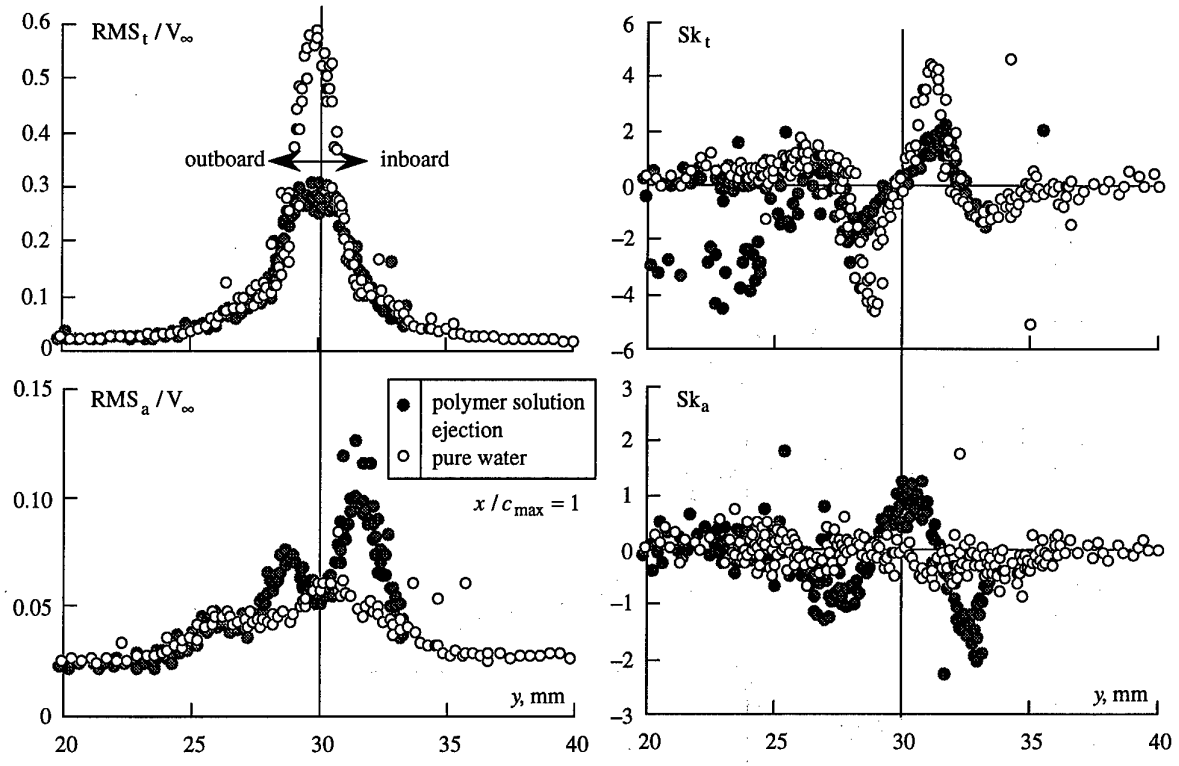


Figure 5 : Root mean square and skewness of the velocity fluctuation at one maximum chord downstream the foil tip for water and polymer solution ejection.

Skewness

For water and polymer ejection, distance has very limited effect on skewness of the tangential velocity ; the slopes of the linear region remain the same as well as the maximum and minimum amplitudes. For polymer ejection, in the outboard potential region the scatter is extremely large whatever the distance to the foil tip. This contrasts with the behaviour in pure water ; nearly free of scatter in the potential region. The skewness of the axial velocity in pure water shows a near zero level in the potential region for all the stations. In the core region and for the closest station to the tip, negative values occur. They decay very rapidly downstream and level off at one chord where the zero level is reached everywhere. With the polymer solution ejection, the mean level in the potential region is nearly constant and close to zero without any significant scatter. In the core region, the very distinct shape developed at the station closest to the tip decays when moving downstream but remains still significant at one chord.

Cross moment

The cross moment in pure water is characterized, for x/c_{max} equal to or larger than 0.50, by a single negative bucket centred on the vortex axis surrounded by a flat, zero value region, corresponding to the potential part of the flow both on and outboard. The ejection of the polymer solution develops, for x/c_{max} equal to or larger than 0.25, a peculiar pattern mainly associated, as it will be seen next, to the large axial velocity deficit. The absolute values of the maximum and minimum are comparable, showing the absence of a non symmetrical contribution due to the "true" turbulence, as in the case of pure-water flow.

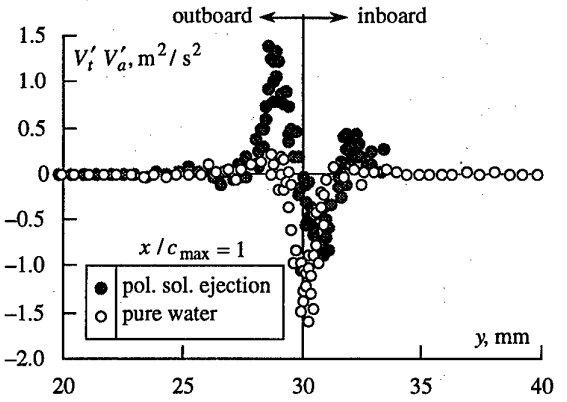


Fig. 6 : Cross moment of the tangential and axial velocity fluctuations at one maximum chord downstream the foil tip for water and polymer solution ejection.

4. DISCUSSION AND INTERPRETATION

4.1 Critical cavitation numbers

Tests performed in the range of Reynolds numbers encountered at the ENCT display an improvement of up to 30% in the cavitation numbers as the polymer solution is ejected in the vortex core. Thus, for given reference

pressure and angle of attack, the free stream velocity can be increased up to 15% with the polymer ejection without cavitation inception. Since the lift coefficient of the foil measured during the ejection tests did not show any distinguishable difference as compared to pure water, the reduction of the critical cavitation numbers can not be ascribed to a reduction of the foil bound circulation in the mid-plane. Cavitation tests conducted with water ejection at a flow rate of 5.5 cm^3/s did not display changes of the critical cavitation numbers. Moreover, Fruman ([14], [7]) and Chahine *et al.* [8] showed that a water-glycerine solution with a viscosity larger than the one associated with the polymer solution used during these measurements, does not lead to a modification in the measured critical cavitation numbers. Hence, the observed delay is neither the result of mass addition in the vortex core nor caused by improved diffusion due to increased viscosity. Only the polymer viscoelastic properties can be made responsible of the observed effects.

Furthermore, for the experimental conditions tested, no significant effect of the ejection rate was noticed. This can be associated to the saturation effect shown by Fruman and Aflalo [7] to exists in their tests for a 1000 ppm polymer solution at ejection rates larger than 0.7 cm^3/s and a Reynolds number of 0.2×10^6. Since the ejection rate scales with the Reynolds number, for the present tests at a Reynolds numbers of about 10^6 the lower limit for saturation will be 3.5 cm^3/s, value corresponding to the minimum selected for performing the experiments. The physical explanation for this saturation effect can be traced to the existence of a maximum possible jet swelling, as shown by Fruman *et al.* [15] in the case of jets ejected in stagnant fluids, and to the fact that, for axisymmetric jets, swelling increases only as the 1/3 power of the ejection velocity (Ouibrahim *et al.* [16]).

For an axisymmetric vortex, the radial equilibrium equation is given by,

$$\frac{\partial}{\partial r}(p-\sigma_{rr})=\rho\frac{V_t^2}{r}-\frac{\sigma_{\theta\theta}-\sigma_{rr}}{r} \qquad (7)$$

where σ_{rr} and $\sigma_{\theta\theta}$ are the normal stresses along the radial and tangential directions. If we assume that $\sigma_{rr} = 0$ for a point situated at a large distance to the vortex axis, then, the integration between infinite and the axis gives,

$$(P-\sigma_{rr})_0 = P_\infty - \rho\int_0^\infty \frac{V_t^2}{r}dr - \int_0^\infty \frac{\sigma_{rr}-\sigma_{\theta\theta}}{r}dr \qquad (8)$$

The pressure at the axis of the vortex can be modified either by the modification of the tangential velocity profile or the introduction of normal stresses associated with the viscoelastic behaviour of the ejected polymer solution.

For a Newtonian fluid, the contribution of the second normal stress difference, $\sigma_{rr} - \sigma_{\theta\theta}$, is zero and the pressure coefficient at the vortex axis, Cp, can be determined from the tangential velocity profiles,

$$Cp = 2\frac{P_0 - P_\infty}{\rho V_\infty^2} = -\frac{2}{V_\infty^2}\int_0^\infty \frac{V_t^2}{r}dr \qquad (9)$$

In Figure 7, the pressure coefficients (with sign changed) computed using expression (9) are plotted as a function of the downstream distance for the no ejection and polymer ejection cases. The corresponding desinent cavitation numbers with and without polymer ejection are also indicated.

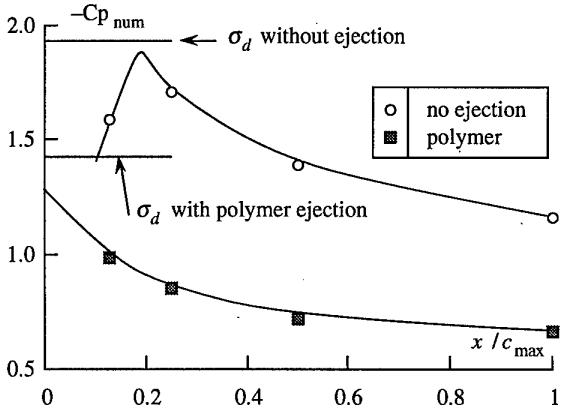


Fig. 7 : Computed pressure coefficient as a function of the downstream distance ($\alpha = 10°$, $Re = 10^6$).

The no ejection data clearly indicate that a minimum could exist in between the 0.125 and 0.25 c_{max} stations as clearly demonstrated by previous investigations (Fruman *et al.* ([11], [12])). The minimum pressure coefficient will be thus larger than the value corresponding to 0.25 c_{max}, estimated to be –1.71. This value is higher than the desinent cavitation number (with sign changed), –1.93, but reasonable close as the tentative curve fitting shows.

With polymer ejection a tentative extrapolation of the pressure coefficient data indicates that the minimum occurs probably nearer the tip that in the case of no ejection. At the tip, the extrapolated value can be estimated to be about –1.3, larger but reasonably close to the desinent cavitation number with sign changed, –1.49.

To our knowledge, only the swelling of the jet issuing from the ejection port has been made responsible of the increase of the pressure coefficient and the decrease of the critical cavitation numbers. Fruman and Aflalo [7] stated that "the polymer solution ejected at the tip of the wing swells when exiting the capillary tube and modifies the roll-up process by creating a displacement effect", readily seen in Figure 4 to be of about 0.35 mm at the station nearest the tip. If it is assumed that this increase corresponds to the swelling of the jet issuing from the ejection port, the relative swelling (ratio of the swollen jet diameter to the port diameter) will be of 1.7. Fruman and Galivel [17] have investigated the behaviour of wall polymer jets ejected from two dimensional slits into a coflowing stream and shown that the relative swelling was about 2 for a free stream velocity of nearly 8 m/s, an ejection velocity over slit thickness of 4200 s^{-1} and a polymer concentration of 2000 ppm. Because in the present situation the free stream velocity is larger (12.5 m/s), the concentration smaller (1000 ppm) and the ejection velocity to port diameter ratio slightly larger (≈6000 s^{-1}), the value estimated above seems to be reasonable. Moreover, an explanation based on the

modification of the core dimension is consistent with the fact that the growth of the jet persists over long distances as a result of the known coherence of polymer jets and decreased diffusion of polymer solutions.

4.2 LDV measurements

All LDV velocity and velocity fluctuations measurements are directly affected by the slope and curvature of the ideal instantaneous velocity profile. The reason lies in the fact that over the finite dimension of the measuring volume, particles will have different velocities depending on their position. As a result, the histograms of velocities will extend between the minimum and the maximum of the portion of the instantaneous velocity profile included in the measuring volume with a probability favouring the faster particles. To this purely mechanical histogram, giving the impression of apparent velocity fluctuations, a turbulence effect will be additioned. If the ideal instantaneous velocity profile is subjected to motions in space, vortex wandering in the present case, the measuring volume will be, in appearance, extended to incorporate the vortex wandering amplitude. This amplitude plus the measuring volume length is the spatial bias which has to be accounted for if the velocities and velocity fluctuations are to be interpreted. To do this, authors have proposed different approaches for example Devenport *et al.* [18] for their hot wire velocity measurements in tip vortices have assumed a probability distribution within the spatial bias. Fruman et al. [19] and Fruman and Billard [10] have developed a simple approach consisting of computing the statistical first and higher moments of a velocity profile making use of equations (2) to (5), assuming that the velocity is an ergodic function and substituting thus a time dependent integration by a spatial integration. This assumption implies that all particles have the same probability (independent of their velocities) to be within the spatial bias. A more sophisticated approach, consisting on building a full histogram by summing individual weighted Gaussian distributions, one for each local velocity comprised within the spatial bias, has been recently proposed (Le Guen [20]). The weight of the Gaussian distribution accounts for the fact that particles having large velocities have a larger probability to cross the measuring volume than slowly moving particles. An example of the first approach is given below.

The measured tangential velocity profile at $x/c_{max} = 1$ during polymer ejection has been fitted using the following expression,

$$\frac{V_t}{V_\infty} = \sum_i \left\{ \frac{\Gamma_i}{2\pi(y-y_0)} \left(1 - \exp\left[-\left(\frac{y-y_0}{a_i} \right)^2 \right] \right) \right\} \qquad (10)$$

with Γ_i is the intensity of a vortex centred on the axis, a_i is the radius of a vortex core and y_0 is the abscissa of the vortex axis. The adjustment was conducted by selecting the Γ_i and a_i in order to minimize the root mean square of the differences between measured and adjusted values. Three vortices were sufficient to achieve a very good fit. Then, the different moments, over a sliding window of length δ, were computed using expressions (2) to (5) and twenty discrete values of the fitted velocity profile. The values of the skewness increase in a non physical way in the region far from the vortex core if they are normalized with the third power of the computed RMS, whose values are very small in this region. To avoid this situation, a background uniform fluctuation, equal to 0.007 of the upstream velocity, was added to all computed values of the apparent RMS. Figure 8 shows the experimental and adjusted velocity profiles, the RMS and the skewness for a span $\delta = 3.8$ mm. This value has to be compared to the core radius, of about 1.75 mm, and the length of the measuring volume, of about 0.5 mm. The maximum of the apparent velocity fluctuation and the minimum of the skewness are respectively 0.33 and –1.83. The experimental values are 0.3 and –1.85, in very good agreement with the estimated ones.

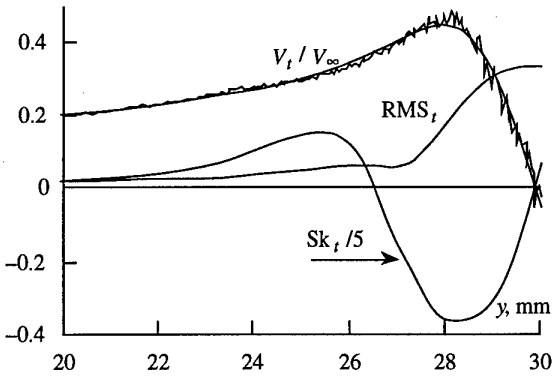


Figure 8 : Adjusted tangential velocity profile at x/c_{max}=1, apparent velocity fluctuation (RMS) and skewness (Sk) distributions due to an assumed excursion of the spatial bias of length equal to 3.8 mm. Free stream velocity 12.5 m/s, polymer solution ejection flow rate 4.7 cm^3/s.

An analogous procedure was followed for the axial velocity profile, who was fitted using

$$\frac{V_a}{V_\infty} = 1 - \Delta V_a \exp\left[-k (y-y_0)^2 \right] \qquad (11)$$

where ΔV_a is the velocity deficit on the vortex axis and k is an adjustment constant. Figure 9 shows that the adjusted velocity profiles fits pretty well the experimental one. The RMS and the skewness were computed as above for the same span δ and plotted in Figure 9. The extreme values of the RMS and the skewness are 0.074 and –1.32 respectively. These values are to be compared to the experimental ones of 0.1 and –1.3 (Figure 5).

Finally, the cross moment, Figure 10, indicates an estimated maximum of 1.74, larger than the experimental value of 1.5, but still reasonable taking into account the numerous approximations made. Table 1 offers a summary of these comparisons.

It seems therefore plausible to conclude that the ejection of a semi-dilute polymer solution into the core of a tip vortex results in the near complete suppression of the contribution of turbulence to the velocity fluctuations. Most, if not all, of the velocity fluctuations are associated to the spatial bias due to the finite length of the measuring volume of the LDV and the excursion of the tip vortex (wandering). In the

case of pure water flow without polymer ejection, both vortex wandering and turbulence contributes to the velocity fluctuation ; the first contribution being much larger than the second one.

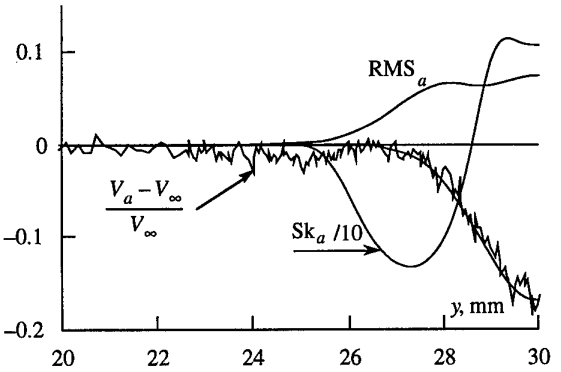


Figure 9 : Adjusted axial velocity profile at $x/c_{max}=1$, apparent velocity fluctuation (RMS) and skewness (Sk) distributions due to an assumed excursion of the spatial bias of length equal to 3.8 mm. Free stream velocity 12.5 m/s, polymer solution ejection flow rate 4.7 cm^3/s.

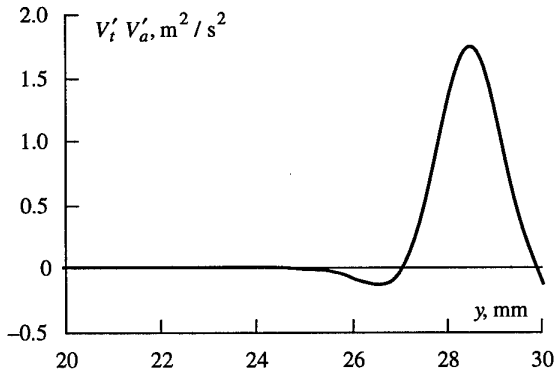


Figure 10 : Cross moment distribution for the adjusted velocity profiles of Figure 8 and 9 due to an assumed excursion of the spatial bias of length equal to 3.8 mm. Free stream velocity 12.5 m/s, polymer solution ejection flow rate 4.7 cm^3/s.

Table 1 : Comparison of experimental and predicted key values of the velocity fluctuation characteristics with polymer injection.

		Experimental	Predicted
Axial velocity	max. RMS	0.1	0.074
	min. Sk	-1.3	-1.32
Tangential velocity	max. RMS	0.3	0.33
	min. Sk	-1.85	-1.83
Maximum cross moment		1.5	1.74

Finally, it is interesting to note that the cross moment for pure water is consistently negative and that this behaviour can only be associated to the true turbulence. However, the physical significance of this behaviour is not as yet well understood. Another question still unanswered is related to the very large scatter of the skewness of the tangential velocity fluctuations in the potential region for polymer solution ejection.

5. CONCLUSIONS

An investigation on the modification, as a result of a localized semi-dilute drag-reducing polymer ejection at the tip of an elliptical wing, of the critical cavitation numbers and of the axial and tangential velocities and velocity fluctuations of the tip vortex was conducted. As established in a previous investigation at much smaller Reynolds numbers, the present results show that tip vortex cavitation inception and desinence can be reduced by as much as 30% provided the polymer ejection rate is scaled with the Reynolds number.

Earlier results concerning the increase, during polymer ejection, of the radius of the core region of the tangential velocity profiles situated several chords downstream the tip have been confirmed and extended to the very near region, within one chord from the tip. The axial velocity profiles show the occurrence of a wake effect (velocity deficit) in the core region for both water and polymer solution ejection. However, the effect is larger in the latter case.

Based on the cavitation and velocity results, it appears that jet swelling, caused by the relaxation of normal stresses associated with the viscoelastic properties of the polymer solutions, is responsible of the thickening of the viscous core which in turn is probably the unique cause of the tip vortex cavitation inhibition.

A simple analysis showed that the velocity fluctuations, in the case of polymer solution ejection, are essentially due to the spatial bias associated to the finite size of the measuring volume and the vortex wandering, and have little, if not nothing, to do with an increase of the background turbulence in the core region. In the case of pure water, it appears that some limited "true" turbulent velocity fluctuations exists in the core region besides the apparent large contribution due to the spatial bias.

ACKNOWLEDGEMENTS

This work was partly supported by the Direction des Recherches, Etudes et Techniques of the Ministry of Defence, France.

REFERENCES

1. McCormick, B.W., "On cavitation produced by a vortex trailing from a lifting surface", Journal of Basic Engineering, Sept. 1962, pp 369–379.

2. Billet, M.L., Holl, J.W., "Scale effects on various types of limited cavitation", ASME International Symposium on Cavitation Inception, New York, USA, Dec. 1979, pp 11-23.

3. Arndt, R.E.A., Keller, A.P., "Water quality effects on cavitation inception in a trailing vortex", Journal of Fluids Engineering, 114, 1992, pp 430-438.

4. Green, S.I., "Correlating single phase flow measurements with observations of trailing vortex cavitation", Journal of Fluids Engineering, 113, March 1991, pp 125-129.

5. Fruman, D.H., The "Action Concertée Cavitation-Research Program and accomplishments". International Symposium on Cavitation, CAV '95, Deauville, France, Proceedings, 1995, pp 211-217.

6. Aflalo, S.S., "Inhibition de la cavitation de tourbillon marginal". Thesis, University Paris VI, 1987.

7. Fruman, D.H., Aflalo, S.S, "Tip vortex cavitation inhibition by drag-reducing polymer solution", Journal of Fluids Engineering, 111, 1989, pp 211–216.

8. Chahine, G.L., Frederick, G.F., Bateman, R.D., "Propeller tip vortex suppression using selective polymer injection", Journal of Fluids Engineering, 115, 1993, pp 497-503.

9. Fruman, D.H., Pichon, T., Cerrutti, P., "Effect of a drag-reducing polymer solution ejection on tip vortex cavitation", Journal of Marine Science and Technology, 1, 1995, pp 13-23.

10. Fruman, D.H., Billard, J-Y., "The tip vortex : effect of a drag reduction agent on confined turbulence", ASME FED-Vol. 237, 1996, pp 217-224.

11. Fruman, D. H., Dugué, C., Pauchet, A., Cerrutti, P., Briançon-Marjollet, L., "Tip vortex roll-up and cavitation", Nineteenth Symposium on Naval Hydrodynamics, Seoul, National Academy Press, Washington, D.C., 1994, pp 633-651.

12. Fruman, D.H., Cerrutti, P., Pichon, T., Dupont, P., "Effect of hydrofoil planform on tip vortex roll-up and cavitation", Journal of Fluids Engineering, 117, 1995, pp 162-169.

13. BURSTware User's Guide, Dantec, 1991.

14. Fruman, D.H., "Tip vortex cavitation in polymer solutions", Cavitation and Multiphase Flow Forum, ASME FED-Vol 64, 1988, pp 81-83.

15. Fruman, D.H., Perrot, P., Boughechal, J., "On the swelling of submerged jets of dilute and semi-dilute polymer solutions", Chem. Eng. Commun., 27, 1984, pp 101–118.

16. Ouibrahim, A., Galivel, P., Barigah, M., Fruman, D.H., "Anomalous jet effects during thin-slit drag-reducing polymer solutions", International Symposium on Flow Visualization, Bochum, Proceeding by Hemisphere Publ. Co., 1980.

17. Fruman, D.H., Galivel, P., "Near-field viscoelastic effects during thin-slit drag-reducing polymer ejection", Journal of Rheology, 24, 5, 1980, pp 627–646.

18. Devenport, W.J., Rife, M.C., Liapis, S.I., Follin, G.J., "Turbulence structure and scaling in trailing vortices", Journal of Fluid Mechanics, 312, 1996, pp 67-106.

19. Fruman, D.H., Castro, F., Pauchet, A., Pichon, T., "On tip vortex turbulence, wandering and cavitation occurrence", Second International Symposium on Cavitation, Tokyo, Japan, Proceedings, H. Kato ed., 1994, pp 151–157.

20. Le Guen, A., Viot, X., Billard, J-Y., Fruman, D.H., "Fluctuations de vitesse et biais spatial dans le tourbillon marginal", 6èmes Journées de l'Hydrodynamique, Nantes, France, 1997, Proceedings pp 325-336.

CAVITATION SELF-OSCILLATIONS INTENSIFY TECHNOLOGICAL PROCESSES

V.V.Pilipenko
I.K. Man'ko
V.A. Zadontsev

Institute of Technical Mechanics of the National Academy of Sciences of Ukraine
Hydromechanical System Dynamics Division
320600 Dniepropetrovsk-5, Leshko-Popelya str, 15.

SUMMARY

Characteristic features are presented for high-frequency, high-amplitude self-oscillations in a hydraulic system with a local hydraulic resistance of a venturi nozzle type whose physical nature is due to a periodically - stalled cavitation (growth, break-off, carry-over and collapse of a cavity diffuser-like part). Analytical expressions are given to determine the frequencies and amplitudes of pressure oscillations occuring in the hydraulic system with a local hydraulic resistance under realization of the periodically- stalled cavitation regime. The possibility to utilize cavitation self- oscillations for various technological processes intensification is shown.

List of Symbols

p_1^* - total pressure at the nozzle inlet;

$\overline{p}_1$ - nozzle inlet pressure under steady-state conditions;

$\overline{p}_2$ - nozzle outlet pressure under steady-state conditions;

m - mass flow rate of liquid under steady-state conditions;

β - venturi -nozzle diffuser flare angle;

ρ - liquid density;

Sh_m - modified Strouhal number;

r_{cr} - radius of the venturi - nozzle restricted section;

μ - venturi - nozzle flow coefficient;

l_{cav} - cavitation cavity length;

τ - cavitation criterion parameter for the steady-state conditions, roughly equal to the pressure ratio ($\tau \approx \overline{p}_2 / \overline{p}_1$);

p_{cr} - nozzle restricted section pressure;

f - cavitation self - oscillation frequency;

J_d - inertial resistance coefficient of the venturi - nozzle diffuser;

V_{cav} - cavitation cavity volume;

c - sound velocity in a liquid;

v_{cr} - liquid jet velocity across the venturi - nozzle restricted section;

F_2 - sectional area of the exit pipeline;

ΔP_2 - peak-to-peak amplitude of pressure oscillations;

$|\delta p_2|$ - amplitude of pressure oscillation;

$|\delta \overline{V}_к|$ - amplitude of cavitation formation volume oscillations;

ϖ - cyclic frequency.

Bar over parameters denotes steady-state conditions.

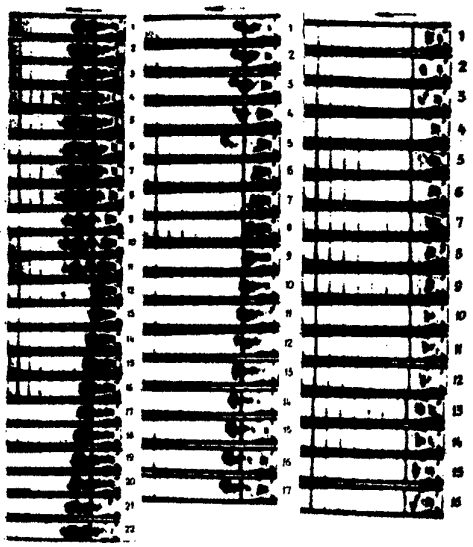
For a number of years the investigations on self-oscillation regimes in hydraulic systems with cavitating local hydraulic resistances have been conducted at the Institute of Technical Mechanics of NAS of Ukraine [1-6].

In studying the cavitation phenomena in local hydraulic resistances liquid flow regimes have been revealed under which in the channel of the local hydraulic resistance of the venturi - nozzle type large cavitation formations periodical nucleation and their growth to certain sizes take place. On reaching the maximum sizes in accordance with the given flow regime the cavitation formation break-off occurs that is followed by its further carry-over and collapse as a whole in a pressure zone that involves a pressure pulse in the flow. A flow regime of this kind has been called by us a "periodically stalled" cavitation regime [1,2].

The distinguishing feature of such a regime is that the large cavitation formations collapse does not take place on the channel wall, but in the liquid flow, and the process of cavity nucleation, break-off, carry-over and collapse is strictly periodical. Fig. 1 shows the cinematographic records of the process of the large cavitation formations nucleation, growth to certain sizes, break-off, carry-over and collapse that occurs in the flow passage of the local hydraulic resistance of the venturi - nozze type at various cavitation parameter values [3,5].

Fig. 2, e.g., presents the oscillogram of pressure self- oscillations in the liquid flow past this resistance due to cavitation formations collapse. The

Paper presented at an AGARD FDP Workshop on "High Speed Body Motion in Water", held in Kiev, Ukraine, 1-3 September 1997, and published in R-827.



$\tau = 0{,}15$ $\tau = 0{,}2$ $\tau = 0.3$

Fig. 1 Cinematographic records of the inception, growth to some sizes, break-off, carry-over and collapse of large cavitation formations that originate in flow passage of local hydraulic resistance of venturi-nozzle type under constant pressure at the inlet and different values of the cavitation parameter τ.

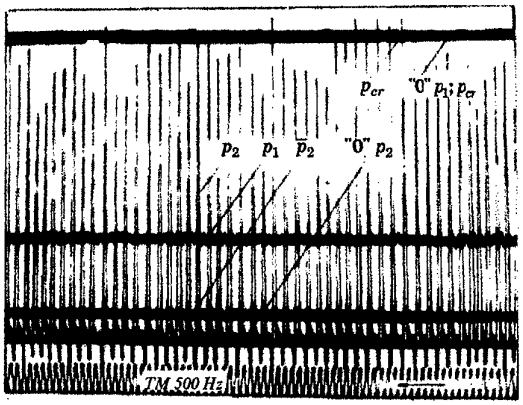


Fig. 2 Oscillogram of pressure in liquid flow past local hydraulic resistance of a venturi-nozzle type that is due to the collapse of large cavitation formation, where: p_1 - is the pressure at the hydraulic resistance inlet; p_{cr} - is the pressure in restricted section of the hydraulic resistance, p_2; $\overline{p}_2$ - is the pressure at the hydroresistance outlet.

oscillation frequency is determined both by the channel geometry [4] and flow parameters and may be assigned in a range of 100 - 2000 Hz.

As an example, in Fig.3 the oscillation frequency versus the pressure ratio $\overline{p}_2 / \overline{p}_1$ in the hydraulic

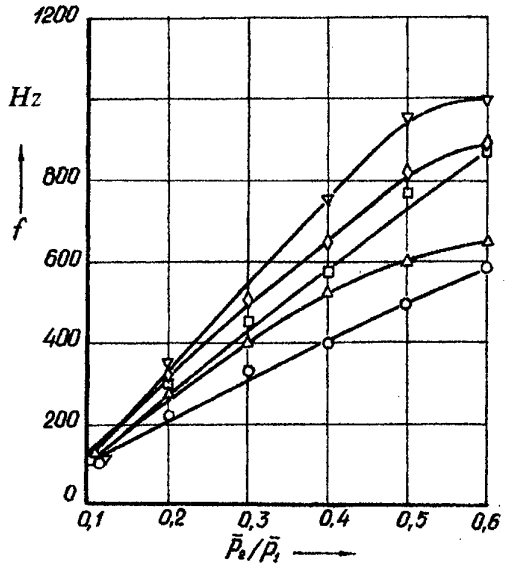


Fig. 3 Frequency dependencies of the pressure ratios $\overline{p}_2 / \overline{p}_1$ in the hydraulic system with the venturi-nozzle at various pressures $\overline{p}_1$ at the nozzle inlet: O – $\overline{p}_1$ = 1,0 MPa; Δ - $\overline{p}_1$ = 2,0 MPa; □ - $\overline{p}_1$ = 3,0 MPa; ◊ – $\overline{p}_1$ =4,0 MPa; ∇ – $\overline{p}_1$ =5,0 MPa.

system with the venturi - nozzle at various nozzle inlet pressures $\overline{p}_1$ is shown. It follows from this figure that at a constant nozzle inlet pressure practically linear frequency dependences on the pressure ratio $\overline{p}_2 / \overline{p}_1$ are obtained, in this case the frequency increases with the increase of the $\overline{p}_2 / \overline{p}_1$ value. Besides, at a constand value of $\overline{p}_2 / \overline{p}_1$ the oscillation frequency increases with the increase of the nozzle inlet pressure. The peak-to-peak amplitude dependences on the pressure ratio $\overline{p}_2 / \overline{p}_1$ at a constant venturi - nozzle inlet pressure $\overline{p}_1$ are nonlinear and have the maximum at $\overline{p}_2 / \overline{p}_1 \approx 0{,}3$. At constant values of $\overline{p}_2 / \overline{p}_1$ with the increase in the venturi - nozzle inlet pressure $\overline{p}_1$ the peak-to-peak amplitude of oscillations increases too (see fig.4).

Formula is obtained for determining the frequency of high-frequency cavitation self-oscillations on geometrical and regime parameters of the local hydraulic resistance of the venturi-nozzle type [6].

$$f = Sh_m \sqrt{\frac{2\left(p_1^* - p_{cav}\right)}{\rho}} \times \frac{tg\frac{\beta}{2}}{r_{cr}\left(\sqrt{\frac{\mu}{1-\sqrt{1-\overline{\tau}}}} - 1\right)} \qquad (1)$$

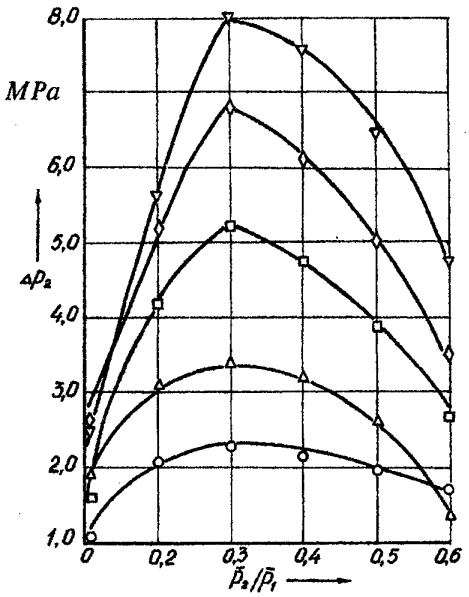


Fig. 4 Peak-to-peak amplitude dependencies of pressure ratios $\bar{p}_2 / \bar{p}_1$ in the hydraulic system with the venturi-nozzle at various nozzle inlet pressures where: O – $\bar{p}_1$ = 1,0 MPa; Δ - $\bar{p}_1$ = 2,0 MPa; □ - $\bar{p}_1$ = 3,0 MPa; ◊ – $\bar{p}_1$ =4,0 MPa; ∇ – $\bar{p}_1$ =5,0 MPa.

This formula with due regard for an experimentally obtained Strouhal number dependence on the cavitation parameter provides a satisfactory agreement of predicted and experimentally obtained frequency dependences in a Venturi-nozzle diffuser angles range from 16 to 120°.

The formula for estimating the peak amplitudes of high-frequency cavitation self-oscillatins in the local hydraulic resistance is obtained in the form :

$$\left|\delta p_2\right|_{\max} = \rho v_{cr}^2 (2\pi)^2 Sh_m^2 \times \frac{J_d}{\sqrt{1 + \frac{(2\pi)^2 v_{cr}^2 J_d^2 F_2^2}{l_{cav}^2 c^2}}} \times \frac{\left|\delta V_{cav}\right|}{l_{cav}^2} \qquad (2)$$

This formula gives an acceptable agreement between predicted and experimentally measured amplitudes of pressure oscillations at the outlet of the venturi-nozzle type local hydroresistance in a diffuser angles range of 16-30°.

The peak-to-peak amplitude of oscillations at the prescribed geometrical values of the venturi-nozzle channel is determined on flow parameters but its maximum value (if common water is used as a working fluid) exceeds the steady-state pressure value at the channel inlet by factor 1,5-5,0. Peak pressure values at the local hydraulic resistance exit at oscillations of an impact character maintain their values downstream at up to several meters distance practically without damping. Upstream of a special geometry channel the oscillations do not propagate. It allows oscillations of certain frequency and amplitude to be superimposed on the liquid flow or to transform a steady liquid flow into a pulsating one. This has resulted in developing a cavitation generator of high-frequency, high-amplitude liquid pressure oscillations without rotating and moving parts. The cavitation generator permitting to transform a steady-state liquid flow into a pulsating one has been used in developing a device for hydraulic hot fire-scale cleaning with pulsating water jets. A schematic of the scale cleaning device collector is shown in Fig.5. Pulsating jets application has allowed to decrease metal spoilage caused by fire-scale pressing-in by factor 2-5.

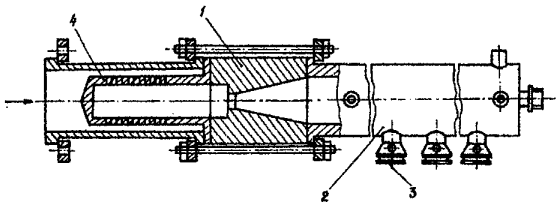


Fig. 5 Schematic of the collector of the hydraulic fire-scale cleaning device using pulsating jets: 1 – cavitation generator; 2 – collector; 3 – nozzles; 4 – filter.

The "periodically-stalled" cavitation regime has been utilized in developing a drilling hydrovibrator to superimpose axial vibrational accelerations on the rock cutting tool (diamond crowns, hard-alloy rock rollers) in the rotary drilling of 76 mm-diameter boreholes in medium-hard and hard rocks of IV-XII drillability category accompanied by face cleaning with flushing fluid. A schematic of the drilling tool with the drilling hydrovibrator is presented in Fig.6.

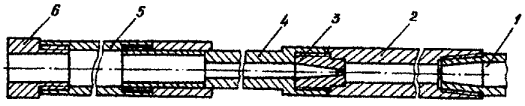


Fig. 6 Schematic of the drilling tool with drilling hydrovibrator: 1 – drill pipe string; 2, 4 – reducers; 3 – hydrovibrator; 5 – core barrel; 6 – diamond crown.

In this case vibrational accelerations have been obtained on the rock cutting tool with the amplitude not less than 2000 m/s² in a frequency range from 300 to 2000 Hz at the expense of flushing fluid energy. The hydrovibrator application enables :

- to increase a drilling rate in medium-hard and hard rocks by factor 1,5-5,0 as compared to a rotary drilling with diamond and hard-alloy tools;
- increase more than twice rock cutting tool durability;
- increase core output percent in fractured rock;
- decrease drilling power consumption.

The absence of moving parts is responsible for the hydrovibrator's high reliability and ease of operation.

At our Institute a hydrodynamic cavitation plant for dispersing the pastes of aqueous dispersion paints has been developed , manufactured and successfully tested whose schematic representation is shown in Fig.7. As compared to existing similar purpose devices the stated plant is noted for:
- low specific current consumption;
- simple design;
- servicing ease;
- small mass and overall dimensions;
- insignificant operating costs;
- applicability to existing production lines for dispersing suspensions.

Technical Data:
- output, max, kg/h – 15000;
- specific current consumption, kW/kg – 2×10^{-3};
- overall dimensions, m – 3,7×2,6×2,2;
- mass, kg, max 3000

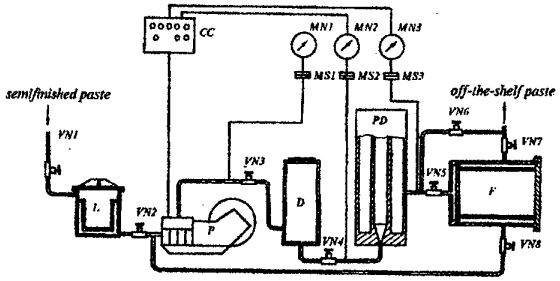


Fig. 7 Schematic of the hydrodynamic cavitation plant for dispersing the pastes of aqueous – dispersion paints: VN1 - VN8 – valves; L - trap; P - pump; CC - 6control cabinet; MN1 - MN3 – manometers; MS1 - MS3 - membrane separator; PD - powder dispenser; F - filter; D - damper.

It should be noted that novel original designs utilized by us in the developed plant are fit for head- and mass interchange processes intensification, production of finely dispersed emulsions and suspensions and may be used as well in food-stuff production practice, in chemical, wood-pulp and paper industries, for preparing drilling fluids, increasing the convective heat exchange in a shell-and-tube heat exchanger, washing the process pipelines etc.

A hydrodynamic device for increasing the efficiency of water well development and recovering has been created. The device is designed on the original principal of liquid pressure pulses action on water-bearing horizon.

Technical Data:
- diameter of the mechanically treated well, inch – 4 and more;
- pulse frequency, Hz, within the range – 100 – 2000.

Time of well mechanical treatment, h:
- using an independent pump – 4 –8;
- using an immersion pump – 200.

Increase of specific yield, percents – 50 –120.

The device may be employed for wells of any depth in any hydrogeological conditions with and without a filter. We consider this device to be applicable for raising the oil and gas pools yield too.

Thus, our investigations show that cavitation regimes of liquid flows in local hydroresistances may be used for practical purposes to intensify diverse technological processes.

REFERENCES

1. On Highfrequency Pressure and Flow Oscillations in a Hydraulic System past Cavitating Venturi-Tube/ V.V. Pilipenko, V.A. Zadontsev, I.K. Man'ko, N.I. Dovgot'ko// Proceedings, XIII ALL Union Meeting on Hydraulic Automation/ June 24-26, 1974, t. Kaluga/. – Kaluga: Publish. House of the – Inst. Of Contr. Probl. AS USSR, 1974, pp. 199-201.
2. Pilipenko V.V., Zadontsev V.A., Man'ko I.K., Dovgot'ko N.I. Studies of High-Frequency Self-Excited Oscillations in Hydraulic System With Venturi Tube / Cavitation Self-Excited Oscillations in Pump System. – Kyiv: Naukova Dumka, 1976, - p.2, p.p. 104-113.
3. Man'ko I.K. Visual Studies of Cavitation Oscillations in Hydraulic System with Transparent Venturi Tube (Abidem – p.p. 113-118).
4. Man'ko I.K. Effect Of the Venturi Tube Diffuser Angle on Frequency and Level of Maximum Values of High-Frequency Cavitation Self-Excited Oscillation Pressure/ Cavitation Self-Excited Oscillations and Dynamics of Hydraulic System – Kyiv: Naukova Dumka, 1977. p.p. 34-39.
5. Pilipenko V.V., Man'ko I.K. Experimental Determination of the Cavity Length and its Dependence on the Diffuser Angle of the Venturi Tube and its Operation (Abidem. p.p. 39-43).
6. Pilipenko V.V. Cavitation Self-Oscillations. – Kyiv: Naukova Dumka, 1989. p.316. – ISB N 5-12000537-3

Control of Cavity Parameters at Supercavitating Flow

Yu.D.Vlasenko
National Academy of Sciences - Institute of Hydromechanics
8 / 4 Zhelyabov str., Kiev, 252057
Ukraine

1. SUMMARY

Some methods of control of fully developed cavity parameters by varying geometrical characteristics of a cavitating body are considered. Results of experimental investigations of cavitators with variable frontal drag and constant edge of free streamline separation and also some types of nonsymmetrical cavitators are presented. The possibility and a number of features of the fully developed cavity control independently on the cavitation number and cavitation regime (vapor or gas) are shown.

2. INTRODUCTION

First of all, the possibility of supercavity control is of interest from point of view of the optimal flow regime maintenance for unsteady conditions: at changes of mainstream velocity or depth, abrupt difference of the external pressure value etc. For ventilated supercavities, at relatively moderate motion velocities the main cavity characteristics (the cavitation number, cross dimensions and length of a cavity) depend on the rate of gas, which is being blown to a cavity. Therefore, for such cavities the supply rate regulation may be considered as one of possible methods of the cavity control. The physical side of the processes in ventilated supercavities and quantitative dependences for basis parameters of such flows have been studied enough in detail [1, 2, 3] for conditions of steady flow regimes.

At the same time, performed experiments have shown that the supply value regulation as a method of the cavity control has very low speed even in the simplest case of a cavity past a disk cavitator [4]. Some characteristic results of these experiments are presented in Fig. 1. The typical graph of the cavity length increase after the supply beginning (Fig. 1,a) and the dependence of the maximal speed of the cavity length increase $\overline{V}_{cmax} = \frac{V_{cmax}}{V_0}$ and the relative value of the cavity formation period $\overline{t}_f = \frac{t_f}{t_c}$ on a value of the supply rate coefficient $\overline{Q}_g = \frac{Q_g}{V_0 D_n^2}$ (Fig. 1,b) are shown. Here, we designated: V_0 is the mainstream velocity; D_n is the cavitator diameter; L_c is the cavity length; t is the time; $V_c = \frac{\partial L_c}{\partial t}$ is the speed of the cavity length increase; Q_g is the blown gas rate; t_f is the complete time of the cavity formation; $t_c = \frac{L_c}{V_0}$ is the time for passing by cavitator the distance L_c. It is seen from graphs that maximal values of speed of the cavity length increase is lower than the velocity of the cavitator motion in stream greater than by an order. Moreover, in the case of presence of a body moving in a cavity past a cavitator the cavity formation process becomes considerably complicated. The cavity control by the gas blowing is impossible at motion velocity increase and approximation to the vapor cavitation regime.

We have applied another approach to the problem on control of the supercavity parameters. The basis supercavity dimensions - the mid-section diameter D_c and length L_c - are determined with enough accuracy by asymptotic relations [1, 5]

$$\frac{D_c}{D_n} = \sqrt{\frac{c_{x0}(1+\sigma)}{\sigma}}; \quad \frac{L_c}{D_n} = \frac{1}{\sigma}\sqrt{c_{x0}(1+\sigma) ln \frac{1}{\sigma}},$$

where $\sigma = \frac{p_0 - p_c}{\rho V_0^2/2}$ is the cavitation number; p_0 и p_c are the pressures, respectively, in the free stream and in the cavity; ρ is the fluid density; $c_{x0} = \frac{c_x}{1+\sigma}$, $c_x = \frac{X}{S_n \rho V_0^2/2}$ is the cavitator drag coefficient; X is the frontal cavitator drag; S_n is the area bounded by line of free streamline separation on a cavitator. An analysis of these relations shows a possibility in principle of control of the cross dimension and length of a cavity by means of the control parameter c_{x0} at saving the constant cavitator diameter D_n [6].

The scheme of realization of such method of the cavity control is given in Fig. 2 in the most general view. The cavitator represents a solid body 1 with fixed edge 2 of the free streamline separation and variable geometry of the streamlined surface located in front of this edge. The variation of the cavitator drag coefficient and, hence, values of the frontal hydrodynamic drag, cavity length and diameter are attained by means of changing, for example, the height h of its streamlined profile at sav-

Paper presented at an AGARD FDP Workshop on "High Speed Body Motion in Water", held in Kiev, Ukraine, 1-3 September 1997, and published in R-827.

ing the constant cavitator diameter D_n. Using the one-valued behaviour of dependences $X(h); L_c(h)$ and $D_c(h)$ at the constant cavitation number, we have a possibility to vary the cavity characteristics by varying one parameter. The supercavity control possibility due to these cavitators was experimentally investigated in the hydrodynamic laboratory of the IHM.

3. HARDWARE AND METHODS TO CARRY OUT THE EXPERIMENTS

The experiments were carried out using the cavitators of enough rigid structure ensuring the one-valued check of the streamlined surface geometry. The scheme variants of the cavitators with variable drag are shown in Fig. 3. The applied cavitators have combined design including the outer body 1 with sharp frontal edge having the diameter D_n and the central element 2 with the same diameter located in tne outer body. Variation of the streamlined surface geometry and, as a result, the cavitator drag at its constant diameter was realized by changing relative positions of the body 1 and the central element 2. Bodies of revolutions of various types can serve as a central element for considered cavitators. This has certain applied significance. For example, the type of cavitators shown in Fig. 3,a with central element close to a paraboloid of revolution assumes using the frontal surface to locate devices, which are not functionally connected with cavitator, so as the axial water inlet, sensors etc.

The experiments with pointed cavitators were carried out in the small hydrodynamic tunnel having glass working section with dimension 0.34 x 0.34 x 2.0 m at constant mainstream velocity $V_0 = 8.9$ m/s. The tested cavitators were fixed along the stream axis, the supercavity was created by air-supply to the zone past the cavitator. The scheme of experiment in the working part of the hydrodynamic tunnel is presented in Fig. 4. The photographs of the nose of cavities past the cavitators of pointed types are shown in Fig. 5.

The cavitator having variable drag and a cone-shaped central element shown in sketch (Fig. 3, b) has been chosen for systematic experimental investigations. Results of these researches are submitted below. In this case the choose of the central body shape is due to that the hydrodynamic characteristics of cones was enough well studied at cavitation flow around them [1, 2, 7]. Since, the drag coefficient of this cavitator definitively depends on the value x of displacement of the central element 2 relatively to frontal sharp edge of the body 1, then the pointed linear parameter x will be named as a working stroke of the cavitator with variable drag. The photographs of the cavitator applied in the experiments with diameter $D_n = 20$ mm are shown in Fig. 6 at two extreme positions of the conic central element relatively to the body.

The quantitative characteristics of the cavitators were measured for four values of a cone angle of the central element : $2\beta = 60^o; 90^o; 120^o; 180^o$ (disk). According to a dependence $C_{x_o}(2\beta)$ adduced in Fig. 7 the range of the drag coefficient variation for the pointed cones is $C_{x_o} = 0.34 \div 0.82$ at the zero cavitation number [2]. During experiments the cavity parameters L_c and D_c and the frontal drag value X of the cavitator as a function of the value x of its working stroke were being measured by means of photoregisration and tensometer for the pointed values of cone angles. To ensure a comparison of results these measurements were executed for steady cavities at constant values of the cavitation number.

Moreover, the experiments on study of nonstationary supercavities were carried out. Their purpose was to determine the speed of the cavity control by means of the considered cavitators. The experiments with cavities past flat cavitators having shape differing from circular one were performed too.

4. RESULTS OF EXPERIMENTS

Variation of the cavitator drag coefficient C_x depending on a cone angle of the central element and the working stroke value x is shown in Fig. 8 by experimental graphs $C_x/C_{xd}(x/D_n)$ и $C_x/C_{xd}(x/h)$. They characterize a possibility of the frontal drag control by means of the given cavitators (here, C_{xd} is the drag coefficient for disk). Graphs show that both the range of the drag coefficient regulation and the cavitator working stroke value increase at decrease of a cone angle of the central element (Fig. 8,a). The lower limit of this range corresponds to $x/D_n = 0$ and is defined by value C_x for appropriate cone. The upper limit of regulation of C_x does not depend on the central element shape and is reached when the working stroke value x is close to the profile height h of the central element, that is $x/h \geq 0.9$ for all cones (see Fig. 8, b). In this case the limit value for ratio $\left(\frac{C_x}{C_{xd}}\right)_{max} \simeq 1.17$ is reached. From here, we obtain the limit value of the drag coefficient $C_{x_0} \simeq 0.96$ for cavitators of considered type with account that for disk at $2\beta = 180^o$ $C_{x_0} \simeq 0.82$. Thus, for cone angle of the central element, for example, $2\beta = 60^o$, we obtain almost triple change of the cavitator drag coefficient in limits of the working stroke value.

The stated above is confirmed by experimental graphs of dependence of the supercavity length and diameter on the relative value of the cavitator working stroke $\frac{x}{h}$ at the constant cavitation num-

ber (Fig. 9,a,b). We can see also from these graphs that the effective range of the cavitator working stroke is $\frac{x}{h} = 0 \div 0.9$.

The control of steady supercavity dimensions due to varying the cavitator drag is illustrated by photographs submitted in Fig. 10. In this case we compare the cavities obtained at equal cavitation numbers and two limit values of the cavitator working stroke corresponding to minimal ($x/h = 0$) and maximal ($\frac{x}{h} = 0.91$) values of the drag coefficient C_x.

As it was pointed, the stated results refer to steady regimes of the supercavitating flow. The question about the supercavity evolution speed at influence of the control parameter C_x and also about the cavity deformation behaviour at unsteady regimes due to abrupt changes of the cavitating body drag are of interest too. It is enough obvious from general physical concepts that the cavity shape change should be realized with mainstream velocity in this case. This assumption was checked in the special experiments, where we have realized two enough quick regimes of the frontal drag change: from maximal value to minimal one and on the contrary, from minimal value to maximal one.

This is attained by means of free motion of one of the cavitator elements – the outer body or the central element – about the rigidly fixed second element in the longitudinal direction. In the initial position the mobile element was fixed in forward (in opposite to the mainstream) position. After that the mobile element of the cavitator was displaced to the extreme back position due to the velocity head effect, and the snapshot of the cavity shape with exposure time about $\frac{1}{1000}$ s was being realised after given time interval t_{sn}. The maximal initial value of the frontal drag was being ensured at use of the outer cavitator body as a mobile body. The minimal initial drag of the cavitator was being ensured at mobile central element. The drag jump value was defined by cone angle of the central element.

The scheme of the experiment is presented in Fig. 11. The behaviour of changing C_x and L_c for time at abrupt drag reduction (Fig. 11, a) and also the scheme of the longitudinal cavity deformation registration ΔL_c for time t_{sn} (Fig. 11, b) are shown there. The initial steady cavity is plotted by dotted line. Measurement of the photographs confirms that the cavity change as a result of the cavitating body drag change happens with the mainstream velocity, i. e. $\frac{\Delta L_c}{t_{sn}} = V_0$.

The supercavity transformation behaviour for time is illustrated by photographs in Figs. 12, 13 and 14 at processes described above. Three qualitatively various types of the unsteady supercavity deformations are presented there. The presented photograph selections are not cinegrams (sequential frames), but are only registration of typical phases of the considered processes.

The sequential stages of the unsteady cavity deformation due to quick reduction of the cavitator drag are presented in Fig. 12 at a moderate value of the drag difference ΔC_x. In this case the well expressed boundary between the initial cavity and new formed cavity contours is observed. This boundary in the form of a ring wave moves with mainstream velocity along the cavity without its discontinuity.

The stages of analogous process realized for more abrupt form are shown in Fig. 13. This is attained by means of both the increase of the value ΔC_x difference and the higher speed of this process. In this case we obtain the unsteady regime, when the cavity transformation is accompanied by discontinuity between the new formed and initial parts of the cavity.

In contrast to the stated above the unsteady cavity transformation process stipulated by abrupt increase of the cavitator drag is going on in relatively smoothed form without sharply expressed boundary between the initial and new formed parts of the cavity (Fig. 14).

We should note also that at all the considered unsteady regimes the supercavity (or its parts as in Fig. 13) saves a smooth surface due to preservation of the constant edge of free streamline separation at the cavitator drag change.

The analysis of obtained results shows a possibility of simulation of the unsteady cavitation processes by means of the control of the cavitating body drag. In this way, for example, in the conditions of inverted motion the simulation of the unsteady cavitation flow processes stipulated by variation of the velocity and depth of the cavitating body motion is possible at constant mainstream velocity. Then, the unsteady regimes stipulated by the cavitator drag $C_x(t)$ reduction correspond to the motion velocity V_0 reduction in noninverted motion and, on the contrary, the motion with increasing velocity is simulated by increase of the drag $C_x(t)$. According to this we note that a qualitative analogy of the unsteady cavity shapes presented in Fig. 12, 13, 14 and cavities registered at water dive of bodies with abrupt change of the velocity along the trajectory is observed [8]. The cavity smooth surface preservation for all the control regimes is also an essential property for practical applications. This is stipulated by constancy of the free streamline separation line of the cavitating body.

The question about possibility of control of the

shape of cavity cross sections by changing the shape of the cavitating edge in the plane, which is perpendicular to the flow axis, is of certain interest from point of view of the general problem on control of the supercavity parameters. We have carried out experiments on study of geometry of the steady cavities past flat cavitators having the cavitating edge shapes differing critically from circular one: rectangles with different side ratio, rhombuses, disks with local protrusions and hollows etc. The experiments were carried out at small hydrodynamic tunnel of the IHM at the mainstream velocity $V_0 = 8.9$ m/s. Cavities have been photographed in two planes. The evolution of cross section shape along the cavity length has been studied by using results of measurement of the cavity contour projections. Some characteristic results of these experiments are submitted in Figs. 15 and 16.

Photographs of two projections of cavities past cavitator having shape of an elongated rectangle with side ratio 1 : 6 are presented in Fig. 15 at $\sigma = 0.0364, Fr_d = 24.2$ and various cavitator orientations in the stream: with vertical (a) and horizontal (b) position of the long side. Here, $Fr_d = \frac{V_0}{\sqrt{gd_n}}$, d_n is the diameter of a disk equivalent in area. It is well seen from photographs that the intensive cavity expansion happens directly past the cavitator in the plane, which is parallel to its short side. At the same time the cavity cross dimensions are changed considerably weaker in the plane, which is parralel to the long side. Graphs of changing the section aspect ratio $\lambda = \frac{D_1}{D_2}$ of these cavities along the length are given in Fig. 16. Here, D_1 and D_2 are the cavity cross dimensions in the planes, which are parallel to long and short sides of the cavitator, respectively. Graphs in Fig. 16,a show that the cavity section shape intensively tends to circular one just past the cavitator and transforms into circular in the part of cavity in front of its mid-section. Behind the mid-section the cavity sections transform in different way in dependence on the cavitator orientation. This is a result of the gravity influence. The graph of dependence $\lambda(\bar{x})$ at $Fr = \infty$ obtained by means of processing the same experimental data by approximate methods [9] is presented in Fig. 16,b. The obtained graph illustrates the process of the cavity section reorientation about the cavitating body position without distortions caused by gravity influence.

The experiments permit also to detect some features of the cavity section formation due to specific configuration of local parts of the cavitating edge of a nozzle (protrusions, hollows etc.). As in the above considered case the cavity repeats the nozzle shape only on the very small distance from it. The cavity section deformation along the length is not reduced to the smoothing the initial perturbations and has a more complex behaviour. Local features of the cavitator contour, as sharp angles or hollows, cause to formations with opposite sign on the cavity surface, i.e., a longitudinal hollow arises past a sharp protrusion of the cavitator on the small distance from it, and a hollow presence on the cavitator creates longitudinal protruding crest on the cavity surface. These formations are stable along the length and give the complex shape, which consists of parts with alternating curvature, to the cavity sections.

5. CONCLUSIONS

The possibility of control of the supercavity parameters by varying the drag coefficient of the cavitating body at preservation of the constant cavitating edge has been experimentally shown. The obtained results have shown the real possibility to realize control for wide range of variation of the cavitator drag coefficients and the cavity length and cross dimension dependent on it. The considered approach has the advantage permiting the cavity control to realize indepenidently on the cavitation number or regimes (vapor or gas). It is shown that the variation of the cavity shape and dimensions happens with mainstream velocity. This is maximal possible velocity for the cavity control. It is essential also that the cavity control method by means of cavitators having the variable drag may be applied to simulate the unsteady cavitation processes in the inverted motion conditions at the constant mainstream velocity. The cavity free surface remains always smooth due to saving the constant separation line of free streamlines of the cavitating body at all the control regimes.

The experiments have shown the limit of possibilities to influence on a shape of the cavity cross sections by changing the cavitating body edge shape in view of a complexity of processes of the cavity section transformation past noncircular cavitators.

REFERENCES

1. Logvinovich, G.V., "Hydrodynamics of Flows with Free Boundaries", Kiev, USSR, Naukova dumka, 1969, 208 P. (in Russian)

2. Epshtein, L.A., "Methods of Theory of Dimensionality and Similarity for Problems of Ship Hydromechanics", Leningrad, USSR, Sudostroenie, 1970, 207 P. (in Russian)

3. Epshtein, L.A., Blyumin, V.I., Starodubtzev, P.S.," Influence of Cavitation and Froude Numbers on Cavity Dimensions and Volume of Air for Its Maintenance", J. Proceeding of CAHI, 824, 1961. (in Russian)

4. Vlasenko, Yu.D., Korolev, V.I., Boyko, V.T.,"

Experimental Investigation of Cavity Evolution at Unsteady Gas Cavitation", J. Hydromechanics, 24, 1973, pp 79 – 83. (in Russian)

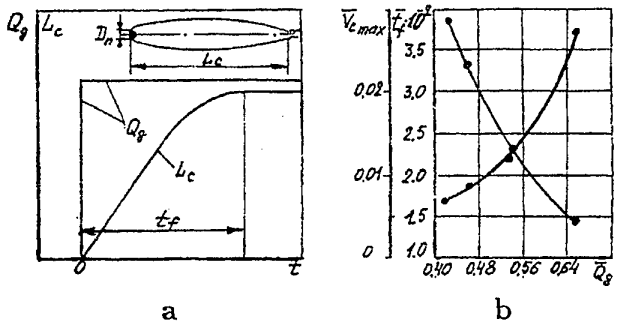
5. Savchenko, Yu.N., Semenenko, V.N., Serebryakov, V.V., "Experimental Check of Asymptotic Formulae for Axisymmetrical Cavities at $\sigma \rightarrow 0$" in "Problems of high-speed hydrodynamics", Cheboksary, Russia, 1993, pp 117 – 122. (in Russian)

6. Savchenko, Y., Semenenko, V., Naumova, Y., Varghese, A., Uhlman, J., Kirschner, I., "Hydrodynamic Characteristics of Polygonal Contours in Supercavitating Flow", Papers of Third International Symposium on Performance Enhancement for Marine Applications.–Newport RI, USA, 6-8 May 1997.

7. Cnapp, R.T., Daily, J.W., Hammitt, F.G. "Cavitation", New York, USA, Mograw–Hill Book C^o, 1970, 687 P.

8. Logvinovich, G.V., Yakimov, Yu.L., "Water Dive of Bodies with High Velocities" in book " Unsteady Water Flow with High Speeds", Moscow, USSR, Nauka, 1973, pp 85 – 92 (in Russian).

9. Buyvol, V.N., Vlasenko, Yu.D., Zhuravlev, Yu.F., Shevchuk, Yu.R., "Slender Cavities past Elliptic Cavitators", J. Applied Machanics, **15**, 10, 1978, pp 110 – 118 (in Russian).



a b

Fig. 1. Graph of the cavity length increase after the supply beginning (a) and dependence of the length increase speed $\overline{V}_{cmax}$ and the cavity formation period $\overline{t_f}$ on the gas supply value.

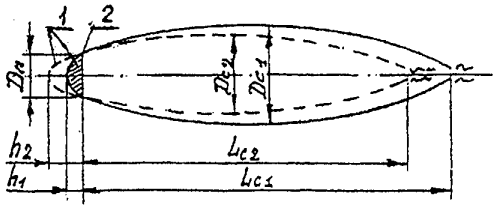
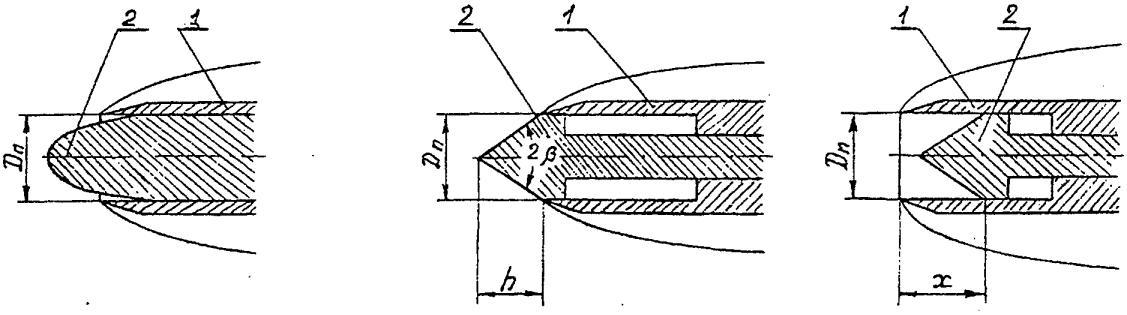


Fig. 2. Scheme of control of the cavity parameters by changing the cavitator drag.



a b

Fig.3. Schemes of cavitators with variable drag.

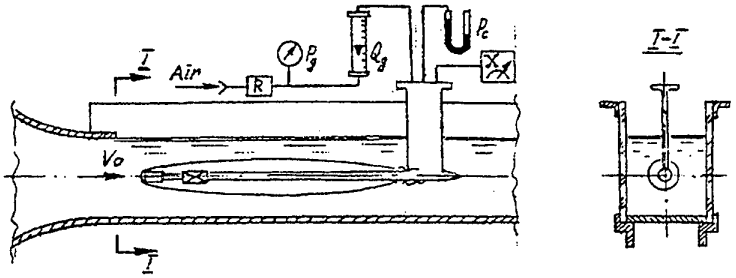


Fig. 4. Scheme of the experiment in the working section of the hydrodynamic tunnel.



a b

Fig. 5. Photographs of the nose of cavities past cavitators with variable drag.

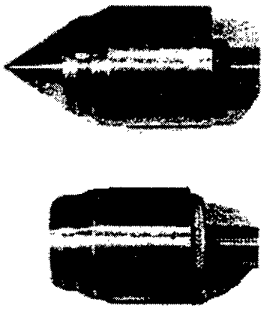


Fig. 6. Photographs of the cavitator with variable drag at two extreme positions of the central element relatively to the body.

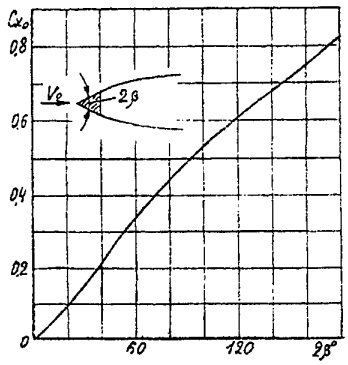
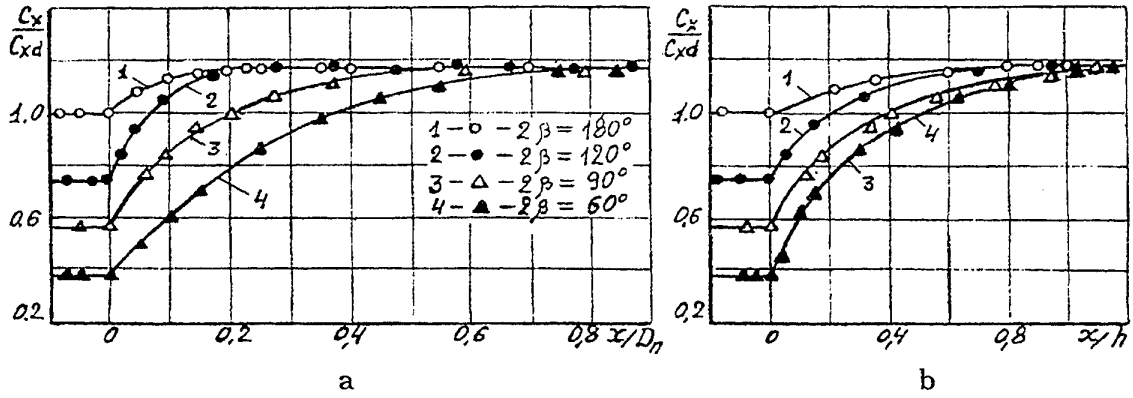


Fig. 7. Dependence of the drag coefficient of cones on the cone angle at the zero cavitation number [2].



a b

Fig. 8. Dependenence of the cavitator drag coefficient on the working stroke value.

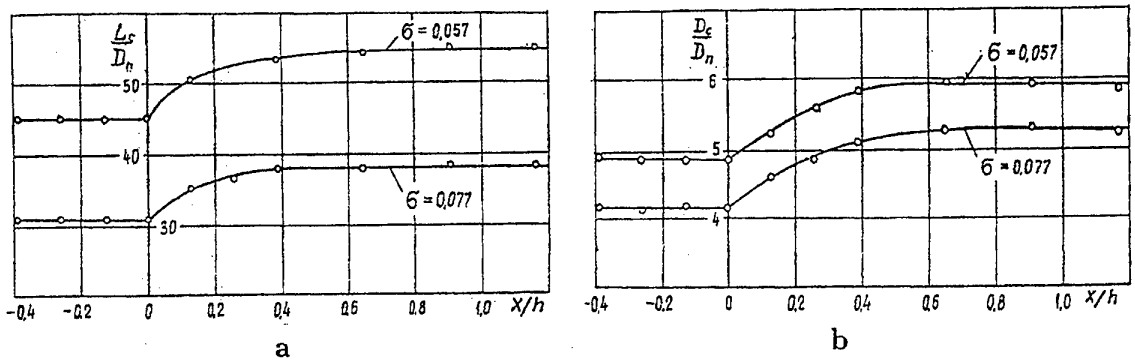


Fig. 9. Dependence of the cavity length and diameter on the cavitator working stroke at constant cavitation number.

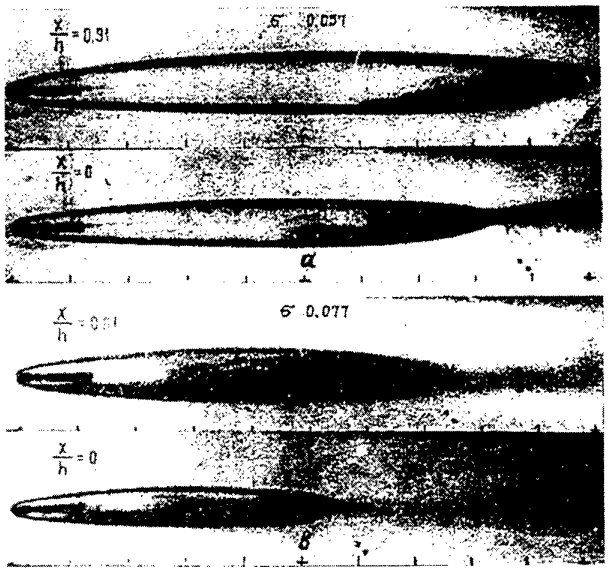


Fig. 10. Photographs of the cavities past the cavitator with variable drag at constant cavitation number and various value of the cavitator working stroke.

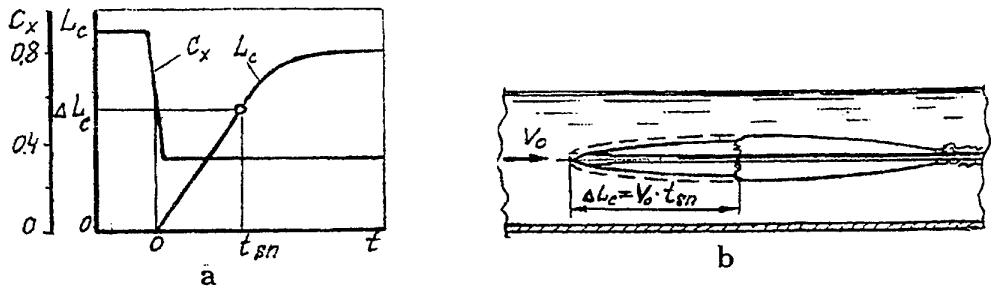


Fig. 11. Scheme of determination of the speed of changing the cavity shape.



Fig. 12. Deformations of unsteady cavity without its discontinuity at abrupt reduction of the cavitator drag.

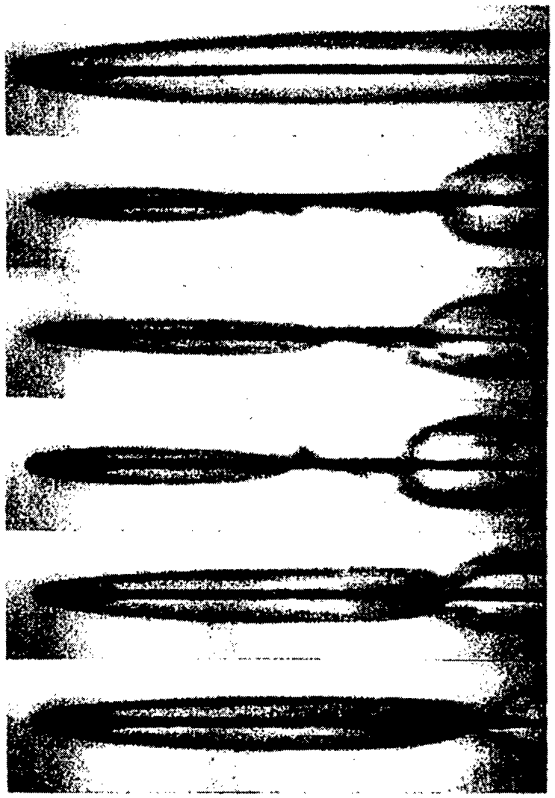


Fig. 13. Discontinuity of unsteady cavity at abrupt reduction of the cavitator drag.

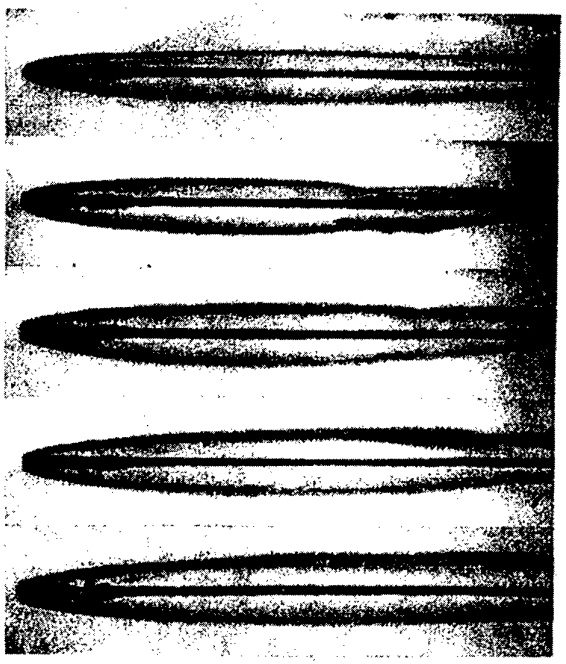
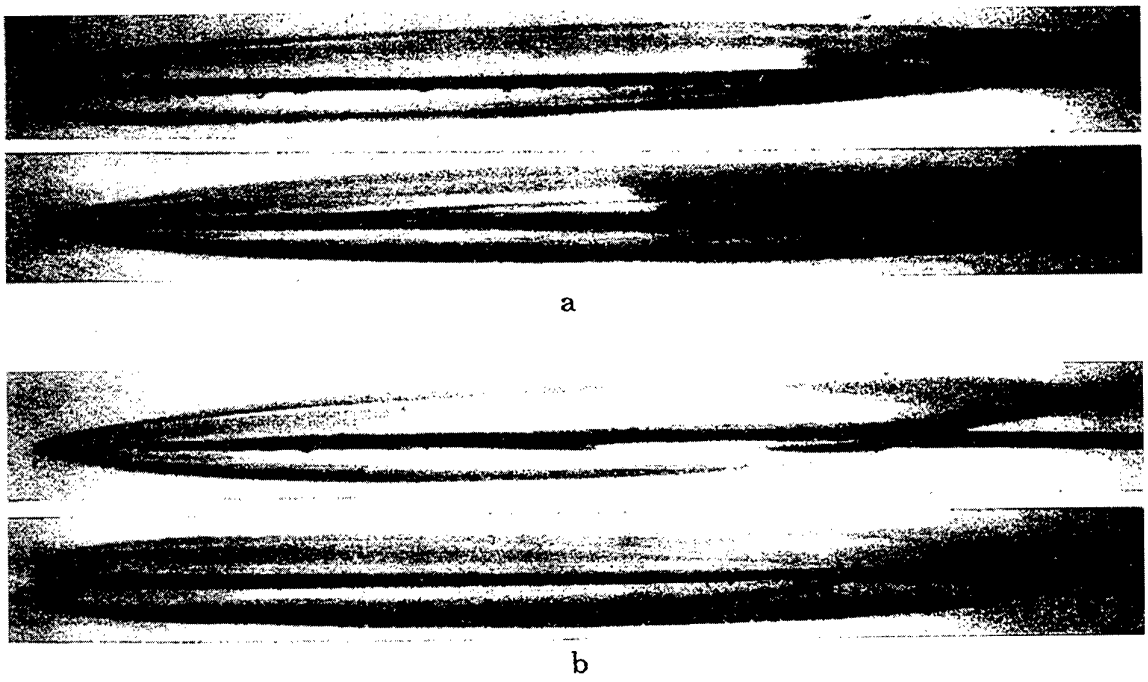


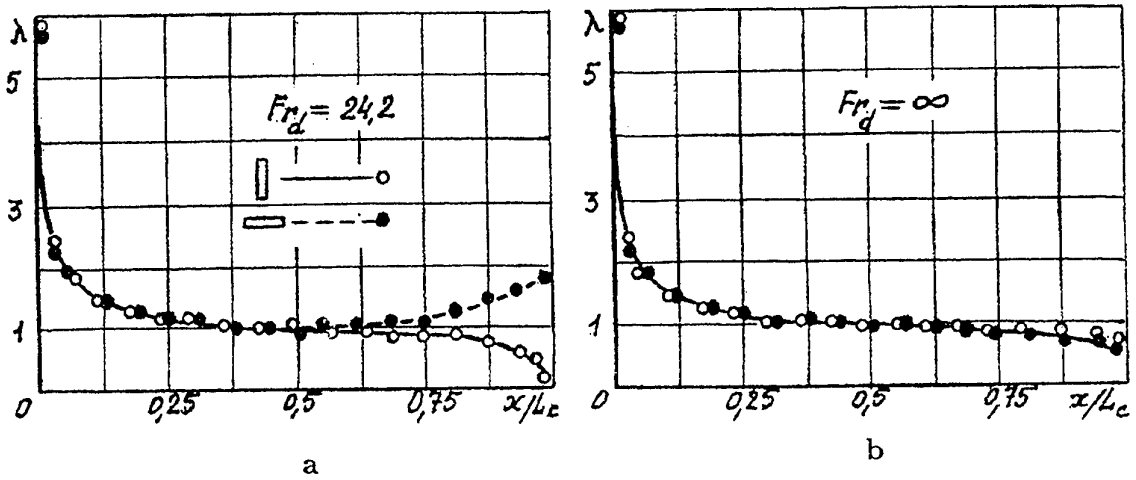
Fig. 14. Unsteady cavity deformations at abrupt increase of the cavitator drag.



a

b

Fig. 15. Photographs of cavities past the rectangular cavitator with side ratio 1 : 6 at $\sigma = 0,0364, Fr_d = 24,2$ and various orientation of cavitator in the stream.



a b

Fig. 16. Changing the section aspect ratio along the length of cavity past a rectangular cavitator with side ratio 1 : 6.

HIGH SPEED BODY MOTION AND SOUND GENERATION

Victor T. GRINCHENKO

Institute of Hydromechanics National Academy of Sciences
8/4 Zhelyabov Str., 252057 Kyiv, Ukraine

SUMMARY

The accurate prediction of the sound field generated by moving in water bodies is important to control sources and reduce noise. Measurement and processing of hydrodynamic noise can give important information about structure of flow around body. One important feature of high speed flows around bodies is the presence of cavitation. An accurate simulation of the flow field past cavitation body is the first requisite in the computation of the radiated noise. The available models of flows that describe the cavitation flows do not give adequate picture of the flow in all domain. So the data on noise in cavitation flows are based on experimental measurement. Some such experiments are discussed in the article. The estimation of acoustic efficiency of different kinds of flows is presented. Analysis of experimental data provides estimation of Struchal numbers in flows with different cavitation number.

I. INTRODUCTION

The sound field is one of a number of disturbances arising from a moving in fluid body. This specific disturbance can be detected at a great distance. Although only very small part of kinetic energy of the moving body transforms to sound the study of characteristics of the sound is practically important. The problem of sound radiation by moving body in a fluid has received attention for a long time [1]. The general case of motion in ideal compressible fluid of both rigid and compliant bodies has a simple integral description by the Kirchhoff's formula [2]. But some important features of the fluid-body interaction can not be considered in the scope of ideal fluid models.

We consider the problem of sound radiation by a body moving at a high speed. Taking into account the acoustical aspect of the problem it is not possible to determine uniquely specific feature of high speed body motion. The structure of the flow past body is strictly dependent on form of the body. The main interest in the article is concentraded on sharp-edged bluff bodies. For such kind of bodies one can say that high velocity motion in water is certain to create the cavity in the wake of the bodies. It is a flow with free boundaries [3].

Cavitating flow has been studied quite extensively in the past in the Institute of Hydromechanics of the National Academy of Sciences of Ukraine [3, 4]. Now the interest to the problem has quickened in connection with possibility to achieve the body velocity close sound speed in water in so-called supercavitation regime [5]. Hydrodynamic characteristics of body moving in cavitation regime are estimated, as a rule, in scope of the model of ideal incompressible fluid. Taking into account the compessibility of fluid results only in insignificant effect on geometrical and force characteristics of flow up to Max number of $M = 0.7$[5].

It is essential to notice that all approaches to model description of cavitation flows are founded on a very crude model of flow in closure region of cavity. The structure of the flow in this small domain can be unimportant with respect to integral force characteristics but be very important with respect to sound generation process. Up to now no clear-cut physical model of the flow in this domain exists. This does not allow to develop a mathematical model to calculate characteristics of sound and efficiency of radiation. Because of this a knowledge about sound radiation in cavitation flow is based on qualitative description of the flow in closure region and on experimental data.

II. SOUND GENERATION BY RIGID BODY

Preparatory to consider some data for sound generation in cavitation flows we will first discuss the views of the process in flow without cavitation. The prediction of flow-induced noise is based on the Lighthill's acoustic analogy [6] and extension of that on rigid body motion case by Curle [7]. A general analysis of this problem, starting from first principles, is hardly possible, and in this phase of the study we must rely on experimental data relating the interaction forces to parameters describing the flow field and the body. The first data of the direct numerical estimation of noise using acoustic analogy [8] are also very important.

The structure of the flows past rigid bodies is mostly determined by the Reynolds number $R = \frac{VD}{\nu}$, where D, V, and ν denote the freestream velocity,

Paper presented at an AGARD FDP Workshop on "High Speed Body Motion in Water", held in Kiev, Ukraine, 1-3 September 1997, and published in R-827.

characteristic dimension of the body, and kinematic viscosity of the fluid.

For sufficiently small Reynolds numbers, as in many problems of sound radiation in hydroacoustics, the sound radiation is the most important mechanism of vibration damping. The viscous drag is small and proportional to relative velocity. As the relative speed increases the other mechanisms of dissipation become important.

For Reynolds numbers within the boundaries ($300 < R < 10^4$) strong periodic components of the fluid motion in the wake can be seen. For example, in the wake behind a cylinder a set of vortices is shad off the cylinder surface forming the Karman vortex street. The formation of vortex set produces a periodic oscillatory transverce momentum component of the fluid motion in the vicinity of the cylinder. As a result a sound field is produced equivalent to that of an oscillatory volume force acting on the fluid.

The radiated sound spectrum has a peak at frequency f given by

$$f = \frac{StV}{D} \tag{1}$$

where D is diameter of cylinder and St is Strouchal number. Experimentally, the Strouchal number is approximately constant ($St \simeq 0.2$) over the mentioned range of Reynolds numbers.

The magnitude of the transverce force per unit length of the cylinder can be estimated by

$$F_1 = \beta \frac{\rho V^2}{2} D \tag{2}$$

where β is an empirical coefficient and ρ is density of the fluid. As a mean value of this coefficient one can use $\beta \simeq 1$. The characteristic wavelength of radiated sound for frequency in (1) is

$$\lambda \simeq 5D\frac{c}{V} \tag{3}$$

where c is sound velocity in the fluid. It may be concluded that even for $M \approx 1$ the diameter is small with regard to wavelength. The correlation length of the vortices Δ is typically three or four times the diameter and can be considered as a value small relative to wavelength. Thus for $M < 1$ the sound radiated by length Δ of the cylinder is the same as that produced by point force

$$F_i = \beta \frac{\rho V^2}{2} D\Delta \exp^{-i2\pi ft} \tag{4}$$

The corresponding sound field is the sound field of a moving dipole and is given in [10]. For relatively small Mach number emitted power is

$$W_a \simeq \frac{\pi}{12} St^2 \beta^2 \frac{\rho V^3}{2} \Delta^2 M^3 \tag{5}$$

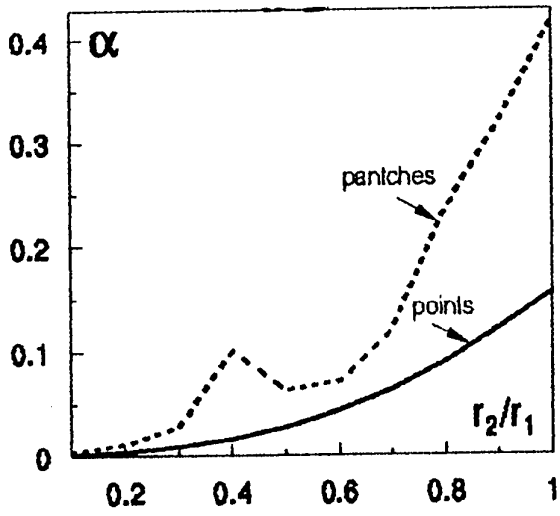


Figure 1:

It is natural to compare this acoustic power with the total flow-energy loss from drag force on the cylinder. Taking into account some empirical relation one can get

$$W_d \simeq 1.3 \frac{\rho V^3}{2} D\Delta \tag{6}$$

The coefficient of acoustic efficiency of the system η can be determined as

$$\eta = \frac{W_a}{W_d} \simeq 0.01 M^3 \frac{\Delta}{D} \tag{7}$$

It may be concluded that the source under consideration is not efficient.

The sound field that we have just discussed corresponds only to the fluid motion near the cylinder boundary. Some acoustic radiation will be a result of interaction of coherent structures in wake of the cylinder. The estimation of efficiency of such type of sources can be obtained from numerical data for a set of vortices. The coefficient of acoustic efficiency can be given in the form $\eta_{ad} = \alpha M^5$. The value of the coefficient α as the function of ratio of vorticity is shown in Fig. 1. The solid line corresponds to set of two point vortexes. Taking into account finite dimension of vortex kernel can produce some increase of radiated sound (dashed line). The flow in the wake of the cylinder has a more complicated structure. But some times interaction of a set of sources does not produce more intensive sound. One can see that interaction of coherent structures does not produce intensive sound. In the case under consideration the dipole sources are more important. Such conclusion is in good agreement with the results of direct numerical implementation of the Lighthill's analogy equation [11].

Both presented estimations contain Mach number as more important characteristic of the flows. That

estimations are correct only under the condition that Mach number is small. It is not essential restriction for many practical problems because the discussed results are applicable up to $M \simeq 0.3$. When M increases the structure of the flow can change sufficiently . Cavitating flow around body can define specific structure of wake and formation of new sources of sound.

III. SCHEMES OF CAVITATION FLOWS

We have just considered the estimation of sound radiation by separate flow past cylinder. For many other bodies the picture of the flow will be the same in a qualitative sence. When velocity of the flow increases its structure can differ substantially from those considered earlier. In the flow past bodies the cavitation nucleus can originate.The cavitation number

$$\sigma = \frac{2(p_\infty - p_c)}{\rho V_\infty} \qquad (8)$$

is an important parameter to characterize the flow.

In general several stages of cavitation flows are distinguished. After the bubble and cavitation vortex form, the stationary cavity related with body is generated as the cavity number decreases. The bubble cavitation has been, for several decades, a subject of considerable interest of both hydrodynamics and acoustics. Even though the study of dynamics of a single bubble isolated in a liquid is a difficult problem [14]. Many important quantitative characteristics of cavitation motion, including acoustical ones, have been found experimentally. Here we will discuss only some acoustical data for moving body with stable cavity.

Many hydrodynamic aspects of flows with stable cavity can be understood and described quantitatively in scope of the model of ideal incompressible fluid. To study the acoustical phenomena in hydrodynamic flow it is necessary to know the source function in wave equation [9]. Existing models of cavitation flows do not give an appropriate basis for development of corresponding acoustical model. There are three schemes of closure of the cavitating motion [11]. The schemes are shown in Fig. 2. One can see there three different approaches to solution of the problem of cavity closure. The structure of flows according to these schemes in closure region is completely different. The hydrodynamic problem is solved in the scope of the hypothesis that disturbances near the ends of the cavities do not affect the flow structure near leading edges. The assumption is natural in scope of the ideal incompressible fluid model but it does not give a foundation to develop a sound field estimation algorithm.

The influence of compressibility on characteristics of cavitating motion is very small as far as $M \simeq 1$

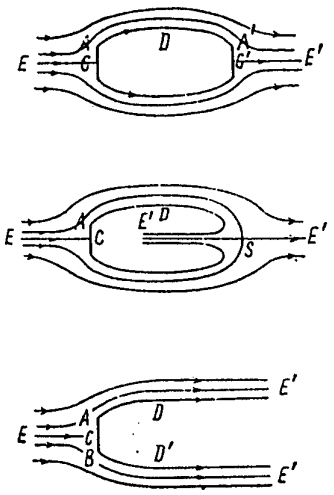


Figure 2:

[5]. At the same time the compressibility effects are the determining factor with respect to acoustical aspects of the cavitation motion. The fact that the compressibility properties have slight influence on hydrodynamic characteristics of cavitating motion gives a ground for important qualitative conclusion. One can say that cavitation motion also forms very weak mechanism for transformation of energy of the flow into energy of sound waves. And yet if the noticeable discrepancies in 3-4% between compressible and incompressible solutions [5] were related with sound production the source would be much more effective than the cylinder in separated flow.

IV. ANALYSIS OF EXPERIMENTAL DATA

At the very beginning of the development of cavity in flow past body one can not see a great change in acoustical properties of the flow. The support for such conclusion gives the analysis of the experimental data [15]. The authors present the experimental result for the cavitation number σ in the range from 5 to 15. The cross flow past equilateral triangle prisms was studied. Measurement of pressure pulsation in wake gives the functions $St = f(\sigma)$. The functions for different positions of prism with respect to filling flow direction are presented in Fig. 3. One can see that Strouchal number is practically identical to that for cylinder in section I. It is reasonable to suppose that action of the bodies on the flow will be similar to concentrated oscillating force. The typical [15] power spectrum of pressure fluctuation for $\sigma = 8.58$ is shown in Fig. 4. The dominant frequency of the radiation is close to $50Hz, \lambda = 30m$ so the source region can be considered as compact. The authors [15]

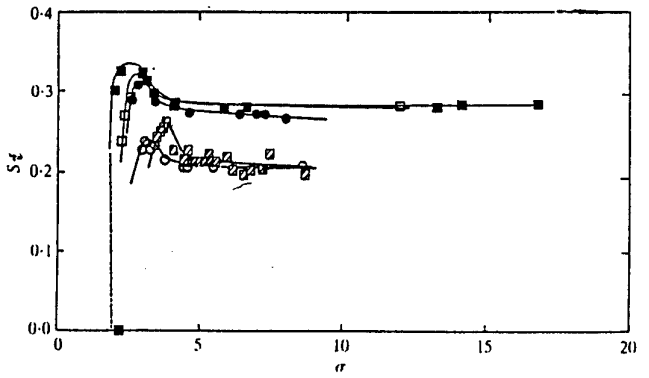


Figure 3:

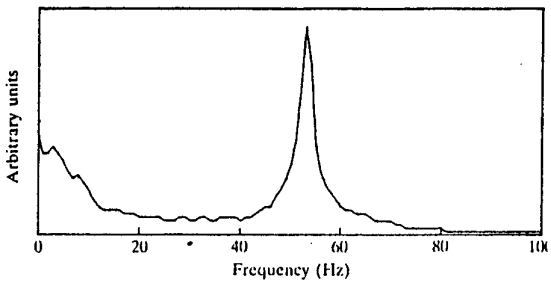


Figure 4:

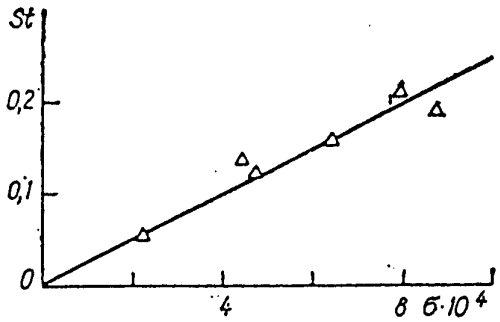


Figure 5:

noticed that at very low cavitation number the spectra do not indicate a clear dominant frequency. In light of concrete experimental data the question calls for further investigation. From the data [15] it is clear that region with $\sigma < 5$ is interesting for discussion.

The early observations of the cavitation phenomena have been performed for many decades ago. A review of the first facts was given by Epshtain L.A. [12]. He also performed first experimental observations of acoustical phenomena in cavitation flows in region of relatively small cavitation numbers. The first things to note in the cases of ship screw cavitation are that strong vibrations are arising. One can say that some effective mechanisms of transformation of flow energy into sound and vibration energy are created.

The experimental investigation [12] of sound radiation by cavitation was carried out in cavitation water tunnel. The circular cylinder of diameter $D = 10mm$ formed the basic test body. The characteristics of sound were measured in air at the distance of $0.2m$ from the test section. The initial data and some results of measurements are presented in Table 1. The table contains data for several important parameters of the experiments. One can see there data for velocity and pressure of the approaching flow. It is interesting to consider the acoustical characteristics. The Strouchal number is calculated with respect to diameter of cylinder.

First of all one can notice the irregular dependence of main frequency of sound on cavitation number. So high level of radiated sound without any doubt shows that cavitation creates new type of sound source. The character of the radiation shows existence of some resonance phenomena. So sharp dependence of eigenfrequency of the fundamental mode on cavitation number does not have any explanation. Importance of resonance effects in the sound radiation by the single vortex was noted in [13]. Here the resonance frequencies of the cavity were identified in the experimental noise spectra. The author notes very strong dependence of the main radiating frequency on cavitation number. He explains the dependence as a result of effective excitation of different modes. One can say that a source of monopole type was created in flow and that produced sound was a result of forced oscillation of the cavity. The type of radiating mode can be strongly dependent on disturbances in coming flow.

The important characteristic of periodical structure of the flows is the Strouchal number. For the supercavitation motions the number strongly dependends on cavitation number. The corresponding experimental data are presented in Fig. 5. Here the triangles show the experimental measurements. The last can be rather accurately approximated by the linear function $St = 120\sigma$.

The mechanism of initiation of the forced oscillation may be connected with dynamical behavior of the cavities in flow. Despite lack of adequate models of the flow in closure region the experimental observation clearly shows an existence of a periodical process in change of cavity volume. Figures 6 and 7 display the character of flow in closure region of cavities for two different types of motion. The periodic character of the wake structure is obvious.

The presented pictures show that new important source of sound is in the wakes of cavitating motion. It is the sequence of bubbles. The single bubble is a

very effective source of sound. The collapse of single bubbles produces strong sound [13] with efficiency coefficient $\eta \approx 0.3$. But experimental data for bubble cavitation show that the value of this coefficient is only $\eta \approx 3.10^{-3}$. Thus the difference is $20dB$. The physical reason is that interaction in bubble ensemble is a governing factor.

The bubble cavitation is also characterized by specific spectra of the radiated sound [13]. The spectra does not contain any strong separated frequencies. So there is no basis to consider the experimental data in table 1 as a result of bubble cavitation. The existence of some strong periodic regimes in cavity oscillation is predicted in scope of theory of auto-oscillation [16]. The author considered different kinds of cavities. It is interesting that existing strong periodic regimes are typical for natural vapor cavity.

To this point the cavity near moving body has been considered as a source of sound. It is interesting to consider the cavity near body as the element of a mechanism to control sound radiation. In Fig. 8 a test equipment is presented. At the top of part 1 a hydrophone is situated. In region 4 there is a sound radiator. The signals from hydrophone were considered for two cases. First the equipment was put in flow without cavity. The flow velocity was small to produce natural cavity. In the latter case the artificial cavity 2 was created near the head part of equipment. In both cases the same value of electric voltage was used as an exciting force of the sound radiator in region 4.

The results of sound measurement are given in Fig. 8. The line crossing square points corresponds to the first case. The crosses identified the line corresponding to the second one. It is naturally that the presence of cavity sufficiently change the conditions of work for hydrofone. The nearby sources of sound are working similar to acoustically soft surface. One can see that cavity plays a role of such surface in very wide frequency band. This result may be interesting with respect to mentioned difference in the radiation efficiency of single bubble and ensemble of bubbles. In Fig. 8 we can see the same difference in 20 dB between sound levels of source.

CONCLUSION

The problem of estimation of acoustical properties of cavitating flow is very complicated. The lack of any complete schemes of flow past stable cavity does not give a way for analytical and numerical description of the acoustical problem. Experimental data give the basis to consider the stable cavity as a monopole type source of sound. Such sources are more effective than sources in flows without cavity. The cavity near body can be used to control characteristics of hydrophons placed at cavitation body.

REFERENCES

1. Blochincev, D.I., "Acoustics of inhomogeneous moving medium", Moskow, Nauka, 1981, 206 p.
2. Farassat F. and Myers M. K.,"Extension of Kirchhoff's formula to radiation from moving sources", Journal Sound and Vibration, 1988, **133**(3), pp. 451-460
3. Logvinovich, G.V., "Hydrodynamics of Flows with Free Boundaries", Kiev, Naukova Dumka, 1969, 208 p. (In Russian)
4. Savchenko,Y.N., "Hydrodynamics of separated flows", Applied Hydromechanics, Naukova Dumka, Kiev,1989, pp. 161-191. (in Russian)
5. Savchenko,Y.N., Semenenko,V.N., Serebryakov,V.V. "Experimental Research into Supercavitating Flows at Subsonic Speeds", Doklady AN Ukrainy, No 2,1993,pp.64-69. (In Russian)
6. Lighthill M. J., "On sound generated aerodynamically: I. General Theory", Proceedings of the Royal Society of London, Ser.A, Vol. 211, No. 1107, 1952, pp. 564-587.
7. Curle N., The influence of solid boundaries upon aerodynamic sound. Proc. Royal Soc.of London,Ser.A, Vol.231, No 1187, pp. 1788-1796.
8. Wang M., Lele S. K., and Moin P., Computation of quadrupole noise using acoustical analogy. AIAA Journal, vol.34, No 11, 1996, pp. 2247-2254.
9. Dowling A. P., Ffowcs Williams J. F. Sound and sources of sound,Ellis Horwood Limited, 1983, p. 321
10. Morse, F.M. and Ingard, K.U."Theoretical acoustics". McGraw-Hill, 1968, 927 p.
11. Gurevich, M.I.,"Theory of Jets in Ideal Fluid", Moskow, Nauka, 1979,
12. Epschtain,L.A.,"Origin and Development of Cavitation",TSAGI,Moskow,1959, pp. 41-118. (In Russian)
13. Levkovsky Yu.L., Structure of cavitating flows, Sudostroenie, 1978, 222 p.
14. Dassie G. and Reali M., Dynamics of oscillating spherical gas/vapor bubble. Journal Ac. Soc. Am.,**100**,5, 1996, pp.3088-3097.
15. Balachandar R. and Ramamurthy A.S., Wake and cavitation characteristics of equilateral prisms at incidence. Journal of fluid and structure, 1992, **6**, 6, pp. 671-680.
16. Semenenko,V.N.,"Computer modeling of pulsations of blowed supercavities", Hydromechanics, 1997, Issue 71, Kiev, pp. 110-118.(In Russian)

Table 1: Experimental measurement of sound produced by cavitation flow past rigid cylinder

$p_\infty[kg/cm^2]$	$v_\infty[m/\sec]$	$L[dB]$	$f[Hz]$	σ	St	P
3,31	11,7	69	650	4,80	0,555	0,048
3,24	12,3	77,5	400	4,30	0,325	0,130
3,16	12,9	94	950	3,80	0,736	0,90
3,13	13,18	90	700	3,60	0,530	0,56
3,08	13,6	86	680	3,35	0,500	0,38
3,02	14,0	73	788	3,10	0,563	0,084
3,02	14,0	73	760	3,10	0,542	0,084
3,08	13,6	85	680	3,35	0,500	0,325
3,13	13,18	92	700	3,60	0,530	0,72
3,16	12,9	96	950	3,80	0,736	1,16
3,24	12,3	78	380	4,30	0,309	0,136
3,31	11,7	61	620	4,80	0,530	0,035

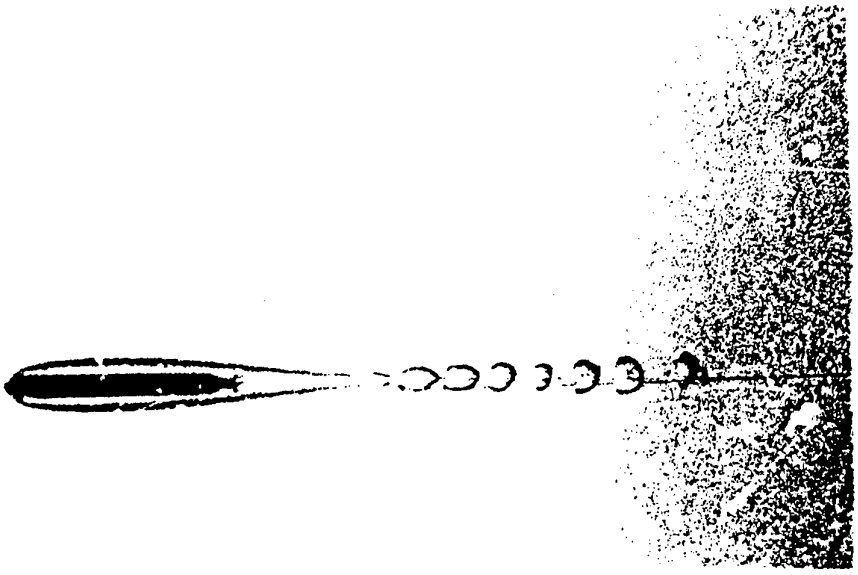


Figure 6: Structure of cavitation flow after air-water boundary penetration

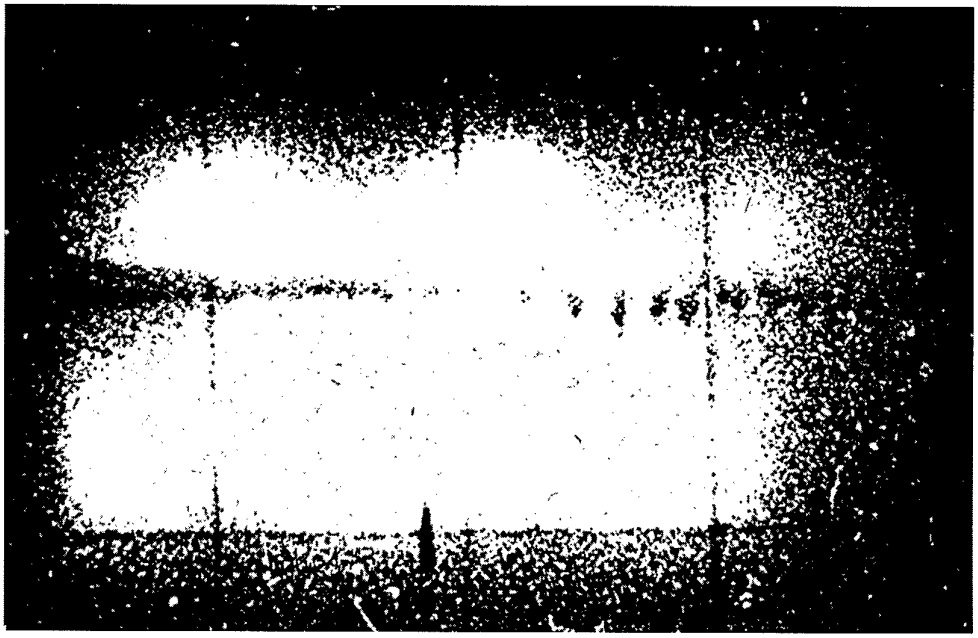
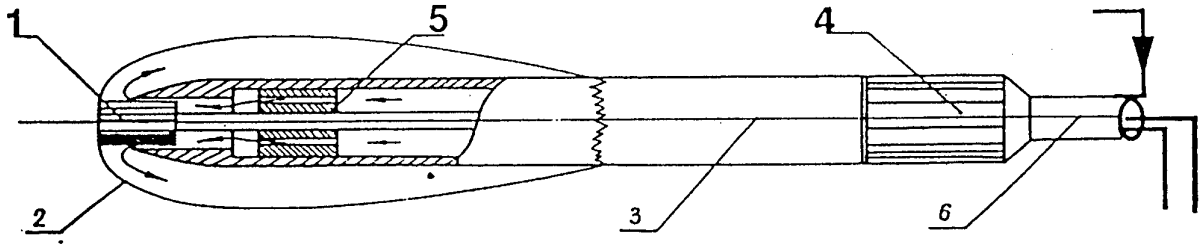
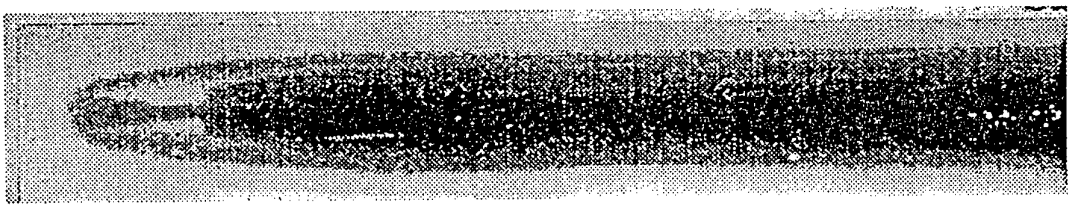


Figure 7: Structure of supercavitation flow in closure region $M = 0.5$





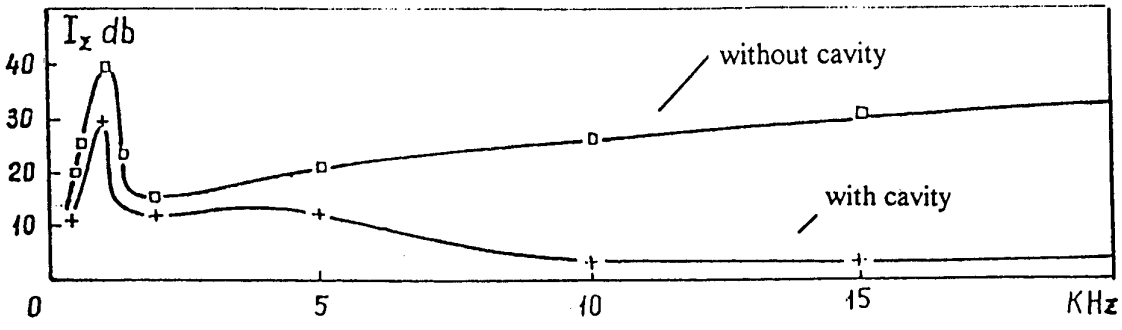


Figure 8: Control of sound radiation by a cavity near a hydrophone

ABSTRACT:

SUPERCAVITATING PROJECTILE EXPERIMENTS AT SUPERSONIC SPEEDS

Ivan, N. KIRSCHNER
Naval Undersea Warfare Center Division
Launcher and Missile Systems Department
Newport, Rhode Island 02841 U.S.A.

Selected results of research and development in the topic area of supercavitating high-speed bodies were presented. A United States underwater speed record was set on 17 July 1997 with successful launch of a supercavitating projectile from a fully-submerged gun. The projectile followed a stable trajectory along most of a 17-m test range before impacting the safety containment. The gun launcher employed a conventional powder propellant, but was fitted with a special waterproof breech and a special sealing system. The bow shocks of other projectiles launched at supersonic speeds are clearly visible in high-speed film images captured during the test series(see Figure 1. Figure 2 presents a composite image of a projectile traveling at approximately 1220 mls).

This effort was sponsored by the Office of Naval Research, the Defense Advanced Research Projects Agency, and the Naval Undersea Warfare Center (NUWC) Division Newport under a program that has evolved since the 1980s. Under this program, the theory of high-Mach-number underwater flows has been investigated since 1994. Ongoing research involves the interaction between shockwaves and the cavity, along with firs-principles modeling of projectile dynamics and stability.

The NUWC Division Newport Supercavitating High-Speed Bodies Test Range has been designed for safely testing projectiles traveling at over 1 km/s. The launch depth is approximately 4m. The main challenges for such experimentation are launcher alignment and triggering of various instrumentation.

The research and development team led by NUWC Division Newport included the participation of General Dynamics Armament Systems (the designer and fabricator of the underwater launcher), the Army Research Laboratory, Cornell University, Tracor Systems Engineering, and other organizations.

Future development might include tests at faster speeds over longer ranges. A more comprehensive physics modeling capability is also being developed.

Paper presented at an AGARD FDP Workshop on "High Speed Body Motion in Water", held in Kiev, Ukraine, 1-3 September 1997, and published in R-827.

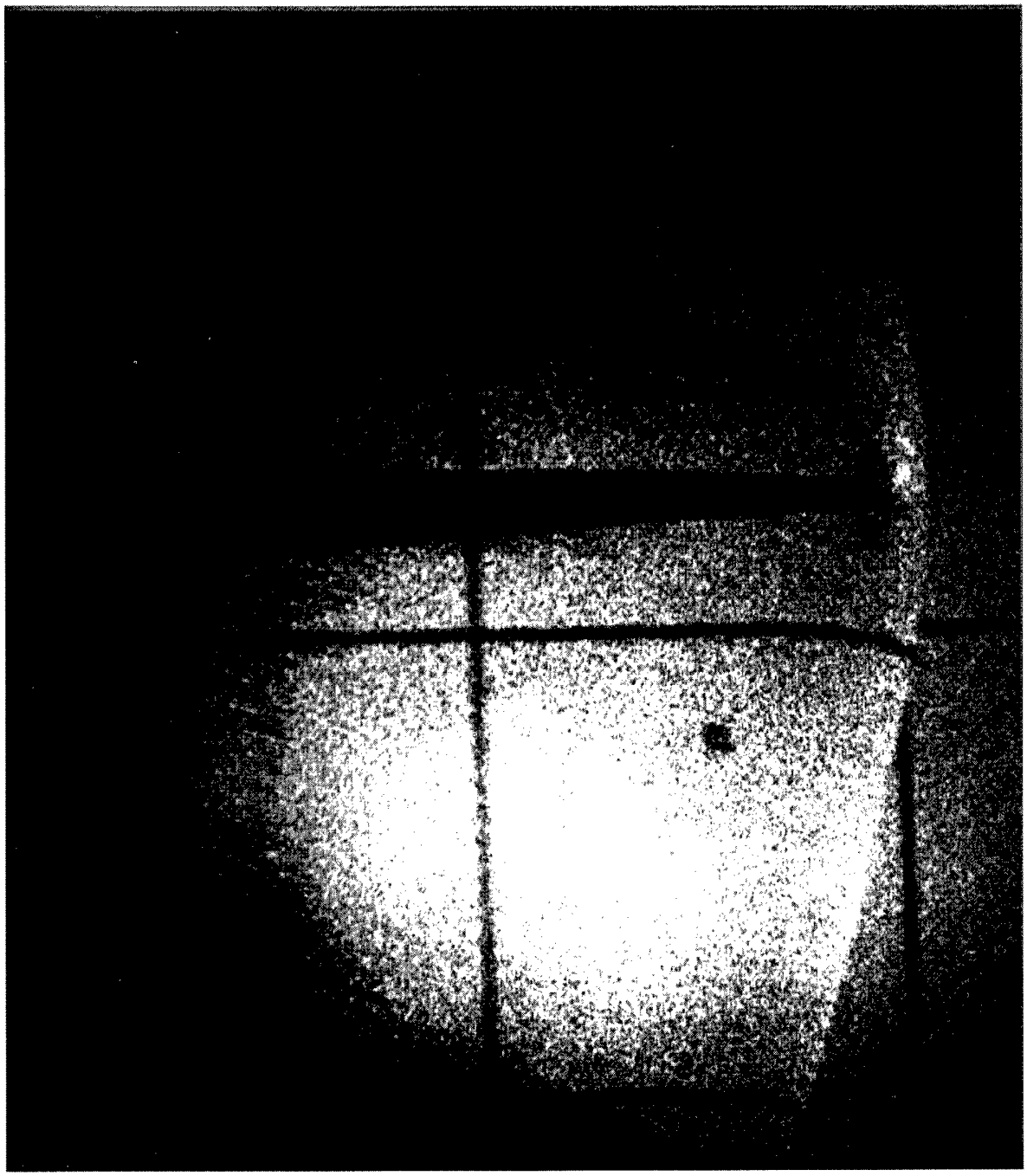


Figure 1
Back-Lit image of a projectile launched
at supersonic speeds underwater

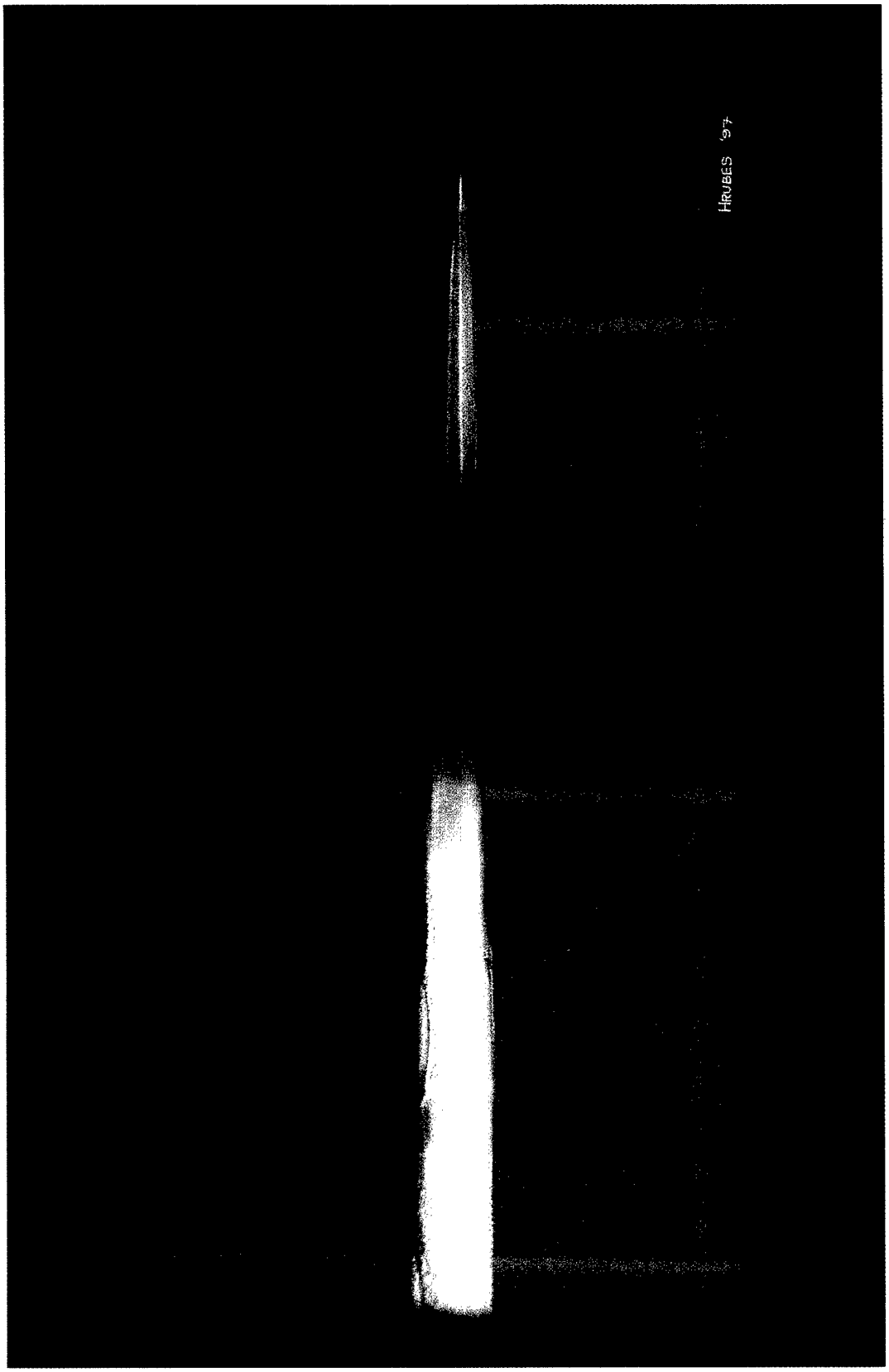


Figure 2
Composite image of a projectile
traveling at approximately 1220 mls

REPORT DOCUMENTATION PAGE

1. Recipient's Reference	2. Originator's Reference	3. Further Reference	4. Security Classification of Document
	AGARD-R-827	ISBN 92-836-1071-7	UNCLASSIFIED/ UNLIMITED

5. Originator Advisory Group for Aerospace Research and Development
North Atlantic Treaty Organization
7 rue Ancelle, 92200 Neuilly-sur-Seine, France

6. Title
High Speed Body Motion in Water

7. Presented at/sponsored by
This report is a compilation of the proceedings of a Fluid Dynamics Panel Workshop held at the National Academy of Sciences in Kiev, Ukraine, 1-3 September 1997.

8. Author(s)/Editor(s)	9. Date
Multiple	February 1998
10. Author's/Editor's Address	**11. Pages**
Multiple	352

12. Distribution Statement There are no restrictions on the distribution of this document. Information about the availability of this and other AGARD unclassified publications is given on the back cover.

13. Keywords/Descriptors

Hydrodynamics
Hydromechanics
Boundary layer flow
Cavitation
Swimming
Bionics
Drag
Reduction
Propulsion
Efficiency
Hydrofoils
Turbulent boundary layer
Water flow
Vortices
Shear flow
Transition flow
Boundary layer control
Computerized simulation

14. Abstract

This report is a compilation of the edited proceedings of a Workshop on "High Speed Body Motion in Water" held at the National Academy of Sciences in Kiev, Ukraine, 1-3 September 1997. Technical Topics covered during the workshop included Hydrobionics, Boundary Layer Flows, Supercavitating Flows, Air-water Penetration and Control of Cavitation.

The material assembled in this report was prepared under the combined sponsorship of the NATO Partnership for Peace Program, the AGARD Fluid Dynamics Panel, the Institute of Hydromechanics in Kiev, and the United States Air Force European Office of Aerospace Research and Development.

AGARD

NATO OTAN

7 RUE ANCELLE • 92200 NEUILLY-SUR-SEINE

FRANCE

Télécopie 0(1)55.61.22.99 • Télex 610 176

DIFFUSION DES PUBLICATIONS

AGARD NON CLASSIFIEES

L'AGARD détient un stock limité de certaines de ses publications récentes. Celles-ci pourront éventuellement être obtenus sous forme de copie papier. Pour de plus amples renseignements concernant l'achat de ces ouvrages, adressez-vous à l'AGARD par lettre ou par télécopie à l'adresse indiquée ci-dessus. *Veuillez ne pas téléphoner.*

Des exemplaires supplémentaires peuvent parfois être obtenus auprès des centres de diffusion nationaux indiqués ci-dessous. Si vous souhaitez recevoir toutes les publications de l'AGARD, ou simplement celles qui concernent certains Panels, vous pouvez demander d'être inclus sur la liste d'envoi de l'un de ces centres.

Les publications de l'AGARD sont en vente auprès des agences de vente indiquées ci-dessous, sous forme de photocopie ou de microfiche. Certains originaux peuvent également être obtenus auprès de CASI.

CENTRES DE DIFFUSION NATIONAUX

ALLEMAGNE
Fachinformationszentrum Karlsruhe
D-76344 Eggenstein-Leopoldshafen

BELGIQUE
Coordonnateur AGARD - VSL
Etat-major de la Force aérienne
Quartier Reine Elisabeth
Rue d'Evere, B-1140 Bruxelles

CANADA
Directeur - Gestion de l'information
(Recherche et développement) - DRDGI 3
Ministère de la Défense nationale
Ottawa, Ontario K1A 0K2

DANEMARK
Danish Defence Research Establishment
Ryvangs Allé 1
P.O. Box 2715
DK-2100 Copenhagen Ø

ESPAGNE
INTA (AGARD Publications)
Carretera de Torrejón a Ajalvir, Pk.4
28850 Torrejón de Ardoz - Madrid

ETATS-UNIS
NASA Center for AeroSpace Information (CASI)
Parkway Center, 7121 Standard Drive
Hanover, MD 21076

FRANCE
O.N.E.R.A. (Direction)
29, Avenue de la Division Leclerc
92322 Châtillon Cedex

GRECE
Hellenic Air Force
Air War College
Scientific and Technical Library
Dekelia Air Force Base
Dekelia, Athens TGA 1010

ISLANDE
Director of Aviation
c/o Flugrad
Reykjavik

ITALIE
Aeronautica Militare
Ufficio Stralcio AGARD
Aeroporto Pratica di Mare
00040 Pomezia (Roma)

LUXEMBOURG
Voir Belgique

NORVEGE
Norwegian Defence Research Establishment
Attn: Biblioteket
P.O. Box 25
N-2007 Kjeller

PAYS-BAS
Netherlands Delegation to AGARD
National Aerospace Laboratory NLR
P.O. Box 90502
1006 BM Amsterdam

PORTUGAL
Estado Maior da Força Aérea
SDFA - Centro de Documentação
Alfragide
P-2720 Amadora

ROYAUME-UNI
Defence Research Information Centre
Kentigern House
65 Brown Street
Glasgow G2 8EX

TURQUIE
Millî Savunma Başkanliği (MSB)
ARGE Dairesi Başkanliği (MSB)
06650 Bakanliklar - Ankara

AGENCES DE VENTE

NASA Center for AeroSpace Information (CASI)
Parkway Center, 7121 Standard Drive
Hanover MD 21076
Etats-Unis

The British Library Document Supply Division
Boston Spa, Wetherby
West Yorkshire LS23 7BQ
Royaume-Uni

Les demandes de microfiches ou de photocopies de documents AGARD (y compris les demandes faites auprès du CASI) doivent comporter la dénomination AGARD, ainsi que le numéro de série d'AGARD (par exemple AGARD-AG-315). Des informations analogues, telles que le titre et la date de publication sont souhaitables. Veuiller noter qu'il y a lieu de spécifier AGARD-R-nnn et AGARD-AR-nnn lors de la commande des rapports AGARD et des rapports consultatifs AGARD respectivement. Des références bibliographiques complètes ainsi que des résumés des publications AGARD figurent dans les journaux suivants:

Scientific and Technical Aerospace Reports (STAR)
STAR peut être consulté en ligne au localisateur de ressources uniformes (URL) suivant:
http://www.sti.nasa.gov/Pubs/star/Star.html
STAR est édité par CASI dans le cadre du programme NASA d'information scientifique et technique (STI)
STI Program Office, MS 157A
NASA Langley Research Center
Hampton, Virginia 23681-0001
Etats-Unis

Government Reports Announcements & Index (GRA&I)
publié par le National Technical Information Service
Springfield
Virginia 2216
Etats-Unis
(accessible également en mode interactif dans la base de données bibliographiques en ligne du NTIS, et sur CD-ROM)

Imprimé par le Groupe Communication Canada Inc.
(membre de la Corporation St-Joseph)
45, boul. Sacré-Cœur, Hull (Québec), Canada K1A 0S7

AGARD

NATO OTAN

7 RUE ANCELLE • 92200 NEUILLY-SUR-SEINE

FRANCE

Telefax 0(1)55.61.22.99 • Telex 610 176

DISTRIBUTION OF UNCLASSIFIED

AGARD PUBLICATIONS

AGARD holds limited quantities of some of its recent publications, and these may be available for purchase in hard copy form. For more information, write or send a telefax to the address given above. *Please do not telephone.*

Further copies are sometimes available from the National Distribution Centres listed below. If you wish to receive all AGARD publications, or just those relating to one or more specific AGARD Panels, they may be willing to include you (or your organisation) in their distribution.

AGARD publications may be purchased from the Sales Agencies listed below, in photocopy or microfiche form. Original copies of some publications may be available from CASI.

NATIONAL DISTRIBUTION CENTRES

BELGIUM
Coordonnateur AGARD - VSL
Etat-major de la Force aérienne
Quartier Reine Elisabeth
Rue d'Evere, B-1140 Bruxelles

CANADA
Director Research & Development
Information Management - DRDIM 3
Dept of National Defence
Ottawa, Ontario K1A 0K2

DENMARK
Danish Defence Research Establishment
Ryvangs Allé 1
P.O. Box 2715
DK-2100 Copenhagen Ø

FRANCE
O.N.E.R.A. (Direction)
29 Avenue de la Division Leclerc
92322 Châtillon Cedex

GERMANY
Fachinformationszentrum Karlsruhe
D-76344 Eggenstein-Leopoldshafen

GREECE
Hellenic Air Force
Air War College
Scientific and Technical Library
Dekelia Air Force Base
Dekelia, Athens TGA 1010

ICELAND
Director of Aviation
c/o Flugrad
Reykjavik

ITALY
Aeronautica Militare
Ufficio Stralcio AGARD
Aeroporto Pratica di Mare
00040 Pomezia (Roma)

LUXEMBOURG
See Belgium

NETHERLANDS
Netherlands Delegation to AGARD
National Aerospace Laboratory, NLR
P.O. Box 90502
1006 BM Amsterdam

NORWAY
Norwegian Defence Research Establishment
Attn: Biblioteket
P.O. Box 25
N-2007 Kjeller

PORTUGAL
Estado Maior da Força Aérea
SDFA - Centro de Documentação
Alfragide
P-2720 Amadora

SPAIN
INTA (AGARD Publications)
Carretera de Torrejón a Ajalvir, Pk.4
28850 Torrejón de Ardoz - Madrid

TURKEY
Millî Savunma Başkanliği (MSB)
ARGE Dairesi Başkanliği (MSB)
06650 Bakanliklar - Ankara

UNITED KINGDOM
Defence Research Information Centre
Kentigern House
65 Brown Street
Glasgow G2 8EX

UNITED STATES
NASA Center for AeroSpace Information (CASI)
Parkway Center, 7121 Standard Drive
Hanover, MD 21076

SALES AGENCIES

NASA Center for AeroSpace Information (CASI)
Parkway Center, 7121 Standard Drive
Hanover MD 21076
United States

The British Library Document Supply Centre
Boston Spa, Wetherby
West Yorkshire LS23 7BQ
United Kingdom

Requests for microfiches or photocopies of AGARD documents (including requests to CASI) should include the word 'AGARD' and the AGARD serial number (for example AGARD-AG-315). Collateral information such as title and publication date is desirable. Note that AGARD Reports and Advisory Reports should be specified as AGARD-R-nnn and AGARD-AR-nnn, respectively. Full bibliographical references and abstracts of AGARD publications are given in the following journals:

Scientific and Technical Aerospace Reports (STAR)
STAR is available on-line at the following uniform resource locator:
http://www.sti.nasa.gov/Pubs/star/Star.html
STAR is published by CASI for the NASA Scientific and Technical Information (STI) Program
STI Program Office, MS 157A
NASA Langley Research Center
Hampton, Virginia 23681-0001
United States

Government Reports Announcements & Index (GRA&I)
published by the National Technical Information Service
Springfield
Virginia 22161
United States
(also available online in the NTIS Bibliographic Database or on CD-ROM)



Printed by Canada Communication Group Inc.
(A St. Joseph Corporation Company)
45 Sacré-Cœur Blvd., Hull (Québec), Canada K1A 0S7

ISBN 92-836-1071-7